

DTIC FILE COPY



AD-A223 123

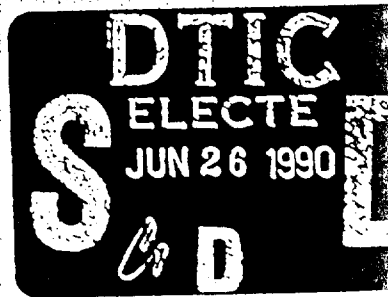
AIR FORCE OFFICE OF
SCIENTIFIC RESEARCH
UNITED STATES AIR FORCE
RESEARCH INITIATION
PROGRAM

CONDUCTED BY
UNIVERSAL ENERGY SYSTEMS
U.E.S.

1988

TECHNICAL REPORT

VOLUME 1 OF 4



RODNEY C. DARRAH
PROGRAM DIRECTOR, UES

SUSAN K. ESPY
PROGRAM ADMINISTRATOR, UES

LT. COL. CLAUDE CAVENDER
PROGRAM MANAGER, AFOSR

DISTRIBUTION STATEMENT A

Approved for public release
Distribution Unlimited

REPORT DOCUMENTATION PAGE

Form Approved
OMB No. 0704-0188

Public reporting burden for this collection of information is estimated to average 1 hour per response, including the time for reviewing instructions, searching existing data sources, gathering and maintaining the data needed, and completing and reviewing the collection of information. Send comments regarding this burden estimate or any other aspect of this collection of information, including suggestions for reducing the burden, to Washington Headquarters Service, Directorate for Information Operations and Reports, 1215 Jefferson Davis Highway, Suite 1204, Arlington, VA 22202-4302, and to the Office of Management and Budget, Paperwork Reduction Project (0704-0188), Washington, DC 20503.

1. AGENCY USE ONLY (Leave blank)		2. REPORT DATE	3. REPORT TYPE AND DATES COVERED	
		1988 Vol. 1 of 4	Technical Report	
4. TITLE AND SUBTITLE			5. FUNDING NUMBERS	
United States Air Force Research Initiation Program			61102F 3484/D5	
6. AUTHOR(S)				
Rodney C. Darrah Lt Col Claude Cavender				
7. PERFORMING ORGANIZATION NAME(S) AND ADDRESS(ES)			8. PERFORMING ORGANIZATION REPORT NUMBER	
Universal Energy Systems			AFOSR-TR 90 0707	
9. SPONSORING / MONITORING AGENCY NAME(S) AND ADDRESS(ES)			10. SPONSORING / MONITORING AGENCY REPORT NUMBER	
AFOSR/XOT Bld 410 Bolling AFB DC 20332-6448			F49620-88-C-0053	
11. SUPPLEMENTARY NOTES				
12a. DISTRIBUTION / AVAILABILITY STATEMENT			12b. DISTRIBUTION CODE	
Unlimited				
13. ABSTRACT (Maximum 400 words)				
See Attached				
14. SUBJECT TERMS			15. NUMBER OF PAGES	
			16. PRICE CODE	
17. SECURITY CLASSIFICATION OF REPORT	18. SECURITY CLASSIFICATION OF THIS PAGE	19. SECURITY CLASSIFICATION OF ABSTRACT	20. LIMITATION OF ABSTRACT	
Unclassified	Unclassified	Unclassified	N/A	

INTRODUCTION

Research Initiation Program - 1988

AFOSR has provided funding for follow-on research efforts for the participants in the Summer Faculty Research Program. Initially this program was conducted by AFOSR and popularly known as the Mini-Grant Program. Since 1983 the program has been conducted by the Summer Faculty Research Program (SFRP) contractor and is now called the Research Initiation Program (RIP). Funding is provided to establish RIP awards to about half the number of participants in the SFRP.

Participants in the 1988 SFRP competed for funding under the 1988 RIP. Participants submitted cost and technical proposals to the contractor by 1 November 1988, following their participation in the 1988 SFRP.

Evaluation of these proposals was made by the contractor. Evaluation criteria consisted of:

1. Technical Excellence of the proposal
2. Continuation of the SFRP effort
3. Cost sharing by the University

The list of proposals selected for award was forwarded to AFOSR for approval of funding. Those approved by AFOSR were funded for research efforts to be completed by 31 December 1989.

The following summarizes the events for the evaluation of proposals and award of funding under the RIP.

- A. Rip proposals were submitted to the contractor by 1 November 1988. The proposals were limited to \$20,000 plus cost sharing by the universities. The universities were encouraged to cost share since this is an effort to establish a long term effort between the Air Force and the university.
- B. Proposals were evaluated on the criteria listed above and the final award approval was given by AFOSR after consultation with the Air Force Laboratories.
- C. Subcontracts were negotiated with the universities. The period of performance of the subcontract was between October 1988 and December 1989.

Copies of the Final Reports are presented in Volumes I through IV of the 1988 Research Initiation Program Report. There were a total of 92 RIP awards made under the 1988 program.

UNITED STATES AIR FORCE
1988 RESEARCH INITIATION PROGRAM

Conducted by
UNIVERSAL ENERGY SYSTEMS, INC.

under
USAF Contract Number F49620-88-C-0053

RESEARCH REPORTS
VOLUME I OF IV

Submitted to
Air Force Office of Scientific Research

Bolling Air Force Base
Washington, DC

By
Universal Energy Systems, Inc.

April 1990



Accession For	
NTIS CPAS	<input checked="" type="checkbox"/>
DTIC TAB	<input type="checkbox"/>
Unannounced	<input type="checkbox"/>
Justification	
By	
Distribution	
Availability	
Dist	
A-1	

TABLE OF CONTENTS

<u>SECTION</u>	<u>PAGE</u>
INTRODUCTION	i
STATISTICS	ii
PARTICIPANT LABORATORY ASSIGNMENT	vii
RESEARCH REPORTS	xvii

INTRODUCTION

Research Initiation Program - 1988

AFOSR has provided funding for follow-on research efforts for the participants in the Summer Faculty Research Program. Initially this program was conducted by AFOSR and popularly known as the Mini-Grant Program. Since 1983 the program has been conducted by the Summer Faculty Research Program (SFRP) contractor and is now called the Research Initiation Program (RIP). Funding is provided to establish RIP awards to about half the number of participants in the SFRP.

Participants in the 1988 SFRP competed for funding under the 1988 RIP. Participants submitted cost and technical proposals to the contractor by 1 November 1988, following their participation in the 1988 SFRP.

Evaluation of these proposals was made by the contractor. Evaluation criteria consisted of:

1. Technical Excellence of the proposal
2. Continuation of the SFRP effort
3. Cost sharing by the University

The list of proposals selected for award was forwarded to AFOSR for approval of funding. Those approved by AFOSR were funded for research efforts to be completed by 31 December 1989.

The following summarizes the events for the evaluation of proposals and award of funding under the RIP.

- A. Rip proposals were submitted to the contractor by 1 November 1988. The proposals were limited to \$20,000 plus cost sharing by the universities. The universities were encouraged to cost share since this is an effort to establish a long term effort between the Air Force and the university.
- B. Proposals were evaluated on the criteria listed above and the final award approval was given by AFOSR after consultation with the Air Force Laboratories.
- C. Subcontracts were negotiated with the universities. The period of performance of the subcontract was between October 1988 and December 1989.

Copies of the Final Reports are presented in Volumes I through IV of the 1988 Research Initiation Program Report. There were a total of 92 RIP awards made under the 1988 program.

STATISTICS

PROGRAM STATISTICS

Total SFRP Participants	153
Total RIP Proposals submitted by SFRP	121
Total RIP Proposals submitted by GSRP	5
Total RIP Proposals submitted	126
Total RIP's funded to SFRP	85
Total RIP's funded to GSRP	3
Total RIP's funded	88
Total RIP's Proposals submitted by HBCU's	8
Total RIP's Proposals funded to HBCU's	4

LABORATORY PARTICIPATION

<u>Laboratory</u>	<u>SFRP Participants</u>	<u>RIP's Submitted</u>	<u>RIP's Funded</u>
AAMRL	10	8 (1 GSRP)	5
AFWAL/APL	8	8	4
ATL	8	9 (1 GSRP)	8 (1 GSRP)
AEDC	5	5 (1 GSRP)	4 (1 GSRP)
AFWAL/AL	8	8	4
ESMC	1	0	0
ESD	2	2	2
ESC	8	7	5
AFWAL/FDL	10	9 (1 GSRP)	6 (1 GSRP)
FJSRL	7	5	4
AFGL	12	7	5
HRL	14	13	9
AFWAL/ML	12	9	6
OEHL	4	3	3
AL	8	7	6
RADC	12	8	8
SAM	16	9	8
WL	6	7 (1 GSRP)	4
WHMC	2	2	1
Total	153	126	88

LIST OF UNIVERSITIES THAT PARTICIPATED

Akron, University of	- 1	Louisiana Tech. University	- 1
Alabama, University of	- 1	Lowell, University of	- 2
Albany College	- 1	Maine, University of	- 1
Arizona State University	- 1	Meharry Medical College	- 1
Arizona, University of	- 1	Miami University	- 1
Arkansas State University	- 1	Miami, University of	- 1
Arkansas, University of	- 2	Michigan State University	- 1
Auburn University	- 1	Michigan Tech. University	- 1
Austin Peay State Univ.	- 1	Michigan, University of	- 2
Ball State University	- 1	Minnesota, University of	- 1
Boston College	- 1	Missouri Western State Coll.	- 1
California State Univ.	- 2	Missouri, University of	- 2
California, Univ. of	- 1	Montana, University of	- 1
Calvin College	- 1	Montclair State College	- 1
Carnegie Mellon University	- 1	Morehouse College	- 1
Central State University	- 3	Muhlenberg College	- 1
Central Wesleyan College	- 1	Murray State University	- 1
Cincinnati, University of	- 3	Nebraska, University of	- 1
Clarkson University	- 2	New Hampshire, Univ. of	- 3
Clemson University	- 1	New Mexico, University of	- 1
Colorado State University	- 2	New York State University	- 2
Columbia Basin College	- 1	New York, City College of	- 1
Dayton, University of	- 5	North Carolina State Univ.	- 1
Delta State University	- 1	North Carolina, Univ. of	- 2
East Texas State University	- 1	Northern Illinois Univ.	- 1
Eastern New Mexico Univ.	- 1	Ohio State University	- 2
Fairleigh Dickinson Univ.	- 1	Oklahoma State University	- 1
Fayetteville State Univ.	- 1	Oral Roberts University	- 1
Florida Inst. of Technology	- 1	Oregon Inst. of Technology	- 2
Florida, University of	- 1	Oregon State University	- 1
Francis Marion University	- 1	Pennsylvania State Univ.	- 1
George Mason University	- 1	Polytechnic University	- 1
Georgia Inst. of Technology	- 2	Prairie View A&M Univ.	- 2
Georgia, University of	- 1	Presbyterian College	- 1
Gonzaga University	- 1	Purdue University	- 1
Hampton University	- 1	Redlands, University of	- 1
Illinois Inst. of Technology	- 1	Lehigh Polytechnic Inst	- 1
Indiana University	- 1	Rice University	- 1
Iowa State University	- 1	Rochester Inst. of Tech.	- 1
Jackson State University	- 3	Rose-Hulman Inst. of Tech.	- 1
Jacksonville State Univ.	- 1	Saint Paul's College	- 1
Jarvis Christian College	- 1	San Francisco State Univ.	- 1
Kentucky, University of	- 1	Santa Clara University	- 1
LaVerne, University of	- 1	Southeast Oklahoma State U.	- 1
Louisiana State University	- 2	Southern Mississippi, Univ.	- 1

LIST OF UNIVERSITIES THAT PARTICIPATED
Continued

Southern University	- 2	Tuskegee University	- 1
Southwest Missouri State U.	- 1	Virginia Polytechnic Inst.	- 1
St. Norbert College	- 1	Warren Wilson College	- 1
Staten Island, College of	- 1	Wayne State University	- 1
Syracuse University	- 1	Wesleyan College	- 1
Taylor University	- 1	West Florida, University of	- 1
Tennessee Space Inst., Univ.	- 1	West Texas State Univ.	- 1
Tennessee Tech. University	- 2	West Virginia Tech.	- 1
Tennessee, University of	- 1	Western Illinois University	- 1
Texas A&I University	- 1	Western Michigan University	- 1
Texas Lutheran College	- 1	Widener University	- 1
Texas, University of	- 4	Wilberforce University	- 1
Towson State University	- 1	Wisconsin-Madison, Univ. of	- 1
Trinity University	- 1	Wright State University	- 5
		Total	153

PARTICIPANTS LABORATORY ASSIGNMENT

PARTICIPANT LABORATORY ASSIGNMENT

AERO PROPULSION LABORATORY

(Wright-Patterson Air Force Base)

Dr. Suresh K. Aggarwal (1987)
University of Illinois at Chicago
Specialty: Aerospace Engineering

Dr. Mingking K. Chyu
Carnegie Mellon University
Specialty: Heat Transfer

Dr. Derek Dunn-Rankin
University of California
Specialty: Laser Diagnostics (combustion)

Dr. Wayne A. Eckerle
Clarkson University
Specialty: Experimental Fluid Mechanics

Dr. Arthur A. Mason (1986)
University of Tennessee Space Institute
Specialty: Physics

Dr. Douglas G. Talley
University of Michigan
Specialty: Combustion

Dr. Richard Tankin (1987)
Northwestern University
Specialty: Mechanical Engineering

Dr. Cheng-Hsiao Wu (1987)
University of Missouri
Specialty: Solid State Physics

ARMAMENT LABORATORY

(Eglin Air Force Base)

Dr. Ibrahim A. Ahmad
Northern Illinois University
Specialty: Statistics and Operations

Dr. Charles Bell (1987)
Arkansas State University
Specialty: Mechanical Engineering

Dr. Stephen J. Dow
Univ. of Alabama in Huntsville
Specialty: Discrete Mathematics

Dr. Joseph J. Feeley (1987)
University of Idaho
Specialty: Electrical Engineering

Dr. Manuel A. Huerta
University of Miami
Specialty: Plasma Physics

Prof. Anastas Lazaridis
Widener University
Specialty: Ablation, Solar Energy

Dr. Kwang S. Min
East Texas State University
Specialty: Signal Processing

Dr. Joseph J. Molitoris
Muhlenberg College
Specialty: Nuclear Physics

Prof. Wafa E. Yazigi
Columbia Basin College
Specialty: Solid Mechanics

Harry G. Armstrong Aerospace Medical Research Laboratory
(Wright-Patterson Air Force Base)

Dr. Charles D. Covington
University of Arkansas
Specialty: Digital Signal Processing

Dr. Donald Robertson (1987)
Indiana University of PA
Specialty: Psychology

Dr. Barry P. Goettl
Clemson University
Specialty: Engineering Psychology

Dr. Joseph E. Saliba
University of Dayton
Specialty: Engineering Mechanics

Dr. David G. Payne
SUNY Binghamton
Specialty: Human Memory

Dr. Sanford S. Singer
University of Dayton
Specialty: Enzymology

ARNOLD ENGINEERING DEVELOPMENT CENTER
(Arnold Air Force Base)

Mr. Ben A. Abbott (GSRP)
Vanderbilt University
Specialty: Electrical Engineering

Prof. William M. Grissom
Morehouse College
Specialty: Combustion Diagnostics

Dr. Eustace L. Dereniak
University of Arizona
Specialty: Infrared Physics

Dr. William Sutton (1985)
University of Oklahoma
Specialty: Heat Transfer

Dr. Ahmad D. Vakili
Univ. of Tennessee Space Inst.
Specialty: Unsteady Flows

ASTRONAUTICS LABORATORY
(Edwards Air Force Base)

Dr. Gurbux S. Alag (1987)
Western Michigan University
Specialty: Systems Engineering

Dr. David W. Jensen
Pennsylvania State University
Specialty: Advanced Composite Materials

Dr. Clarence Calder
Oregon State University
Specialty: Stress Wave Propagation

Dr. John Kenney (1987)
Eastern New Mexico University
Specialty: Physical Chemistry

Mr. David B. Chenault (GSRP)
University of Alabama
Specialty: Physics

Dr. Mark A. Norris
Virginia Polytechnic Inst. & State Univ.
Specialty: Structural Dynamics &
Controls

ASTRONAUTICS LABORATORY

(Edwards Air Force Base)

(continued)

Dr. Phillip A. Christiansen
Clarkson University
Specialty: Physical Chemistry

Dr. Susan T. Collins
California State University
Specialty: Matrix Isolation Spectroscopy

Dr. Rameshwar P. Sharma
Western Michigan University
Specialty: Fluid Mechanics

Dr. Siavash H. Sohrab (1986)
Northwestern University
Specialty: Engineering Physics

AVIONICS LABORATORY

(Wright-Patterson Air Force Base)

Prof. William K. Curry (1987)
Rose-Hulman Inst. of Technology
Specialty: Computer Science

Dr. Gerald W. Grams
Georgia Tech.
Specialty: Atmospheric Physics

Dr. David Hemmendinger
Wright State University
Specialty: Logic Programming

Dr. Periasamy K. Rajan
Tennessee Tech. University
Specialty: Digital Signal Processing

Dr. Mateen M. Rizki
Wright State University
Specialty: Modeling and Simulation

ENGINEERING AND SERVICES CENTER

(Tyndall Air Force Base)

Dr. Wayne A. Charlie
Colorado State University
Specialty: Geotechnical Engineering

Dr. David H. DeHeer
Calvin College
Specialty: Molecular Biology

Dr. Deanna S. Durnford
Colorado State University
Specialty: Groundwater

Dr. Neil J. Hutzler
Michigan Tech. University
Specialty: Environmental Engineering

Dr. Peter Jeffers (1987)
S.U.N.Y.
Specialty: Chemistry

Dr. Richard S. Myers
Delta State University
Specialty: Experimental Physical Chem.

Dr. William Schulz (1987)
Eastern Kentucky University
Specialty: Chemistry

Dr. Dennis Truax (1987)
Mississippi State University
Specialty: Civil Engineering

ELECTRONIC SYSTEMS DIVISION

(Hanscom Air Force Base)

Mr. George N. Bratton
Austin State Peay State Univ.
Specialty: Statistics

Dr. John F. Dalphin
Towson State University
Specialty: Computer Science

Dr. Stephan Kolitz (1986)
University of Massachusetts
Specialty: Operations Reserach

FLIGHT DYNAMICS LABORATORY

(Wright-Patterson Air Force Base)

Dr. Peter J. Disimile (1986)
University of Cincinnati
Specialty: Fluid Mechanics

Dr. James A. Sherwood
University of New Hampshire
Specialty: Solid Mechanics

Mr. Thomas Enneking (GSRP), (1987)
University of Notre Dame
Specialty: Civil Engineering

Dr. Gary Slater (1987)
University of Cincinnati
Specialty: Aerospace Engineering

Dr. Awatef Hamed
University of Cincinnati
Specialty: Engineering

Dr. Kenneth M. Sobel
The City College of New York
Specialty: Eigenstructure

Dr. Yulian B. Kin
Purdue University Calumet
Specialty: Stress Analysis

Dr. Forrest Thomas (1987)
University of Montana
Specialty: Chemistry

Dr. Oliver McGee (1987)
Ohio State University
Specialty: Engineering Mechanics

Mr. David F. Thompson (GSRP)
Purdue University
Specialty: Computer Information

Dr. William E. Wolfe
Ohio State University
Specialty: Geotechnical Engineering

FRANK J. SEILER RESERACH LABORATORY

(United States Air Froce Academy)

Dr. Richard Bertrand (1985)
University of Colorado
Specialty: NMR Spectroscopy, Atomic Spectroscopy

Dr. Tammy J. Melton
St. Norbert College
Specialty: Inorganic Synthesis

FRANK J. SEILER RESERACH LABORATORY

(United States Air Froce Academy)

(continued)

Dr. Dan R. Bruss
Albany College of Pharmacy
Specialty: Physical Organic Chemistry

Dr. Charles M. Bump (1987)
Hampton University
Specialty: Organic Chemistry

Dr. Michael L. McKee
Auburn University
Specialty: Molecular Orbital Theory

Dr. Patricia L. Plummer
Columbia Univ. of Missouri
Specialty: Quantum Chemistry

Dr. Howard Thompson (1987)
Purdue University
Specialty: Mechanical Engineering

Dr. Melvin Zandler (1987)
Wichita State University
Specialty: Physical Chemistry

GEOPHYSICS LABORATORY

(Hanscom Air Force Base)

Dr. Lucia M. Babcock
Louisiana State University
Specialty: Gas Phase Ion-Molecule Chem.

Dr. Pradip M. Bakshi
Boston College
Specialty: Quantum Theory

Dr. Donald F. Collins
Warren Wilson College
Specialty: Optics, Image Processing

Dr. Lee Flippin (1987)
San Francisco State University
Specialty: Organic Chemisty

Dr. Janet U. Kozyra
University of Michigan
Specialty: Space Physics

Dr. Steven Leon (1987)
Southeastern Massachusettes
Specialty: Mathematics

Dr. John P. McHugh
University of New Hampshire
Specialty: Fluid Mechanics

Dr. Timothy Su (1987)
Southeastern Massachusetts Univ.
Specialty: Physical Chemistry

HUMAN RESOURCES LABORATORY

(Brooks, Williams and Wright-Patterson Air Force Base)

Dr. Ronna Dillion (1987)
Southern Illinois University
Specialty: Educational Psychology

Dr. J. Kevin Ford
Michigan State University
Specialty: Industrial/Organ. Psychology

Dr. Jorge L. Mendoza (1986)
Texas A&M University
Specialty: Psychology

Dr. Philip D. Olivier (1986)
University of Texas
Specialty: Electrical Engineering

HUMAN RESOURCES LABORATORY

(Brooks, Williams and Wright-Patterson Air Force Base)
(continued)

Dr. Hugh. P. Garraway, III
Univ. of Southern Mississippi
Specialty: Computer Based Learning

Dr. Douglas E. Jackson
Eastern New Mexico University
Specialty: Math/Statistical Information

Dr. Charles E. Lance
University of Georgia
Specialty: Industrial/Organizational Psy.

Dr. Thomas L. Landers
University of Arkansas
Specialty: Reliability & Maintainability

Dr. Mufit H. Ozden
Miami University
Specialty: Operations Research

Dr. Dharam S. Rana
Jackson State University
Specialty: Quantitative Techniques

Dr. Jonathan M. Spector
Jacksonville State University
Specialty: Logic

Dr. Charles Wells (1987)
University of Dayton
Specialty: Management Science

Dr. Robert K. Young
University of Texas
Specialty: Experimental Psychology

LOGISTICS COMMAND

(Wright-Patterson Air Force Base)

Dr. Ming-Shing Hung (1986)
Kent State University
Specialty: Business Administration & Management Science

MATERIALS LABORATORY

(Wright-Patterson Air Force Base)

Dr. Bruce Craver (1987)
University of Dayton
Specialty: Physics

Dr. Parvis Dadras
Wright State University
Specialty: Mechanics of Materials

Dr. David A. Grossie
Wright State University
Specialty: X-ray Crystallography

Dr. Gordon Johnson (1987)
Walla Walla College
Specialty: Electrical Engineering

Dr. L. James Lee
The Ohio State University
Specialty: Polymer & Composite
Processing

MATERIALS LABORATORY

(Wright-Patterson Air Force Base)

(continued)

Dr. Barry K. Fussell
University of New Hampshire
Specialty: Systems Modeling & Controls

Dr. Michael Sydor
University of Minnesota
Specialty: Optics, Material Science

Dr. John W. Gilmer (1987)
Penn State University
Specialty: Physical Chemistry

Dr. Richard S. Valpey
Wilberforce University
Specialty: Organic Synthesis

OCCUPATIONAL AND ENVIRONMENT HEALTH LABORATORY

(Brooks Air Force Base)

Dr. Steven C. Chiesa
Santa Clara University
Specialty: Biological Waste Treatment

Dr. Gary R. Stevens
Oklahoma State University
Specialty: Stochastic Processes

Dr. Larry R. Sherman
University of Akron
Specialty: Organotin Chemistry

Dr. Shirley A. Williams (1986)
Jackson State University
Specialty: Physiology

ROME AIR DEVELOPMENT CENTER

(Griffiss Air Force Base)

Dr. Keith A. Christianson
University of Maine
Specialty: Electronic Materials

Dr. David Sumberg (1987)
Rochester Institute of Tech.
Specialty: Physics

Dr. Hugh K. Donaghy
Rochester Inst. of Technology
Specialty: Natural Language Processing

Dr. Donald R. Ucci
Illinois Inst. of Technology
Specialty: Adaptive Arrays

Dr. Oleg G. Jakubowicz
State University of New York
Specialty: Neural Nets

Dr. Peter J. Walsh
Fairleigh Dickinson University
Specialty: Superconductivity

Dr. Louis Johnson (1987)
Oklahoma State University
Specialty: Electrical Engineering

Dr. Kenneth L. Walter
Prairie View A&M University
Specialty: Chemical Engineering Process

Dr. Samuel P. Kozaitis
Florida Institute of Tech.
Specialty: Optics, Computer Architecture

Dr. Gwo-Ching Wang
Rensselaer Polytechnic Inst.
Specialty: Surface Sciences

SCHOOL OF AEROSPACE MEDICINE

(Brooks Air Force Base)

Dr. Ronald Bulbulian
University of Kentucky
Specialty: Exercise Physiology

Dr. John A. Burke, Jr.
Trinity University
Specialty: Inorganic Compounds

Dr. Hoffman H. Chen (1986)
Grambling State University
Specialty: Mechanical Engineering

Dr. Frank O. Hadlock (1986)
Florida Atlantic University
Specialty: Mathematics

Dr. Eric R. Johnson
Ball State University
Specialty: Protein Biochemistry

Dr. Harold G. Longbotham
Univ. of Texas - San Antonio
Specialty: Nonlinear Digital Filtering

Dr. Mohammed Maleque (1987)
Meharry Medical College
Specialty: Pharmacology

WILFORD HALL MEDICAL CENTER

(Lackland Air Force Base)

Dr. David R. Cecil
Texas A&I University
Specialty: Algebra (Finite Fields)

WEAPONS LABORATORY

(Kirtland Air Force Base)

Dr. Albert W. Biggs (1986)
University of Alabama
Specialty: Electrical Engineering

Dr. Parsottam J. Patel (1986)
Meharry Medical College
Specialty: Microbiology

Dr. William Z. Plachy
San Francisco State University
Specialty: Physical Chemistry

Dr. Ralph Peters (1987)
Wichita State University
Specialty: Zoology

Dr. Thomas R. Rogge
Iowa State University
Specialty: Finite Element Analysis

Prof. Sonia H. Sawtelle-Hart
Univ. of Texas - San Antonio
Specialty: Exercise Physiology

Dr. Wesley Tanaka (1987)
University of Wisconsin
Specialty: Biochemistry

Dr. John R. Wright
Southeast Oklahoma State Univ.
Specialty: Biochemistry

Dr. Donald Welch (1986)
Texas A&M University
Specialty: Microbiology

Dr. William M. Jordan
Louisiana Tech. University
Specialty: Composite Materials

WEAPONS LABORATORY

(Kirtland Air Force Base)

(continued)

Dr. Lane Clark
University of New Mexico
Specialty: Graph Theory

Dr. David A. Dolson
Murray State University
Specialty: Laser Spectroscopy

Dr. Arkady Kheyfets
North Carolina State Univ.
Specialty: Mathematical Physics

Dr. Barry McConnell (1987)
Florida A&M University
Specialty: Computer Science

Dr. William Wheless (1987)
New Mexico State University
Specialty: Electrical Engineering

RESEARCH REPORTS

MINI-GRANT RESEARCH REPORTS
1988 RESEARCH INITIATION PROGRAM

<u>Technical Report Number</u>	<u>Title and Mini-Grant No.</u>	<u>Professor</u>
Volume I Armament Laboratory		
1	Statistical Analysis of Residual Target Performance and for Measures of Target Partial Availability Pending Approval 210-9MG-010	Dr. Ibrahim A. Ahmad
2	Synergistic Effects of Bomb Cratering, Phase II 760-7MG-025	Dr. Charles Bell (1987)
3	Automated Motion Parameter Determination from an Image Sequence 210-9MG-025	Dr. Stephen J. Dow
4	Modeling and Simulation on Micro-computers, 1989 760-7MG-070	Dr. Joseph J. Feeley (1987)
5	Two Dimensional MHD Simulation of Accelerating Arc Plasmas 210-9MG-090	Dr. Manuel A. Huerta
6	Modeling Reactive Fragments 210-9MG-011	Prof. Anastas Lazaridis
7	Target-Aerosol Discrimination for Active Optical Proximity Sensors 210-9MG-016	Dr. Kwang S. Min
8	The Dynamics of Impact 210-9MG-008	Dr. Joseph J. Molitoris
9	Report Not Acceptable at this Time 210-9MG-015	Prof. Wafa E. Yazigi

Arnold Engineering Development Center

- | | | |
|----|--|---------------------------|
| 10 | Multigraph Kernel for Transputer Based Systems
21-9MG-087 | Mr. Ben A. Abbott (GSRP) |
| 11 | MTF Studies of IR Focal Plane Arrays at Low Flux Levels
210-9MG-020 | Dr. Eustace L. Dereniak |
| 12 | Droplet Size Distributions and Combustion Modeling in a Pintle Injector Spray
210-9MG-069 | Prof. William M. Grissom |
| 13 | Multiple Scattering in Solid Fuel Rocket Plumes
760-0MG-091 | Dr. William Sutton (1985) |
| 14 | Influence of Forced Disturbances on the Vortex Core and the Vortex Burst
210-9MG-056 | Dr. Ahmad D. Vakili |

Astronautics Laboratory

- | | | |
|----|--|------------------------------|
| 15 | Large Space Structure Parameter Estimation
760-7MG-042 | Dr. Gurbux S. Alag (1987) |
| 16 | Integrated Strain Measurement in Composite Members Using Embedded Constantan Wire
Pending Approval
210-9MG-076 | Dr. Clarence Calder |
| 17 | Calibration of the Infrared Spectropolarimeter
210-9MG-026 | Mr. David B. Chenault (GSRP) |
| 18 | Computer Code to Include Core Polarization in Effective Potential Basis Set Expansion Studies
210-9MG-092 | Dr. Phillip A. Christiansen |
| 19 | Fluorescence Spectra of Matrix-isolated Lithium
210-9MG-115 | Dr. Susan T. Collins |

- | | | |
|--|--|------------------------------|
| 20 | Calibration of Composite-Embedded
Fiber-Optic Strain Sensors
Pending Approval
210-9MG-052 | Dr. David W. Jensen |
| 21 | Energy-And Time-Resolved Photophysics
and Photochemistry of High Energy
Cryogenic Metal-Containing Rocket Fuels
760-7MG-019 | Dr. John Kenney (1987) |
| 22 | Experimental Verification and Develop-
ment of Structural Identification
Techniques on a Grid
210-9MG-045 | Dr. Mark A. Norris |
| 23 | Report Not Available at this Time
210-9MG-103 | Dr. Rameshwar P. Sharma |
| 24 | Experimental Investigation of the
Stability of Jets Near the Critical
Point
760-6MG-110 | Dr. Siavash H. Sohrab (1986) |
| Electronics Systems Division | | |
| 25 | HF Network Evaluation
210-9MG-012 | Mr. George N. Bratton |
| 26 | Report Not Available at this Time
210-9MG-023 | Dr. John F. Dalphin |
| 27 | Reliability in Satellite Communication
Networks
Pending Approval
760-6MG-094 | Dr. Stephan Kolitz (1986) |
| Engineering and Services Center | | |
| 28 | High Intensity Compressive Stress Wave
Propagation Through Unsaturated Sands
210-9MG-075 | Dr. Wayne A. Charlie |
| 29 | Decontamination and Elisa Analysis
of Blood Group Substances from Human
Tissue
Pending Approval
210-9MG-112 | Dr. David H. DeHeer |

- | | | |
|----|---|---------------------------|
| 30 | Estimation of Jet Fuel Contamination
in Soils
210-9MG-074 | Dr. Deanna S. Durnford |
| 31 | Extraction of Volatile Organic Chemicals
from Unsaturated Soil: Experimental
Results and Model Predictions
210-9MG-059 | Dr. Neil J. Hutzler |
| 32 | Homogeneous Hydrolysis Rate Constants
for Selected Chlorinated Methanes,
Ethanes, Ethenes, and Propanes
760-7MG-038 | Dr. Peter Jeffers (1987) |
| 33 | Sorption Kinetics of Volatile Organic
Compounds on Aquifer Materials
210-9MG-047 | Dr. Richard S. Myers |
| 34 | Report will be Submitted Under
Mini-Grant 210-10MG-095 | Dr. William Schulz (1987) |
| 35 | Report Not Available at this Time
760-7MG-105 | Dr. Dennis Truax (1987) |

Volume II

Frank J. Seiler Research Laboratory

- | | | |
|----|---|-----------------------------|
| 36 | NMR Studies of Alkylammonium-Chloro-
oaluminate Room-Temperature Electrolytes
760-0MG-095 | Dr. Richard Bertrand (1985) |
| 37 | Mechanistic Studies on the Thermal
Decomposition of NTO by High
Performance Liquid Chromatography
210-9MG-111 | Dr. Dan R. Bruss |
| 38 | Aromatic Nitrations in Chloroaluminate
Melts
760-7MG-076 | Dr. Charles M. Bump (1987) |
| 39 | Calculated C-NO ₂ Bond Dissociation
Energies (Part I) and A MCSCF Study of
the Rearrangement of Nitromethane to
Methyl Nitrite (Part II)
210-9MG-054 | Dr. Michael L. McKee |
| 40 | Sodium as an Electrode for Chloroaluminate
Melts
210-9MG-098 | Dr. Tammy J. Melton |

41	Report Not Available at this Time 210-9MG-097	Dr. Patricia L. Plummer
42	Transient Shock Waves in a Mach 3 Flow 760-7MG-071	Dr. Howard Thompson (1987)
43	Ab-initio and Semi-Empirical Molecular Orbital Studies of Energetic Materials (Nitrogen Heterocyclics) and Polymers 760-7MG-092	Dr. Melvin Zandler (1987)
Geophysics Laboratory		
44	Radiative Association in Ion-Molecule Reactions: Reactions of Some Carbon Cations 210-9MG-086	Dr. Lucia M. Babcock
45	Impulse Approximation Formalism for Atom Molecule Collisions 210-9MG-109	Dr. Pradip M. Bakshi
46	Stellar Photometry, Vehicle Glow, and Advanced Image Analysis 210-9MG-100	Dr. Donald F. Collins
47	Synthesis of Organometallic Reagents for SIFT Studies of Electron Attachment Reactions 760-7MG-056	Dr. Lee Flippin (1987)
48	Theoretical and Observational Studies of Geomagnetic Storm-Related Ion and Electron Heating in the Subauroral Region 210-9MG-084	Dr. Janet U. Kozyra
49	Algorithms for Generalized Exponential Inversion 760-7MG-036	Dr. Steven Leon (1987)
50	Report Not Available at this Time 210-9MG-125	Dr. John P. McHugh
51	Trajectory Calculations of High Tempera- ture and Kinetic Energy Dependent Ion- Polar Molecule Collision Rate Constants 760-7MG-040	Dr. Timothy Su (1987)

Rome Air Development Center

- | | | |
|----|---|---------------------------|
| 52 | Aging Studies of GaAs Schottky Barriers
210-9MG-073 | Dr. Keith A. Christianson |
| 53 | Report Not Available at this Time
210-9MG-094 | Dr. Hugh K. Donaghy |
| 54 | Neural Network for Aiding Intelligent
Analysis
Pending Approval
210-9MG-124 | Dr. Oleg G. Jakubowicz |
| 55 | Supply Line Testing in CMOS Digital
Circuits
760-7MG-050 | Dr. Louis Johnson (1987) |
| 56 | Characterization of Detectors for
Optical Pattern Recognition
210-9MG-018 | Dr. Samuel P. Kozaitis |
| 57 | Fiber Optic Distribution for Phased
Array Antennas
Pending Approval
760-7MG-113 | Dr. David Sumberg (1987) |
| 58 | Continuation Study of the Effect of
Nonlinearities of High Speed Analog-
to-Digital Converters on Digital
Beamforming Arrays
210-9MG-040 | Dr. Donald R. Ucci |
| 59 | Analysis of Microwave Surface Impedance
of High Temperature Superconductors
210-9MG-072 | Dr. Peter J. Walsh |
| 60 | Report Not Available at this Time
210-9MG-113 | Dr. Kenneth L. Walter |
| 61 | X-Ray Pole-Figure Analysis of $\text{YBa}_2\text{Cu}_3\text{O}_{7-x}$
Thin Film on $\text{SrTiO}_3(100)$ Prepared by RF
Diode Sputtering
210-9MG-077 | Dr. Gwo-Ching Wang |

Weapons Laboratory

- | | | |
|----|---|----------------------------|
| 62 | Slow Wave Transmission Line Transformers
760-6MG-072 | Dr. Albert W. Biggs (1986) |
|----|---|----------------------------|

- | | | |
|----|--|----------------------------|
| 63 | Report Not Available at this Time
210-9MG-119 | Dr. Lane Clark |
| 64 | Vibrational Energy Transfer in Sulfur
Monoxide
210-9MG-101 | Dr. David A. Dolson |
| 65 | Development of an Experimental Program
to Evaluate Laser Composite Material
Damage Models
210-9MG-034 | Dr. William M. Jordan |
| 66 | Report Not Available at this Time
210-9MG-114 | Dr. Arkady Kheifets |
| 67 | Report Not Available at this Time
760-7MG-047 | Dr. Barry McConnell (1987) |
| 68 | Slow to Fast Wave Transition Analysis
760-7MG-068 | Dr. William Wheless (1987) |

Volume III

Air Force Wright Aeronautical Laboratories

Aero Propulsion Laboratory

- | | | |
|----|--|-------------------------------|
| 69 | Vaporization Behavior of Pure and
Multicomponent Fuel Droplets in a
Hot Air Stream
760-7MG-061 | Dr. Suresh K. Aggarwal (1987) |
| 70 | Effects of Injection-To-Mainstream
Density Ratios on Film Cooling Heat
Transfer
Pending Approval
210-9MG-096 | Dr. Mingking K. Chyu |
| 71 | Accurate Temperatures Using Cars in
Droplet Laden Flows
Pending Approval
210-9MG-055 | Dr. Derek Dunn-Rankin |
| 72 | Report Not Available at this Time
210-9MG-019 | Dr. Wayne A. Eckerle |
| 73 | Report Not Available at this Time
760-6MG-099 | Dr. Arthur A. Mason (1986) |
| 74 | Report Not Available at this Time
210-9MG-022 | Dr. Douglas G. Talley |

- 75 Vortical Structures in 2-D Slot Dr. Richard Tankin (1987)
 Burner-Cold Flow
 760-7MG-051
- 76 Calculations of Interface-State Occupation Dr. Cheng-Hsiao Wu (1987)
 Function and GaAs/Ge Heterostructure Solar
 Cell Efficiency
 760-7MG-093
- Avionics Laboratory**
- 77 Computer Simulation of Adaptive Resource Prof. William K. Curry (1987)
 Management in Real-Time
 760-7MG-081
- 78 Study of Sky Backgrounds and Subvisual Dr. Gerald W. Grams
 Cirrus
 Pending Approval
 210-9MG-120
- 79 Proving Equivalence of High-and Low-Level Dr. David Hemmendinger
 Architectural Descriptions in VHDL
 210-9MG-108
- 80 Report Not Available at this Time Dr. Periasamy K. Rajan
 210-9MG-051
- 81 Applications of Evolutionary Learning Dr. Mateen M. Rizki
 Strategies to Pattern Recognition Tasks
 210-9MG-058
- Flight Dynamics Laboratory**
- 82 The Effect of a Roughened Surface on Dr. Peter J. Disimile (1986)
 Turbulent Boundary Layer Separation
 at Mach 6.0
 760-6MG-075
- 83 A Stochastic Model of Fatigue Crack Mr. Thomas Enneking (GSRP)
 Growth Due to Random Loading for (1987)
 Application to Aircraft Wheels
 760-7MG-124
- 84 An Investigation of the Flow Field in Dr. Awatef Hamed
 Shock Wave/Boundary Layer/Bleed
 Interactions
 Pending Approval
 210-9MG-061

- | | | |
|-----------------------------|--|------------------------------|
| 85 | Fatigue Characteristics of F-16 Composite Transparency Material Determined by Long-Term and Accelerated Methods
210-9MG-038 | Dr. Yulian B. Kin |
| 86 | Convergence of Upper-Bound Optimum Design of Large-Scale Structures with Specified Frequency Bands
760-7MG-115 | Dr. Oliver McGee (1987) |
| 87 | Report Not Available at this Time
210-9MG-088 | Dr. James A. Sherwood |
| 88 | Robustness with Positive Real Controllers for Large Space Structures
760-7MG-088 | Dr. Gary Slater (1987) |
| 89 | Robust Eigenstructure Assignment for Flight Control Design
210-9MG-035 | Dr. Kenneth M. Sobel |
| 90 | Comparative Burning Rates and Duplex Loads of Solid Propellants
760-7MG-080 | Dr. Forrest Thomas (1987) |
| 91 | Optimal and Sub-Optimal Loop Shaping in Quantitative Feedback Theory
Pending Approval
210-9MG-106 | Mr. David F. Thompson (GSRP) |
| 92 | Low Velocity Impact of Composite Materials
760-7MG-102 and 210-9MG-082 | Dr. William E. Wolfe |
| Logistics Command | | |
| 93 | Aircraft Availabilty Model: Feasibility Study for POM Forecasting
760-6MG-105 | Dr. Ming S. Hung (1986) |
| Materials Laboratory | | |
| 94 | Tunable Absorption in Doping Superlattices
760-7MG-097 | Dr. Bruce Craver (1987) |
| 95 | Joining of Carbon-Carbon Composites
210-9MG-004 | Dr. Parviz Dadras |
| 96 | Report Not Available at this Time
210-9MG-064 | Dr. Barry K. Fussell |

- | | | |
|---|---|-----------------------------|
| 97 | Characterization of the Phase Separation Behavior of Poly(p-phenylene benzobisthiazole)/Amorphous Nylon Molecular Composites by Small Angle Light Scattering
760-7MG-013 | Dr. John W. Gilmer |
| 98 | Structural Analysis of Model Compounds with Potential Second and Third Order Nonlinear Optical Properties
210-9MG-080 | Dr. David A. Grossie |
| 99 | Liquid Crystal Biomolecules for use as Optical Filters
760-7MG-075 | Dr. Gordon Johnson (1987) |
| 100 | Knowledge Development for the Rule Based Process Automation of Resin Transfer Molding
210-9MG-063 | Dr. L. Jmaes Lee |
| 101 | Photoreflectance Measurements of the Quality of Undoped GaAs
210-9MG-031 | Dr. Michael Sydor |
| 102 | Synthesis of 2, 6-Diformyl Pyridobisimidazoles
210-9MG-029 | Dr. Richard S. Valpey |
| Volume IV | | |
| Human Systems Division Laboratories | | |
| Harry G. Armstrong Aerospace Medical Research Laboratory | | |
| 103 | Auditory Modeling
210-9MG-060 | Dr. Charles D. Covington |
| 104 | Assessing the Cognitive Demands of Tracking Strategies
210-9MG-078 | Dr. Barry P. Goettl |
| 105 | Report Not Available at this Time
210-9MG-121 | Dr. David G. Payne |
| 106 | Effect of System Reliability on Probabilistic Inference
Pending Approval
760-7MG-094 | Dr. Donald Robertson (1987) |

- 107 Optimization of the Nonlinear Discrete Dr. Joseph E. Saliba
Parameter Model of the Seated Human
Spine
210-9MG-071
- 108 In Vitro Modeling of Perfluoro-N-Decanoate Dr. Sanford S. Singer
Effects on Enzymes of Fatty Acid Metabolism
210-9MG-002
- Human Resources Laboratory
- 109 Report Not Acceptable at this Time Dr. Ronna Dillion (1987)
760-7MG-100
- 110 An Investigation of Training Content Dr. J. Kevin Ford
Validity and Training Efficiency in the
Air Force Airmen Basic-In-Residence
Training Course
210-9MG-066
- 111 An Intelligent Tool to Facilitate the Dr. Hugh P. Garraway, III
Development of Qualitative Process Models
in Novice Programmers
210-9MG-007
- 112 On the Effect of Range Restriction on Dr. Douglas E. Jackson
Correlation Coefficient Estimation
210-9MG-027
- 113 Validation of an Enlisted Air Force Dr. Charles E. Lance
Specialty Task Taxonomy and Cross-AFS
Ease-of-Movement Predictions
210-9MG-017
- 114 Proportional Intensity Reliability Dr. Thomas L. Landers
Analysis for Repairable Items
210-9MG-104
- 115 A Monte Carlo Comparison of Validity Dr. Jorge L. Mendoza (1986)
Generalization Procedures
760-6MG-136
- 116 A Network Tutor Based on the Heuristic Dr. Philip D. Olivier (1986)
of Polya
760-6MG-032
- 117 Graphical Programming of Simulation Dr. Mufit H. Ozden
Models in an Object-Oriented Environment
210-9MG-028

- | | | |
|---|--|--------------------------------|
| 118 | Report Not Available at this Time
210-9MG-043 | Dr. Dharam S. Rana |
| 119 | Refinement Considerations for an
Advanced Instructional Design Advisor
210-9MG-021 | Dr. Jonathan M. Spector |
| 120 | Engineering Design with Decision Support:
An Application of Goal Decomposition
760-7MG-046 | Dr. Charles Wells (1987) |
| 121 | Report Not Available at this Time
210-9MG-099 | Dr. Robert K. Young |
| Occupational and Environment Health Laboratory | | |
| 122 | Solvent Extraction of Boron from
Industrial Wastewaters
210-9MG-102 | Dr. Steven C. Chiesa |
| 123 | Comparison of Asbestos Analysis by
SEM-EDXA and TEM-SAED
210-9MG-122 | Dr. Larry R. Sherman |
| 124 | An Examination of Kriging Techniques
for Ground Water Monitoring
210-9MG-070 | Dr. Gary R. Stevens |
| 125 | Cortisol Prevention of Chronic Beryllium
Disease in Postpartum Rats: A Pilot Study
760-6MG-078 | Dr. Shirley A. Williams (1986) |
| School of Aerospace Medicine | | |
| 126 | Blood Flow Distribution in the Non-
Working Forearm During Exercise
210-9MG-057 | Dr. Ronald Bulbulian |
| 127 | Photophysics and Photochemistry of
Transition Metal Complexes
210-9MG-091 | Dr. John A. Burke, Jr. |
| 128 | Serum Squalene and Cholesterol Ratio as
Risk Predictor for Coronary Artery Disease
760-6MG-118 | Dr. Hoffman H. Chen (1986) |
| 129 | A Feasibility Study for a Computerized
ECG Database
760-6MG-073 | Dr. Frank O. Hadlock (1986) |

- | | | |
|------------------------------------|--|---------------------------------|
| 130 | Development of a New Ultrasensitive Cholesterol Assay System for the Determination of Free Cholesterol in Biological Fluids
210-9MG-105 | Dr. Eric R. Johnson |
| 131 | Application of Nonlinear Filters to VEP Data
210-9MG-033 | Dr. Harold G. Longbotham |
| 132 | Effects of Low Dose Soman on CNS Neurotransmitters
760-7MG-078 | Dr. Dr. Mohammed Maleque (1987) |
| 133 | Cleansing of Bone-Marrow by Lymphokine Activated Killer Cells (LAK-Cells)
760-6MG-131 | Dr. Parsottam J. Patel (1986) |
| 134 | Transcutaneous Oxygen Delivery
210-9MG-042 | Dr. William Z. Plachy |
| 135 | Report Not Acceptable at this Time
760-7MG-091 | Dr. Ralph Peters (1987) |
| 136 | A Computer Model of the Human Systemic Arterial Tree
210-9MG-003 | Dr. Thomas R. Rogge |
| 137 | The Effect of Age, Family Status, and Physical Activity on Select Dietary Components of TAC Pilots
210-9MG-095 | Prof. Sonia H. Sawtell-Hart |
| 138 | Comprehensive Lipoprotein Analysis by High-Performance Molecular Exclusion Chromatography
760-7MG-043 | Dr. Wesley Tanaka (1987) |
| 139 | Nmr and Temperature-Dependence Studies of the Metal-Ion Catalyzed Chemiluminescence of Luminol
210-9MG-037 | Dr. John R. Wright |
| Wilford Hall Medical Center | | |
| 140 | Enhancements to PC-Mainframe Interface for Data Entry
210-9MG-048 | Dr. David R. Cecil |

141

Effect of Hyperoxia on the Permeability
of the Blood-Brain Barrier in Several
Laboratory Species and on Organotypic
Explant Tissue Cultures of Hamster Brain
760-6MG-091

Dr. Donald Welch (1986)

FINAL REPORT NUMBER 1
STATISTICAL ANALYSIS OF RESIDUAL TARGET
PERFORMANCE AND FOR MEASURES OF TARGET PARTIAL AVAILABILITY
PENDING APPROVAL
Dr. Ibrahim A. Ahmad
210-9MG-010

1987 USAF-UES RESEARCH INITIATION PROGRAM

Sponsored by the
AIR FORCE OFFICE OF SCIENTIFIC RESEARCH

Conducted by the
Universal Energy Systems, Inc.

FINAL REPORT

SYNERGISTIC EFFECTS OF BOMB CRATERING, PHASE II

Prepared by: Charles J. Bell, Jr.
Academic rank: Professor
Department and Engineering
University: Arkansas State University
Research Facility: Air Force Armament Test Laboratory
Clusters and Warheads Branch
Eglin Air Force Base, Florida
USAF Researcher: Albert L. Weimorts, Jr.
Date: May 5, 1989
Contract No: F 49620-85-C-0013

SYNERGISTIC EFFECTS OF BOMB CRATERING, PHASE II

by

Charles J. Bell, Jr.

ABSTRACT

A computer program was developed to simulate explosions of multiple charges beneath runways. The program is user friendly in that it requests from the operator the data required for each run. One, two, or three rounds may be selected, and the multiple rounds may be detonated simultaneously or with time delay. When using three rounds, either in-line or triangular configurations are possible.

ACKNOWLEDGEMENTS

I wish to thank the Air Force Systems Command and the Air Force Office of Scientific Research for sponsorship of this research. Universal Energy Systems must be mentioned for their concern and help to me in all administrative and directional aspects of this program.

Mr. Keith Blocker, an engineering degree candidate at Arkansas State University wrote the original computer program. His work was indispensable. Mrs. Maxine Smith provided essential secretarial support. Dr. Albert Mink gave administrative assistance. Dr. William Crumpton and Dr. Lyle Rhea made their computer expertise available in times of need.

NOMENCLATURE

A	parameter of variable units
d	depth below runway bottom surface
f_c	compressive failure strength of concrete
h	slab thickness in feet
I_{ap}	applied specific impulse
I_c	critical specific impulse in psi-sec
$P_{\underline{a}}(R)$	peak pressure at point R in psi
$P(R, t)$	pressure at r at time t
R	distance from CG in feet
t	time in seconds
W	explosive mass in pounds
θ	time constant in seconds
ρ_c	concrete density in lb/cu ft

I. INTRODUCTION

Synergistic effects offer an opportunity for significant enhancement of the damage wrought by clustered kinetic energy penetrators. Exploitation of synergism requires knowledge of the effects of projectile depths at detonation, detonation time intervals, and projectile spacing upon synergism. Target structure and surrounding media are also factors that must be considered in a plan of attack.

The number of variables involved in this problem dictates that a mathematical model be developed for determining the spacing, depth, and timing of detonations that should be used in a given situation. A model proposed by Bell (1) has been modified and programmed in Turbo Basic to allow analytical estimates of synergistic effects using up to three projectiles. The program is reproduced in the Appendix.

II. THE MODEL

Cole (2) has summarized years of work on underwater explosions. The model proposed in his work has been used for almost every subsequent analysis in a number of media including soils and concrete. This adaptation has been accomplished by the simple expedient of adjusting exponents and coefficients to suit the particular application. The model proposed in (1) is based upon, but slightly different than, that presented by Cole (2).

The basic difference between the model used here and that proposed by Cole (2) is in the treatment of the charge weight (W) and the distance (R) from the charge center of gravity (CG). The classic model of Cole used the parameter $W^{1/3}/R$ raised to some power in calculating maximum pressure (P_m), applied impulse (I_{ap}), and pressure (P) at distance R from the CG. the reasons for using this modified model may be found in (1).

The equations for a spherical charge are:

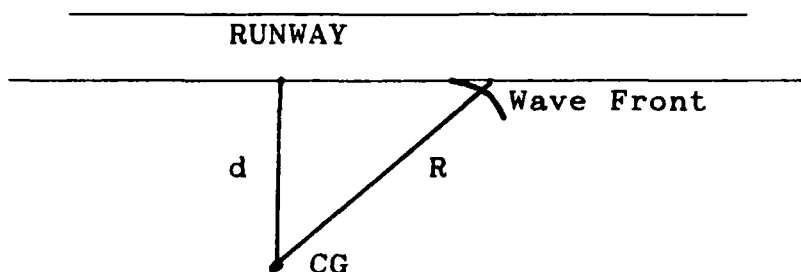
$$P_m(R) = AW^{1/3}/R^n \quad (1)$$

$$P(R,t) = P_m(R)e^{-t/\theta} \quad (2)$$

$$I(R) = \int_0^{a\theta} P(R,t) dt \quad (3)$$

The appropriate values for A, n, and θ depend upon soil type, soil moisture, explosive type, and soil preparation. These equations are valid on a spherical surface at radius R from the CG of a spherical charge. For a cylindrical charge used to attack a plane target, the equations must be modified.

The impulse due to a wave striking a plane surface must be modified to include only that component normal to the plane surface.



The normal component of the impulse (I) is given by:

$$I_n = I_x d / R \quad (4)$$

The preceding four equations apply to the spherical charges detonated in a uniform medium. If the projectile has only partially penetrated the structure or is not deeply buried in the subsoil, a correction should be made in the values of pressure and impulse. Drake and Little (4) present curves that may be used for this purpose. These curves were fit to equations using the least squares method, and the resulting equations were programmed to calculate a coupling factor (F) which corrects for both cylindrical shape and depth of penetration into the soil below the runway. The coupling factor is always less than one and is applied to the peak pressure. The applied impulse is thus affected to the same extent since impulse is directly proportional to peak pressure. The equation for applied impulse at the bottom surface of the runway is therefore given by:

$$I_{ap} = F x I_x d / R \quad (5)$$

where I is calculated from equation (3).

Breaching occurs in concrete when some critical condition is exceeded. Ross (3) gives the critical impulse for breaching as:

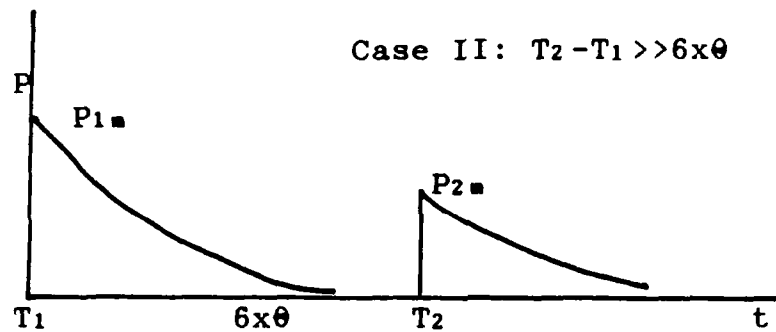
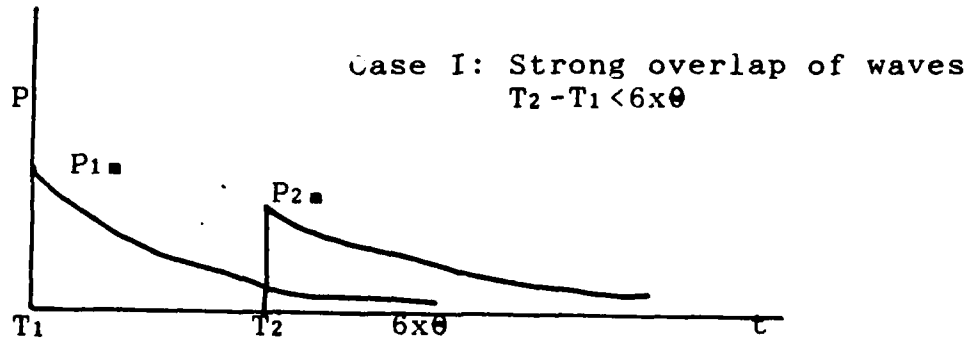
$$I_c = 0.005h(\rho_c f_c)^{1/2} \quad (6)$$

Breaching is presumed to occur when $I_{ap} \geq I_c$. For a single charge equations 1-6 are used to determine the breach dimensions when the criterion above is met.

Multiple charges can produce synergism at a point provided the pressure waves arrive at the point with adequate combined strength and with a short enough time interval between arrivals. Definitive data on the effect of time of arrival is not available. Therefore, some assumptions must be made regarding addition of impulses of two or more waves arriving

at a point. A brief discussion follows.

The sketches below apply to two pressure waves arriving at a particular point. The time constant θ is taken to be the same for both waves despite the fact that this is not necessarily the case. See Cole (2) for some data on waves in water.



It is assumed here that if $T_2 - T_1$ is greater than $6x\theta$, there will be no synergism, while if $T_2 - T_1$ is less than $6x\theta$ synergism will occur. In the case of no synergism, the individual pressure waves only need be considered. At those points where synergism does occur a method of adding the impulses must be specified. The method chosen here is simply to add the individual impulses at those points where the times of arrival of the waves are within $6x\theta$ of one another. Note that the individual impulses are given by the areas under their respective P vs t curves.

The computer program is based upon the model described above.

III. RECOMMENDATIONS

The model utilized here could be improved in a variety of ways. Among the improvements that might be considered would be utilization of the cylindrical shape calculations as reported by Ross (3). Another obvious improvement would be

to take into account the different characteristics of layers of soil and rubble that lie below the slab. Shock waves are significantly altered during passage from one medium into another, and this phenomenon is not accounted for in the present model.

The computer program could be improved in a number of ways. A first step would be incorporation of an advanced model as proposed above. Even though the existing model were retained, the program could be extended to cases in which the charges were detonated at different depths, rather than at identical depths as is now the case for multiple charges. The program could also be modified to require less execution time. The triple triangular configuration can take up to 50 seconds execution time with the existing program.

The most crucial recommendation is that additional experimental data be gathered for use in developing an improved model and a better computer program. Without this additional data, the benefits of further work on the model and/or program might prove to be marginal. The high cost of full scale experimental work indicates that data should be obtained from scaled models. It is therefore recommended that data be obtained using models scaled to, say, two inches thick concrete specimens. Dimensional analysis should be applied to the overall problem to find an acceptable method of scaling to an economical level.

REFERENCES

1. Bell, C. J., "Synergistic Effects of Bomb Cratering", USAF-UES Summer Faculty Program Report, 1987.
2. Cole, Robert H., Underwater Explosions, Princeton University Press, 1948.
3. Ross, C. A., et al, Concrete Breaching Analysis, AFATL-TR-81-105, Eglin AFB, FL, 1981.
4. Drake, J. L. and Little, C. D., Jr., "Ground Shock from Penetrating Conventional Weapons", The Interaction of Non-Nuclear Munitions with Structures Symposium, U. S. Air Force Academy, 1983.

**Appendices can be obtained from
Universal Energy Systems, Inc.**

Automated Motion Parameter Determination
from an Image Sequence

by

Stephen J. Dow
Department of Mathematics & Statistics
The University of Alabama in Huntsville

Final Report
Research Initiation Program
Sponsored by Air Force Office of Scientific Research
Conducted by Universal Energy Systems, Inc.
Contract no. P.O. S-210-9MG-025

July 1989

Abstract

A system for extracting the 6 parameters describing the motion of a known rigid object from an image sequence is discussed. A manual version of the system uses graphics overlay to visually line up an object model with the actual object in the images frames. Methods are developed here for automating the matching process. These methods involve the use of graphics generation, edge extraction, distance transformation, and match optimization. The matching step uses the average distance from a graphics silhouette pixel to the nearest edge pixel as a function to be minimized.

Acknowledgements

I would like to thank the Air Force Office of Scientific Research, Universal Energy Systems, and the Air Force Systems Command for sponsoring this research. This research also would not have been possible without the administrative and technical coordination provided by George Weekly, whose efforts are very much appreciated.

1. Introduction

Motion parameter determination from image sequences is a problem which has received considerable attention in recent years. Much of the research in this area has concentrated on constructing an optical flow field [4] or on deriving motion parameters from frame-to-frame feature point correspondences [7]. These approaches attempt to develop motion information directly from the image data independent of the specific object(s) undergoing motion. The methods discussed here assume that information about the object and imaging process are available. Specifically our problem is to compute values of 6 parameters describing the motion in space of a known rigid object; values of the parameters are desired for each time step corresponding to a frame in an image sequence. Object measurement data, camera parameters such as focal length, and initial frame motion parameter estimates are assumed to be known. This information allows the creation of a graphics image which can be compared to the real image data.

A system at Eglin AFB uses this technique to extract the motion parameters of falling munitions from film images. The system generates a graphics image of the object of interest for arbitrary hypothesized motion parameter values. The graphics image is overlaid on an image frame and an operator uses joysticks to adjust the

motion parameters until the camera and graphics images line up. The objective of this research effort was to develop methods of automating the matching process.

A simple system of automated matching has been developed and implemented in Fortran. The basic steps in the method developed here are (1) graphics generation, (2) edge extraction, (3) distance transformation, and (4) match optimization. A graphics generation module produces a silhouette or outline of the object of interest for arbitrary input values of the 6 motion parameters. The edge extraction and distance transformation steps are applied to each digitized input frame of the gray level image sequence. These operations enable computation of a measure of goodness of match between the graphics silhouette and edges found in the real images, based on the average distance between a silhouette pixel and its closest edge pixel. The match optimization process automates the process of making small adjustments in the motion parameters to obtain the best match. The details of each step are described in the subsequent sections.

2. Preliminaries

Some basic concepts from computer graphics and digital image processing are discussed here to make the report self-contained. Here the term digital image will simply

mean a 2-dimensional array of numbers such as may be declared in a Fortran subroutine by the statement

```
INTEGER IMG(NUMCOL, NUMROW)
```

An index pair (J,I) into this array is referred to as a pixel and the number IMG(J,I) is referred to as a pixel value. For gray level images, the number IMG(J,I) represents the gray level at pixel (J,I); that is, at the Jth column starting from the left and the Ith row starting from the top. (Standard raster-scan order is used for storing images; the top row of pixels is stored first from left to right, then the second row, and so on. The row index I appears second in Fortran arrays because in Fortran the first index varies most rapidly.)

Certain standard terminology has developed concerning the adjacency of pixels. Two pixels are said to be 4-adjacent or are said to be 4-neighbors of one another if one is immediately above, below, to the left, or to the right of the other. Thus the 4-neighbors of pixel (J,I) are (J,I-1), (J,I+1), (J-1,I), and (J+1,I). The 8-neighbors of pixel (J,I) are the 4-neighbors just listed together with (J+1,I+1), (J-1,I+1), (J+1,I-1), (J-1,I-1).

There are several places where the algorithms involve stepping along a path in the pixel grid. A sequence of pixels in which each successive pixel is a 4-neighbor (or 8-neighbor) of the preceding pixel will be called a 4-path (or 8-path). Such a path may be represented efficiently by

a chain code, which is a sequence of integers representing the direction taken at each step in the path. The directions taken to each of the 8-neighbors of a pixel C may be numbered as shown below:

```

      8 1 2
      7 C 3
      6 5 4
  
```

Then the 8-path indicated below starting at pixel Q would have chain code 2, 3, 4, 4, 3, 3, 2, 8.

```

      P P      P
      Q      P      P
      P P P
  
```

The 8-neighbor of pixel (J,I) in direction DIR has coordinates (J + JDEL(DIR), I + IDEL(DIR)) where the offsets IDEL, JDEL are as shown below:

DIR	1	2	3	4	5	6	7	8
JDEL	0	1	1	1	0	-1	-1	-1
IDEL	-1	-1	0	1	1	1	0	-1

The offsets may be conveniently stored in static arrays used as lookup tables when generating the pixels along an 8-path. The information needed to generate a path by this technique consists of the initial pixel coordinates, the path length, and the chain code.

The last concept to be discussed here is connectivity on the pixel grid. A set of pixels is said to be 4-connected (or 8-connected) if the set contains a 4-path (or 8-path) joining any two of its pixels. This definition is

usually applied to the set of pixels having a given value in an image. For example in the small image shown below, the set of 0-valued pixels is 8-connected but not 4-connected.

```

0 0 0 0 0 0 0 0
0 0 0 0 1 0 0 0
0 0 0 1 0 1 0 0
0 1 1 0 0 0 1 0
0 1 0 0 0 0 1 0
0 0 1 1 0 1 0 0
0 0 0 0 1 0 0 0
0 0 0 0 0 0 0 0

```

The fact that the set of 0-valued pixels above is not 4-connected can be more fully described by saying that this set has two 4-connected components, one component consisting of the 0-valued pixels 'outside' the ones and a second component consisting of those 'inside' the ones. A 4-connected component of a set is defined as a maximal 4-connected subset; more precisely a 4-connected component of a set S is a 4-connected subset C of S with the property that for any pixel P in C, C consists of exactly those pixels Q in S for which there is a 4-path contained in S joining P and Q.

3. Graphics Generation

Techniques for the graphics generation step have been described in a previous report [2]. The approach used here involves generating a wireframe model of the object, transforming the model to image coordinates, scan-

conversion, and boundary tracking. The final output is a chain code representing the silhouette of the object. A brief discription of the techniques is included here.

The wireframe model consists of vertices and edges. The portion of the object modeled as a solid of revolution involves a grid of such vertices and edges; for each interval along the axis of revolution a series of vertices and edges approximating a circle are generated. The remaining vertices and edges are given directly as input data.

Transformations convert the model from its real-world dimensions in a camera-centered coordinate system to image (screen) coordinates dimensioned in pixels. The first transformation consists of a translation and rotation using the 6 motion parameters which are to be determined. During the matching process these 6 parameters are adjusted. The remaining transformations involve perspective projection and a 2-dimensional scaling and translation. This portion of the transformation process is fixed for the whole image sequence. The component transformations are combined into a single 4x4 transformation matrix A. Details of the construction of A are given in the previous report. Each vertex (x,y,z) in the object model is converted to image coordinates (x',y') by the following equations:

$$[x \ y \ z \ 1] A = [u \ v \ 0 \ w]$$

$$\begin{aligned} x' &= u/w \\ y' &= v/w \end{aligned}$$

The edges of the model are stored as pairs of indices into the vertex array. Only the vertex coordinates are affected by the transformation above; their indices do not change. After the transformation has been applied, each edge is scan-converted to produce an 8-path of pixels approximating a line segment. Bresenham's algorithm is used here for computational efficiency (see [3] for details). The pixels of these scan-converted edges are set to 1 in an initially all-zero graphics image. After this step is complete we have a binary image whose 1-valued pixels form a picture of the wireframe model. The next step is silhouette extraction.

A boundary tracking algorithm for silhouette extraction has been employed. Two assumptions needed for this algorithm to work correctly are (1) that the object is entirely contained within the image, so that the first and last rows and columns of the graphics image are all zeros, and (2) that the set of model pixels (1-valued pixels) is 8-connected. Under these conditions the set of 0-valued pixels has one 4-connected component containing the outer part of the image, which represents the background surrounding the object of interest. The desired silhouette consists of those model pixels having a 4-neighbor in this

background component. Thus the silhouette forms the interface between the object and background. This silhouette is extracted as a single 8-path running clockwise around the object. An initial pixel is found by examining pixels in raster-scan order until a 1-valued pixel is encountered. The algorithm, which is coded as Fortran subroutine TRACK8, then steps from pixel to pixel, at each step performing clockwise search of the 8-neighbors of the current pixel to find the next pixel. This search starts with the 8-neighbor in direction $DIR - 2 \pmod{8}$, where DIR is the direction taken at the previous step. The result is returned as a chain code representing an 8-path which begins and ends at the same pixel.

4. Edge Extraction

Edge detection is a major area of computer vision research, reflecting the importance of edge location in interpreting images. Edges represent boundaries between meaningful regions, and are identified as locations of sudden change in the image intensity values. Often a gradient operator is involved. It produces two output images, a magnitude image and a direction image, from the input gray-level image. The magnitude and direction values at a given pixel may be interpreted as a vector pointing in the direction of greatest increase in image

intensity and whose length represents the magnitude of that increase. The Sobel gradient operator used here computes the output values from the 8-neighbors of an input pixel as follows. The horizontal and vertical components of the gradient vector are computed using the convolution masks:

$$\begin{array}{ccc} -1 & 0 & 1 \\ -2 & 0 & 2 \\ -1 & 0 & 1 \end{array} \quad \begin{array}{ccc} -1 & -2 & -1 \\ 0 & 0 & 0 \\ 1 & 2 & 1 \end{array}$$

This means that the components GX and GY at pixel (J,I) are

$$\begin{aligned} GX &= (IMG(J+1, I-1) + 2*IMG(J+1, I) + IMG(J+1, I+1)) \\ &\quad - (IMG(J-1, I-1) + 2*IMG(J-1, I) + IMG(J-1, I+1)) \\ GY &= (IMG(J-1, I+1) + 2*IMG(J, I+1) + IMG(J+1, I+1)) \\ &\quad - (IMG(J-1, I-1) + 2*IMG(J, I-1) + IMG(J+1, I-1)) \end{aligned}$$

The ordinary magnitude and direction of this vector would be $MAG = \text{SQRT}(GX**2 + GY**2)$, $THETA = \text{ARCTAN}(GY/GX)$; different formulas were used in the actual code to avoid the floating point computations and to discretize the direction to one of the 8 direction numbers discussed above for chain codes.

A simple edge extraction can be performed by thresholding the magnitude output; i.e. choose some threshold value and classify as edge pixels those pixels whose magnitude value is above the threshold. This generally results in a noisy edge image needing further processing.

A contour following approach [1] was used here to process the Sobel output. For a pixel to be classified as

an edge pixel by the contour following algorithm it must not only have a high gradient magnitude but also belong to a connected sequence of such pixels having some minimum length. Each pixel sequence is generated by stepping from pixel to pixel so as to follow the peak magnitudes while also keeping the gradient direction close to perpendicular to the direction of the path. These requirements help to eliminate locations of random fluctuations in image intensity from the final edge image. The following listing contains the essential parts of the contour following Fortran code while omitting some housekeeping details:

```

DO 20 I = 1, NUMROW
DO 20 J = 1, NUMCOL

MAG = M(J,I)
IF (MAG .LT. THRESH) GO TO 20
C(J,I) = LABEL
LENGTH = 0

DO WHILE (MAG .GT. THRESH)
DIR = D(J,I)
DMOVE = direction among DIR + 1, DIR + 2, DIR + 3
maximizing M(J + JDEL(DMOVE), I + IDEL(DMOVE))
J = J + JDEL(DMOVE)
I = I + IDEL(DMOVE)
IF (C(J,I) .EQ. LABEL) GO TO 10
C(J,I) = LABEL
MAG = M(J,I)
LENGTH = LENGTH + 1
CHAINCODE(LENGTH) = DMOVE
END DO

10 IF LENGTH < MINLENGTH THEN
retrace the contour setting C(J,I) = 0
20 CONTINUE

```

In the actual code being used a slightly different labeling scheme allows the arrays C and D above to coincide,

conserving space. This array is relabeled at the end to produce a binary output edge image.

5. The Distance Transformation

The distance transformation has as input a binary image and as output an image containing distance values. The two values in the input image will be assumed to be 0 and 1. The value of a pixel in the output image is that pixel's distance from the nearest 1-valued pixel in the input image. An example input and output array are shown below:

0	0	0	0	0	0	0	0	4	3	3	2	1	2	3	4
0	0	0	0	1	0	0	0	3	2	2	1	0	1	2	3
0	0	0	1	0	1	0	0	2	1	1	0	1	0	1	2
0	1	1	0	0	0	1	0	1	0	0	1	2	1	0	1
0	1	0	0	0	0	1	0	1	0	1	1	2	1	0	1
0	0	1	1	0	1	0	0	2	1	0	0	1	0	1	2
0	0	0	0	1	0	0	0	3	2	1	1	0	1	2	3
0	0	0	0	0	0	0	0	4	3	2	2	1	2	3	4

Formally the value of output image B at a given pixel (J,I) is given in terms of the input image A by

$$B(J,I) = \min \{ \text{dist}((J,I), (M,N)) : A(M,N) = 1 \}.$$

The pixel-to-pixel distance function used here is

$$\text{dist}((J_1,I_1), (J_2,I_2)) = \text{abs}(J_1 - J_2) + \text{abs}(I_1 - I_2)$$

where abs denotes absolute value. The algorithm used to perform the distance transformation was first introduced by Rosenfeld and Pfaltz [5]. It generates the output image given by the equations above but does not explicitly use

those equations. Rather the transformation is accomplished in two sequential scans of the image; one in standard raster scan order and the second in reverse order (starting in the lower right corner of the image and proceeding to the left and up). The distance transformation is used here to provide a measure of distance from silhouette pixels to edge pixels; therefore we apply the distance transformation to the edge image. The details of how it is used are discussed in the next section.

6. Match Optimization

As mentioned in the introduction the matching process involves comparison of the graphics silhouette output and the edge image. Let $\underline{u} = (x, y, z, a, b, c)$ denote the vector of motion parameters. Here x, y, z are translation parameters in a camera centered coordinate system and a, b, c are rotation parameters (Euler angles) about the 3 axes of this coordinate system. As discussed in section 3 and further in [2], values of these parameters are used in constructing the transformation matrix which in turn is used in the graphics generation process to produce an 8-path of silhouette pixels. Because the silhouette represents the boundary between the object and its background we expect the silhouette pixels to coincide with a subset of the edge pixels if the motion parameters are

correct. Motion parameters close to their true values will produce silhouette pixels close to the edge pixels. Thus we will measure match quality by taking the average distance between a silhouette pixel and the closest edge pixel to it. This match quality function will be denoted $f(\underline{u})$. The match optimization process consists of varying \underline{u} in order to minimize $f(\underline{u})$ locally.

Values of $f(\underline{u})$ are computed by getting the silhouette path corresponding to \underline{u} , summing the values of $D(J,I)$ over the pixels (J,I) along this path, and dividing by the length of the path. Here D is the distance image; $D(J,I)$ thus is the distance from pixel (J,I) to the nearest edge pixel. Since $D(J,I)$ is a nonnegative integer for every pixel, $f(\underline{u})$ is a nonnegative real number. In the ideal case where all silhouette pixels are also edge pixels, $f(\underline{u})$ is 0.

The minimization of $f(\underline{u})$ is a local minimization, that is, over a domain consisting of a neighborhood of the current value of \underline{u} . This is really only a restriction for the first frame, since in later frames the previously computed values can be used to get an initial estimate for the current frame. One reason for the need to restrict to a local minimization is that in a global formulation there are bound to be multiple values of \underline{u} minimizing $f(\underline{u})$. This can be seen from the fact that as the object moves away

from the camera the graphics model will shrink to a single pixel, and for certain values of the parameters this pixel will be an edge pixel, resulting in $f(\underline{u}) = 0$. This situation could be overcome by formulating the problem as a minimization over a large but depth-restricted domain. The more fundamental problem is that the function f as defined does not lend itself to analytic methods of computing minima directly; rather the minima must be found by a numerical search. The search becomes computationally prohibitive if too large an area is involved. However, as mentioned above, the local minimization restriction is not a problem under the assumptions of good initial frame estimates. To automate the initial frame parameter estimation would probably require techniques quite different from those discussed here; in particular it seems likely that additional computer vision techniques for extracting information from the images (beyond simple edge extraction) would be needed.

The minimization techniques which have been considered so far are iterative methods of incrementing \underline{u} based on the effects on $f(\underline{u})$ of small increments in each of the motion parameters. Let dx, dy, dz, da, db, dc denote these small increments and $\underline{u} = (x, y, z, a, b, c)$. The corresponding differentials in f are

$$f_1 = f(x + dx, y, z, a, b, c) - f(\underline{u}),$$

$$f_2 = f(x, y + dy, z, a, b, c) - f(\underline{u}),$$

...

$$f_6 = f(x, y, z, a, b, c + dc) - f(\underline{u}).$$

The vector $g(\underline{u}) = (f_1, f_2, \dots, f_6)$ is a discrete approximation to the gradient of f at \underline{u} . Several techniques of updating \underline{u} based on $g(\underline{u})$ have been implemented for experimental consideration and will be discussed here. A textbook approach is the method of steepest descent (see [6]). The method uses the fact that under mild assumptions a function of several variables decreases most rapidly in the direction of its negative gradient. The update step suggested by this method is to replace the current \underline{u} by $\underline{u} - c * g(\underline{u})$, where c is a positive constant. Our implementation of this method normalizes the update vector magnitude by taking $c = 1/r$, where

$$r = \text{sqrt}(f_1^2 + f_2^2 + \dots + f_6^2).$$

There is no absolute normalization involved here; it depends on the units in which the motion parameters are denominated. For the test data these units were inches and degrees. The update step in the direction $-c * g(\underline{u})$ is repeated as long as $f(\underline{u})$ decreases. Then a new $g(\underline{u})$ is computed, the process of updating \underline{u} repeated, and so on. This procedure continues until $f(\underline{u})$ falls below some tolerance or until a value of \underline{u} is found for which the prescribed update does not decrease $f(\underline{u})$.

Another strategy under consideration is to increment

along one of the 6 motion parameter coordinate axes rather than in the negative gradient direction. One approach to this strategy is to cycle through the six parameters, performing a minimization with respect to each variable in turn. Perhaps a better method is to find the coordinate giving the best response, minimize with respect to that coordinate, and repeat. A version of this technique has been implemented and works as follows. The values f_1, f_2, \dots, f_6 are computed as above, using positive increments dx, dy, \dots and then 6 more values g_1, g_2, \dots, g_6 are computed using increments $-dx, -dy, \dots$. The minimum of these 12 values indicates the coordinate and the increment sign (positive or negative) giving the best response. This direction is used as before, with repeated increments until no further improvement in $f(\underline{u})$ is obtained.

The discussion so far has dealt with how to proceed on a single frame, given initial estimates of the motion parameters. For the first frame these initial estimates must be generated by some manual interaction, such as is currently performed on the Eglin system. For the second frame the process uses the final value of \underline{u} from the first frame. After the second frame an initial estimate can be computed as the previous frame value plus the change in \underline{u} between the previous two frames.

7. Testing

There has not been time in this effort to perform much testing on the techniques developed here; all that can be done here is to give a rough description of how the methods performed on two sequences of images used during its development. The first sequence involved an object which turned out to be nonrigid, causing problems in obtaining an accurate match for the first frame. However it provided test images for the early development of the edge extraction and distance transformation steps and their integration with the graphics generation. Both image sequences involved dark objects against a much lighter background; as might be expected the edge extraction algorithm performed well on this data. Although accurate matching was unattainable for the first sequence, the match optimization algorithms were able to iterate toward an improved match from initial offsets. The data (image, object, and camera data) for the second frame sequence were obtained with a couple months left in the period of performance and transferred to the development system. Further development was needed to display overlays for verifying visually the match quality. On this second sequence the algorithms were able to track the object frame to frame in several tests with success varying depending on the parameter values input for the initial frame. In the

successful runs the system generated motion parameters resulting in a very close match (average distance along contour less than 2 pixels) for each frame in the sequence without intervention after the initial frame inputs. The match quality was also verified visually by overlay of the graphics on the image frames. However, for reasons not yet clear, the motion parameters generated do not match those generated by the Eglin system.

8. Recommendations

While this research effort has resulted in much progress toward the development of techniques and algorithms for automated motion parameter determination, the implementation and testing of those techniques is obviously far from complete. The results stated in the previous section are very preliminary and there was no time to perform and document carefully controlled tests. The match optimization algorithms continue to be refined as this report is being written and will almost certainly require further development. Although the testing done so far is rather sketchy, seeing the graphics overlay track the object across several frames of at least one image sequence leads one to conclude that the techniques discussed here merit further study.

At some point it would be useful to transport the

methods discussed in this report from the workstation developmental environments to the GADS (graphic attitude determination system) specific hardware. Without getting into all the technical details here, initially this would only involve conversion of the graphics display calls. This would allow direct comparison of the graphics generated by the two methods for equal motion parameter values. After verifying agreement of the graphics output, comparisons could be made of the motion parameters output by manual and automated matching. Later, when the automated algorithms have been further developed and tested, the algorithms could be converted to the specialized image processing hardware for computational speed.

References

- [1] S. J. Dow, Contour following and region extraction methods for digital images, Final report to U.S. Army Missile Command, Contract DAAH01-87-D-0021, D.O. 52, June 1988.
- [2] S. J. Dow, Model drawing algorithms for a matching problem, Final report, Air Force Summer Faculty Research Program, August 1988.
- [3] J. D. Foley and A. van Dam, Fundamentals of Interactive Computer Graphics, Addison-Wesley, 1982.
- [4] B. K. P. Horn and B. G. Schunck, Determining optical flow, Artificial Intelligence 17 (1981) 185 - 203.
- [5] A. Rosenfeld and J. L. Pfaltz, Sequential operations in digital picture processing, JACM 4 (1966), 471 -494.
- [6] G. R. Walsh, Methods of Optimization, John Wiley & Sons, New York 1975.
- [7] Y. Yasumoto and G. Medioni, Robust estimation of three-dimensional motion parameters from a sequence of image frames using regularization, IEEE Trans. on Pattern Anal. and Machine Int. 8 (1986), 464-471.

MODELING AND SIMULATION ON MICROCOMPUTERS, 1989

Proceedings of the SCS Western Multiconference
on Modeling and Simulation on Microcomputers
4-6 January 1989
San Diego, California

Edited by
R. Wade Allen
Systems Technology, Inc.



A Society for Computer Simulation International (Simulation Councils, Inc.) publication
San Diego, California

Bank-to-turn missile/target simulation on a desk-top computer

Michael. E. Wallis and Joseph J. Feeley
Electrical Engineering Department
University of Idaho
Moscow, Idaho 83843

ABSTRACT

Recent aerial combat studies (Arrow 1985) indicate bank-to-turn (BTT) missiles may have certain advantages over skid-to-turn (STT) missiles during short to medium range engagements. This has revitalized interest in the missile guidance and control problem and prompted a re-examination of the methods available to design and simulate guidance and control systems. This paper describes a simulation program written in Microsoft QuickBASIC for IBM PC-compatibles which greatly enhances the usefulness of an earlier microcomputer FORTRAN program. It permits interactive management of initial conditions and data files, displays animated multi-window graphics during the simulation, shows graphics plots for most program variables, and exports data to other programs. The program simulates a simple three-degree-of-freedom target model pursued by a six-degree-of-freedom BTT missile model with nonlinear features such as speed and altitude dependent aerodynamics, fuel consumption effects on mass and moments of inertia, second-order actuator and sensor dynamics with saturation, and noisy discretized signals. Guidance laws include classical proportional navigation and modern laws based on stochastic optimal control theory and differential game theory. The thoroughly commented source code is designed for clarity and easy modification through use of procedures and modules. A copy of the program is available on request.

INTRODUCTION

The design and verification of a missile guidance and control system typically includes a series of high-fidelity computer simulations followed by an analysis of the missile's simulated dynamics. Ideally these simulations are interactive and graphically oriented so that many options may be examined quickly. This paper describes a simulation program which satisfies those needs for bank-to-turn air-to-air missiles.

The simulation program is an enhanced version of an existing program (Shelton 1986), and models the pursuit and evasion dynamics of a missile and target engaged in 3-dimensional air-to-air combat. Missile dynamics are modeled by six-degree-of-freedom (6DOF) nonlinear differential equations that include speed and altitude effects influenced by aerodynamic forces and moments, and time-varying mass, center-of-gravity and inertia moments caused by fuel depletion. Actuators and sensors are modeled by second-order differential equations with limiting. Digital autopilot and guidance signals subject to noise, level saturation and discretization roundoff are also modeled. The target is modeled as an acceleration-limited point mass with three-degree-of-freedom (3DOF) dynamics and response times typical of a modern fighter aircraft.

A post-processor part of the program reads a binary output file containing over 150 variables saved during a simulation run. It can plot variables to the screen

and also save certain groups of variables in ASCII file format for further processing by other analysis programs such as PC-MATLAB.

A summary of requirements for the BTT steering policy is found in (Reidel 1980). A comparison of BTT and STT steering policies is found in (Reichert 1981). A status report of recent BTT control developments is found in (Arrow 1985). An assessment of current air-to-air missile guidance and control technology, with 80 references, is found in (Cloutier et. al. 1988). A recent paper on 6DOF BTT missile simulation and autopilot design is (Langehough and Simons 1988).

6DOF SIMULATION OF MISSILE DYNAMICS

This section develops the equations describing the missile's inertial motion and the aerodynamic and gravitational forces acting on it. A derivation of the equations in this section will be published in (Feeley, Wallis and Li 1989).

Reference Frames

Analyzing a dynamic problem with six degrees of freedom is simplified if critical parts of the problem are isolated with respect to certain special Cartesian coordinate systems. A good account of reference frame theory based on aerodynamics is found in (Etkin 1972). Five reference frames are used in the simulation.

Inertial Frame. Used to describe the absolute changes in velocity which cause Newtonian forces and moments. The Earth's rotation is negligible so its surface is used as a local inertial frame.

Body Frame. Used to sum all forces and moments acting on the missile. The body frame is fixed to the missile airframe with origin located at the missile's time-zero center-of-gravity (CG_0). The missile's true center-of-gravity (CG) moves along the body frame X-axis as fuel burns.

Relative Frame. Used to describe target location relative to missile. Its origin is located at CG_0 so the relative frame moves with the missile, but its axes remain parallel with the inertial frame axes. The relative frame is rotated into the body frame with yaw, pitch and roll Euler angles ψ , θ and ϕ .

Seeker Frame. Used to locate the target with simulated measurements of error angles σ_{EY} and $\sigma_{E\theta}$ relative to a gimballed platform fixed to the missile airframe. The seeker frame is rotated into the body frame with gimbal yaw and pitch angles ψ_c and θ_c .

Wind Frame. Used to describe aerodynamic forces and moments acting on the missile's airframe. The wind frame X-axis is defined parallel to the missile's

velocity vector. The body frame is rotated into the wind frame with aerodynamic elevation (attack) angle α and azimuth (sideslip) angle β .

Variable-Mass Dynamics

During flight a missile loses considerable mass as fuel burns, causing CG to move forward with respect to CG_0 . A further complication arises because the missile in this simulation is modeled with variable thrust, causing mass loss to vary with time. The simulation accommodates a two-stage thrust profile:

Thrust = 0 time < t_0
 Thrust = Th_1 $t_0 \leq$ time < t_1
 Thrust = Th_2 $t_1 \leq$ time < t_2
 Thrust = 0 $t_2 \leq$ time

The thrust profile is smoothed at the breakpoints by using small time-constant exponential functions.

Since the thrust profile is essentially a piecewise linear function of time all variable-mass effects are modeled as piecewise linear time functions which are smoothed together during the thrust transition periods. These functions are synthesized by assuming that the time-derivative of the missile's mass and moments of inertia are directly proportional to the rocket impulse time-derivative, where impulse is the time integral of thrust:

$$\text{Impulse} = \int \text{Thrust} \cdot dt \approx Th_1 \cdot (t_1 - t_0) + Th_2 \cdot (t_2 - t_1)$$

First, three impulse-fraction constants are defined:

$$\begin{aligned} \text{ImpFrac}_1 &= Th_1 / \text{Impulse} \\ \text{ImpFrac}_2 &= Th_2 / \text{Impulse} \\ \text{ImpFrac}_3 &= (\text{ImpFrac}_1 - \text{ImpFrac}_2) \cdot (t_1 - t_0) \end{aligned}$$

These constants allow the impulse to be re-described as a normalized linear function of time t :

$$\begin{aligned} \text{ImpNorm} &= 0 && t < t_0 \\ \text{ImpNorm} &= \text{ImpFrac}_1 \cdot t && t_0 \leq t < t_1 \\ \text{ImpNorm} &= \text{ImpFrac}_2 \cdot t + \text{ImpFrac}_3 && t_1 \leq t < t_2 \\ \text{ImpNorm} &= 1 && t_2 \leq t \end{aligned}$$

Missile mass is now represented by a time function:

$$\text{Mass}(t) = \text{Mass}_0 - \text{ImpNorm}(t) \cdot d\text{Mass}$$

where Mass_0 is the missile's time-zero mass and $d\text{Mass}$ is defined so $[\text{ImpNorm}(t_2 - t_0) \cdot d\text{Mass}]$ is the total mass lost from t_0 to t_2 . The missile's principal moments of inertia are similarly defined:

$$\begin{aligned} I_{xx}(t) &= I_{xx0} - \text{ImpNorm}(t) \cdot dI_{xx} \\ I_{yy}(t) &= I_{yy0} - \text{ImpNorm}(t) \cdot dI_{yy} \\ I_{zz}(t) &= I_{zz0} - \text{ImpNorm}(t) \cdot dI_{zz} \end{aligned}$$

Finally, CG is located along the body frame positive X-axis using yet another time function:

$$X_{cg}(t) = \text{ImpNorm}(t) \cdot dCG$$

I_{xx} , I_{yy} , I_{zz} and X_{cg} , and their derivatives, and Mass are then included in the derivation of the missile dynamic equations. The time-derivative of Mass is accounted for in the rocket thrust term.

Aerodynamic Relationships

External forces and moments are impressed on the missile because of aerodynamic lift and drag. These effects depend on the missile's orientation relative to its velocity vector, as well as its Mach number and the local dynamic air pressure.

Dynamic air pressure DynPrs is a function of the local air density ρ and the magnitude of the missile's body frame inertial velocity \bar{V}_b :

$$\text{DynPrs} = \frac{1}{2} \cdot \rho \cdot V_b^2$$

Mach number is a normalized function of V_b and the local speed-of-sound SOS :

$$\text{Mach} = V_b / \text{SOS}$$

SOS and ρ are in turn functions of the missile's inertial altitude H , and are modeled using equations fitted to a set of tabulated data (McCormick 1979).

Forces and Moments. The aerodynamic forces and moments acting on the missile airframe can now be described as functions of Mach number, angles α and β , and "effective" fin deflection angles δ_p , δ_q and δ_r .

As mentioned earlier, angles α and β orient the wind frame with respect to the body frame. The angle-of-attack α describes the angle between the missile's body frame velocity vector \bar{V}_b and the body frame XY plane, while the sideslip angle β describes the angle between \bar{V}_b and the body frame XZ plane. Nonzero values of α and β indicate changes in aerodynamic lift along the body-frame Z- and Y-axes respectively, and changes in aerodynamic drag along the body-frame X-axis. These lift and drag variations in turn indicate that aerodynamic forces and moments acting on the missile airframe are also changing.

δ_p , δ_q and δ_r are called "effective" roll, pitch and yaw angles because they are synthesized from the missile's four physical fin deflections to portray equivalent rolling, pitching and yawing motions of the missile about its XYZ body axes. Nonzero deflections alter the cross-sectional area of the missile, thus modifying lift and drag. The synthesis of effective fin deflections is discussed in (Cronvich 1986).

Stability Derivatives. The aerodynamic forces (F_x, F_y, F_z) and moments (L, M, N) acting on a missile are described in terms of the partial derivatives of the forces and moments with respect to the missile's body frame linear velocities (U, V, W), angular velocities (P, Q, R) about the body-frame XYZ axes, velocity vector orientation angles α and β , and fin deflection angles δ_p , δ_q and δ_r . A complete set of partial derivatives are called the stability derivatives for the missile. An excellent general reference on stability derivative theory is found in (Nielsen 1960).

Stability derivative values are usually not defined by mathematical functions. They are instead interpolated from aerodynamic coefficient arrays tabulated from empirical values measured during wind-tunnel testing of the missile. This simulation uses 15 aerodynamic coefficient arrays taken from Shelton's program (Shelton 1986). Their parameter dependence is indicated parenthetically:

- $C_{D_0}(\delta_q, \text{Mach}, \alpha)$ - drag from pitch fin deflection
- $C_{D_T}(\text{Mach}, \alpha)$ - base drag due to Mach
- $C_{L_\beta}(\text{Mach}, \alpha)$ - roll moment from sideslip
- $C_{L_\delta}(\text{Mach}, \alpha)$ - roll moment from roll fin deflection
- $C_{L_P}(\text{Mach}, \alpha)$ - roll damping moment from pitch rate
- $C_{M_\alpha}(\text{Mach}, \alpha)$ - pitch moment from angle of attack
- $C_{M_\delta}(\text{Mach}, \alpha)$ - pitch moment from pitch fin defl.
- $C_{M_q}(\text{Mach}, \alpha)$ - pitch moment from pitch fin defl.
- $C_{N_0}(\text{Mach})$ - lift due to Mach
- $C_{N_\delta}(\text{Mach}, \alpha)$ - lift from pitch fin deflection
- $C_{N_\beta}(\text{Mach}, \alpha)$ - yaw moment from sideslip
- $C_{N_\delta}(\text{Mach}, \beta)$ - yaw moment from yaw fin deflection
- $C_{N_r}(\text{Mach}, \beta)$ - yaw damping moment from yaw rate
- $C_{Y_\beta}(\text{Mach}, \alpha)$ - side force from sideslip
- $C_{Y_\delta}(\text{Mach}, \beta)$ - side force from yaw fin deflection

Force and Moment Coefficients. The aerodynamic coefficients are multiplied by dynamic parameter values to form three XYZ body frame force coefficients and three coefficients describing moments about the body frame XYZ axes. The body frame force coefficients are

$$\begin{aligned} C_x &= C_D + C_{DT} \\ C_y &= C_{Y\beta}*\beta + C_{Y\delta_r}*\delta_r \\ C_z &= C_{N\alpha}*\alpha + C_{N\delta_q}*\delta_q \end{aligned}$$

while the moment coefficients are

$$\begin{aligned} C_l &= C_{L\delta_p}*\delta_p + C_{Lp}*P*L_{2v} + C_{L\beta}*\beta \\ C_m &= C_{M\delta_q}*\delta_q + C_{Mq}*Q*L_{2v} + C_{M\alpha} \\ C_n &= C_{N\delta_r}*\delta_r + C_{Nr}*R*L_{2v} + C_{N\beta}*\beta \end{aligned}$$

where

$$L_{2v} = L_{ref}/2*V_b$$

and L_{ref} is an effective reference missile length used to describe moments about CG. The conceptual meaning of L_{ref} is similar to the definition of an effective cross-sectional area of a three-dimensional object.

Aerodynamic Forces and Moments. The aerodynamic force coefficients are converted into forces by multiplication with the local dynamic pressure, the missile effective cross-sectional area S_{ref} , and missile mass:

$$\begin{aligned} F_x &= C_x * DynPrs * S_{ref} * Mass \\ F_y &= C_y * DynPrs * S_{ref} * Mass \\ F_z &= C_z * DynPrs * S_{ref} * Mass \end{aligned}$$

The moment coefficients are similarly converted into aerodynamic moments about the body frame XYZ axes by multiplying with $DynPrs$, S_{ref} and L_{ref} :

$$\begin{aligned} L &= C_l * DynPrs * S_{ref} * L_{ref} \\ M &= C_m * DynPrs * S_{ref} * L_{ref} \\ N &= C_n * DynPrs * S_{ref} * L_{ref} \end{aligned}$$

Equations of Motion

A complete set of 6DOF equations can now be described by summing all external forces and moments acting on the missile and setting them equal to the forces and moments caused by inertial acceleration. Inertial and external components are indicated by i and e subscripts, respectively.

First, the inertial accelerations acting on the missile may be expressed in the body frame as

$$\begin{aligned} A_{ix} &= \ddot{U} + Q*W - R*V + \dot{X}_{cg} - X_{cg}*(Q^2 + R^2) \\ A_{iy} &= \ddot{V} + R*U - P*W + 2*R*\dot{X}_{cg} + X_{cg}*(P*Q + \dot{R}) \\ A_{iz} &= \ddot{W} + P*V - Q*U - 2*Q*\dot{X}_{cg} + X_{cg}*(P*R - \dot{Q}) \end{aligned}$$

The second derivative of X_{cg} is retained to model effects during rocket thrust transients.

These inertial accelerations are set equal to the accelerations caused by external forces, which include the aerodynamic forces plus rocket thrust and gravity G transformed into the body frame:

$$\begin{aligned} A_{ex} &= F_x/Mass + G_{bx} + Thrust/Mass \\ A_{ey} &= F_y/Mass + G_{by} \\ A_{ez} &= F_z/Mass + G_{bz} \end{aligned}$$

Next, the inertial moments about the body frame XYZ axes are described by

$$\begin{aligned} L_1 &= \dot{P}*I_{xx} + P*\dot{I}_{xx} + Q*R*(I_{zz} - I_{yy}) \\ M_1 &= \dot{Q}*I_{yy} + Q*\dot{I}_{yy} + R*P*(I_{zz} - I_{xx}) \\ N_1 &= \dot{R}*I_{zz} + R*\dot{I}_{zz} + P*Q*(I_{yy} - I_{xx}) \end{aligned}$$

These are set equal to the sum of external moments acting on the missile, which include the aerodynamic moments and two CG terms:

$$\begin{aligned} L_o &= L \\ M_o &= M - Mass*G_{bz}*X_{cg} \\ N_o &= N + Mass*G_{by}*X_{cg} \end{aligned}$$

These equations may be simplified to increase program speed by ignoring the small magnitude inertial terms, most of which include derivatives of the CG dependent variables.

3DOF SIMULATION OF TARGET DYNAMICS

A controllable target is included to test the missile's tracking and steering capabilities. The target uses simple evasive algorithms to realistically model the characteristics of a human-piloted aircraft.

The target maintains its initial heading while remaining at constant altitude and velocity until the missile-target relative separation is less than 6000 feet. The target then makes a 45° maneuver out of the inertial XY plane by setting its normal X and Z accelerations to equal-magnitude values. A given set of acceleration magnitudes and signs define each algorithm. At one second to estimated closest approach the target makes a 180° roll maneuver by setting its Y and Z accelerations to 0 and 9 G's.

The target's response to acceleration commands is governed by a simple differential equation of the form

$$\dot{\bar{A}} = (\bar{A}_c - \bar{A})/\tau$$

where \bar{A} is the actual body acceleration, \bar{A}_c is the commanded acceleration, and τ is the response time-constant of the target. Commanded accelerations are restricted to a range representing the limits of a human pilot's mental alertness, ± 9 G's.

NAVIGATION SYSTEM

This section describes how the missile's sensing and control systems are simulated.

Gimballed Seeker

The seeker is typically a gimballed platform which is used to track an evading target and provide electronic signals for the autopilot system. The seeker reference frame is fixed to this platform, and is defined by two gimbal angles, ψ_c and θ_c , which represent the measured yaw and pitch of the seeker frame relative to XZ and XY planes of the body frame. Two error angles, σ_{EY} and σ_{EP} , represent the measured azimuth and elevation of the target in the seeker frame. Non-zero values of σ_{EY} and σ_{EP} cause feedback signals which realign the seeker platform.

Measured Error Angles σ_{EY} and σ_{EP} . The error angles are simulated by transforming the target's perfect-information displacements from the relative frame into the seeker frame and the forming a set of perfect-information angles locating the target in the seeker frame. These angles are then noise-corrupted to model measurement error, and discretized and limited to mimic an analog-to-digital conversion.

The relative frame displacements are first brought into the body frame by a transformation using Euler

angles ψ , θ and ϕ . They are then rotated into the seeker frame with gimbal angles ψ_G and θ_G , providing the closed feedback loop necessary to drive σ_{EY} and σ_{EP} to zero. Once in the seeker frame the displacements are used to form orthogonal pitch and yaw angles lying in the seeker XY and XZ planes.

Gaussian-distributed wideband noise is added to these angles to model measurement errors. Both angles are then discretized by a sequence of multiplication and division by 1000, with an intermediate integer truncation. The pitch and yaw angles are finally limited to $\pm 4^\circ$ and $\pm 2^\circ$ respectively to form "measured" pitch and yaw angles σ_{EP} and σ_{EY} .

Filtered Error Angles ψ_E and θ_E . The measured error angles are then treated as a set of electric control signals used to re-orient the seeker platform. They are passed through a second-order under-damped system simulating the dynamics of the seeker drive mechanism. The output of this system is taken as the seeker yaw and pitch error angles ψ_E and θ_E , and their first derivatives.

LOS Error Angles ψ_{LOS} and θ_{LOS} . The filtered error angles and rates are then scaled, added and limited to form a set of Line-of-Sight (LOS) error angle rates:

$$\begin{aligned} \dot{\psi}_{LOS} &= \dot{\psi}_E + 30\psi_E & -75^\circ/\text{sec} \leq \dot{\psi}_{LOS} \leq 75^\circ/\text{sec} \\ \dot{\theta}_{LOS} &= \dot{\theta}_E + 30\theta_E & -75^\circ/\text{sec} \leq \dot{\theta}_{LOS} \leq 75^\circ/\text{sec} \end{aligned}$$

The LOS rates are made proportional to the error angles in the event measured error angles σ_{EY} and σ_{EP} are limited, in which case filtered error angles ψ_E and θ_E are also limited and have zero derivatives.

Gimbal Angles ψ_G and θ_G . The LOS error angle rates are identical with the gimbal angle rates once the inertial rotation of the missile is removed. This is accomplished by transforming the inertial angular velocity $\bar{\omega}$ of the body frame from the body frame into the seeker frame and removing it from the LOS rates.

After integrating, gimbal angles ψ_G and θ_G are produced. In the event the seeker platform is highly unaligned with the target, ψ_G is limited to $\pm 65^\circ$ and θ_G is limited to $\pm 70^\circ$ to represent the mechanical constraints of the seeker platform.

GUIDANCE SYSTEM

The missile guidance system uses measured relative target range and (optionally) range-rate to generate commanded horizontal and vertical body-frame accelerations A_{YC} and A_{ZC} . These acceleration commands are sent to the missile autopilot system and converted into fin deflection commands which steer the missile.

The default guidance system is based on a proportional navigation guidance law with user-defined gain. Provisions have been made to include guidance laws based on stochastic optimal control and differential game theory.

MISSILE AUTOPILOT

The autopilot converts body acceleration commands A_{YC} and A_{ZC} generated by the guidance system into commanded fin deflection angles F_{1C} , F_{2C} , F_{3C} and F_{4C} . References on BTT autopilot design may be found in (Aarow 1982), (Williams and Friedland 1986) and (Cronvich 1986).

The missile is steered by four tail-mounted fins whose orientations are given by fin deflection angles F_1 , F_2 , F_3 and F_4 . These angles are algebraically related to the effective roll, pitch and yaw deflection angles δ_p , δ_q and δ_r which are used to compute values of the aerodynamic coefficients.

The acceleration commands from the guidance system are first used to form a commanded roll angle:

$$\phi_c = \text{ArcTan}(A_{YC}/-A_{ZC})$$

If A_{ZC} is zero, the ArcTan argument is sign indeterminate so ϕ_c is set to $\pm \pi/2$ depending on the sign of the actual body roll rate P . ϕ_c is made zero if the magnitudes of A_{YC} or A_{ZC} are less than certain minimum values, thus providing a noise threshold that prevents a roll command unless both commanded body accelerations are sufficiently large.

Commanded accelerations A_{YC} and A_{ZC} and commanded roll angle ϕ_c are combined with other parameters such as angles α and β , dynamic pressure and missile mass to form body rotation rate commands P_C , Q_C and R_C . The commanded body rotation rates are then combined with the true body rotation rates P , Q and R , α and β , mass, dynamic pressure, and certain of the aerodynamic coefficients to form a set of commanded effective fin deflections δ_{pC} , δ_{qC} and δ_{rC} .

These effective fin deflection commands are then algebraically transformed into fin deflection commands F_{1C} , F_{2C} , F_{3C} and F_{4C} which are treated as signals used to drive a set of mechanical fin actuators. The fin actuators are modeled as second-order under-damped systems, and limiting is used to model maximum fin deflections and rates. If the difference between a commanded and actual deflection is less than $.05^\circ$, it is set to zero to provide a noise threshold.

SIMULATION PROGRAM

The simulation program is presented to the user as a sequence of text menus which are branched through using single alphanumeric keystrokes. Simulation data may be entered directly into the program at the lower levels of each menu branch. All keyboard entries are monitored by a "smart" line editor which ignores invalid selections, range checks data entries, and monitors timebase information to prevent conflicts with the numerical integration and other procedures sensitive to the simulated time frame.

As the simulation begins a graphics screen appears and is updated at menu-specified intervals. Missile and target flight paths are shown as three orthographic projections which are dynamically scaled as either aircraft moves offscreen. Three other simple orthographic views show the missile's inertial orientation. A final window shows a representation of the missile's four physical fin deflections. A text sidebar lists components of the missile's inertial location, scaling factors for the flight path windows, real and simulated elapsed times of the simulation, missile Mach number, and estimated target range and time-to-go before closest approach. Figure 1 shows an actual screen display of a completed simulation.

The simulation may be stopped at any time or manually stepped to closely examine changes in the graphics displays. The program branches back to the main selection menu after the simulation terminates normally or is manually aborted.

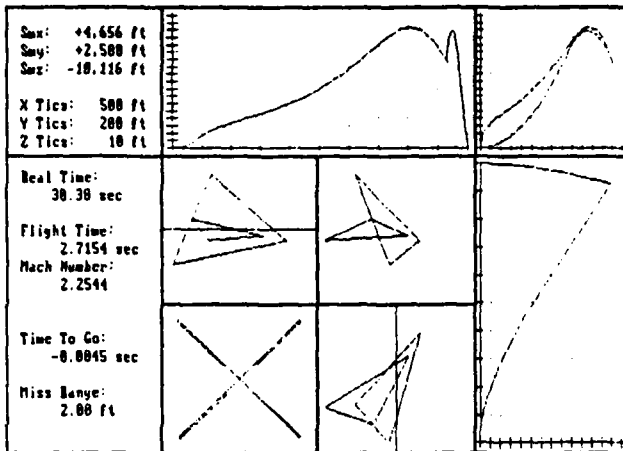


FIGURE 1: Graphics Screen Display of Simulation.

All menu-selectable program initial conditions are stored in named text files which may be loaded, altered or resaved using menu selections.

Over 150 simulation variables are automatically stored in a named file at menu-specified intervals. Data is saved in binary form to reduce running time and conserve disk space. The output filename may be changed with a menu selection, or the data storage feature may be turned off.

Other menu options include

- guidance law
- integration options: 1st, 2nd and 4th-order Runge-Kutta and adaptive Runge-Kutta-Fehlberg methods; time-step, minimum time-step and error tolerance
- missile altitude, Mach number and measurement noise
- initial target range, azimuth and elevation angles, flight aspect angle, and response time-constant
- general options such as output file and screen update intervals, and a "speed" switch causing the simulation to ignore higher-order effects

DATA POST-PROCESSOR PROGRAM

The data post-processor is used to read any of the binary output files created by the simulation program. One menu selection allows replaying the simulation program's graphics screen at high speed. Another selection allows plotting any two program variables against each other. Future enhancements will allow simple mathematical operations such as summing and multiplying variables before plotting.

Other menu selections allow the export of pre-defined groups of variables as ASCII text files. These files may be read by other programs such as PC-MATLAB for further analysis.

HARDWARE AND SOFTWARE INFORMATION

Until recently comprehensive nonlinear analysis has been carried out exclusively on mainframe and mini-computers, but advances in desktop personal computer (PC) technology have permanently altered this situation. PC machines have always enjoyed certain key advantages over larger machines, such as easy access and low cost, but lately they also have acquired the speed and data storage needed for computationally intensive projects.

The highly competitive market in PC programming languages has also produced a variety of inexpensive and easy-to-use integrated development packages which have no counterpart on larger machines. This simulation, for example, represents over 10,000 lines of commented source code developed and tested over a six month period using Microsoft QuickBASIC 4.00b, a development environment with an integrated "smart" editor-debugger which reduces program development to an almost ideal run-edit cycle.

Some of the compiled QuickBASIC features which differ from standard interpreted BASIC include

- multi-module programs with include files
- true subprograms and functions which allow mixed-language support with procedures written in other Microsoft languages, including C and FORTRAN
- modern structured programming functions such as SELECT CASE and block IF... THEN
- alphanumeric labels with no required line numbers
- unlimited array size up to available system memory
- IEEE number format; use of 80x87 math coprocessors
- automatic syntax checking as code is typed in
- context-sensitive on-line help menus.
- debugging tools: watch variables, single-step trace mode, fixed or conditional breakpoints, etc.

The compiled programs run on most PC-compatible computers with a minimum of 320k of memory, an 80x87 math coprocessor, single floppy drive and CGA, EGA or Hercules graphics adapter. Working with the source code in QuickBASIC's editor/debugger requires a full 640k of memory and a hard disk. The programs were tested on the following PC class computers: an 8Mhz 8088-2 based XT clone, a 6Mhz 80286 based IBM AT, an 8Mhz 80826 based Hewlett-Packard Vectra, and a 20Mhz 80386 based Dell 310. Using 4th-order Runge-Kutta integration with 5ms time-steps, the simulator runs about 10 to 30 times slower than real-time on a Dell 310, depending on other program options, and runs an additional 5 times slower on a HP Vectra.

ACKNOWLEDGEMENTS

This research was partially funded by the Air Force Office of Scientific Research, Bolling AFB, D.C., under contract F49620-85-C-0013/SB5851-0360. Special thanks are also given to Dr. James R. Cloutier and Lt. Roger Smith of the Air Force Armament Laboratory for their assistance.

REFERENCES

- Aarow, A. 1982. "An Analysis of Aerodynamic Requirements for Coordinated Bank-to-Turn Missiles." NASA CR 3644.
- Aarow, A. 1985. "Status and Concerns for Bank-to-Turn Control of Tactical Missiles." *Journal of Guidance and Control*, vol. 8, no. 2 (Mar-Apr): 267-274.
- Cloutier, J.R.; J.H. Evers and J.J. Feeley. 1988. "An Assessment of Air-to-Air Missile Guidance and Control Technology." In *Proceedings of the 1988 American Control Conference* (Atlanta, GA, June 15-17). ACC, 133-142.
- Cronvich, L.L. 1986. "Aerodynamics Considerations for Autopilot Design." *Progress in Astronautics and Aeronautics (Tactical Missile Aerodynamics)*, vol 104: 3-42.

Etkin, B. 1972. *Dynamics of Atmospheric Flight*, John Wiley & Sons, Inc.

Feeley, J.J.; M.E. Wallis and G. Li. 1989. "A Game Theoretic Guidance Law for Bank-to-Turn Air-to-Air Missiles." To be published.

Langehough, M. A. and F. E. Simons. 1988. "6DOF Simulation Analysis for a Digital Bank-to-Turn Autopilot." In *Proceedings of the 1988 American Control Conference* (Atlanta, GA, June 15-17). ACC, 573-578.

McCormick, B.W. 1979. *Aerodynamics, Aeronautics and Flight Mechanics*. John Wiley & Sons, Inc. pp. 16-22, 624, 625.

Nielsen, J.N. 1960. *Missile Aerodynamics*. McGraw-Hill Book Company, Inc.

Reichert, R. T. 1981. "Homing Performance Comparison of Selected Airframe Configurations Using Skid-to-Turn and Bank-to-Turn Policies." NASA CR 3420.

Reidel, F. W. 1980. "Bank-to-Turn Control Technology Survey for Homing Missiles." NASA CR 3325.

Shelton, L.C. 1986. "6-DOF Bank-to-Turn Missile Simulation of the ILAAT Missile with Look-Up Tables for the Aerodynamic Coefficients", Air Force Armament Laboratory, unpublished. A copy is available on request from the authors of this paper.

Williams, D.E. and B. Friedland. 1987. "Modern Control Theory for Design of Autopilots for Bank-to-Turn Missiles." *Journal of Guidance and Control*, vol. 10, no. 4 (Jul-Aug): 378-386.

**RESEARCH INITIATION PROGRAM FINAL REPORT
SUBMITTED TO UNIVERSAL ENERGY SYSTEMS, INC.
UNDER 1988 USAF-UES SUMMER FACULTY RESEARCH PROGRAM**

Principal Investigator: Dr. Manuel A. Huerta
Professor of Physics
Soc. Sec. No. 262-70-9459
Telephone No. (305) 284-2323
Physics Department
University of Miami
Coral Gables, FL 33124

Minigrant Period of Performance: 1 January 1989 through 31 December 1989.

Title: Two dimensional MHD simulation of
Accelerating Arc Plasmas

Summer 88 Research Location: AFATL/SAH
Eglin AFB, FL 32542-5000

USAF Research Contact: Mr. Kenneth K. Cobb
AFATL/SAH
Eglin AFB, FL 32542-5000
Tel No. (904)-882-0360

Signed: Manuel A. Huerta

Dr. Manuel A. Huerta
Professor of Physics

Date: Jan. 12, 1990

**Two Dimensional Simulation of
Railgun Plasma Armatures**

by
Manuel A. Huerta

ABSTRACT

We have developed a fully heat conducting two dimensional MHD code to simulate the internal dynamics of a railgun plasma armature. We use the equations of resistive MHD, with an energy equation that includes Ohmic heating and heat transport in the radiation diffusion approximation. We use an explicit Flux Corrected Transport code to advance all quantities in time. We completed a run of our simulation that consumed 50 hours of CPU time in a ETA10 supercomputer. The run shows what appear to be secondary arcs.

Acknowledgements

My graduate student, Mr. G. Christopher Boynton, and I would like to thank Universal Energy Systems, the Air Force Systems Command, and the Air Force Office of Scientific Research for the Research Initiation Minigrant that enabled us to perform this research. We also thank the Florida State University Computer Center for a grant of 120 hours of CPU time in their ETA10 supercomputer.

I. Introduction

The work under this minigrant was a followup to the work that my graduate student, Mr. G. C. Boynton, and I did at AFATL/SAH under the 1988 UES-USAF Summer Faculty Research Program. Most of the work was done during the summer months of 1989, although some work continued until the end of the grant period.

Our work has centered on developing a two dimensional time dependent simulation of plasma armatures. We model the plasma with the equations of resistive MHD and we use a two dimensional fully explicit flux corrected transport code to advance all quantities in time. The physical effects that we include in our model are the same as in the steady, one dimensional model of Powell and Batteh¹. Therefore we leave out viscosity, and other effects that can be important in a boundary layer. A good deal of effort has also been expended on developing graphical methods that allow convenient display of the results.

II. Results

Since the beginning of this grant two papers have appeared based on our previous work. The first paper² used an adiabatic energy equation and constant electrical conductivity with a density cutoff. Our second paper³ treated the plasma as isothermal, also with a density cutoff for the electrical conductivity. In those papers we treated the temperature in a simplified way because the large temperature gradients that exist in the plasma were giving us trouble with our algorithms.

Our main effort under this minigrant was to develop a code with a full energy equation with heat transport in the radiation diffusion approximation. We are pleased that we have succeeded in running a simulation with the complete energy equation. Our run consumed 50 hours of CPU time at the ETA10 supercomputer of the Florida State University Computer Center. We found that the ETA10 could run our program about 20 times faster than a VAX 8650. A grant of 120 hours of free supercomputer time from the FSUCC made our calculations possible.

We show some figures that are representative of our results. Figure 1 shows a plot of the component of the current density J_y across the entire computational region. The simulation uses a grid with 120 cells in the direction of travel and 10 cells in the rail to rail direction, with a time step of $.23 \times 10^{-9}$ sec. We show the plasma armature after 886,000 time steps. The elapsed time since firing is 3.228×10^{-4} sec, by which time the velocity of the projectile is 4.9×10^3 m/sec, and the 2 gm projectile has traveled 9.5×10^{-1} meter down the barrel. In Figure 1 a disturbance seems to be present in J_y near the rear of the plasma. Figure 2 shows an enlarged view in which we just show J_y toward the rear, from cells 40 to 120, after 886,000 time steps. Figure 3 shows J_y after 887,000 time steps, the disturbance is growing, and is detaching from the main arc (1,000 time steps amount to .23 microsec). Figure 4 shows J_y after 890,000 time steps, a clear secondary arc has formed. Figure 5 shows J_y after 895,000 time steps, the secondary arc is falling behind so far that it is getting out of our computational region. Figure 6 shows the temperature at 890,000 time steps, the same as in Figure 4. The temperature has risen in the rear where the currents are building up. Figure 7 shows the current J_y at 890,000 time steps as in Figure 4, but here it is shown for the entire computational grid. Clearly the secondary arc that looks so large in Figure 4 actually carries only a small fraction of the total current.

We believe that adding ablation to the model will increase the strength of the secondary arcs because of the increased material at the rear. The secondary arcs are clearly not the result of some numerical instability. Actually we have figures that show a secondary arc starting to form, but then decaying.

III. Recommendations

Recently Hawke⁴ et al. have reported on the effects believed to prevent the attainment of high velocities in the HELEOS rail launcher. These effects were first discussed by Parker^{5,6} who pointed out that rail ablation, secondary arc formation or restrike, and viscous drag, represented important loss mechanisms. These effects were discussed intensively at the recent Workshop on Secondary Arcs and Hybrid Armatures organized by Keith Jamison and Dennis Keefer, held at the College of Engineering of the University of New Mexico in Albuquerque, N. M., during September 12 and 13, 1989. Dr. Huerta presented some partial results about secondary arc formation in our successful run at that workshop. Since then we have examined our output more thoroughly and are very excited because our simulation shows secondary arc formation pretty much in the way that they appear in the experimental data presented at the workshop.

It would be interesting to understand the instabilities in the temperature, or possibly other quantities, that trigger the secondary arc formation in the figures we presented above. A possible mechanism might be that there is a local increase of temperature that increases the electrical conductivity and the current density so much that the heat diffusion is unable to get rid of the Ohmic heat, leading to further heating. Eventually the heat conductivity might increase sufficiently to stop the growth.

We believe that it is essential to include rail ablation in the model if one hopes to simulate secondary arcs that really resemble the observed ones. It is easy to treat rail ablation by adding mass to the computational cells that are adjacent to the rails. The ablated mass would be added at rest relative to the rails and would tend to fall behind in the armature. Some of it might possibly be left behind altogether and not contribute much to an ablation drag force. Some of the ablated mass could get entrained into the forward movement of the armature, however, and constitute a drag force that would reduce the acceleration of the armature. The entrainment is something that cannot be easily modeled, the way the amount of the ablated mass can be, and only a simulation can illustrate it. There would undoubtedly be interesting flows and other arc phenomena influenced by the ablation. We are fully confident that we can do this work provided we have the computer time. A run of our fully explicit code should take some 50 hours of supercomputer time. This might be reduced if we can run a code in which the diffusion equations for the temperature and the magnetic fields are treated implicitly.

References

1. Powell, J. D., and Batteh, J. H., "Plasma Dynamics of an Arc-Driven Electromagnetic Projectile Accelerator," J. Appl. Phys., 52, 2717 (1981)
2. M. A. Huerta and G. C. Boynton, "Two-dimensional time dependent simulation of plasma armatures", IEEE Trans. Mag., 25, 238 (1988).
3. G. C. Boynton and M. A. Huerta, "Two-dimensional MHD simulation of isothermal plasma armatures", IEEE Trans. Plasma Sci., 17, 468 (1989).
4. R. S. Hawke, et al., "Armature Formation in a Railgun Using a Two-Stage Light Gas Gun Injector", IEEE Trans. Plasma Sci. 17, 378 (1989).
5. J. V. Parker, "Why Plasma Armature Railguns Don't Work (and what can be done about it)", IEEE Trans. Mag., 25, 418 (1988).
6. J. V. Parker, "Experimental measurement of ablation effects in plasma armature railguns", IEEE Trans. Mag., 22, 1633 (1986).

ETIME = 3.228197E-04S
GFRM = 7.54E+06M/S^2
VFRM = 4.9E+03M/S
SFRM = 9.5E-01M
MAX = 2.2E+09
MIN = -9.2E+06

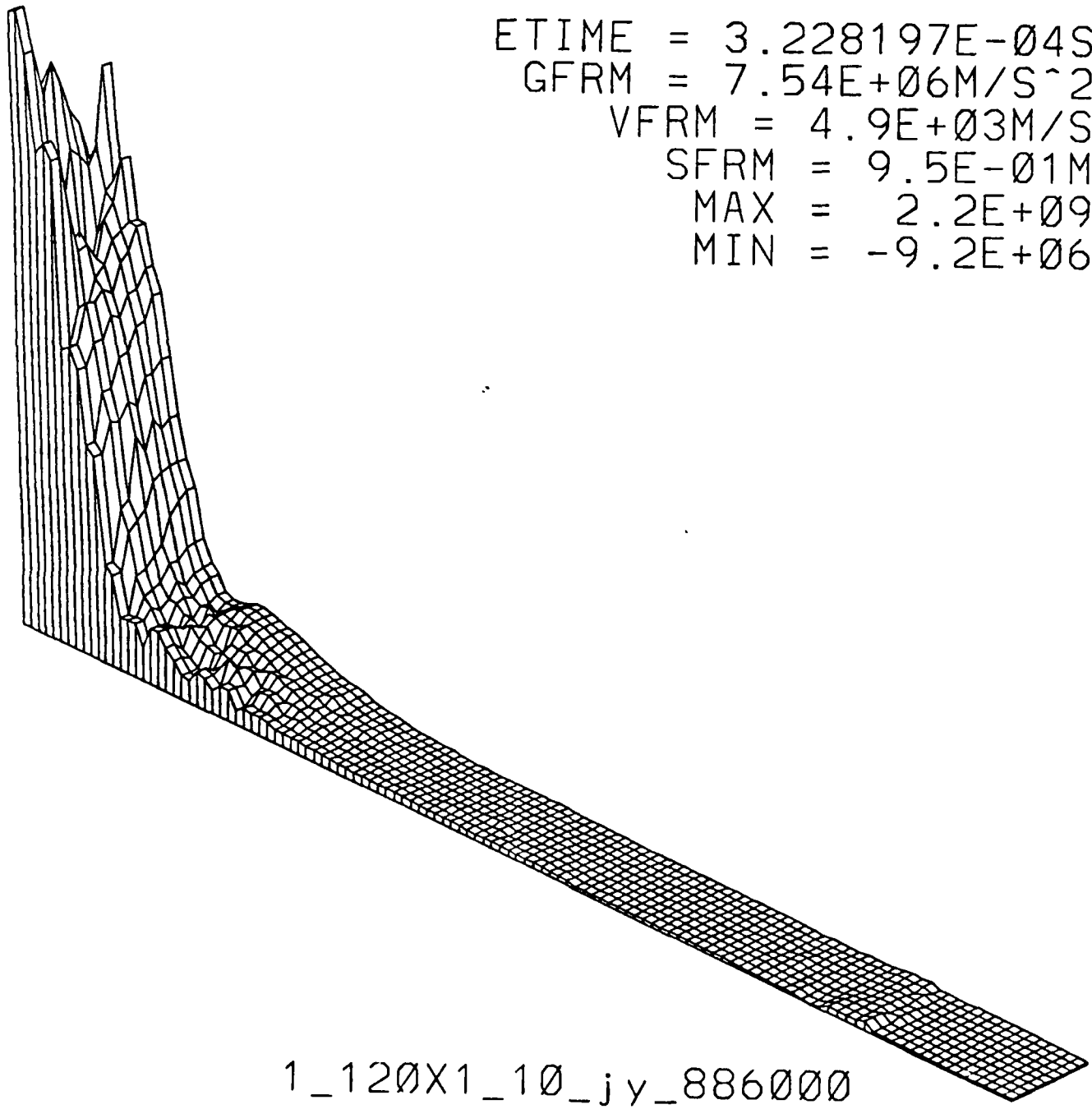
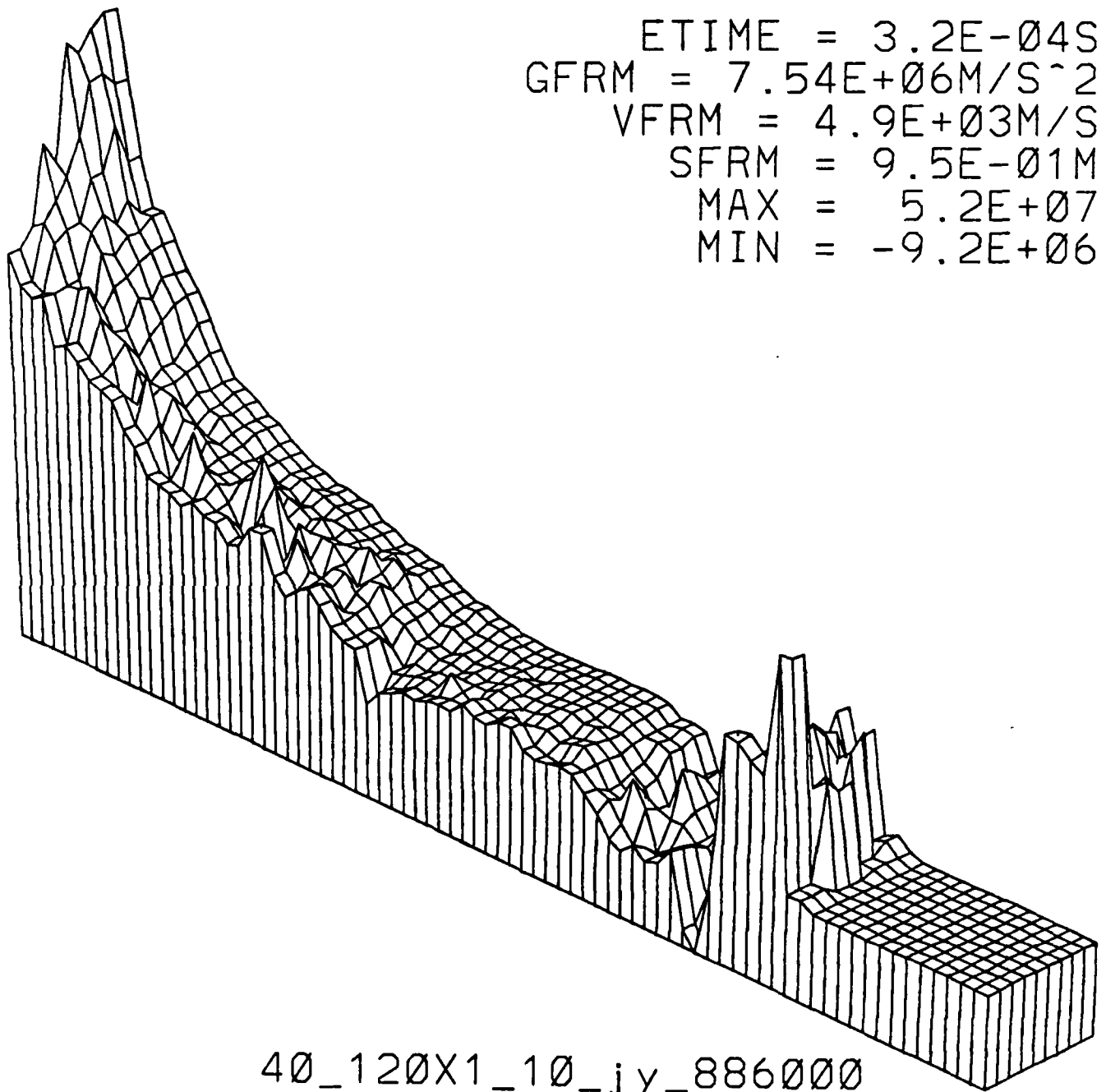


FIGURE 1



ETIME = 3.2E-04S
GFRM = 7.54E+06M/S^2
VFRM = 4.9E+03M/S
SFRM = 9.5E-01M
MAX = 5.2E+07
MIN = -9.2E+06

FIGURE 2

ETIME = 3.2E-04S
GFRM = 7.50E+06M/S^2
VFRM = 4.9E+03M/S
SFRM = 9.5E-01M
MAX = 5.2E+07
MIN = -2.3E+06

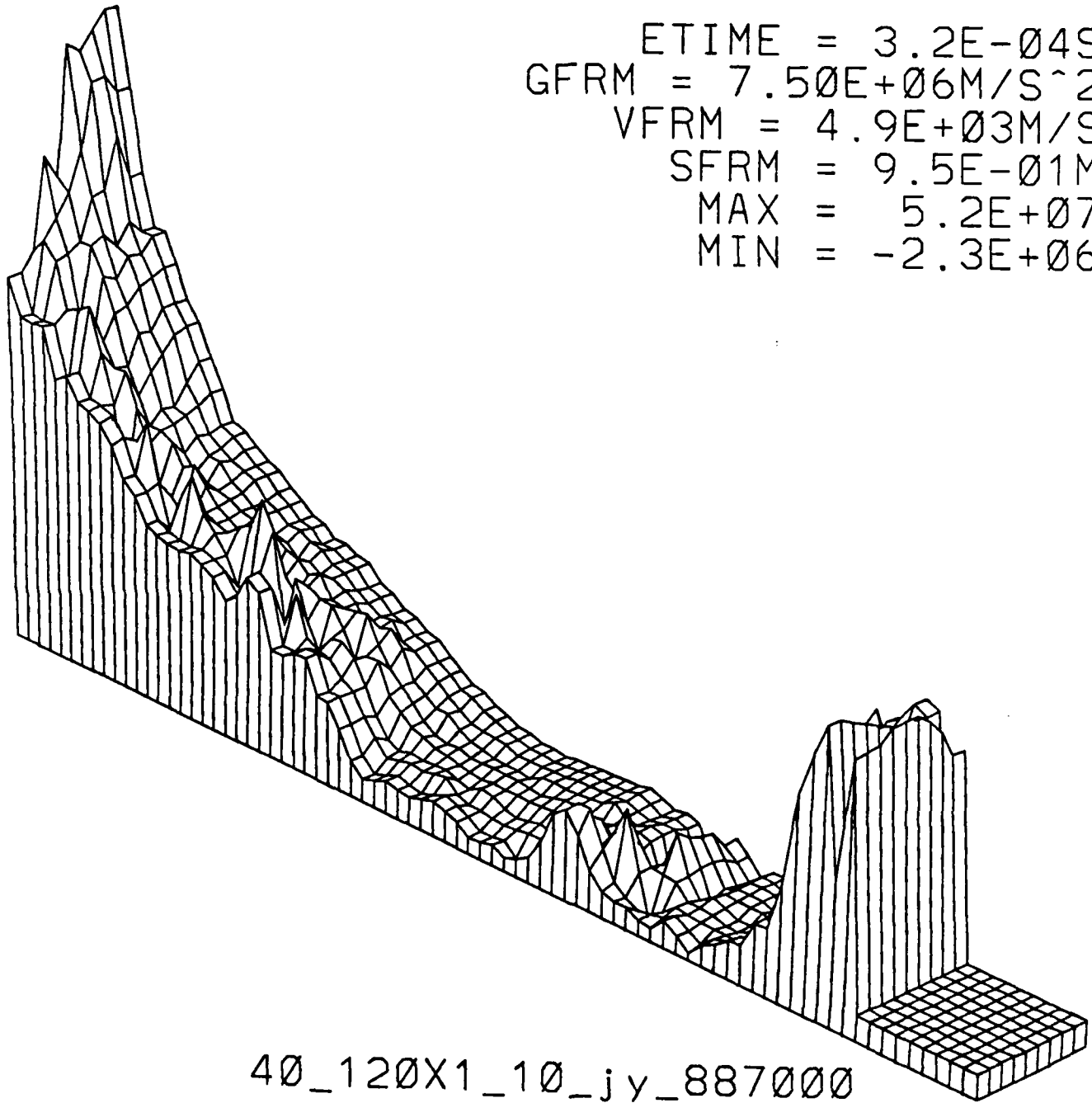


FIGURE 3

ETIME = 3.2E-04S
GFRM = 7.57E+06M/S^2
VFRM = 4.9E+03M/S
SFRM = 9.5E-01M
MAX = 5.4E+07
MIN = -3.6E+06

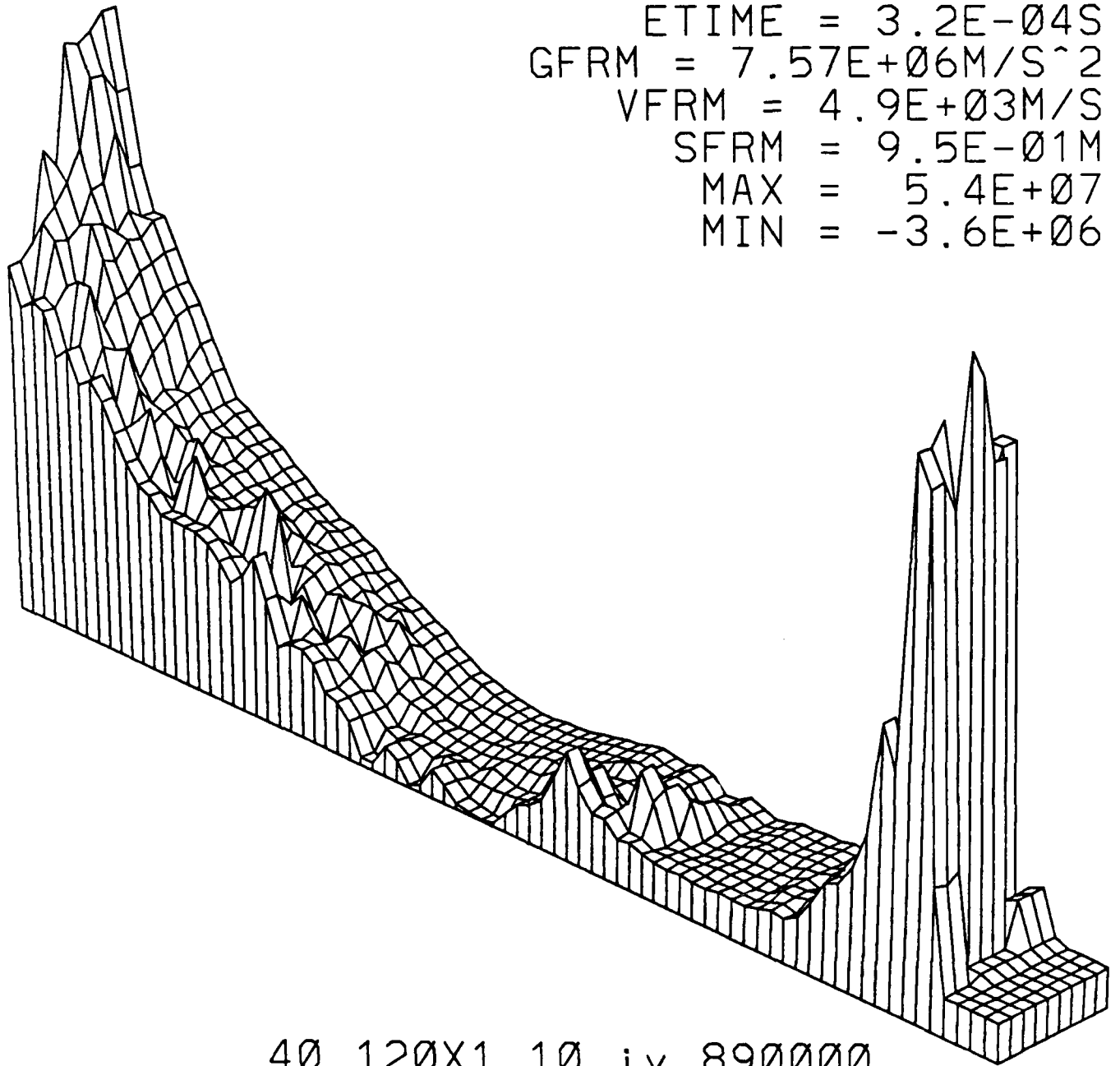
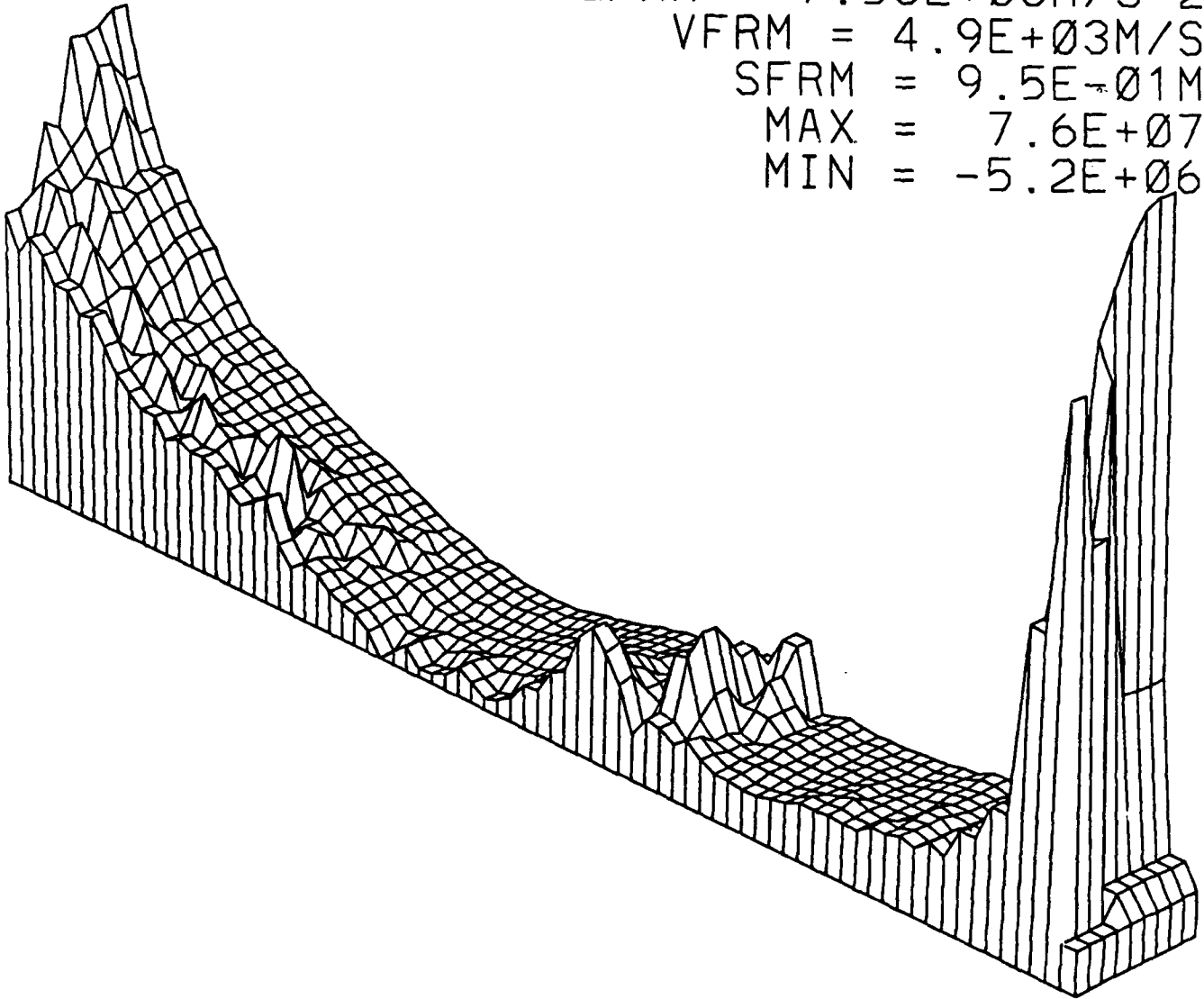


FIGURE 4

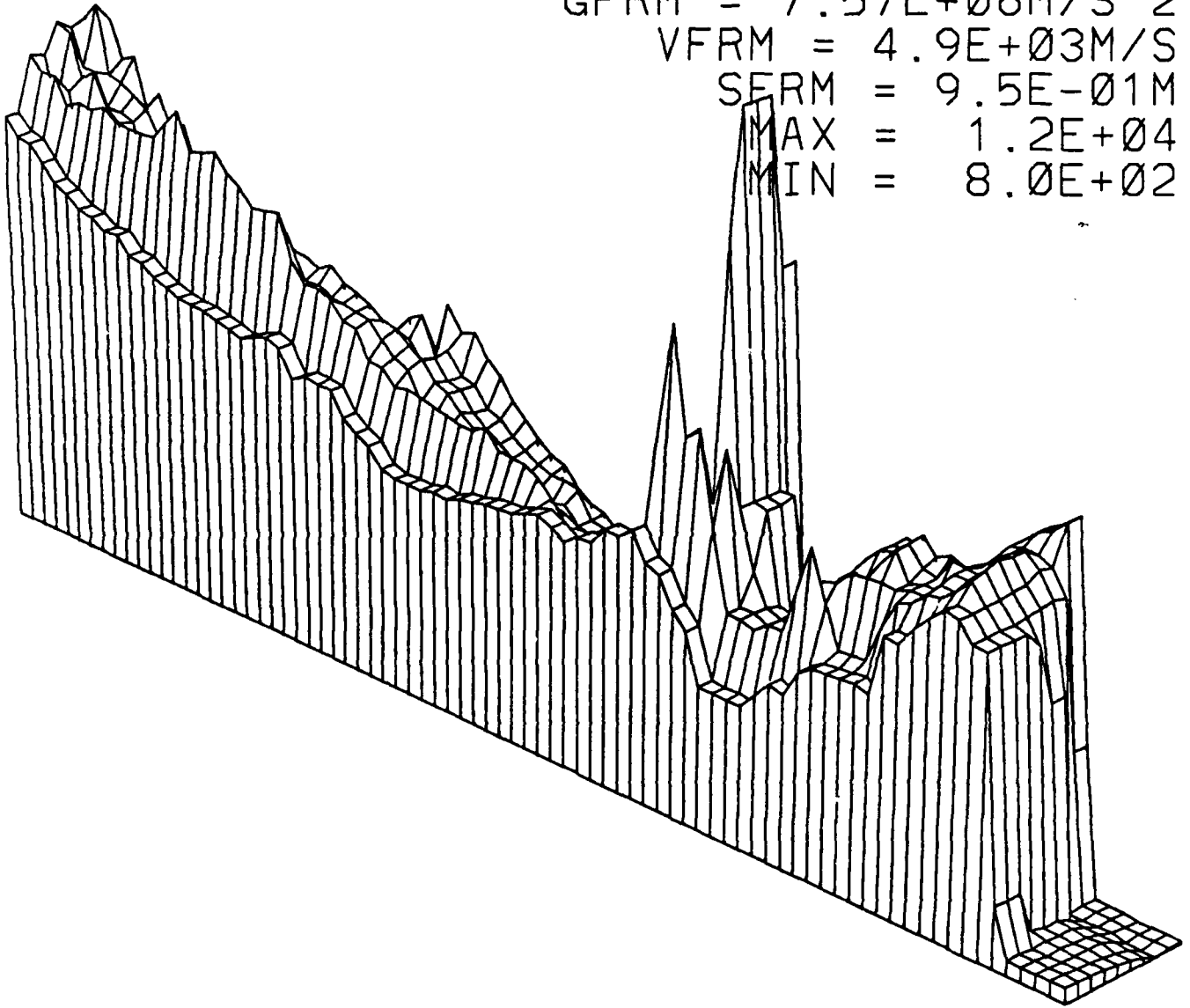
ETIME = 3.2E-04S
GFRM = 7.53E+06M/S^2
VFRM = 4.9E+03M/S
SFRM = 9.5E-01M
MAX = 7.6E+07
MIN = -5.2E+06



40_120X1_10_jy_895000

FIGURE 5

ETIME = 3.2E-04S
GFRM = 7.57E+06M/S^2
VFRM = 4.9E+03M/S
SERM = 9.5E-01M
MAX = 1.2E+04
MIN = 8.0E+02



40_120X1_10_tmp_890000

FIGURE 6

ETIME = 3.230816E-04S
GFRM = 7.57E+06M/S^2
VFRM = 4.9E+03M/S
SFRM = 9.5E-01M
MAX = 2.2E+09
MIN = -3.6E+06

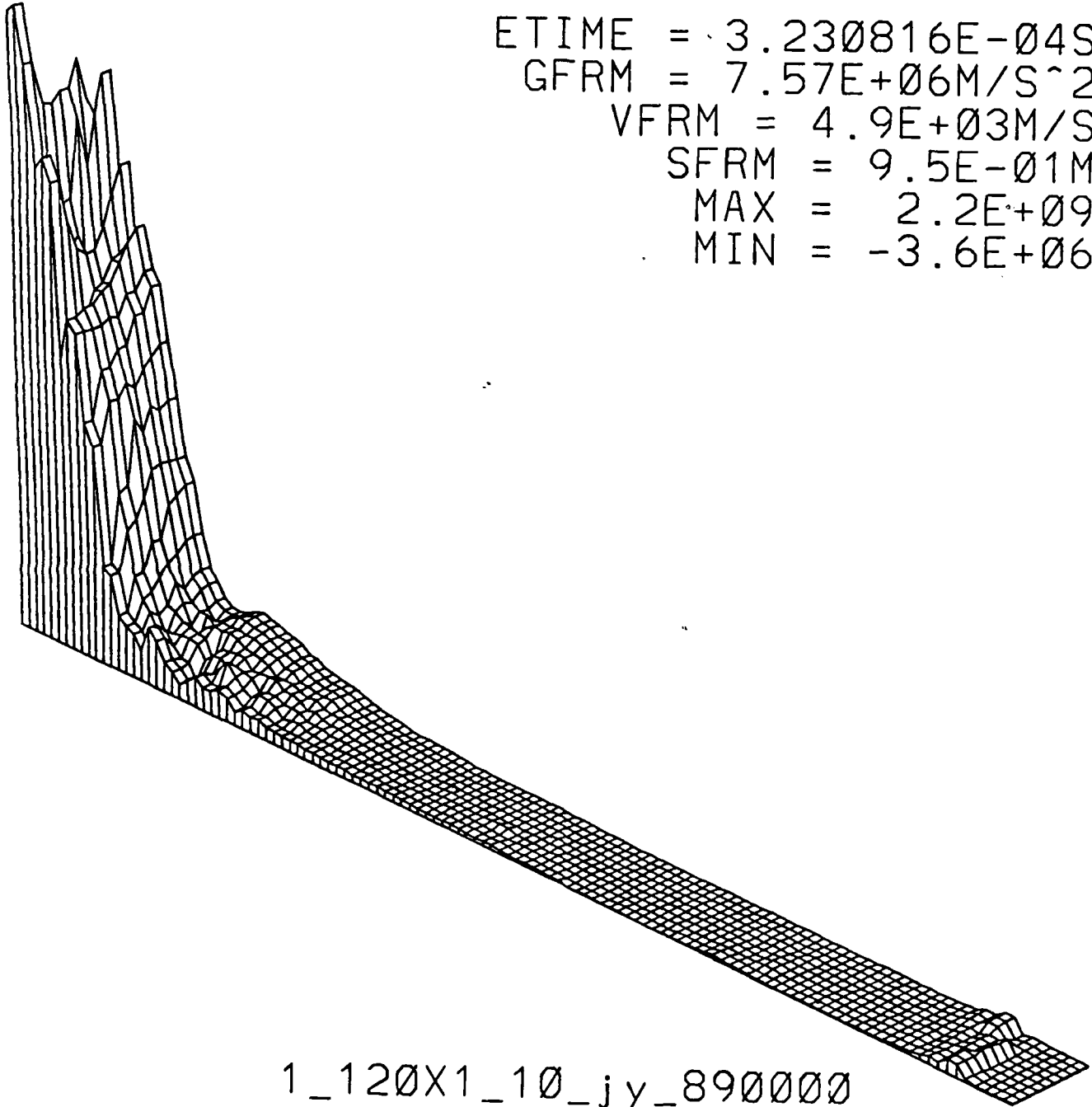


FIGURE 7

1988 USAF-UES MINIGRANT RESEARCH PROGRAM

Sponsored by the
AIR FORCE OFFICE OF SCIENTIFIC RESEARCH
BOLLING AFB, D.C.

Conducted by the
Universal Energy Systems, Inc.

FINAL REPORT

MODELING REACTIVE FRAGMENTS

Prepared by:	Anastas Lazaridis
Academic Rank:	Associate Professor
Department:	Mechanical Engineering
University:	Widener University
Research Location:	Widener University
USAF Researcher:	Joseph C. Foster
Date:	January 20, 1990
Contract No:	F49620-88-C-0053/SB5881-0378

ABSTRACT

Quantitative prediction of damage caused by reactive fragments has proved to be a challenge despite the success of several field tests. This difficulty can be attributed to the many variables that control the interaction of a reactive projectile with its target and the lack of a systematic study of vaporific phenomena.

This report expands the work of an earlier investigation performed under contract number F49620-87-R-0004. It discusses the findings of a new literature survey in the general area of vaporifics with emphasis on rapid metal oxidation reactions. It summarizes mathematical techniques for the study of metal combustion and extends current theories to obtain hypergolic limits of aluminum. The adaptability of existing propellant evaluation programs to the study of the reactive fragment is also discussed.

As a result of this effort, a proposal has been submitted to the Armament Laboratory at Eglin AFB for continued investigation of impact activated metal-oxidizer reactions. This proposal has been evaluated for its technical merit and is awaiting funding.

ACKNOWLEDGMENTS

I wish to thank the Air Force Office of Scientific Research for funding this investigation. My appreciation also goes to the Air Force Armament Laboratory at Eglin Air Force Base for providing the opportunity to perform this study. Special thanks go to Dr. Joseph C. Foster and Mr. David Wagon for their cooperation, technical assistance, and encouragement during the performance of this work. I also wish to acknowledge the friendly assistance received from everyone I contacted at Universal Energy Systems throughout this year.

I. INTRODUCTION

Reactive fragments are projectiles that carry a small quantity of a highly reactive substance and are designed to break up from a warhead in a similar manner to that of the standard rod fragments. Upon impact, the reactive material is released and the potential for a fast chemical reaction with behind-the-target debris or other stored fuel becomes a possibility. If the proper conditions are present, such a reaction can generate enough energy to cause excessive damage to the target.

The concept of the reactive fragment was demonstrated with large scale tests in which single projectiles filled with a highly reactive oxidizer were shot at normal incidence onto a number of typical military targets. Damage was assessed qualitatively by comparison with results from the impact of inert projectiles on similar targets. This comparative experimentation technique showed that fuel tanks can be made to explode catastrophically,¹ and that other land or air targets can be damaged extensively.²⁻⁷ It was also reported that the energy release payoff of reactive projectiles can be as high as 4:1 compared to conventional explosives⁸ and that the total impulse delivered can be twice as much as the same weight of a high explosive.²

The interaction of a reactive fragment with its target is a complicated process that is associated with several physical phenomena. In general, impact and penetration through the

skin of a target involve shock waves that produce behind-the-target spall and vaporific effects. The latter are the result of vigorous chemical reactions between metal and oxidizer usually followed by secondary combustion of other materials present in the vicinity. Other phenomena include air entrainment behind the projectile, melting, ablation, particle dispersion and mixing in and around an expanding reactive turbulent jet. Although vaporific effects were observed almost half a century ago, a systematic quantitative analysis of the processes leading to them has not been conducted.⁹

The processes associated with the reactive fragment are similar to those of vaporifics. The basic difference between them lies in the fact that the former is designed specifically to carry a predetermined amount of a highly reactive substance while the latter occurs as a result of a vigorous oxidation reaction between metal particles behind the target and atmospheric oxygen entrained in the wake of the impact. The reactive oxidizer of the fragment is typically a very active chemical compound. It may attack metal particles or other potential fuels behind the target commensurate with its chemical preference for such materials. Depending on existing environmental conditions, the ensuing reaction can be so rapid as to cause detonation or it may move slower resulting in incendiary combustion. Predicting the results is currently a very difficult task. The problem is that much quantitative information is lacking in the areas of metal combustion,

reaction kinetics, and the dynamics of reactive flows.

Existing hydrodynamic codes are capable of monitoring the internal energy of striker and target as functions of their geometry, relative impact velocity, and materials involved, and can define the state and phase of these materials after impact. They do not include the particle sizes of the spall behind the target and lack the capability of estimating the enhancement in the energy deposition associated with the oxidation reactions of the spall material.⁹ Some attention has recently been given to estimating particle size of spall¹⁰ and applying the results to existing hydrocodes.¹¹ To model the effects of the reactive fragment quantitatively, these computer codes must be expanded to include the contributions of spall material particle size distribution, pressure and temperature conditions of the medium behind the target, appropriate reaction kinetics, and dispersion and mixing of the reactants. The last two processes are dependent on flow characteristics, molecular diffusion, and target internal geometry.

A partial survey of literature during the summer of 1988 uncovered pertinent information and provided a list of topics for future research.¹² An important aspect of that work was the identification of more than five hundred references associated with individual phenomena of vaporifics, which led to a recommendation for further study of the subject. The ultimate goal of such an undertaking would be to understand the intricacies of vaporifics and to provide a method of

estimating their contribution to blast effects. Tests had demonstrated the potential lethality of reactive fragments, but generated little data that could be used in a vulnerability model. It was indicated that several important questions remained unanswered. These included behind-the-target spall sizes and their compatibility with metal ignition/oxidation requirements, chemical reaction kinetics of potential reactants, dispersion and mixing characteristics of fuel and oxidizer at different impact velocities and angles of obliquity, the effect of the presence of moisture in the environment, and the lack of information involving conditions of low atmospheric temperatures in oxygen-starved atmospheres especially with a target moving at high speeds. As a result, future experimental and theoretical work was recommended.

II. BACKGROUND

Military targets may be broadly identified by location, such as land, sea, or air targets. They can also be classified more specifically according to function, such as fuel storage tanks, airplanes, ships, communication antennae, or ground vehicles. These targets come in a variety of shapes and sizes, and consist of many different materials. Despite these differences, however, all are made of solid materials that either protect internal components or store a strategic fluid such as a fuel. This leads to another convenient classification. The first group contains targets consisting of one or more layers of solid materials, such as plates of pure metals or alloys or sheets of organic composites,

followed by air and other solid components, while the second group comprises targets of one or more solid, typically metallic, layers followed by a liquid fuel confined within this boundary. It is to be noted that under proper conditions all materials can become potential fuels.

Current interest in the reactive fragment concept arises from the success of field tests with either simulated targets or components of real military targets. These tests have demonstrated the ability of reactive projectiles to cause catastrophic failure to metallic tanks containing hydrocarbon fuel while solid projectiles produced less damage caused mainly by induced secondary combustion.¹ Full tanks of fuel were reported to suffer greater damage than those that were partially filled especially when the reactive compound was released in the vapor region of the tank.⁴ Since the reactive substance used in the projectile is known to react vigorously with most hydrocarbons, these results are not surprising. The discrepancy in reaction rates of reactive compound with fuel in the liquid vis-a-vis the vapor state may be explained by the additional ram effect occurring on the liquid. Tests with an airplane wing and simulated radar antennae showed the ability of the reactive projectile to incapacitate such solid components of air and land targets. Solid projectiles, on the other hand, caused relatively minor damage.²⁻⁴ This difference in the results caused by the two projectiles indicated that impact induced vaporific effects are enhanced by chemical reactions taking place between target constituent

materials and the reactive substance released by the projectile.

Although several explanations were offered to account for the observed results, prediction of the extent of damage in all of these tests proved to be a challenge. Since damage can be correlated to the rate of energy deposition on the target and its total value, it is probably easier to estimate for a liquid fuel stored in a tank than it is for all the processes that take place behind the skin of an airplane wing after penetration by a projectile. Among these processes are turbulent mixing of spall with reactive material, vigorous chemical reactions that may continue to completion or terminate earlier depending on local conditions and geometry, and secondary combustion with entrained air. An important aspect of this set of events is rapid oxidation of metallic spall which can lead to detonation or to milder combustion based on existing conditions. In this work emphasis has been placed on the combustion of metals and especially aluminum since it is present in many air, land, and sea targets.

III. OBJECTIVES

The overall goal of this research is to isolate the phenomena associated with the interaction of a reactive fragment and its target, assess the relative contribution of pertinent parameters, establish a quantitative cause and effect relationship between them, and combine the results to generate a model that can be incorporated in a hydrocode.

The objective of the work reported in this document was to continue the literature survey, research mathematical techniques that could be used in modeling vaporific processes behind the target boundary surface, and establish an ongoing relationship of scientific cooperation with Armament Laboratory personnel at Eglin Air Force Base. Specific tasks included:¹³

1. Updating and expanding the literature survey reported earlier.¹² Areas to be emphasized were fuel/oxidizer reactions, fuel combustion, their chemical kinetics, reactive turbulent flows, theoretical and experimental methods.
2. Research of mathematical techniques toward developing a computer algorithm for metal oxidation.
3. Extending current theories to obtain hypergolic limits for aluminum and other metals of interest.
4. Studying the adaptability of the PEP program to existing hydrocodes for estimating the effects of the interaction between target and reactive fragment.

IV. DISCUSSION

A literature search was conducted to identify the most recent work in high-temperature metal oxidation. The scientific and technical network STN International's CA, COMPENDEX, ENERGY, MATH, METADEX, and PHYS databases were searched. CA is the chemical abstracts database of the

American Chemical Society covering literature from all areas of chemistry and chemical engineering since 1967. COMPENDEX covers the worldwide literature in engineering and technology corresponding to Engineering Index Monthly from 1973 onwards. ENERGY contains references of worldwide energy research and technology for all kinds of energy sources starting from 1974. MATH is a database of mathematics and mathematical methods. METADEX covers the worldwide literature on metals and metallurgy with citations since 1966. PHYS is a database of physics that emphasizes non-conventional and Eastern European literature since 1979.

IV.1. LITERATURE UPDATE

An earlier report listed forty-four references on various aspects of the reactive fragment problem.¹² Approximately half of these references covered work in metal combustion. Except for some theoretical studies that can be applied to oxidizing agents other than oxygen, almost all the literature deals with combustion of metals in the presence of oxygen.

Friedman and Macek performed some of the early work on the combustion of aluminum. They investigated the ignition and burning of single aluminum particles injected axially into a hot stream of gas which had a uniform temperature, composition, and flow velocity.¹⁴⁻¹⁶ The gas was produced by burning propane in oxygen and adjusting the flame temperature by introducing nitrogen to the mixture. Ignition and burning of aluminum particles were studied photographically and by

means of microscopic examination of original and burned particles. Consistent with the theory of D. A. Frank-Kamenetskii, ignition occurred only if the gas temperature exceeded a critical value that depended on oxygen concentration. A correction had to be applied to the original theory to account for the melting of aluminum oxide and the associated resistance to oxygen transport. Thus, expressions were derived for the ignition time delay

$$t = \rho d^2 \{c \ln[(T_a - T_o)/(T_a - T_i)] + L/(T_a - T_m)\}/12k \quad (1)$$

and the ignition limit

$$T_{ai} = T_{mo} - (Qd/2k) K (P_{OX}/RT_{mo})^n \quad (2)$$

where d is particle diameter, ρ is particle density, k is thermal conductivity of ambient gas, L is the heat of fusion at the particle melting point T_m , c is particle heat capacity, T_a is the temperature of the gas stream, T_o is particle initial temperature, T_i is particle ignition temperature, T_{ai} is the limiting ignition temperature, Q is exothermicity, T_{mo} is the melting point of the oxide, P_{OX} is partial pressure of oxygen, and the quantity $K(P_{OX}/RT_{mo})^n$ represents the rate of surface oxidation through the solid layer of the oxide at its melting point. Moisture content of the hot ambient gas was found to have no influence on the ignition process. The pre-ignition reaction was observed to be controlled by diffusion through the oxide layer coating the particle, and ignition occurred only when the oxide layer melted regardless of the gas composition. The combustion of

aluminum particles, on the other hand, was affected by the presence of water in the gas stream. In the absence of water vapor, diffusion and combustion took place freely in the gas phase whereas moisture in the gas impeded this process and confined it to a smaller region.

Markstein reviewed the fundamental aspects of metal combustion and gave a synopsis of previous work.¹⁷ He suggested that the products of metal combustion were highly stable condensed-phase substances because of their large exothermic enthalpies of formation. Their presence together with condensed-phase reactants implied a predominance of heterogeneous reaction processes. The latter were also the subject of a later paper by the same author.¹⁸ A proposed sequence of events describing the mechanism of metal combustion was discussed. It started with the preheating of metal particles to their ignition temperature, a process that yields spherical droplets of molten metal covered by a thin oxide coating. Continued increase in temperature to a level needed to sustain combustion leads to either surface burning of the metal behind the oxide layer or vapor-phase burning in the ambient gas. Criteria advanced by Glassman¹⁹ and modified by Brzustowski and Glassman²⁰ were used to specify the conditions in which one or the other process occurred. These criteria stated that surface burning takes place when the oxide is more volatile than the metal or if the boiling point of the metal exceeds that of the oxide. Conversely, vapor-phase burning occurs when the metal is more volatile

than its oxide. An excess of the boiling point of the oxide over that of the metal is a necessary condition for this process, but it does not guarantee its occurrence. Suppression of vapor-phase burning may result from the formation of a protective oxide layer, reduction of the flame temperature below the metal boiling point because of radiation losses, or both. Finally, the oxide coating formed around the metal particles is blown up by the evaporating metal "like a soap bubble". This frees the surface of the metal to come in direct contact with the oxidizer. Fragmentation may take place in this stage if the metal droplet exceeds a critical diameter beyond which the force of surface tension can no longer balance that of metal-vapor pressure.

This project has identified some significant studies in the Russian literature. Three papers, in particular, are worth mentioning. Merzhanov presented an analytical method for predicting metal particle ignition and conditions for sustained combustion.²¹ Considering a metal particle in a gaseous oxidizer at the same temperature as the metal or above it, he wrote the equations for thermal balance and oxidation kinetics associated with the chemical reaction of metal and oxidizer. The reaction rate was determined by the processes of metal/oxidizer transfer through a film of a solid protective coating formed by the initial reaction. A numerical solution of the equations after appropriate simplifications gave the time-dependence of particle temperature and amount of oxidized metal. Temperature-time

curves were obtained experimentally for the combustion of tantalum and tungsten in oxygen, and titanium in a nitrogen atmosphere using an electrothermographic technique. These graphs are of the same form as the theoretically calculated curves. The last figure of the paper shows the growth of nitride film at the induction period prior to ignition. Experiments involving the ignition mechanism of aluminum in oxygen, oxygen-nitrogen mixtures, and carbon dioxide atmospheres showed that ignition and self-heating can occur only in the first two cases. In carbon dioxide, aluminum ignited at the melting point of the protective film, but self-heating was completely absent at temperatures below it. The high-temperature interaction between aluminum and oxygen followed a parabolic law. Merzhanov drew four major conclusions from this study. 1) The oxide film thickness grew considerably in the induction period. 2) The experimental studies provided qualitative support to the theoretical results that showed the presence of self-accelerating temperature growth and pre-explosion self-heating. 3) The critical temperature showed only slight dependence on particle size. 4) Rigorous quantitative comparisons were hindered because of lack of information on the kinetics of high temperature interaction between metal and gas. A recommendation was made for further experimental work to study the kinetics of heat evolution in high temperature oxidation. Derevyaga, Stesik, and Fedorin studied the combustion of aluminum, zinc, and magnesium in air, and determined critical conditions for their ignition in different oxygen

concentrations.^{22,23} The experiments were conducted with 99.8% pure 2-3 mm spherical samples of zinc, 99.5% pure 3-4 mm spheres of aluminum, and 99.9% pure 3-6 mm spheres of magnesium. The oxidizing gas was air moving at 15-20 cm/sec. The results for aluminum confirmed that the oxide film became permeable at temperatures below the ignition point of the metal, which was found to be $1780 \pm 20^\circ\text{C}$. This was a constant for all samples irrespective of any previous oxidation history. Past the ignition point a sharp intensification of the removal of condensed reaction products into the flow was observed in the combustion regime. It was concluded that complete combustion of the metal would occur if ambient conditions were favorable to heating the metal close to its boiling point. A common pattern of ignition with subsequent combustion or extinction is evident in all three papers, even though the reactants differ. This is an indication that further research may lead to the construction of a generalized theory.

The multidimensional combustion of condensed samples of rectangular cross-section was investigated analytically and experimentally by Volpert, et al.²⁴ Pressed iron-zirconium samples of various densities and calorific values were used and comparison was made between the experimental data and the theoretical results. Yukhvid modeled the interaction of molten slag with a metal matrix in exothermic combustion heating of a powder mixture.²⁵ Metal inclusions and gas voids in the molten slag layer were considered including thermal

conditions for layer separation. The mathematical model was applied to welding. Kudryavtsev, et al., proposed a model for the combustion of metal particles based on the diffusion theory of combustion.²⁶ They described a calculation procedure applicable to both low and high pressure combustion. Aluminum burning in steam was used as an example. Two papers presented studies of laser activated thermochemical reactions of condensed media. Bonch-Bruevich, et al., formulated a phenomenological theory of nonisothermic reactions using laser induced oxidation of metals in air as an example.²⁷ An experimental and theoretical study of laser induced ignition and combustion of metals in air was performed by Arzuov, et al.²⁸ The oxidation of metal is considered according to a parabolic law. It is shown that interference phenomena in the oxide-metal system play an important role in the ignition process for tungsten.

In an effort to uncover kinetic oxidation data for aluminum and other metals, shock-wave studies were reviewed. Tyte used data for aluminum, magnesium, and lead to conclude that shock-wave to particle interaction was best explained by a combustion model.²⁹ Hodgson and Mackie studied the oxidation of magnesium in a shock tube.³⁰ Their experimental results in shocked argon-oxygen or argon-air environments were interpreted by a homogeneous gas-phase reaction model. The rate coefficient for the reaction $Mg + O_2 \rightarrow MgO + O$ was figured at 2000 K as $(5 \pm 3) \times 10^{10} \text{ cm}^3/(\text{mole} \cdot \text{sec})$.

Other related bibliography includes the analytical work of Harwell, et al., which was an attempt to predict the interaction of a projectile with its target and correlate the resulting damage by measuring the radiation emitted from the impact.³¹ Glickstein used finite-element and time-marching techniques along with phase change, liquid metal flow, and appropriate models of oxidation kinetics to develop a computer program for the combustion of titanium.³² The model predicts metal ignition due to radiation, frictional heating, and exposure to high ambient temperature. Kennedy and Nunziato investigated the behavior of shock waves in the chemically reacting solid explosive PBX-9404 by laser interferometry.³³ Their experimental results showed a sequence of growth, decay, and growth in the evolution of the shock wave in the explosive. The pyrophoricity of fine powders of iron and titanium were considered by Evans, et al.³⁴ A qualitative discussion of vapor explosion was given by Witte, et al.³⁵ while Ishihama and Enomoto presented an experimental method for studying dust explosions.³⁶ Glassman and Dryer's results with hydrocarbon fuels may not be directly applicable, but their experimental technique using a turbulent flow reactor may be useful in the study of reactive fragments.³⁷

IV.2. MATHEMATICAL METHODS

Exothermic metal oxidation may lead to rapid self-heating of metal particles at high temperatures depending on thermal conditions and the rate of reaction. This process can bring the metal to its ignition point in much the same way as the

thermal explosion of a solid explosive. Whether the metal burns beyond this point depends on the rate of heat transferred away from the particle vis-a-vis the rate of energy released by the reaction. If environmental conditions are favorable, cooling by heat transfer at the surface of the particle can not catch up with the rate of energy generated by the oxidation, the particle temperature continues to grow, and self-acceleration of the reaction can lead to detonation. The basis for this process is the exponential dependence of the chemical reaction rate on temperature according to Arrhenius' law, which is of the form

$$d\mu/dt = K_0 \exp(-E/RT) C^n f(\mu) \quad (3)$$

where $\mu = m(t)/m_0$, $m(t)$ is the quantity of metal that reacts during time t , m_0 is particle mass, E is activation energy, T is particle temperature, C is oxidizer concentration, n is the order of the reaction, K_0 is the Arrhenius pre-exponential factor, and $f(\mu)$ is the kinetic function. According to the early theory of Frank-Kamenetskii,³⁸ the energy balance around a solid undergoing a chemical reaction is given by

$$\rho c(dT/dt) = k \nabla^2 T + \rho Q(d\mu/dt) \quad (4)$$

where ρ is the density, c is specific heat capacity, T is particle temperature, t is time, k is thermal conductivity, Q is energy generated by the reaction, and μ is the normalized mass of the particle that is oxidized in time t . Considering only one-dimensional heat transfer and combining equations (3)

and (4), a nonlinear equation is obtained for the temperature. Making the approximations that the temperature of the solid prior to the explosion is close to the initial temperature and the reaction before the explosion is slight, and using new variables for space and temperature, this equation is reduced to the form

$$\alpha(\partial\theta/\partial t) = \partial^2\theta/\partial x^2 + (\beta/x)(\partial\theta/\partial x) + \delta \exp(\theta) \quad (5)$$

where $\alpha = \rho cL^2/k$, $\theta = E(T-T_0)/\rho T_0^2$, x is dimensionless length normalized by a characteristic length L , $\beta=0$ for a slab, $\beta=1$ for a cylinder, $\beta=2$ for sphere, $\delta = \rho QL^2K_0E/kRT_0^2$, and T_0 is the initial particle temperature. A steady state solution of this equation under a uniform boundary condition of constant temperature at the surface gives a critical value for δ , which leads to a critical ambient temperature over which there will always be explosion. This formulation of the problem considers a finite volume of a solid explosive in which both convective and radiative heat transfer at the boundary is neglected. Because of the non-linearity of equation (5) only approximate or numerical methods can be used to solve it. This gives the explosion time as a function of the surface temperature.

Merzhanov considered the combustion of small metallic particles and assumed that they can be lumped to a point mass with uniform temperature. Then, he modified the energy conservation equation to include convection and radiation.

This lumped capacitance method gave the equation

$$\rho c(dT/dt) = \rho Q(d\mu/dt) - h(S/V)(T-T_0) - \epsilon\sigma(S/V)(T^4-T_0^4) \quad (6)$$

where (S/V) is the ratio of surface area to the volume of the particle, ϵ is the emissivity of the particle surface, σ is the Stefan-Boltzmann constant, and h is the heat transfer coefficient that can be calculated from an expression of the form

$$h = (k/L) f(Ra, Re, Pr) \quad (7)$$

The conduction term does not appear in equation (6) because the particle is assumed to be at a uniform temperature. Using these equations, Merzhanov derived critical parameters that determine whether the particle proceeds to ignition and further combustion.

As a result of this effort, a proposal has been submitted to the Armament Laboratory for continued investigation of impact activated metal-oxidizer reactions (see Appendix). Assuming no interparticle influences, similar equations will be written and solved according to proper oxidation kinetics. The non-linearity of the equations of this section suggests the use of approximate or numerical methods for their solution. At this stage of the research it appears that the overall problem can be described by the combined effect of all the particles in the space behind the damaged skin of the target assuming a random distribution of metal fragments in oxidizer surroundings based on target geometry. More than one

oxidizer can be considered in this model.

IV.3. HYPERGOLICITY OF ALUMINUM

The ability of materials to react spontaneously and vigorously upon contact with a reagent in the environment under a specified set of conditions is known as hypergolicity. It is possible for fine particles to be heated to their ignition temperature by exothermic surface oxidation. A large metal surface to volume ratio and heat transfer from the environment may assist this process. According to Beltran there are four general mechanisms associated with the autoignition and subsequent combustion of a material in an oxidizing atmosphere.³⁹ The most fundamental of these is the spontaneous accelerating oxidation of a pure surface, which requires very small particles. The others are the spontaneous reaction of the oxidizing atmosphere with a reactive chemical intermediate compound formed from the metal, the oxidation of a metal induced by mechanical energy, and the autoignition of metal particles caused by friction induced electrostatic charges. In this section Beltran's method is used with necessary modifications to obtain the hypergolic properties of aluminum.

In his investigation Beltran assumes an adiabatic spherical particle which is heated by the energy generated from surface oxidation. This guarantees the determination of the maximum particle size for hypergolicity, although he argues that any heat transfer from the particle is probably

negated by external heat transfer to the particle in an environment of many particles. He also assumes that no dimensional changes occur during oxidation of the spherical particle, the density of the oxide is approximately the same as that of the metal, the oxide formed is infinitesimally thin in comparison to the particle diameter, and the specific heat of the particle is constant. This gives the expression for particle diameter

$$d = 6t.\delta h/c.(T_i-T_p) \quad (8)$$

where t is the thickness of the oxide layer, δh is its heat of formation per unit mass, c is the specific heat of particle material, T_i is the ignition temperature, and (T_i-T_p) is the temperature rise above the initial temperature of the particle, T_p . If one accounts for the difference in the densities of metal and its oxide, this equation becomes

$$d = 6t.d_r.\delta h/c.(T_i-T_p) \quad (9)$$

where d_r is the ratio of oxide to metal densities. Although the specific heat of liquid aluminum remains approximately constant at 0.26 cal/g.K, its value for aluminum in the solid phase changes significantly as shown in fig. 1. This variation in the specific heat leads to another modification of equation (8) so that

$$d = (6t.d_r.\delta h)/C \quad (10)$$

$$\text{where } C = \int_{T_p}^{T_i} c \, dT. \quad (10a)$$

The thermodynamic data of fig. 1 was approximated by first, second, and fourth order polynomials. Although the latter is the most accurate representation of the data, the linear relationship

$$c = 0.213 + 0.000113T \quad (T \text{ in } ^\circ\text{C}) \quad (11a)$$

or

$$c = 0.182 + 0.000113T \quad (T \text{ in } \text{K}) \quad (11b)$$

deviates from it by no more than $\pm 1.5\%$. With equation (11b), the integral in equation (10) takes the form

$$C = (T_i - T_p) (0.182 + 0.000113T_{\text{ave}}) \quad (12)$$

where $T_{\text{ave}} = (T_i + T_p)/2$. Hypergolicity of pure and preoxidized aluminum is shown in fig. 2 and fig. 3, respectively. Both figures are drawn under the assumption that the thickness of the oxide layer formed is of the order of one atomic diameter and the ratio $d_r = 1$.

The ignition temperature of pure aluminum is approximately 945K while that of a particle protected by an oxide layer is assumed to occur at 2220K, the melting temperature the aluminum oxide. Application of these values gives the hypergolic diameter of a spherical particle as a function of its initial temperature. Fig. 4 and fig. 5 present this relationship for particles of pure and preoxidized aluminum, respectively, which have undergone rapid oxidation to a thickness of one atomic diameter.

The factor $\delta h/C$ equals the ratio of particle mass to that of the oxide mass needed to bring the particle to its ignition temperature. This means that hypergolicity is enhanced by a large value of $\delta h/C$. It is for this reason that the ratio $\delta h/C$ is termed the ignition factor. Fig. 6 is a plot of the ignition factor for aluminum calculated on the basis of a constant specific heat. According to Beltran autoignition is assured in a cloud of particles if the fraction of oxide mass produced to the original particle mass is equal to the inverse of the ignition factor and there is pure metal surface exposed to the oxidizer.

Once oxidation begins, the temperature will increase rapidly, which can accelerate the oxidation process. It is, therefore, reasonable to assume that oxidation will continue beyond one atomic monolayer. If the particles are not spherical, the above equations can be modified to include the difference in the surface area by defining the ratio of particle surface area to that of a sphere, S_r . Then, equation (10) becomes

$$d = (6t_m \cdot d_p \cdot N \cdot S_r) \cdot (\delta h/C) \quad (13)$$

where t_m is the atomic monolayer of one atomic diameter and N is the number of such atomic monolayers of oxide produced. This equation is graphed in fig. 7 as a function of the $N \cdot S_r$ product for $d_p=1$ and constant specific heat, which shows the increase in hypergolicity with surface roughness. Note that the curve of $N \cdot S_r=1$ is the same as that of fig. 2.

Hypergolicity of agglomerates is considered in terms of the specific surface area of the particles, A_S , which is the total surface area per unit mass. Beltran gives an expression for this parameter to satisfy conditions of hypergolicity. This relation is derived on the basis of the assumptions discussed earlier and has the form

$$A_S = (C/\delta h) \cdot (1/\rho \cdot N \cdot t_m) \quad (14)$$

where ρ is the particle density. Fig. 8 gives the hypergolic limits of aluminum in terms of the specific surface area, which is a function of the temperature rise and the number of atomic diameters associated with the oxidation process. Ignition occurs for all points on the graph that are below and to the right of the line associated with the proper oxide thickness. The curves show that hypergolicity increases both with surface area and oxide thickness, as expected.

IV.4 STUDY OF PEP PROGRAM

The PEP or propellant evaluation program was developed by the Naval Weapons Center to obtain thermodynamic properties at high temperatures and estimate performance characteristics of propellant systems.⁴⁰ It had been suggested as a tool to estimate the energy released by the interaction of the reactive substance in a fragment with target material, which could be correlated to observed damage.

As a result of this investigation it is concluded that the PEP program would be inefficient and limited in scope

because both the model used and the assumptions associated with it are not consistent with this application. The model consists of an isobaric, adiabatic combustion followed by an isentropic expansion through a nozzle. It is also assumed that chemical equilibrium is attained in the combustion process because the reaction kinetics are sufficiently fast. Neither of these conditions is exactly correct in the case of the reactive fragment. Combustion may be so vigorous that it may lead to rapidly increasing pressure and detonation, and expansion is not isentropic. Adapting a different program such as the TIGER routine may be more advantageous. This program was developed to calculate thermodynamic properties of nonideal heterogeneous systems and especially detonating explosives. Its model appears to be more consistent with the conditions of the reactive fragment.

V. CONCLUSIONS AND RECOMMENDATIONS

The thermal model of metal combustion is applicable to the reactive fragment problem. A proposal to continue this work has already been submitted to the Armament Laboratory at Eglin AFB.

Although ignition of single particles appears to favor small particles, there is evidence that sizes larger than those obtained by the method of Beltran may ignite. The criteria seem to be the existence of a large particle surface area to volume and the continuous generation of fresh metal surfaces.

Experimental data corresponding to realistic conditions of the reactive fragment are needed to correlate the influence of all the important parameters. Some recommendations for such a program were made in an earlier report.¹²

REFERENCES

1. Tulis, A. J., "Liquid Filled Pellets," Report No. AFATL-TR-78-70, Air Force Armament Laboratory, Eglin AFB, FL 32542 (July 1978).
2. Martin Marietta Aerospace, "Reactive Fragment Tests Against Radar Antenna Targets," Report No. OR 18,268, Air Force Armament Laboratory, Eglin AFB, FL 32542 (March 1985).
3. Cunningham, J. E., "Reactive Fragment Investigation," Report No. AFATL-TR-82-52, Air Force Armament Laboratory, Eglin AFB, FL 32542 (August 1982).
4. Cunningham, J. E., "Reactive Fragment Warhead," Report No. AFATL-TR-85-47, Air Force Armament Laboratory, Eglin AFB, FL 32542 (October 1985).
5. Remar, J. and Gagliano, J., "Reactive Projectile Study for SDI Application," Report No. AFATL-TR-87-09, Air Force Armament Laboratory, Eglin AFB, FL 32542 (April 1987).
6. Watt, R. M., "Hypervelocity Impact Tests of Reactive Projectiles," Report No. AEDC-TSR-86-V24, Arnold Engineering Development Center, Tullahoma, TN (September 1986).
7. Watt, R. M., "Reactive Projectile Test," Data Package for Report No. AEDC-TSR-86-V24, Arnold Engineering Development Center, Tullahoma, TN (August 1986).
8. Cunningham, J. E., "Reactive Warhead Handling Technology and Application Assessment," Report No. AFATL-TR-86-12, Air Force Armament Laboratory, Eglin AFB, FL 32542 (June 1986).
9. Backofen, J. E., Jr., Kennedy, D. R., and Golovin, M. N., "Enhanced Energy Coupling Phenomena: A State-of-the-Art Survey and Assessment," Air Force Armament Laboratory, Eglin AFB, FL 32542 (April 1980).
10. Grady, D. E., "A Strain-Rate-Dependent Spall Mechanism Transition in Metals," SAND-87-0741C, Sandia National Laboratories, Thermomechanical and Physical Division, Albuquerque, N.M. 87185-5800 (1987).
11. Holmquist, T. J. and Johnson, G. R., "Behind Armor Debris Predictions With the EPIC-2 Code," Honeywell Inc., Armament Systems Division, MN (March 1989).

12. Lazaridis, A., "Modeling Reactive Fragments," Report submitted to Air Force Armament Laboratory, Eglin AFB, FL 32542 (August 1988).
13. Lazaridis, A., "Modeling Reactive Fragments," Proposal for research (Submitted to UES: August 1988, Funded by the AFOSR with a minigrant: December 1988, Duration: One year.)
14. Friedman, R. and Macek, A., "Ignition and Combustion of Aluminum Particles in Hot Ambient Gases," *Combust. Flame*, Vol. 6, pp. 9-19 (1962).
15. Friedman, R. and Macek, A., "Combustion Studies of Single Aluminum Particles," Ninth Symposium (International) on Combustion, pp. 703-712, Academic Press; N.Y. (1963)
16. Macek, A., "Fundamentals of Combustion of Single Aluminum and Beryllium Particles," Eleventh Symposium (International) on Combustion, pp. 203-217, Academic Press, N.Y. (1967).
17. Markstein, G. H., "Combustion of Metals," *AIAA J.*, Vol. 1, pp. 550-562 (1963).
18. Markstein, G. H., "Heterogeneous Reaction Processes in Metal Combustion," Eleventh Symposium (International) on Combustion, pp. 219-234, Academic Press (1967).
19. Glassman, I., "Combustion of Metals - Physical Considerations," Solid Propellant Rocket Research, pp. 253-258, Academic Press (1960).
20. Brzustowski, T. A. and Glassman, I., "Spectroscopic Investigation of Metal Combustion," Princeton University Aeronautical Engineering Report No. 586 (October 1961).
21. Merzhanov, A. G., "Thermal Theory of Metal Particle Ignition," *AIAA Journal*, Vol. 13, No. 2, pp. 209-214 (February 1975).
22. Derevyaga, M. E., Stesik, L. N., and Fedorin, E. A., "Ignition and Combustion of Aluminum and Zinc in Air," *Fizika Goreniya i Vzryva*, Vol. 13, No. 6, pp. 852-857 (November-December 1977).
23. Derevyaga, M. E., Stesik, L. N., and Fedorin, E. A., "Critical Conditions for the Ignition of Magnesium," *Fizika Goreniya i Vzryva*, Vol. 14, No. 6, pp. 44-49 (November-December 1978).
24. Volpert, V. A., Dvoriankin, A. V., and Strunina, A. G., "Multi-dimensional Combustion of Samples of Rectangular Cross-Section," *Fiz. Goreniya Vzryva*, Vol. 19, pp. 10-13 (July 1983).

25. Yukhvid, V. I., "Dynamic Interaction of a High Temperature Multiphase Melt With the Metallic Matrix," *Izv. Akad. Nauk SSSR, Met.*, No. 6, pp. 130-135 (1988).
26. Kudryavtsev, V. M., Sukhov, A. V., Voronetskii, A. V., and Shpara, A. P., "Combustion of Metals at High Pressure (Three-Zone Model)," *Fiz. Goreniya Vzryva*, Vol. 15, No.6, pp. 50-57 (1979).
27. Bonch-Bruevich, A. M., Libenson, M. N., Gagarin, A. P., Kotov, G. A., Makin, V. S., Pudkov, S. D., and Shandybina, G. D., "Laser Activation of Thermochemical Reactions on Condensed Medium Surfaces," *Poverkhnost*, No. 3, pp. 13-24 (1982).
28. Arzuov, M. I., Barchukov, A. I., Bunkin, F. V., Konov, V. I., and Luk'yanchuk, B. S., "Combustion of Metals Under the Action of CW CO₂ Laser Radiation," *Sov. J. Quantum Electron.* Vol. 9, No. 6, pp. 787-789 (June 1979).
29. Tyte, D. C., "Interaction of Metallic Powders with a Shock Wave through an Oxidizing Atmosphere," *J. Appl. Phys.*, Vol. 37, No. 2, pp. 802-806 (February 1966).
30. Hodgson, A. and Mackie, J. C., "A Shock-Tube Study of the Kinetics of Evaporation and Oxidation of Magnesium," *Combust. Flame*, Vol.35, pp. 323-334 (1979).
31. Harwell, K. E., Pell, K. M., and McCay, T. D., "Analytical Model of the Flash Produced in Aluminum-Aluminum Hypervelocity Impacts," *J. Spacecraft*, Vol. 9, No. 9, pp. 682-689 (September 1972).
32. Glickstein, M. R., "Computer Modeling of Titanium Combustion," Accession Number: 82(10):72-414, Air Force Wright Aeronautical Laboratories, Wright-Patterson AFB, OH 45433 (1980).
33. Kennedy, J. E. and Nunziato, J. W., "Shock-Wave Evolution in a Chemically Reacting Solid," *J. Mech. Phys. Solids*, Vol. 24, pp. 107-124 (1976).
34. Evans, J. P., Borland, W., and Mardon, P. G., "Pyrophoricity of Fine Metal Powders," *Powder Metallurgy*, No. 1, pp.17-21 (1976).
35. Witte, L. C., Cox, J. E., and Bouvier, J. E., "The Vapor Explosion," *J. Metals*, pp.39-44 (February 1970).
36. Ishihama, W. and Enomoto, H., "New Experimental Method for Studies of Dust Explosions," *Combust. Flame*, Vol. 21, pp. 177-186 (1973).

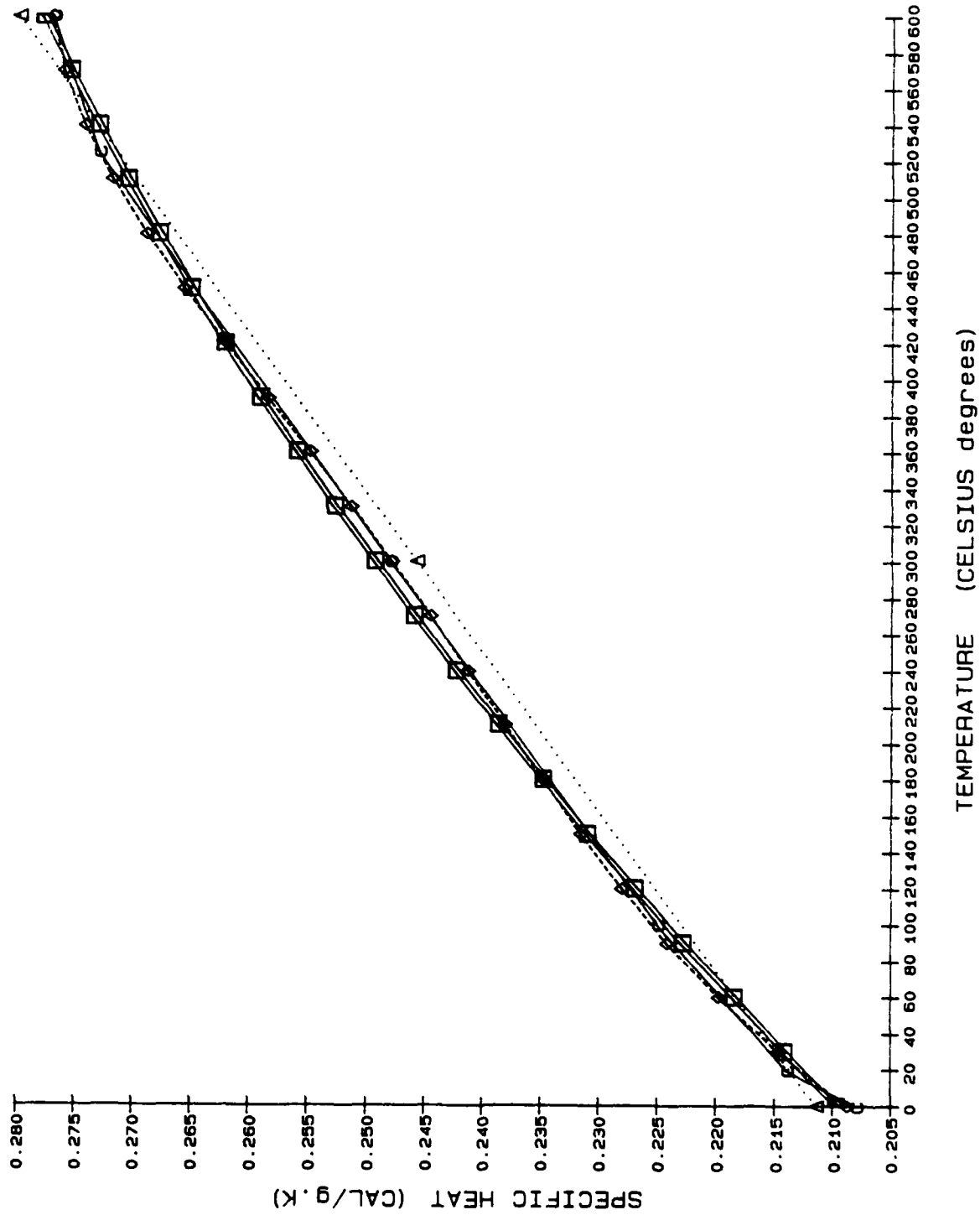
37. Glassman, I. and Dryer, F. L., "Oxidation Kinetics of Hydrocarbon Fuels," Report No. AFOSR-TR-78-0061, Air Force Office of Scientific Research, Bolling AFB, Washington, D.C. 20332 (December 1977).
38. Frank-Kamenetskii, D. A., Diffusion and Heat Exchange in Reaction Kinetics (translated by N. Thon), Princeton University Press, Princeton, N.J. (1955).
39. Beltran, M. R., "Pyrophoric and Hypergolic Properties of Boron," Report No. AD-B089-774L, JANNAF 21st Combustion Meeting 2, pp. 65-99 (October 1984).
40. Cruise, D. R., "Theoretical Computations of Equilibrium Compositions, Thermodynamic Properties, and Performance Characteristics of Propellant Systems," Report No. NWC TP 6037, Naval Weapons Center, China Lake, Ca 93555 (April 1979).

F I G U R E S

CAPTIONS TO FIGURES

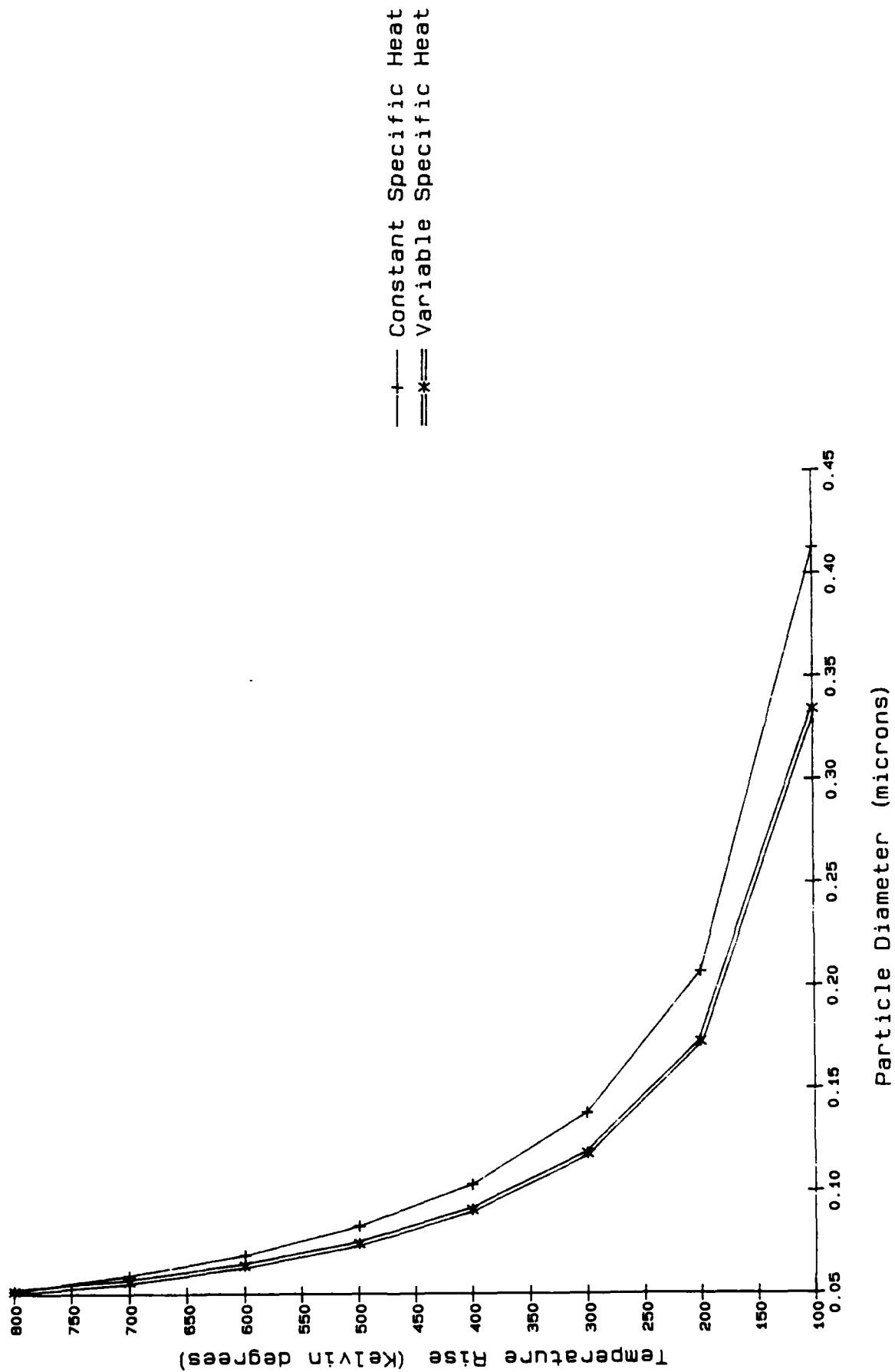
- Figure 1. Specific heat of aluminum as a function of temperature.
- Figure 2. Hypergolic diameter of a single aluminum particle as a function of the temperature rise from its initial condition.
- Figure 3. Hypergolic diameter of a single preoxidized aluminum particle as a function of the temperature rise from its initial condition.
- Figure 4. Hypergolic diameter of a single aluminum particle as a function of its initial temperature.
- Figure 5. Hypergolic diameter of a single preoxidized aluminum particle as a function of its initial temperature.
- Figure 6. The ratio of particle mass to that of its oxide necessary to bring the particle to ignition as a function of the temperature rise from the initial condition.
- Figure 7. Hypergolic size of an aluminum particle as a function of the product of number of atomic monolayers of oxide and surface roughness ratio, and temperature rise from the initial condition.
- Figure 8. Specific particle surface area of aluminum agglomerates as a function of the number of atomic monolayers of oxide formed and the temperature rise from the initial condition.

SPECIFIC HEAT of ALUMINUM

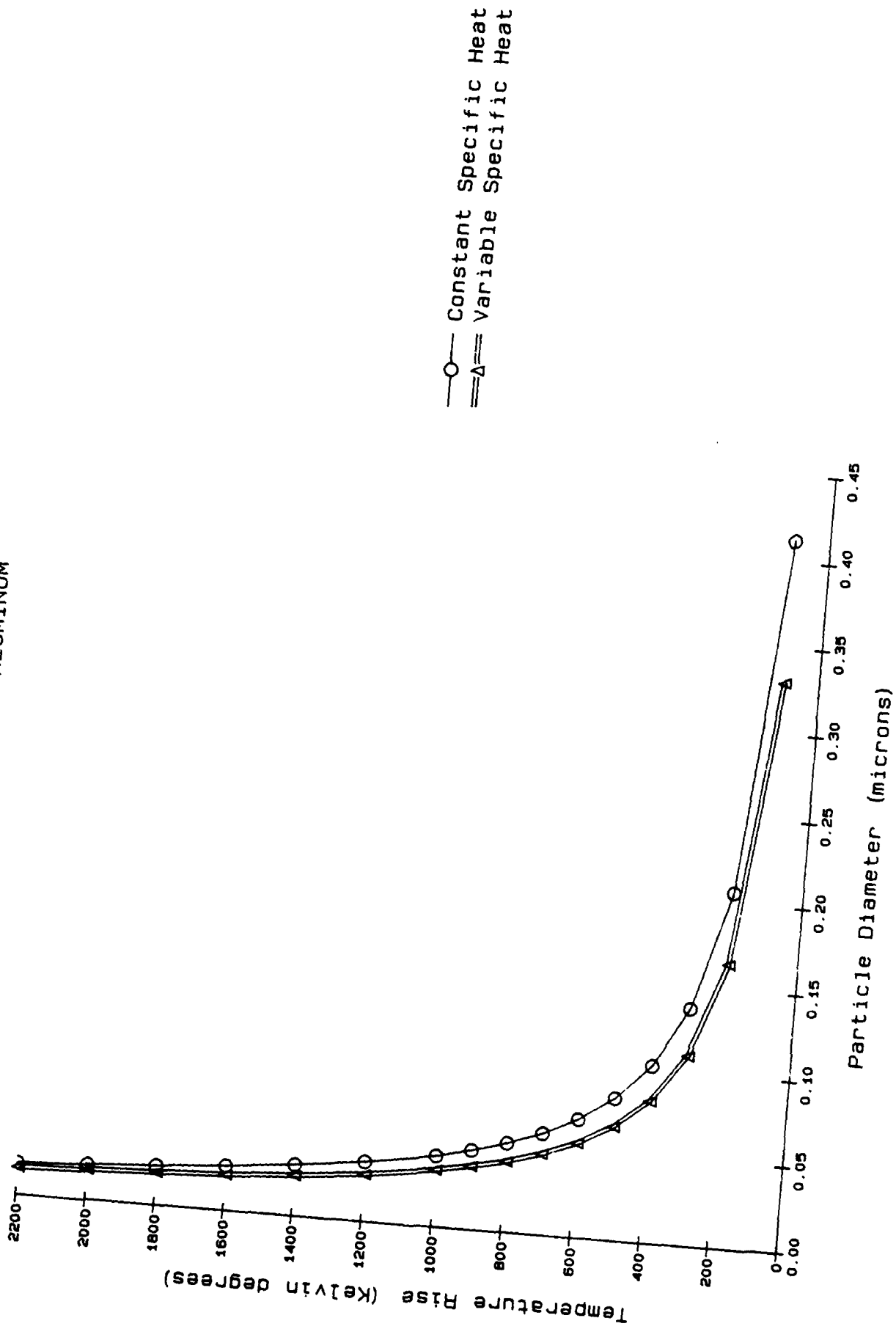


—C— DATA
=□= 2ND ORDER
.....Δ..... LINEAR
- - - - -◇- - - - - 4TH ORDER

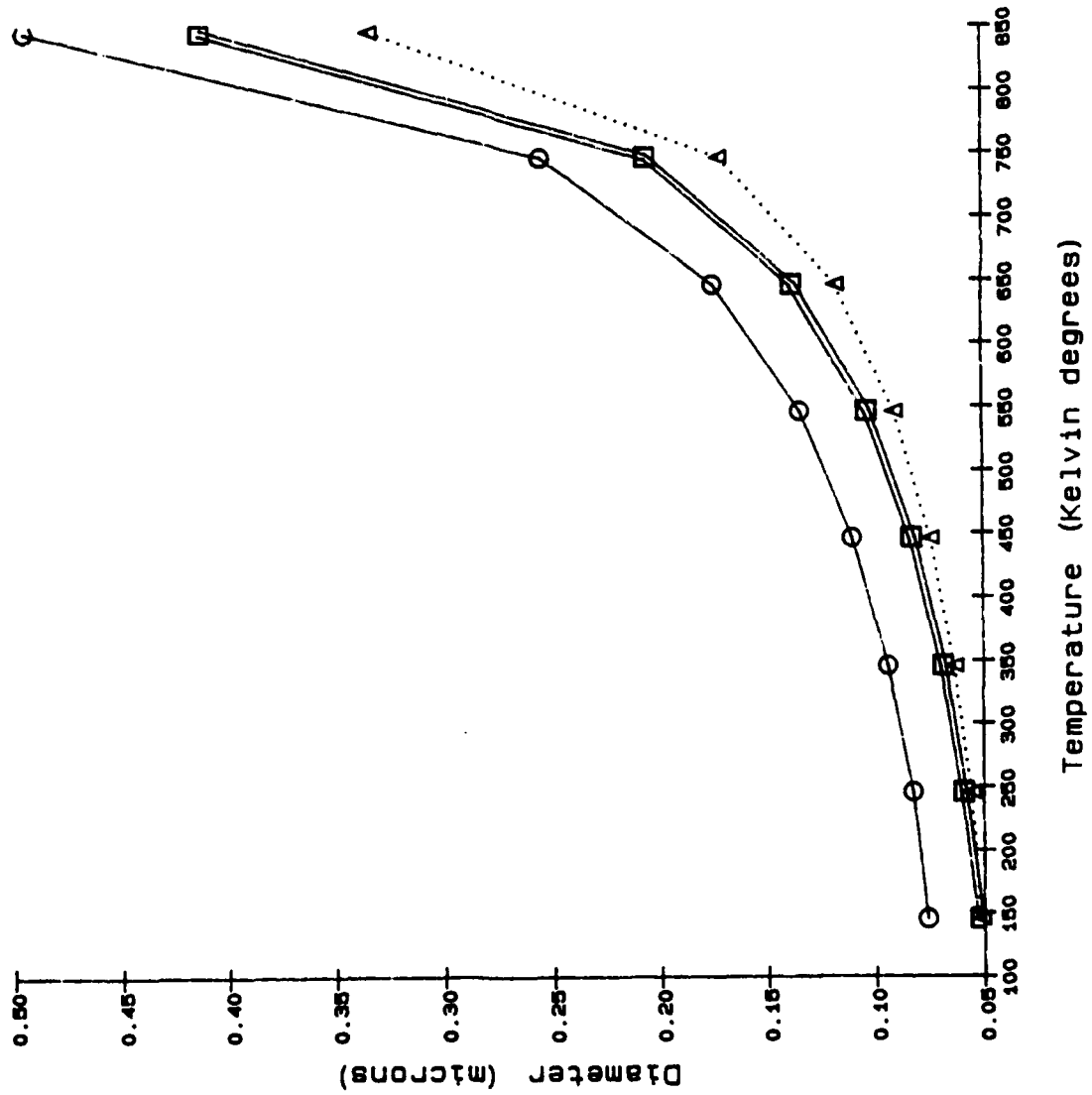
HYPERGOLICITY OF PURE ALUMINUM



HYPERGOLICITY OF OXIDIZED ALUMINUM

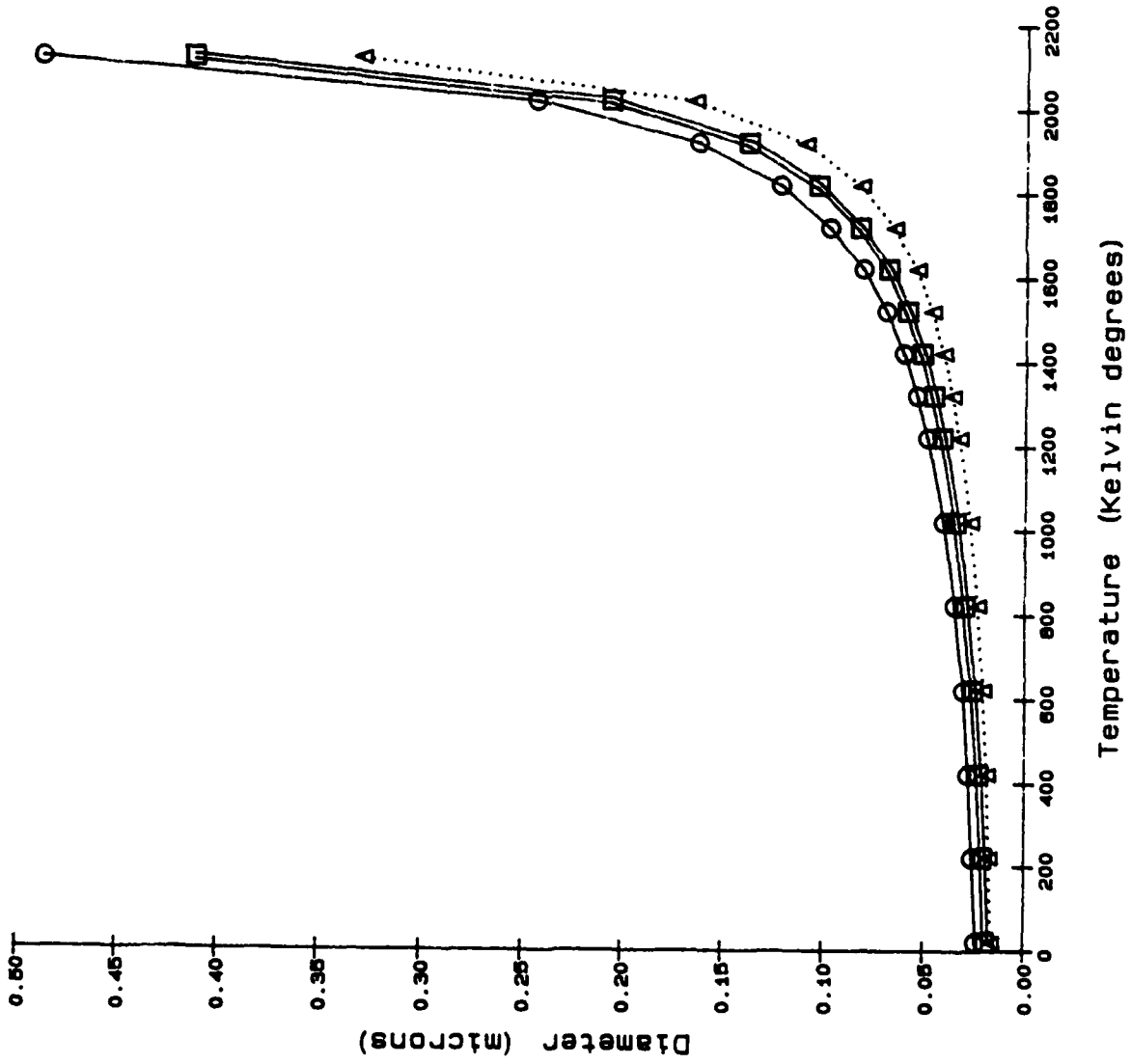


PARTICLE DIAMETER vs. TEMPERATURE for ALUMINUM



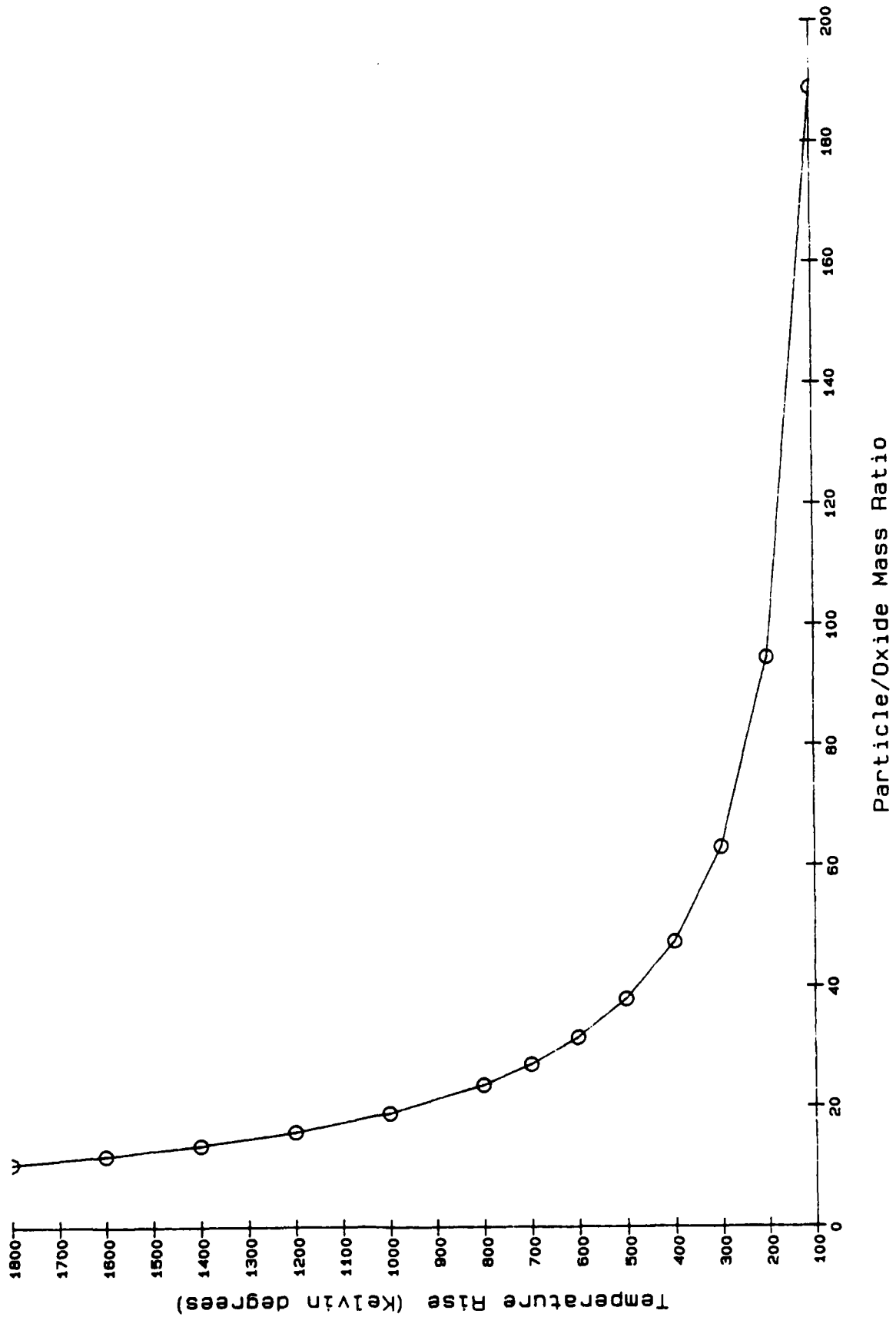
○ Equation (10)
 □ Equation (8)
 △ Variable c. Density ratio 1

PARTICLE DIAMETER VS. TEMPERATURE for PREOXIDIZED ALUMINUM

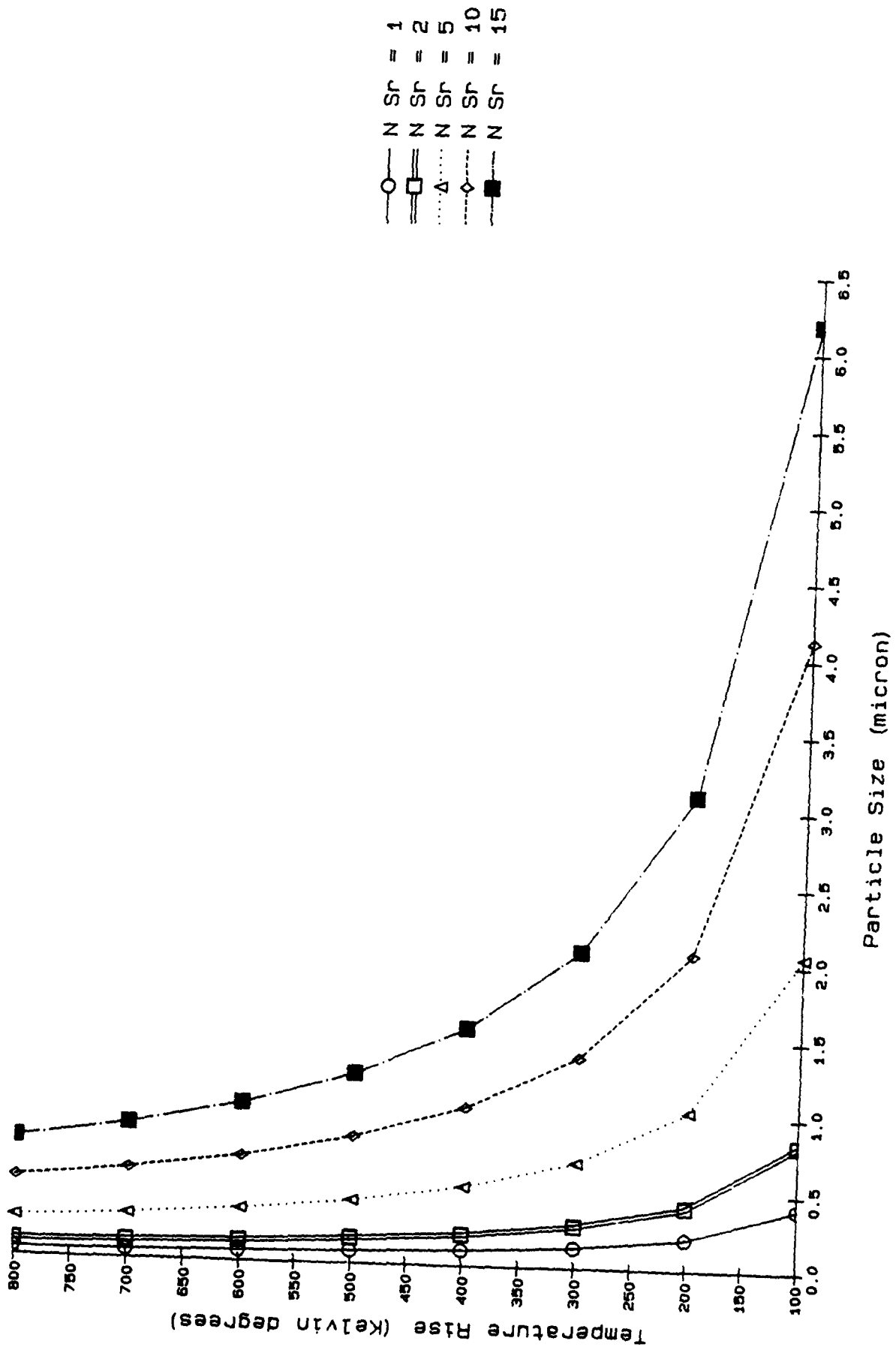


○ Equation (10)
□ Equation (8)
△ Variable c. Density ratio 1

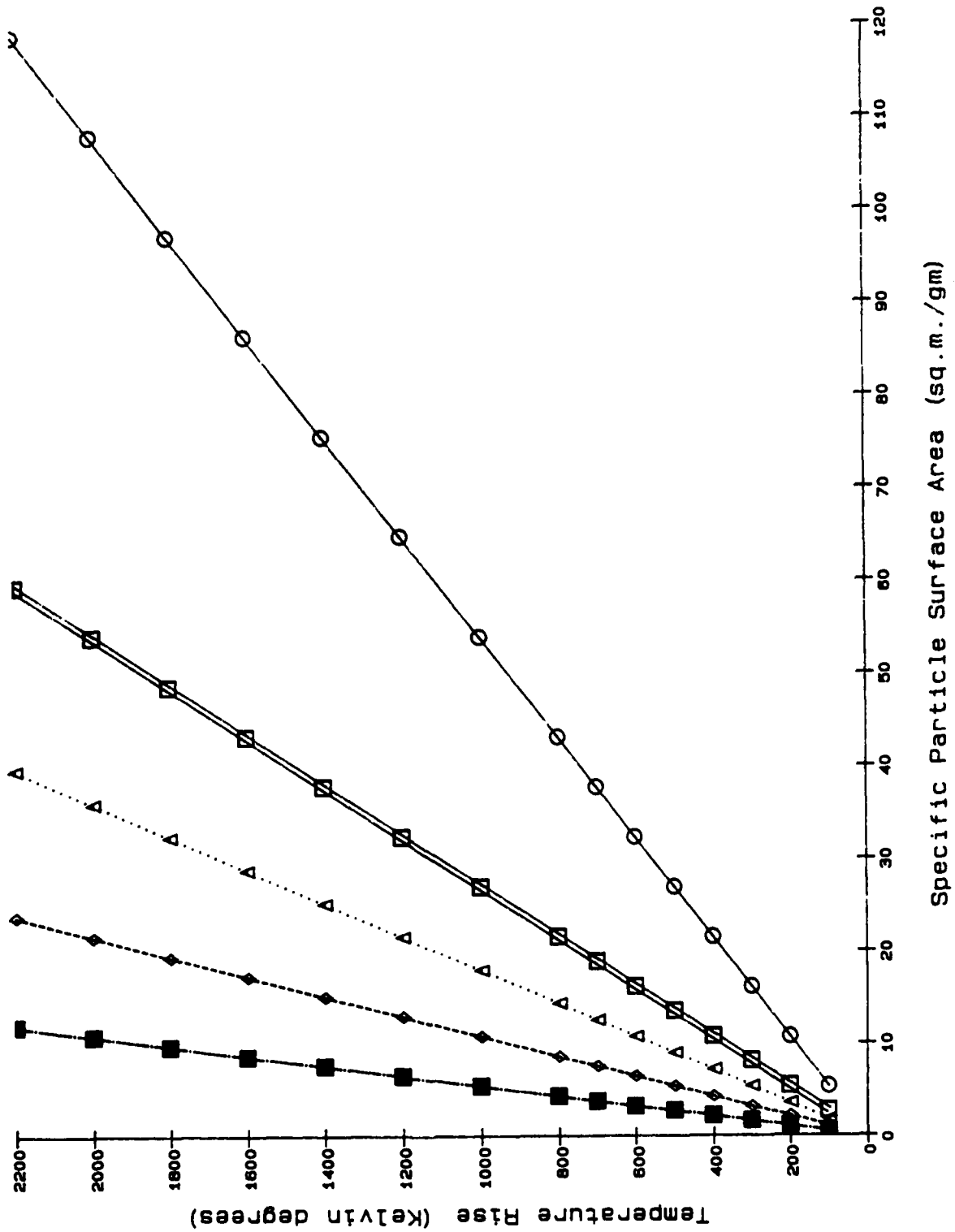
IGNITION FACTOR FOR ALUMINUM



HYPERGOLICITY OF ALUMINUM



EFFECT OF PARTICLE SURFACE AREA ON HYPERGOLICITY OF ALUMINUM



○ N = 1
 □ N = 2
 △ N = 3
 ◇ N = 5
 ■ N = 10

A P P E N D I X

APPENDIX

PROPOSAL

The objective of this work is to generate a mathematical model and a computer solution of the pertinent equations for single particle oxidation, develop a theory for multiparticle oxidation consistent with experimental data to be obtained at the Armament Laboratory, and provide consultation in the performance of relevant experiments.

Procedure and Schedule

The proposed work falls into three categories:

1. Theoretical Study: Develop a realistic model for the oxidation of a single metal particle consistent with experimental results.
 - a. Reproduce and expand published studies, especially Merzhanov's. (First 1.5 years.)
 - b. Refine the Merzhanov theory to include phase transformations and compare it to experimental results. (Second year.)
 - c. Commence the development of a theory for multiparticle metal oxidation under dynamic conditions. (Third year.)
 - d. Update the literature survey periodically throughout the duration of this project. (Periodically for three years.)

- e. Investigate the feasibility of identifying a model for the oxidation of liquid hydrocarbons. (Final year.)
2. Computational Work: Write a computer program to solve the mathematical equations obtained in the theoretical study. These equations are expected to be highly nonlinear because of the presence of radiation and the typically nonlinear nature of the reaction rate function. Consequently, special numerical techniques may be needed for their solution.
- a. Solve the pertinent equations of the mathematical model using appropriate functions for the reaction rates between metal and oxidizer. (First two years.)
 - b. Consider the use of different oxidizers and fit kinetic data to the model as dictated by experiment. (Third year.)
 - c. Gain familiarity with the most recent version of the EPIC-2 program. (First 2 years.)
3. Experimental Activity: Work with the Armament Laboratory to define experiments and identify methods for obtaining data not available in the literature.
- a. Provide consulting services as necessary.
 - b. Assist in data interpretation.

1989 USAF-UES RESEARCH INITIATION PROGRAM

Sponsored by the

AIR FORCE OFFICE OF SCIENTIFIC RESEARCH

Conducted by the

Universal Energy Systems, Inc.

FINAL REPORT

Prepared by: Kwang S. Min, Ph.D.
Hisook L. Min, M.S.

Academic Rank: Professor
Research Associate

Department and Physics Department

University: East Texas State University

Research Location: Jan.- May East Texas State U.
June - Dec. AFATL/MNF
Eglin AFB Fl. 32542

USAF Researcher: Mr. Robert Orgusaar
Capt. Michael Caraway

Date: Dec. 31, 1989

Contract No. F49620-88-C-0053/SB5881-0378

Target-Aerosol Discrimination for
Active Optical Proximity Sensors

- 0. Cover Sheet, Abstract, and Acknowledgement
 - I. Introduction
 - II. Objectives
 - III. Progress on Primary Task
 - A. Enhancement of Algorithms
 - B. Processing of Data
 - C. Hardware Implementation
 - D. Further Considerations
 - IV. Progress on Associated Research
 - A. Applications of Artificial Neural Nets
 - B. Applications of Parallel Processing
 - V. Conclusions
 - VI. Recommendations
- References
- Appendices
- A. Examples of Target-Aerosol Discrimination
 - B. Neural Nets Illustrations
 - C. Example of Parallel Processing Program

Target-Aerosol Discrimination for
Active Optical Proximity Sensors

by

Kwang S. Min and Hisook L. Min

ABSTRACT

In order to assist the development of all-weather Active Optical Proximity Sensors, the algorithms previously proposed in AFATL-TR-88-137 were enhanced. This advancement was validated against all of the realistic target-cloud data sets recently taken in severe aerosol condition at the Climatic Laboratory of Eglin Air Force Base. Hardware implementation of the algorithm is under way.

In seeking additional aids for solving the problem, two newer technologies (neural nets and parallel processing) have been explored and applied to target-aerosol discrimination and associated problems.

Recommendations for improved sensor design and a proposal for a new mode of target detection are also included.

Acknowledgements

We would like to thank the Air Force Systems Command and the Air Force Office of Scientific Research for the funding and support of this research. Deep appreciation goes to Universal Energy Systems for their kind concern and all administrative arrangement of the program. The principal investigator is deeply obligated to Dr. Bill Frawly, director of development, and Dr. Ray Houston, manager of analytical techniques, of E-Systems, Inc., Greenville Div. for providing him with access to the DAP-510 systolic array computer to carry on parallel processing work in the first half of this research. Our research activities at AFATL are rewarding and enlightening. Dr. Sam Lambert, chief scientist of the laboratory, and Mr. Ron Boulet, branch chief, gave continuous encouragement. Mr. Robert Orgusaar and Capt. Michael Caraway with whom we collaborated closely, furnished a great deal of help during the course of this research. Interactions with Bob Erhart, Dick Mabry, Scott Turner, David Hayden, Larry Lewis, Dennis Goldstein, David Gray, Otto Martinez, Rochelle Tyra, Karen Likens, and Malinda Reaves of the laboratory were productive. Help in computing with the Sun workstations and the NP computer provided by Joe Majors and Brian Robertson was deeply appreciated. The image processing and Radar Signal Processing Laboratory staffs of AFATL furnished invaluable assistance regarding image related work.

I. Introduction

Advances made by the recipients of the mini-grant in the research relevant to the target-aerosol discrimination problem are summarized in this report. The period covered is from January 1, 1989 through December 31 of 1989. The first half of the research was carried out at the East Texas State University (January through May), and the later half has been in progress at the Air Force Armament Laboratory at Eglin Air Force Base, Fl.

The principal investigator was assigned as a University Resident Research Professor at the Air Force Armament Laboratory at Eglin Air Force Base effective June, 1989 and has been located there since. The coinvestigator has taken a leave of absence from her teaching assignment at Jarvis Christian College for a year to assist in this research.

In addition to the originally proposed method of solving the discrimination problems utilizing conventional signal processing techniques, two additional relevant activities occurred: [1] formulation of special types of neural nets which may be useful for the target-aerosol discrimination problem, and [2] familiarization with a Single Instruction Multiple Data (SIMD) parallel computer which provides the formulation of efficient algorithms for target detection.

The primary task, application of signal processing to target-aerosol discrimination, has progressed as planned. AFATL/MNF provided excellent support by performing a large scale

aerosol-target pulse return measurement experiment in the Climatic Laboratory. This required extensive electronic design work and the generation of artificial snow. The data has been thoroughly analyzed and will be presented in a AFATL technical report. The effort is continuing and a series of new experiments has been planned. The author is considering submitting a paper based on this work to the SMOKE/OBSCURANT CONFERENCE to be held in April, 1990.

The study of neural nets and their application to the armament system began in January at East Texas State with partial support from this grant and is continuing and broadening in scope at EGLIN AFB. A paper entitled "Applications of Neural Nets to Munition Systems" which we have written has been accepted for presentation at the Society of Photo and Instrumentation Engineers (SPIE) Conference, Aerospace Sensing-90 at Orlando in April, 1990.

Through an arrangement with an area industry (E-Systems, Inc., Greenville Division), the principal investigator was given access to an AMT 510 - a systolic array parallel computer. This unit has 1024 processing units. The computer was used extensively to formulate [1] signal processing algorithms utilizing SIMD computer and [2] multi-target tracking algorithms of upto 1024 targets utilizing Kalman filtering. A paper based on this second work was presented at the Fourth SIAM Parallel Computing Conference at Chicago in December, 1989.

II. Objectives

The Air Force Armament Laboratory is interested in developing a workable all-weather fuze which is robust under adverse weather conditions. Numerous efforts and programs have had only limited success in the last two decades.

During the summer of 88, we participated in the research under the UES, SFRP and SSRP fellowships and initiated three innovative techniques of target-aerosol discrimination. Our effort was presented in AFATL-TR-88-137.

For the mini-grant(RIP), we proposed to further the algorithms and extend the capability of the proposed discrimination techniques. It is strongly felt that systematic testing with realistic data is essential for the validation of the algorithm. Looking into a possible real-time implementation is also one of the important goals.

The immediate goals for the present research are:

- [1] Formulate an effective algorithm to discriminate the target signal from interfering aerosol returns in adverse weather conditions using digital signal processing techniques.
- [2] Investigate any candidate technology available (currently or in the near future) and assess its enhancement possibility in building a robust target-aerosol discriminator for an active optical sensor.
- [3] Formulate and propose new concepts which may be helpful in solving the target-aerosol discrimination problem in general.

An ideal algorithm is illustrated in the figure below.



Figure 1.

III. Progress of Primary Task

Recently, an engineer (R. Orgusaar) at AFATL/MNF performed a series of experiments to obtain Ladar pulse returns in a dense aerosol environment. The measurement was carried out in the AFATL Climatic Laboratory at the end of June, and a technical report [2] has been published based on this experiment and related design descriptions. Since a fresh set of data was available, it was an excellent opportunity to test the algorithms proposed last year.

Data was taken at varied aerosol densities/visibilities ranging from infinity to 15 ft (4.5 m). For low and medium density data, the algorithm discriminated the target from cloud returns easily.

However, for the extremely dense aerosol it was necessary to enhance the algorithm for effective discrimination. Several new techniques have been tried to make the algorithm robust in severe aerosol conditions. After long and tedious enhancement processes, it was confirmed that the algorithm developed works for all the data sets taken.

The method used in this work is based on the Waveform Extraction Method and the Spectral Extraction Method, which have been explored in TR-88-137. Due to the complexity of the experimental data, application of the spectral extraction technique for the entire domain of the data set was ineffective. Segmentation of a significant portion of the domain prior to application of the technique was essential. The significant portion is defined as the interval which includes aerosol and target return signals only. The following is the outline of the enhanced algorithm:

- (1) Smooth the data distribution curve
- (2) Using the waveform extraction technique, identify the critical interval which may represent the target return signal, if any
- (3) Segment the neighborhood which includes the critical interval and the aerosol return signal, if any
- (4) Find transform coefficients for the segmented interval
- (5) Apply appropriate bandpass filtering to the transform coefficients
- (6) Reconstruct a signal using the filtered transform coefficients
- (7) Enhance the reconstructed signal

Target discrimination from aerosol can be achieved by steps 1 and 2, which use the waveform extraction technique. However, the discrimination is reinforced by the spectral selection technique used in the steps 3 through 7. The following describes the above algorithm.

A. Enhancement of Algorithms

1. Segmentation

- (1) Remove the noise from the original data distribution by applying 7 points neighborhood averaging. Let $f(n)$ be the smoothed data.
- (2) Find derivatives $f'(n)$ of the data $f(n)$ for n in the domain. Smooth $f'(n)$ using the same 7 points averaging.
- (3) Using $f'(n)$ distribution, find the interval $[nr, nf]$ where nr is the rising point of $f(n)$ and nf is the falling point of $f(n)$ immediately after nr .
 - a. If $f'(nr-1) \leq 0$, $f'(nr-2) \leq 0$, $f'(nr) > 0$, $f'(nr+1) > 0$, and $f'(nr+2) > 0$ then nr is the rising point of $f(n)$
 - b. If $f'(nf-1) \geq 0$, $f'(nf) < 0$, and $f'(nf+1) < 0$ then nf is the falling point of $f(n)$
- (4) Find a point p such that $f'(p) = \max\{f'(n)\}$ for every n in $[nr, nf]$. If $f'(p) > c$ for a given positive constant c , then proceed to the second derivative test.
- (5) Find $f''(n)$ for every n in $[nr, nf]$. Find nh such that $f''(nh) = \max\{f''(n)\}$ for every n in $[nr, nf]$.

Similarly, find nl such that $f''(nl) = \min\{f''(n)\}$ for every n in $[nr, nf]$.

If $f''(nh) > ch$ for a given positive number ch and

$f''(nl) < cl$ for a given negative number cl

then $nr \leq n \leq nf$ can be claimed as the interval where $f(n)$ is the target return signal for every n in the interval.

Repeat (2) - (5) until a critical interval or the end of the data set is encountered.

(6) Find n_s such that $n_s < n_r$ and $| f(n_s) - f(n_r) | < \delta$ for $\delta > 0$ a small number.

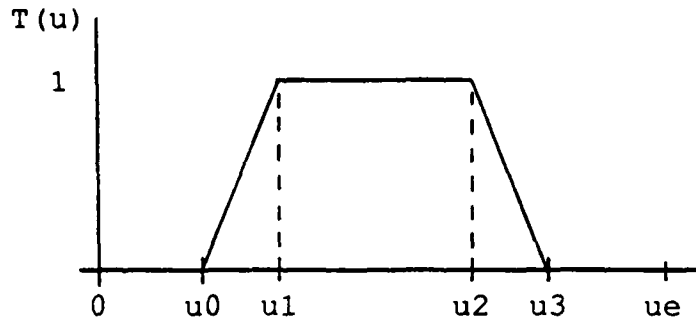
Similarly, find n_e such that $n_e > n_r$ and $| f(n_e) - f(n_r) | < \delta$. Choose all n such that $n_s \leq n \leq n_e$ to proceed with filtering.

2. Band Pass Filtering

(1) $f(n)$ for $[n_s, n_e]$ are transformed using DFT to find the transform coefficients $F(u)$ of $f(n)$ for $[0, u_e = n_e - n_s]$.

(2) A trapezoidal band pass filter $T(u)$ shown below is applied to $F(u)$ to find the band pass frequency function $G(u)$, where

$$G(u) = T(u) \times F(u)$$



$$\begin{aligned} u_0 &= u_e/20 \\ u_1 &= u_0 + u_e/10 \\ u_2 &= u_e - u_0 \cdot u_e/100 \\ u_3 &= u_e - u_1 \cdot u_e/100 \end{aligned}$$

where $u_e = n_e - n_s$

Figure 2. Band Pass Filter

(3) The inverse transform of $G(u)$ is computed to reconstruct the band pass filtered signal $g(n)$.

When the density of aerosol was very high, it was extremely difficult to find $g(n)$ in which the target signal can be totally discriminated from those of aerosol. To enhance this point, use the following techniques:

- (1) Set $g(n) = 0$ if $g(n) < 0$ for $ns < n < ne$.
- (2) Compute the average value m of $g(n)$ for $ns < n < ne$
- (3) Find $A(n) = g(n) - m$ for each n $ns < n < ne$
- (4) Set $A(n) = 0$ if $A(n) < 0$
- (5) Compute $V(n)$ such that $V(n) = (A(n))^{**2}$ for every n on $[ns, ne]$.

This $V(n)$ represents the target signal slightly modified from the original $g(n)$.

A more detailed description of the algorithm and the results will be presented in the proposed Technical Report:

"Digital Processing Techniques for Active Optical
Fuze Sensors"

by H. Min, R. Orgusaar, and K. Min

B. PROCESSING OF DATA

A total of 41 sets of usable data and an equal number of reference leg data are taken at varied visibility conditions ranging from 15 ft to near infinity. Typical data at various aerosol conditions are illustrated using the compressed forms in Figure A1 in Appendix A.

Transform and filtering are performed with newly implemented enhancement in the preprocessing. For all transforms, the signal separation appears to work.

It has been validated that all the realistic ladar pulse return data collected in the AFATL Climatic Laboratory on June 30, 1989 can be analyzed effectively by using this enhanced algorithm.

Separation of mixed target and cloud signals utilizing these signal processing techniques was successful as shown in Figures A2 - A7 in Appendix A. Newly enhanced techniques in the time domain tends to expedite and complement our earlier discrimination techniques.

C. Hardware Implementation

Implementation of these algorithms to realistic systems needs to be studied with caution. In view of stringent requirements on fuzing functions, (1) extremely short response time and (2) miniature processing elements, systematic studies should be carried out to implement them successfully. With currently available technology, it should be feasible to implement these algorithms.

Several companies, including Texas Instruments, Motorola, and AT & T, have been active in advancing signal processing VLSI technologies. AFATL/MNF elected to procure a development board utilizing the newest 32 bit floating point high speed DSP chip, TMS320C30, which was delivered during the month of October [3]. The main board has been installed and the software partially tested. The C-compiler for the TMS320C30 [4] arrived in the middle of November and the preliminary work towards the hardware implementation of the algorithm has been commenced.

Recent development in ASIC technology claims that it is feasible to build a chip which performs 256 point FFT in microseconds. The price of these IC's are decreasing drastically and implementation of a specific algorithm can be easily achieved.

Systematic studies of the appropriate implementation of proposed algorithms and testing will be continued with the full utilization of all the resources currently available or under development.

D. Further Considerations

1. Future Experiments

While the analysis was in progress, the need for a measured data set with known controlled parameters was realized. It is especially so for the extremely dense condition to confirm the effectiveness of the algorithm. The present data set does not have a time marker indicating when the pulse was emitted and there is an ambiguity in confirming the target pulse with confidence in a severe aerosol condition.

We plan to perform a controlled experiment in AFATL/MNF's Bay-9. Use of a more powerful Ladar emitter may improve the detectability of the target considerably by improving the signal to noise ratio. Recent advances in laser diode technology makes it possible to have a relatively inexpensive powerful emitter available for this type of experimentation. Generation of artificial fog has been discussed with an expert of the Test Wing, Dr. Register. Further experiments with aerosol, smoke, or other obscurants may be carried out in the future.

2. Use of Multi-beam Configuration and Two-dimensional Arrays

One of the most powerful techniques in signal detection and classification is the use of cross correlation measures utilizing known templates. Our previously proposed correlation method in

signal separation [1] has some similarity in the basic concepts except that it does not use a prestored template. This method is effective in identification of the target and localization of a high value spot in the target. A continued study of this approach is urged, but it requires high speed and possibly parallel processing.

As an extension to our correlation method work in the last year, which correlates the active IR returns for two-dimensional array of emitter-sensors and extracts the target signature, larger array size configurations are simulated. Array size has been increased to 64 (8 x 8) and the algorithm has been implemented to PC-AT and Sun-3 workstation. A number of larger array cases will be studied with NP in the near future.

A small size preliminary experiment utilizing a 4-sensor (2 x 2) array is being considered for the near future.

3. IR Sensing and Image Based Fuze

Recent development in high speed sensing and imaging technology may make it possible to develop an image based fuze. Active or passive IR imaging can be accomplished, and matching filters may be utilized for the target recognition using prestored templates. The motion of the target can be estimated by observing the time sequence of the target images, and the optimum burst point may be readily determined.

Acquisition and construction of a high speed digitizer and efficient (optical or any other form of parallel processing) image and logic processing devices are essential in this application.

Meanwhile, another alternative has been considered to make the image fuzing possible by implementing a new and fast "object" processing technique. It is based on a simplified array made of 64 sensors (8 x 8) and a new approach to processing. It employs a quick identification/classification scheme being developed by the participant under the separate heading of Neural Nets Applications. Hopefully it will meet the time requirement of fuzing with a "quick recognition" capability.

An algorithm for fuzing based on passive sensor signal processing has been developed by detecting the image changes and estimating the motion. For the present, the algorithm is not overly concerned about the time requirement and is scaled for a small array of 64 sensors (8 x 8).

Various refinements to meet the practical requirements are forthcoming. Part of this work is carried out in the Radar Signal Processing Laboratory (RSPL) and Image Processing Laboratory (IPL) of AFATL.

4. Adaptive Processing

The importance of adaptive processing of data in the enhancement of the algorithm has become evident during the course of this research. Aids provided by parallel computing and neural nets are likely to be of great value.

In addition to the Air Force, other branches of the Armed Services are utilizing these technologies in the munition systems. We also attempted to study and utilize them as much as possible. Our activities will be described in the next section.

IV. Progress on Associated Research

As stated earlier, two candidate technologies which may provide some assistance in achieving an all-weather sensor have been studied. They are (1) artificial neural nets, and (2) parallel processing. Activities for each subject are described below.

[A] Applications of Neural Nets to Target Detection

Artificial neural nets are taken as effective classifiers and their applications to Air Force armament systems are considered. This activity includes the formulation of special artificial neural nets as efficient discriminator/classifiers and their applications to

[1] Target-Aerosol Discrimination

[2] Image Based Fuze

Founding work was started at the beginning of the year at East Texas State Univeristy under the Mini Grant, and has been in progress steadily. The work will continue through the URRP period (June 1990), and will culminate in the form of a proposed AFATL Technical Report:

"Applications of Neural Nets to Air Force Munition Systems"

by K. Min and H. Min

In addition to that, the following conference presentation has been accpted.

SPIE Aerospace Sensing-90 at Orlando, April 1990

"Applications of Neural Nets to Munition Systems"

by K. Min and H. Min

This work is still in progress and many practical applications are yet to be validated. However, some encouraging results in the ground work along with over all strategy for its utilization to target-aerosol discrimination will be given below.

The neural nets constructed are similar to the Kohonen type [5] which is known to be an effective classifier. Another reason for choosing this type is that it can be pre-adapted (trained) using a group of probable candidate templates for specific tasks, and it does not require tedious iterative processes in performing a discrimination/classification.

Adaptation(training) of the associative memory is very fast, and the response time of the nets to do a classification is remarkably short. It can discriminate a very large number of templates with only a small number of input neurons. For example, using only 8 input neurons we did not encounter any difficulty in distinguishing several hundred different patterns.

In one of a few formulations, we used a block of 64 (8 x 8) pixels to represent a pattern. Each pixel carries binary information and our figure is a black and white image.

To start out, each row (image) vector is coded with an identification number 0 through 255. We have developed a simple scheme for this representation, and it does not require storing 256 patterns in memory to identify them.

For any desired template, form an 8-dimensional vector with an identification number for each of the row vectors. This vector will represent this specific template and will be used to discriminate it from all other templates.

The desired number of templates are selected, and the nets undergo very short adaptation process with them to establish an optimum associative memory.

Once this process is completed, it is quite efficient to identify the input pattern. The strengths of these nets are

[1] it can tolerate noise or imperfection of data

[2] it picks the closest candidate in the absence of an exact match and gives the measure of closeness.

Figure B1 in Appendix B illustrates an example of this net identifying several noisy input figures properly. These nets are implemented on PC-AT and Sun-3 workstations using C-language.

Taking advantage of noise tolerance, fast response time, and the pretraining capability, it is feasible to use these nets as a sensitive discriminator/classifier. It detects the designated types of signal change and demonstrates the possibility of utilization for the target-aerosol discrimination.

The optimum utilization of the nets by detecting the characteristics of the mixed Ladar returns for this purpose is yet to be determined. Further experimentation and study will be required.

For the image interpretation and motion detection for the fuzing purpose, it is necessary to build several echelons of nets. The basic approach is [1] use an 8 x 8 block as an unit, [2] make a small image of a few of these blocks and [3] make a large of a few small images. Thus it is possible to construct a hierachy of structures to represent a large sized image. It will make the segmentation procedure simpler.

Though many details still need to be developed, some of ground work in the image detection has been done. They are described below.

- [1] To warrant more accurate identification, an 8 x 8 basic input block will be examined in two directions. In addition to the row vector identification scheme, a column vector identification will be carried out at the same time. As a result, a figure will have two identification vectors, one made of row vector ID's and the other made of column vector ID's.
- [2] Having two identification schemes has the advantage of having a double checking capability. If a *minimum closeness measure of an input figure is above a certain threshold in one direction, then try the other direction for a better fit. If both measures are above a respective threshold, then we conclude that the input figure does not have an acceptable match.*
- [3] We noticed that many figures or patterns are related to each other. For example, a mirror image of a pattern can be associated with the figure by a simple scheme. Upon analysis, we developed algorithms to generate 15 other related patterns out of the original by performing complement, mirror image, left rotation, right rotation, and double rotation. This

fact is extremely helpful in reducing the number of templates that must be stored for the discrimination/classification. The fewer the number of templates, the quicker the identification. Preprocessing of an input figure into 16 different appearances takes very little time with our algorithm. Identification will stop as soon as any one form closely matches any reference template stored. Figure B2 of Appendix B shows 16 different "looks" of a pattern.

Motion detection, size change estimation and other important algorithms are under study. So far, all work has been with binary images, but its extension to a multi-level image will be carried out in the near future.

[B] Applications of Parallel Processing

Noting the necessity of parallel processing in the signal processing and image interpretation, substantial amount of effort was put in parallel processing prior to the move to Eglin.

Using all 1024 processing units of the AMT-510 systolic array processor [6], the tasks listed below were performed. It is a Single Instruction Multiple Data (SIMD) machine and is especially suitable for these kinds of computation.

[a] Digital Signal Processing

[b] Multi Target Tracking using Kalman filtering

For digital signal processing, several basic algorithms including orthogonal transforms, filtering, pulse processing, cross correlation evaluation, and phased array simulation were worked out using AMT Fortran-plus.

The machine has excellent graphics displaying 1024 x 1024 pixels with 256 colors. In processing a triangular transform on 8K data, it required than a minute. This included data generation, transform, inverse transform, and display of all of the above. The code is very compact due to the parallel nature as shown in Appendix C.

For multiple target tracking with Kalman filtering, up to 1024 targets are tracked simultaneously and displayed on the screen. Upto 6 different versions of tracking algorithms were run concurrently and their results displayed on the screen for comparison. A small simulation program of several targets going through cloud regions was worked out in relation to a target-aerosol discrimination problem.

Recent development in parallel computers indicates a possible availability of a very small unit which may be used for a munition system in the near future. Some have been ruggedized already and are used in helicopters. With the advancement of the technology in the next few years, it may not be a mere dream to utilize a parallel computing "chip" for the target-aerosol discrimination.

V. Conclusions

Upon pursuing the objectives of the present research, the following conclusions are made:

1. The newly enhanced target-aerosol discrimination algorithm successfully separated the target signals from interfering background in severe aerosol conditions.
2. If a Ladar emitter with higher power is used, the discrimination algorithm may be simplified by taking advantage of a better signal to noise ratio (SNR).
3. Implementation of parallel algorithms in digital signal processing will improve the speed and boost the capability of target detection by allowing more complex processings.
4. Utilizing special types of artificial neural nets may improve the robustness of the munition system. Preliminary results of the present study are encouraging.
5. Utilization of emerging technology, focal plane arrays with passive IR, may be an addition to future fuzing by providing an image based fuze/seeker.
6. Multi-mode and multi-sensor fusion may be a necessity for genuine all-weather sensing.

VI. Recommendations

For the development of the all-weather fuze, the following recommendations are made:

1. Continue systematic in-house research in target-aerosol discrimination with continually improving experimental design. The experiments needed are neither too expensive nor elaborate.
2. Continue to upgrade the discrimination algorithm as new sets of data are collected. Move toward simpler algorithms to improve the response time which is critical for a fuzing action. Research in hardware implementation of the algorithm should continue using the appropriate development board.
3. Continue research in the implementation of parallel algorithms in signal processing for the fuze/seeker system. It will be an integral part of a future munition system, and necessary hardware is approaching within reach.
4. Continue research in special types of neural nets. Their applications for specific missions will enhance the robustness of the munition systems.
5. Emphasize a systematic study of "sensor fusion" using a multi-mode, multi-sensor munition system. Parallel processing and neural nets may provide needed help.
6. Continue to develop a working model of an image based fuze/seeker utilizing focal plane arrays, parallel algorithms, and neural nets.

References

- [1] Kwang S. Min and Hisook L. Min: Target Aerosol Discrimination Techniques for Active Optical Sensors, AFATL-TR-88-137, Air Force Armament Laboratory, 1988.
- [2] Robert H. Orgusaar: Optical Fuzing Sensor Data Collection, AFATL-TR-89-73. Air Force Armament Laboratory, 1989.
- [3] Texas Instruments: Third_generation TMS320 User's Guide, 1988
- [4] Texas Instruments: TMS320C30 C Compiler User's Guide, 1988
- [5] T. Kohonen: Self-Organization and Associative Memory, 2nd ed., Springer Verlag, 1987
- [6] D. J. Hunt: AMT DAP - A Processor Array in a Workstation Environment, Computer Systems Science and Engineering Vol 4 No 2, pp. 107-114, April 1989

Appendices can be obtained from
Universal Energy Systems, Inc.

1989 USAF-UES RESEARCH INITIATION PROGRAM

Sponsored by the
AIR FORCE OFFICE OF SCIENTIFIC RESEARCH

Conducted by the
Universal Energy Systems, Inc.

FINAL REPORT

The Dynamics of Impact

Prepared by:	Dr. Joseph J. Molitoris
Academic Rank:	Professor
Department and College:	Physics Muhlenberg
Research Location:	Muhlenberg College Department of Physics Allentown, PA 18104
USAF Researcher:	Joseph C. Foster, Jr.
Date:	01 December 1989
Contract No:	F49620-88-C-0053

The Dynamics of Impact

by

Joseph J. Molitoris

ABSTRACT

The physics of impact and penetration is relevant to both the development of armor and armor penetrators. This dynamic process was studied through the use and development of one-dimensional physics models and a two-dimensional hydrodynamic code. The appropriateness of the physics assumptions in these models was verified by comparison with both final state and time resolved data.

ACKNOWLEDGEMENTS

The hospitality of the Munitions and Warheads branch is gratefully acknowledged. I express my appreciation to Joe Foster, without whom this research would not have been possible. The support of Leo Wilson, Joel House, Don Lorey, and Dave Lambert was also much appreciated. Joel especially made a good effort to keep me in the communications loop. In particular, I am grateful for the data provided by Leo and Joel and the Hull simulations run by Don. Discussions with Stan Jones are acknowledged.

I am indebted to Sam Lambert for his support and an overview plus a tour of the base. I thank the Air Force Systems Command, the Air Force Office of Scientific Research, and Universal Energy Systems for the sponsorship and administration of this program.

I. INTRODUCTION

The mechanism of the deformation of metals at high velocities is of both practical and fundamental interest. The basic question is: what is it that happens when a projectile interacts with a target? The entire event has a duration of only 100 μ s with much that is essential occurring during the first 10 μ s. The answer to this question is dependent on the velocity of the projectile, the geometry of the interaction, and the material properties of both the projectile and the target.

The Anti-Armor group of the Munitions and Warheads branch at the Armament Laboratory of Eglin Air Force Base has many years of experience with the dynamics of impact and penetration. Furthermore, the recent Intermediate range Nuclear Forces treaty makes armor and anti-armor technologies a national interest. As noted in a recent New York Times article on the subject: "Since the dawn of man, there has been a never-ending race between the makers of swords and the makers of shields."¹

This type of research effort also has relevance to the Strategic Defense Initiative. Directed beams damage a target by depositing their energy in a thin layer on the surface.² The surface vaporizes and momentum transfer to the target causes damage by shear, buckling, and/or spall.

In materials as well as my former field of nuclear physics, one speaks of the projectile impacting the target. Shock waves are formed and propagate in the projectile and target material. For a rod impactor in particular, elastic and plastic waves also propagate in the rod and conspire to decelerate and deform it. Through studying collisions at different velocities and with different elements, one hopes to learn about the material equation of state.

II. OBJECTIVES OF THE RESEARCH EFFORT

My goal for the year was to become further acquainted with the state of the art techniques of the Munitions and Warheads branch and more cognizant of this active research field. The Anti-Armor group is interested in simple engineering/physics models of the impact and penetration of a target by a rod. These include the Taylor theory for the impact of a specimen against an anvil³ and the Tate theory (which makes use of the Bernoulli equation) for the penetration of a rod into a target.⁴

Upon impact, a shock wave and slower elastic wave propagate from the front end of the rod backwards. Like any stress wave, they are reflected and inverted at the free end. Such stress waves are attenuated both mechanically and thermally in an exponential manner.⁵ Strong shock waves and tensile

waves can also produce strain hardening, defects, and void growth in the material.

The approach followed in researching the field was both analytical and computational. Analytical methods were employed wherever possible. But I also utilized data from the FORTRAN codes Hull and Epic and wrote my own code. During my previous summer research, I had become acquainted with the various experimental facilities including the high frame rate camera, the X-ray examination of metal samples, and the 50 and 120 mm gun ballistics apparatus.

The major items of work performed as part of the research were:

1. Search the literature and maintain a bibliography.
2. Set up and utilize the Zenith computer hardware and software.
3. Study and modify the one dimensional models of impact and penetration.
4. Develop FORTRAN programs for simulation and data analysis.
5. Analyze time resolved impact data as obtained by Leo Wilson and the AFATL-MNW Anti-Armor group.
6. Document results in this final report.

III. SHOCK PHYSICS

One dimensional models^{3,4,6-9} have their place in understanding the complicated process of impact and penetration. The practical goal is to predict as well as possible the results of a particular penetrator-armor combination with a model that is either analytic or at least solvable with small computer programs. These simple physics models are hence useful in the design process.

For a rod impacting an anvil at $t = 0$, the initial conditions are those of a shock. In the reference frame where the shock is at rest, the particle velocity of the unshocked matter is $u_0 = u_s$ and that of the matter through which the shock wave has passed is $u = u_s - u_p$. Conservation of mass across the shock front gives

$$\rho_0 u_0 = \rho u \quad (1)$$

and conservation of momentum implies

$$\rho_0 u_0^2 - \rho u^2 = p - p_0 \quad (2)$$

whereas the statement of conservation of energy is

$$1/2 u_0^2 + p_0/\rho_0 + e_0 = 1/2 u^2 + p/\rho + e \quad (3)$$

The Rankine-Hugoniot energy equation gives the locus of end states reachable by shock transition from the initial state at pressure p_0 and specific volume $\nu_0 = 1/\rho_0$.

A simple application of these ideas equates the pressure in

the target to that in the projectile

$$\rho_p u_p u_{sp} = \rho_t u_t u_{st} \quad (4)$$

Together with the fact that $u_p + u_t = v$ and a linear parameterization for the dependence of shock velocity on particle velocity,¹⁰ this allows one to calculate the velocity dependence of the variables by solving a quadratic equation. For definiteness, consider Cu impacting steel.^{9,10} As the impact velocity ranges from 100 to 300 m/s, the particle velocity in the copper varies from 51 to 152 m/s and the shock velocity in the copper ranges from 3.99 to 4.14 km/s. For comparison purposes, the elastic wave velocity for Cu is $c_o = \sqrt{Y_m/\rho} = 3.73$ km/s. In Figure 1 of reference 9 is shown the pressure at the interface over this velocity range. The pressure is quite high, going from 18.1 kbar at 100 m/s to 56.1 kbar at 300 m/s. By way of comparison, the Young's modulus of Cu is 1240 kbar and the typical dynamic yield⁹ is 4.5 kbar.

Since this shock pressure only exists for a very short time $\tau < 10 \mu s$, the dynamic strength properties of the solid at high strain rate are probed. Indeed, at the higher velocities, the effect resembles a small explosion: most solids are then damaged by plastic flow and fracture.

IV. TAYLOR MODEL

The classic theory of impact is the Taylor model.³ By eliminating target damage in the Taylor model, one hopes to more clearly study the behavior of the projectile. The Taylor impact test is generally used for velocities in the 100-300 m/s range where the strain rates are $\dot{\epsilon} \approx 10^2-10^4$ sec⁻¹. In this regime, the impact pressure and material strength are related by $p < Y_T$ and $p \cong Y_p$: the projectile deforms but the target does not. This is a complicated impact regime since strength effects, large particle displacements, and failure mechanisms all may come into play.

Consider the impact of a rod of initial length l_0 and area $A_0 = \pi r_0^2$ onto a semi-infinite rigid boundary. Let the front end of the rod be just at the boundary at $t = 0$. Denote the instantaneous length of the rod by l , the location of the back end by s , and the distance from the boundary to the plastic interface by h . The back end velocity of the rod is then

$$v = ds/dt = \dot{s} \quad (5)$$

and the velocity of the plastic front is

$$\lambda = dh/dt = \dot{h} . \quad (6)$$

The geometry of the model then requires that $l_0 = h + l + s$, from which we find

$$dl/dt = \dot{l} = - (\lambda + v) . \quad (7)$$

Thus the rod decreases in length due to the motion of both the back end and the plastic front.

Now consider the balance of mass in the dynamic plastic deformation of the front end of the rod. The amount of mass lost during an infinitesimal time step dt is just $\rho ds A_0$ and the amount of matter eroded is $\rho dh (A - A_0)$. Hence we obtain the fluid dynamic continuity equation:

$$(\lambda + v) = \gamma \lambda \quad (8)$$

where $\gamma = A/A_0$.

In Taylor's view, the momentum of the plastically deformed wafer is changed by a force gradient. The Taylor model assumes that the pressure $Y = Y_p$ is constant across the plastic interface. The material properties are thus idealized by hypothesizing perfect plasticity: there is a constant stress exerted by the material when it deforms plastically. The impulse-momentum theorem then implies (see reference 9 for a derivation)

$$\rho (\lambda + v) v = Y (\gamma - 1) . \quad (9)$$

In the context of the Taylor model, this momentum equation and the continuity equation uniquely determine the parameters λ and γ . The final physics ingredient is the equation which governs the deceleration of the undeformed length of rod. This follows from Newton's second law:

$$dv/dt = \dot{v} = -Y/\rho l . \quad (10)$$

Equations (9) and (10) may be combined to give

$$\dot{\lambda} v + \lambda \dot{v} = -Y\gamma/\rho \quad . \quad (11)$$

Note that this last equation has elements of both mass and momentum loss. One may obtain the approximate Taylor yield strength of a material by assuming that λ is constant and the average velocity is $v_o/2$. This value is given in terms of the final length l_1 and undeformed length l_f :

$$Y_T = \rho v^2 (l_o - l_f) / [2 (l_o - l_1) \ln(l_o/l_f)] \quad . \quad (12)$$

Other one-dimensional models tend to amount to a different relationship between λ and v . In the Taylor model, λ decreases slightly with velocity or grows with time during the impact. In an energy based approach,⁶ the value of λ is smaller than in the Taylor model at high velocities and strains. Hawkyard's statement of conservation of energy gives

$$\gamma \rho v^2 / 2Y + \gamma - 1 = \gamma \ln \gamma \quad (13)$$

which may be solved numerically for $\gamma = \gamma(v)$. In the Jones-Foster model⁷, the value of λ is assumed to be a constant which can be extracted from experiment.

These models were examined in a time dependent way using simple FORTRAN programs. The results were compared to time resolved Taylor anvil data and the codes Hull and Epic-2. The fluid mechanics computer code includes strength effects and material failure; it solves the complete set of continuum equations. Word processing, data analysis, and

programming were all be done on a Zenith personal computer.

V. FLUID DYNAMICS

HULL is a program for solving dynamic continuum mechanics problems¹¹ in Eulerian or Lagrangian formats. Heat conduction and viscous effects are not included.

The equations solved express the conservation of mass, momentum, and energy:

$$\partial\rho/\partial t + \nabla \cdot (\rho\vec{u}) = 0 \quad (14)$$

$$\rho \, d\vec{u}/dt = -\rho\vec{g} + \nabla \cdot \vec{S}$$

$$\rho \, de/dt = -\rho\vec{u} \cdot \vec{g} + \nabla \cdot (\vec{S} \cdot \vec{u})$$

where ρ is the material density, $\vec{u} = \vec{u}(r,t)$ is the material velocity, \vec{S} is the stress tensor, \vec{g} is the gravitational force per unit mass, and e is the total specific energy.

The fluid dynamic equations are solved with the method of finite differences using a mesh of discrete intervals Δx_i , Δy_j in the radial and axial coordinates, respectively. The solution is advanced explicitly from the initial conditions by discrete time steps. Computations were performed with a VAX computer at Eglin AFB.

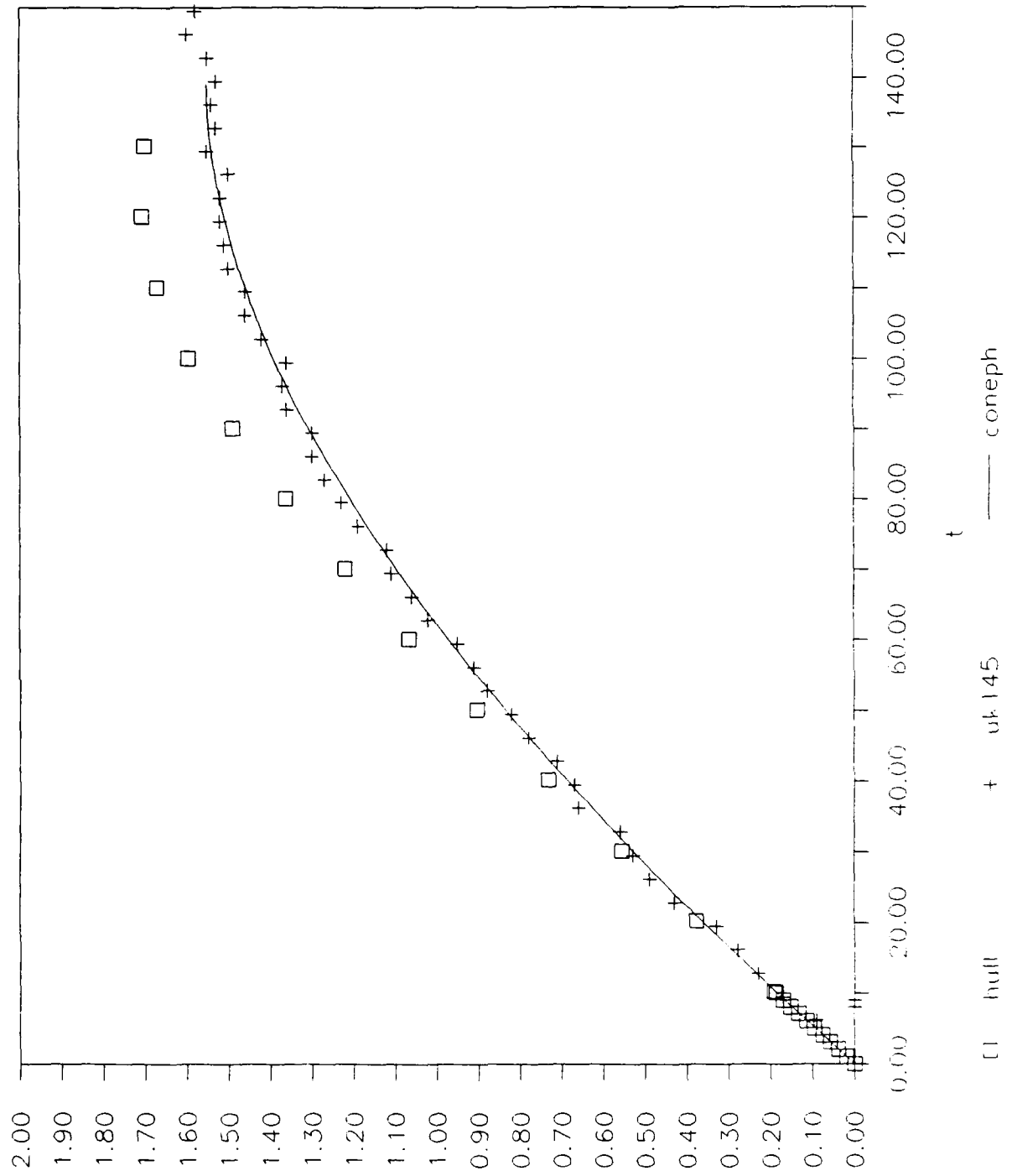


Figure 1

VI. EXPERIMENT

The Taylor anvil setup consisted of a 30 caliber barrel, through which rods were fired using 1-5 grains of red dot propellant and a polypropolux obturator. Data collected by Leo Wilson and Joel House from a high speed camera with a frame rate of 300,000 - 1,000,000 frames per second was available for analysis. This enables time resolution at the 1 μ s level. The camera is a Cordin 330A streak and framing camera, which uses a nitrogen driven rotating mirror. Standard 35 mm Tri-X ASA 400 film was used.

The shot UK-145 was chosen for a detailed analysis. This shot consisted of an OFHC Cu rod impacting a 4340 steel anvil. The rod had dimensions $l_o = 5.72$ cm and $r_o = .380$ cm (30 caliber). The camera was set at a frame rate of 300,000 frames per second. The velocity as determined from the pressure transducers was 18,900 cm/s. From the pre-impact pictures, a least squares velocity of 18,800 cm/s was determined. In Figures 1 and 4, this is the slope at $t = 0$.

The final dimensions of the specimen were total length $l_1 = 4.17$ cm and undeformed length $l_f = 1.65$ cm. In dimensionless form, these are two parameters $p_1 = l_1/l_o = .729$ and $p_2 = l_f/l_o = .288$. The approximate Taylor yield from equation (12) is 3.3 kbar. Solving equations (5) to (10) numerically, one can fit p_1 with $Y = 4.0$ kbar or p_2

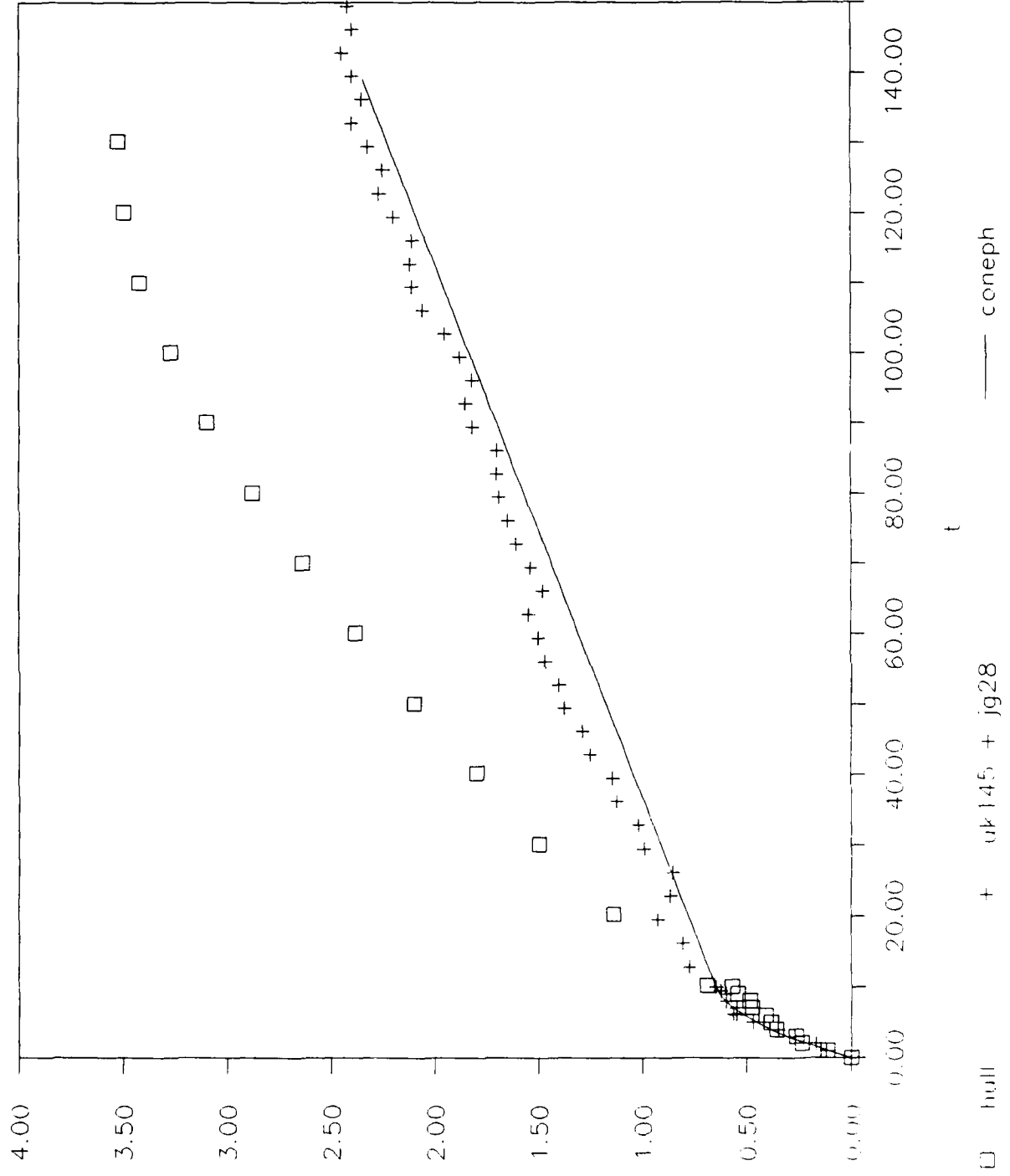


Figure 2

with $Y = 3.4$ kbar in the full Taylor model. The Jones-Foster model has the same ambiguity, giving yields of 3.7 and 3.1 kbar, respectively, taking the value of λ from the experiment. In the Hawkyard model, these values are 4.1 and 3.5 kbar. However, note that it is better to fit p_1 since this gives the correct total final length. The amount of stopping is thus correctly predicted.

In Figures 1 and 4, the deceleration function for the back end of the rod is shown for all times and for early times, respectively. All measurements were made using a vernier caliper from 8x10 viewgraphs blown up from the 35 mm negatives. The Taylor model with $Y = 4.0$ kbar fits the deceleration function perfectly!⁹ However, the modified Taylor model and the Jones-Foster model provide equally good agreement with the data. As seen in the figure, a calculation with the fluid dynamic code Hull also comes very close.

The point where the rod first undergoes deformation may be located from the time resolved data and in the fluid dynamic simulations. This quantity is

$$h = \int_0^t \lambda dt.$$

Refer to Figures 2 and 5. The full Taylor model given by solving equations (5) to (10) gives a value of h which is not linear with time. Coincidentally, the final value of h will fit the data even though λ is an increasing function of

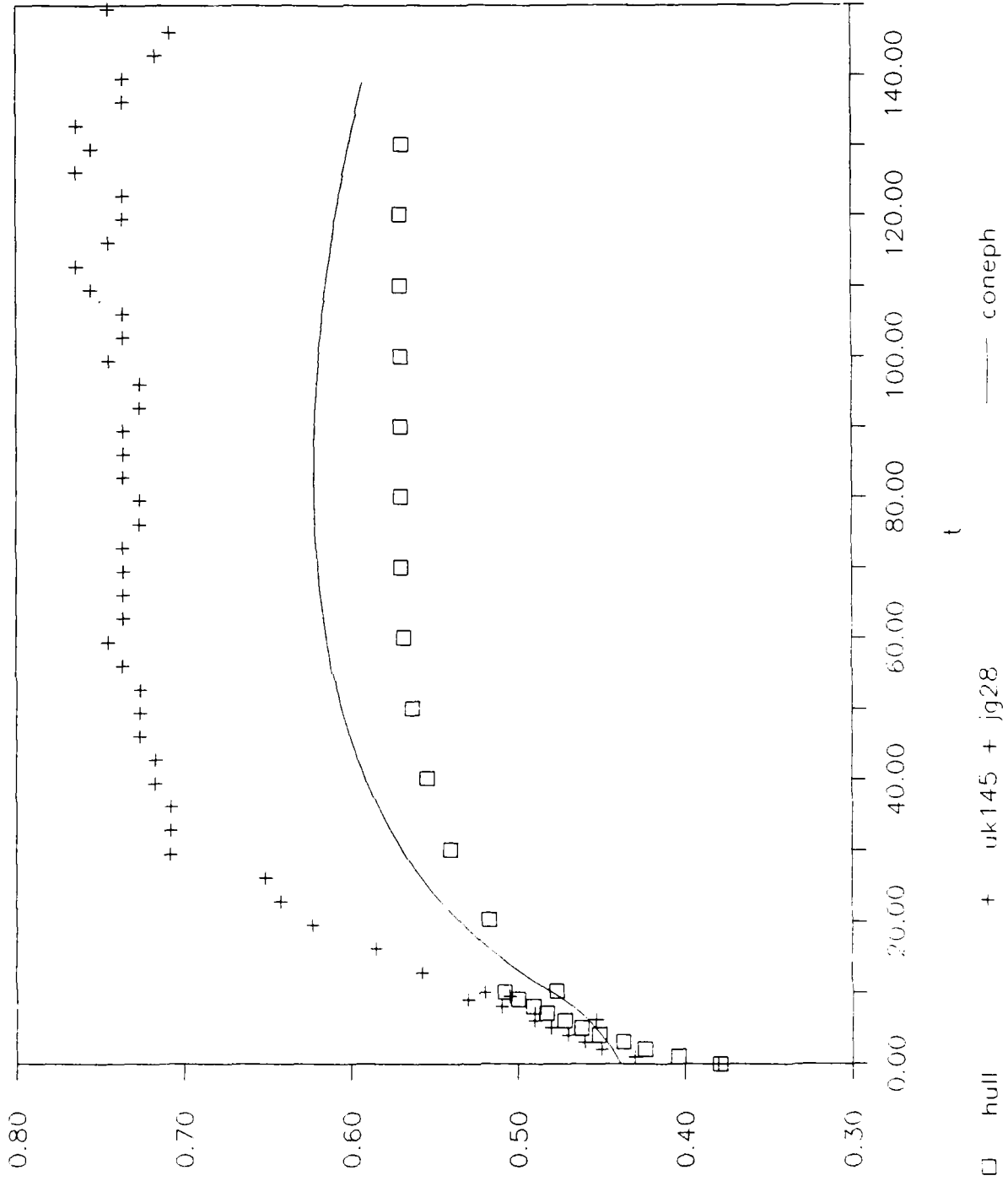


Figure 3

time or a decreasing function of velocity in the full Taylor model. Note that the experimental data does not support this Taylor model time dependence. At $t = 0$, the data gives $\lambda \geq 1.16$ km/s. For later times $5 < t < 135 \mu\text{s}$, the data is linear with least squares slope 13,140 cm/s.

The Hull simulations support a large value for the plastic front velocity initially, but disagree with the constant late time behaviour. The Taylor model may be modified to have $\lambda = 13,140$ cm/s by rejecting equation (9). This is shown by the line labeled Taylor in Figure 3 of reference 9.

The last question to be addressed is that of radial growth. According to the Taylor model, the radius of each wafer is fixed as it is plastically formed. Hence, the radius at the anvil interface is a constant $r = .585$ cm in the full Taylor model and $r = .593$ cm in the modified Taylor model. Both the Jones-Foster and the Hawkyard models also lack radial growth. The data shows this growth at the anvil interface up to about $50 \mu\text{s}$. Refer to Figures 3 and 6. The experimental value for the final radius is $.737$ cm, much in excess of any of the model predictions. The occurrence of radial growth as well as the freeze-out time is predicted by the fluid dynamic simulation. However, the final radius is not predicted correctly.

What was learned in my previous research⁹ was that the

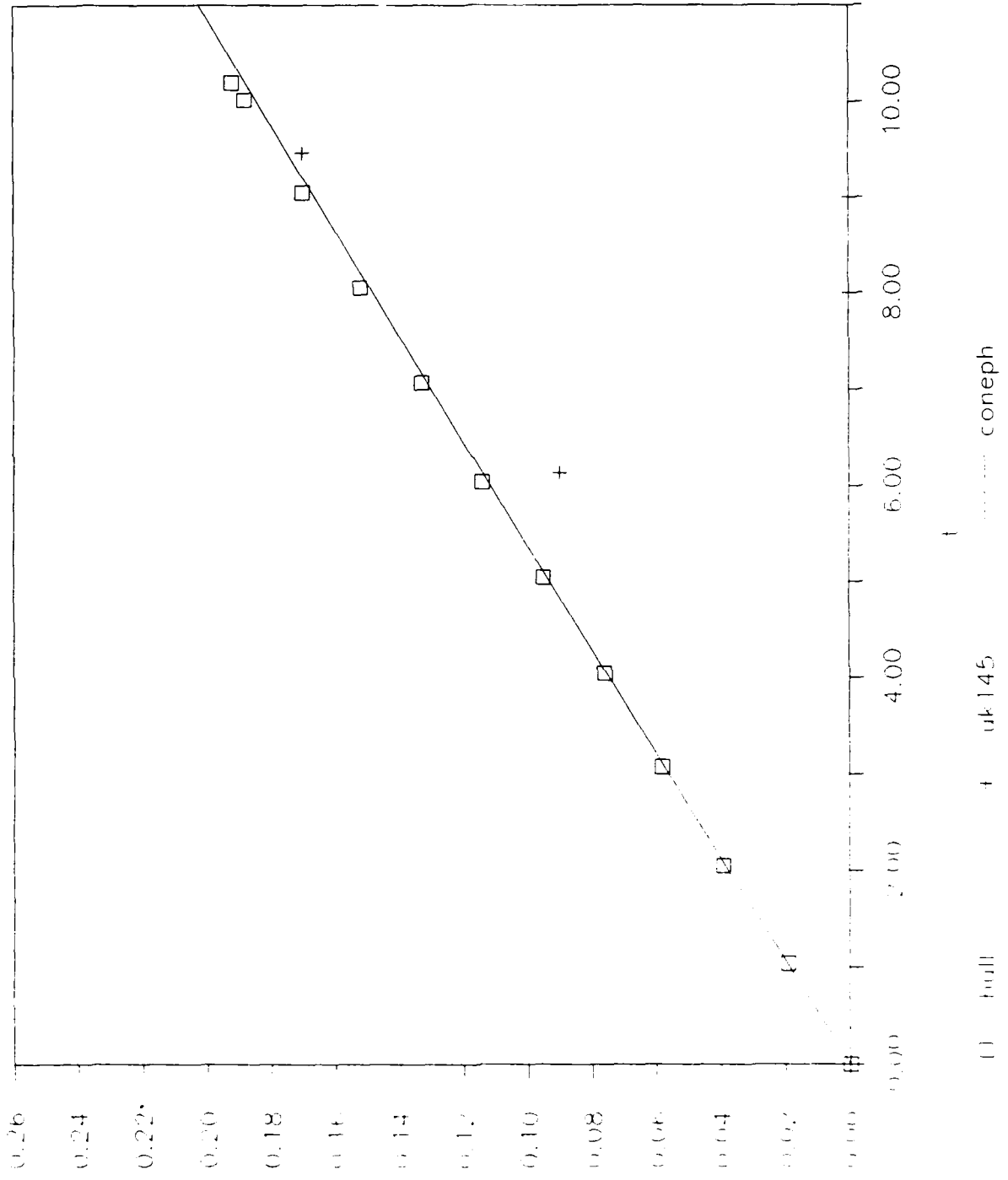


Figure 4

Taylor model can't describe the deformation front data (Figures 2 and 5) because it lacks the proper initial conditions. Dynamically, the Taylor model is a failure. The continuity equation (8) may be solved to get $\lambda = v/(\gamma-1)$. Since λ is big at $t = 0$, this means that $\gamma-1$ must be small. Later, when λ is smaller, γ must be larger. This would give a bizarre and unrealistic shape for the deformed cylinder since $\gamma = A/A_0$.

A more general (than (8)) conservation of mass equation is

$$\int_0^t \rho(\lambda + v)A_0 dt = \rho V(r,h) \quad (15)$$

where $V(r,h)$ is the volume of the deformed part of the projectile. A simple choice for $V(r,h)$ is a portion of a cone with volume $1/3 \pi h(r^3 - r_0^3)/(r - r_0) + \pi r_0^2 h$, where r is the time dependent radius at the anvil interface.

The volume as a function of time is known from equations (5)-(7) and the initial conditions. Hence the radius may be found by solving a quadratic equation

$$r = -r_0/2 + \sqrt{3V/\pi h - 3r_0^2/4} \quad (16)$$

Surprisingly, for $\lambda = 13,140$ cm/s, the radius is actually found to decay with time in this model! However, if we specify two parameters $\lambda(0) = 116,000$ cm/s and $\lambda(10 \mu s) = 13,140$ cm/s with an assumed linear dependence in the first phase ($t < 10 \mu s$) and constant behavior in the second phase ($t > 10 \mu s$), the results are quite different.

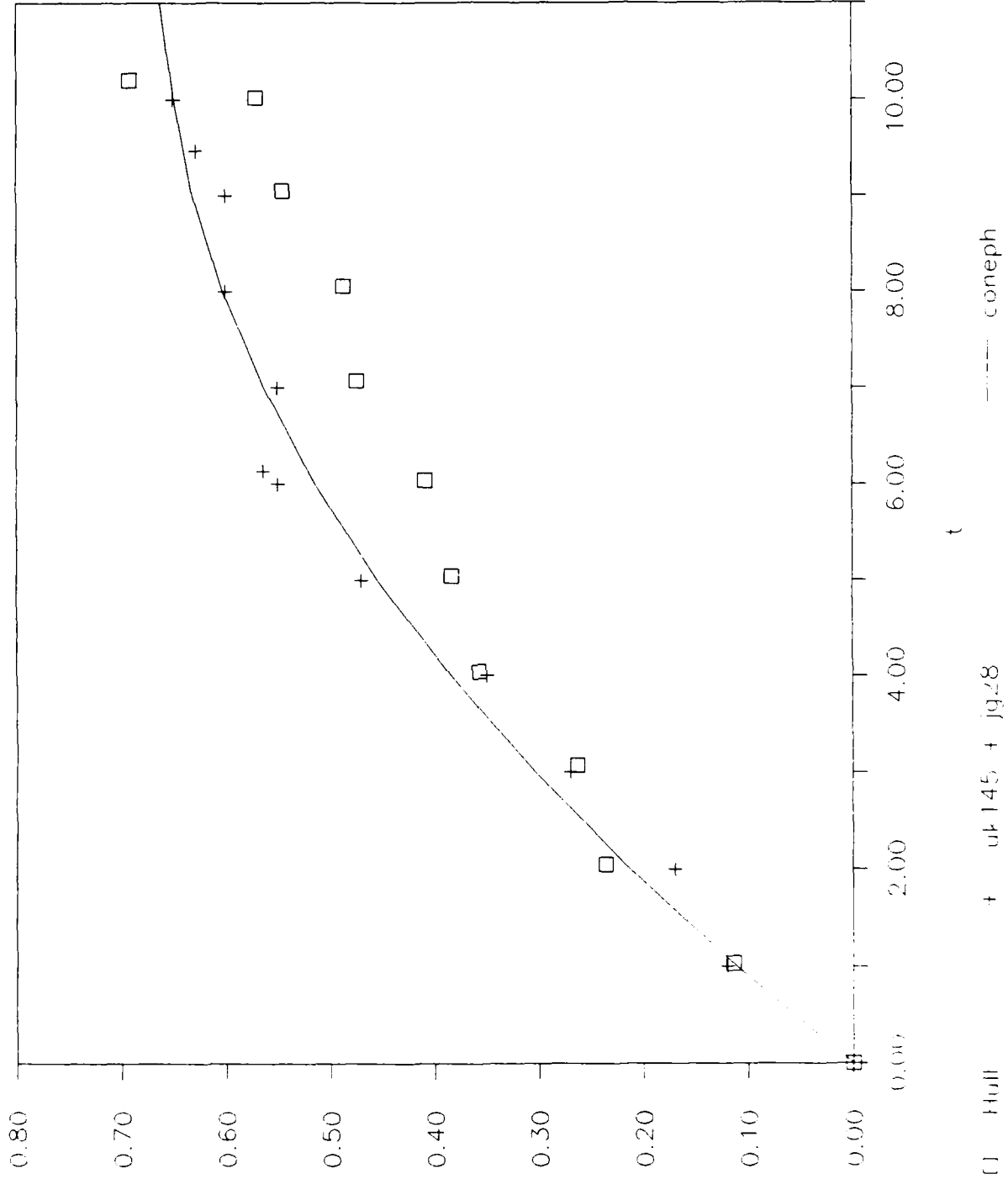


Figure 5

In Figures 1,2,3,4,5, and 6 we compare the results of this two phase cone model to the experimental data. The deceleration function is fit perfectly for both late (Figure 1) and early times (Figure 4). The propagation of the deformation front is also fit quite well (Figures 2 and 5); but this is no surprise with the two parameters used in the model. The interesting and new physics is in the radial growth at the anvil interface (Figures 3 and 6). The cone model described here does what the Taylor, Hawkyard, Jones-Foster, and many other models have not done: it predicts radial growth!

VII. RECOMMENDATIONS

Time resolved Taylor anvil data simultaneously at 300,000 and 1,000,000 frames per second over a range of velocities - $v = 100, 200, \text{ and } 300 \text{ m/s}$ - would be most useful for the same material (e.g., OFHC Cu) and fixed l_0/d_0 . It is essential to have 5 to 10 frames before impact and the other 65 to 70 after impact, if possible including some of the rebound. A charge coupled device could be used to eliminate the film and thus improve the sharpness of the images. This is essential to precisely extract the radial growth function and the deformation front velocity.

I would like to continue this analysis and extend it with

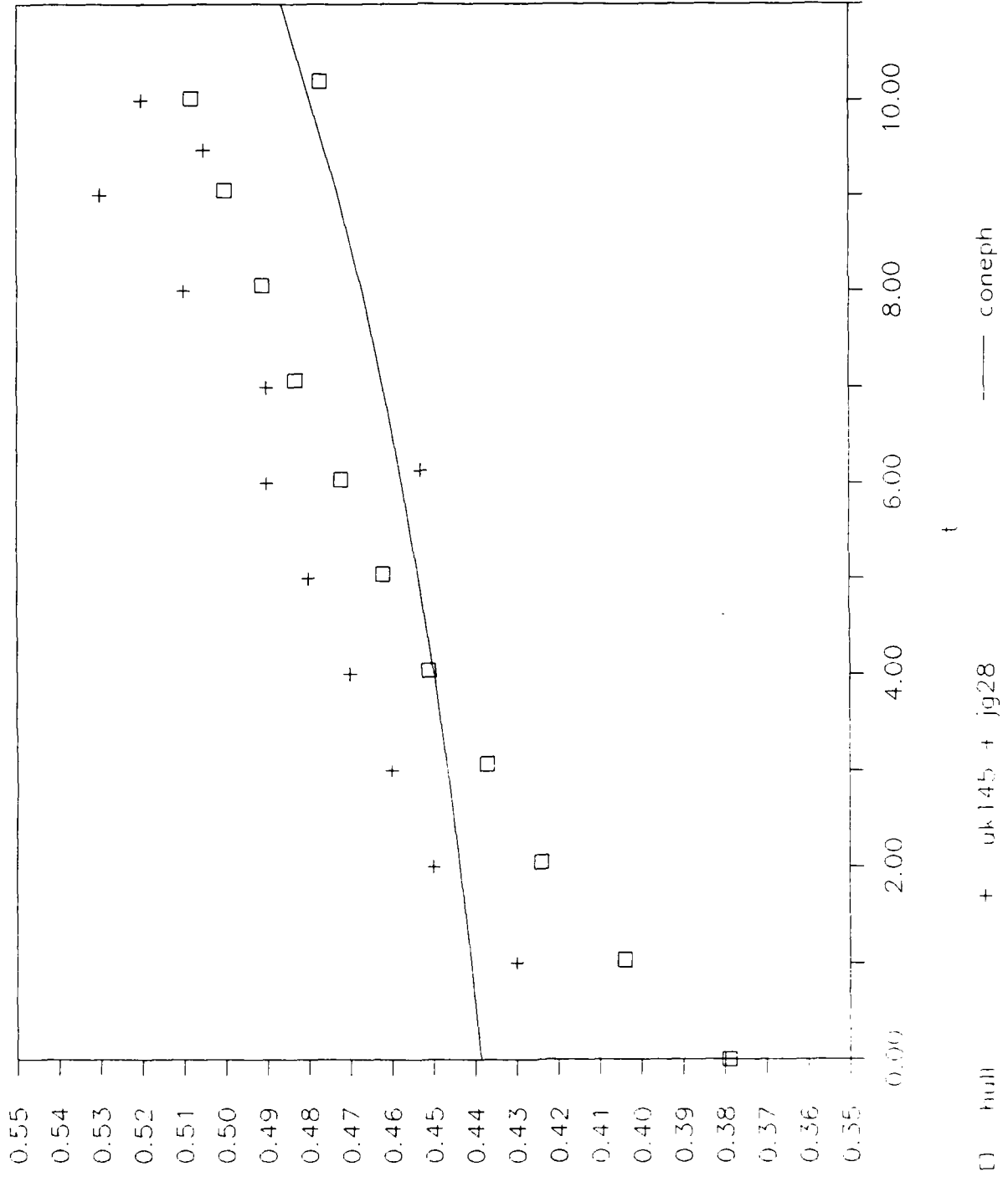


Figure 6

higher frame rate (up to 2,000,000 frames per second) data and other materials. The cone model requires modification to both explain the two parameters $\lambda(0)$ and $\lambda(10)$ and to more correctly model the radial growth. This higher frame rate data will provide insight into the dynamics of the first 10 μ s of impact, where the physics of the shock process must be included.

Hydrodynamic simulations can continue to provide insight into the effects of the material equation of state. Improvements in the hydrodynamic codes might be suggested by comparison to experiment and the one dimensional models.

I propose to also investigate in future work the validity of the physics assumptions of one dimensional penetration models.

REFERENCES

1. New York Times, July 18, 1989.
2. K. Froeschner, D. Maiden, H. Chau, J. Appl. Phys. 65 (1989) 2964.
3. G. Taylor, Proc. Roy. Soc. A194 (1948) 289.
4. A. Tate, J. Mech. Phys. Sol. 15 (1967) 387.
5. S. Treitel, J. Appl. Phys. 31 (1960) 391.
6. G. Hawkyard, Int. J. Mech. Sci. 11 (1969) 313.
7. S. Jones, P. Gillis, J. Foster, J. Appl. Phys. 61 (1987) 499.
8. S. Jones, P. Gillis, J. Foster, J. Mech. Phys. Sol. 35 (1987) 121.
9. J.J. Molitoris, Universal Energy Systems Summer Research Program Proceedings, 1988.
10. LASL Shock Hugoniot Data, ed. S. Marsh, Berkeley: UC Press, 1980.
11. D. Matuska and J. Osborne, HULL Users Manual, Shalimar, FL: Orlando Technology Inc., 1987.

Appendix I
Summary of Expenses

1. Wages

\$1240	Spring 1989
6200	Summer 1989
1240	Fall 1989
2500	Muhlenberg College (MC) Faculty Research Grant
1150	MC Student Research Grant
\$8680	Total RIP Wages
\$3650	Total MC Wages

2. Equipment

\$7971	computer hardware
1800	MC equipment contribution
312	computer software and supplies
2200	MC software/supplies contribution
\$8283	Total RIP Equipment
\$4000	Total MC Equipment

3. Travel

\$645	Technical conference
300	Eglin AFB trip
\$945	Total RIP Travel
\$1000	MC travel contribution

4. Reference and Publication

\$74 books

\$17982 Total RIP Funds to Date

1998 Owed Muhlenberg College

8650 Total MC Contributions

Appendix II

More Complete Bibliography

- J. Aidun and Y. Gupta, J. Appl. Phys. 65 (1989) 1898.
- G. Alers and Y. Liu, Trans. Metall. Soc. AIME 236 (1966) 482.
- S. Altan and A. Eringen, J. Appl. Phys. 65 (1989) 4587.
- R. Asaro, Mech. of Mat. 4 (1985) 343.
Material Modelling and Failure Modes in Metal Plasticity.
- M. Backman and W. Goldsmith, Int. J. Eng. Sci. 16 (1978) 1.
- P. Bennett and G. Sinclair, Trans. ASME June (1966) 518.
- G. Birkhoff, D. MacDougall, E. Pugh, G. Taylor, J. Appl. Phys. 19 (1948) 563.
- V. Boiko, A. Gulidov, A. Popyrin, V. Fomin, Y. Shitov, J. Appl. Mech. and Tech. Phys., 5 (1982) 705.
Experimental-Theoretical Investigation of the Rebound of Short Rods from a Rigid Barrier.
- D. Brillhart, R. De Angelis, A. Preban, J. Cohen, P. Gordon, Trans. Metall. Soc. AIME 239 (1967) 836.
Quantitative Study of the Substructure and Properties of Shock-Loaded Copper.
- D. Carley, Atomic Weapons Res. Est. Report O49/78 (1978).
- W. Carrington and M. Gayler, Proc. Roy. Soc. A 194 (1947) 323.
- V. Celli, M. Kabler, T. Ninomiya, R. Thomson, Phys. Rev. 131 (1963) 58.
- S. Chang and S. Ohr, J. Appl. Phys. 52 (1981) 7174.
Dislocation free zone model of fracture.
- D. Christman and J. Gerring, J. Appl. Phys. 37 (1966) 1579.
- R. Clifton, in Mechanics Today, ed. S. Nemat-Nassar, vol. 1, p. 102, NY: Pergamon, 1973.
- R. Cook, J. Appl. Phys. 65 (1989) 1902.
- D. Curran, L. Seaman, D. Shockey, Phys. Rep. 147 (1987) 253.
- W. Davis, Sci. Amer. May 1987, 106.

- L. Davison and R. Graham, Phys. Rep. 55 (1979) 256.
- J. Doyle, Exp. Tech. Jan. (1988) 29.
- R. Dragsdorf, J. Appl. Phys. 31 (1960) 434.
- J. Dugdale and D. MacDonald, Phys. Rev. 89 (1953) 832.
- G. Duvall, p. 165 in Response of Metals, ed. Shewman and Zackay, NY: Interscience, 1961.
- P. Duwez and D. Clark.
An Experimental Study of the Propagation of Plastic Deformation Under Conditions of Longitudinal Impact.
- R. Eichelberger, J. Appl. Phys. 27 (1956) 63.
- A. Eringen, Int. J. Eng. Sci. 4 (1966) 179.
A Unified Theory of Thermomechanical Materials.
- R. Eykholt, S. Trugman, D. Solovitz, J. Appl. Phys. 65 (1989) 4198.
The dynamics of free straight dislocation pairs I.
- R. Eykholt, D. Solovitz, J. Appl. Phys. 65 (1989) 4204.
The dynamics of free straight dislocation pairs II.
- A. Fine and H. Kraus, J. Appl. Mech. 33 (1966) 514.
- P. Follansbee and U. Kocks, Acta. Metal. 36 (1988) 81.
(need p. 82, 83, 91)
- A. Freudenthal, J. Appl. Phys. 31 (1960) 434.
- K. Froeschner, D. Maiden, H. Chau, J. Appl. Phys. 65 (1989) 2964.
- P. Fuller and J. Price, Nature 193 (1962) 262.
- P. Gillis and S. Jones, J. Appl. Phys. 48 (1977) 2845.
- A. Griffith, Phil. Trans. R. Soc. London A221 (1921) 163.
- W. Gust, J. Appl. Phys. 53 (1982) 3566.
- M. Hashmi, P. Thompson, Int. J. Mech. Sci. 19 (1977) 273.
- F. Hauser, Exp. Mech., Aug. (1966) 395.
- J. Hawkyard, Int. J. Mech. Sci. 11 (1969) 313.
- J. Hawkyard, D. Eaton, W. Johnson, Int. J. Mech. Sci. 10 (1968) 929.

- F. Helie, *Traite de balistique experimentale*, Paris: Dumaine, 1980.
- R. Hill, E. Lee, S. Tupper, *Proc. Roy. Soc. London A* 188 (1947) 273.
The Theory of Wedge Indentation of Ductile Materials.
- R. Hixson, D. Boness, J. Shaner, J. Moriarty, *PRL* 62 (1989) 637.
- K. Hoge, *J. Bas. Eng.* June (1966) 509.
- K. Hoge and A. Mukherjee, *J. Mat. Sci.* 12 (1977) 1666.
- J. House, AFATL-TR-89-41, Sept. 1989.
Taylor Impact Testing.
- J. House and L. Wilson, unpublished.
- I. Hutchings, *J. Mech. Phys. Sol.* 26 (1979) 289.
- I. Hutchings and T. O'brien, *Int. J. Mech. Sci.* 23 (1981) 255.
- G. Johnson and W. Cook, *Eng. Frac. Mech.* 21 (1985) 31.
- G. Johnson and W. Cook, *Seventh Int. Symp. on Ballistics*, The Hague, Netherlands, 1983.
- G. Johnson and T. Holmquist, *J. Appl. Phys.* 64 (1988) 3901.
- J. Johnson and F. Addesio, *J. Appl. Phys.* 64 (1988) 6699.
- S. Jones, P. Gillis, J. Foster, *J. Appl. Phys.* 61 (1987) 499.
- S. Jones, P. Gillis, J. Foster, *J. Mech. Phys. Sol.* 35 (1987) 121.
- T. Karman and P. Duwez, *J. Appl. Phys.* 21 (1950) 987.
- M. Keshavan and P. Gillis, *J. Phys. F* 5 (1975) 903.
On Dislocation Multiplication.
- K. Kim and W. Sachse, *J. Appl. Phys.*, 65 (1989) 4234.
- J. Kleiman, R. Heimann, D. Hawken, N. Salansky, *J. Appl. Phys.* 56 (1984) 1440.
- P. Klooster, N. Trappeniers, S. Biswas, *Physica* 97B (1979) 65.
Effect of Pressure on the Elastic Constants of Noble Metals.

- E. Lee and S. Tupper, J. Appl. Mech. 21 (1954) 63.
Analysis of Plastic Deformation in a Steel Cylinder Striking
a Rigid Target.
- C. Maiden and S. Green, J. Appl. Mech. 33 (1966) 496.
- L. Malvern, Q. of Appl. Math. 8 (1951) 405.
Plastic Wave Propagation in a Bar of Material Exhibiting a
Strain Rate Effect.
- D. Marsh, J. Sci. Instr. 38 (1961) 229.
- D. Marsh, Proc. Roy. Soc. London A279 (1964) 420.
- D. Matuska and J. Osborne, AFATL-TR-81-69 (1981).
- F. McClintock, J. Appl. Mech. 35 (1968) 363.
- R. McQueen, J. Hopson, J. Fritz, Rev. Sci. Instr. 53 (1982)
245.
- R. McQueen and S. Marsh, J. Appl. Phys. 31 (1960) 1253.
- R. Medrano, P. Gillis, C. Hinesley, H. Conrad, J. Strain
Anal. 9 (1974) 146.
- G. Miller, T. Ahrens, E. Stolper, J. Appl. Phys. 63 (1988)
4469.
- C. Munroe, Am. J. Sci., 3 (1888) 48.
- C. Munroe, Pop. Sci. Mo., 56 (1900) 444.
- S. Novikov and A. Chernov, J. Appl. Mech. Tech. Phys. 5
(1982) 703.
- K. Oh and P. Persson, J. Appl. Phys. 65 (1989) 3852.
- R. Pack and W. Evans, Proc. Phys. Soc. London B64 (1951) 293
and 303.
- M. Parrinello and A. Rahman, J. Appl. Phys. 52 (1981) 7182.
- M. Peach and J. Koehler, Phys. Rev. 80 (1950) 436.
The Forces Exerted on Dislocations and the Stress Fields
Produced by Them.
- A. Rajendran, M. Dietenberger, D. Grove, J. Appl. Phys. 65
(1989) 1521.
- S. Reid, R. Edmunds, W. Johnson, J. Mech. Eng. Sci. 23
(1981) 85.
- D. Reynolds and S. Czyzak, J. Appl. Phys. 31 (1960) 94.

- Z. Rosenberg and M. Forrestal, Trans. ASME 55 (1988) 236.
- Z. Rosenberg, Y. Partom, M. Mayseless, J. Falcovitz, J. Appl. Phys. 56 (1984) 1434.
- Z. Rosenberg, D. Yaziv, Y. Parton, J. Appl. Phys. 51 (1980) 4790.
- V. Sample, G. Fitzsimons, A. DeArdo, Acta. Metall. 35 (1987) 367.
- Y. Sano, J. Appl. Phys. 65 (1989) 3857.
- S. Schiferl, LAUR89-260.
- R. Sedgewick, L. Hageman, R. Herrman, J. Waddell, Int. J. Eng. Sci. 16 (1978) 859.
- A. Sengupta, C. Wigglesworth, S. Ghosh, W. Johnson, S. Reid, J. Mech. Eng. Sci. 24 (1982) 31.
- J. Smith and C. Arbogast, J. Appl. Phys. 31 (1960) 99.
- D. Steinberg, Int. J. Impact Eng. 5 (1987) 603.
- D. Steinberg, LLNL preprint, 1988.
- D. Steinberg, S. Cochran, M. Guinan, J. Appl. Phys. 51 (1980) 1498.
- D. Steinberg and C. Lund, J. Appl. Phys. 65 (1989) 1528.
- J. Sternberg, J. Appl. Phys. 65 (1989) 3417.
- D. Tabor, Proc. Roy. Soc. London 192 (1948) 247.
A Simple Theory of Static and Dynamic Hardness.
- A. Tate, J. Mech. Phys. Sol. 15 (1967) 387.
- A. Tate, J. Mech. Phys. Sol. 17 (1969) 141.
- A. Tate, Int. J. Eng. Sci. 16 (1978) 845.
- A. Tate, Int. J. Mech. Sci. 28 (1986) 535.
- A. Tate, Int. J. Mech. Sci. 28 (1986) 599.
- G. Taylor, Proc. Roy. Soc. A145 (1934) 362.
The Mechanism of Plastic Deformation of Crystals I.
- G. Taylor, Proc. Roy. Soc. A145 (1934) 388.
The Mechanism of Plastic Deformation of Crystals II.

- G. Taylor, Proc. Roy. Soc. A194 (1948) 289.
The use of flat-ended projectiles for determining dynamic yield stress I.
- T. Ting, J. Appl. Mech. (Trans. ASME) 33 (1966) 505.
- D. Tonks, Los Alamos 88-2459, 1988.
Rate-Dependent Plasticity of Copper and Stainless Steel Under Shock Compression.
- V. Torrey, Pop. Sci. Mo. 146 (1945) 65.
- K. Toukan, F. Carrion, S. Yip, J. Appl. Phys. 56 (1984) 1455.
- C. Tracy, J. Test. and Eval. 15 (1987) 14.
- N. Trappeniens, S. Biswas, C. Seldam, Physica 85B (1977) 20.
Effect of Pressure on the Shear Modulus.
- S. Treitel, J. Appl. Phys. 31 (1960) 391.
- J. Walsh, M. Rice, R. McQueen, F. Yarger, Phys. Rev. 108 (1957) 196.
- W. Webb, J. Appl. Phys. 31 (1960) 194.
- C. Weir, E. Lippincott, A. Valkenburg, E. Bunting, J. Res. Nat. Bur. Stand. 63A (1959) 55.
- A. Whiffin, Proc. Roy. Soc. A194 (1948) 300.
The use of flat-ended projectiles for determining dynamic yield stress II.
- J. Wilbeck, AFML-TR-77-134 (1978).
- M. Wilkins and M. Guinan, J. Appl. Phys. 44 (1973) 1200.
- L. Wilson, J. Foster, S. Jones, P. Gillis, Int. J. Imp. Eng. 8 (1989) 15.
- T. Wright, BRL Technical Report, page 85.
- F. Young and T. Noggle, J. Appl. Phys. 31 (1960) 604.
- F. Zerilli and R. Armstrong, J. Appl. Phys. 61 (1987) 1816.

FINAL REPORT NUMBER 9
REPORT NOT ACCEPTABLE AT THIS TIME
Prof. Wafa E. Yazigi
210-9MG-015

MULTIGRAPH KERNEL FOR TRANSPUTER BASED SYSTEMS

Final Report Submitted to:
USAF-UES Summer Faculty Research Program
Graduate Student Research Program

Contract Number:
F49620-88-C-0053/SB5881-0378

Sponsored by the:
AIR FORCE OFFICE OF SCIENTIFIC RESEARCH

conducted by:
Universal Energy Systems

Submitted by:
Dr. D. Mitchell Wilkes
Ben Abbott
Department of Electrical Engineering
School of Engineering
Vanderbilt University

5-29-1989

Abstract

This report describes the research accomplished under the USAF-UES Summer Research Program (SRP) mini-grant awarded for the period January 1, 1989 to May 31, 1989. The main thrust of the research consisted of continued development of the MULTIGRAPH Kernel (MGK) targeted for the INMOS Transputer. As a result of this grant, it is now possible to graphically model a system using the MULTIGRAPH Programming Environment (MPE) and have the system builder map the model to a parallel graph which is in turn executed in parallel by a set of Transputers.

1 Acknowledgements

Many thanks to the Air Force Systems Command and the Air Force Office of Scientific Research for sponsoring this research. Universal Energy systems has my gratitude for their concern and help to me in all the administrative and directional aspects of this program. Thanks as well to AEDC/DOTR for the much needed use of equipment.

There is no doubt this work would not have been successful without the patience and insight of Lt. Ted Bapty. Thanks to Amit Misra for the use and explanations of his Beamforming system. And as always, thanks are required for the founders of the MPE, Dr. Janos Sztipanovits, Dr. Gabor Karsai, and Dr. Csaba Biegl without whom there would be no MULTIGRAPH.

2 Introduction

The MGK provides a generic execution environment for parallel programs built by the various tools comprising the MULTIGRAPH Programming Environment (MPE). This environment provides an extremely high level of programmer interface. The user normally works with interactive graphical languages allowing him to concentrate on declaring a system model rather than on program functions. These high level tools subsequently map the user's model of the required system into a parallel graph computation to be executed under the MGK. The MGK hides the underlying parallel hardware structure by providing a virtual machine, the MULTIGRAPH Virtual Machine (MVM). This paper describes the specific details of the Transputer version of the MGK. Minor familiarity with the MGK and MPE is assumed by this paper. For details about MPE see: [4]. For details about MGK see: [5]. This paper proceeds in the following manner: 1) it states the goals of this phase of research in light of previous work, 2) it describes the equipment purchased under this grant and its function as applied to the work, 3) it details the steps and issues involved in each of the specific goals, 4) it describe a Beamforming system used to test the Transputer MPE, and 5) it explains what is planned for the 1989 SRP and research further on.

3 Research Goals

Work on a Transputer based MGK began while Ben Abbott participated in the 1988 SRP at Arnold Engineering Development Center (AEDC). During the summer research period the MVM was successfully implemented on a single Transputer system by porting previously developed code to AEDC's Transputer configuration. The intention of the research under this grant was to extend this MVM to use an arbitrary configuration of Transputers as well as to provide an interface to the various high level tools of the MPE.

To accomplish the above goals, proposed development was to proceed in the following stepwise fashion [6]:

1. Complete the basic message routing system started during the SRP 1988.
2. Interface the MGK with this message routing system.
3. Set up a UNIX/KCL based host.
4. Interface the system builder functions to the Transputer platform.

Each of these steps was successfully completed and will be individually described in the section after next.

4 Transputer Development System

A large portion of the money provided by this grant went directly into the purchase of the equipment required to provide a Transputer development system compatible with the AEDC platform. Figure 1 shows the basic pieces of the system purchased. This system will be transported to AEDC during the summer of 1989 while Ben Abbott participates in the SRP for the second time. Due to the compatibility of this system with those of AEDC, effort to port the work of this phase onto AEDC hardware will be minimal.

The Everex 386/20 provides the user interface of MPE. It runs a System V Unix. The portion of the MGK running on the 386 is a mixture of Kyoto Common Lisp (KCL) and C. A Unix device driver provides access to the Transputer network by way of the CSA PART.4A-820-3. This board converts the PC parallel bus to the INMOS serial protocol as well as hosting one Transputer. The CSA Part.1-820 was not purchased under this grant and is on loan to Vanderbilt from AEDC. It provides the computing powerhouse of the platform with its four Transputers. The Logical Systems C is a cross-compiler hosted on the 386 and targeted for the Transputers. Having the source code to the compiler, runtime library, and utility programs allowed the modifications necessary for special MGK requirements such as dynamic loading and Lisp interface. One of the main differences between this system and that of AEDC is the lack of graphics support in this system (i.e., X windows). Graphics were purposely neglected during this phase of the research due to cost constraints. Instead, those portions of the MPE requiring graphics during this phase were developed on an HP 350 under HP-X-Windows MPE. Intermediate files on the HP were then copied to the Transputer development system where they were processed by it alone.

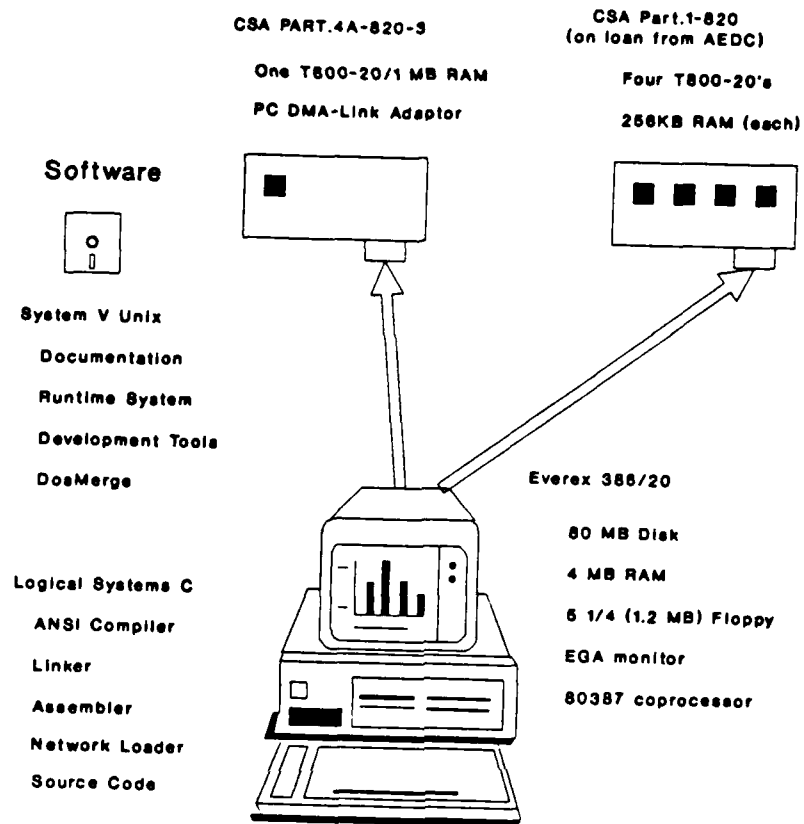


Figure 1: Transputer development system purchased under this grant.

5 Research Period Breakdown

As a result of this grant, it is now possible to graphically model a system using the MPE and have the system builder map the model to a parallel graph which is in turn executed in parallel by a set of Transputers.

Thus, the goals set for this phase of research were accomplished. The following subsections provide the basic flow of the work that was accomplished under this grant. The last of these sections describes a Beamforming signal processing system that has been used to test the functionality of the system. Performance benchmarks, although not the thrust of this research, are provided as well.

5.1 Basic Message Routing System

The Transputer hardware supports a form of synchronized point to point message passing utilized by the OCCAM programming language [2]. The communication requirements posed by the MVM and trade-offs were described using the guidelines set out by Reed and Fujimoto [1] in the 1988 SRP final report [6]. Briefly, the decisions made during that period entailed:

- Transport Mechanism: Store and Forward since it is the only viable solution allowing the embedded DMA mechanism to be utilized.
- Routing mechanism: distributed tables (actually graphs for MGK)
- Buffer Management: Use of MGK dynamic memory manager. This allows types to be easily transferred along with size and data information.
- Flow Control: Use the basic MGK return code mechanism as a send/acknowledge protocol. Use datanode queuing model and environment priority for further control.

A new concept developed during this research period was incorporated into the communication system as well. Specifically, the communication system itself is made up of special purpose MGK actors and datanodes. This produces an extremely flexible and portable communication system without excessively taxing overhead. Figure 2 depicts this set of communicating

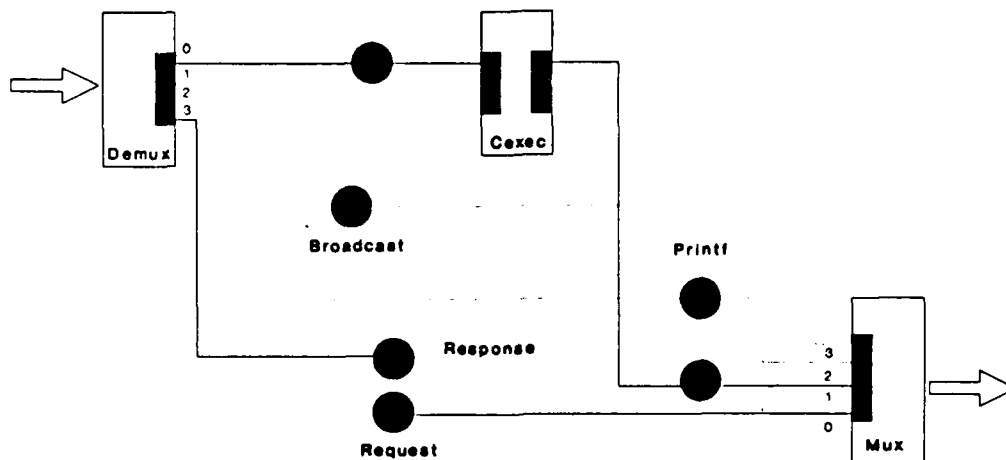


Figure 2: Set of communicating actors. One set is associated with each physical Transputer link.

actors. In the Transputer sense, there is one set of actors per bidirectional physical link (i.e., four sets of communicating actors).¹

The rolls of each of the actors are as follows:

- *Demux*: Wait for a MGK data structure to be received from a physical link. Create the same structure on this Transputer node. Propagate this structure to the appropriate datanode which is in turn expected to be connected to the appropriate actor.
- *Mux*: Execute when data is written into a datanode connected to one of its input ports. Transmit the data, port index, and data type

¹This idea of using actors themselves as the communication system was first hinted at by the work of Agha and Hewitt [10]

across the physical link to a *Demux* actor.

- *Cexec*: Always connected to port 0 and 1 of *Demux* and *Mux* respectively. When data is received, execute it as a remote procedure call and provide the resulting MGK code out through the *Mux*.

The four *Request* and *Response* datanode pairs provide access to remote procedure calls on the four neighbor processors connected by the physical links. String data structures written into the *Printf* datanode are propagated down an acyclic graph toward the Host system to be displayed on the host console. Conversely, writing into the *Broadcast* datanode causes information to be propagated away from the Host in an acyclic graph to all of the connected transputers.

5.2 Interface the Message Routing to MGK

Since the communication system is written above the basic MGK (i.e., actors and datanodes), interface to the kernel for the most part comes automatically. However, some new functions were needed.

In the Transputer version of MGK, a MGK task [5] is a Transputer. To allow graphs and subgraphs to be built on a particular transputer, the kernel must provide some way to call the graph building routines targeted for that particular machine. This job is handled by the Host system (in this case the 386). During initialization, the Host leap frogs across the set of Transputers creating a graph connected to a *Cexec* on each Transputer. This leap frog graph is shown in Figure 3. Then, to control any particular Transputer, the Host need only write a request into its local datanode associated with the desired Transputer and await the response on the corresponding datanode. Routines added to the kernel to allow this graph to be built follow:

- `MUX_ACTOR(physical_link_index)` : returns the actual address of the actor associated with a physical link.
- `DEMUX_ACTOR(physical_link_index)` : returns the actual address of the actor associated with a physical link.
- `CEXEC_ACTOR(physical_link_index)` : returns the actual address of the actor associated with a physical link.

- `CONNECT_FREE_OUTPUT(actor_pointer, datanode_pointer, connect_mode)` : Connects the first free output port of an actor to a datanode using the provided connection criteria. Returns the index to the port actually allocated.
- `CONNECT_FREE_INPUT(data_node_pointer, actor_pointer)` : Connects a datanode to the first free input port of an actor. Returns the index to the port actually allocated.
- `BUILD_COMMAND_JUMPER(from_index, to_index)` builds a jumper from the communication set connected with the physical link of one transputer to control a neighbor processor. Returns the port allocated on the `from_index` *Demux* actor.
- `BUILD_STATUS_JUMPER(from_index, to_index)` builds a jumper from the communication set connected with the physical link of one transputer to control a neighbor processor. Returns the port allocated on the `to_index` *Mux* actor.

With these basic primitives the Host can build up graphs across Transputers. Each subgraph is scheduled by the MVM scheduler on that Transputer. The Host version of the MVM goes further to hide the hops and connections across Transputers such that the user need not be aware of the communicating actor sets at all. These concepts are mainly implemented in Lisp and are described in the next subsection.

5.3 Unix/KCL Host

An integral part of the Transputer based MPE is the Host system. It provides centralized building² and model interpretation. A version of MGK with a Lisp environment is used as the Host and is a direct port of a previous Unix-based MGK. The communicating actors and a special Unix device driver provide access to the Transputer MGKs. Thus, there is a MGK running on the 386 as well as each Transputer. The Lisp interface is used to hide the separate machines from the user allowing him to simply create actors (associated with tasks) and datanodes (independent of tasks) and connect them in arbitrary fashions without worrying about the hops

²not execution control flow which is distributed

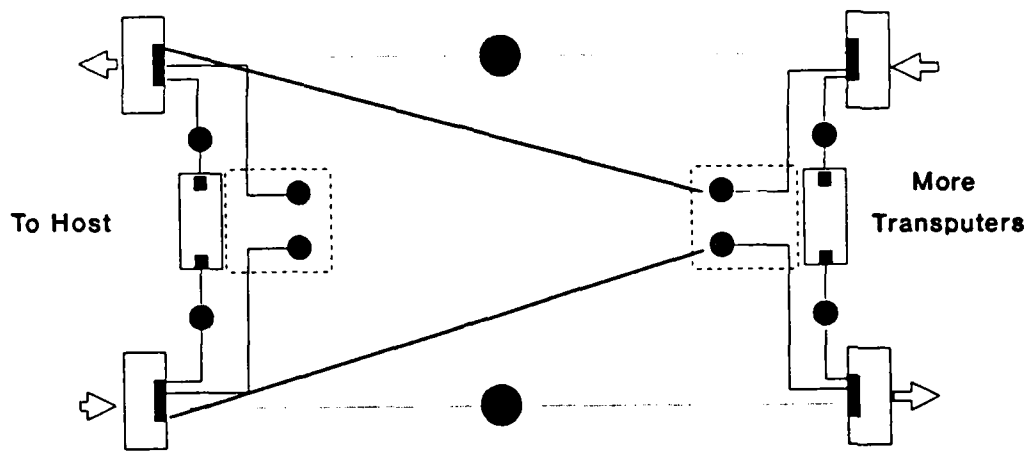


Figure 3: Leap frog connection of communicating actors with Host.

or even the path needed to get from one item to another. This concept of a virtual machine entails many details that had to be handled.

The bulk of these are broken out below:

- Port of Austin Kyoto Common Lisp (AKCL) to the 386. AKCL is a public domain Common Lisp available in source code format. The port was straightforward (but large).
- MGK on 386. Again the port held few unexpected outcomes. However, entry points had to be modified to check for data structures associated with Transputers. A special routine to allow the keyboard to be checked without hanging up was incorporated.
- Add Lisp code to hide the Transputers. This entailed modifying the standard MGK data structures to incorporate a field indicating what type they are (actually this field was already there in the form of a pointer to the associated task). Then, routines to calculate and build the path needed to get from one Transputer to another were added. The path itself is calculated from a global Lisp vector indicating the connectivity of the Transputer network. Routines to hold the symbol table of each Transputer allow dynamic linking and remote procedure calls.

When the Lisp call to connect two nodes is entered, the nodes are first checked for type. If one of them is a Transputer node the special routines are used. If the nodes are on different transputers, a series of virtual datanodes are created and hooked together through *MUX / DEMUX* actor pairs across Transputers until the connection may be made locally. Thus, simply by the graph structure the message routing is established.

- Dynamic Linker for Transputers. At build or runtime different actor scripts may need to be loaded onto different Transputers. The Logical Systems Linker and loader [8] were modified to allow this capability. The Host version of MGK keeps track of all of the MGK tasks in the system. If the task is a Transputer, the Host also keeps track of a symbol table file associated with that Transputer. When a new script needs to be loaded to an already executing graph, the linker is called with a special switch that forces it to preload the symbol table

with the items already on that Transputer. Linking then proceeds as usual. Upon linking completion, the symbol table of the associated Transputer is updated and the executable object module is loaded by a special loader that makes a remote procedure call from the Host to the appropriate Transputer.

5.4 Interface of System Builder

One of the most interesting reasons for porting the MPE to a Transputer platform is the availability of high level programming tools that allow the user to model the desired system rather than program specific functions. These tools map the users model into a parallel graph to be executed by the MVM. Most of these tools use the HDL [4] as a starting point or in the case of the graphical languages as an intermediate description of the declared model. HDL is a Lisp-like declarative language with an interpreter written in Lisp to provide the mapping to the MVM. On the X-Windows machines, HDL provides a "deck of cards" menu system for user commands. The HDL has been ported to the 386 with modifications only to the menu system (these have been replaced with 386 PC function keys). Thus, a graphical editing session on the HP 350 may be used to produce HDL files which are in turn used by the HDL running on the 386 to produce a parallel graph running on the Transputer system.

6 Testing the Transputer MPE with a Beam-forming System

Testing the Transputer MPE was done by choosing an adaptive signal processing system currently being developed under the XIEDIT graphical programming environment [4] of the MPE. The system chosen estimates the directions of arrival of signals impinging on an array of sensors using Beam-forming techniques. It does so by taking the spatial transforms of the signals received and estimates the energy in the signals arriving from various directions. Then it looks for the peaks in the spectrum thus obtained. For further information about Beamforming refer to [9].

The important issue about this test is the generic nature of the MPE. This independently produced system (i.e., all development work was done

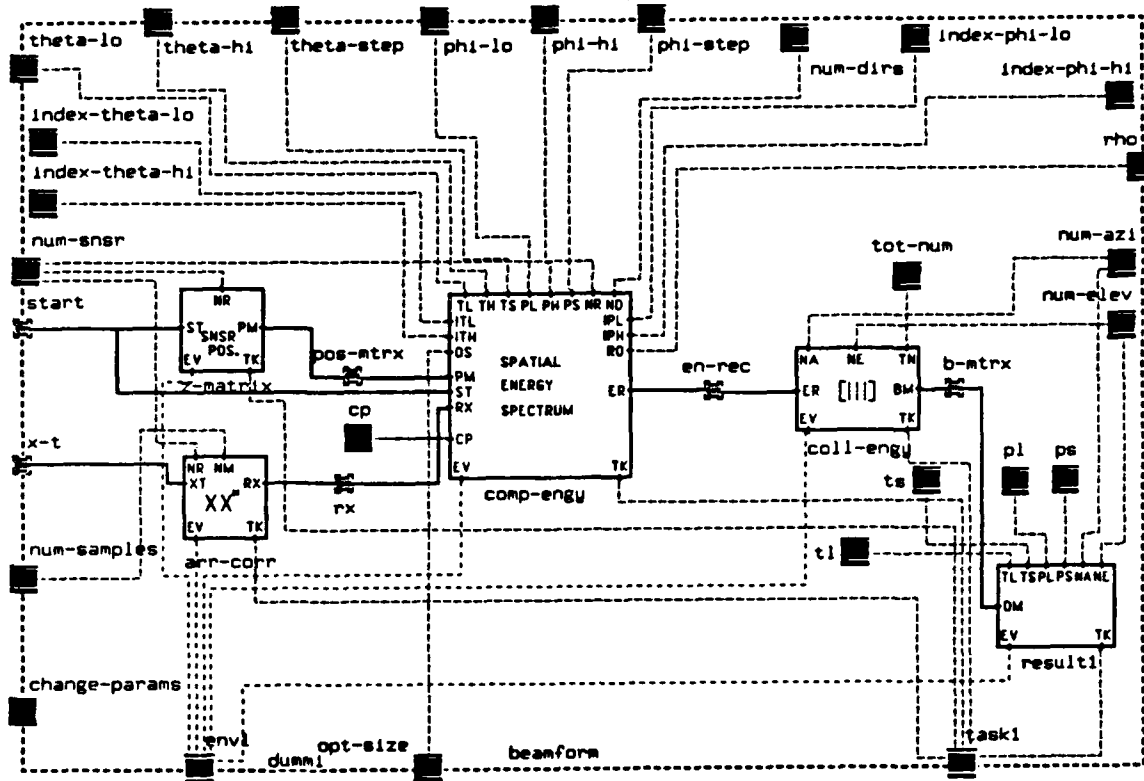


Figure 4: Portion of the graphical description of the test system.

on the monoprocessor version of the MPE hosted on a HP 350) required only minor changes to the actor scripts³ and no changes to the HDL.

³In the monoprocessor version of MGK actor scripts can get away with the unadvisable programming technique of shared global variables. Just such an anomaly was the problem in this case. Actually, the system ran with no changes when HDL was told to map to a single Transputer. The updated scripts were of course capable of correct execution under the monoprocessor MGK.

```

;;; Definition for |collect-energy|.

(DEFPRIMITIVE |collect-energy| :IFANY
  ((|en-rec| :STREAM) -> (|b-mtrx| :STREAM)) NIL
  ((|num-azi| NIL) (|num-elev| NIL) (|tot-num| NIL)) NIL (|env1|)
  (|task1|) ((|Structural| . "cllt-engy.icon"))
  ((|Structural| (BOX 113 91 540 365) (TEXT 189 344 |collect-energy|)
    (|env1| (TEXT 74 340 |env1|)) (|task1| (TEXT 391 339 |task1|))
    (|en-rec| (TEXT 5 161 |en-rec|))
    (|b-mtrx| (TEXT 483 161 |b-mtrx|))
    (|num-azi| (TEXT 31 16 |num-azi|))
    (|num-elev| (TEXT 129 16 |num-elev|))
    (|tot-num| (TEXT 226 16 |tot-num|))
    (|env1| (ICON |Environment| 80 356))
    (|task1| (ICON |Task| 403 355))
    (|en-rec| (ICON |Stream| -7 180))
    (|b-mtrx| (ICON |Stream| 534 179))
    (|num-azi| (ICON |StaticParameter| 48 -11))
    (|num-elev| (ICON |StaticParameter| 148 -12))
    (|tot-num| (ICON |StaticParameter| 243 -12))))
  "collect_engy")

```

Figure 5: Portion of the equivalent HDL moved to the Transputer MPE.

A top level block diagram taken directly from the graphical editing environment may be seen in figure 4⁴. As stated previously, from this graphical description, the HDL declarative language representation is automatically produced. A small section of the HDL of this system is shown in figure 5.

The Transputer architecture chosen for this test was that of a pipeline structure utilizing only two of the links of each of the Transputers. This architecture was chosen to force a mapping of the execution graph to make hops across Transputers and is not considered optimal. Execution time for the test system are as follows:

- On the HP 350: 5.22 seconds.

⁴This system actually has several layers of hierarchy not included here for the sake of brevity. For a more complete description of HDL and XIEDIT see [4]. Work on this particular Beamforming system as yet is unpublished

- 1 Transputer : 3.14 seconds.
- 2 Transputers: 1.66 seconds.
- 4 Transputers: 1.02 seconds.

7 Plans for Continuation

The present state of the Transputer MPE shows it to provide an extremely powerful execution environment that remains compatible with the previously developed MPE's. During the SRP 1989 the Transputer MPE will be used at AEDC to implement the CADDMAS system for real-time monitoring and frequency analysis of jet engine turbine test data. Future plans involve the use of multiple aspect modeling and structurally adaptive techniques [3] to include in the model and graph building process the architecture of the Transputer network. Under this scenario, a reasonable solution to the assignment problem may be possible. The use of a crossbar switch to allow dynamic changes of the architecture adds an even more exciting variable to this future research.

References

- [1] Reed, D. and Fujimoto, R.
Multi-computer Networks Message-Based Parallel Processing, Cambridge, Massachusetts, *MIT Press*, 1987.
- [2] D. Poutain, A tutorial introduction to OCCAM programming, *INMOS Limited*, March 1987.
- [3] Sztipanovits, J: "Toward Structural Adaptivity,"
Proc. of the 1988 IEEE International Symposium on Circuits and Systems, Espoo, Finland, pp. 2359-2362, 1988.
- [4] Karsai, G.: "Declarative Programming Techniques for Engineering Problems", Ph.D. Thesis, Vanderbilt University, 1988.
- [5] Biegl, C.: "Design and Implementation of an Execution Environment for Knowledge-Based Systems", Ph.D. Thesis, Vanderbilt University, 1988.
- [6] Abbott, B.: "MULTIGRAPH Kernel for Transputer Based Systems", *Final Report for USAF-UES SRP*, Contract no. F49620-88-C-0053, Sept, 1988.
- [7] Abbott, B.: "MULTIGRAPH Kernel for Transputer Based Systems", *Proposal USAF-UES SRP Minigrant*, October 1988.
- [8] Bailey, K., et.al., C Users Guide, Provo, Utah, *Computer Systems Architects*, 1988.
- [9] Van Veen, B. and Buckley, K.: "Beamforming: A Versatile Approach to Spatial Filtering", *IEEE ASSP Magazine*, April 1988.
- [10] Agha, G. "Actors : a model of concurrent computation in distributed systems ", Cambridge, Mass., *MIT Press*. 1986.

FINAL REPORT
MTF STUDIES OF IR FOCAL PLANE ARRAYS
AT LOW FLUX LEVELS

Prepared by

Eustace L. Dereniak
The Optical Sciences Center
University of Arizona
Tucson, Arizona 85721
(602) 621-1019

Prepared for

Universal Energy Systems Inc.
4401 Dayton-Xenia Road
Dayton, Ohio 45432-1894

This research was supported by

Contract No. F49620-88-C-0053/SB5881-0378.
Air Force Office of Scientific Research
Bolling AFB, DC

6 February 1990

ABSTRACT

This report summarizes our research on measurement of the modulation transfer function (MTF) of infrared (IR) focal-plane arrays at low-background flux. The two methods that have been emphasized during this program are the laser-speckle method, which is most feasible under cryogenic conditions, and the interference method, which has a higher signal-to-noise ratio.

ACKNOWLEDGMENT

Our thanks to Marshall Kingery and Arnold Engineering Development Center for support of this project, to CALSPAN, and its personnel: Dave Elrod, Neill Fry, and Lavelle Whitehead.

I. INTRODUCTION

We hope that the methods developed here eventually will be implemented into the Focal Plane Characterization Chamber (FPCC) at the Arnold Engineering Development Center (AEDC), Arnold Air Force Base, Tullahoma, Tennessee.

II. OBJECTIVES

We studied the development of feasible methods to measure the modulation transfer function (MTF) of an infrared focal plane array at cryogenic temperature in a low-background flux environment, such as in the FPCC.

III. THEORY AND EXPERIMENTAL APPROACH

After studying the relevant literature,¹⁻⁸ we determined that the spatial-frequency domain approach had the highest feasibility.

It is well known that the modulation transfer function (MTF) of a two-dimensional system relates the spatial power spectra of input and output signals in the following manner:

$$S_{out}(\xi,\eta) = [MTF(\xi,\eta)]^2 S_{in}(\xi,\eta) \quad (1)$$

where $MTF(\xi,\eta)$ is the modulation transfer function of the system and ξ,η are spatial frequency variables. The $MTF(\xi,\eta)$ can be calculated if both input and output power spectra are known. The output power spectrum can be evaluated numerically by taking the Fourier transform of the output signal from the system. The question then is how to form an input signal with known spatial power spectrum. Furthermore, to avoid aliasing, the input power spectrum must be controllable so that the cut-off frequency of the spectrum is less than or equal to the Nyquist frequency of the imaging system.

Two methods were focused on in this research project: 1) using laser speckle patterns; and 2) using interference fringe patterns. A 4-mW 3.39- μm HeNe laser, two integrating spheres, and optical and electronic components were purchased to set up proper trial experiments to evaluate the feasibility, advantages, and disadvantages of each approach.

A. Speckle Method

A speckle pattern is formed when coherent radiation is either reflected from a rough surface or propagated through a medium with random refractive-index (or thickness) fluctuations. The coherent radiation scattered from a random scatterer (e.g., a rough surface) is dephased randomly because of random optical pathlengths. Therefore, a random intensity distribution that results from the interference of the randomly dephased radiation can be observed at any plane beyond the scatterer. The spatial power spectrum can be described by the autocorrelation of the squared modulus of the radiation amplitude distribution function in the scattering aperture.³ For a uniformly irradiated aperture with dimension L , the spatial power spectrum at a distance Z from the aperture is a triangle function that cuts off at $L/\lambda Z$. It is obvious that aliasing easily can be avoided by choosing parameters L and Z equal to the Nyquist frequency of the focal plane array, which is the reciprocal of the pixel spacing. This is one major advantage of the speckle method.

Laser speckle has been used to measure the MTF of a PtSi charge-coupled array at the University of Arizona. A speckle pattern was formed by directing an expanded laser beam on a piece of transmitting ground plate.

In this research program, the above experiment was partially repeated with a slightly different setup. An expanded laser beam was directed on a piece of sandblasted aluminum plate; thus a speckle pattern was produced by the reflected (scattered) laser radiation. This change offers a higher signal level (no fresnel losses as using a transmitting medium) and the feasibility for different wavelengths (metals are highly

reflective in the infrared and far-infrared region). This approach is also more feasible under low temperature. The major drawback of using a diffusing plate (reflecting or transmitting) is that the radiation distribution at the aperture must be measured. If the distribution is not uniform enough, then the spatial power spectrum of the speckle must be calculated numerically from the distribution function.

A very different approach has been focus on recently. When laser radiation is fed into an integrating sphere (IS), a uniform speckle pattern will be formed at its output port. Therefore, the spatial power spectrum is known (i.e., a triangle-shaped function is one dimension). Another advantage of using an IS is that no optical component is needed to expand the laser beam. This make the integrating sphere the best candidate for use under cryogenic conditions. The major difficulty, however, is that the signal-to-noise ratio (SNR) is very low because of the numerous reflections (losses) of radiation inside the IS. To boost the SNR, computer software was developed. However, no significant improvement was achieved. Another difficulty of the speckle method is that a large number of frames of data must be averaged because the properties of speckle are statistical.

B. Interference Method

A Twyman-Green interferometer has been designed and major optical components have been purchased to develop the interference approach. A plane mirror in the Twyman-Green interferometer is replaced by a concave mirror so that a series of concentric fringes with the fringe spacing decreasing along the radial direction (Newton's rings) can be produced. This type of fringe pattern contains a wide range of spatial-frequency components. Therefore, the MTF can be calculated with just one interference pattern, which requires just one adjustment trial. On contrast, the single-frequency approach using sinusoidal interference patterns, requires at least several different adjustments to obtain the MTF at different spatial frequencies.

The interference patterns have higher SNR. The drawbacks of this method include the expensive optics and difficult optical adjustments. The feasibility under cryogenic condition requires further investigation.

IV. RECOMMENDATIONS

Because using an IS has many advantages, great efforts should be put on pursuing this method. The only major problem is the low SNR. New computer software must be developed to boost SNR further. However, the ultimate limit of the SNR is determined by the power of the laser, the sensitivity of testing arrays, and the size and reflectivity of the interior wall of the IS. The smaller the IS, the larger its output ($1/R^2$).⁵ However, if the size of the IS is too small, the distribution at its output port might not be uniform enough, which is contradictory to the reason of using an IS. The reflectivity of the inner wall of the IS can be increased by plating it with gold. It should also be noted that at longer wavelength in the IR, stronger laser sources are available, such as CO² laser-pumped FIR lasers.

V. CONCLUSION

The speckle method using an integrating sphere is the best candidate for measuring the MTF of an IR focal plane array because it is less complex and more economical than the interference method to be implemented, especially under cryogenic conditions. The interference method remains to be a candidate because of its higher signal-to-noise ratio.

REFERENCES

1. M. Francon, *Laser Speckle and Application in Optics*, p. 136 (Academic Press, New York, 1979).
2. P. Hariharan, "Evaluation of the modulation transfer function of photographic materials using a laser speckle pattern," *Appl. Opt.* **9**, 1482 (1970).
3. J. W. Goodman, in *Laser Speckle and Related Phenomena*, J.C. Dainty, ed., p. 40 (Springer-Verlag, New York, 1975).
4. G. Boreman, "Measurement of Modulation Transfer Function and Spatial Noise in Infrared Charge-Coupled Devices," PhD Dissertation, University of Arizona (1984).
5. H. Tang, "The Study of Untuned Cavities for Use with Pulsed FIR Lasers," MS Thesis, University of Alabama (1988).
6. M. Born and E. Wolf, *Principles of Optics*, Fifth Ed., p. 289 (Pergamon Press, Oxford, 1975).
7. M. Zaja and A. Persin, "MTF measurement of thermal imaging system from the edge response function," *Opt. Eng.* **22**, 743 (1983).
8. G. Boreman, Y. Sun, and A. James, "Generation of laser speckle with an integrating sphere," to be published in *Opt. Eng.* (1990).

**DROPLET SIZE DISTRIBUTIONS AND COMBUSTION MODELING
IN A PINTLE INJECTOR SPRAY**

FINAL REPORT

DECEMBER 1989

**William M. Grissom
Physics Department
Morehouse College
Atlanta, Georgia 30314**

**Contract: F49620-85-C-00137/SB5851-0360
Purchase Order: S-760-7MG-022
Universal Energy Systems, Inc.**

sponsored by Air Force Office of Scientific Research

1.0 INTRODUCTION

To properly model the three dimensional turbulent combustion in a liquid rocket engine, knowledge of the droplet size distribution, mass density, and velocities at each spatial position in the combustion chamber is needed. These, in turn, determine how the droplet combustion should be modeled.

The goal in the present study was to develop an experimental system to measure droplet size and velocity distributions at different spatial positions in an injector spray of interest to Arnold Engineering Development Center. A droplet sizing instrument developed by the author on a previous UES/AFOSR minigrant for the Astronautics Lab (Reference 1) was employed towards this goal.

2.0 BACKGROUND

2.1 Importance of Droplet Sizing

Liquid rocket turbulence models are very sensitive to the droplet sizes and size distributions input into the model. Droplet combustion is normally limited by the vaporization rate of the droplets, and the vaporization rate per volume is inversely proportional to the droplet diameter to a power between 1.5 and 2, as shown in Section 5.0.

In one early liquid rocket combustion model (SDER) the results were so sensitive to the mean droplet size input into the model that the assumed diameter was adjusted to "calibrate" the model to engine test data. Since little reliable data on the actual droplet sizes existed, this procedure was warranted. However, this did not allow for a critical test of the model.

In a more thorough study of the sensitivity of modeling to the assumed droplet sizes, Ferrenberg and Varma (Reference 2) found an inverse proportionality between the Sauter mean diameter assumed and the amount of unreacted fuel ejected from the engine. They also found an equally strong sensitivity to the assumed shape of the droplet size distribution. Broader distributions, in which more of the volume is contained in the larger droplets, showed the largest amount of unvaporized droplets ejected.

At present there is only limited data on droplet size distributions in liquid rocket injectors, mostly obtained with the hot-wax technique described below. The author is aware of only measurements in like-like doublet elements and unlike doublet elements (References 2 and 3). Apparently no data has ever been taken in a pintle injector.

2.2 Droplet Sizing Methods

The various droplet sizing methods can be divided into two main classes: (1) "spatial" distributions which give a count based on a picture of the droplets frozen in space and (2) "flux" distributions which give a count based on the flux of droplets crossing a counting station. To explain the difference, consider an analogous problem of determining the distribution of vehicles travelling along a highway. A spatial distribution, based on still photographs, would overcount the true flux distribution of slower-moving bicycles along a road. Likewise, spatial droplet sizing techniques overcount the true flux of the smaller droplets, which normally move slower after injection into the engine. Some techniques are able to measure simultaneous droplet size and velocity, in which case either flux or spatial distributions can be generated. A review of most droplet sizing techniques is given by Azzopardi (Reference 4).

The flux distribution is normally of interest in combustion modeling. Ferrenberg and Varma (Reference 2) used a simple simulation of droplet drag to show that a spatial measurement technique can lead to distributions with Sauter mean diameters 30% less than the flux averages. Other anomalies such as bi-modal distributions can arise when a normally-distributed flux distribution is sampled spatially.

2.2.1 Spatial sizing methods:

The earliest droplet sizing method was photographic. While still attempted today, it has fallen out of favor due to problems with establishing acceptable focus criteria and problems with processing the voluminous photographs needed for a statistically-significant sample size. Double-flash photography allows simultaneous droplet size and velocity to be obtained. Holographic photography overcomes the focusing problems, but not the data analysis difficulties.

The most common droplet sizing instrument is based upon the forward diffraction "Airy rings" which arise when a laser beam is passed through a spray (Reference 5). As marketed by Malvern Instruments, Ltd. it is a simple, turn-key system. Besides being a spatial method, it also gives a spatially averaged distribution, weighted along the "line-of-sight" of the laser beam through the spray. While it is possible to determine the actual size distribution at each point in the spray (Reference 6) by computed tomography, this has not yet been accomplished. Such a "line-of-sight" average is not sufficient for a single element spray, where large spatial variations are expected.

2.2.2 Flux sizing methods:

The earliest of these methods replaced the actual spray liquids with various waxes, which would solidify after spraying, and could then be sieved into size distributions and weighed. The greatest problem with this technique is in properly scaling the hot wax properties to those of the actual fuel and oxidizer used. There are also questions as to the wax properties where droplet breakup occurs, as the wax begins cooling before atomization (Reference 2).

Later techniques have evolved from the Laser Doppler Velocimeter (LDV). The earliest of these attempted to correlate the visibility of the signal to the droplet size (Reference 7). Due to the complicated nature of Mie scattering, it has proven difficult to design a system in which the visibility is a monotonic function of the droplet size.

An approach which overcomes this problem is to simultaneously collect the light scattered at two different angles in the forward direction. The phase shift between the two visibility signals is a monotonic function of the droplet size. This technique, being developed by Aerometrics, Inc. has shown success in actual sprays (Reference 8).

All of the LDV-based systems must use elaborate noise rejection techniques to resolve the weak, high frequency signal and without a skilled operator, erroneous measurements are possible. To improve signal detection, forward-scattered collection at small angles to the beam is generally used. It is likely that in a dense spray the interference pattern would be easily disturbed by the upstream droplets through which the beams must travel.

A more direct approach is to use the intensity of the light scattered when a droplet crosses a laser beam as a size indication. This yields a strong signal which is easily detected. If the droplet crosses an area of uniform intensity, the intensity scattered is proportional to the cross-sectional area of the droplet. Interference effects, described by the Mie solution, cause oscillations about this exact area proportionality, but for droplets greater than about 5 μm in diameter, with large collection angles, the interference effects average out.

The main difficulty is that laser beams normally have a Gaussian intensity profile. A droplet crossing the beam at different locations would generate different pulse heights, a problem termed "Gaussian ambiguity". Deconvolution techniques have been developed to correct the raw data for this problem (Reference 9 and 10), and an instrument employing these corrections is presently marketed by Insitec. Other attempts have been made to generate a more uniform ("tophat") intensity profile, with marginal success (Reference 11).

One means of eliminating the Gaussian ambiguity, developed by Spectron Development Labs (Reference 12), is to use an LDV probe volume to define the center of the main beam. This allows simultaneous measurement of the droplet velocity. The LDV probe volume diameter must be several times larger than the droplet diameter and the main beam diameter must be about 5 times larger than LDV beam. Also, the LDV signal requires forward collection optics, which views the main beam at an oblique angle, increasing the probe volume size still further. This makes it more likely that more than one droplet will be in the probe volume at a time in a dense spray, somewhat limiting the applications of the instrument.

2.3 Injector Spray Characteristics

Most liquid rocket injectors consist of numerous single element injectors. The single elements typically consist of two or more impinging liquid jets. The liquid jets may be of the same propellant, or consist of a combination of oxidizer and fuel jets. Other singlet elements such liquid-gas atomizers (used with gaseous H₂ fuel) or a jet impacting a "splash plate" are used. The singlet sprays merge to form the total injector spray. Normally the attempt is to obtain uniform properties over the bulk of the chamber area, with fuel rich conditions near the walls.

The pintle injector in the TRW Lunar Module Descent Engine, which was the focus of the present project consists of a single element located on the centerline of the engine. Single element injectors are common in small rocket engines where the lower flow rates do not allow a multi-element design. Other claimed advantages in the TRW engine are simplicity, reliability, and less likelihood for combustion instability (Reference 13).

The liquid oxidizer flows inside an axial tube and the fuel flows in a coaxial sheet down the outside of the tube. At the end of the tube the oxidizer is directed outward in a radially-expanding fan which crosses the downward flowing fuel sheet, causing intimate mixing and droplet formation. The designers also intended that the sudden reaction of the hypergolic propellants would aid in atomizing the liquids.

A concern with all optical diagnostics in a dense spray is light attenuation in passing through the spray. A simple analysis for a standard multi-element injector allows an assessment. Consider a mono-disperse spray of droplets of diameter d , with spacing ℓ between droplets in a square lattice. Equating the volume flow rate of liquid through the orifices in the injector to that of the droplets in the spray:

$$v_o A_o = \frac{\pi}{6} \left(\frac{d}{\ell} \right)^3 v_d A$$

where v_o is the axial velocity of the jet issuing from the orifice, v_d is the droplet velocity, A_o is the total area of the orifices in the plane of the injector face, and A is the total area of the injector face. The spacing between droplets is then:

$$\frac{\ell}{d} = \left[\frac{\pi}{6} \frac{(v_d)(A)}{(v_o)(A_o)} \right]^{1/3}$$

Droplet drag calculations suggest that the droplets decelerate to about $0.8 v_o$ after entering the chamber, and are then accelerated by the expanding combustion gases, so one might take $v_d = v_o$ as a good approximation.

Including diffraction, each droplet scatters away all light incident upon an area twice its cross-section, so that a beam of diameter A_b will be attenuated by a fraction $e = \pi D^2 / (2A_b)$. The number density of droplets is $n = 1/\ell^3$, so that in a path length L the beam will intercept LA_b/ℓ^3 droplets. Assuming a linear absorption law, the fraction of intensity transmitted is:

$$T = \exp(-eN) = \exp(-\alpha L)$$

$$\text{where: } \alpha = \frac{\pi}{2d} \frac{(d)^3}{(1)} = \frac{3}{d} \frac{(v_o)(A_o)}{(v_d)(A)}$$

This can be easily extended to a poly-disperse spray by replacing the diameter above with a "reciprocal weighted" average diameter:

$$\frac{1}{d_{\text{avg}}} = \frac{1}{N} \sum \frac{1}{d}$$

The smaller droplets are most important in determining the total attenuation, but are not as significant in a combustion model. Therefore, beam attenuation is not very useful as a diagnostic method.

A representative multi-element injector ("StarTech") was tested by the author and Michael Powell of AFAL (Reference 14). $A/A_o = 121$ for this injector, so that the spacing between droplets was 4 drop diameters, as given above. The circular injector was 3.5 inches in diameter. Initially the flow rates were set 11 times too low. From the measured transmission, the reciprocal weighted average diameter was calculated to be $173 \mu\text{m}$. The analysis above suggests an enormous attenuation for a more reasonable average diameter of $50 \mu\text{m}$. Indeed, when operating at the correct flow rates no transmission was detected. This suggests that it is impossible to optically access the interior of a large, multi-element injector spray. For this reason, droplet sizing is better attempted in a small single element spray.

3.0 EXPERIMENTAL SYSTEM

3.1 Optics

The droplet sizing instrument used was developed as a previous minigrant project for the Astronautics Laboratory, and is described more fully in Reference 1. The scattered intensity when a droplet passes through the probe volume is used to determine the droplet size. A small "locater beam", coaxial with the main beam, defines a region of uniform intensity in the center of the main beam. The locater beam is of a different color (yellow) than the red main beam. Originally, laser beams of different polarizations were used, but significant cross-talk was noted as the polarization was altered by scattering. In fact, this "depolarization" effect is the basis of a droplet sizing method by Beretta (Reference 15).

As shown in Figure 1 and Photo 1, the locater beam is expanded to 40 mm diameter by a 40x microscope objective and converged by an f/6.5 achromatic lens to a minimum spot size of 5 μm diameter. The main beam is expanded with a 20x lens and gradually converged at f/40 to a minimum size of 33 μm diameter. A spatial filter is used with the main beam to give a uniform Gaussian profile. The main beam is brought coaxial with the locater beam by a small 6 mm diameter mirror inserted in the center of the expanded locater beam. By moving the focusing lenses, the beam diameters at the probe volume can be varied. Normally the main beam is adjusted to 500 μm diameter at the probe volume and the locater beam is about 20 μm diameter.

A lens at 90° to the laser images the laser beams onto the main slit. The slit width, together with the beam diameter defines the size of the probe volume. The two colors are separated by an edge filter. The red light, from the main beam, is reflected into a photomultiplier. The yellow light, from the locater beam, passes through a lens which re-images the droplet and forms an image of the main slit on the "locater slit". The locater slit views only the center of the main slit, ignoring those droplets which are partially obscured by the edges of the main slit. Therefore, the "locater photomultiplier" triggers a measurement only when a droplet passes through the center of the main beam and is centered in the view of the main slit. While conceived independently, both ideas of a coaxial locater beam and a double slit imaging system have been used previously (References 16 and 17, respectively). However, the first used forward scattering and the second used an incoherent source with the two slits in parallel, rather than series.

For alignment, a white object is placed in the laser beams and translated until it is in the probe volume, as determined by viewing the image at the main slit. The scattered light is bright enough to be traceable through the collection optics. The image of the main slit on the locater slit is visible, and is centered

over the smaller locator slit. By a slight rearrangement, the collection lenses can project a magnified image of the probe volume onto a screen, allowing the beams to be aligned coaxial. Since the intensity profile cannot be measured, the beam diameters can only be approximated. The receiving optics are covered with black plastic after alignment.

3.2 Electronics

Rocket injectors have pressure drops of about 100 psi. From Bernoulli's Equation, the droplet velocities for water are about 37 m/s. The droplets would cross the 400 μm main beam in 11 μs . This requires that the electronics have frequency response of at least 45 kHz.

A 50 μm droplet would scatter 1.5% of the 5 mW main beam. The f/5.2 lens covers 0.23% of the total angle, and at 90° the scattered intensity is about 10% of the isotropic value, so that a power of $1.7 \cdot 10^{-8}$ W is collected. For 70% transmission in the collection optics and 5% photomultiplier quantum efficiency, $6.5 \cdot 10^{-15}$ J of energy will be detected during the 11 μs the droplet spends in the laser beam. This corresponding to 20,700 photons at the 632.8 nm wavelength. According to Poisson statistics the pulse signal would vary by +/- 0.7%, which is negligible.

The current outputs of the photomultipliers are converted to voltage by dropping across a 500 Ω resistor. Assuming 200 pF capacitance in the photomultiplier and input cable, this acts as a low pass filter with a 1.6 MHz cut-off frequency. An op amp circuit, with slew rates of 13 V/ μs , amplifies the voltage signals. It was necessary to hand wire a dynode chain for the main photomultiplier, with zener diodes and capacitors in the last stages, to maintain linearity.

Originally, analog signal processing was tried, using a single channel pulse height analyzer (Ortec 550). One difficulty was that the count rate was very low, since a single channel analyzer disregards most of the valid pulses. Another problem was that the analyzer was intended for use with the much shorter scintillation pulses in nuclear spectroscopy and did not work well with the slower droplet pulses. Any ripples on the pulses were mistakenly identified as peaks.

The signal processing presently consists of a Rapid Systems model 2000, 20 MHz, 2 channel A/D converter. A pulse from the locator photomultiplier triggers digital acquisition of the pulse. The digitized pulse is fit to a Gaussian curve. The pulse peak determines the droplet diameter and the pulse width determines the droplet speed. These are tabulated to give drop size and velocity distributions and cross-correlations. Since both size and velocity are obtained simultaneously, either a flux or spatial distribution can be generated.

Representative digitized data shown in Figure 2. This was acquired by an interactive program which stores the time series binary data on hard disk, a utility which converts the files to Lotus 1-2-3 format, and importing and plotting in Quattro Pro. However, this manual procedure cannot be used to process the vast number of pulses needed to obtain a statistically-significant sample. Drivers are provided to control the A/D converter from a C program.

Note that in Figure 2, only 3 droplets passed through the center of the main beam and generated a locator signal ($>1V$), although 8 droplets passed through the main beam somewhere. There is no direct correlation between the locator signal and the droplet size. Even a very small droplet can generate a strong trigger signal. The spray seems to be sparser than could be tolerated, since the pulses do not come close to overlapping. At the rate of 6 measurements per second, it would take 5 minutes to acquire a minimum 2000 counts needed for an accurate size distribution. The beam diameters could be increased to improve the count rate.

3.3 Calibration

Originally uniform glass spheres were circulated in a glass container with a magnetic stirrer, but problems with deposition on the sides and obtaining the proper density resulted. Presently a glass pipet is drawn to a very thin diameter, cleaved and vibrated with a speaker and audio generator to generate a stream of mono-disperse droplets, as shown in Photo 2 (Reference 18). The droplet stream is translated to pass through the center of the probe volume.

Since exactly one droplet is generated each cycle, the droplet size can be calculated from the flow rate by a simple mass balance. Additionally, the spacing between the droplets can be measured using a strobe light, allowing the droplet velocity to be measured. Knowing the droplet velocity, the beam diameter can be determined from the pulse width.

Some problems have been encountered with the tubes becoming clogged. More careful filtering is needed. It is also difficult to obtain a sharply cleaved edge on the tube, which allows a thin jet to issue from the tube. Commercial droplet generators are available, but are quite expensive.

3.4 Translation System

Designing and assembling the translation system was the major task of the project and considerable time was spent in designing a system which met the budget constraints. To implement the "scattering tomography" corrections for beam attenuation, discussed in Section 4.1, it was initially considered

necessary to provide rotation of the beam about the collection axis, so that the spray could point either up or down. A large rotator (Velmex B4872TS) with a stepper motor accomplishes this. Axial translation is provided by a manual stage (Velmex A2509). Rotation about the spray axis is accomplished with a small stage with a DC/encoder drive (Oriental Motor 13048). Translation over an axial cross-section is done with two stages with DC/encoder drives (Oriental Motor 16138). To insure alignment with the optics, the translation system is mounted on a rail extending from the optics table. The assembly is shown in Photos 1 and 2.

The three DC motors and the stepper motor are controlled by a single board in the AT computer bus (Precision Micro Control DCX). A driver is provided to send motion commands from a C program.

3.5 Model Injector and Flow System

The actual TRW pintle injector has a 6.7 cm diameter and a total flow around 1000 L/min. Besides exceeding the space and flow limitations of the facilities at Morehouse College, the light attenuation through such a dense spray would be tremendous. For these reasons it was necessary to confine testing to a smaller scale model.

To limit the beam attenuation to 50% over a 4 cm path through the spray requires (Section 2.3):

$$\alpha = -[\ln(0.5)] / (0.04 \text{ m}) = 17 \text{ m}^{-1}$$

Assuming 50 μm droplets moving at 50 m/s, this restricts the volume flow rate to:

$$\dot{V} = v_O A_O = (17 \text{ m}^{-1}) (50 \mu\text{m}) (1.3 \cdot 10^{-3} \text{ m}^2) (50 \text{ m/s}) / 3 = 18.4 \text{ cc/s}$$

or 1.1 L/min, which is considerably less than in the actual injector.

The model injector is shown in Figure 3 and in Photos 3-5. The "oxidizer" and "fuel" are discharged through circular openings of 3.4 mm diameter. For a pressure drop of 20 psi in each, the discharge velocity of water would be 17 m/s. For flows of 9.2 cc/s through each opening, the gap required is 50 μm . Actually, there is a "discharge coefficient" for each opening, due a vena contracta in the opening, so that the actual gap might be as large as 100 μm .

There were not enough funds to build the model injector at an outside shop. There is a machine shop in the Physics Department, but it is currently occupied by Atlanta University and Morehouse faculty are not allowed access. It was necessary to construct the injector with the authors personal tools,

consisting of a drill press, bandsaw, and Dremel tool. The design reflects these limitations.

The stainless steel tubing was chucked in the drill press and rotated, while cut with the Dremel tool, giving a square edge. It was press fit into the aluminum block. Interchangeable brass plates, with a centered hole, are placed over the tube. The gap between the plate and tube controls the "fuel" flow. The hole in the plate is sized with a tapered hand reamer to give a uniform clearance with an adjustable hole size. The round head of a brass screw closes the end of the tube. A thin wire is twisted around the screw and the ends protrude between the tube and screw head, forming a gap which controls the "oxidizer" flow. The wires are trimmed flush with the Dremel tool.

It proved easy to maintain a uniform gap for the "oxidizer" at the end of the tube. A fine radial sheet was formed, which broke into fine droplets. It was more difficult to control the "fuel flow". The liquid would run down the tube in streams, rather than forming a uniform cylindrical sheet. More work is needed to solve this problem.

A gear pump provides operating pressures up to 100 psi. A single pump is used, since both the "oxidizer" and "fuel" flows are distilled water, at present. Each flow has a separate rotameter and pressure gage, as shown in the Photo 6. The spray comes out at a very wide angle and contains many fine droplets which tend to settle on the optics. To control this, the spray is directed into the suction tube of a shop vacuum. This distorts the droplet trajectories somewhat, but the result is probably closer to the streamlines in the rocket engine. The vacuum also allows the spray to be rotated upward without affecting the spray. The water collected in the vacuum returns to the pump.

4.0 DATA ANALYSIS

4.1 Beam Attenuation

In a dense spray the attenuation of the laser beam in traveling through the spray to the probe volume can become significant. Obviously, droplet sizing methods which rely upon the intensity of the scattered light are directly affected by beam attenuation. This is one claimed advantage of alternative methods such as the Airy diffraction (Malvern) or LDV techniques which, to a first approximation, are intensity independent. Actually, the Malvern instrument was found to give an 8% change in the indicated mean diameter with 60% beam attenuation (Reference 6). Also, the droplet size distribution was distorted, both apparently due to multiple scattering. While this is better than the 37% decrease in mean diameter which would result for an intensity technique (recall D^2 relationship), it is not negligible.

No careful studies of the effects of beam attenuation on the LDV techniques are known. It is expected that passing through numerous droplets in the spray would significantly distort the interference pattern at the probe volume, destroying the visibility signal. In one attempt by Rocketdyne Corp. to employ an LDV Instrument (Spectron Development Labs), it was not possible to make measurements closer than 12 inches downstream of a rocket injector.

4.1.1 Time-averaged Intensity

A. Input beam attenuation

Actually, it is not difficult to correct for beam attenuation in the intensity techniques. By passing the beam to the measurement volume from each side of the spray, in turn, it is possible to determine the intensity of the beam at the measurement point. The geometry is shown in Figure 4.

The intensity fraction transmitted across the total path through the spray is denoted as $T (=I_t/I_0)$. The transmittance to the probe volume is denoted as t_ℓ when the beam is from the left, or t_r when the beam is from the right. Then,

$$T = t_\ell t_r = (t_r/t_\ell) t_\ell^2$$

Thus,

$$t_\ell = [(t_\ell/t_r)T]^{1/2}$$

Implicit in this derivation is the assumption that the transmittances are the same for either direction of the beam. In terms of the intensities defined in Figure 4, this assumption means that $I_\ell/I_0 = I_t/I_r$. This assumption is actually identical to assuming that Beer's linear absorption law holds. Since the attenuation is due to scattering rather than absorption this assumption is not perfectly valid, although it works well even at attenuations of 99%.

The result is expressed in terms of the ratio t_ℓ/t_r . This ratio is easily determined from the measured pulse height distributions with the beam from the left and right, in turn. While the collected light is also attenuated, it is the same fraction in each case so that the ratios are unaffected. Therefore, the distributions should be similar in shape, with the abscissa simply scaled by the intensity ratio. Ratioing the mean pulse heights of each distribution gives the intensity ratio at the probe volume, which is equal to the ratio t_ℓ/t_r . The total transmittance (T) along the path is simply the ratio t_ℓ/t_r at a point at the right edge of the spray. In practice the spray has no "edge", so T must be determined by extrapolating the t_ℓ/t_r values for a number of points along the path. T could also be measured with a separate detector.

This analysis procedure is termed "scattering tomography". By determining t_ℓ at a number of points along a line, the absorptivity at every point on the line can be determined. It is a much simpler technique than the well known absorption tomography, which requires that the absorptivity at many points over an entire area be simultaneously determined.

It is not actually necessary to pass a separate beam from the right. Instead, the same geometry can be obtained by rotating the spray 180° about the collection axis. This is not very convenient as it leaves the spray pointing upward, but was preferred in the present study to generating two separate input beams.

B. Input and Collection Attenuation

To apply this result to droplet sizing, attenuation along the collection path must also be considered. While this would seem to complicate the data analysis, it actually reduces the complexity, as will be seen. By rotating the spray 90° about a vertical axis through the probe volume, as shown in Figure 5, the former beam path, with known transmissivity t_1 can be made to coincide with the collection axis.

Denote the mean of the measured pulse height distribution by $P_{k\theta}$, where $k=\ell$ or r for the beam from the left or right, respectively, and $\theta = 0^\circ$ or 90° for the spray at the original orientation or rotated 90° about the vertical, respectively. Considering both the beam and collection attenuations, the corrected mean (P) is then:

$$P = P_{\ell 0^\circ} / (t_1 t_3)$$

From the previous analysis:

$$t_1 = [(P_{\ell 0^\circ} / P_{r 0^\circ}) T_1]^{1/2}$$

and

$$t_3 = [(P_{\ell 90^\circ} / P_{r 90^\circ}) T_2]^{1/2}$$

substituting,

$$P = \frac{[P_{\ell 0^\circ} P_{r 0^\circ} P_{\ell 90^\circ}]^{1/2}}{[P_{r 90^\circ} T_1 T_2]}$$

Note that $P_{\ell 0^\circ} = P_{r 90^\circ} (= t_1 t_3 P)$, so more simply,

$$P = \frac{[P_{r 0^\circ} P_{\ell 90^\circ}]^{1/2}}{[T_1 T_2]}$$

Actually, a number of other combinations are possible. To generalize, note that $P_{r0^\circ} = t_2 t_3 P$ and $P_{l90^\circ} = t_1 t_4 P$. Substituting,

$$P = \begin{bmatrix} t_1 t_2 t_3 t_4 & PP \\ T_1 & T_2 \end{bmatrix}^{\frac{1}{2}}$$

Since $T_1 = t_1 t_2$ and $T_2 = t_3 t_4$ this gives an identity, which could have been used as the starting point for the derivation, although it would seem a bit inspired.

Referring to Figure 5, the possibilities for the numerator are:

$$\begin{aligned} (t_1 t_3 P)(t_2 t_4 P) &= P_{l0^\circ} P_{l180^\circ}, P_{l0^\circ} P_{r270^\circ}, P_{r90^\circ} P_{l180^\circ}, \text{ or } P_{r90^\circ} P_{r270^\circ} \\ \text{and} \\ (t_1 t_4 P)(t_2 t_3 P) &= P_{l90^\circ} P_{r0^\circ}, P_{l90^\circ} P_{l270^\circ}, P_{r180^\circ} P_{r0^\circ}, \text{ or } P_{r180^\circ} P_{l270^\circ} \end{aligned}$$

These can be summarized as two basic procedures:

- (1) after the first measurement, rotate the spray 180° about the vertical axis, or
- (2) after the first measurement, rotate the spray 90° about the vertical axis, then rotate 180° about the collection axis (to pass the beam from the right side).

For each of these, there are four possibilities, since the first measurement could be made along any of the four segments. Several of these possibilities could be used and averaged to increase the accuracy. (In fact, one is not constrained to only these four segments, since any ray through the probe volume is a valid starting point, however, the data tabulation is easier if measurements are confined to points in a rectangular grid.)

The first procedure is much easier since the spray remains pointing down. This result was not predicted from the previous scattering tomographic analysis, which was as far as the author had worked when the proposal was submitted. Indeed, considerable time and expense was spent in designing and assembling the translation system to allow rotation about the collection axis, which is seen to be unnecessary. However, the upward rotation is useful in determining the total path transmittance without a separate measurement, as described in Section A.

4.1.2 Fluctuations in Beam Intensity

A related problem is that the attenuation of the beam is not constant, due to statistical fluctuations in the number of droplets along the path to the probe volume. Attenuation of the collected light also fluctuates, but is not significant due to the much larger number of droplets in the cone of collected light.

It is assumed that a droplet scatters all of the light incident upon its cross-sectional area away from the beam. An equal amount of light is diffracted

by the droplet, but is not considered here since most of the diffracted light remains within the confines of the beam over the short distance to the probe volume. For simplicity, the beam is assumed to have uniform intensity over the e^{-2} beam diameter (D), and the droplets in the spray are assumed to be mono-disperse. The fraction of beam intensity scattered by a droplet of diameter d is $(d/D)^2$. Using the linear attenuation law, the total fraction attenuated is: $A = 1 - \exp[-N(d/D)^2]$; where N is the number of droplets in the beam. According to Poisson statistics, this attenuated fraction will fluctuate by an rms fraction of $1/\sqrt{N}$, so that the rms fluctuation of the beam intensity will be:

$$I_{\text{rms}}/I = A/\sqrt{N}$$

Expressing in terms of the attenuation,

$$I_{\text{rms}}/I = (d/D) A[-\ln(1-A)]^{-1/2}$$

For both very low and very high attenuations there is little fluctuation in the intensity. In the latter case this is because there are numerous droplets in the beam, so that the statistical variation in the number is very small. The maximum fluctuation occurs at an attenuation of 71.5% in which case $I_{\text{rms}}/I = 0.638(d/D)$. For the design case of 50 μm droplets in a 500 μm diameter main beam, the maximum intensity fluctuation would be $\pm 6.4\%$, corresponding to a fluctuation in measured diameter of $+3.2\%$, -3.3% . Since the main beam converges as it approaches the probe volume, it is actually larger over much of the path, making the fluctuations even smaller. This intensity fluctuation would cause an artificial spread in the drop size distribution which could be corrected by a convolution method. However, the effect is fairly negligible.

For comparison, Hess (Reference 19) measured intensity fluctuations of $\pm 14\%$, with a beam attenuation of 5%. The beam was attenuated by a spray far upstream of the probe volume. The intensity fluctuations at the probe volume were monitored by passing a mono-disperse stream of 73 μm droplets through the probe volume. The beam diameter was about 600 μm at the probe volume, and somewhat larger in the spray. Since the attenuating droplets were so far upstream, a factor of 2 should be added to the droplet area in the analysis above to account for diffraction. The analysis would then predict: $I_{\text{rms}}/I = \sqrt{2}(d/D)(0.221)$. To agree with the analysis, the droplets in the spray would have to have been an average of 269 μm in diameter, which is large, but not unreasonable. Since the properties of the spray were not stated, this gives only an order of magnitude comparison.

The upstream droplets also cause spatial non-uniformities in the beam intensity profile, more simply termed "shadows". Diffraction smooths out these shadows as the beam propagates. A droplet moving through the probe volume gives a scattered pulse with ripples on the basic Gaussian shape due to these

shadows in the profile. This was a problem with the earlier analog system, which could process only smooth pulses. The present digital processing fits the pulse to a Gaussian shape, averaging over these ripples and eliminating any concerns.

4.1.3 Multiple Scattering

A final concern is that the attenuation is not due to absorption, but rather to scattering. The light is not really lost, as in absorption, but is simply redirected. After scattering repeatedly among the droplets in the spray, some of the scattered light is redirected along the beam path, recontributing to the beam.

Initially, the light is moving in the beam direction. After scattering off of the first droplet, it is redistributed, as given by the Mie theory, with most of the light travelling in the forward direction. However, after numerous scatterings, the light becomes isotropic, spreading equally in all directions. This transition from a directed beam to isotropic radiation was observed by the author and Michael Powell at AFAL (Reference 14) in passing a laser beam through a 3.5 inch diameter multi-element injector spray. As viewed from the side, the beam gradually spread until about half-way through the spray it "bloomed" into a spherical shape. A similar experiment was performed by Leslie Allen, as a student project at Morehouse College, with more quantitative results.

In a single element injector spray, the attenuation would not be so large. Simple energy considerations would argue that for attenuations of even 90% very little of the multiply scattered light would re contribute to the beam. In fact, in a student lab at Morehouse College, using transparent slides, attenuations of even 99% show no deviation from the Beer-Lambert Law. In fact, the contribution of multiply scattered light to the beam could be easily determined by measuring the intensity close to the beam direction.

The main effect of multiply scattered light is a steady background glare against which the droplet is seen. In a system which measures a DC level, such as the Malvern forward diffraction method, this glare contributes directly to the signal. However, in single particle counters where the signal is a pulse, the multiply scattered light simply causes an increase in the baseline level, which is easily eliminated. The proper question is whether the presence of a droplet in the probe volume would change the amount of multiply scattered light directed into the collection angle. At high attenuations, where multiple scattering becomes significant, it is also isotropic so that a spherical droplet could not send it in a preferred direction.

A final consideration is whether the assumption that the collected light would be attenuated by the same fraction as the input beam over the same path

is valid. Initially, it might appear that the lens would collect much of the light scattered from the collection path. However, for the scattered light to contribute to the image at the slit it must not only strike the lens, but be directed at a specific angle. This has the same probability as for light scattered from the beam to be redirected along the beam direction.

4.2 Counting Statistics

While Figure 2 shows that a small droplet can generate as large a locator pulse as can a large droplet, this does not mean that large and small droplets will trigger measurements with equal probabilities. This is a problem with all single particle counters, yet it appears that other investigators have not always considered the potential for such a triggering bias.

In the case of a triggering volume much larger than any of the droplets, the volume occupied by a droplet is not significant in the analysis, so that each droplet might be considered as located at a point in space. Each droplet would then have an equal probability of being within the triggering volume, and assuming that every droplet could trigger a measurement when it was in the trigger volume, there would be no bias. However, in a dense spray a minimal probe volume is required to avoid having more than one droplet in the probe volume at a time and the trigger volume must be smaller still to adequately define the center of the probe volume.

In the present instrument the locator beam diameter is about $10 \mu\text{m}$. Of course, it is difficult to speak of the "edge" of the locator beam, since the intensity falls off exponentially. Assume that if the edge of any droplet crosses the e^{-2} radius, a measurement is triggered. Assume also that whenever even part of a droplet image falls on the locator slit it triggers a measurement. These are reasonable assumptions since, as seen in Figure 2, the locator pulses are very large and the pulse heights seem to be independent of the droplet size.

With these assumptions, a measurement would be triggered whenever the center of a droplet is within a cylinder of diameter $(D_1 + d)$, and length $(S + d)$, where D_1 is the e^{-2} diameter of the locator beam, d is the droplet diameter, and S is the locator slit width. The relative probabilities for a droplet of diameter d_1 to trigger a measurement, versus one of diameter d_2 is simply the ratio of their respective trigger volumes:

$$\frac{p_1}{p_2} = \frac{(S+d_1)(D+d_1)^2}{(S+d_2)(D+d_2)^2}$$

It is possible to experimentally determine the counting statistics, although time has not permitted a verification. At certain frequencies the vibrating glass capillary tube generates a large and a small droplet every cycle.

The diameters can be measured by the instrument. While close to the tube exit the droplets follow exactly the same path, at some distance downstream they spread out somewhat randomly over space. The probe volume can be scanned over the stream at a constant rate to average over any nonhomogeneities. (In fact a steady scan over the concentrated stream, close to the tube exit, would also work). The ratio of measured count rates determines the relative counting probabilities. A similar procedure could use a mixture with two sizes of glass beads.

5.0 COMBUSTION MODELING

There have been several assumptions as to the mechanics of droplet combustion. These can be divided into several classes:

- (1) rapid vaporization and subsequent diffusion burning of the vapor
- (2) individual droplet combustion with a flame front surrounding each droplet
- (3) individual droplet combustion with a burning wake behind each droplet
- (4) group combustion of droplets with a flame region surrounding a group of droplets

The distinction between each of these modes is a function of the droplet size, number density, and velocity. Very small droplets (< 50 microns) tend to vaporize quickly, as in mode 1, while large droplets (> 150 microns) are observed to burn individually (Reference 20). In most practical cases, with a continuous droplet distribution, all of these modes exist simultaneously (References 21, 22).

5.1 Droplet Vaporization Analysis

The first mechanism can be easily modeled by considering an isolated droplet moving relative to a uniform body of hot gas. This assumes that the flame is far enough from the droplet that it does not affect the evaporation rate. At high evaporation rates the surface of the droplet can be assumed to be at the saturation temperature (T_S), so that a heat balance gives:

$$\dot{m} = -hA\Delta T/\lambda$$

where λ is the latent heat of vaporization, h is the heat transfer coefficient, $\Delta T = T_g - T_S$, and $A = \pi D^2$.

The heat transfer coefficient to a moving sphere is given by "Frossling's Equation" (Reference 23, Equation 13.3-1):

$$Nu = 2.0 + 0.60 Pr^{0.333} Re^{\frac{1}{2}}$$

where $Nu = h_0 D/k$, k and Pr are the thermal conductivity and Prandtl number of the gas, and Re is the Reynold's number based upon the droplet diameter.

The vapor generated decreases the heat transfer coefficient through transpiration, by a factor:

$$\frac{h}{h_0} = \frac{\ln(1+B)}{B} \quad ; \quad \text{where: } B = \frac{C_p \Delta T}{\lambda}$$

The parameter B is termed the "Spalding Transfer Number". This correction factor has been questioned, and some authors have stated that it has no theoretical basis. Actually it is easily derived from existing transpiration analyses, as shown in Reference 24. There is a slight correction for the gas to vapor molecular weight ratio which is neglected here.

When convection is negligible, $h_0 = 2k/D$, giving:

$$\dot{m} = -[2\pi k(h/h_0)\Delta T/\lambda] D$$

When convection is dominant, $h_0 = 0.6kPr^{0.333}(\rho V/\mu)^{1/2} D^{-1/2}$, giving:

$$\dot{m} = -[0.6\pi kPr^{0.333}(\rho V/\mu)^{1/2}(h/h_0)\Delta T/\lambda] D^{1.5}$$

Since the droplets are injected into a rocket engine at velocities around 50 m/s, convection is usually dominant.

5.2 Single Droplet Experiments

Numerous experiments have measured the evaporation time of a single droplet in a quiescent atmosphere, with the droplet hanging on the end of a thin wire. A flame front surrounds the droplet and the heat causes natural convection.

The droplet diameter is found to vary with time as (Glassman, Equation 6-26):

$$D^2 = D_0^2 - \beta t$$

where D_0 is the initial diameter (at $t=0$) and β is an experimental constant. Using $V = \pi D^3/6$ and $m = \rho V$ the mass evaporation rate per droplet is:

$$\dot{m} = -[\pi\rho\beta/4] D$$

Note that the dependance of the droplet evaporation rate upon the diameter is almost linear in all of these cases.

5.3 Energy generation density

The important quantity in a turbulent flow model of a rocket engine is the energy generation per volume, which is given by:

$$\dot{q}''' = n \dot{m} H_r$$

where n is the droplet number density and H_r is the heat of reaction. By conservation of mass, the number density depends upon the volume flow of liquid per cross-sectional area (V_ℓ), droplet velocity (v_d), and diameter as: $n = 6V_\ell / (\pi v_d D^3)$, so:

$$\dot{q}''' = [6V_\ell H_r / (\pi v_d)] \dot{m} / D^3$$

Substituting the evaporation rates above, the energy generation density is seen to vary inversely with the diameter to either the 1.5 or 2 power, depending upon the evaporation mechanism. In either event, the results of a rocket combustion model are seen to be very sensitive to the assumed droplet diameters.

6.0 RESULTS TO DATE AND FUTURE PLANS

The translation system, model injector, and flow system have been designed and assembled and preliminary results have been obtained. The programming to translate the spray and analyze the data have not been completed, primarily because the author had to begin learning to program in C when the need became obvious. Presently, the Oriel rotation stage is out for warranty repairs to the encoder, partially incapacitating the system. More progress was expected to date. The greatest difficulty was that the author spent considerable time completing a Technical Report (for the same AEDC group) as a formal record of work on minigrant from last year.

It is planned to continue measurements with the present system in an effort to determine correlations between the droplet size distributions and the spray parameters. Unfortunately, the funds are almost exhausted. Therefore it will probably not be possible to use different liquids in the testing, since such would require an additional gear pump, and funds for materials.

Additionally, the author has applied for a minigrant to follow work on a singlet oxygen spray generator at the Weapons Laboratory. This work would include additional development of a uniform droplet generator. This would aid calibration of the present droplet sizing instrument, if the minigrant is approved.

REFERENCES

1. Grissom, W. M., "Droplet Size Distribution Measurements in a Single Element Liquid Rocket Injector", Final Report, UES/AFOSR Contract F49620-85-C-0013/535851-0360, Dec. 1987.
2. Ferrenberg, A.J. and Varma, M.S., "Atomization Data Requirements for Rocket Combustor Modeling", 21st JANNAF Combustion Meeting, CPIA Publ. 412, Vol. 1, Oct 1984, p. 369.
3. Gill, G.S. and Nurick, W.H., Liquid Rocket Injector, NASA SP-8089, March 1976.
4. Azzopardi, B.J., "Measurement of Drop Sizes", Int. Journal of Heat and Mass Transfer, 22, 1979, p. 1245.
5. Swithenback, J., et. al., "A Laser Diagnostic Technique for the Measurement of Droplet and Particle Size Distributions", AIAA Paper no. 76-69, Jan. 1976.
6. Yule, A.J., et. al., 18th Symposium (International) on Combustion, 1981, p. 1501.
7. Chigier, N.A., et. al., 17th Symposium (International) on Combustion, 1979, p. 315.
8. Bachalo, W.D., et.al., "Evolutionary Behavior of Sprays Produced by Pressure Atomizers", AIAA-86-0296, Jan. 1986.
9. Muzutani, Y., et. al., "Doppler-Mie Combination Technique for Determination of Size-Velocity Correlation of Spray Droplets", Combustion and Flame, 44, 1982.
10. Holve, D.J. and Annen, K. "Optical Particle Counting and Sizing using Intensity Deconvolution", Optical Engineering, 23(5), 591-603 (1984)
11. Eauret, P.R. et al, "Measurement of Drop Size and Velocity in Vaporizing Sprays, in Proceedings, Second Int. Conf. of Liquid Atomization and Spray Systems. Madison, Wisconsin. June 20-24, 1982, p.261
12. Hess, C.F., "An Instrument to Measure the Size and Velocity of Particles in Particle Laden Flows", AIAA-85-1443, July 1985.

13. "Characteristics of the TRW LUNAR MODULE DESCENT ENGINE, Vol.1", (2nd revision), TRW Systems Group, June 30, 1977, p. 2-39.
14. Grissom, W.M. "A Feasibility Study of Liquid Rocket Engine Combustion Diagnostics", UES/AFOSR Summer Faculty Research Program Report, 1986.
15. Beretta, F., et. al. "Drop Size and Concentration in a Spray by Sideward Laser Light Scattering Measurements", Combustion Science and Technology, Vol. 36 (1984), pp. 19-37
16. Wang, J.C.F. and Hencken, K.R., "In situ Particle Size Measurements using a Two-Color Laser Scattering Technique", Applied Optics, 25, no. 5, March 1986.
17. Umhauer, H., "Particle Size Distribution Analysis by Scattering Light Measurement using an Optically Defined Measurement Volume", Journal of Aerosol Science, 14, no. 6, 1983, p. 765.
18. Sakai, T., et. al., "Uniform Size Droplets by Longitudinal Vibration of Newtonian and non-Newtonian Fluids", Proc. 2nd Int. Conf. on Liquid Atomization and Spray Systems (ICLASS), Madison, Wisconsin, June 1982.
19. Hess, C.F. "Nonintrusive Optical Single-Particle Counter for measuring the Size and Velocity of Droplets in a Spray", Applied Optics, Vol. 23, no. 23 (December 1984), pp 4375-4382.
20. Bolado, R. and Yule, A.J. "The Relationship Between Atomization Characteristics and Spray Flame Structures", Proc. 2nd Int. Conf. on Liquid Atomization and Spray Systems (ICLASS), Madison, Wisconsin, June 1982, p. 221.
21. Presser, C., et.al. "Velocity and Droplet Size Measurements in a Fuel Spray", AIAA-86-0297, Jan. 1986.
22. Sohrab, S.H. "Studies on Combustion of Liquid Fuel Sprays in Stagnation Flows", AFOSR/UES Summer Faculty Research Program, AFRPL, Sept. 1985.
23. Bird, R.B., Stewart, W.E., and Lightfoot, E.N. Transport Phenomena. Wiley (1960)
24. Grissom, W.M. "Liquid Film Cooling in Rocket Engines", AEDC-TR (being finalized), also as Final Report UES/AFOSR minigrant 1988.

- L - Lens
- M - Mirror
- SF - Spatial Filter
- S - Slit
- EF - Edge Filter
- F - Interference Filter
- PMT - Photomultiplier Tube

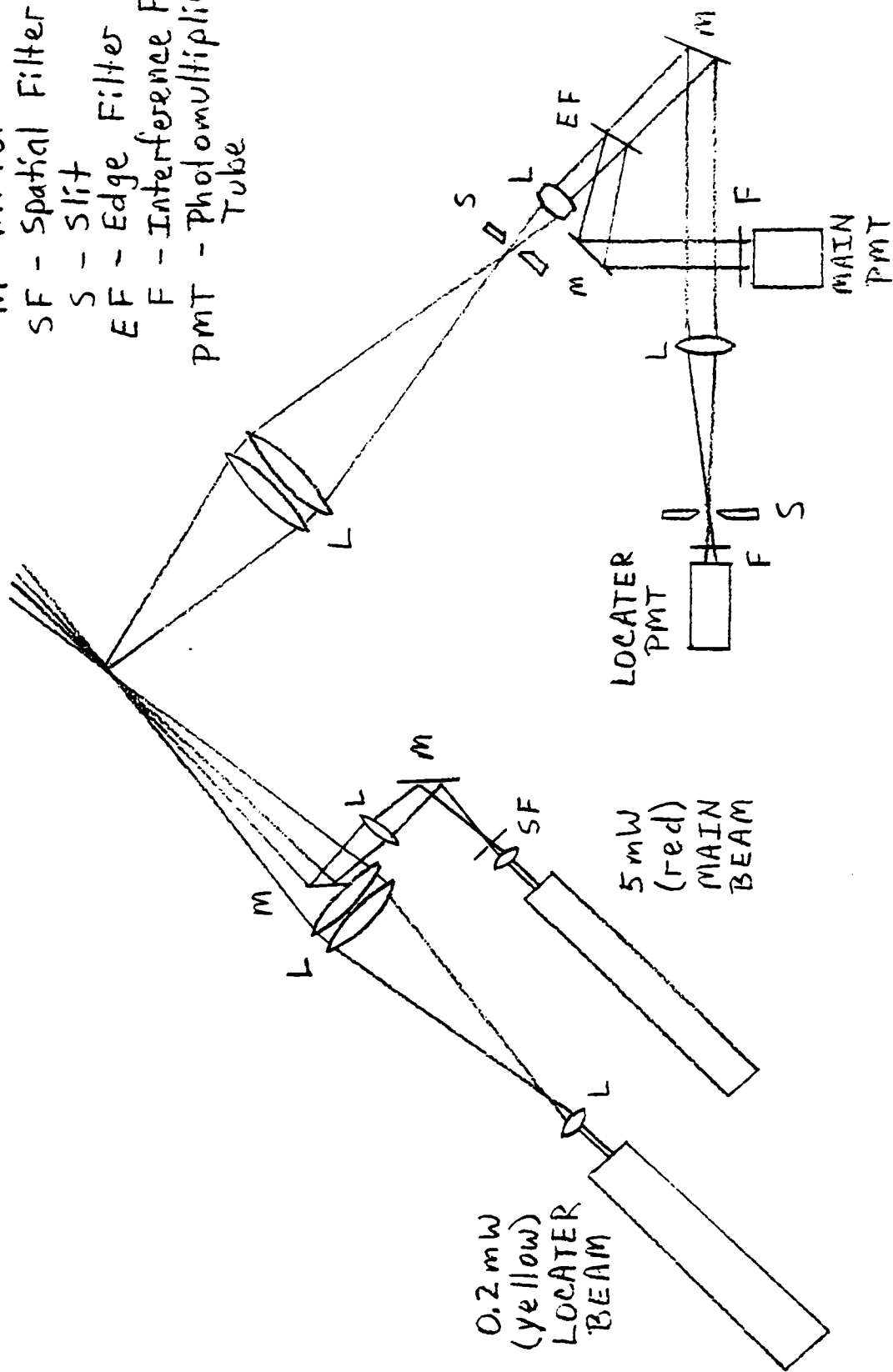


Figure 1. Optics arrangement

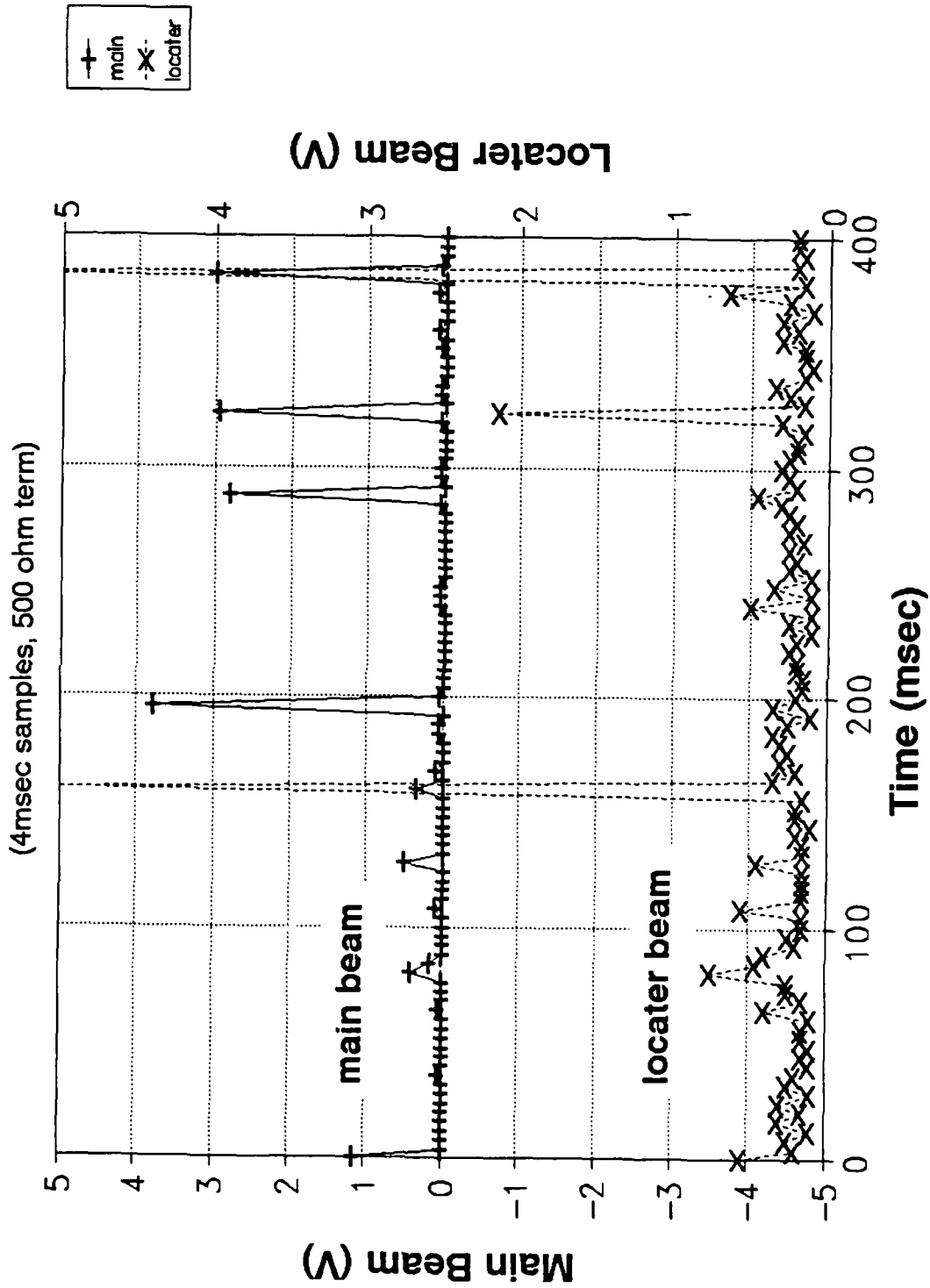


Figure 2. Photomultiplier Signals

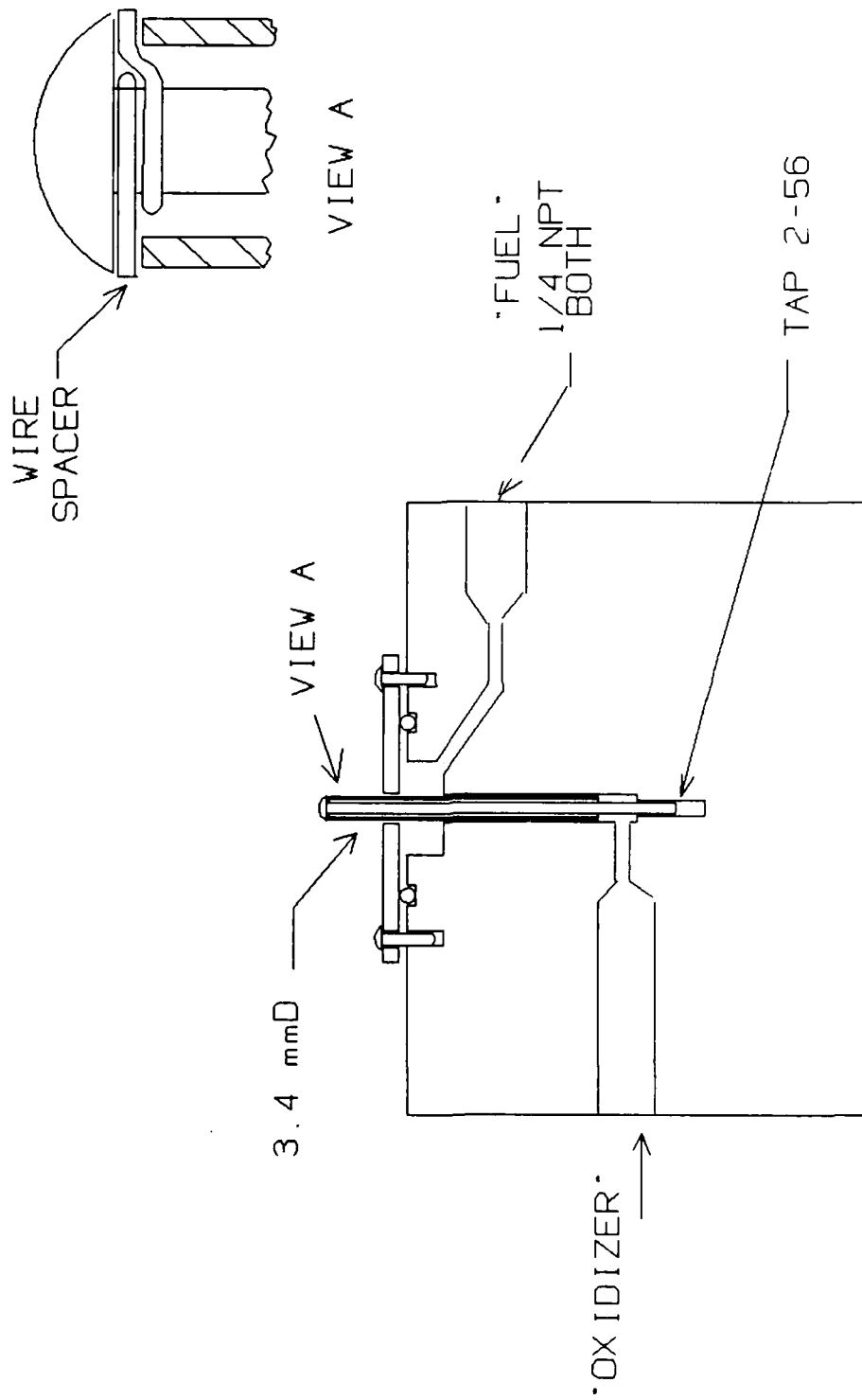


Figure 3. Test injector assembly

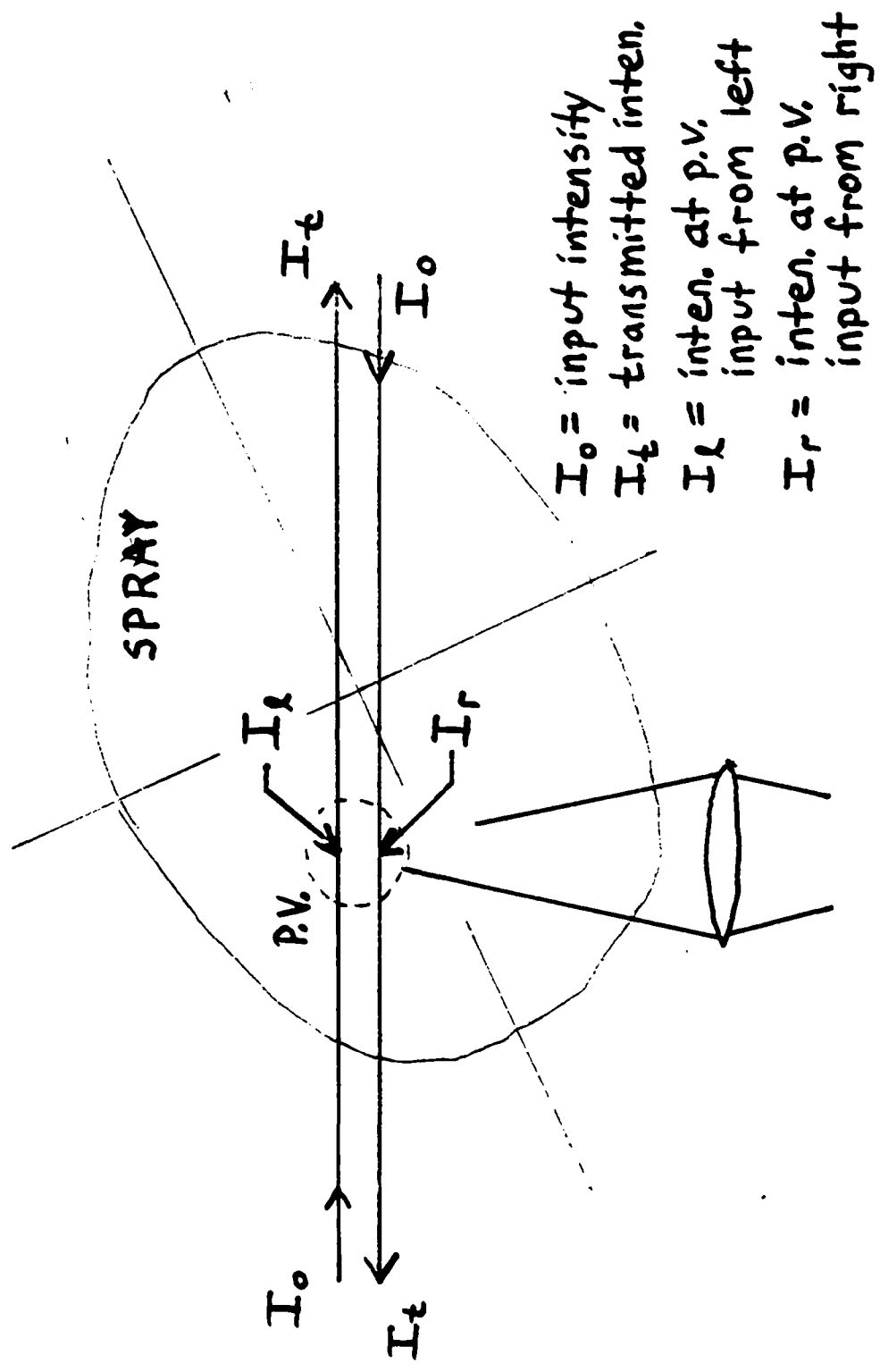


Figure 4. Scattering tomographic geometry

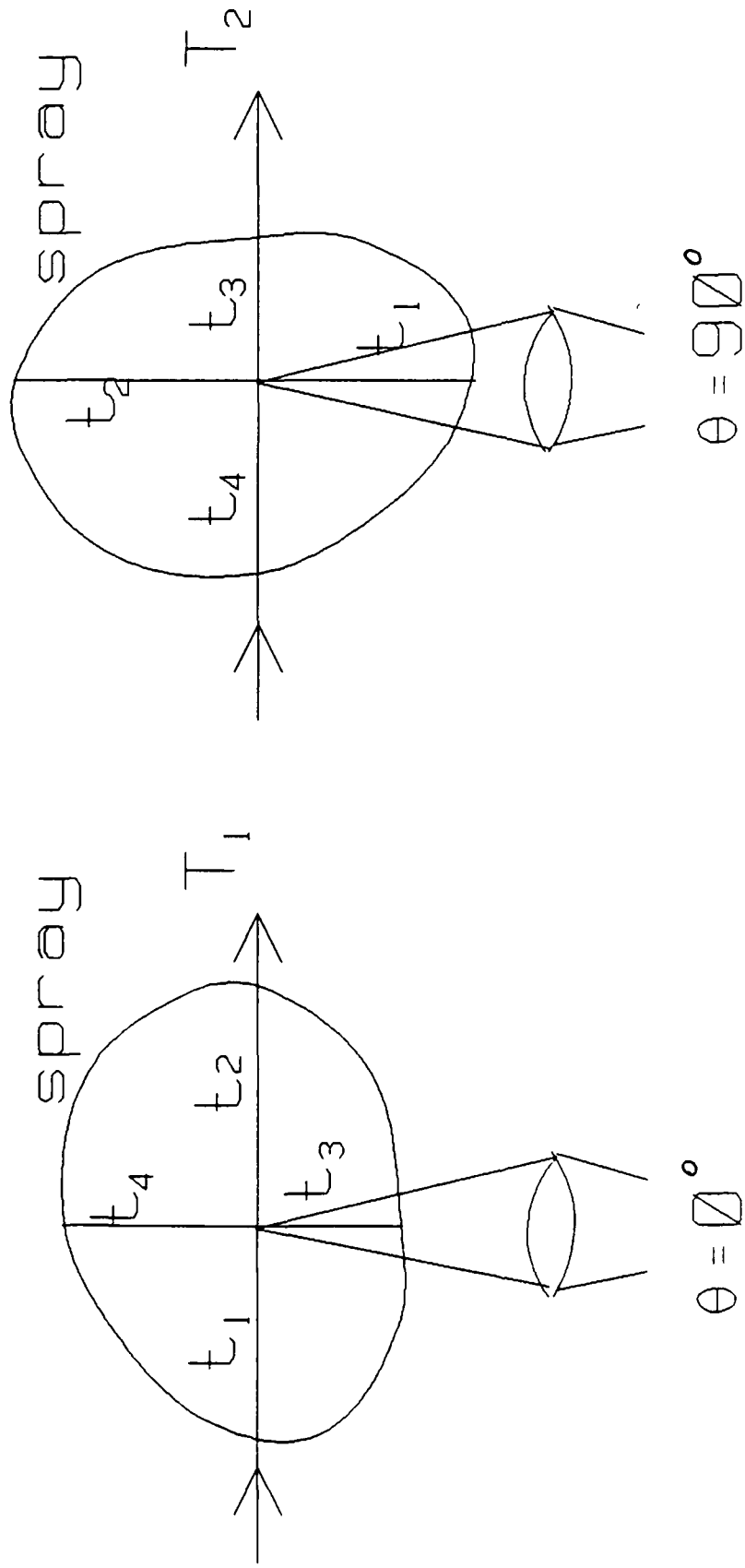


Figure 5. Input and Collection Attenuations

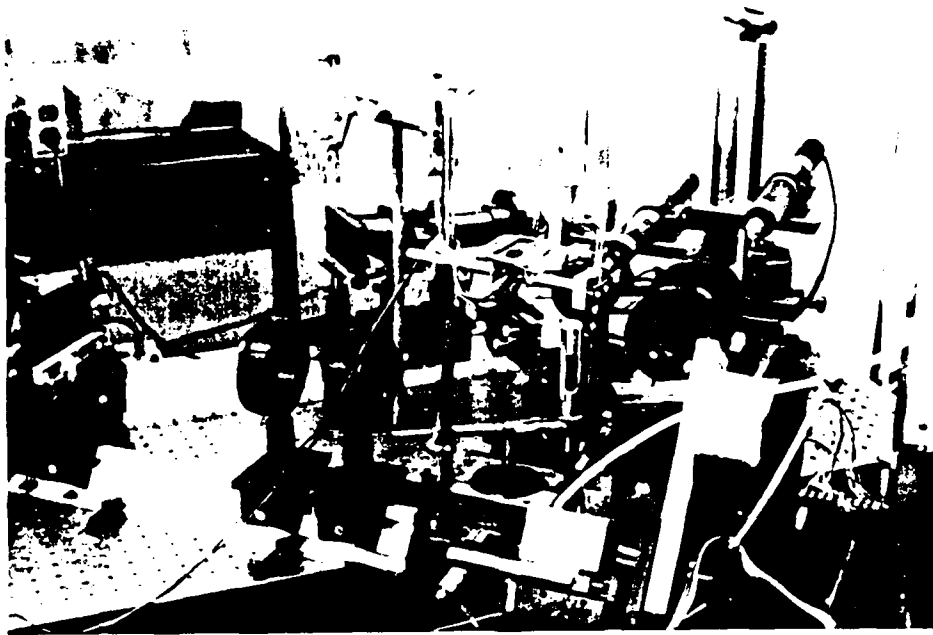


PHOTO 1. Optics Table and Translation System

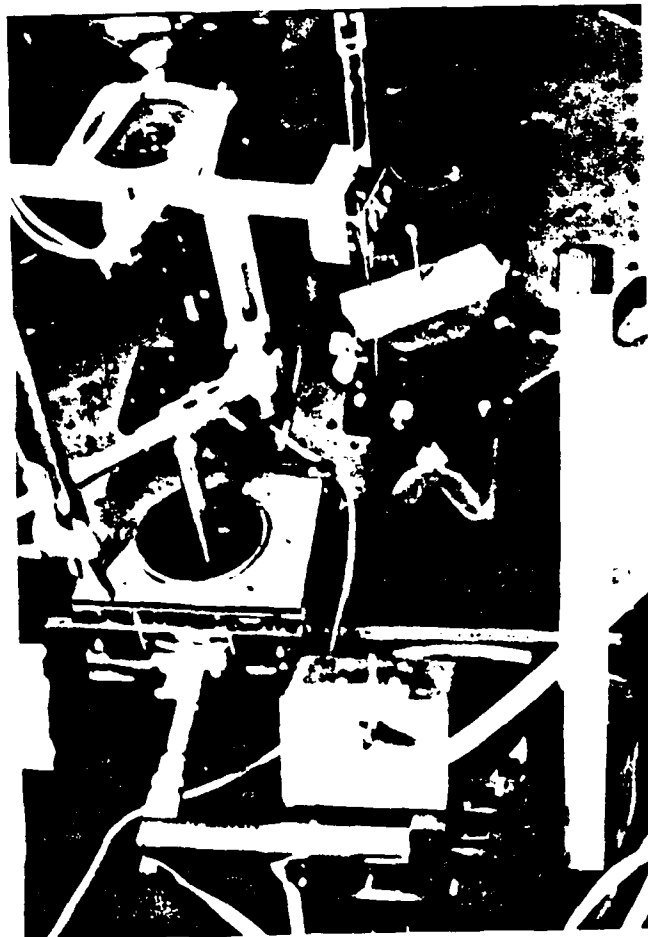


PHOTO 2.
Calibration



PHOTO 3. Injector spray with beam passing to left

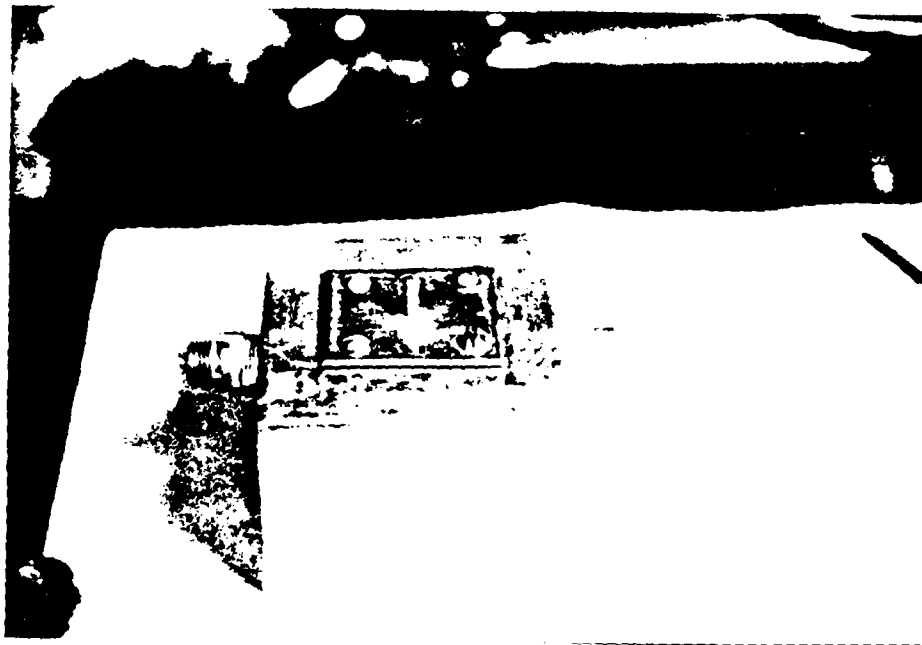


PHOTO 4. Test injector assembled

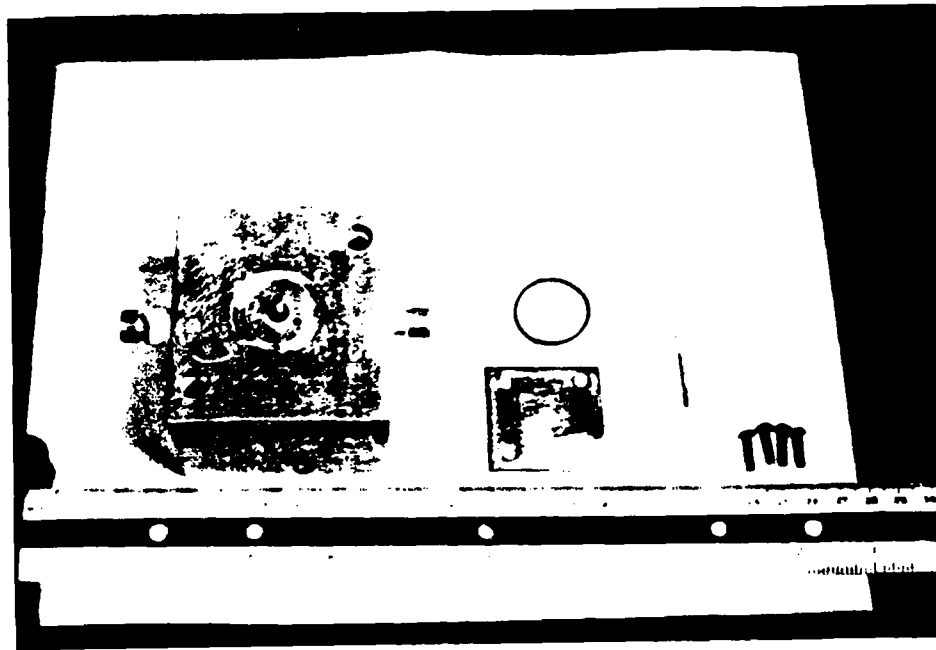


PHOTO 5. Test Injector disassembled

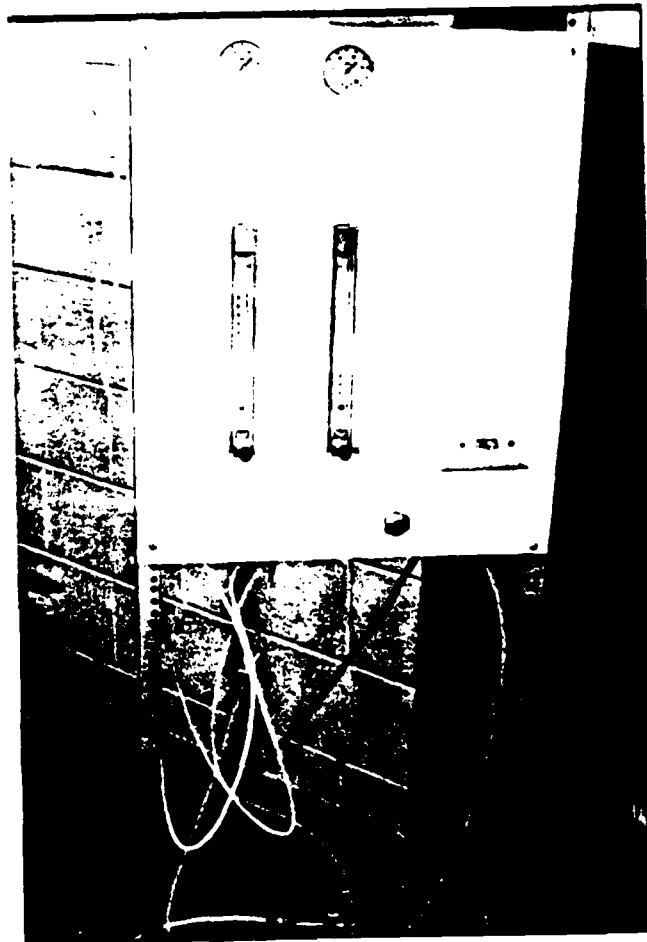


PHOTO 6.
Flow Bench

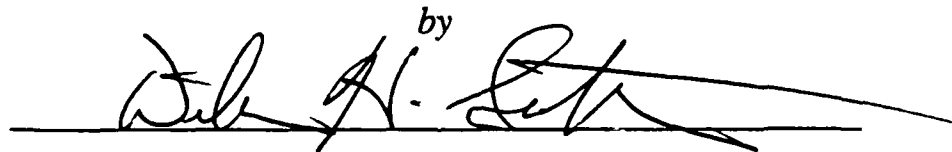
**Multiple Scattering
in
Solid Fuel Rocket Plumes**

**AIR FORCE OFFICE
OF
SCIENTIFIC RESEARCH**

RESEARCH INITIATION

**UES CONTRACT
S-760-OMG-091**

FINAL REPORT

by


William H. Sutton, Associate Professor

**School of Aerospace and Mechanical Engineering
College of Engineering
University of Oklahoma
Norman, OK 73019**

ABSTRACT

High resolution modeling of participating thermal radiation from exhaust plumes of solid fuel rocket motors containing low molecular weight metals was the goal of this project. Volumetric scattering of thermal radiation in such applications poses problems for nozzle base heating, performance diagnostics, and for infrared signature work. High resolution modeling, when used in conjunction with appropriate infrared testing, can provide valuable insight into the underlying physics and properties of solid fuel rocket plumes. The research here represents a beginning effort for such a code which could eventually be used to validate simpler models such as those in SIRRM.

A finite, cylindrically symmetric, variable property, and anisotropically scattering numerical solution to the monochromatic radiative transfer equation has been formulated using a discrete ordinates method. This model allows closer representation of the rocket plume than previous Six-Flux and Monte Carlo solutions. The solution is currently undergoing testing for simpler situations compared to other methods.

"This document was prepared under the sponsorship of the Air Force. Neither the US Government nor any person acting on behalf of the US Government assumes any liability resulting from the use of the information contained in this document or warrants that such use will be free from privately owned rights."

I. OBJECTIVES OF THE RESEARCH

The radiative transfer modelling in the JANNAF rocket plume computer codes is known to be rather poor in certain situations when used in a diagnostic sense. The codes perform well when performance is the required result. However, when near field information concerning structure of the plume, chemistry, or particle physics is needed such as in a test environment, the input data must usually be adjusted somewhat to match the performance. These problems seemed insignificant until failure of several of the space shuttle Inertial Upper Stage (IUS) solid fuel rockets in space. Careful examination of previous tests and additional work indicated that the particles in the core of the rocket plume were radiating much more strongly than the SIRRM code predicted. This kind of problem has many implications, including loss of performance and increased base heating to the rocket nozzle and adjacent satellite components. The Payload Assist Module (PAM) would appear to have similar characteristics except with more fuel and higher particulate loading, the radiation is likely to be more pronounced. One possible cause of the higher radiation could be that solids were remaining molten beyond the exit plane of the nozzle; a Graduate Summer Fellow under my direction, David W. Young, solved this problem. Another possibility was that scattering was producing effects beyond the capabilities modeled in SIRRM; that was the basis for this proposed research on high resolution modeling of multiple scattering thermal radiation. SIRRM uses either the Two-Flux or Six-Flux radiation models for the particulates overlaid onto gaseous modeling. The beauty of the Two-Flux and the Six-Flux methods lies in computer speed and ability to model scattering. Unfortunately, the models appear to give erroneous results for highly scattering media or near edges of multidimensional regions. They are also poor for appli-

cation to media with significant spatial distribution of properties.

In some instances the Two-Flux model in SIRRM is superior to the Six-Flux model of the same problem compared to the test data. The objective of the current research is to provide both an efficient benchmark of the Flux methods and a usable alternative to available Monte Carlo schemes. The current research uses a discrete ordinates approach to allow for variable properties and anisotropic scatter in a cylindrically symmetric region. The method can be loosely tied to Multi-Flux models except that the angles represent quadrature. There is also no tie to adding and doubling schemes as in the current SIRRM formulation. These features allow a smoother representation of the scattering phase function and avoid tying the spatial grid to uniform optically thin distortion. Errors of the method should tend to be minor systematic roundoff with solutions approaching the exact results as the grid spacing approaches zero as opposed to the statistical and targeting problems associated with Monte Carlo solutions. The method shares the flexibility of Six-Flux and Monte Carlo with the added capability of adding higher quality resolution without significant modification. Such a method is very well suited for both far field linear signature work and the near field diagnostic and performance testing done at AEDC.

II. INTRODUCTION

Analysis of thermal radiation for solid fuel rocket plumes is greatly complicated by emission from hot particles and multiple scattering from fairly dense dispersions of adjacent particles into a given direction of observation. Such problems require the solution (or at least simulation) of the participating radiative transfer equation. The net effect of absorption, emission and scattering in the rocket plume is to greatly redistribute radiative energy compared to line of sight calculation used for simple gaseous radiation and for single scattering models. For the particular needs associated with rocket plume diagnostics and to gain the maximum information from the fewest tests, numerical solution of the radiative transfer equation up to the limits of infrared imaging resolution would greatly enhance interpretation of sometimes ambiguous test results. This type of solution and the coordination in its usage with AEDC form the basis of this research.

There are several variations of problem solutions similar to the proposed research which have appeared in the literature under the general heading of transport theory since the late 1950s. Most work has been done in neutron transport although more recently thermal radiation and electron transport have attracted considerable interest owing to the similarity of formulation. A brief summary is given here for those methods and problems directly related to the proposed research; a detailed literature review prior to 1977 is given by Crosbie and Linsenhardt[1] and a more recent review is given by Kisomi and Sutton[2].

The Six-Flux and the Two-Flux methods are available in the JANNAF SIRRM computer code at AEDC. These methods are based on ideas first posed by Joule[3] for a gas dynamics problem with equal collision probability in all directions. Flux type methods consist of expressing the beam direction in terms of Dirac delta functions and performing

solid angle integration to yield specific direction fluxes. The Six-Flux method was applied to early anisotropic scattering problems by Churchill, et al[4,5]. More recent results by Meador and Weaver[6] indicate that the Six-Flux method artificially distributes too much radiation into transverse scattering(side scatter). This would account for the observation of SRRM users that the Two-Flux model often yields better results than Six-Flux. It is also possible that certain curvature effects are missing from the current Six-Flux model[7] due to conformal fitting of a rectangular radiation model to a nearly cylindrical plume geometry. The effects of curvature on radiation are discussed by Pomraning and Stevens[8] for a toroidal neutron transport problem.

The Monte Carlo approach to solving radiative transfer has been used on several related problems. Perlmutter and Howell[9] were among the first to use this method in cylindrical participating radiation problems although not related to plume work. Stockham and Love[10] analyzed the search-light problem for an anisotropically scattering cylindrical plume with emphasis on nozzle base heating. This statistically based ray tracing approach is closely tied to the quality of physics modeled by beam interactions and the resolution of the capture grid, however the method is widely applied to complex problems. The limitations of the method pose little difficulty when used for hemispherically integrated quantities, such as heat flux; however recent work on directional emittance of a slab by Lin, Sutton, and Love[11] indicates that radiance may be significantly in error for Monte Carlo schemes.

The Discrete Ordinates method, first developed by Carlson[12], uses a finite difference representation for the directional derivative of the monochromatic radiance with iteration for the in-scattering integral. Like Six-Flux and Monte Carlo, this solution approach is very flexible. Early multidimensional solutions were quite limited due to computer space limitations; three dimensional anisotropically scattering radiation problems, although

computationally fast, can easily require 10 to 20 megabytes of computer memory. The advent of inexpensive computer memory and accessibility to supercomputers has made solution of such large scale problems more straightforward. Recent works by Five-land[13] for a constant property cylinder and by Kamath[14] for a three dimensional multilayered rectangular medium illustrate the flexibility of the method. Sutton[15] recently formulated the anisotropically scattering, variable property, cylindrical cone medium problem for a solid fuel rocket plume using a discrete ordinates approach as a portion of Air Force Summer Fellow research at AEDC. Testing of that computer code for the problem continues at this time.

III. FORMULATION OF THE PROBLEM

The current formulation of a solution to the Radiative Transfer Equation using a discrete ordinates or S_N method follows roughly that given by Fiveland [13] for a cylindrically symmetric medium with uniform properties and linearly anisotropic scatter. The discrete ordinate method is generally described as a finite difference method spatially with discrete angular directions represented by quadrature points for later angular integration. The right hand side of the Radiative Transfer Equation, which is referred to here as the Source Function, is iterated through the solution until converged.

There are several significant deviations here from Fiveland's work. In his paper the grid resolution is fairly coarse (6x10, radial to axial). The angular definition used a symmetric area weighted quadrature for S_n , where the number of angles is stated as $N(N+2)$. The author's previous work in slab geometry indicates that at least 17 spatial nodes are required to produce benchmark accuracy up to an optical thickness of 5. For three dimensional work [14], 9 nodes in each direction will give benchmark accuracy for optical thicknesses less than 2. Computer core space usually limits one to no greater resolution in three dimensional problems. Although Fiveland states that $N = 4$ (24 angle directions) gives sufficient accuracy, no angular quantities were stated.

The Radiative Transfer Equation in a cylindrically symmetric medium is expressed in terms of spectral radiative intensity, I , (or radiance per standard military usage) as

$$\frac{\sin \theta \cos \phi}{r} \frac{\partial (r I)}{\partial r} + \cos \theta \frac{\partial I}{\partial z} - \frac{1}{r} \frac{\partial (\sin \theta \sin \phi I)}{\partial \phi} + \beta I = S \quad (1)$$

where the source function is defined as

$$S = (\beta - \sigma) B + \frac{\sigma}{4 \pi} \int_{\phi=0}^{\pi} \int_{\theta=0}^{\pi} \hat{P}(\theta, \phi, \theta', \phi') I \sin \theta' d\theta' d\phi'$$

The symmetric scattering phase distribution function is given by

$$\hat{P}(\theta, \phi, \theta', \phi') = P(\theta, \phi, \theta', \phi') + P(\theta, -\phi, \theta', \phi')$$

where

$$P(\theta, \phi, \theta', \phi') = \sum_{n=0}^N A_n P_n(\cos \theta_0)$$

and

$$\cos \theta_0 = \sin \theta \sin \theta' \cos(\phi - \phi') + \cos \theta \cos \theta'$$

The intensity is next split into 4 quadrants based on symmetry

(i.e., unique direction cosines),

$$\begin{aligned} I(r, z, \phi, \theta) &= A^1(r, z, \phi, \theta); \quad 0 \leq \phi \leq \frac{\pi}{2}, \quad 0 \leq \theta \leq \frac{\pi}{2} \\ &= A^2(r, z, \phi, \pi - \theta); \quad 0 \leq \phi \leq \frac{\pi}{2}, \quad \frac{\pi}{2} \leq \theta \leq \pi \\ &= A^3(r, z, \pi - \phi, \pi - \theta); \quad \frac{\pi}{2} \leq \phi \leq \pi, \quad \frac{\pi}{2} \leq \theta \leq \pi \\ &= A^4(r, z, \pi - \phi, \theta); \quad \frac{\pi}{2} \leq \phi \leq \pi, \quad 0 \leq \theta \leq \frac{\pi}{2} \end{aligned}$$

The geometry of the model is sketched in Figure 1. The plume may take on any finite non-singular cylindrically symmetric shape within the radiation boundaries and the model will remain well posed. Clearly the choice of a finite cylindrical geometry will greatly aid the rocket base heating analysis because the model extends radially beyond the nozzle. However, care needs to be taken at the upper finite boundary since optical thickness and length of the plume will force the problem to be nearly semi-infinite.

The Radiative Transfer Equation is now recast for the split intensities transformed to the

angular range $0 \leq \theta \leq \frac{\pi}{2}, 0 \leq \phi \leq \frac{\pi}{2}$

$$\frac{\sin \theta \cos \phi}{r} \frac{\partial (r A^1)}{\partial r} + \cos \theta \frac{\partial A^1}{\partial z} - \frac{1}{r} \frac{\partial (\sin \theta \sin \phi A^1)}{\partial \phi} + \beta A^1 = S^1$$

$$\frac{\sin \theta \cos \phi}{r} \frac{\partial (r A^2)}{\partial r} - \cos \theta \frac{\partial A^2}{\partial z} - \frac{1}{r} \frac{\partial (\sin \theta \sin \phi A^2)}{\partial \phi} + \beta A^2 = S^2$$

$$-\frac{\sin \theta \cos \phi}{r} \frac{\partial(r A^3)}{\partial r} - \cos \theta \frac{\partial A^3}{\partial z} - \frac{1}{r} \frac{\partial(\sin \theta \sin \phi A^3)}{\partial \phi} + \beta A^3 = S^3$$

$$-\frac{\sin \theta \cos \phi}{r} \frac{\partial(r A^4)}{\partial r} + \cos \theta \frac{\partial A^4}{\partial z} - \frac{1}{r} \frac{\partial(\sin \theta \sin \phi A^4)}{\partial \phi} + \beta A^4 = S^4$$

The Source Function is also recast in terms of these intensities as

$$S = (\beta - \sigma) B + \frac{\sigma}{4\pi} \int_{\phi'=0}^{\pi} \int_{\theta'=0}^{\pi} \left[\hat{P}(\theta, \phi, \theta', \phi') A^1(r, z, \phi', \theta') + \hat{P}(\theta, \phi, \pi - \theta', \phi') A^2(r, z, \phi', \theta') + \hat{P}(\theta, \phi, \pi - \theta', \pi - \phi') A^3(r, z, \phi', \theta') + \hat{P}(\theta, \phi, \theta', \pi - \phi') A^4(r, z, \phi', \theta') \right] \sin \theta' d\theta' d\phi'$$

where successively,

$$S^1(r, z, \phi, \theta) = S(r, z, \phi, \theta)$$

$$S^2(r, z, \phi, \theta) = S(r, z, \phi, \pi - \theta)$$

$$S^3(r, z, \phi, \theta) = S(r, z, \pi - \phi, \pi - \theta)$$

$$S^4(r, z, \phi, \theta) = S(r, z, \pi - \phi, \theta)$$

The finite difference solution of these equations starts with known boundaries (or symmetry) and marches away from them assuming the source function is known. The boundaries at the nozzle exit plane and down stream, respectively, of the model are given by

$$A^1(r, 0, \phi, \theta) = I_0(r, \phi, \theta) ; 0 \leq r \leq r_a$$

$$A^4(r, 0, \phi, \theta) = I_0(r, \pi - \phi, \theta) ; 0 \leq r \leq r_a$$

$$A^2(r, z_0, \phi, \theta) = 0 ; r \leq r_0$$

$$A^3(r, z_0, \phi, \theta) = 0 ; r \leq r_0$$

Here, $I_0(r, \phi, \theta)$ represents a specified (or calculated) nozzle exit radiance at the lower boundary. The upper boundary is taken as having negligible re-entrant radiance at this stage of the model development; this can be easily modified to reflect a semi-infinite condition. Radial boundary conditions represent symmetry and a free boundary for the plume axis and radial edge respectively as,

$$A^1(0, z, \phi, \theta) = A^4(0, z, \phi, \theta) ; 0 \leq z \leq z_0$$

$$A^2(0, z, \phi, \theta) = A^3(0, z, \phi, \theta) ; 0 \leq z \leq z_0$$

$$A^4(r_0, z, \phi, \theta) = 0 ; 0 \leq z \leq z_0$$

$$A^3(r_0, z, \phi, \theta) = 0 ; 0 \leq z \leq z_0$$

No boundary condition exists for the ϕ -derivative. The implied symmetry of the special angle $\phi = 0$, yields a radiative transfer equation free of the ϕ -derivative. This solution then starts by differencing from $\phi = 0$ to $\phi = \frac{\pi}{2}$ in the transformed angular range.

Representing each term in the split intensities as

$$[\text{I}] = \sin \theta \cos \frac{\phi}{r} \frac{\partial(r A^\alpha)}{\partial r}$$

$$[\text{II}] = \cos \theta \frac{\partial(A^\alpha)}{\partial z}$$

$$[\text{III}] = -\frac{1}{r} \frac{\partial(\sin \theta \sin \phi A^\alpha)}{\partial \phi}$$

the terms are operated on with

$$\int_{\Delta V} dV \int_{\Delta \phi} d\phi = \int_{\Delta z} 2\pi r dr dz \int_{\Delta \phi} d\phi$$

The subscripts represent either forward or backward differencing in a given direction. For example,

$$[\text{I}]_{br} = \int_{r_{i-1}}^{r_i} 2\pi r \int_{\Delta z} \int_{\Delta \phi} [\text{I}] d\phi dz dr$$

$$[\text{I}]_{fr} = \int_{r_{i+1}}^{r_i} 2\pi r \int_{\Delta z} \int_{\Delta \phi} [\text{I}] d\phi dz dr$$

are used respectively for inward and outward directions based on known starting conditions. In summary the resultant terms based on integration where possible and the mean value theorem otherwise [2] are

$$[\text{I}]_{br} = 2\pi \sin \theta_l \overline{\cos \phi_k} \Delta \phi_k \Delta z \left[r_i A_i^\alpha - r_{i-1} A_{i-1}^\alpha \right]_{j,k,l}$$

$$\left[\text{I} \right]_{fr} = 2\pi \sin\theta_l \overline{\cos\phi_k} \Delta\phi_k \Delta z \left[r_{i+1} A_{i+1}^\alpha - r_i A_i^\alpha \right]_{j,k,l}$$

$$\left[\text{II} \right]_{bz} = 2\pi \cos\theta_l \Delta\phi_k \bar{r}_i \Delta r \left[A_j^\alpha - A_{j-1}^\alpha \right]_{i,k,l}$$

$$\left[\text{II} \right]_{fz} = 2\pi \cos\theta_l \Delta\phi_k \bar{r}_i \Delta r \left[A_{j+1}^\alpha - A_j^\alpha \right]_{i,k,l}$$

$$\left[\text{III} \right]_{b\phi} = 2\pi \Delta r \Delta z \left[\sin\phi_k A_k^\alpha - \sin\phi_{k-1} A_{k-1}^\alpha \right]_{i,j,l} \sin\theta_l$$

Applied to each equation, the difference forms yield the following symbolic set

$$\left[\text{I} \right]_{br} + \left[\text{II} \right]_{bz} + \left[\text{III} \right]_{b\phi} + \overline{\beta}_{i,j}^{-1} V_{i,j} \overline{A}_{i,j,k,l}^{-1} \Delta\phi_k = \overline{S}_{i,j,k,l}^{-1} V_{i,j} \Delta\phi_k$$

$$\left[\text{I} \right]_{br} - \left[\text{II} \right]_{fz} + \left[\text{III} \right]_{b\phi} + \overline{\beta}_{i,j}^{-2} V_{i,j} \overline{A}_{i,j,k,l}^{-2} \Delta\phi_k = \overline{S}_{i,j,k,l}^{-2} V_{i,j} \Delta\phi_k$$

$$- \left[\text{I} \right]_{fr} - \left[\text{II} \right]_{fz} + \left[\text{III} \right]_{b\phi} + \overline{\beta}_{i,j}^{-3} V_{i,j} \overline{A}_{i,j,k,l}^{-3} \Delta\phi_k = \overline{S}_{i,j,k,l}^{-3} V_{i,j} \Delta\phi_k$$

$$- \left[\text{I} \right]_{fr} - \left[\text{II} \right]_{bz} + \left[\text{III} \right]_{b\phi} + \overline{\beta}_{i,j}^{-4} V_{i,j} \overline{A}_{i,j,k,l}^{-4} \Delta\phi_k = \overline{S}_{i,j,k,l}^{-4} V_{i,j} \Delta\phi_k$$

The barred quantities represent finite difference cell-averaged terms.

The numerical procedure, in order, is to start with $A^4(r, z, \phi, \theta)$ at the base edge of the plume and simultaneously difference inward, upward and away from $\phi = 0$. Then $A^3(r, z, \phi, \theta)$ is differenced from the top edge inward downward and away from $\phi = 0$. Symmetry then specifies A^1 and A^2 at $r = 0$. The differencing now proceeds in an outward direction for these two intensities. Next, the source function is calculated. Finally, iterative convergence of the source function is obtained.

IV. RESULTS AND CONCLUSIONS

A code was developed called CYLRAD (listed in the appendix) based on the analysis in this report. The code is fully functional for a portion of the desired parameters. For instance, the code gives reasonable accuracy for radiance (intensity) through intermediate optical thicknesses and most scattering values. Results are shown in Figure 2 for the case for a uniformly emitting and isotropically scattering plume with radius of 0.5 and length of 2.0 in consistent units. The extinction coefficient is 1.0 and the scattering coefficient is 0.5 uniformly over the geometry. capabilities. The results are consistent with both one dimensional slab and cylinder geometries when the other dimension is stretched by an order of magnitude. The heat flux quantities tend to not be symmetric for symmetrically "loaded" problems. This was believed to be a function of curvature effects, the finite difference scheme, and spatial resolution used for the detail required. Variable properties were not tested here, but the scheme used has been successful in three dimensional rectangular coordinates[14]. To find out why flux agreed poorly with the problem physics, several approaches were tried. Of particular concern was the possibility of "flux streaming" noted in reference [16]; the lack of symmetry in quadrature used in the solid angle integrations apparently affects the angular partial differential term in the directional derivative. Thus, the integrations which are tied closely to the forward or backward differencing scheme give forward or backward looking integrations. An area weighted quadrature scheme utilizing complete rotational symmetry was tested in conjunction with several ideas that follow.

A one dimensional version (Q123) of the three dimensional code was developed to evaluate curvature effects and quadrature. The analysis used for Q123 may be found

in reference[17] for a single treatment of slab (1), cylinder (2) or sphere (3) cases. This code shows excellent agreement with published results[2] for exit flux of a uniformly emitting and isotropically scattering infinite cylinder as shown in Table 1. An interesting feature of Q123 is the use of diamond differencing interpolation (extrapolation) of intermediate cell points used in the finite difference representation of the radiative transfer equation. Figure 3 shows, however that the intermediate flux distribution results under or over predict radial heat flux. Since this behavior might be attributed to either curvature or differencing, a two dimensional non-curvature model analogous to that already in SIRRM was developed. This particular code gave excellent results for all isotropically scattering cases (anisotropic not modelled). This demonstrated the method but did not give a clear answer on curvature/quadrature. As a side-line to this, the method of adding and doubling (such as used in SIRRM) should be applied with extreme caution, since numerical results for transmission and reflection are also multidimensional and nonseparable (at least to this point). As an alternative approach for curvature and quadrature, a commercially available two dimensional multigroup discrete ordinates transport code was obtained and tested on the IBM 3081. The code, TWOTRAN II [18], used the uniformly weighted quadrature of [16] but was unwieldy to use for radiative heat transfer (conversion of to non-multigroup, and translation of terminology). However the code does work for cases attempted, and has the advantages of extensive long term benchmarking and maintenance. Modification of the code to eliminate some of the "features" was not possible due to the way subroutines were overlaid in the FORTRAN source; subcode to pre-process or post-process, as needed, would have been a good approach, however the methods were so similar to the one dimensional version created here that a simpler two dimensional model following their

analysis was attempted. That model used a combination of the analysis of Lee[16], Fiveland[13], and Lathrop[18] instead of the methods presented here. Despite several months of extensive effort, that model SNFIVE, could never converge to more than 2 decimal accuracy and required extensive intervention for underflow/ overflow control. The integration over solid angle was very efficient and angular differencing was split as an independent variable from the quadrature. The numerical diamond differencing appears to be the main convergence problem in the method. Attempts were made to incorporate a synthesis of SNFIVE with the method here of differencing over actual nodes (instead of half nodes) for the intensity at the half node (which is never explicitly evaluated). These attempts, though promising, were inconsistent with the contractual schedule here.

An alternative route to check curvature effects was to obtain a portion of the original work of Stockham[10]. The Monte Carlo scheme used for that plume model was slightly modified to FORTRAN 77 and the most recent random number methods. The results tended to lag about 5% below those published despite using a greater number of emission histories. This was also true for comparison simple one dimensional versions of the cases considered. The best guess on the difference in results is that modern random number generators are not concerned with yielding the same output for a given input (which is how the generator used behaved). Thus the results do not represent a totally random sample, but one that runs random within ranges (clusters) and is prone to repeat. Another alternative by Edwards[19] is to use a good approximation such as the diffusion approximation as input to the formal solution along an arbitrary beam path. This method has been applied to early plume problems, but has not received significant attention. It would be a simple matter to use a two flux model or discrete

ordinates (without scatter, it reduces to a better than diffusion non-iterative case) to reiterate a single directional derivative along a path required for measurement.

In conclusion, several codes were developed to solve the radiative transfer equation in cylindrical geometry. Further work in benchmarking the main code presented here needs to be done, before accuracy in a predictive mode can be expected. Alternative methods of attacking the problem were addressed. Most promising for direct application is the semi-iterative Edwards[19] model. A commercially available working code, TWOTRAN II, was found for the problem although it is tailored toward neutron transport. The problem with the six flux in SIRRM appears more likely to be either curvature or non-conservation of radiative flux by layers, than a problem in side scatter.

V. REFERENCES

1. Crosbie, A.L. and Linsenbardt, T.L., *Two-Dimensional Isotropic Scattering in a Semi-Infinite Medium*, *J. Quant. Spectrosc. Rad. Transfer*, Vol.9, P.157, 1978.
2. Kisomi, A.N. and Sutton, W.H., *Source Expansion Solutions for Radiative Transfer in Plane Parallel, Spherical and Cylindrical Geometries*, *AIAA 20th Thermophysics Conference*, AIAA-85-0946, June, 1985.
3. Chandrasekhar, S., *Radiative Transfer*, Dover Publications, New York, 1960.
4. Chu, C.M. and Churchill, S.W., *Numerical Solution of Problems in Multiple Scattering of Electromagnetic Radiation*, *J. Phys. Chem.*, Vol.59, P.855, 1955.
5. Chin, J.H. and Churchill, S.W., *Anisotropic, Multiply Scattered Radiation from an Arbitrary, Cylindrical Source in an Infinite Slab*, *ASME J. Heat Transfer*, Vol.87, P.167, 1965.
6. Meador, W.E. and Weaver, W.R., *Six-Beam Models in Radiative Transfer Theory*, *Applied Optics*, Vol.15, P.3155, 1976.
7. Reed, R.A., *Modified Six-Flux Approximation for Multiple Scattering Radiative Transfer*, *Grumman Research Memorandum*, RM-713, 1981.
8. Pomraning, G.C. and Stevens, C.A., *Transport and Diffusion Equations in Toroidal Geometry*, *Nucl. Sci. Eng.*, Vol.55, P.359, 1974.
9. Perlmutter, M. and Howell, J.R., *Radiant Transfer Through a Gray Gas Between Concentric Cylinders Using Monte Carlo*, *ASME J. Heat Transfer*, Vol.86, P.169, 1964.
10. Stockham, L.W. and Love, T.J., *Radiative Heat Transfer from a Cylindrical Cloud of Particles*, *AIAA J.*, Vol.6, P.1935, 1968.
11. Lin, J.D., Sutton, W.H., and Love, T.J., *Solution of Directional Emissivity from Isothermal Dispersions by Source Function Expansion Technique*, *AIAA 23rd Aerospace Sciences Conference*, AIAA-85-0405, 1985.
12. Carlson, B.G., *The Numerical Theory of Neutron Transport in Methods in Computational Physics*, Vol.I, Alder, Fernbach, and Rotenberg Eds., Academic Press, New York, 1963.
13. Fiveland, W.A., *A Discrete Ordinates Method for Predicting Radiative Heat Transfer in Axisymmetric Enclosures*, *ASME Technical Paper*, ASME 82-HT-20, 1982.

14. Kamath, R., *M.S. Thesis, University of Oklahoma, A Numerical Study of Multilayer Radiative Heat Transfer in a Three-Dimensional Participating Media*, 1985.
15. Sutton, W.H., *Final Report, USAF-UES Summer Faculty Research Program, Particle Scattering in Plumes*, July, 1985.
16. Lee, C.L., *Los Alamos Scientific Laboratory, LA-2595, TID-4500(17th Ed.), The Discrete Sn Approximation to Transport Theory*, 1962.
17. Schaeffer, N.M., *U.S. Atomic Energy Commission, TID-25951, Reactor Shielding for Nuclear Engineers*, 1973.
18. Lathrop, K.D. and Brinkley, F.W., *Los Alamos Scientific Laboratory, LA-4848-MS, TWOTRAN II: An Interfaced, Exportable Version of the TWOTRAN Code for Two-Dimensional Transport*, 1973.
19. Edwards, R.H. and Bobco, R.P., *Hughes Aerospace Technology Laboratory, Report 3, Radiant Heat Transfer from Isothermal Dispersions with Isotropic Scattering*, 1965.

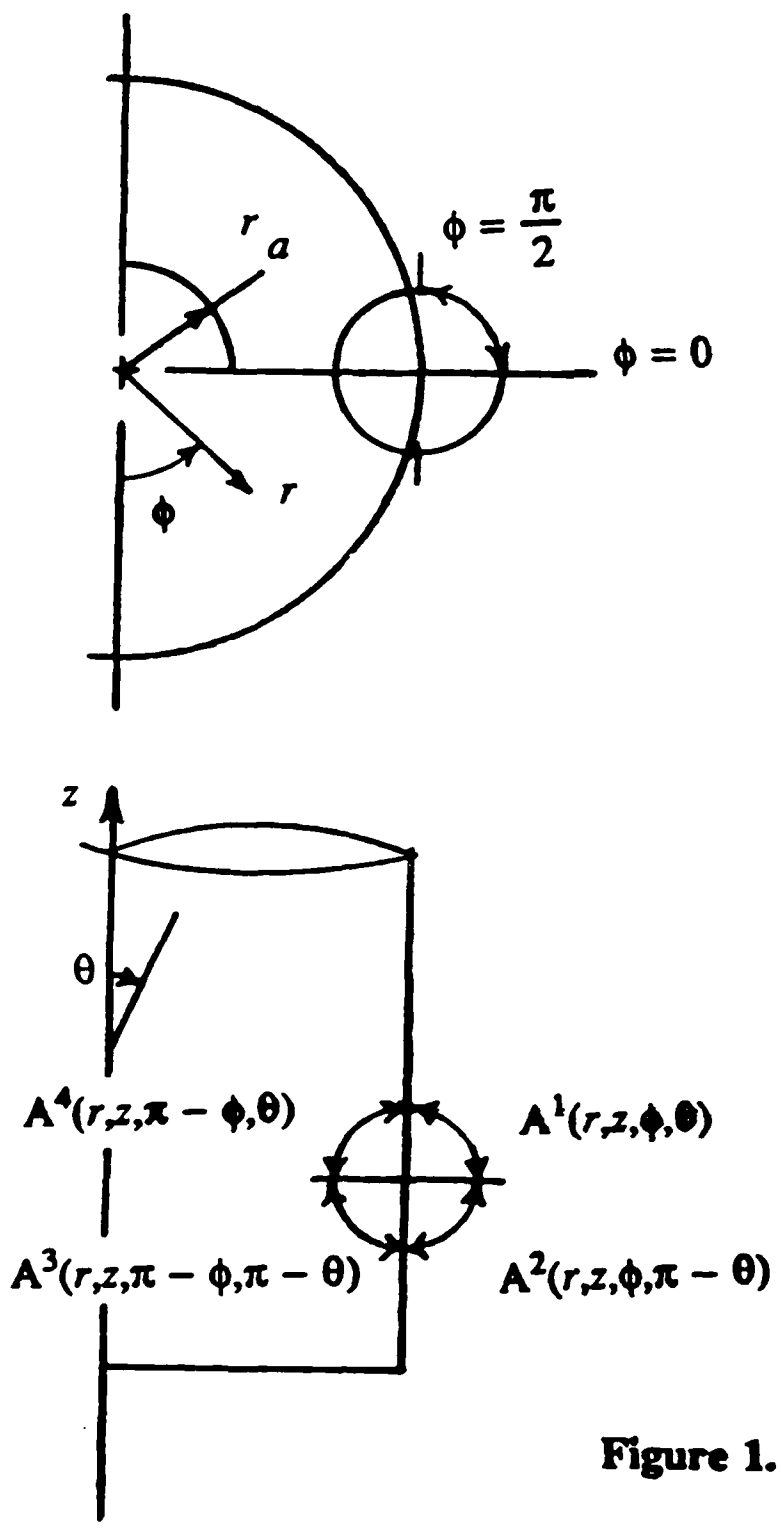


Figure 1. Model Geometry

COMPARISON OF Q123 WITH S-1 & EXACT RESULTS IN
 DETERMINING THE EXIT HEAT FLUX OF A CYLINDER

ALBEDO	METHOD	2Ro = 1.0 *	2Ro = 2.0 *
0.2	Q123	1.98503	2.48427
	S-1	2.33882	2.78165
	EXACT	2.34237	2.7847
0.5	Q123	1.41427	1.93495
	S-1	1.79462	2.25321
	EXACT	1.85353	2.32477
0.9	Q123	0.34912	0.58132
	S-1	0.52127	0.76571
	EXACT	0.55292	0.90477

* EXACT RESULTS FROM HEASLET & WARMING

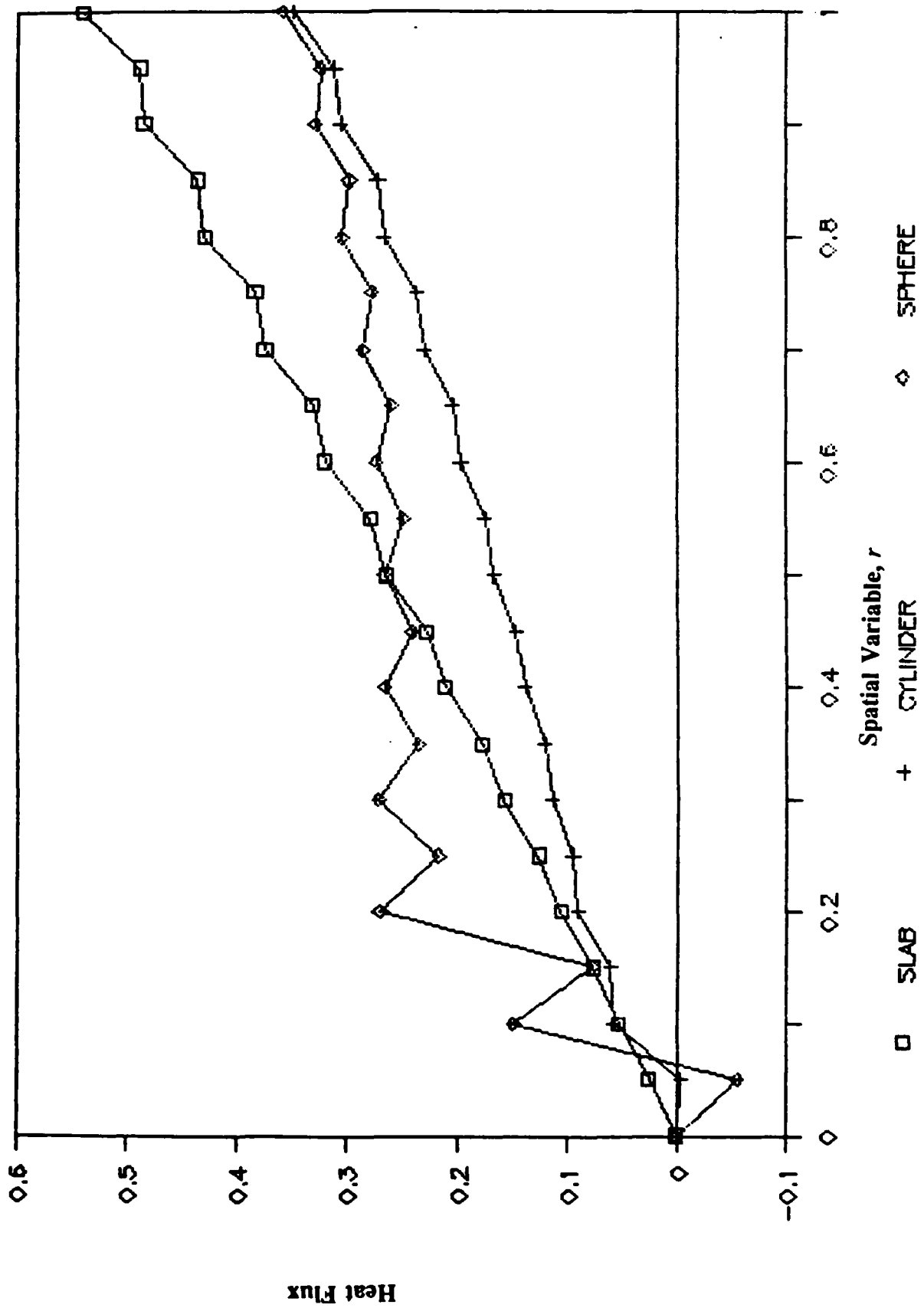


Figure 2 Discrete Ordinates; Slab, Cylinder, Sphere

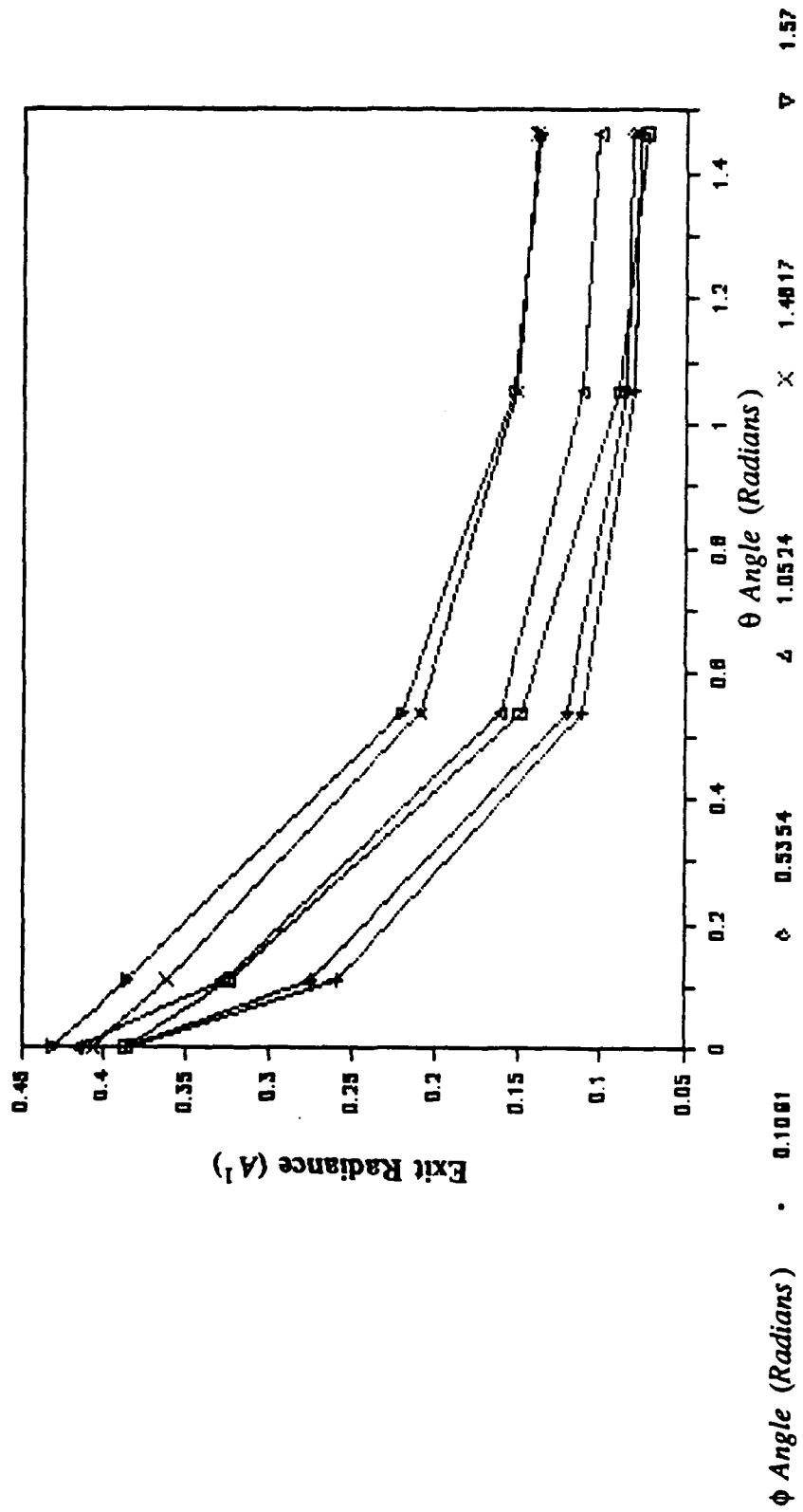


Figure 3 Cylindrical Exit Intensity (Radiance)

Program Listing

```

COMMON/ANIS/AN(10), NUM
DIMENSION A1(9,9,5,5), A2(9,9,5,5), A3(9,9,5,5)
S, A4(9,9,5,5), S1(9,9,5,5), S2(9,9,5,5), S3(9,9,5,5)
$, S4(9,9,5,5), SS1(9,9,5,5), QR(9,9), QZ(9,9), BT(9,9)
$, SC(9,9), B(9,9), Z(25), R(17), U1(11), W1(11), X(10), V(10)
READ(5,1) IL, JL
1 FORMAT(2I3)
IM1=IL-1
JM1=JL-1
KL=5
LL=KL
PI=3.14159265359
PIH=PI/2.
X(1)=-0.861136311594053D0
X(2)=-0.339981043584856D0
V(1)=0.347854845137454D0
V(2)=0.652145154862546D0
X(3)=-X(2)
X(4)=-X(1)
V(3)=V(2)
V(4)=V(1)
U1(1)=0.0
DO 3 L=2, LL
U1(L)=PIH*X(L-1)/2.0+PIH/2.0
3 W1(L)=PIH*V(L-1)/2.0
READ(5,5) R0, Z0
5 FORMAT(2F10.0)
READ(5,6) BETA, SIGMA, BLK, 3NZ
6 FORMAT(4F10.0)
READ(5,90) NUM
90 FORMAT(1I3)
READ(5,91) (AN(N), N=1, NUM)
91 FORMAT(1F10.0)
DO 7 I=1, IL
DO 8 J=1, JL
B(I, J)=BLK
BT(I, J)=BETA
8 SC(I, J)=SIGMA
7 CONTINUE
DR=R0/IM1
DZ=Z0/JM1
R(1)=0.0
Z(1)=0.0
DO 9 I=2, IL
9 R(I)=R(I-1)+DR
DO 10 J=2, JL
10 Z(J)=Z(J-1)+DZ

```

```

C
C      INITIAL CONDITIONS
C
C      READ(5,11) IN

```

```

11 FORMAT(1I3)
IN=IL
INP1=IN+1
DO 12 I=1, IL
DO 13 J=1, JL
DO 14 K=1, KL
DO 15 L=1, LL
A1(I, J, K, L)=0.0
A2(I, J, K, L)=0.0
A3(I, J, K, L)=0.0
A4(I, J, K, L)=0.0
S1(I, J, K, L)=(BT(I, J)-SC(I, J))*B(I, J)
S2(I, J, K, L)=(BT(I, J)-SC(I, J))*B(I, J)
S3(I, J, K, L)=(BT(I, J)-SC(I, J))*B(I, J)
S4(I, J, K, L)=(BT(I, J)-SC(I, J))*B(I, J)

```

```

15 CONTINUE
14 CONTINUE
13 CONTINUE
12 CONTINUE
    DO 16 K=1, KL
    DO 17 J=1, JL
    DO 18 I=1, IN
    A1(I, 1, K, L) = BNZ
    A4(I, 1, K, L) = BNZ
18 CONTINUE
17 CONTINUE
16 CONTINUE
    ICOUNT=1
100 CONTINUE
    WRITE(6, 504) ICOUNT
504 FORMAT(' ', 4X, '*** ITERATIONS =', I3)
    IF(ICOUNT.GE.31) STOP
    ICOUNT=ICOUNT+1
    DO 20 I=1, IL
    DO 21 J=1, JL
    DO 22 K=1, KL
    DO 23 L=1, LL
    SS1(I, J, K, L) = S1(I, J, K, L)
23 CONTINUE
22 CONTINUE
21 CONTINUE
20 CONTINUE

```

```

C
C     STARTING WITH PHI=0, PI ... AGAIN SPECIAL ANGLES ...
C     THE DIFFERENCING LOOP FOR CALCULATION BEGINS
C

```

```

    DO 30 L=1, LL
    DO 31 I=IM1, 1, -1
    DO 32 J=2, JL
    SA4=(S4(I, J, 1, L)+S4(I+1, J, 1, L)+S4(I, J-1, 1, L)+S4(I+1, J-1, 1, L))
    &/4.0
    RA4=(R(I+1)+R(I))/2.0
    DS1=SIN(U1(L))/DR
    DS2=COS(U1(L))/DZ*RA4
    BA4=(BT(I, J)+BT(I+1, J)+BT(I, J-1)+BT(I+1, J-1))/4.0
    DS4=RA4*BA4/4.0
    A4(I, J, 1, L) = (RA4*SA4 + (DS2-DS4)*A4(I, J-1, 1, L)
    &+ (DS1*R(I+1)-DS4)*A4(I+1, J, 1, L) - DS4*A4(I+1, J-1, 1, L))
    &/ (R(I)*DS1+DS2+DS4)
32 CONTINUE
    DO 33 J=JM1, 1, -1
    SA3=(S3(I, J, 1, L)+S3(I+1, J, 1, L)+S3(I, J+1, 1, L)+S3(I+1, J+1, 1, L))
    &/4.0
    RA3=(R(I+1)+R(I))/2.0
    CS1=SIN(U1(L))/DR
    CS2=COS(U1(L))/DZ*RA3
    BA3=(BT(I, J)+BT(I+1, J)+BT(I, J+1)+BT(I+1, J+1))/4.0
    CS4=RA3*BA3/4.0
    A3(I, J, 1, L) = (RA3*SA3 + (CS2-CS4)*A3(I, J+1, 1, L)
    &+ (CS1*R(I+1)-CS4)*A3(I+1, J, 1, L) - CS4*A3(I+1, J+1, 1, L))
    &/ (R(I)*CS1+CS2+CS4)
33 CONTINUE
31 CONTINUE
    DO 37 J=2, JM1
    A1(1, J, 1, L) = A4(1, J, 1, L)
    A2(1, J, 1, L) = A3(1, J, 1, L)
37 CONTINUE
    DO 34 I=2, IL
    DO 35 J=2, JL
    SA1=(S1(I, J, 1, L)+S1(I-1, J, 1, L)+S1(I, J-1, 1, L)+S1(I-1, J-1, 1, L))
    &/4.0

```

```

RA1=(R(I-1)+R(I))/2.0
AS1=SIN(U1(L))/DR
AS2=COS(U1(L))/DZ*RA1
BA1=(BT(I,J)+BT(I-1,J)+BT(I,J-1)+BT(I-1,J-1))/4.0
AS4=RA1*BA1/4.0
A1(I,J,1,L)=(RA1*SA1+(AS2-AS4)*A1(I,J-1,1,L)
&+(AS1*R(I-1)-AS4)*A1(I-1,J,1,L)-AS4*A1(I-1,J-1,1,L))
&/ (R(I)*AS1+AS2+AS4)
35 CONTINUE
DO 36 J=JM1,1,-1
SA2=(S2(I,J,1,L)+S2(I-1,J,1,L)+S2(I,J+1,1,L)+S2(I-1,J+1,1,L))
&/4.0
RA2=(R(I-1)+R(I))/2.0
BS1=SIN(U1(L))/DR
BS2=COS(U1(L))/DZ*RA2
BA2=(BT(I,J)+BT(I-1,J)+BT(I,J+1)+BT(I-1,J+1))/4.0
BS4=RA2*BA2/4.0
A2(I,J,1,L)=(RA2*SA2+(BS2-BS4)*A2(I,J+1,1,L)
&+(BS1*R(I-1)-BS4)*A2(I-1,J,1,L)-BSA*A2(I-1,J+1,1,L))
&/ (R(I)*BS1+BS2+BS4)
36 CONTINUE
34 CONTINUE
30 CONTINUE

```

C
C
C
C
C

```

*****
MAIN DIFFERENCING SCHEME
*****

```

```

DO 500 L=1,LL
DO 501 K=2,KL
DO 40 I=IM1,1,-1
DO 41 J=2,JL
SAV4=(S4(I,J,K,L)+S4(I+1,J,K,L)+S4(I,J-1,K,L)+S4(I,J,K-1,L)
&+S4(I+1,J-1,K,L)+S4(I+1,J,K-1,L)+S4(I,J-1,K-1,L)
&+S4(I+1,J-1,K-1,L))/8.0
BAV4=(BT(I,J)+BT(I+1,J)+BT(I,J-1)+BT(I+1,J-1))/4.0
RAV4=(R(I+1)+R(I))/2.0
COSA4=(COS(U1(K))+COS(U1(K-1)))/2.0
A4OUT=A4(I+1,J-1,K,L)+A4(I+1,J,K-1,L)
&+A4(I,J-1,K-1,L)+A4(I+1,J-1,K-1,L)
D11=SIN(U1(L))*COSA4/DR
D12=RAV4*COS(U1(L))/DZ
D13=SIN(U1(L))/(U1(K)-U1(K-1))
D14=RAV4*BAV4/8.0
A4(I,J,K,L)=(RAV4*SAV4+(R(I+1)*D11-D14)*A4(I+1,J,K,L)
&+(D12-D14)*A4(I,J-1,K,L)+(D13*SIN(U1(K-1))-D14)*A4(I,J,K-1,L)
&-D14*A4OUT)/(R(I)*D11+D12+D13*SIN(U1(K))+D14)
41 CONTINUE
DO 42 J=JM1,1,-1
SAV3=(S3(I,J,K,L)+S3(I+1,J,K,L)+S3(I,J+1,K,L)+S3(I,J,K-1,L)
&+S3(I+1,J+1,K,L)+S3(I+1,J,K-1,L)+S3(I,J+1,K-1,L)
&+S3(I+1,J+1,K-1,L))/8.0
BAV3=(BT(I,J)+BT(I+1,J)+BT(I,J+1)+BT(I+1,J+1))/4.0
RAV3=(R(I+1)+R(I))/2.0
COSA3=(COS(U1(K))+COS(U1(K-1)))/2.0
A3OUT=A3(I+1,J+1,K,L)+A3(I+1,J,K-1,L)
&+A3(I,J+1,K-1,L)+A3(I+1,J+1,K-1,L)
C11=SIN(U1(L))*COSA3/DR
C12=RAV3*COS(U1(L))/DZ
C13=SIN(U1(L))/(U1(K)-U1(K-1))
C14=RAV3*BAV3/8.0
A3(I,J,K,L)=(RAV3*SAV3+(R(I+1)*C11-C14)*A3(I+1,J,K,L)
&+(C12-C14)*A3(I,J+1,K,L)+(C13*SIN(U1(K-1))-C14)*A3(I,J,K-1,L)
&-C14*A3OUT)/(R(I)*C11+C12+C13*SIN(U1(K))+C14)
42 CONTINUE
40 CONTINUE

```

```

DO 850 J=2, JM1
A1(1, J, K, L)=A4(1, J, K, L)
A2(1, J, K, L)=A3(1, J, K, L)
850 CONTINUE
DO 50 I=2, IL
DO 51 J=2, JL
SAV1=(S1(I, J, K, L)+S1(I-1, J, K, L)+S1(I, J-1, K, L)+S1(I, J, K-1, L)
&+S1(I-1, J-1, K, L)+S1(I-1, J, K-1, L)+S1(I, J-1, K-1, L)
&+S1(I-1, J-1, K-1, L))/8.0
BAV1=(BT(I, J)+BT(I-1, J)+BT(I, J-1)+BT(I-1, J-1))/4.0
RAV1=(R(I-1)+R(I))/2.0
COSA1=(COS(U1(K))+COS(U1(K-1)))/2.0
A1OUT=A1(I-1, J-1, K, L)+A1(I-1, J, K-1, L)
&+A1(I, J-1, K-1, L)+A1(I-1, J-1, K-1, L)
A11=SIN(U1(L))*COSA1/DR
A12=RAV1*COS(U1(L))/DZ
A13=SIN(U1(L))/(U1(K)-U1(K-1))
A14=RAV1*BAV1/8.0
A1(I, J, K, L)=(RAV1*SAV1+(R(I-1)*A11-A14)*A1(I-1, J, K, L)
&+(A12-A14)*A1(I, J-1, K, L)+(A13*SIN(U1(K-1))-A14)*A1(I, J, K-1, L)
&-A14*A1OUT)/(R(I)*A11+A12+A13*SIN(U1(K))+A14)
51 CONTINUE
DO 52 J=JM1, 1, -1
SAV2=(S2(I, J, K, L)+S2(I-1, J, K, L)+S2(I, J+1, K, L)+S2(I, J, K-1, L)
&+S2(I-1, J+1, K, L)+S2(I-1, J, K-1, L)+S2(I, J+1, K-1, L)
&+S2(I-1, J+1, K-1, L))/8.0
BAV2=(BT(I, J)+BT(I-1, J)+BT(I, J+1)+BT(I-1, J+1))/4.0
RAV2=(R(I-1)+R(I))/2.0
COSA2=(COS(U1(K))+COS(U1(K-1)))/2.0
A2OUT=A2(I-1, J+1, K, L)+A2(I-1, J, K-1, L)
&+A2(I, J+1, K-1, L)+A2(I-1, J+1, K-1, L)
B11=SIN(U1(L))*COSA2/DR
B12=RAV2*COS(U1(L))/DZ
B13=SIN(U1(L))/(U1(K)-U1(K-1))
B14=RAV2*BAV2/8.0
A2(I, J, K, L)=(RAV2*SAV2+(R(I-1)*B11-B14)*A2(I-1, J, K, L)
&+(B12-B14)*A2(I, J+1, K, L)+(B13*SIN(U1(K-1))-B14)*A2(I, J, K-1, L)
&-B14*A2OUT)/(R(I)*B11+B12+B13*SIN(U1(K))+B14)
52 CONTINUE
50 CONTINUE
501 CONTINUE
500 CONTINUE

```

```

C
C *****
C CALCULATION OF SOURCE FUNCTION TERMS FOR
C A SYMMETRIC ANISOTROPIC PHASE FUNCTION
C *****
C

```

```

DO 60 I=1, IL
DO 61 J=1, JL
DO 63 K=1, KL
DO 64 L=1, LL
AA1=0.0
AA2=0.0
AA3=0.0
AA4=0.0
BB1=0.0
BB2=0.0
BB3=0.0
BB4=0.0
CC1=0.0
CC2=0.0
CC3=0.0
CC4=0.0
DD1=0.0
DD2=0.0

```

```

DD3=0.0
DD4=0.0
DO 65 L1=2,LL
DO 66 K1=2,KL
AA1=AA1+W1(L1)*W1(K1)*PH(U1(L),U1(K),U1(L1),U1(K1))*
&A1(I,J,K1,L1)*SIN(U1(L1))
AA2=AA2+W1(L1)*W1(K1)*PH(U1(L),U1(K),PI-U1(L1),U1(K1))*
&A2(I,J,K1,L1)*SIN(U1(L1))
AA3=AA3+W1(L1)*W1(K1)*PH(U1(L),U1(K),PI-U1(L1),PI-U1(K1))*
&A3(I,J,K1,L1)*SIN(U1(L1))
AA4=AA4+W1(L1)*W1(K1)*PH(U1(L),U1(K),U1(L1),PI-U1(K1))*
&A4(I,J,K1,L1)*SIN(U1(L1))
BB1=BB1+W1(L1)*W1(K1)*PH(PI-U1(L),U1(K),U1(L1),U1(K1))*
&A1(I,J,K1,L1)*SIN(U1(L1))
BB2=BB2+W1(L1)*W1(K1)*PH(PI-U1(L),U1(K),PI-U1(L1),U1(K1))*
&A2(I,J,K1,L1)*SIN(U1(L1))
BB3=BB3+W1(L1)*W1(K1)*PH(PI-U1(L),U1(K),PI-U1(L1),PI-U1(K1))*
&A3(I,J,K1,L1)*SIN(U1(L1))
BB4=BB4+W1(L1)*W1(K1)*PH(PI-U1(L),U1(K),U1(L1),PI-U1(K1))*
&A4(I,J,K1,L1)*SIN(U1(L1))
CC1=CC1+W1(L1)*W1(K1)*PH(PI-U1(L),PI-U1(K),U1(L1),U1(K1))*
&A1(I,J,K1,L1)*SIN(U1(L1))
CC2=CC2+W1(L1)*W1(K1)*PH(PI-U1(L),PI-U1(K),PI-U1(L1),U1(K1))*
&A2(I,J,K1,L1)*SIN(U1(L1))
CC3=CC3+W1(L1)*W1(K1)*PH(PI-U1(L),PI-U1(K),PI-U1(L1),PI-U1(K1))*
&A3(I,J,K1,L1)*SIN(U1(L1))
CC4=CC4+W1(L1)*W1(K1)*PH(PI-U1(L),PI-U1(K),U1(L1),PI-U1(K1))*
&A4(I,J,K1,L1)*SIN(U1(L1))
DD1=DD1+W1(L1)*W1(K1)*PH(U1(L),PI-U1(K),U1(L1),U1(K1))*
&A1(I,J,K1,L1)*SIN(U1(L1))
DD2=DD2+W1(L1)*W1(K1)*PH(U1(L),PI-U1(K),PI-U1(L1),U1(K1))*
&A2(I,J,K1,L1)*SIN(U1(L1))
DD3=DD3+W1(L1)*W1(K1)*PH(U1(L),PI-U1(K),PI-U1(L1),PI-U1(K1))*
&A3(I,J,K1,L1)*SIN(U1(L1))
DD4=DD4+W1(L1)*W1(K1)*PH(U1(L),PI-U1(K),U1(L1),PI-U1(K1))*
&A4(I,J,K1,L1)*SIN(U1(L1))
66 CONTINUE
65 CONTINUE
S1(I,J,K,L)=(BT(I,J)-SC(I,J))*B(I,J)+SC(I,J)/(4.0*PI)*
&(AA1+AA2+AA3+AA4)
S2(I,J,K,L)=(BT(I,J)-SC(I,J))*B(I,J)+SC(I,J)/(4.0*PI)*
&(BB1+BB2+BB3+BB4)
S3(I,J,K,L)=(BT(I,J)-SC(I,J))*B(I,J)+SC(I,J)/(4.0*PI)*
&(CC1+CC2+CC3+CC4)
S4(I,J,K,L)=(BT(I,J)-SC(I,J))*B(I,J)+SC(I,J)/(4.0*PI)*
&(DD1+DD2+DD3+DD4)
64 CONTINUE
63 CONTINUE
61 CONTINUE
60 CONTINUE
DO 110 I=1,IL
DO 111 J=1,JL
DO 112 K=1,KL
DO 113 L=1,LL
IF(ABS(S1(I,J,K,L)-SS1(I,J,K,L)).GT.1.E-03)GO TO 100
113 CONTINUE
112 CONTINUE
111 CONTINUE
110 CONTINUE
WRITE(6,602)
602 FORMAT(' ',3X,' INTENSITIES AT RADIAL EDGE')
DO 610 J=1,JL
WRITE(6,611)Z(J)
611 FORMAT(' ',3X,' Z=',F8.4)
DO 615 K=1,KL
WRITE(6,616)U1(K)

```

```

616 FORMAT(' ',3X,'PHI=',E12.5)
      DO 600 L=1,LL
        WRITE(6,601)U1(L),A1(IL,J,K,L),A2(IL,J,K,L),A3(IL,J,K,L)
        &,A4(IL,J,K,L)
601  FORMAT(' ',2X,'TH=',F8.4,2X,'A1=',E12.5,2X,'A2=',E12.5,
        &2X,'A3=',E12.5,2X,'A4=',E12.5)
600  CONTINUE
615  CONTINUE
610  CONTINUE
      DO 70 J=1,JL
        WRITE(6,81)Z(J)
81   FORMAT(' ',4X,'Z=',F8.4)
      DO 71 I=1,IL
        QQR=0.0
        QQZ=0.0
      DO 72 L=2,LL
      DO 73 K=2,KL
        SSQ=SIN(U1(L))*SIN(U1(L))
        DOMGR=SSQ*COS(U1(K))
        QQR=QQR+W1(K)*W1(L)*(A1(I,J,K,L)+A2(I,J,K,L)-A3(I,J,K,L)
        &-A4(I,J,K,L))*DOMGR
        DOMGZ=COS(U1(L))*SIN(U1(L))
        QQZ=QQZ+W1(K)*W1(L)*(A1(I,J,K,L)+A4(I,J,K,L)-A2(I,J,K,L)
        &-A3(I,J,K,L))*DOMGZ
73  CONTINUE
72  CONTINUE
      QR(I,J)=2.0*QQR
      QZ(I,J)=2.0*QQZ
      WRITE(6,80)R(I),QR(I,J),QZ(I,J)
80  FORMAT(' ',2X,'R=',F8.4,4X,'QR=',E16.9,4X,'QZ=',E16.9)
71  CONTINUE
70  CONTINUE
      STOP
      END
      FUNCTION PH(TH1,PH1,TH2,PH2)
      COMMON/ANIS/AN(10),NUM
      CSTH0=SIN(TH1)*SIN(TH2)*COS(PH1-PH2)+COS(TH1)*COS(TH2)
      CSTH1=SIN(TH1)*SIN(TH2)*COS(PH1+PH2)+COS(TH1)*COS(TH2)
      SUM=0.0
      DO 1 N=1,NUM
1    SUM=SUM+AN(N)*(PN(N,CSTH0)+PN(N,CSTH1))
      PH=SUM
      RETURN
      END
      FUNCTION PN(N1,Z)
      IF(N1.EQ.1)PN=1.0
      IF(N1.EQ.2)PN=Z
      IF(N1.EQ.3)PN=(3.0*Z*Z-1.0)/2.0
      IF(N1.EQ.4)PN=(5.0*Z*Z*Z-3.0*Z)/2.0
      RETURN
      END

```

**INFLUENCE OF FORCED DISTURBANCES ON
THE VORTEX CORE AND THE VORTEX BURST**

Final Report

for

UNIV ENERGY PO S-210-9MG-056

Prepared by:

Ahmad D. Vakili and Robert S. Eramo

The University of Tennessee Space Institute

Tullahoma, Tennessee 37388

October 1989

Table of Contents

- I. Introduction
- II. Experimental Procedure
- III. Swirl Number Determination
- IV. Technical Discussions
- V. Experimental Observations
- VI. Conclusions
- VII. References

Abstract

A preliminary experimental investigation is conducted to study the effects of external forcing on the vortex in a vortex tube. The vortex tube had a slit entrance tangent to the tube's inner diameter and perpendicular to the tube's axis. Various dye flow visualization methods were used to visualize the vortex flow and the core. Forcing was introduced into the flow by axial periodic blowing and suction or both and by periodic tangential blowing. The vortex core developed helical waves with relatively long wavelength for continuous blowing. Periodic pulsation of the axial flow at various low frequencies resulted in various wavelength helical waves on the vortex core. High frequency forcing was found to result in a tighter core and therefore resulted in the delay of the vortex burst in the divergent segment of the tube. Suction along the core axis at the location of vortex burst was able to eliminate the burst for approximately one vortex tube diameter. Some of the observations reported here are new and therefore justify further investigations.

I. Introduction

The flow within the H1-Heater is highly complex and difficult for accurate analyses without identification of some key dominating variables and their physics. Flow physics of the Arc Heater (H1-Heater) requires further fundamental understanding in order to identify the cause of and remedy for the associated operational problems which exist. Such an understanding is also essential for higher rate of power input and scaling of future arc heaters to be properly incorporated. H1-Heater uses a confined vortex flow to stabilize the arc which is ideally positioned along the vortex core. Numerous parameters affect the arc and the vortex core position along the length of the H1-Heater. One of the most important fluid mechanic processes involved is the vortex stability which may lead to vortex burst.

Early vortex research, performed by Lord Kelvin, first indicated the possible occurrence of inertial waves in swirling flows. Since then, researchers like Benjamin, Escudier, Liebovich, and Sarpkaya have become leaders in the field of Vortex Flow research. A multitude of researchers have studied various aspects of vortex flow. Few, however, have experimented with delaying confined vortex breakdown through the introduction of a forced disturbance. Yao, et al. was one of the few research teams to successfully attempt it. They imposed a harmonic oscillation on one of the guiding vanes in their swirl chamber thus postponing vortex core breakdown through introduction of this inertial wave. They found that a downstream traveling spiral wave, co-rotating with the main vortex and having proper frequency, could effectively delay the vortex breakdown. Fundamental experiment and ideas first proposed by Vakili (1985) were the basis for the study performed by Yao, et al. and also for the present study.

Many studies have been performed on the mechanisms for vortex burst (Liebovich). There is, however, no universal and generally agreed upon specific condition which can be attributed to the vortex burst phenomena. Most of the studies have agree-

ment that stability, adverse pressure gradient and a process analogous to the hydraulic jump are suspected to influence the vortex burst.

In addition to the above mentioned parameters, flow unsteadiness plays an important role on the vortex burst. Escudier et al. 1980, in a thorough study performed LDA measurements of a confined turbulent vortex. Even though their study concerned a steady vortex flow, they observed a vortex burst "bubble" in the main tube only when the flow rate was changed rapidly. That is, the unsteady flow phenomenon associated with the change in the flow rate, caused the vortex to burst at a point where under steady flow conditions no such an event could be established. The vortex breakdown in a tube was investigated by Menne recently using Navier-Stokes equations. His results compared well with the experimental data of Faler & Liebovich. He observed that a small non-axisymmetric perturbation caused drastic changes in the flow structure compared to the purely axisymmetric results. Also, it is well known that vortex flows are extremely sensitive to disturbances created by the probes and the surroundings, (e.g. Holman & Moore).

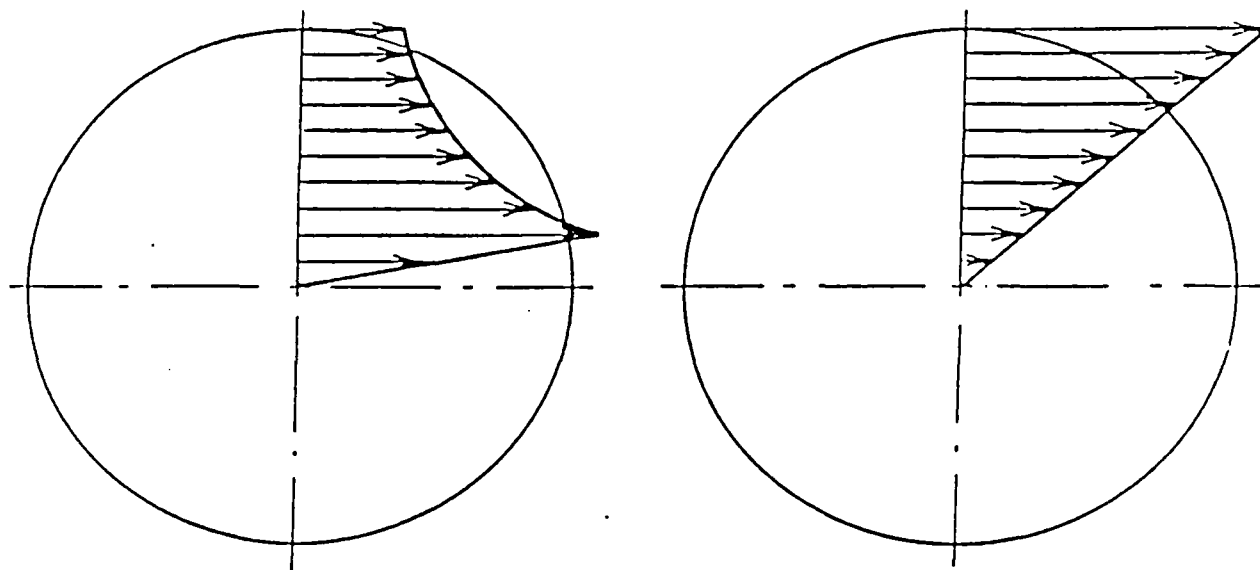
Recent developments in unsteady flow and better understanding of the flow physics have shed light on the significance of even very small unsteady perturbations on mean flows. Many authors have demonstrated that by proper periodic interactions with various shear flows, coherent structures can be created, modified and/or destroyed (see Hussain for more details). Liepmann using surface mounted heat strips was able to eliminate transition and delay its onset. Flow stability can be significantly influenced by acoustic disturbances as have been shown by Gutmark, et al. Stability analysis for a confined steady vortex could be performed as a guide, however, relating the results obtained to real flows requires the support of experimental evidence and knowledge of small disturbances. Stability analysis has been performed on vortex cores by Suzuki and many other authors as referenced by Liebovich (1983). Therefore, a new approach, utilizing the progress in the understanding of unsteady flows must be followed to look for answers.

In studying the phenomenon of energy separation effects in the Ranque-Hilsch tube, Kurosaka, identified that a phenomena "acoustic streaming" (resonance) could change the vortex flow pattern from a free vortex to a forced type vortex, as shown in Figure 1. Studies on the vortex structure inside the Rank-Hilsch tube by many other authors also indicate that the nature of the vortex changes from a Rankine type vortex to a forced vortex during the presence of the Rank-Hilsch effect. Organized acoustic perturbations in the Ranque-Hilsch tube are responsible for the conversion of a Rankine type vortex to a forced vortex. The core of a forced vortex of this nature represents (nearly) the whole vortex. Therefore, as long as the state of forced vorticity is maintained, there can be no vortex burst. In the case of vortical flows, "the Ranque-Hilsch tube," Kurosaka effectively showed that under "resonant" flow conditions a forced vortex is created without forcing.

Kuroda found that the geometry of the outlet also plays an important role on the stability of the forced vortex state. Studying many configurations at the exit of the vortex tube indicated that geometry appears to have a major influence on the forced vortex returning to a Rankine vortex. The axial flow which exists in a forced vortex can be influenced by small changes in the outlet geometry of the tube. Vakili has proposed that the introduction of a forced disturbance, in the form of an axially pulsed flow, may result in two types of interactions, depending on the forcing frequency and amplitude of the pulsed flow.

1. To delay or accelerate the onset of the breakdown point.
2. To enhance the vortex core strength or significantly reduce its strength.

The primary goal of this study is to demonstrate that proper externally-imposed forced harmonic oscillations can provide energy to the vortex such that a vortex may overcome adverse conditions leading to a vortex burst thereby providing supporting evidence for the above mentioned hypothesis. Various types of forcing techniques are incorporated, i.e. axial, radial, circumferential or a combination of these are investigated. Axial pulsing is the main mechanism for introducing the forced dis-



(a) Rankine vortex

(b) Forced vortex

Figure 1. Formation of a forced vortex from a Rankine vortex due to acoustic resonance.

turbance into the experiment.

In short, it appears possible that through forced unsteady excitation, the flow pattern of a confined vortex can be altered in different manners. A fundamental experimental investigation is conducted to answer some basic questions on vortex burst due to external forcing (intentionally provided) to initiate or delay a burst. In this investigation it has been demonstrated that proper forcing can be used to either delay or accelerate the vortex burst and forcing also can be used to increase the strength of vorticity.

II. Experimental Procedure

In a constant area tube under steady conditions, a vortex is subjected to a uniform favorable pressure gradient. Therefore, some increase in the tube area along the flow direction is necessary to provide a level of adverse pressure gradient to accommodate a vortex burst. Different divergence angles would then result in corresponding changes in the pressure gradient along the duct and of the point of vortex burst along the tube. The effect of this parameter on the location of vortex burst is not of primary concern here and therefore is not studied. Only one geometry with a fixed pressure gradient was therefore employed. The approach has been to create a confined vortex in a long cylindrical tube and to adjust the flow and geometry conditions to ensure a vortex burst within the tube.

While maintaining these conditions, various forcing methods are employed. The influence of various forcing harmonics on the location of vortex burst and the strength of vorticity are studied for selected test variables such as: $Re = \frac{U_m D}{\nu}$, swirl number $\Omega = \frac{\Gamma}{U_m D}$ and the nondimensional frequency $k = \frac{f D}{U_m}$ for one pressure gradient along the tube. Where U_m is the mean axial flow velocity, D is the vortex tube inside diameter, Γ is the circulation and ν is the kinematic viscosity. Flow visualization is used to help locate the position of the vortex burst. A vortex in a confined arrangement as shown in Figure 2 can be created by several approaches. Swirl vanes of various geometries have been used by Faler & Liebovich (1977) to generate swirl in the flow entering a vortex tube. Escudier et al. (1980), used tangential flow through a slit in the generator segment of their tube. Due to the advantages associated with the latter approach (see Escudier (1980)), we selected this approach over the swirl vane arrangement. More details on the experimental procedure can be found in the work of Eramo (1989).

The experimental set-up is shown schematically in Figure 2. The plexiglas vortex tube has an inside diameter of $Di = 3''$ and overall length of $L = 79''$. Flow

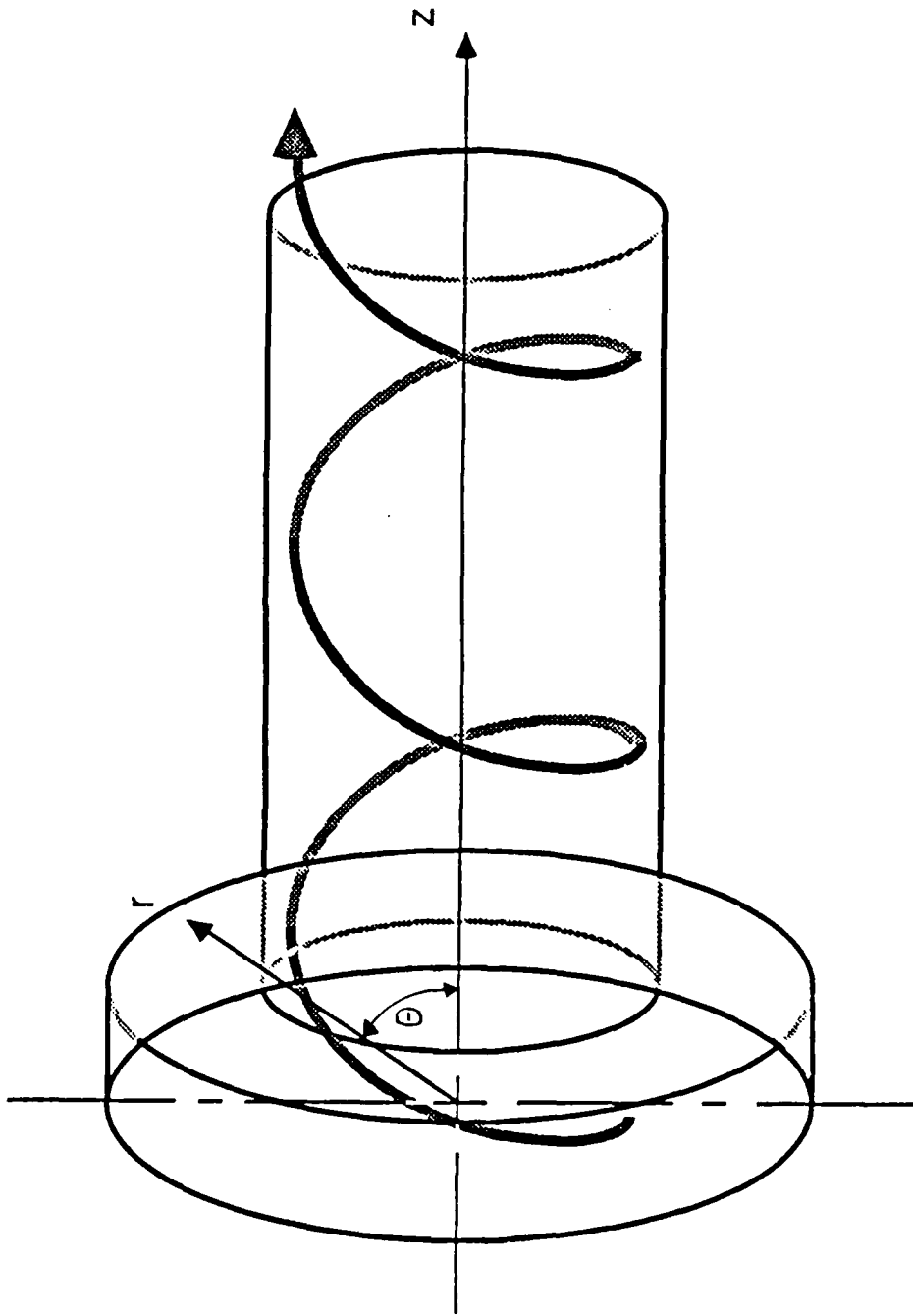


Figure 2. Vortex Tube Coordinate System.

enters the generator section of the tube through a tangential slit with a fixed width $t = 0.125''$. There are three types of inserts made to fit inside the tube. These inserts can be installed in the tube at any desirable axial location. The three inserts are:
a) An orifice-plug b) Two convergent-divergent sections as shown in Figure 3.

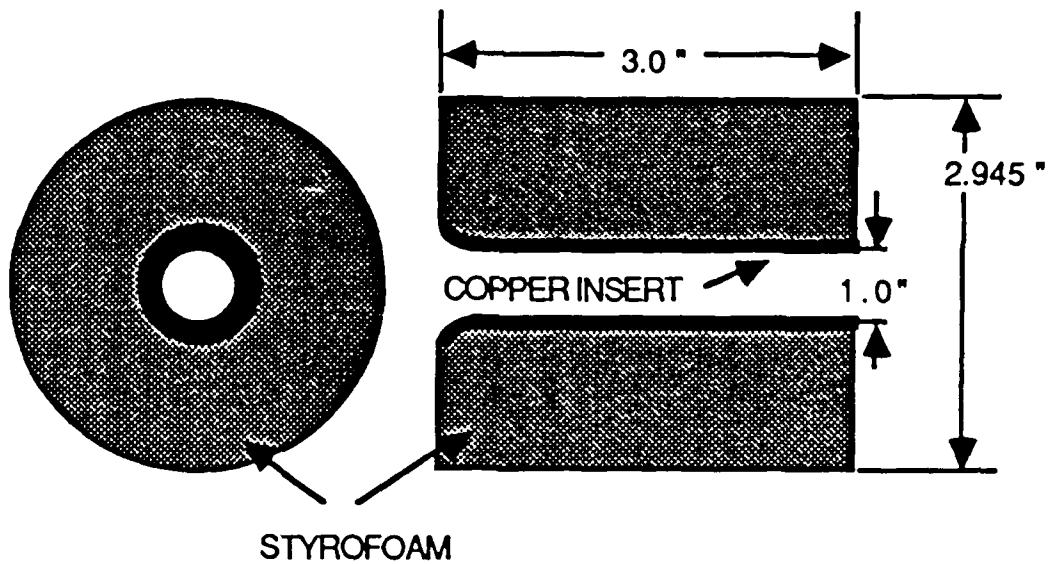


Figure 3a. End Plug Schematic

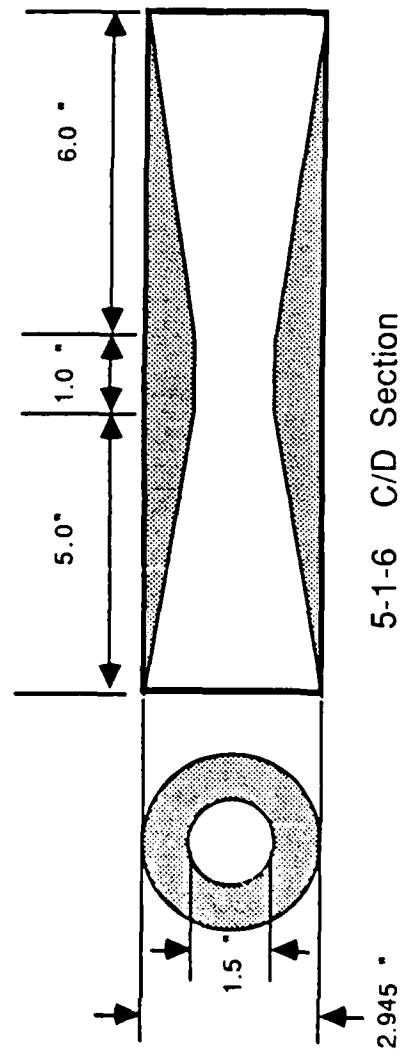
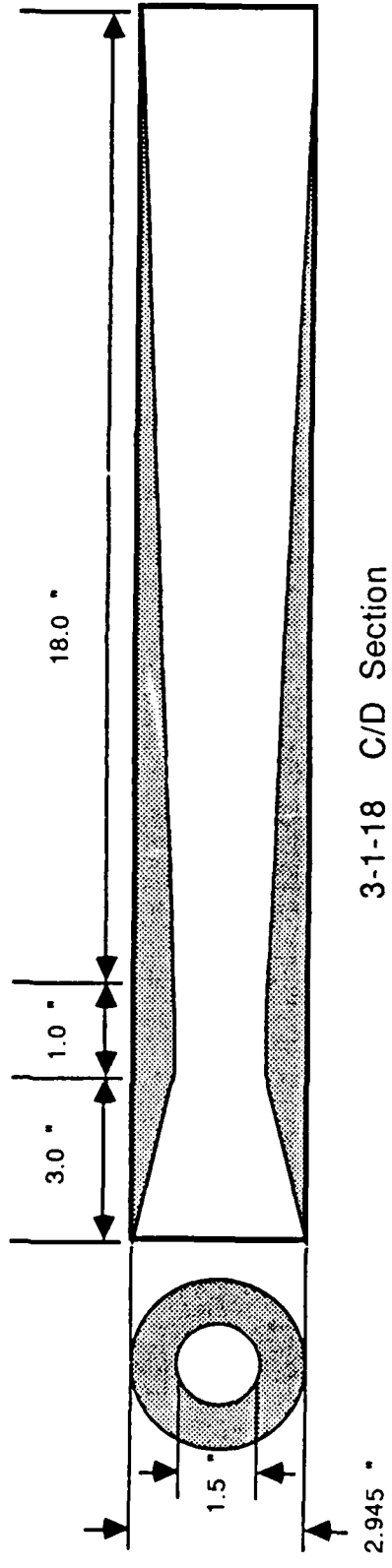


Figure 3b. Converging/Diverging Sections Schematic.

The inserts, once installed, ensure the formation of an organized vortex core and its possible breakdown. The two different geometry convergent-divergent inserts could also be placed in series to create a region in the flow similar to what is available in the mixing region of the arc heater cathode. This is the region where the vortex burst is forced to occur due to the adverse pressure gradient in the divergent section. Various parameters and configurations considered for this study are shown in Table I and Figure 4, respectively.

Flow (GPM)	C_μ ($D = 1.5''$)	V_{slit} (in/sec)	Γ	V_∞	Reynolds number
2.0	8.682	12.32	116.11	4.358	6488
2.5	5.557	15.40	145.14	5.448	8107
3.0	3.855	18.48	174.17	6.537	9726
3.5	2.848	21.56	203.20	7.627	11351
4.0	2.153	24.64	232.23	8.716	12970
4.5	1.702	27.72	261.25	9.805	14589
5.0	1.389	30.80	290.28	10.895	16214
5.5	1.146	33.88	319.31	11.983	17833
6.0	0.972	36.96	348.34	13.074	19458

Table I.

$$V_{SLIT} = \frac{\text{FLOW RATE}}{\text{SLIT AREA}} = \frac{Q(\text{GPM})}{A_{SLIT}}$$

$$V_{SLIT} = 6.160 Q$$

$$\Gamma = \pi D V_{SLIT} \text{ where } D = 3.0''$$

$$V_{\infty} = \left[\frac{4Q}{\pi D_{\text{THROAT}}^2} \right]$$

$$V_{\infty} = [2.179 Q]$$

$$V_{\text{JET}}^2 = \left[\frac{4Q_{\text{JET}}}{\pi D_{\text{JET}}^2} \right]^2$$

$$V_{\text{JET}}^2 = 9.156 \times 10^4 \left(\frac{\text{in}}{\text{sec}} \right)^2$$

$$V_{\text{JET}} = 302.6 \frac{\text{in}}{\text{sec}}$$

$$C_{\mu} = \frac{\left(\frac{Q_{\text{JET}}}{D_{\text{JET}}} \right)^2}{\frac{1}{2} \left(\frac{Q}{D} \right)^2}$$

$$\text{for } D = 1.5'' \quad C_{\mu} = \frac{36.73}{Q^2}$$

$$\text{Reynolds number} = \frac{V_{\infty} D}{\nu} \quad \text{where } D = 3''$$

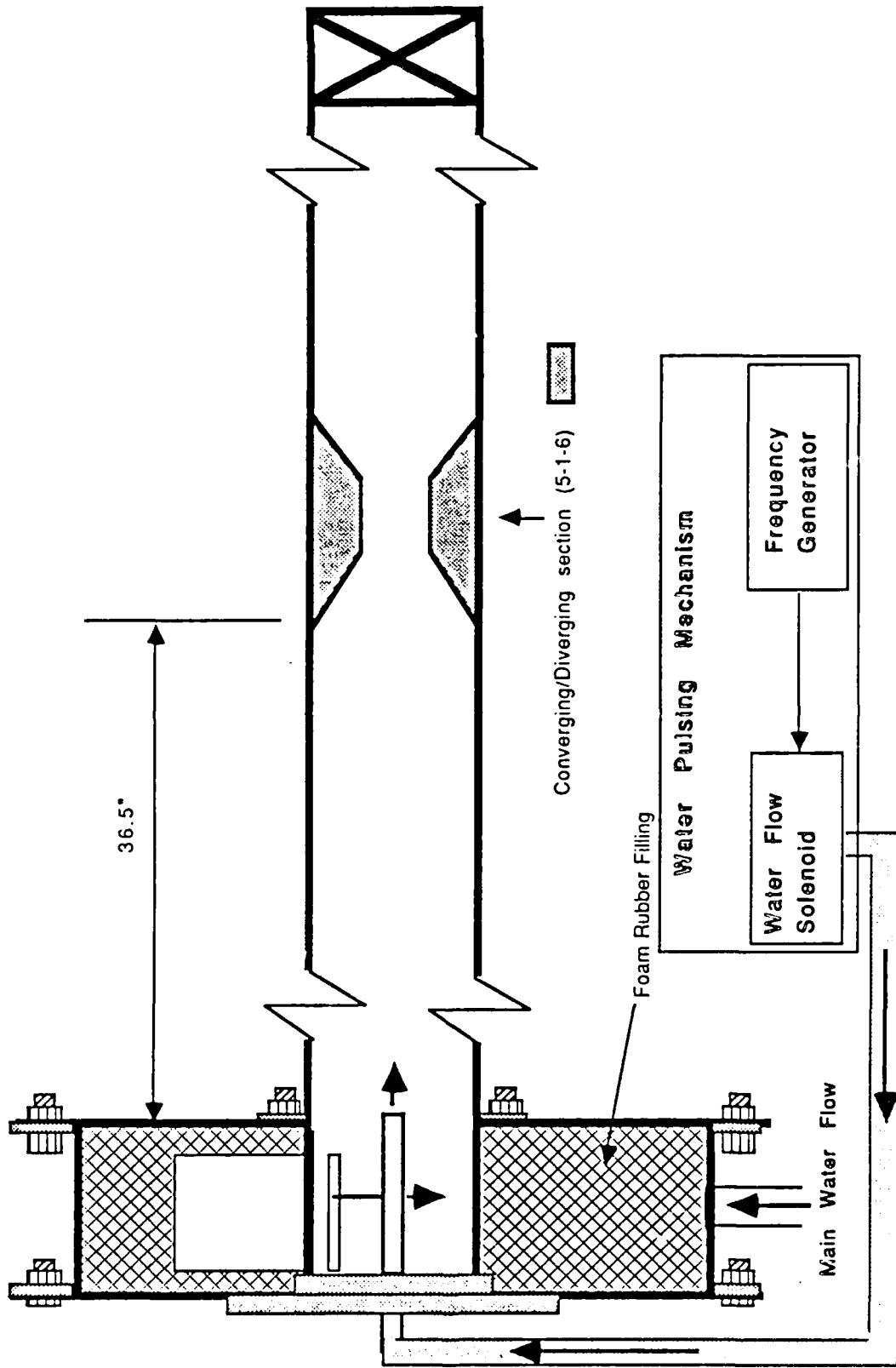


Figure 4a. Second Experimental Set-Up.

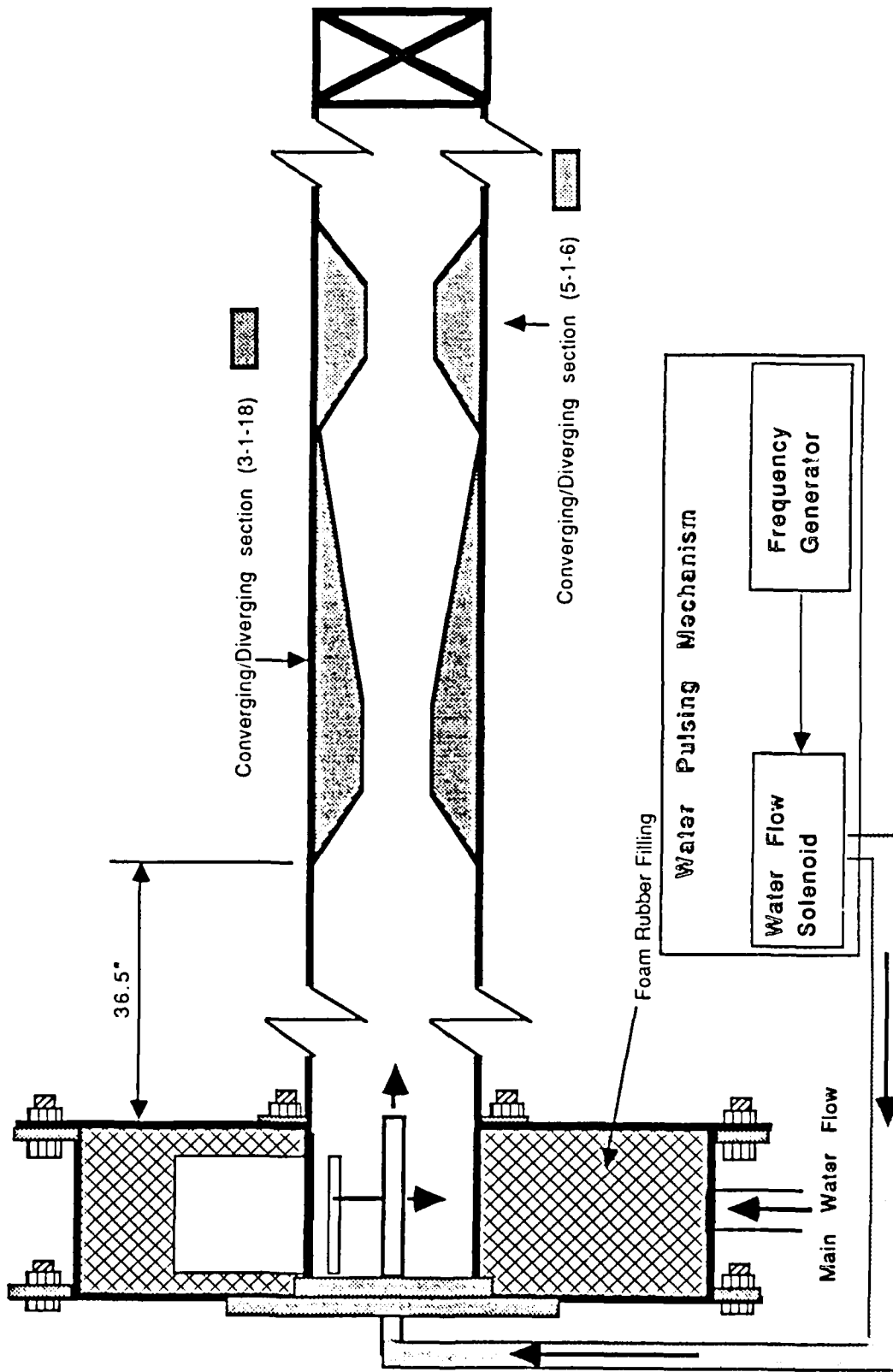


Figure 4b. Third Experimental Set-Up.

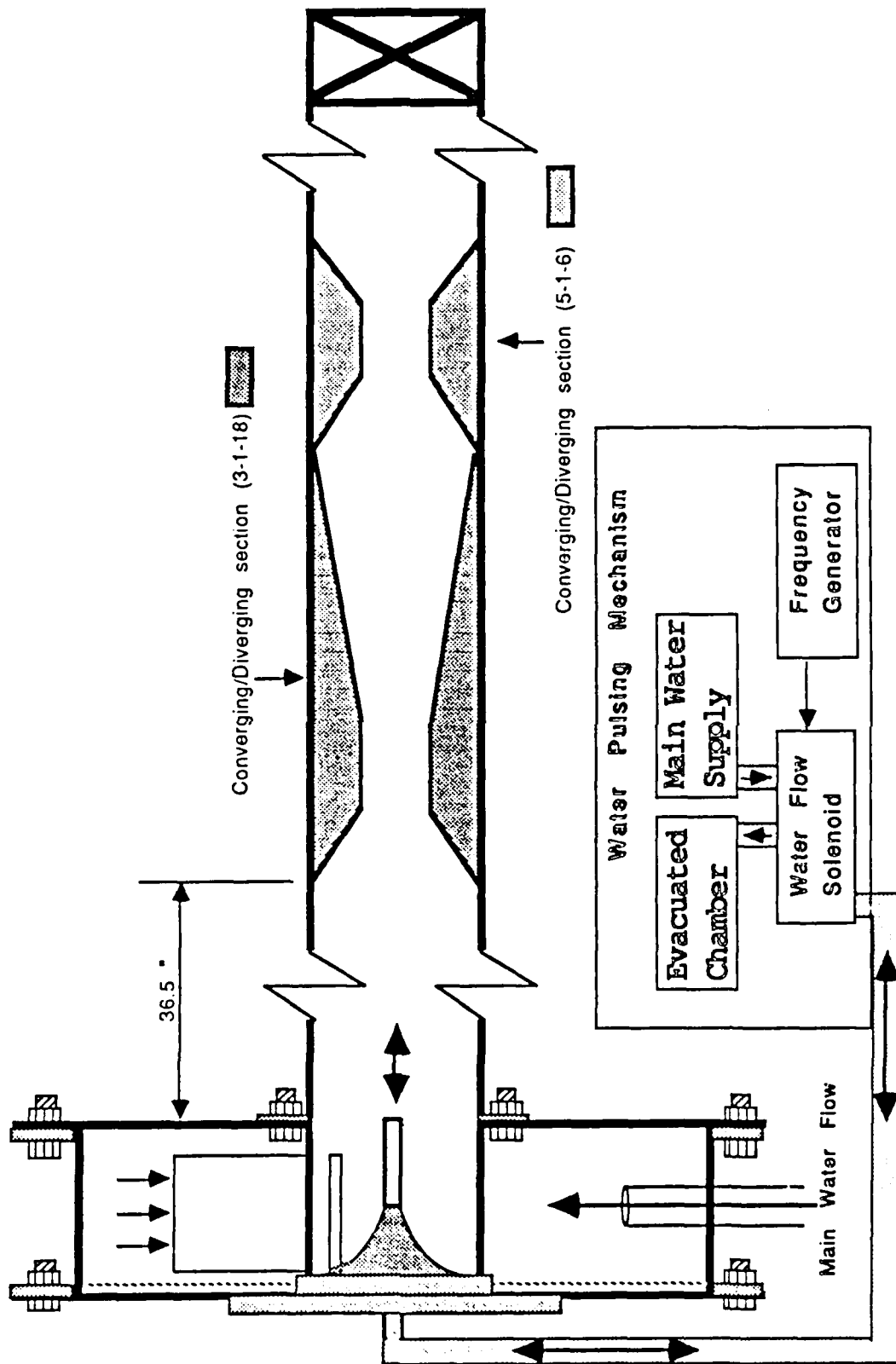


Figure 4c. Final Experimental Set-Up.

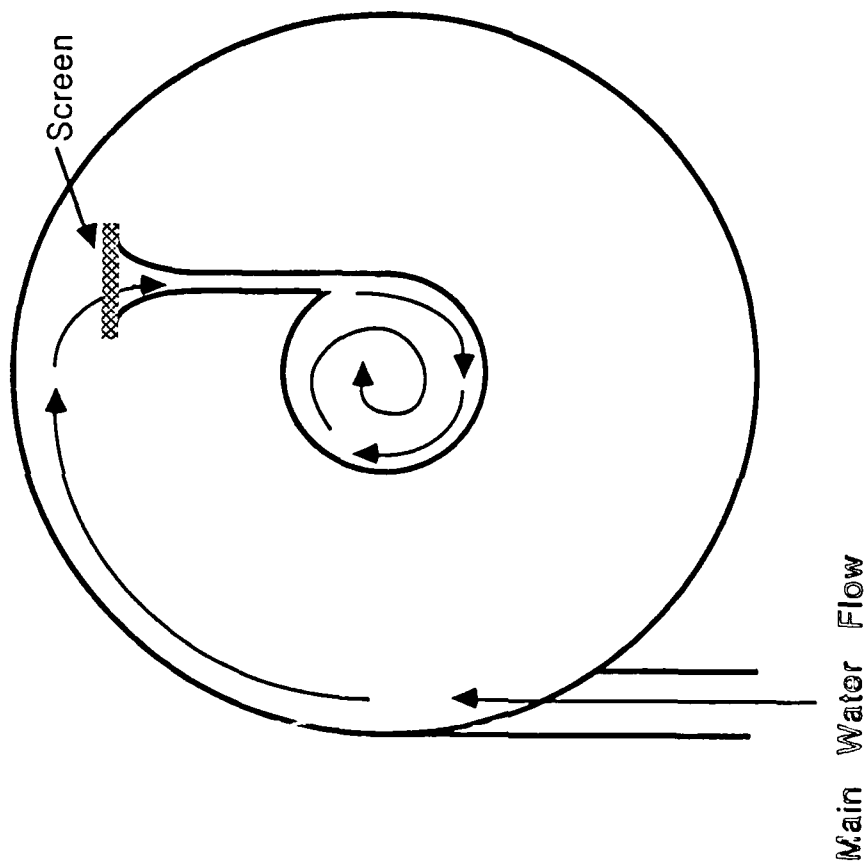


Figure 4d. End-On View of Swirl Generator Section for Experimental Set-Up.

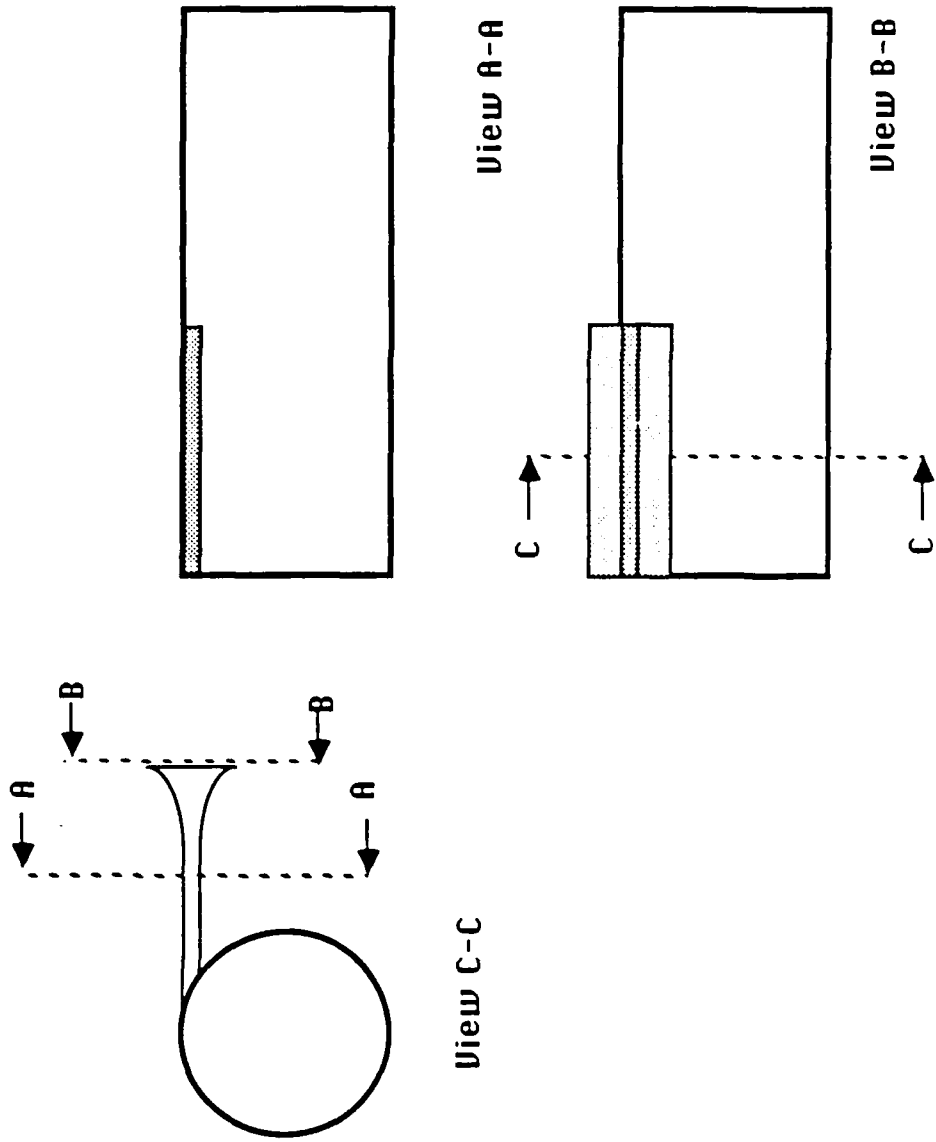


Figure 4e. Close-Up View of Swirl Device.

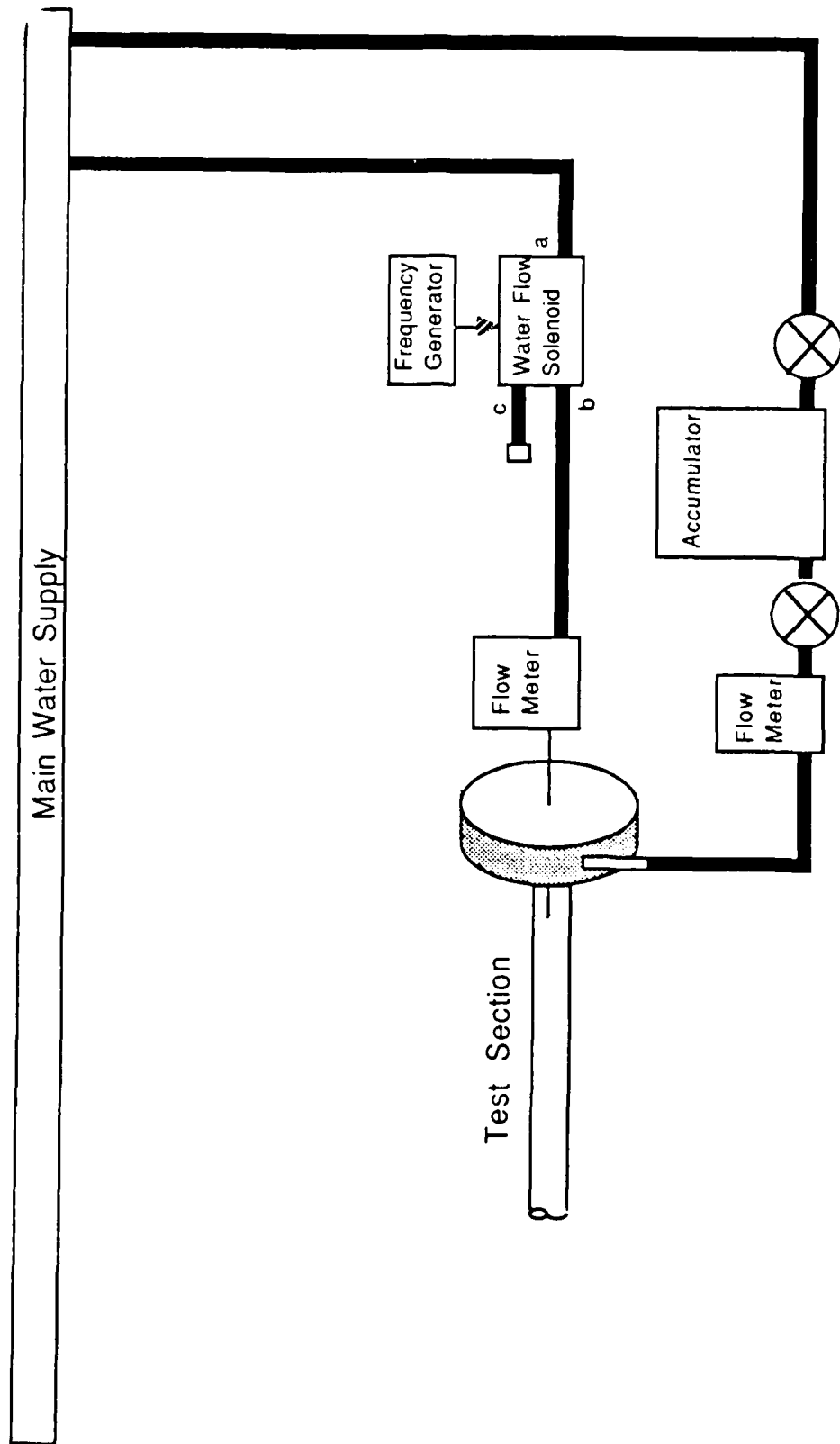


Figure 4f. Schematic of Water Supply for Final Experimental Set-Up.

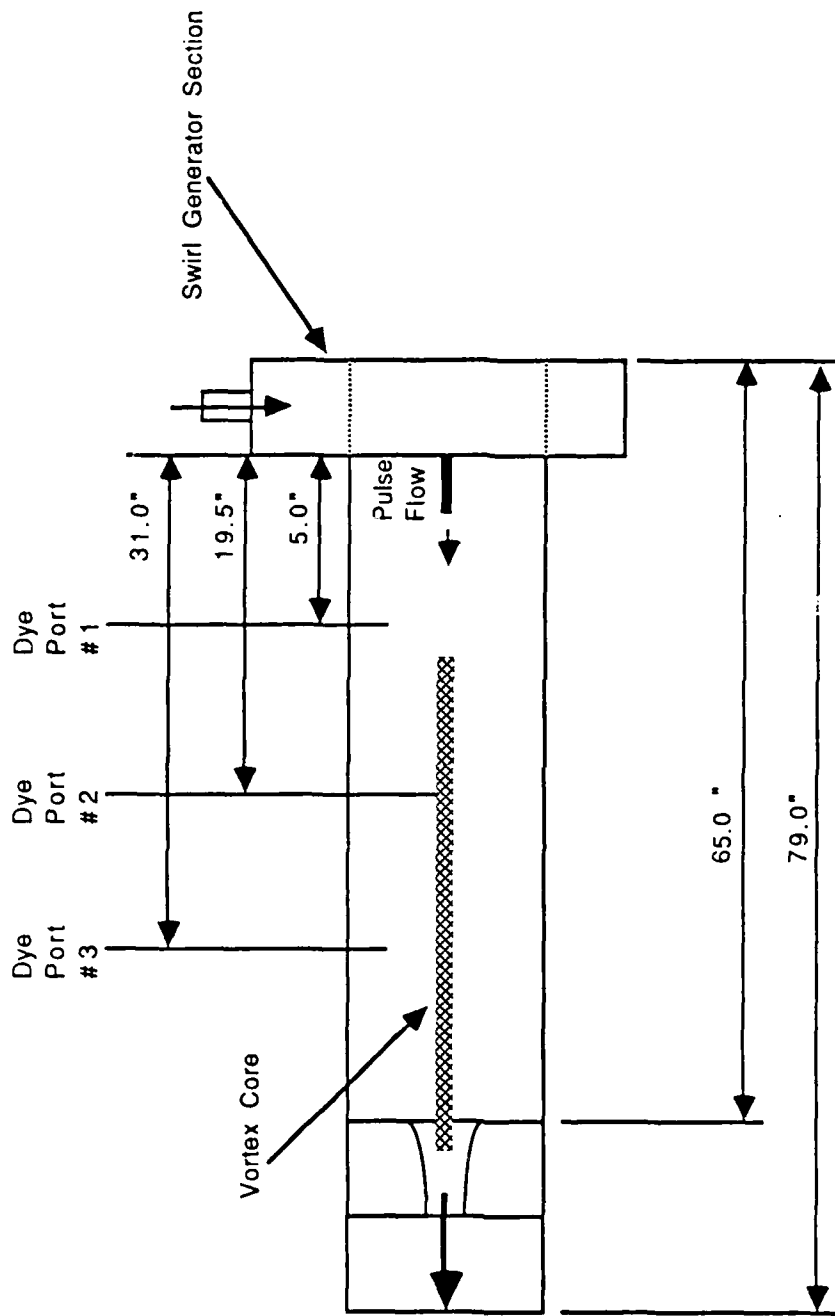


Figure 4g. Typical Dye Probe Locations in Any Set-Up.

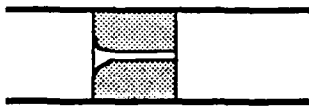
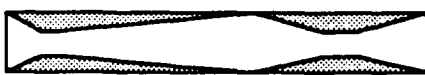
At several axial locations, dye injection probes are used to make the flow visible by releasing a small mixture of dye, water and alcohol (unit density), or fluorescent chemicals. These probes are cylindrical tubes, 0.5mm in diameter and are radially inserted into the vortex tube. In order to make the core visible, a probe is normally positioned near the axis of the vortex tube. Many hours of testing were spent investigating the flow field in each configuration.

Very interesting observations are made which have not previously been reported in a systematic way. Only similar waves have been observed, in the cavitating core of a vortex tube by Hashimoto, without any forcing.

Forcing is provided using periodic blowing through a small orifice ($D_{JET} = 0.170''$) at the exit of a steel tube ($D_{TUBE} = 0.25''$) positioned at two locations. First, axial forcing is provided by introducing the steel tube along the vortex tube axis from the generator section. Second, tangential forcing is introduced by orienting the same steel tube at a selected position, near the axial forcing position, tangent to the inner vortex tube diameter along the swirl direction. Axial suction in the downstream at the location of vortex burst, using the same steel tube is then used to study the suction effect on the vortex burst. This will be discussed separately from the observations made while forcing is applied.

The two different methods to introduce forcing on the flow generally do not create similar types of disturbances. The first approach produces axial - and the second approach results in circumferential-perturbations on the vortex flow in the cylindrical tube. The influence of each of these disturbances on the development of the vortex core and its stability can be addressed as a fundamentally separate problem.

Many configurations under different flow rates and forcing frequencies and amplitudes are studied. Table II shows the range of variables employed for all the conditions investigated. During the discussion of the observed results of particular significance, the conditions are noted as well.

Downstream Geometry	Values of each variable.			
	Flow (GPM)	Pulse Frequency (Hz)	Jet (GPM)	Suction Jet (GPH)
 End Plug	2	0	0	0
	2.5	1.0	0.5	16
	3	1.1		
	3.5	1.2		
	4	1.3		
	4.5	1.4		
	5	1.5		
	5.5	1.6		
	6	1.7		
	 3-1-18/5-1-6 C/D Section	1.8		
1.9				
2.0				
2.25				
2.5				
2.75				
20				
25				
30				
35				
40				

The values in each column indicate the matrix variation of that variable with the ones in the other columns.

Table II

III. Swirl Number Determination

Swirl Number was calculated from the displacement distance X and the circumferential distance C as shown in Figure 5. For swirling flow in a pipe, swirl number is defined as the axial flux of swirl momentum divided by axial flux of axial momentum. The Swirl Number for incompressible flow can be calculated as follows.

$$\text{Swirl Number} \equiv (V_c/V_x)$$

$$V_c \times \Delta t = C \quad \text{where } C \text{ is the circumferential distance the dye travels in time } \Delta t.$$

$$V_x \times \Delta t = X \quad \text{where } X \text{ is the axial distance the dye travels in time } \Delta t.$$

Swirl Number can now be represented

$$\text{Swirl Number} = (C/\Delta t)/(X/\Delta t) = C/X$$

Measurements of X were taken at a point π radians from the dye injection point. This gave the value for C as 1.5π inches. So Swirl Number can be determined from the equation

$$\text{Swirl Number} = \{\pi(1.5)/X\} = \underline{4.71/X}$$

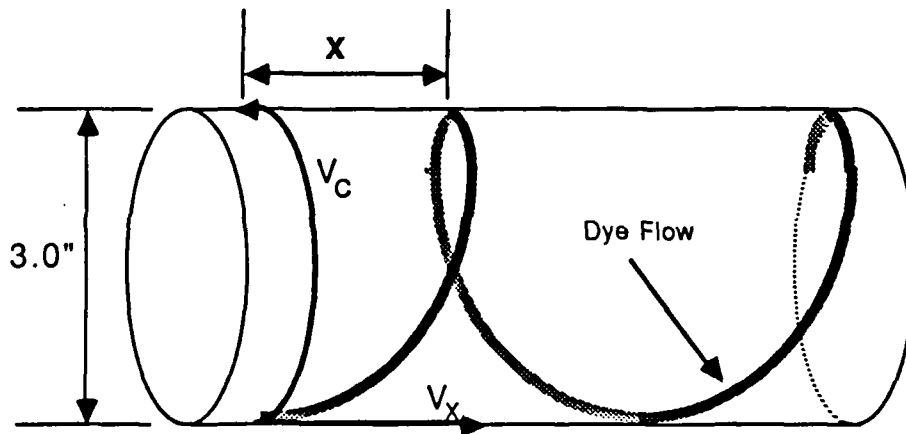


Figure 5. Schematic of Swirl Number Determination Method.

IV. Technical Discussions

In his experimental and theoretical analysis, Hashimoto (1969) developed a theory of induced wave motion in a rotating flow of water with an axial cavity along its axis. His analysis was based on the assumptions that the rotational velocity distribution between the cavity wall and the pipe could be approximated by a quadratic relation based on his experimental results. His analysis was limited to axisymmetric cavity. Therefore, even though he photographed the spiral type of waves, similar to the present observation of spiraling vortex cores, his analysis was carried out for only axisymmetric waves on the cavity.

A non-axisymmetric analysis has been initiated to be developed during the present study. However, this analysis is not completed at this time. The present analysis is for incompressible, nonviscous flow with velocity components (u, v, w) in a system of cylindrical polar coordinates (r, θ, z) . The undisturbed velocity components (U, V, W) and the perturbation components (u', v', w') are assumed to be of the following form.

$$u' = \tilde{u}(r)e^{i(kz+m\theta-wt)}$$

$$v' = \tilde{v}(r)e^{i(kz+m\theta-wt)}$$

$$w' = \tilde{w}(r)e^{i(kz+m\theta-wt)}$$

Complete analysis leading to results which support the experimental observations can be found in the Yao et al. (1989) paper as well as in the works of Hashimoto and Kurosaka. We have attempted a separate approach based on wave superposition which is not complete at this time.

The exact effect of the forced disturbance on the vortex core will depend on whether the frequency chosen for the pulse-jet will add to or cancel existing disturbances inherent in the vortex core and the test apparatus. For example, if a particular disturbance of a given frequency caused a vortex core burst at a specific location and we then introduced a forced disturbance that cancels the effects of the original disturbance, the vortex core burst should change position or disappear

altogether depending on the precise effect of the original disturbance on the vortex core.

Inherent instabilities are not the only cause of vortex core breakdown phenomena. Stability theory only allows one to investigate the amplification or decay of infinitesimally small disturbances imposed on the base vortex flow. Breakdown in then assume to be analogous to laminar-turbulent transition. Adverse pressure gradient and a process analogous to a hydraulic jump are also strong influences. In fact, a pressure gradient, resulting from a diverging test section, is utilized in our experiment to achieve a vortex core breakdown.

The critical state theory is based upon the possibility that a columnar vortex can support axisymmetric standing waves. The supercritical state has low-swirl velocities; and the flow is unable to support these waves. Subcritical flows have high-swirl velocities and are able to support waves. Vortex breakdown can be thought of as the ability of the flow to sustain standing waves.

Ito and his associates researched the critical state theory in 1985 in order to find a theoretical explanation for swirling pipe-flow vortex breakdown phenomena. They found that the internal wave, which may occur in the swirling flow, plays the most significant role in the breakdown phenomena, and that the azimuthal modes of the wave correspond directly to distinct types of flow structures which include the seven types of vortex burst observed by Liebovich.

V. Experimental Observations

In the vortex tube with the plug orifice incorporated, similar results as has been observed in the air cavity core of a vortex tube by Hashimoto were repeated. At low to medium swirl velocities, if air gets trapped in the vortex tube, it forms a cavity around the vortex tube axis. With forcing, or even under natural conditions, (Hashimoto), the air cavity forms a helical wavy shape similar to the observations made by Hashimoto. If the air cavity diameter becomes relatively large, then the helical mode will cease to exist. Under this situation the cavity becomes axially symmetric with respect to the pipe axis. The analysis of Hashimoto is applicable to the axisymmetric waves on the cavity.

With no air and using dye to visualize the core, very similar observations were made. However in this case forcing had to be incorporated to ensure the presence of the helical wave. With no forcing there was no evidence of the helical wave as shown in the photographs in Figures 6, 7, and 8. The wave length of the vortical wave appeared to depend on the forcing frequency. In order to determine, whether there is any relationship between the two the following experiments were performed.

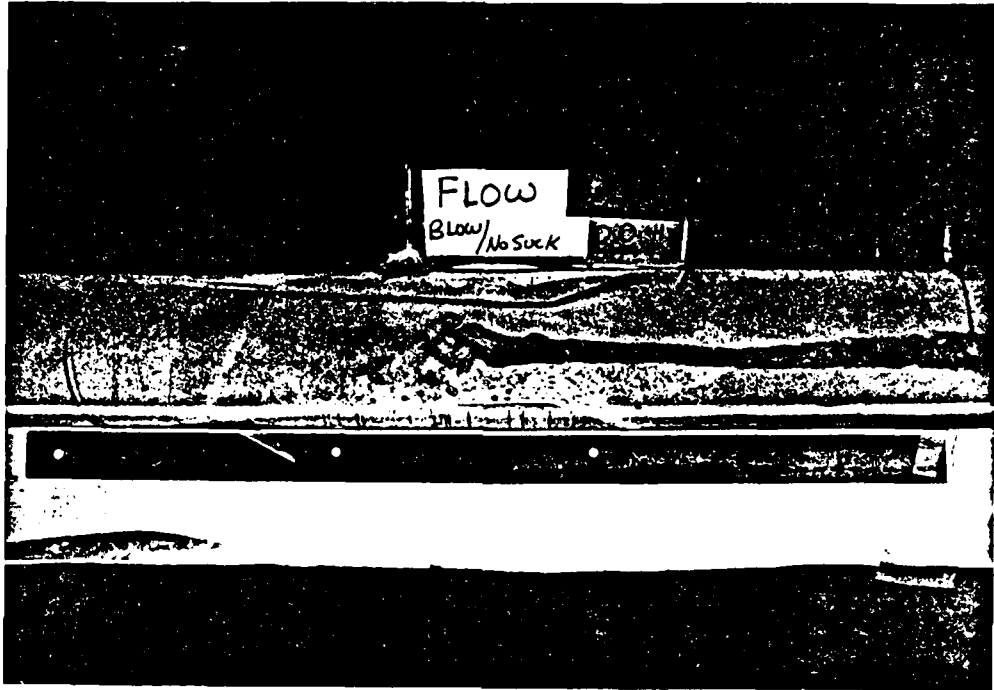


Figure 6. Photograph of Vortex Flow Showing No Evidence of Helical Wave Pattern.

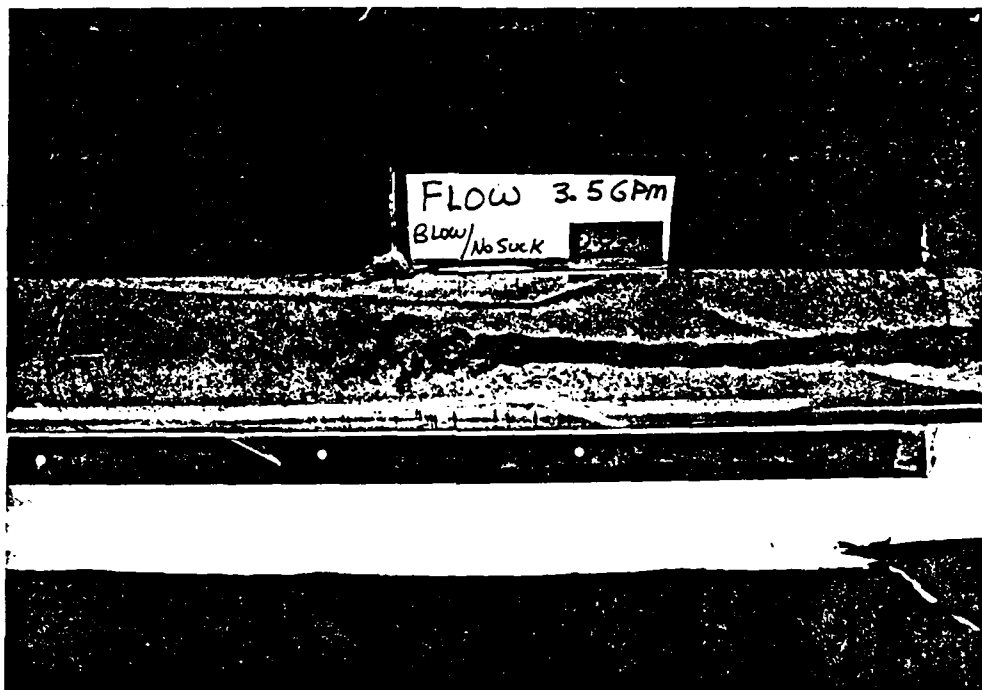


Figure 7. Photograph of Vortex Flow Showing No Evidence of Helical Wave Pattern.



Figure 8. Photograph of Vortex Flow Showing No Evidence of Helical Wave Pattern.

The forcing frequency, the length between the orifice plug and the generator section and the swirl number were varied independently. Since the vortex burst was always located downstream of the plug, very little effect due to pulsation on the vortex burst was observed. Mainly the coupling between the forcing and the helical motion of the core were the focal point of the orifice plug configuration. Several length locations of the orifice plug were investigated. At each location, forcing at several frequencies was tried. The axially symmetric vortex core became helical once the forcing was initiated. Figure 9 shows the helical wave of the core for a typical forcing observation. The distance between the orifice plug and the generator section was selected as multiples of the wave length of the helix observed in the original set-up where this length was 65". The following overall lengths were investigated: $L = 65''$, $57.6''$, $48''$, $43.2''$ and $38.40''$. For the orifice plug at the $65.0''$ length and a flow rate of 5.5GPM, the observed flow contained helical waves on the core with the wavelength shown in Table III.

Forcing Pulse Frequency and Wave Frequency (Hz)	Helix Wavelength (inches)
1.0	4.8
1.1	4.8
1.2	4.8
1.3	4.8
1.4	4.8
1.5	4.8
1.6	4.8
1.7	4.6
1.8	4.0
1.9	3.7
2.0	2.7

Table III.

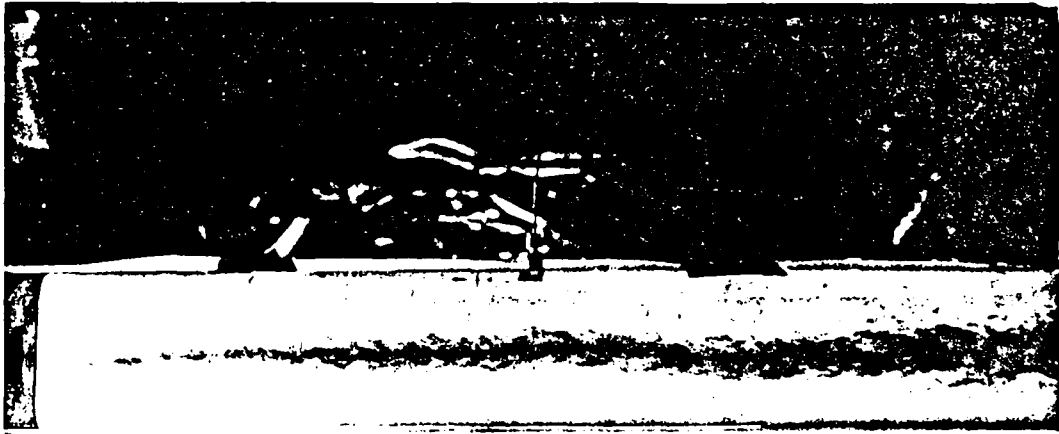


Figure 9a. No Forcing

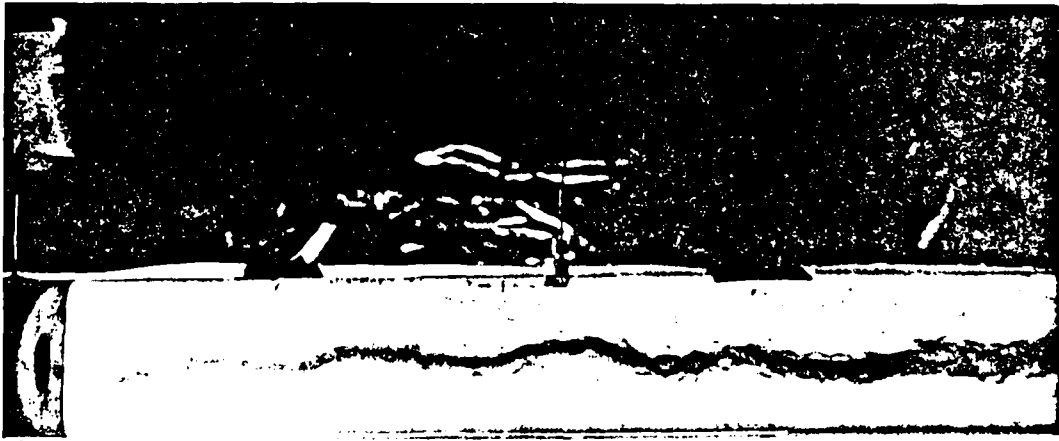


Figure 9b. Axial Forcing at
2.5 Hz



Figure 9. Development of Helical Waves on the Vortex Core Due to Forcing
(flow rate = 5.5 GPM, $Re_D = 17833$).

No interaction between the forcing and the vortex core was observed for the locations $L = 38.4''$ and $43.2''$. It was also observed that the vortex core (even without pulsing) was not very well defined. This may be related, to some extent, to the short distance between the generation section and the orifice plug and the fluctuations in the generation section because of tangential inflow through one slit, see Escudier (1982).

For the orifice plug positioned at $L = 48''$ and the (same) flow rate of 5.5GPM the following forcing frequency effect was observed as shown in Table IV.

Forcing Pulse Frequency (<u>Hz</u>)	Wave Frequency (<u>Hz</u>)	Wavelength of the Helix (<u>inches</u>)
2.00	2.00	6.00''
2.25	2.25	4.40''
2.50	2.50	3.70''
2.75	2.75	3.00''

Table IV.

Many different flow rates and forcing frequencies were tried for this length. Consistent observations, similar to the above were made with wavelength variations as shown in Table IV.

For shorter distances, $L = 24''$ orifice plug position for example, there was small scale evidence of what was observed for the longer length. However, it appeared that the vortex core was not very well defined as was the case for longer distances such as $L = 48''$ and $65''$.

The configuration of the vortex tube was changed to the geometry shown in Figure 4c. In order to change the amplitude and net mass flow of forcing, the blowing arrangement was changed to a Blow-Suction set-up. This was done to accomplish a zero net mass addition to the flow in the vortex tube. Implementing blowing/suction basically did not change any of the previous observations, i.e. that forcing still resulted in a helical wave on the vortex core. It also appeared that

blowing/suction made little difference in the shape of the wave or the position of vortex burst. This observation is a strong point reflecting the fact that the additional mass flow due to blowing is not the cause of the observed helical core.

During transition flows, from low to high flow rates, it was observed that the location where burst occurred was shifted about one diameter downstream. However, the burst location returned to its original position once the flow became steady at the higher flow rate. The reverse process did not result in a similar shift in the vortex core location.

Depending on the forcing frequency, two different forms of interactions were observed. At low frequencies ($0 \leq F < 10\text{Hz}$) the helical wave on the core was the primary result of forcing. For continuous blowing, i.e. no forcing, the core also becomes helical however, with a relatively long and a fixed wavelength of approximately 3 diameters which is independent of blowing rate. A typical core pattern for constant blowing is shown in Figure 10. Once forcing at low frequencies was initiated, then higher frequency helical waves were superimposed on the core as shown in Figure 11. The frequency of these waves was equal to that of the forcing.

Forcing at high frequencies of 20Hz to 40Hz resulted in a different type of interaction. Under these conditions, the position of the vortex burst in the diverging segment of the vortex tube was moved downstream. Figure 12 shows the observed shift due to 30Hz forcing for jet blowing of 0.5GPM . Table V summarizes the results of this experiment and Figure 13 shows plots of $\frac{\text{DISPLACEMENT}}{\text{DIAMETER}}$ vs. PULSE FREQUENCY.

Under certain flow rates, where a vortex core was clearly formed, forcing at high frequencies prevented the formation of a tight and organized vortex core as shown in Figure 14. Vakili et al. (1988) showed that by periodic suction and/or blowing an external vortex over a modified delta wing can be formed and maintained.

<u>Flow (GPM)</u>	<u>Pulse (Hz)</u>	<u>Ruler Burst Position (in)</u>	<u>Downstream Shift Due to Pulsing (in)</u>
3.5	0.0	11.5	0.0
3.5	20.0	10.5	1.0
3.5	25.0	9.5	2.0
3.5	30.0	8.5	3.0
3.5	35.0	8.0	3.5
3.5	40.0	7.0	4.5
3.5	0.0	11.5	0.0
4.0	0.0	11.5	0.0
4.0	20.0	11.0	0.5
4.0	25.0	10.5	1.0
4.0	30.0	10.5	1.0
4.0	35.0	10.0	1.5
4.0	40.0	11.0	0.5
4.0	0.0	11.5	0.0

Table V. Table showing summary of results for the 3-1-18/5-1-6 C/D section experimental set-up at the indicated flow rates and pulse frequencies.

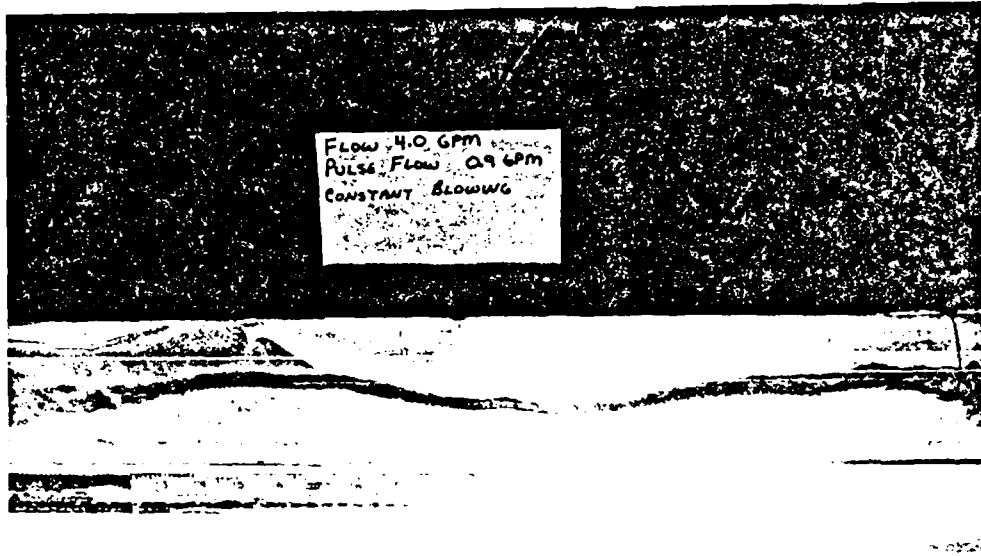


Figure 10. Long Wavelength Helical Wave on the Core Due to Constant Blowing.

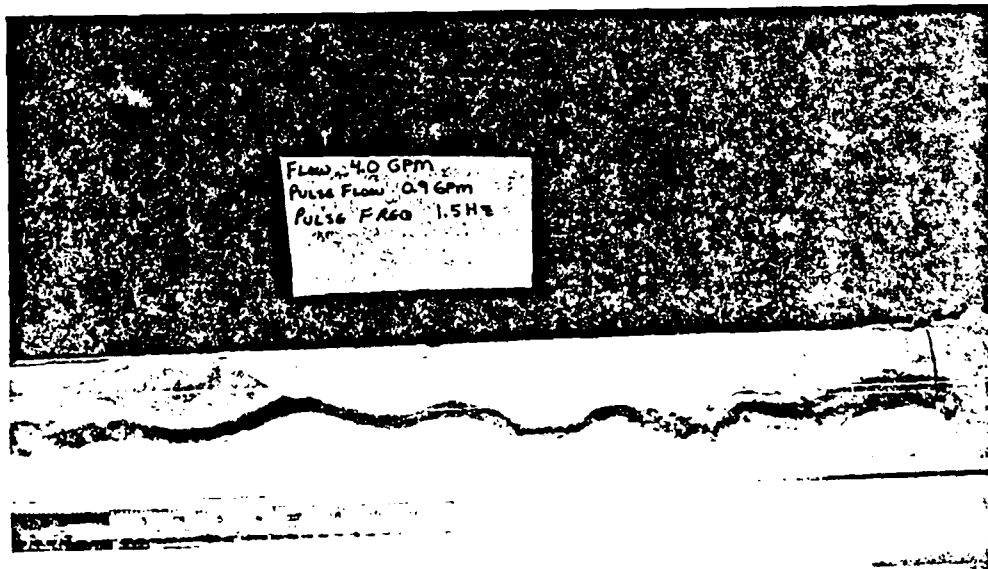


Figure 11. Short Wave Length Helical Waves Superimposed on the Vortex Core Due to Low Frequency Pulsing.

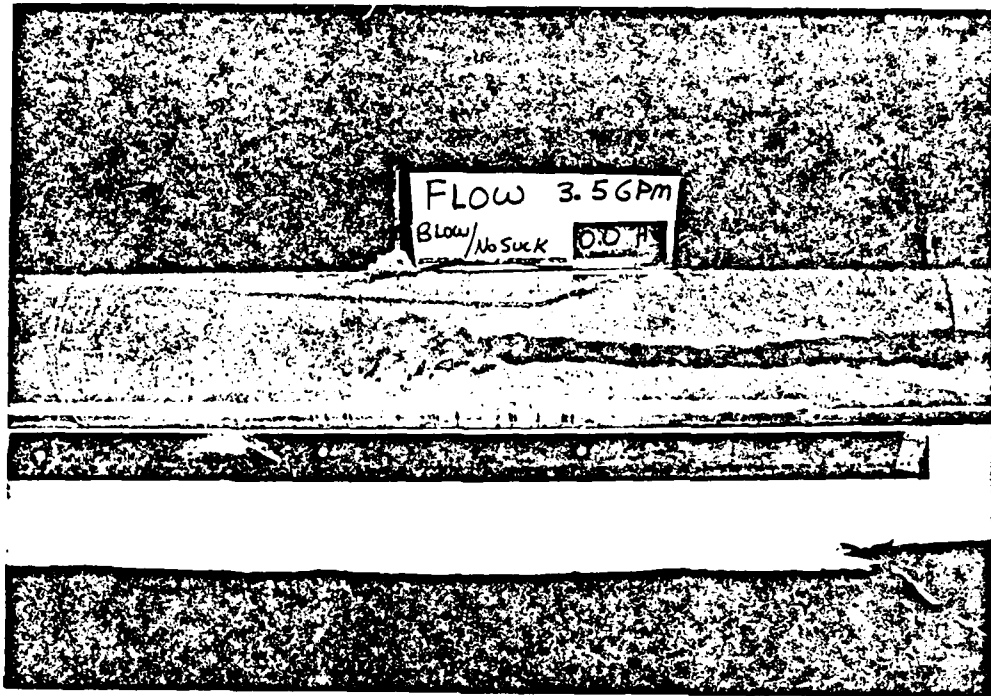


Figure 12a. The Location of Vortex Burst is in the Throat for No Forcing.

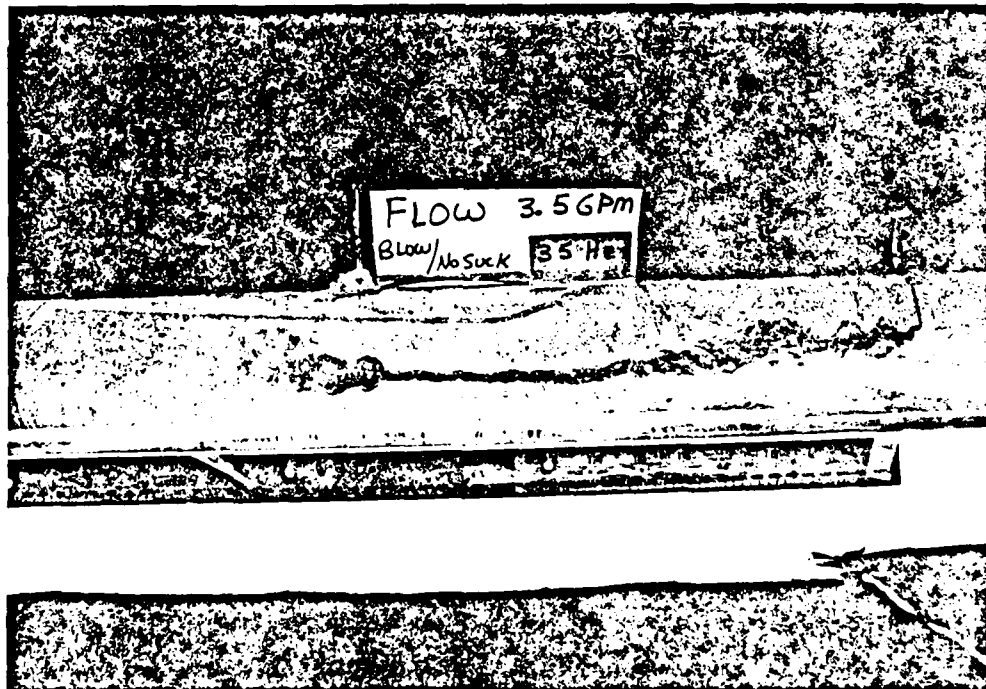


Figure 12b. Pulsing at 35 Hz Delays the Vortex Burst.

Flow Rate of 3.5 GPM

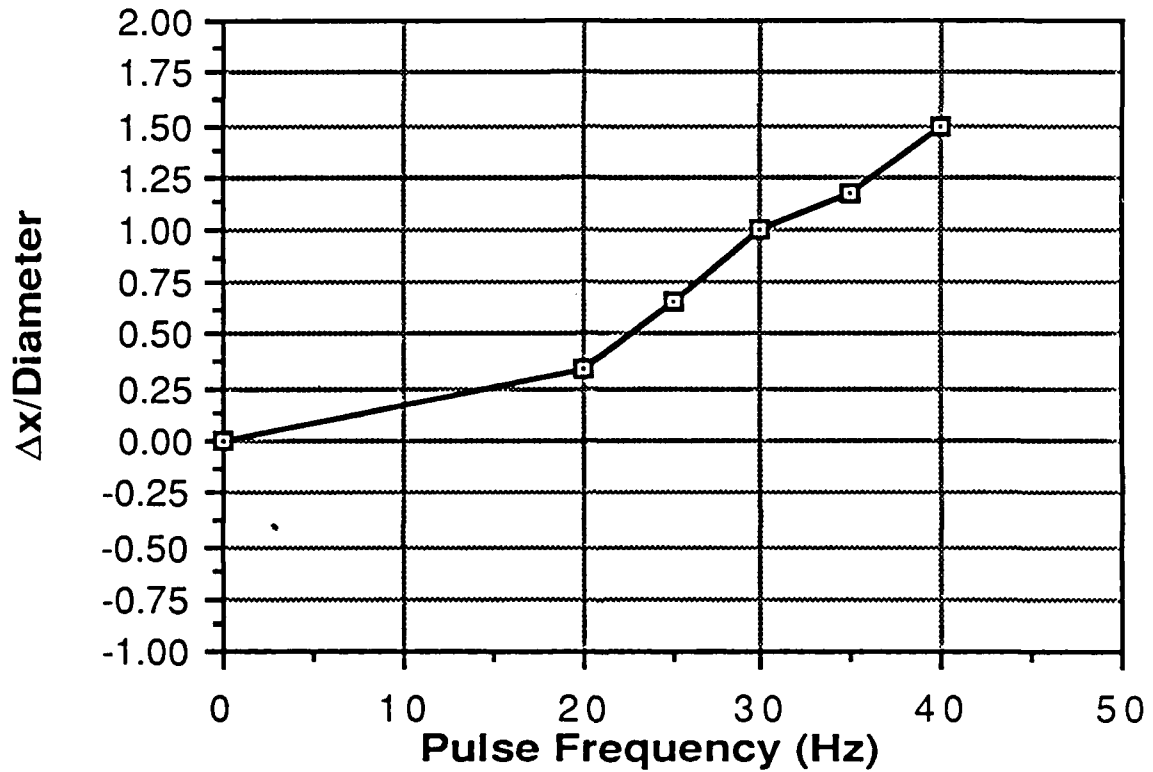


Figure 13a. Plot Showing $\frac{\text{DISPLACEMENT}}{\text{DIAMETER}}$ vs. PULSE FREQUENCY for a Flow Rate of 3.5 GPM.

Flow Rate of 4.0 GPM

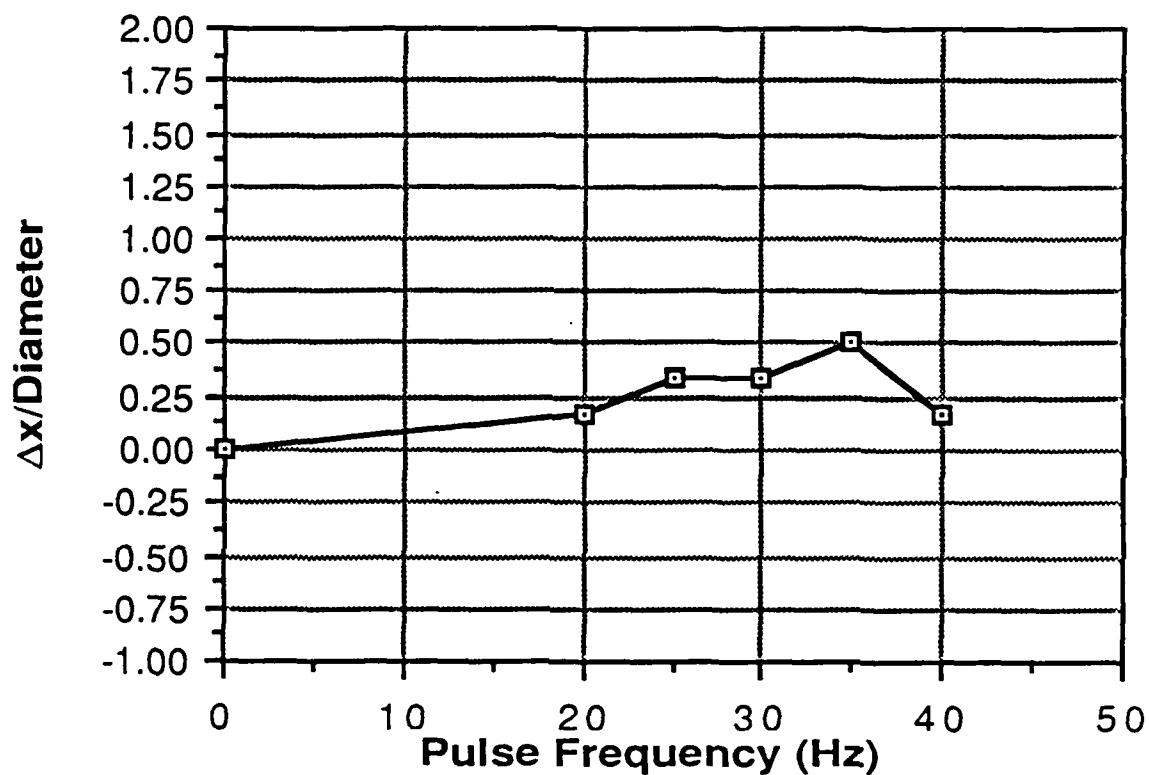


Figure 13b. Plot Showing $\frac{\text{DISPLACEMENT}}{\text{DIAMETER}}$ vs. PULSE FREQUENCY for a Flow Rate of 4 GPM.

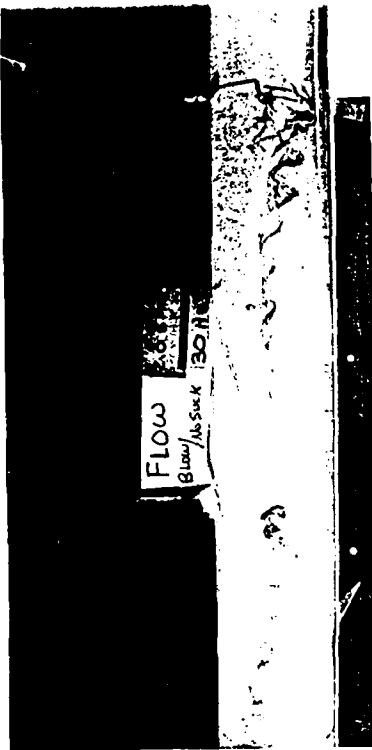


Figure 14a.

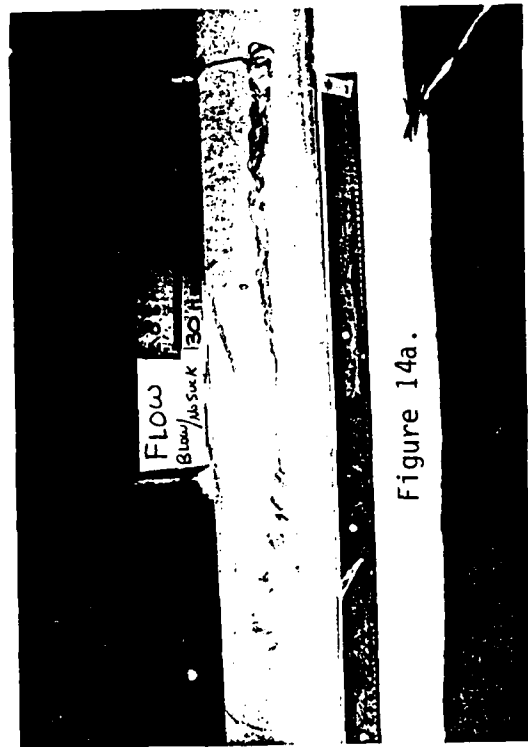


Figure 14b.

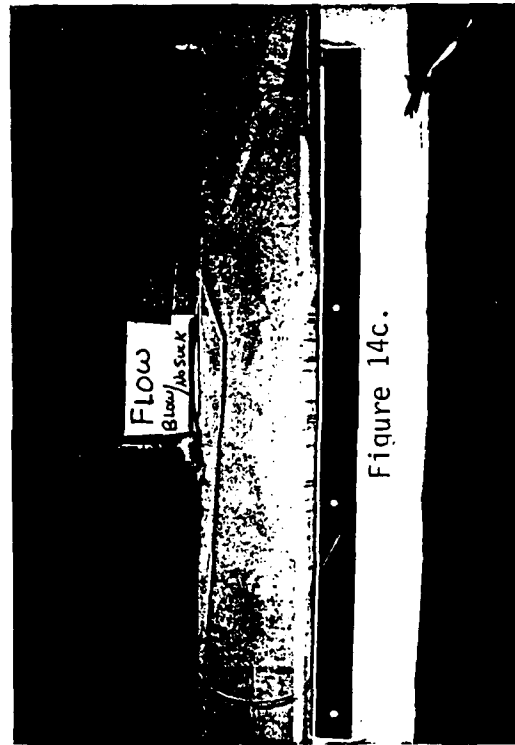


Figure 14c.

Figure 14. Sequence of Photos Showing Degeneration of Vortex Core Once Blowing at 30Hz is Initiated.

For a free vortex steady axisymmetric incompressible flow, using cylindrical coordinates r, θ, z with velocity components u, v and w respectively, if the axial gradients are small compare with radial gradients and $v \ll w$, then it can be shown that $\frac{1}{\rho} \frac{\partial p}{\partial r} = \frac{v^2}{r}$. That is: for an incompressible steady vortex, the axial velocity component u is coupled with the azimuthal component v solely through the axial variation of centrifugal force. Batchelor identified this effect as the key to the understanding of either the inviscid generation of strong axial motion or their subsequent indirect modification by viscosity. The decay of the swirling motion is to increase the pressure in the vortex core and consequently decrease the axial velocity there.

In an unsteady manner similar relationship is expected to exist, that is: we can extend the above idea to quasi-unsteady flows. The utility of this concept in terms of excitation of a vortex using periodicity in the axial direction over a wing was discussed earlier. Yao et al. and Rockwell have also demonstrated that by applying suction at the point of vortex burst and then moving the suction tube downstream the burst location is removed downstream for a few diameters.

A steel tube inserted from the downstream can be positioned at the burst location (see Figure 15). If suction is applied to the steel tube, then the vortex burst can be eliminated as shown in Figures 16 and 17. While the suction is applied, the steel tube can be pulled downstream for some length before the vortex burst reappears. The length that the vortex burst can be moved into the downstream by suction, depends on the pressure gradient. If the divergence angle is small, the pressure gradient is also small, then the delaying length for vortex burst can be expected to be longer than the delay length observed for a larger divergence angle. The divergence angle in the present study is 4.8 degrees in comparison with the 3.4 degrees used by Yao et al.

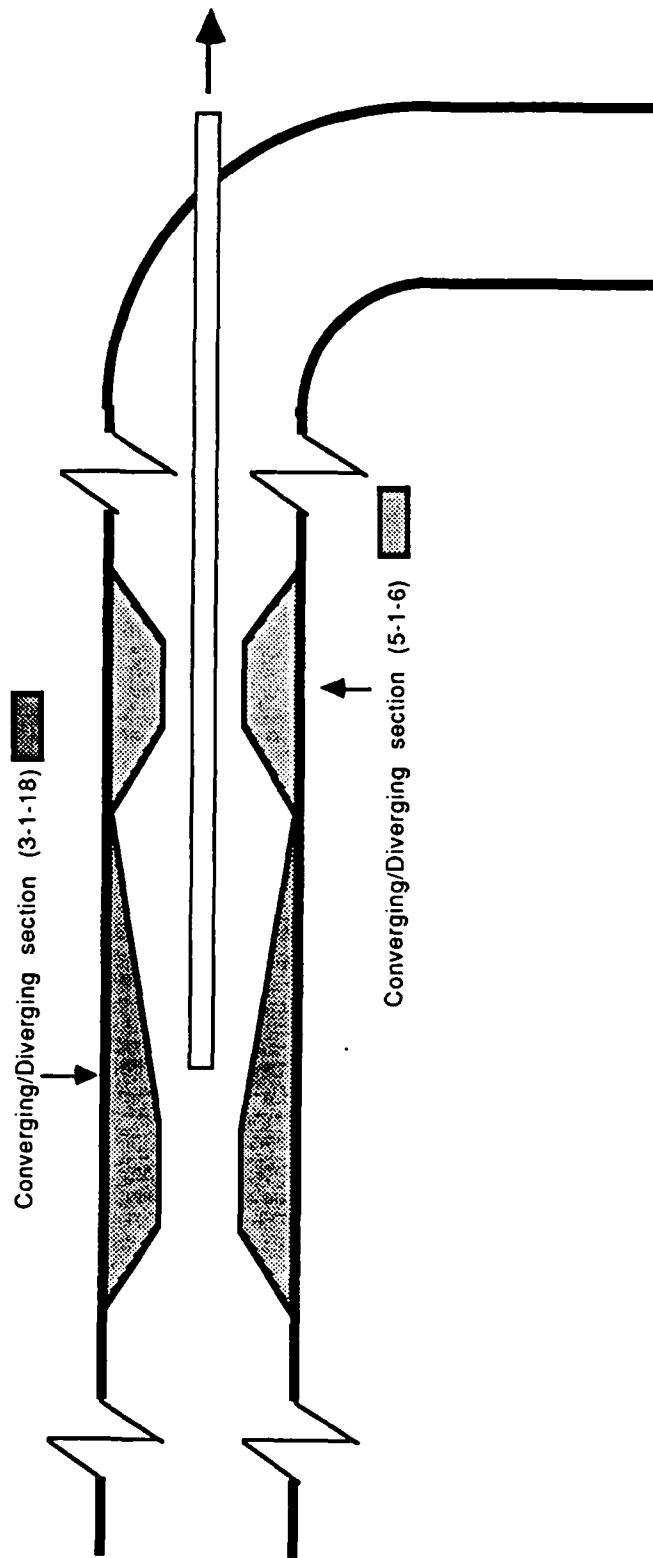


Figure 15. Downstream Suction Experimental Set-Up.

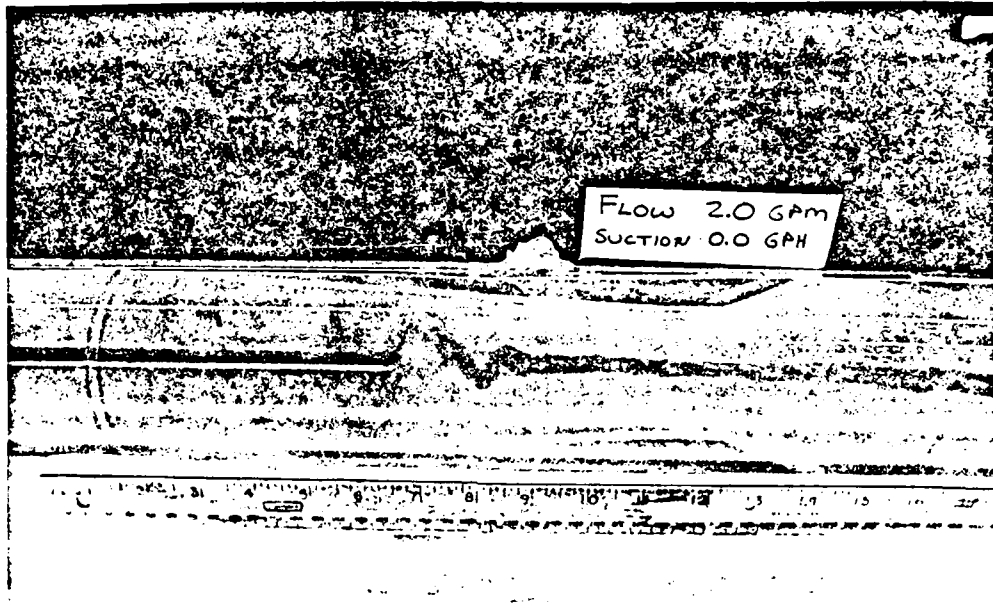


Figure 16a. Vortex Burst Pattern With No Suction Applied.

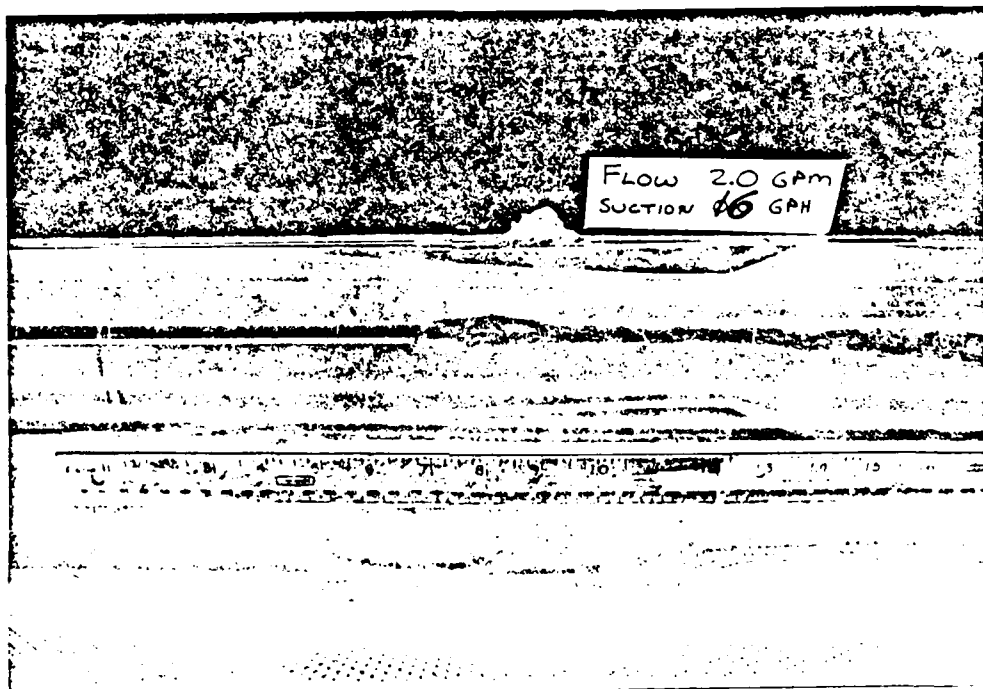


Figure 16b. Vortex Burst Eliminated by Downstream Suction.

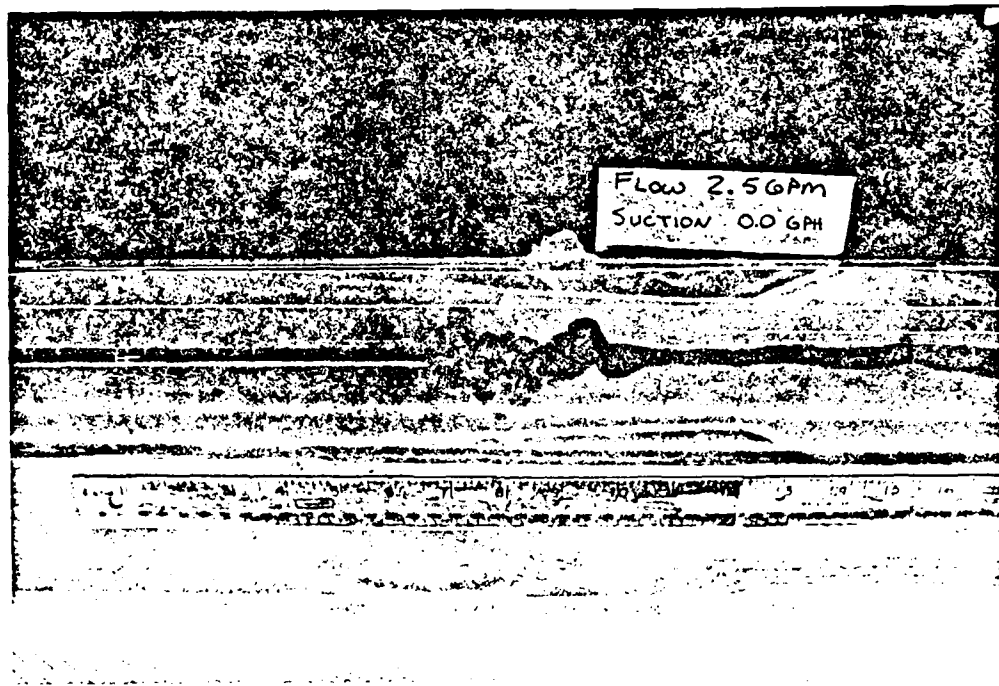


Figure 17a. Vortex Burst Pattern With No Suction Applied.

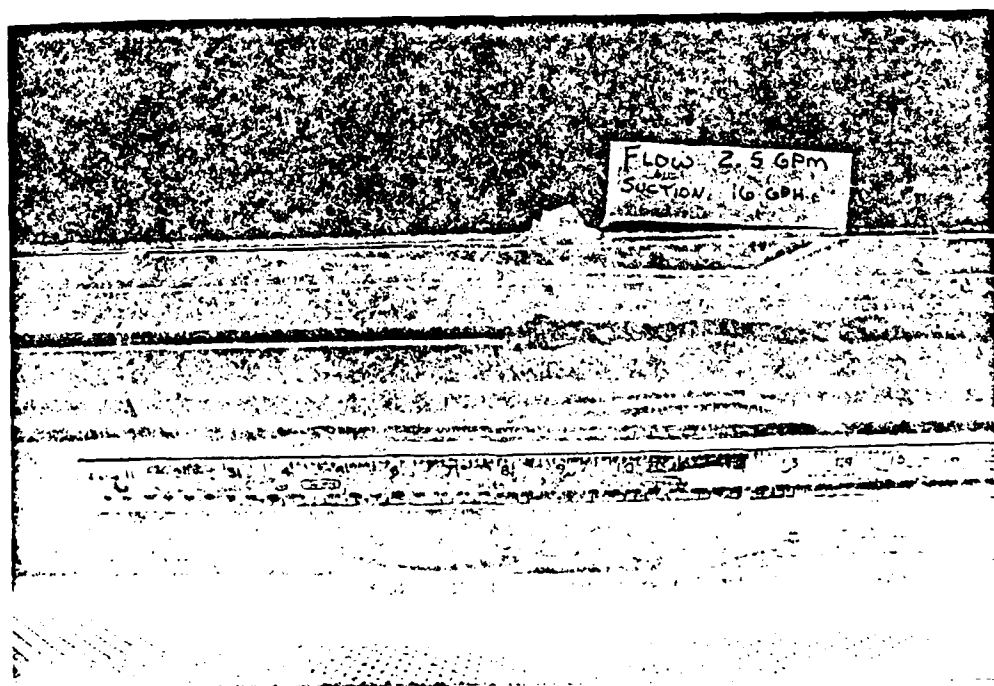


Figure 17b. Vortex Burst Eliminated by Downstream Suction.

VI. Conclusions

A vortex flow established in a vortex tube is documented through measurements and visualization to identify the vortex core and its state. Once a steady vortex flow is established, forcing was introduced to either promote or delay the vortex burst. Axial and circumferential forcing were used in this study. Forcing was provided by periodic blowing and/or blowing suction combination. For the blowing/suction arrangement, net mass flow into the core is nearly zero.

The following flow phenomenon are observed:

- As a result of blowing in the center of the core downstream of the generator section, the core becomes wavy. The helical waves on the core have a relatively long wave length.
- As a result of forcing at low frequencies, helical waves were superimposed on the core. These helical waves had short wavelengths corresponding to the forcing frequencies.
- Forcing at higher frequencies resulted in interactions with the vortex core and caused a delay in the location of vortex burst in the tube.
- Changes in the vortex breakdown position as a function of the reduced frequency, $k = \frac{fD}{U_m}$, are analyzed and correlated for the two types of disturbances and for selected flow parameters.
- Under certain conditions, as observed by flow visualization, forcing resulted in the strengthening of the vortex core and/or in the destruction of the vortex core; which seemingly produced the opposite effect.

Further work is recommended to extend the present observation to compressible flows and with quantitative measurements. Due to constraints on resources these were not performed during this preliminary study.

VII. References

- Batchelor, G. K., "Axial Flow in Trailing Line Vortices," J. Fluid Mech. (1964) 20, Part 4, pp. 645-658.
- Bellamy-Knights, P. C., "A Note on Vortex Breakdown in a Cylindrical Tube," Trans. ASME I, J. Fluid Engng. (1976) 98, p. 322.
- Burggraf, Odus R. and Foster, M. R., "Continuation or Breakdown in Tornado-Like Vortices." Journal of Fluid Mechanics (1977) 80, pp. 685-703.
- Chanaud, R. C., "Observations of Oscillatory Motion in Certain Swirling Flows," J. Fluid Mech. (1985) 21, Part 1, pp. 111-127.
- Chung, T. J. and Sohn, J. L., "Interactions of Coupled Acoustic and Vortical Instability," AIAA Journal (1986) 24, pp. 1582-1596.
- Eramo, R. S., "Effect of Forced Disturbances on the Vortex Burst," M.S. Thesis, UTSI, December 1989.
- Escudier, M. P., Bornstein, J. and Zehnder, N., "Observation and LDA Measurements of Confined Turbulent Vortex Flow," J. Fluid Mech. (1980) 98, Part 1, pp. 49-63.
- Escudier, M. P. and Zehnder, N., "Vortex Flow Regimes," J. Fluid Mech. (1982) 115, pp. 105-121.
- Escudier, M. P. and Keller, J. J., "Recirculation in Swirling Flow: A Manifestation of Vortex Breakdown." AIAA Journal (January 1985) 23, pp. 111-116.
- Faler, J. H. and Liebovich, S., "An Experimental Map of the Internal Structure of a Vortex Breakdown," J. Fluid Mech. (1978) 86, Part 2, pp. 313-335.
- Gutmark, E., Shadow, K. C., Wilson, K. J. and Bicker, C. J., "Acoustic Radiation and Flow Instabilities in Low Supersonic Circular and Elliptic Jets," AIAA, 11th Aeroacoustics Conference, Sunnyvale, CA, AIAA-87-2696.
- Holman, J. P. and Moore, G. D., "An Experimental Study of Vortex Chamber Flow," Trans. ASME. D, J. Basic Engng. (1961) 83, p. 632.
- Hussain, A.K.M.F., Recent Advances in Aerodynamics, ed. by A. Krothpalli and C. A. Smith, Springer Verlag, 1986, 205.

- Ikeda, T., Sakata, M. and Kikuchi, K., "An Experimental Study on Vortex Breakdown in Straight and Divergent Pipes," J. Fac. Engng. (1974) Shishu Univ., Japan 36, p. 1.
- Ito, T., Suematsu, Y., and Hayase, T., "On the Vortex Breakdown Phenomena in a Swirling Pipe-Flow." Memoirs of the Faculty of Engineering Nagoya University (1985) 37, pp. 117-172.
- Jones, J. P., "An Examination of the Hydraulic Jump Theory of Vortex Breakdown" A.A.S.U., No. 265, March 1966 (Typewritten).
- Kelvin, Lord, "Vibrations of a Columnar Vortex," Philos. Mag. (1880) 10, p. 155.
- Krause, E., Menne, S., and Liu, C. H., "Initiation of Breakdown in Slender Compressible Vortices." 10th International Conference of Numerical Methods in Fluid Dynamics (June 23-27, 1986/Beijing, China).
- Kuroda, H., "An Experimental Study of Temperature Separation in Swirling Flow," Ph.D. Dissertation, University of Tennessee, Dec. 1983.
- Kurosaka, M., "Vortex Whistle: an Unsteady Phenomenon in Swirling Flow and Its Effects on Steady Flow Field," AIAA-81-0212.
- Liebovich, S., "Vortex Stability and Breakdown: Survey and Extension," AIAA J. (1983) 22, No. 9, pp. 1192-1206.
- Liepmann, H. W., Brown, G. L. and Nosenchuck, D. M., "Control of Laminar Instability Waves Using a New Technique," J. Fluid Mech. (1982) 118, pp. 187-200.
- Liu, C. H., Krause, Egon, and Ting, Lu., "AIAA-85-1556 Vortex-Dominated Flow with Viscous Core Structure (Invited Paper)," AIAA 18th Fluid Dynamics and Plasma-Dynamics and Lasers Conference (July 16-18, 1985/Cincinnati, Ohio).
- Menne, S., "Simulation of Vortex Breakdown In Tubes," AIAA-88-3573-CP, pp. 164-171.

- Nakamura, Y., Leonard, A., and Spalart, P. R., "AIAA-86-1074 Internal Structure of a Vortex Breakdown," AIAA/ASME 4th Fluid Mechanics, Plasma Dynamics and Lasers Conference (May 12-14, 1986/Atlanta, Georgia).
- Owen, J. M. and Pincombe, J. R., "Vortex Breakdown in a Rotating Cylindrical Cavity," J. Fluid Mech. (1979) 90, pp. 109-127.
- Peckham, D. H. and Atkinson, S. A., "Preliminary Results of Low Speed Wind tunnel Tests on a Gothic Wing of Aspect Ratio 1.0," Aeronautical Research Council C. P. 508, (1957) p. 16, quoted in T. Ito, Y. Suematsu, and T. Hayase, "On the Vortex Breakdown Phenomena in a Swirling Pipe-Flow," Memoirs of the Faculty of Engineering Nagoya University (1985) 37, p. 135.
- Spall, R. E., Gatski, T. B., and Grosch, C. E., "(NASA-CR-178232) On a Criterion for Vortex Breakdown," ICASE Report No. 87-3 (January 1987).
- Suzuki, M., "Theoretical and Experimental Studies on the Vortex Tube," Scientific Papers of Institute of Physical and Chemical Research (Tokyo) (1960) 54, No. 1, pp. 43-87.
- Vakili, A. D., Wu, J. M. and Bhat, M. K., "High Angle of Attack Aerodynamics of Excitation of the Locked Leaside Vortex," Advanced Aerospace Aerodynamics (1988) SAE-SP-757.
- Vakili, A. D., "Organizing Shear Flows by Excitation and Tunable Boundaries." Proposal, The University of Tennessee Space Institute, unpublished. 1985.
- Yao, M., Pan, J., Huang, X., and Wu, J., "AIAA-89-1000 Delaying Vortex Breakdown Waves," AIAA 2nd Shear Flow Conference (March 13-16, 1989/Tempe, Arizona).

FINAL REPORT

AFOSR - Research Initiation Program
Western Michigan University
Kalamazoo, Michigan 49008

Title of Research Project: Large Space Structure Parameter Estimation

Principal Investigator: Gurbux S. Alag, Professor
Dept. of Electrical Engineering
Western Michigan University
Kalamazoo, MI 49008
(616) 387-4057

Duration of Project: December 21, 1987 to December 20, 1988

ABSTRACT

There has been a great deal of interest in experimental modal analysis as a part of an integrated computer aided engineering approach to the solution of structural dynamics problems. Experimental modal analysis refers to the process of determining the modal parameters (frequencies, damping factors, and modal vectors) of a linear, time-invariant system by way of an experimental approach. One common reason for the experimental approach is the verification of the results of the analytical approach, such as finite element analysis.

The determination of modal parameters from experimentally measured data involves the use of parameter estimation techniques. The estimation methods are changing due to the transfer of existing technology from the other fields where estimation techniques have been more commonly used over the past several decades. Various parameter estimation techniques to determine modal parameters from experimentally measured data were investigated as possible candidates for practical implementation.

1. INTRODUCTION

Economic, regulatory, and environmental considerations are forcing industries to build products which weigh less, operate reliably and efficiently, and run with less noise and vibration than in the past. This has led to the use of better testing and analysis tools to assist the design engineers in meeting stringent performance requirements. Many industries have turned to advanced structural dynamics testing for better understanding of structural dynamics¹.

Experimental modal analysis is one such area of dynamics testing and refers to the process of determining the modal parameters using an experimental approach. Experimental modal analysis allows the verification and adjustment of the mathematical model of the structure, is used to locate structural weak points, and eliminate noise or vibration. The objective of all dynamics testing procedure is to excite and identify the modes of vibration of structure under test².

Two different methods of modal testing are used for testing structures.

- * Normal mode method
- * Transfer function method

The transfer function method is faster, easier to perform, and cheaper to implement than the normal mode method and has gained much popularity. In this method, frequency response functions are measured using excitation at single, or multiple points. A very simple and fast method is impact

testing, where a hand held hammer with a load cell mounted on it is used to impact the structure. Accelerometers mounted on the structure measure the response enabling the determination of the frequency response function.

An important phase of the frequency response method is the estimation of modal parameter from the measured data. The frequency response functions are used as input to a modal parameter estimation process to determine the modal parameters. Modal parameter estimation is the estimation of frequency, damping, and modal coefficients from the frequency response function. Many parameter estimation schemes have been developed and changing rapidly due to transfer of existing technology from other fields where estimation methods have been more common^{3,4}.

Several planned USAF Space Systems will pose serious vibration control problems when very precise vibration control of large flexible structures in presence of on board noise is performed. The accuracy of vibration control is dependant on the accuracy of the mathematical structural model. A popular approach for determination of structural model is to perform system identification. There is a proliferation of identification techniques currently being advocated. It is, therefore, essential that various system identification schemes be evaluated in their application to large flexible space structures.

The Air Force Astronautics Laboratory (AFAL), Edwards Air Force Base, is currently developing an in-house capability for experimentally evaluating new techniques in system identification and vibration control for large flexible space structures. Towards this end, a cantilevered two dimensional flexible grid structure has been constructed. Suitable equipment which will enable on-line and off-line identification experiments to be performed, has also been acquired.

Evaluation of various parameter estimation techniques with regard to their implementation and quality of result was undertaken. The work was done at AFAL by the principal investigator during the Summer of 1988.

11. MODAL PARAMETER ESTIMATION

Modal parameter estimation is the estimation of frequency, damping, and modal coefficients from the measured data. The measured data may be either in raw form or in processed form such as frequency response. Regardless of the form of the measured data, the modal parameter techniques have been divided into two categories: (1) Single degree-of-freedom (SDOF) approximations, and (2) multiple degree-of-freedom (MDOF) approximation.

Over the last twenty years, many modal parameter estimation methods have been developed. Often, it seems that these methods are very different and unique. In reality, all

which are in need of analytical model verification. The determination of modal parameters from experimentally measured data involved the use of parameter estimation techniques. With the advent of small, dedicated mini-computer systems it is possible to measure frequency response information and computationally determine the modal parameters. As a result of this improved computational capability, a large number of computational algorithms have been developed in recent years for computing modal information. Numerous parameter estimation methods are available and each has its advantages and disadvantages, and as such, have their own ardent devotees.

A limited study was carried out in respect of evaluation of various parameter estimation techniques during Summer 1987. The study was continued to investigate further estimation techniques and evaluate the ease of difficulty in implementing these techniques and compare the qualities of their results.

The following parameter estimation schemes have already been implemented:

- * Single degree of freedom approximation: In most modal parameter estimation schemes, the typical procedure is to first estimate the eigenvalues (natural frequencies and damping factors) and then to estimate the eigenvectors (modal coefficients). The simplest modal estimation procedure is to measure the magnitude of frequency response at one of the natural frequencies. The natural frequency

for this simple case can be determined by choosing the frequencies where the magnitude of the frequency response reaches a maximum. The damping factor and modal coefficients can be estimated with known techniques⁴.

- * The second method, a MDOF approximation is the Ibrahim time domain method developed to extract the modal parameters from damped complex exponential response information⁵.
- * The third method involves the development of a linearized least squares algorithm. The parameter estimation is done in two steps. In the first step, the frequencies and damping factors are calculated. Using this information, the modal vectors are obtained in the next step.
- * During the Summer of 1988, the principal investigator spent two months at Air Force Astronautic Laboratory, Edwards Air Force Base, Edwards, CA. The laboratory has a software package "IDEAS" developed by Structural Dynamics Research Corporation. The software enables the use of many modal analysis techniques. The capability of the package enables the use of following techniques:

Single-Degree-of-Freedom Technique-

- * 2nd Degree Polynomial Fit
- * Circle Fitting

Multiple-Degree-of-Freedom Techniques

- * Complex Exponential

* Polyreference

* Direct Parameter Estimation

Test data from experimental set-up at AFAL was used to demonstrate the use of the software package "IDEAS". The result obtained for different methods were compared and additional work needs to be done in the area of estimation of modal vectors. "IDEAS" has the capability to enable the determination of mode shapes.

REFERENCES

1. Ramsey, K. A., "Effective Measurements for Structural Dynamics Testing, Part 1", Sound and Vibration, Nov. 1975, pp. 24-35.
2. Richardson, M. K., "Measurement and Analysis of the Dynamics of Mechanical Structures", Notes on course on Modal Analysis, University of Cincinnati, 1987.
3. Allemang, R. J., Brown, D. L., "A Review of Modal Parameter Estimation Concepts", *ibid.*
4. Brown, D. L., R. J. Allemang, R. Zimmerman, M. Mergeay, "Parameter Estimation Techniques for Modal Analysis", SAE paper 790221, 1979.
5. Ibrahim, S. R., Mikulcik, E. C., "A Method for Direct Identification of Vibration Bulletin, Vol. 47, Part 4, 1977, pp. 183-198.
6. "IDEAS" - Users Manual - Structural Dynamics Research Corporation.

FINAL REPORT NUMBER 16
INTEGRATED STRAIN MEASUREMENT IN COMPOSITE
MEMBERS USING EMBEDDED CONSTANTAN WIRE
PENDING APPROVAL
Dr. Clarence Calder
210-9MG-076

1989 USAF-UES Research Initiative Program

Sponsored by the
AIR FORCE OFFICE OF SCIENTIFIC RESEARCH
Conducted by the
Universal Energy Systems, Inc.
Final Report

Calibration of the Infrared Spectropolarimeter

Principal	
Investigator:	Russell A. Chipman
Co-Principal	
Investigator:	David B. Chenault
Prepared by:	David B. Chenault
Academic Rank:	Graduate Student
Department and	Department of Physics
University:	University of Alabama in Huntsville
Research Location:	Huntsville, AL 35899
USAF Researcher:	Mr. Dennis Goldstein
Date:	December 19, 1989
Contract No.	P.O. S-210-9MG-026

Calibration of the Infrared Spectropolarimeter

by

David B. Chenault

ABSTRACT

The infrared spectropolarimeter under development at the University of Alabama in Huntsville has been used to measure the calibration spectra of infrared polarizers. Calibration spectra of several infrared retarders, including the retarders used in the Mueller matrix polarimeter, have also been measured. Initial calibration Mueller matrix measurements have been made. The source and detector stability have been characterized. This report presents the work completed on the spectropolarimeter and presents in detail the development of a technique to measure the linear diattenuation and retardance of samples using a pair of linear polarizers.

1 Introduction

This final report presents the work completed under the Research Initiative Program on the spectropolarimeter at the University of Alabama in Huntsville. The report consists of two parts: a brief summary of calibration steps necessary for accurate measurements with the spectropolarimeter, and the detailed development and results of measurements of linear diattenuation and linear retardance.

There is currently a shortage of data on electrooptical materials in the infrared. Information on materials in this spectral region is becoming increasingly important as seeker technology for Air Force tactical applications evolves. One experimental technique to acquire this information is Mueller matrix infrared spectropolarimetry. The polarization properties of a sample are completely specified if the Mueller matrix of that sample is known. Ideally the Mueller matrix, which is a function of wavelength, should be known for a large region of the infrared spectrum, but for many key materials data at laser wavelengths is still not available. Spectropolarimetry acquires data on samples at laser wavelengths and regions of the spectrum where laser sources do not operate.

The air-to-air guidance section located at the Air Force Armament Laboratory at Eglin Air Force Base has long been concerned with the development of electrooptical materials for the infrared because of their application to advanced sensor systems. Improved spatial light modulators and programmable masks will become necessary in the near future for Air Force tactical missile designs. The construction of the spectropolarimeter at the University of Alabama in

Huntsville is a positive step in the process of characterizing the basic polarization properties of electrooptical materials. The resulting data base is providing key information for infrared modulator development and characterization.

There are several issues that need to be addressed before the instrument can produce accurate and reliable results. These issues include spectral calibration of the polarizing elements of the polarimeter, quantification of the instrumental polarization, and stability of the source and detector over time. These effects have been studied under the Research Initiative Program and are presented in the next section.

2 Objectives and Results

The objectives of the research this year included calibration of the instrument in the process of achieving a fully operational Mueller matrix spectropolarimeter. Calibration of the polarizing elements to be used in the Mueller matrix polarimeter comprised a large part of these efforts. Source and detector stability is a concern since the large number of spectra required to obtain the full Mueller matrix necessitate long measurement times.

The largest errors in spectropolarimetric measurements are believed to arise from the nonideal properties of the polarizing elements. The polarizing and retarding properties are functions of wavelength. In addition, polarizers may contain retardance, and retarders may be polarizing, or diattenuating.

Calibration spectra of parallel and crossed polarizers are shown in Figures 1 and 2. These spectra were ratioed to the spectrum of a single polarizer in the same orientation (the second polarizer of the pair was simply removed) to eliminate instrumental absorption and instrumental polarization effects. Further calibration requires a third polarizer. A third polarizer will be available early in 1990 and additional calibration will be conducted using the data reduction and measurement scheme described in the second half of this report.

The calibration spectra of the retarders used in the Mueller matrix measurements were calculated using the Fourier technique described beginning in the next section. The results of these and other samples will be presented below.

Source and detector stability measurements were made in order to determine the rate of change of the output signal as a function of time. This effect was a concern in the laser polarimeter at Eglin Air Force Base and suggested a similar study for the spectropolarimeter. Measurements were made over approximately eight hours beginning at the time the source was turned on and the liquid nitrogen dewar on the detector was filled. The change in the output signal at a single wavelength as a function of time is shown in Figure 3. As a result of these measurements it was determined that a two hour minimum is required for the source and detector to stabilize. In addition, measurements lasting thirty minutes or less can be made without adjustment for the linear drift apparent on the right side of the plot.

Collaboration between Mr. Goldstein and researchers at the University of Alabama in Huntsville included sharing of algorithms for the correction of small azimuthal and retardance variations. Data with no sample was collected and reduced using these algorithms. The Mueller matrix elements for this calibration measurement should be ones along the diagonal and zeros elsewhere at all wavelengths. As can be seen in Figure 4, the spectra for the Mueller matrix elements do not agree with theory. The large amount of error in retardance is the most likely reason for this error and suggests that the small angle approximations made for this data reduction are violated. Further work on this data reduction is required.

3 Introduction to Linear Diattenuation and Retardance Measurements

The precision calibration of polarizing elements and measurements of potential modulator materials is becoming more important as these devices are utilized in ever increasing numbers [1],[2]. For many optical systems it is also important to know polarization characteristics as a function of wavelength. A technique of measuring linear diattenuation and linear retardation spectra of samples has been employed in an infrared spectropolarimeter, a spectrometer modified by the inclusion of a polarimeter in the sample compartment [3],[4]. The sample is placed in a rotary stage between fixed polarizers. The rotary stage is fixed so that the incident beam remains normal to the rotating sample. A set of spectra are taken with the sample in a series of predetermined orientations. The set of spectra are reduced one wavelength at a time to produce

diattenuation, retardation, and birefringence spectra. These spectra may be used to calibrate polarizing optical elements or to investigate potential modulator materials.

This measurement technique is a variation of previous polarimetric and ellipsometric measurements which have rotated polarizers or retarders in a harmonic fashion [5],[6],[7],[8]. The frequency components of the modulated signal transmitted to the detector are obtained by Fourier analysis and are related to the polarization properties of the sample. In the technique presented here the sample is rotated between fixed polarization elements as shown in Figure 5. Diattenuation and retardance are determined by Fourier analysis of the modulation due to the rotating sample.

The advantage of rotating the sample while holding the polarizers fixed is that instrumental polarization effects are largely eliminated if the polarizers are nearly ideal. Large angles of incidence on fold mirrors and the beamsplitter produce instrumental polarization [5],[9]. Fixed polarizers send the same polarization state to the sample and to the optics following the polarimeter thus eliminating any modulation of the signal transmitted to the detector due to instrumental polarization.

The data reduction and instrumental configuration for measuring diattenuation and retardation spectra are described in Section 5. A monochromatic analysis is presented with a generalization to the dependence on wavelength. The spectropolarimeter configuration and

operation are described in Section 6. Diattenuation and retardation spectra of two achromatic retarders, and a multiple order, $7\lambda/4$ waveplate are presented in Section 7.

4 Background

Many materials and optical devices simultaneously exhibit several polarization altering properties. For example, a birefringent material may be partially linearly polarizing, or a wire grid linear polarizer under strain may exhibit strain birefringence. In such instances a sample acts as a linearly dichroic retarder [10]. In many cases, it may be assumed that the principal axes of linear diattenuation are coincident with the fast and slow axes of retardance. This may occur, for example, in a waveplate where the crystalline anisotropy that gives rise to the birefringence may cause attenuation of a linearly polarized beam parallel or perpendicular to the axis of the anisotropy. The assumption that the axes are coincident is made in this treatment.

Diattenuation, the property of having a transmittance that is dependent on the incident polarization state, is defined [10]

$$\mathcal{D} = \frac{\rho_1 - \rho_2}{\rho_1 + \rho_2} \quad (1)$$

where ρ_1 and ρ_2 are the principal intensity transmittances for linear polarization states. For an ideal polarizer, $\mathcal{D} = 1$, and for a partial polarizer $0 < \mathcal{D} < 1$.

The retardance δ is the difference in phase between the phases δ_1 and δ_2 of the orthogonal eigenpolarization states [9]. The absolute phases δ_1 and δ_2 are lost since these are noninterferometric intensity measurements. All phase information is contained in the retardance $\delta = |\delta_1 - \delta_2|$. The birefringence of single element samples for normally incident light $\Delta n = |n_o - n_e|$, where n_o and n_e are the ordinary and extraordinary indices of refraction, is determined from the retardance

$$\Delta n = \frac{\lambda}{2\pi d} \delta \quad (2)$$

where d is the thickness of the sample and λ is the wavelength.

The polarimeter described here consists of two polarizers and detects the first three elements s_0 , s_1 , and s_2 of the transmitted Stokes vector $\vec{S} = (s_0, s_1, s_2, s_3)^T$. The fourth element of the Stokes vector s_3 , which represents circularly polarized light, cannot be detected. The circular diattenuation and circular retardance of the sample, represented by the fourth row and column of the Mueller matrix, cannot be found with this polarimeter.

In the Jones calculus, the magnitudes of the elements of the Jones matrix are determined, but since the intensity measurements are noninterferometric, the phases of three elements are not determined absolutely but relative to the fourth [6]. Circular polarization effects are not found.

Circularly polarized light incident on a polarizer is transmitted as linearly polarized light but at some fraction

of the incident intensity. Coupling of the linearly polarized light incident on the sample into circular light through circular diattenuation and retardance in the sample is therefore manifested as absorption in this polarimeter. This does not affect the measurements of linear diattenuation and retardance since these quantities are calculated from ratios which remove absorption effects. The terms diattenuation and retardance in the balance of this paper refer to linear diattenuation and linear retardance only.

5 Theory

This section describes the data reduction method for finding the diattenuation and retardance of a sample at a single wavelength and the straight forward extension to measurement of diattenuation and retardance spectra. The Jones calculus is used to model the spectropolarimeter and relate the sample characteristics to the output intensity. The diattenuation and retardation are derived in terms of the coefficients of the Fourier series which describe the intensity modulation of the polarimeter.

A sample with principal intensity transmittances ρ_1 and ρ_2 and phase delays δ_1 and δ_2 whose axes of birefringence and diattenuation are coincident is represented [11] by the Jones matrix J_S

$$J_S = \begin{pmatrix} \sqrt{\rho_1} \exp(-i\delta_1) & 0 \\ 0 & \sqrt{\rho_2} \exp(-i\delta_2) \end{pmatrix}. \quad (3)$$

The coordinate system is chosen so that the principal transmittance ρ_1 is along the x-axis. The system matrix J_{sys} for the sample at an angle θ between parallel polarizers as shown in Figure 5 is

$$J_{sys} = J_p R(-\theta) J_s R(\theta) J_p$$

$$= \begin{pmatrix} 1 & 0 \\ 0 & 0 \end{pmatrix} \begin{pmatrix} \cos\theta & -\sin\theta \\ \sin\theta & \cos\theta \end{pmatrix} \begin{pmatrix} \sqrt{\rho_1} \exp(-i\delta_1) & 0 \\ 0 & \sqrt{\rho_2} \exp(-i\delta_2) \end{pmatrix} \begin{pmatrix} \cos\theta & \sin\theta \\ -\sin\theta & \cos\theta \end{pmatrix} \begin{pmatrix} 1 & 0 \\ 0 & 0 \end{pmatrix} \quad (4)$$

$$= \begin{pmatrix} \sqrt{\rho_1} \cos^2\theta \exp(-i\delta_1) + \sqrt{\rho_2} \sin^2\theta \exp(-i\delta_2) & 0 \\ 0 & 0 \end{pmatrix}$$

where $R(\theta)$ is the rotation matrix and J_p represents a horizontal linear polarizer. The transmitted Jones vector $\vec{E}' = E_x' \hat{x} + E_y' \hat{y}$ with arbitrary incident Jones vector $\vec{E} = E_x \hat{x} + E_y \hat{y}$ is $\vec{E}' = J_{sys} \vec{E}$. The input intensity $|E_x|^2 + |E_y|^2 = 1$ is normalized. The transmitted intensity $I(\theta) = |E_x'(\theta)|^2 + |E_y'(\theta)|^2$ as a function of sample orientation θ , after application of trigonometric identities and rearrangement of terms, is

$$I(\theta) = \frac{3}{8}\rho_1 + \frac{3}{8}\rho_2 + \frac{1}{4}\sqrt{\rho_1\rho_2}\cos\delta$$

$$+ \frac{1}{2}(\rho_1 - \rho_2)\cos 2\theta \quad (5)$$

$$+ \frac{1}{8}(\rho_1 + \rho_2 - 2\sqrt{\rho_1\rho_2}\cos\delta)\cos 4\theta.$$

where $\delta = |\delta_1 - \delta_2|$. Eqn. 5 is a Fourier series in θ with coefficients

$$\begin{aligned}
\alpha_0 &= \frac{3}{8}\rho_1 + \frac{3}{8}\rho_2 + \frac{1}{4}\sqrt{\rho_1\rho_2}\cos\delta, \\
\alpha_2 &= \frac{1}{2}(\rho_1 - \rho_2), \\
\alpha_4 &= \frac{1}{8}(\rho_1 + \rho_2 - 2\sqrt{\rho_1\rho_2}\cos\delta).
\end{aligned}
\tag{6}$$

The principal transmittances, ρ_1 and ρ_2 , and retardance δ are

$$\begin{aligned}
\rho_1 &= \alpha_0 + \alpha_4 + \alpha_2 \\
\rho_2 &= \alpha_0 + \alpha_4 - \alpha_2 \\
\delta &= \cos^{-1}\left(\frac{\alpha_0 - 3\alpha_4}{[(\alpha_0 + \alpha_4)^2 - \alpha_2^2]^{\frac{1}{2}}}\right).
\end{aligned}
\tag{7}$$

$$\tag{8}$$

The diattenuation (from Eqn. 1) is

$$\mathcal{D} = \frac{\alpha_2}{\alpha_0 + \alpha_4}.
\tag{9}$$

Birefringence spectra of single element devices are calculated from the retardance spectra and Eqn. 2.

The quantities α_0 , α_2 , and α_4 are determined by rotating the sample in increments of $\Delta\theta$ to a set of N angles $\theta_n = n\Delta\theta$, $n = 1, 2, \dots, N$, $N\Delta\theta = 360^\circ$, and $N \geq 10$. An intensity measurement is made at each θ_n . The series of intensity measurements may be expressed as a Fourier series

$$\begin{aligned}
I(\theta_n) &= b_0 + \sum_{n=1}^N (b_n \cos\theta_n + c_n \sin\theta_n) \\
&= \alpha_0 + \sum_{n=1}^N \alpha_n \cos(\theta_n - \phi_n)
\end{aligned}
\tag{10}$$

where $a_n^2 = b_n^2 + c_n^2$. The phase of the coefficients ϕ_n is

$$\phi_n = \frac{1}{n} \tan^{-1} \left(\frac{c_n}{b_n} \right). \quad (11)$$

The phase of the second harmonic ϕ_2 gives the orientation of the principal transmittance ρ_1 with respect to the x -axis. The phase of the fourth harmonic gives the orientation of the phase delay δ_1 within an integer multiple of $\pi/2$. The uncertainty is again a result of the nature of intensity measurements; absolute phase information is lost.

Only the dc term a_0 and the coefficients a_2 and a_4 in the Fourier series (Eqn. 10) are used to determine the diattenuation and retardance. The other harmonics $a_1, a_3, a_5, a_6, a_7, \dots$, which should be zero in the absence of noise and systematic errors, provide valuable information on the operation of the polarimeter. For example, beam wander, arising from the rotation of a sample with non plane parallel interfaces, couples strongly into the first harmonic a_1 and decreasingly into the higher harmonics. A nonzero value for a_1 suggests the presence of beam wander.

Diattenuation and retardance are functions of wavelength due to dispersion and absorption bands in the material. This wavelength dependence is easily incorporated into the derivation by allowing the principal transmittances ρ_1 and ρ_2 and the phases δ_1 and δ_2 in Eqn. 3 to become wavelength dependent. Eqns. 4 - 11 become functions of wavelength giving wavelength dependent diattenuation and retardance. Diattenuation and retardance spectra are obtained by making the intensity measurements as prescribed above but at a

number of wavelengths. The data is reduced in like fashion one wavelength at a time. The spectropolarimeter, an instrument capable of making polarimetric measurements at many wavelengths simultaneously, is described briefly in the next section.

6 Experimental

Figure 6 shows the optical configuration of the spectropolarimeter [3],[4]. It is a Fourier transform infrared spectrometer modified by the addition of a polarimeter in the sample compartment. A computer controls all functions of the instrument - data collection, data display, and data storage.

The polarimeter (shown in Figure 5) consists of two fixed wire grid polarizers. The polarizers have approximately 40% transmission of incident unpolarized light from 2.5 to 24 μm . The orientation of the polarizers is determined by rotating one polarizer. The phase of the second harmonic ϕ_2 (Eqn. 11) is used to determine the relative orientation of the polarizer (Section 5). The sample is mounted in a computer controlled rotary stage.

The operation of the spectropolarimeter proceeds as follows: the sample is set at the initial orientation and a spectrum is taken in the normal spectrometer fashion. The sample is rotated through $\Delta\theta$ and another spectrum is taken. This process is repeated until the required number of rotations and measurements are made. The data, placed in temporary storage in the spectrometer computer, is

transferred to a Micro-VAX. The Fourier coefficients and hence diattenuation \mathcal{D} and retardance δ are computed one wavelength at a time.

7 Results

In this section we present diattenuation and retardance spectra of three samples, a multiple plate achromatic retarder, a modified Fresnel rhomb achromatic retarder, and a multiple order quarter wave plate.

The first achromatic wave plate consists of two plates of different birefringent materials whose crystal axes are oriented at right angles to each other and to the optic axis of the instrument. The similarity in the dispersion curves results in a net retardance of nearly one quarter wave over the wavelength range 2.5 to 11 μm . Different materials have been used in similar designs in the visible and ultraviolet [12],[13],[14].

The retardance and diattenuation of the achromatic retarder were measured. Figure 7 shows the diattenuation over the effective transmitting region of the retarder. Figure 8 shows the measured retardance and theoretical prediction using published dispersion relations [15]. The retardance differs from the predicted value but remains largely achromatic out to 14.3 μm . Theoretical predictions for longer wavelengths could not be made because of the lack of birefringence data. Many factors could account for the discrepancy of the measured retardance from theory including misalignment of the fast axes of the two plates, coating and surface imperfections, multiple reflections, or thickness errors. In spite of the variation of retardance with

wavelength, the retarder is superior to conventional single plate designs (cf. Fig. 12) and is useful for many applications, particularly achromatic polarimetry.

Figure 9 shows the second achromatic retarder design, a modified Fresnel rhomb that uses two total internal reflections and one external reflection [16],[17],[18]. The retardance resulting from the internal reflections is nearly wavelength independent. The external reflection allows the exiting beam to be coincident with the incident beam and allows for rotation of the device with minimal beam wander. The measured and predicted linear retardance spectra are shown in Figure 10.

Figure 11 shows spectra of the dc term a_0 and the magnitude of the fourth harmonic coefficient a_4 of a conventional multiple order wave plate. The ambiguity of signs in the computer implementation of the inverse cosine function at the points labelled A in Figure 11 prompted the development of an alternate data reduction scheme for this set of data.

The phase of the variation with wavelength of the dc term and the fourth harmonic coefficients can be related to the retardance. For example, at $10.6 \mu\text{m}$ (Figure 11), the retardance is known to be approximately $7\lambda/4$. Other points (marked B in the Figure) are also multiples of $\lambda/4$. The points A are wavelengths of zero net retardance, and the points C are wavelengths at which the waveplate acts as a $\lambda/2$ retarder.

The Fourier series coefficient spectra of Figure 11 were fitted in a piecewise fashion over several spectral bands to a curve of the form

$$\alpha_0 + \alpha_1 \lambda + \alpha_2 \lambda^2 + \left(\beta_0 + \beta_1 \lambda + \beta_2 \lambda^2 + \beta_3 \lambda^3 + \frac{\beta_4}{\lambda} \right) \cos \left(\gamma_0 + \frac{\gamma_1}{\lambda} + \frac{\gamma_2}{\lambda^2} \right). \quad (12)$$

The known retardance of $7\lambda/4$ at $10.6 \mu\text{m}$ was used to determine the coefficient γ_0 . The retardance at a wavelength λ is then given by the argument of the cosine. Figure 12 shows the retardance spectra calculated from the argument of the cosine and the theoretical retardance [15]. The birefringence computed from the dispersion relations [15] and the measured birefringence are compared in Figure 13. The diattenuation is not subject to sign ambiguities and was computed using Eqn. 9. The diattenuation spectrum of the retarder is shown in Figure 14.

8 Conclusions and Recommendations

Results and achievements ending in December 1989 have been presented. Calibration steps necessary for the full implementation of the Mueller matrix spectropolarimeter have been pursued. The calibration included measurement of the spectra of the polarizing elements used in the spectropolarimeter, and stability measurements of the source and detector with time. One type of data reduction using small angle approximations was found inadequate for the variations of retardance present in the broad wavelength range of the spectropolarimeter.

A technique for calculating spectra of linear diattenuation, linear retardance, and birefringence of transmissive samples with parallel faces and good image quality has been derived and demonstrated. The technique was demonstrated in a spectropolarimeter on achromatic retarders of two different designs, and a single plate, multiple order retarder. The agreement with known birefringence data for the multiple order waveplate demonstrates the validity of the technique. The discrepancy from theory of the more complicated designs of the achromatic retarders indicates the need for the spectral calibration of polarization components. Future work with this technique will include spectral characterizations of magneto- and electro-optic materials by placing the sample in magnetic or electric fields.

The development of the spectropolarimeter has shown that several technically difficult problems remain before the Mueller matrix spectropolarimeter can be considered operational with an acceptable amount of error. While the problems are difficult, they are not impossible and should be surmounted in the coming year. This work has shown the merit of spectropolarimetric measurements. The results of the linear diattenuation and retardance research fully justify the development of the instrument. Full Mueller matrix measurements, which include scattering information, will prove invaluable to developers of modulators. Further work will include placing samples in electric and magnetic fields. New materials useful for modulators in all regions of the mid-infrared, not just laser wavelengths, will result

in improved performance and reliability, a greater choice of materials for varying environmental conditions, and lower cost of these devices.

9 Acknowledgements

The authors would like to acknowledge the useful discussions and comments of Dennis Goldstein at the Air Force Armament Laboratory, Eglin AFB, FL, and James McGuire of the University of Alabama in Huntsville. We wish to acknowledge the work of Dan Brown and Brian Choate in developing and maintaining the curve fitting routines used. We also acknowledge the use of a Cleveland Crystal multiple order wave plate as a sample. The research has been sponsored in part by the Laboratory Graduate Fellowship Program and the Air Force Office of Scientific Research, Bolling AFB, DC. contract # F49620-86-C-0127/SB5861-0436.

FIGURE CAPTIONS

Figure 1: Transmission spectrum of parallel polarizers ratioed against a single polarizer.

Figure 2: Transmission spectrum of perpendicular polarizers ratioed against a single polarizer.

Figure 3: Detector output vs. time. This shows the variation with time of the source and detector after being turned on and filled. Each unit on the x-axis corresponds to 3.75 minutes. The total measurement time is seven hours, forty-five minutes.

Figure 4: Mueller matrix element spectra for no sample corrected for small variations in azimuthal and retardance. Ideally the diagonal elements would be one, all others zero. Each element is ratioed to the 1,1 element.

Figure 5: The rotating sample polarimeter configuration.

Figure 6: The spectropolarimeter. The polarimeter of Figure 5 is located in the sample compartment.

Figure 7: Diattenuation spectrum in per cent against wavelength in microns of the multiple plate achromatic retarder.

Figure 8: Measured (—) and predicted (xxx) retardance spectra in degrees vs. wavelength in microns of multiple plate achromatic retarder. Lack of birefringence data prevented prediction beyond $11\mu\text{m}$.

Figure 9: Modified Fresnel rhomb retarder. Incident and transmitted beams are coincident.

Figure 10: Measured (—) and predicted (xxx) retardance spectra in degrees vs. wavelength in microns of modified Fresnel rhomb retarder.

Figure 11: The dc (top) and fourth harmonic coefficients of single plate, multiple order retarder as a function of wavelength. The vertical axis is in arbitrary intensity. The points marked A are wavelengths where the net retardance is zero, points B are wavelengths where the retardance is a multiple of $\lambda/4$, and points C are multiples of a half-wave of retardance.

Figure 12: Theoretical (xxx) and measured (—) retardance values in degrees for multiple order wave plate vs. wavelength in microns.

Figure 13: Theoretical (xxx) and measured (—) birefringence spectra for multiple order wave plate vs. wavelength in microns.

Figure 14: Diattenuation spectrum in per cent against wavelength in microns for multiple order wave plate.

PARALLEL POLARIZERS

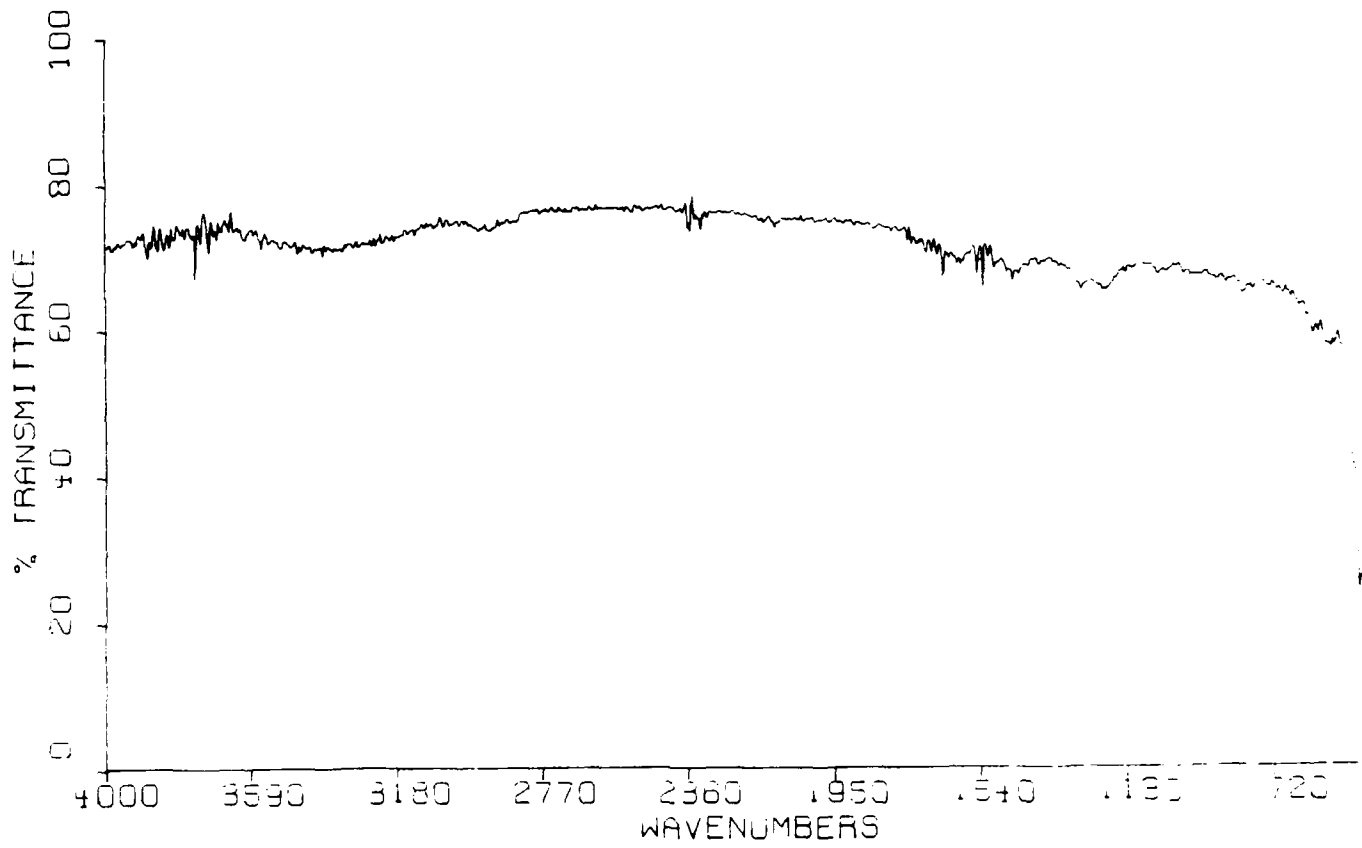


Figure 1

CROSSED POLARIZERS

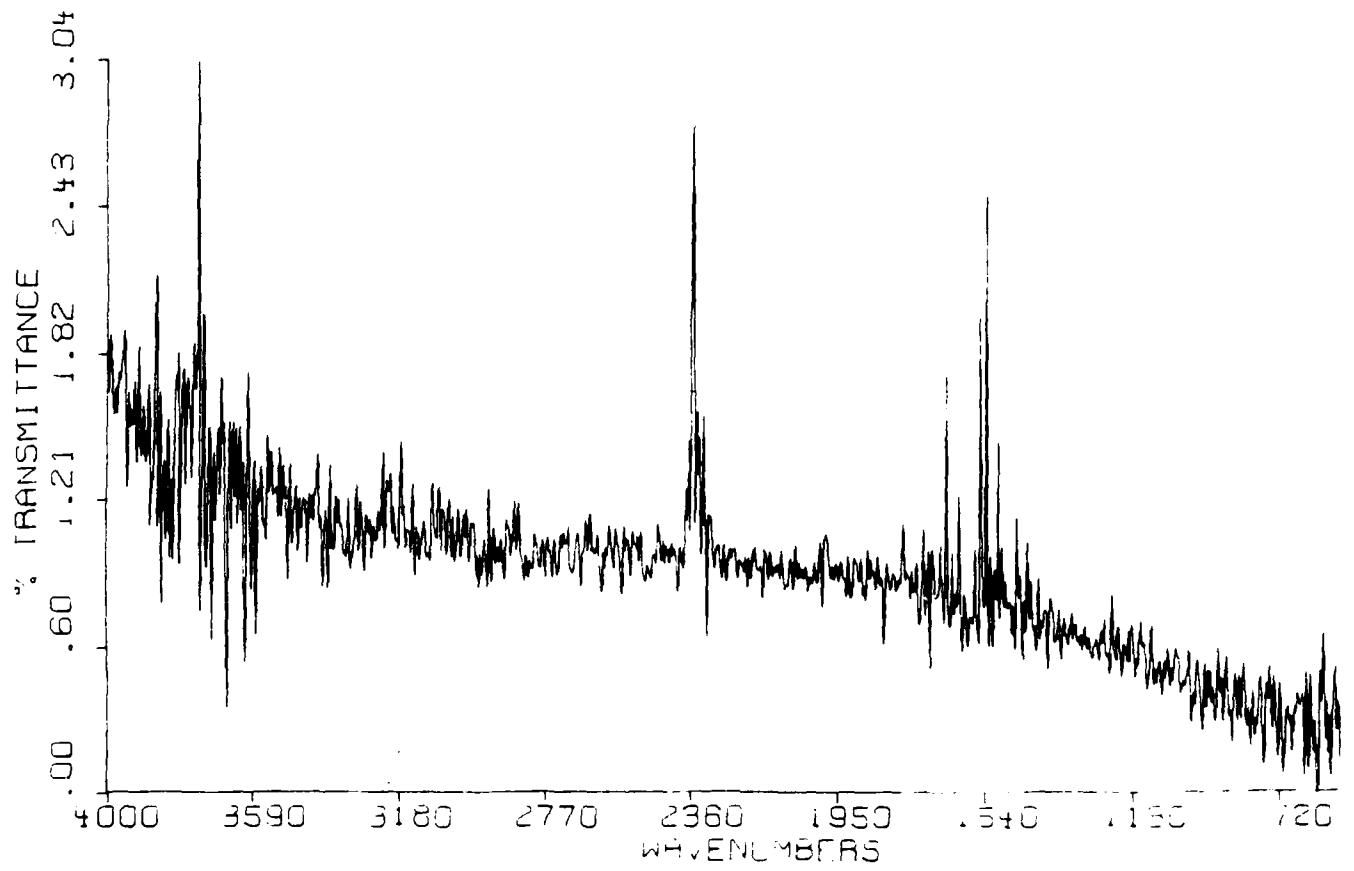


Figure 2

Stability Test

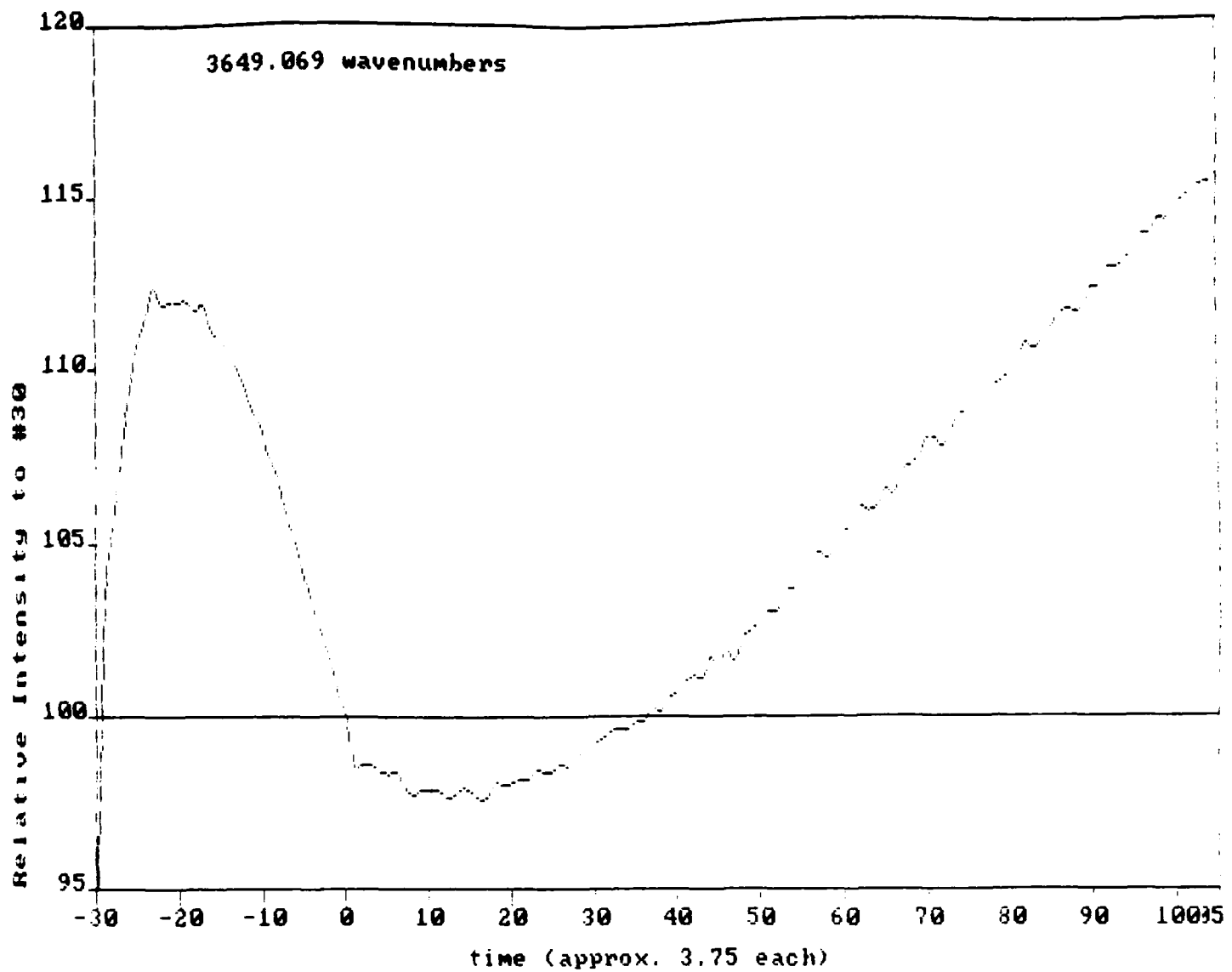


Figure 3

Mueller matrix spectrum

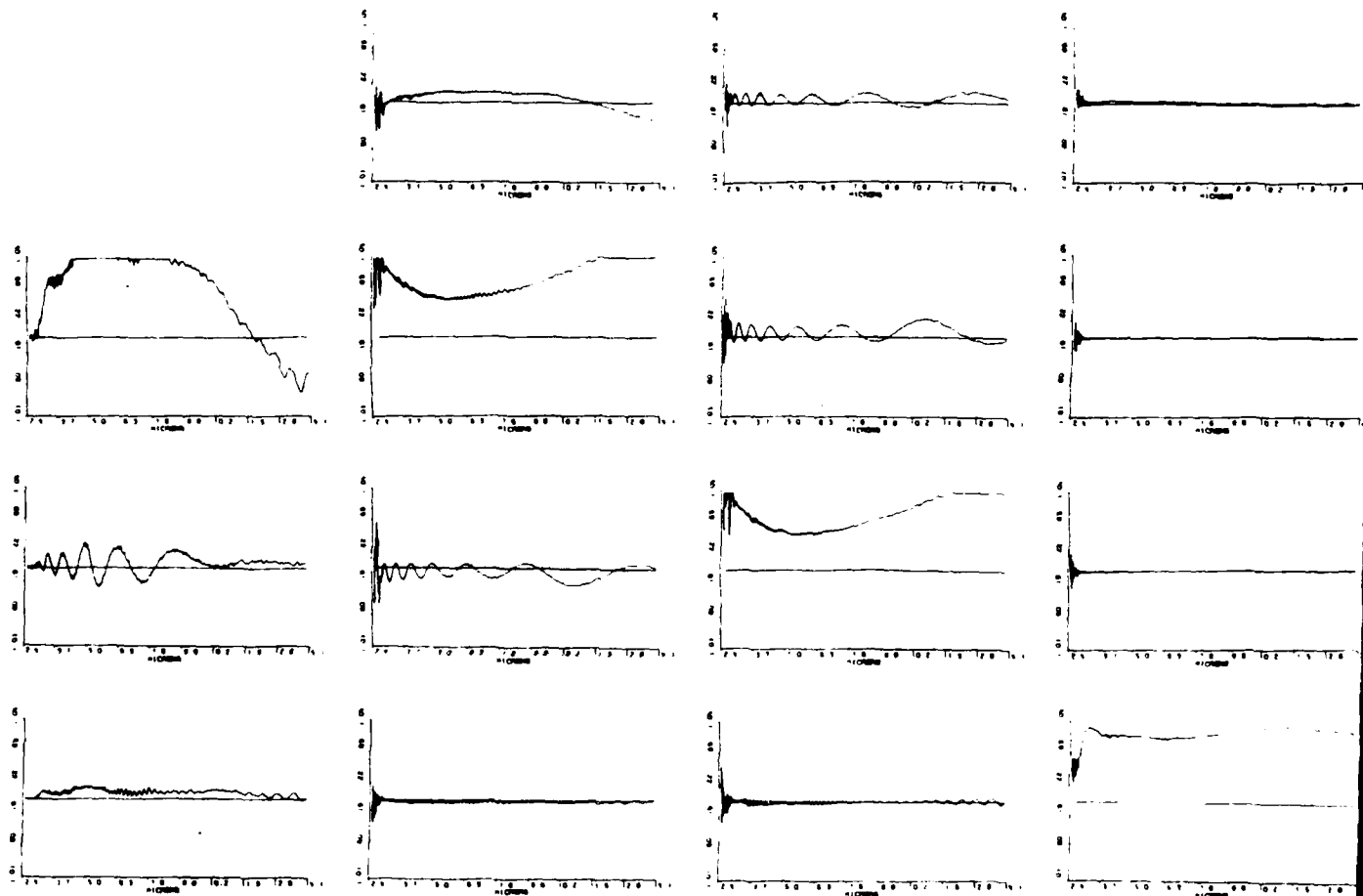


Figure 4

Rotating Sample Polarimeter

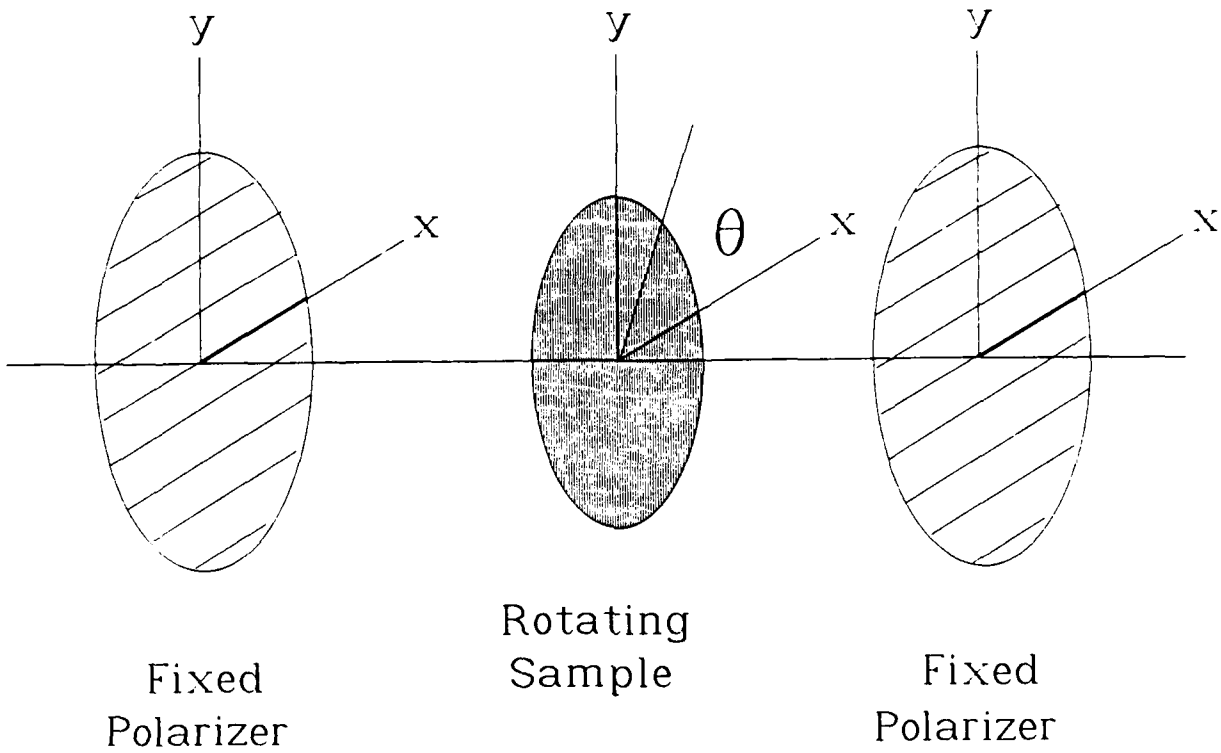


Figure 5

Spectropolarimeter

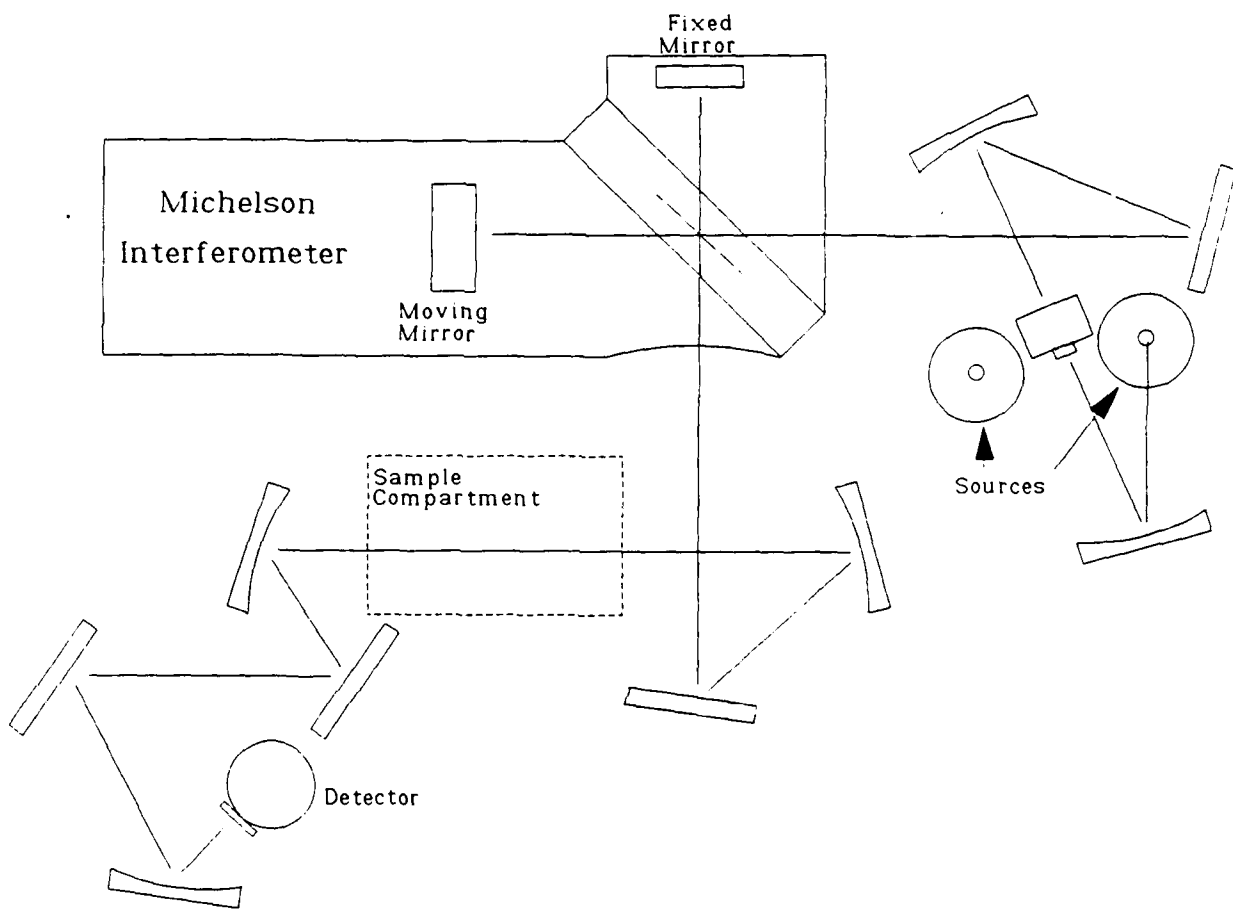


Figure 6

% Diattenuation vs. wavelength (microns)

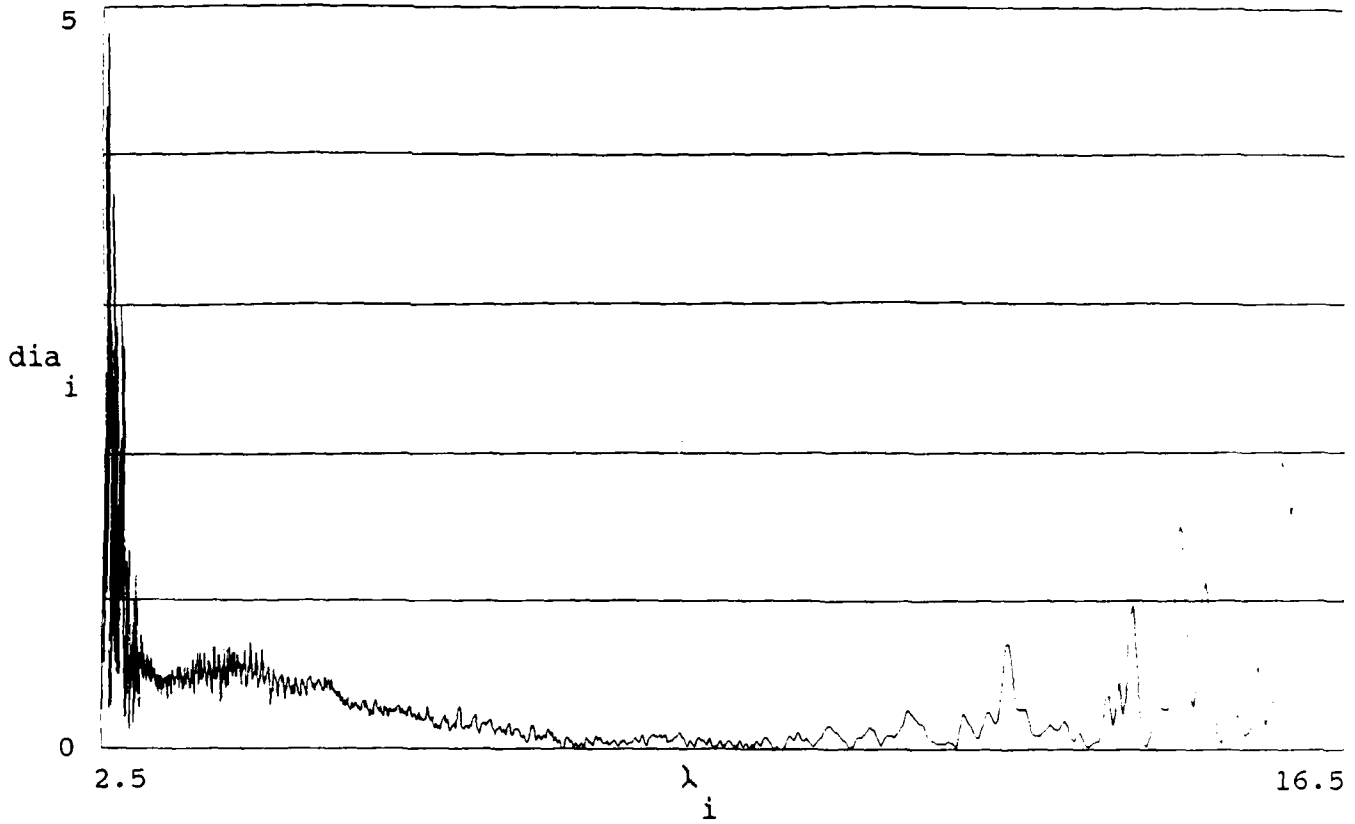


Figure 7

Retardance vs. wavelength

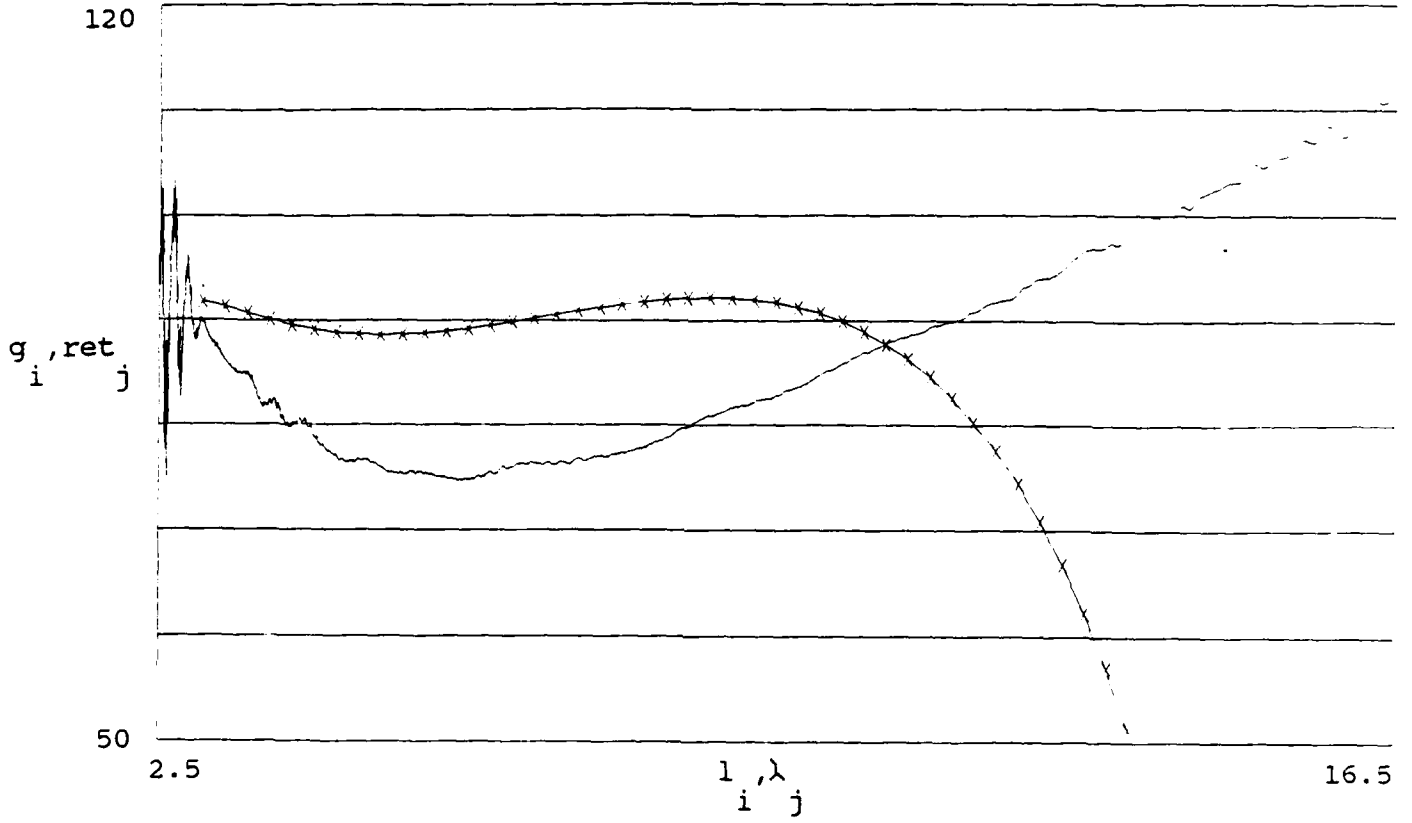


Figure 8

Modified Fresnel rhomb retarder

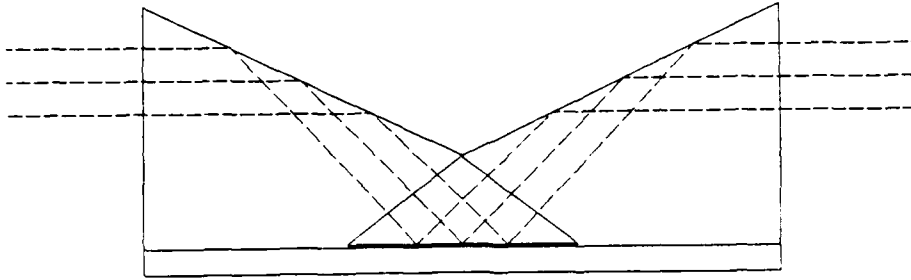


Figure 9

Retardance (degrees) vs. wavelength (microns)

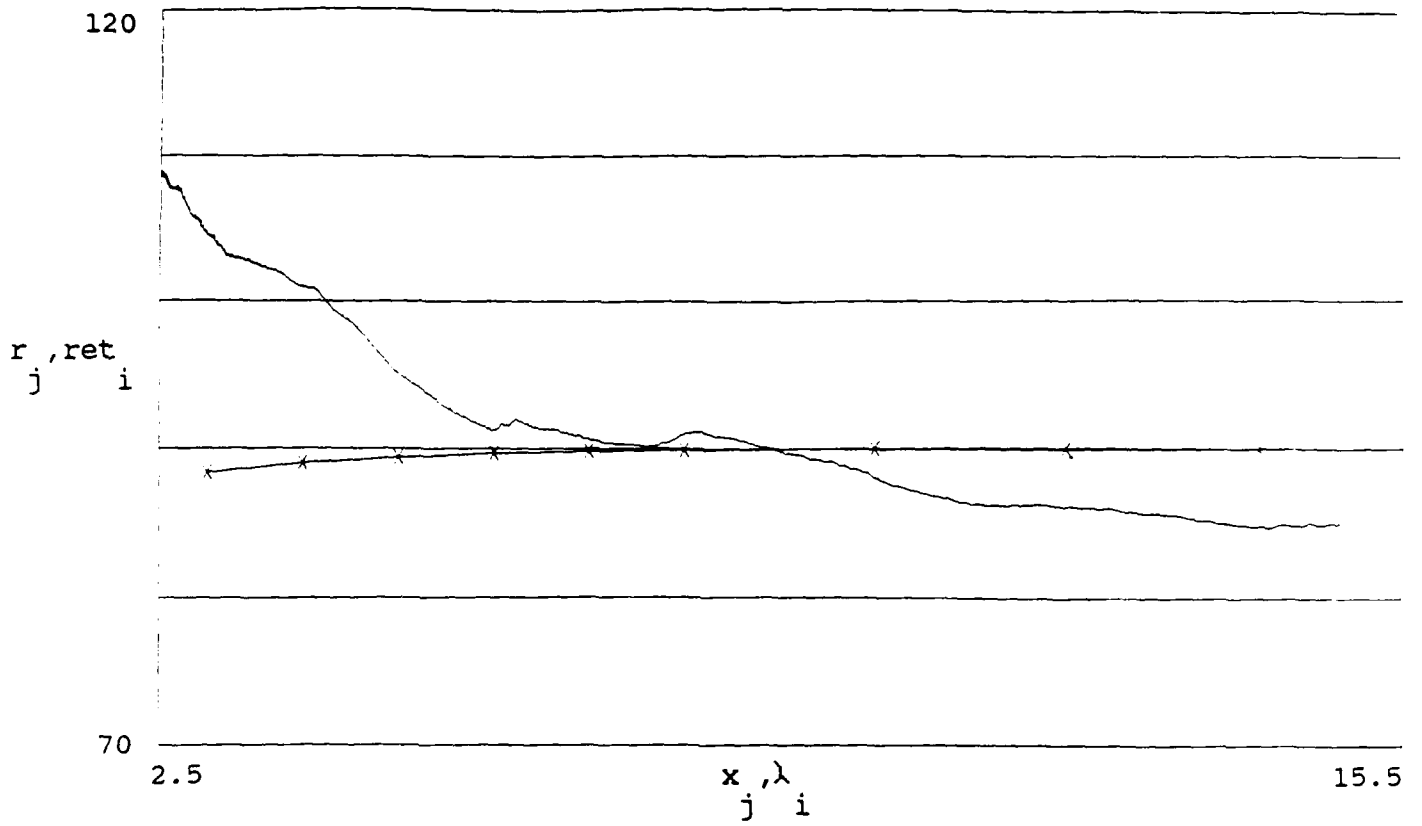


Figure 10

DC and fourth harmonic terms (arbitrary intensity units)
vs. wavelength (microns)

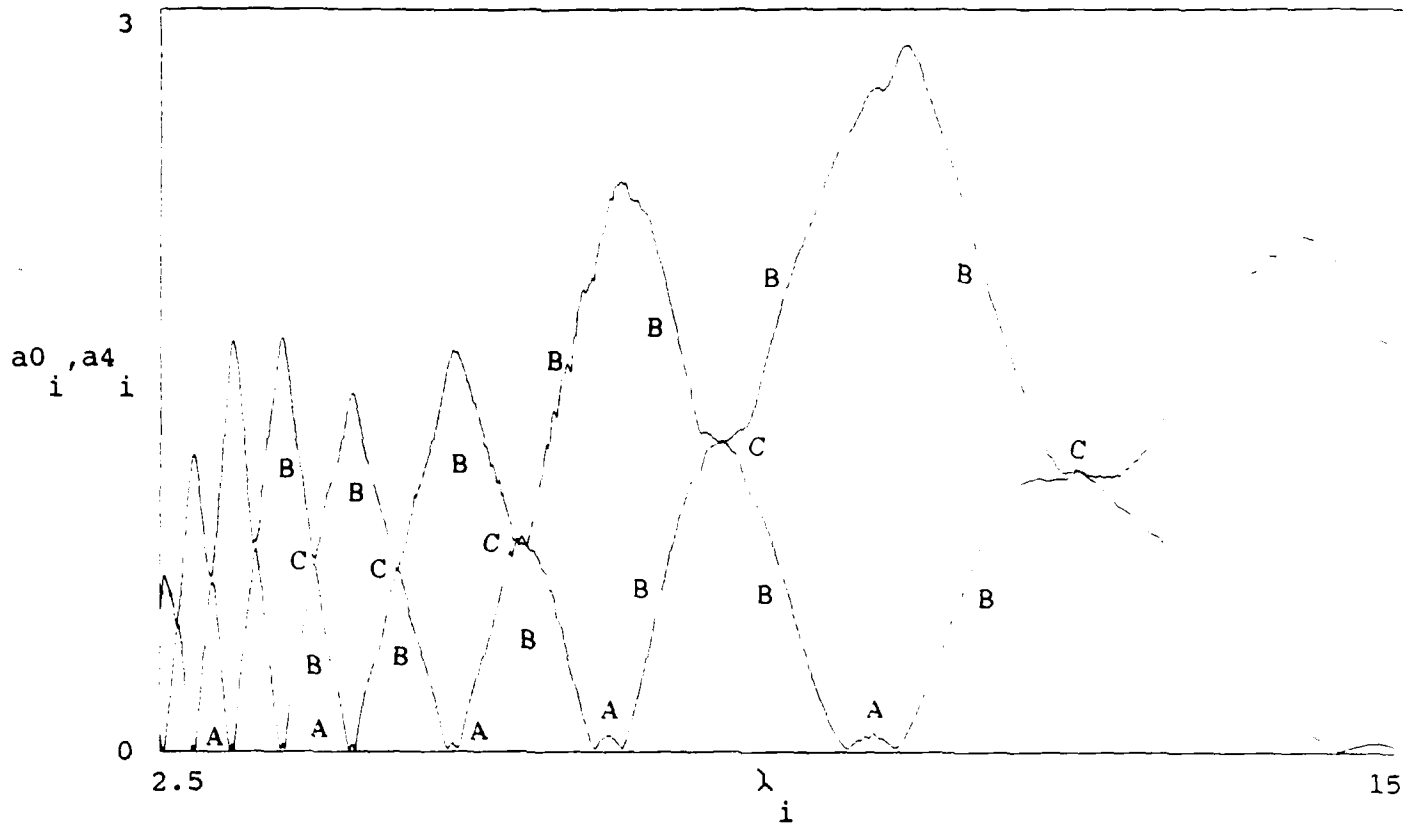


Figure 11

Retardance (degrees) vs. wavelength (microns)
-- = experiment xx = theory

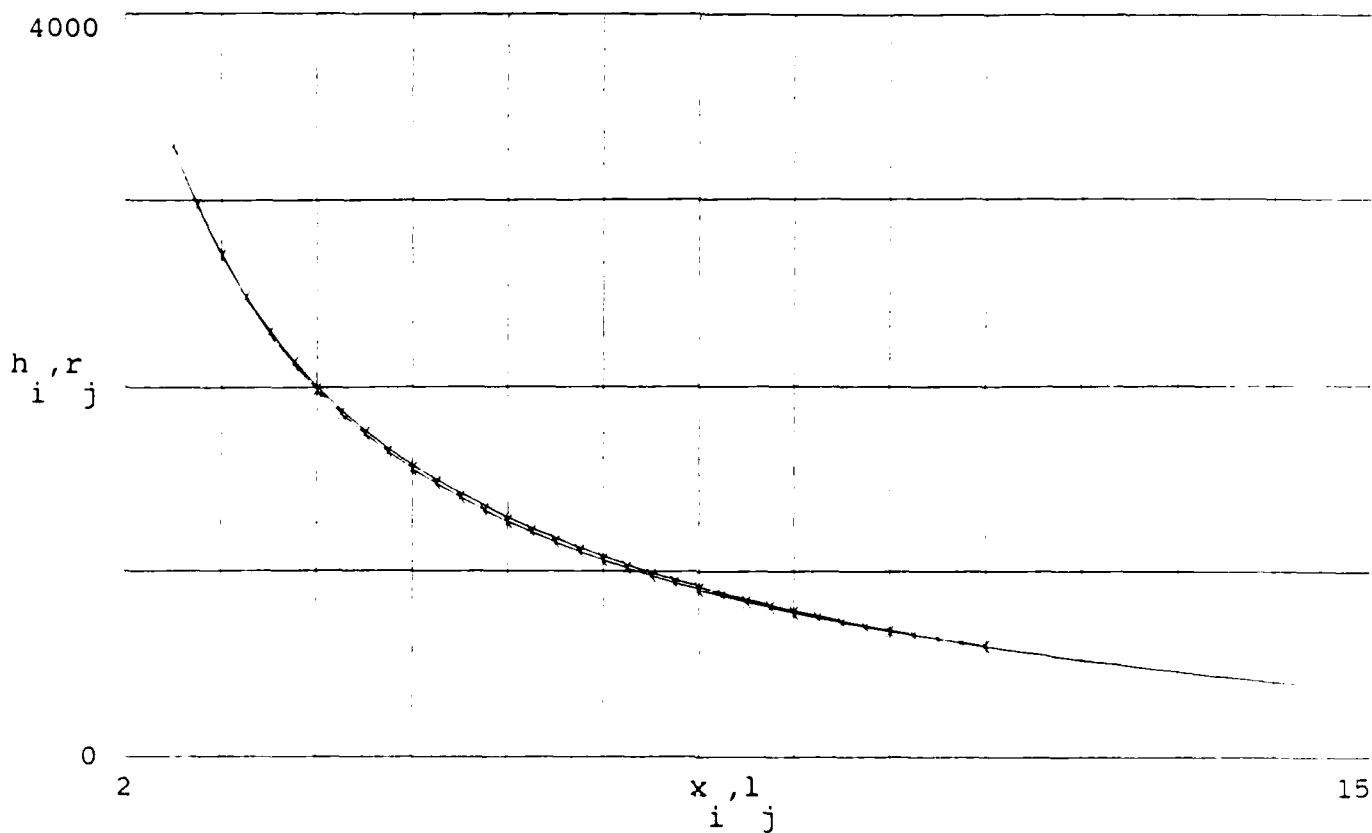


Figure 12

Birefringence vs. wavelength (microns)
-- = experiment xx = theory

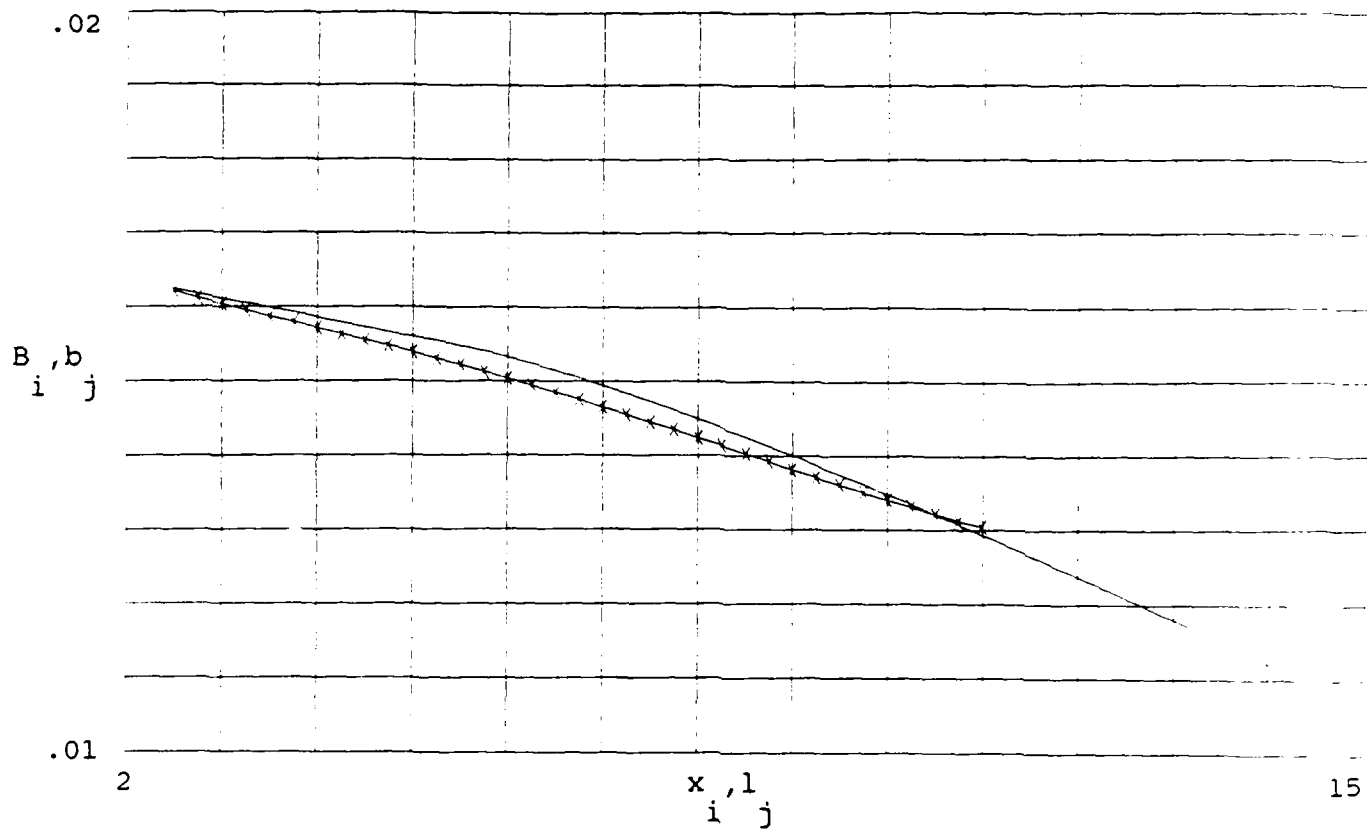


Figure 13

% Diattenuation vs. wavelength (microns)

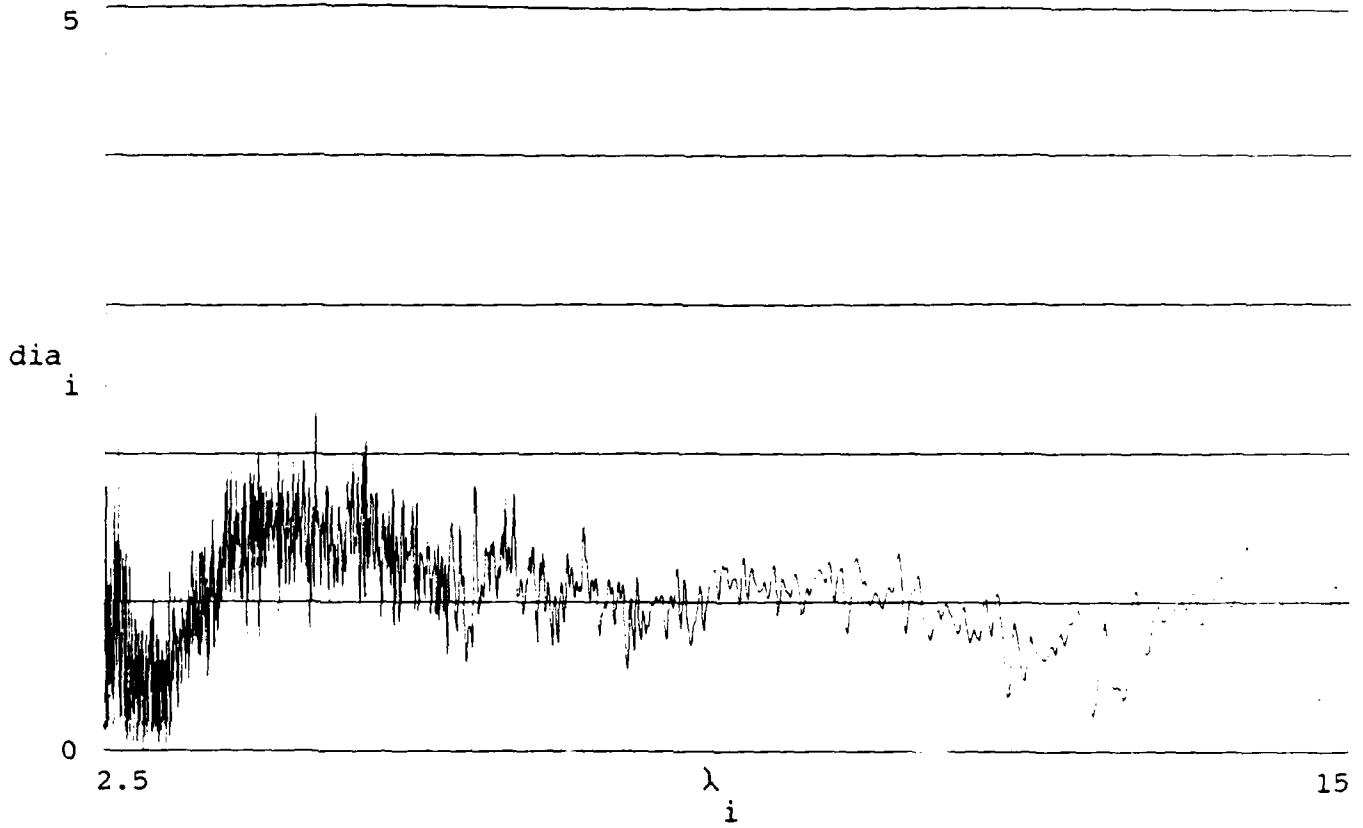


Figure 14

REFERENCES

1. C. Warde and U. Efron, "Guest editorial: materials and devices for optical information processing," *Opt. Eng.* 25 (2), 197 (1986).
2. A. A. Ballman et. al., "Research on nonlinear optical materials: an assessment - V. Inorganic materials for frequency conversion," *Appl. Opt.* 26 (2), 224-227 (1987).
3. D. H. Goldstein, R. A. Chipman, D. B. Chenault, "Infrared Spectropolarimetry," *Opt. Eng.* 28 (2), 120-125 (1989).
4. D. B. Chenault and R. A. Chipman, "Infrared Spectropolarimetry," *Proceedings of the SPIE 1166*, paper 27, in publication (1989).
5. R. M. A. Azzam, "Photopolarimetric measurement of the Mueller matrix by Fourier analysis of a single detected signal," *Opt. Lett.* 2 (6), 148-150 (1978).
6. R. M. A. Azzam, "A simple Fourier photopolarimeter with rotating polarizers and analyzer for measuring Jones and Mueller matrices," *Opt. Comm.* 25 (2), 137-140 (1978).
7. P. S. Hauge and F. H. Dill, "A Rotating-Compensator Fourier Ellipsometer," *Opt. Comm.* 14 (4), 431-437 (1975).
8. D. E. Aspnes, "Photometric ellipsometer for measuring partially polarized light," *JOSA* 65 (11), 1274-1278 (1975).
9. R. A. Chipman, "Polarization analysis of optical systems," *Opt. Eng.* 28 (2), 90-99 (1989).
10. R. M. A. Azzam and N. M. Bashara, Ellipsometry and Polarized Light, p. 76, North-Holland, Amsterdam (1977).
11. Ref. 10, p. 77.

12. I. Filinski and T. Skettrup, "Achromatic optical compensator-modulator," App. Opt. 28 (9), 1720-1726 (1989).
13. V. Chandrasekharan and H. Demany, "Birefringence of Sapphire, Magnesium Fluoride, and Quartz in the Vacuum Ultraviolet, and Retardation Plates," App. Opt. 7 (5), 939-941 (1968).
14. P. D. Hale and G. W. Day, "Stability of birefringent retarders," App. Opt. 27 (24), 5146-5153 (1988).
15. Cleveland Crystals, Inc. Data Sheet, May 1984.
16. J. M. Bennett, "A Critical Evaluation of Rhomb-Type Quarterwave Retarders," App. Opt. 9 (9), 2123-2129 (1970).
17. P. A. Clapham, M. J. Downs, and R. J. King, "Some Applications of Thin Films to Polarization Devices," App. Opt. 8 (10), 1965-1974 (1969).
18. M. Elhanine, R. Farrenq, and G. Guelachvili, "Polarization modulation high resolution Fourier transform spectroscopy," App. Opt. 28 (18), 4024-4029 (1989).

1988 USAF-UES RESEARCH INITIATION PROGRAM

Sponsored by the
AIR FORCE OFFICE OF SCIENTIFIC RESEARCH
Conducted by the
Universal Energy Systems, Inc
FINAL REPORT

COMPUTER CODE TO INCLUDE CORE POLARIZATION IN
EFFECTIVE POTENTIAL BASIS SET EXPANSION STUDIES

Prepared by: Phillip A. Christiansen
Associate Professor
Chemistry Department
Clarkson University
Potsdam, N.Y.
13676

In association with: Dr. Stephen L. Rodgers and
Dr. Daniel D. Konowalow
Air Force Astronautics Laboratory
Edwards AFB, CA
93523-5000

Date: 22 Dec. 1989

Contract No. POS-210-9MG-092

COMPUTER CODE TO INCLUDE CORE POLARIZATION IN
EFFECTIVE POTENTIAL BASIS SET EXPANSION STUDIES

by

Phillip A. Christiansen

ABSTRACT

Core-valence correlation potentials were computed for the alkali elements. The potentials included dipole, quadrapole and higher order corrections within the constraints of the respective basis sets. Conventional electronic structure codes developed for effective potential calculations were modified to include the one and two-electron core polarization corrections. A series of test calculations involving alkali dimers and dimer ions were carried out. Comparisons with previous work indicate that the present approach is probably the most accurate available.

ACKNOWLEDGEMENTS

The support of this work by the Air Force Systems Command, the Air Force Office of Scientific Research, the Air Force Astronautics Laboratory and Universal Energy Systems is gratefully appreciated. I also wish to thank the members of the ARIES group at AFAL, especially Drs. D. D. Konowalow, S. L. Rodgers, M. E. Rosenkrantz and Capt. W. Lauderdale for many useful comments and technical support.

I. INTRODUCTION:

It has been noted within the ARIES group at the Air Force Astronautics Laboratory¹ that there are potential advantages in the use of lighter metals (Li, Be, Al, etc.) as reducing agents in conjunction with liquid hydrogen-oxygen rocket fuels. However to be practical the metals must be stabilized in atomic (or at most very small cluster) form. It has been speculated¹ that the large dipole polarizabilities of some of these metals might make it possible to form at least marginally stable van der Waals complexes involving single metal atoms (or perhaps diatomic molecules) surrounded by H₂ molecules. Liquid hydrogen temperatures would presumably make it possible to keep such complexes intact for sufficiently long time spans for it to be practical.

Relatively little is known about van der Waals complexes in general and almost nothing about these in particular. Only recently have computational electronic structure studies been initiated to determine the stability of various Li-H₂ complexes. Due to the rather small magnitudes of the expected binding energies it is imperative that such studies be as precise as possible. Unfortunately the accuracy of alkali and alkaline-earth electronic structure predictions is greatly complicated by the large core polarizabilities which can cause substantial core-valence correlation errors.² In recent relativistic effective potential quantum Monte Carlo (REP-QMC) simulations we have shown that core-polarization corrections in atomic Al (and its ions) can be treated very accurately by the method previously developed by the author.³

If accurate predictions of van der Waals complex

stabilities are to be made, whether for the alkalis, the alkali-earths or even some of the main group elements (Al, etc.), the problem of core-valence correlation must be resolved. The most economical solution to the problem is to extend the approach used in our REP-QMC work to the more conventional SCF/CI framework.

II. OBJECTIVES OF THE RESEARCH EFFORT:

To facilitate the alkali-hydrogen van der Waals complex work in progress at AFAL it was imperative that polarization potentials and fields be computed for Li and other alkali elements. In addition it was necessary to modify convention electronic structure codes to generate the requisite one and two-electron core-polarization integrals. Codes were then developed to include these integrals in more conventional REP-SCF and CI calculations.

III. ALKALI ELEMENT CORE POLARIZATION:

Core polarization potentials for Li, Rb and Cs were generated using the method described in reference 3. We assumed that the polarization was due primarily to the distortion of ns and np filled shells in the field created by the valence (n+1)s electron. We were therefore able to use the standard nine-electron alkali REPs from the literature.⁴ The individual polarization potentials were computed from the SCF energies for the alkali⁺¹ ions in the presence of a negative point charge positioned a distance r from the nucleus. The point charge of course polarizes the normally spherical wavefunction and the difference between the polarized and unpolarized energies gives a good approximation to an electron-ion scattering potential (at least for large values of r). The potential will include

dipole, quadrupole and higher order corrections if the basis set allows. For small r the potential must be corrected for adiabatic effects. This was accomplished in a manner analogous to reference 3, by multiplying the potential by a cutoff function, $C(r)$, defined as either the square or first power of the fraction of the n_s and n_p electron density inside the radius, r .

Potentials generated in this manner were then used in conjunction with one-electron REPs to compute first ionization potentials for the neutral alkali atoms. By scaling r in the cutoff functions we are able to readily reproduce the experimental ionization energies to within the required four or five significant figures. The one-electron REPs, polarization potentials and corresponding effective field operators (as defined in references 2 through 4) are listed as gaussian expansions in Tables I and II.

VI. ALKALI DIMERS AND DIMER IONS

In conventional electronic structure work the polarization potentials and effective field operators give rise to both one and two-electron integrals as discussed by Muller et al. However in the present case the problem of generating integrals is considerably simplified inasmuch as the potential and field operators are expressed in terms of Gaussian expansions. We have developed computer codes to compute the necessary integrals. These can then be added to the normal REP-SCF one and two-electron integral sets and subsequent calculations carried out in a conventional manner.

In Table I we report the resulting computed spectroscopic

constants for a number of alkali dimer cations. Since in the present formalism the cations are one-electron species our results do not suffer from incomplete configuration expansion difficulties. Where possible we have included the most reliable previous values, (either experiment or theory). The agreement is excellent in all cases. Note the the core polarization corrections increase rapidly for the heavier alkalis, making the Rb and Cs dimers a particularly severe test of the formalism.

Similar results are given in Table IV for the neutral dimers. Note again that the exceptional correlation between our results and the experimental values.

The formalism developed by Muller et al. cannot be extended to the heavier alkalis and is somewhat cumbersome even for the light elements. Furthermore other procedures in the literature have produced erratic results for the heavy alkalis. At the present time our approach appears to be the only method available that is capable of providing reliable results for the alkali elements from the lightest to the heaviest.

V. RECOMMENDATIONS:

In exploratory studies involving light-metal- H_2 van der Waals complexes, lithium is an obvious candidate due to its very large dipole polarizability. However because of its free radical nature, $Li-H_2$ complexes might be relatively unstable with regard to the formation of larger metallic clusters. This might also be true of related Al, B, etc. complexes. Unfortunately the metal-metal binding energies are sufficiently large that the energy required to break the clusters during combustion might cancel out any

advantage the van der Waals complexes would have in a rocket fuel. For this reason it might also be important to carry out studies involving hydrogen complexes of Be or Mg. The Mg polarizability is of roughly the same magnitude as that of Li. Be has obvious health risks but this might not be a serious constraint for propulsion systems operating outside the earth's atmosphere. As with Li, the inclusion of core polarization corrections would be absolutely essential to make accurate predictions. Polarization potentials and effective field operators should probably be computed for all the Group IA, IIA and lighter Group IIIA elements.

The computer codes developed here for the generation of core polarization integrals should be incorporated into the electronic structure packages currently in use at the Air Force Astronautics Laboratory. Core polarization corrections must be included in electronic structure studies involving the alkali, alkaline-earth and similar elements if accurate predictions are to be made. With the modifications discussed above the Air Force Astronautics Laboratory would have access to one of the most advanced computer packages available for the study of molecules containing these elements.

REFERENCES

1. Konowalow, D.D., private communication.
2. Muller, W., Flesch, J., Meyer, W., "Treatment of intershell correlation effects in ab initio calculations by use of core polarization potentials. Method and application to alkali and alkaline earth atoms", J. Chem. Phys. 1984, 80, 3297.
3. Christiansen, P.A., "Core-valence correlation in relativistic effective potentials", Chem. Phys. Lett. 1986, 127, 50.
4. Pacios, L.F., Christiansen, P.A., "Ab initio relativistic effective potentials with spin-orbit operators. I. Li through Ar", J. Chem. Phys. 1985, 82, 2664.

Table I. Core polarization effective field operators.

Lithium

<u>N</u>	<u>Expn.</u>	<u>Coef.</u>
2	0.003000	-0.033771
2	0.026000	0.051340
2	0.002300	0.038903
2	0.116000	0.140688
2	0.295600	0.170258
2	0.471000	0.234780
2	2.366300	-0.516449

Potassium

<u>N</u>	<u>Expn.</u>	<u>Coef.</u>
2	0.0071	0.019590
2	0.0532	0.087389
2	0.2127	0.217919
2	0.2380	0.038199
2	1.7814	-0.807161
2	3.2741	0.638330
2	5.6736	-0.385779
2	8.4367	0.203838

(Table I continued)

Rubidium

<u>N</u>	<u>Expn.</u>	<u>Coef.</u>
2	0.0020	0.005652
2	0.0193	0.052359
2	0.1939	0.381659
2	0.4209	-0.545279
2	2.3860	-0.003641
2	4.2289	0.355908
2	11.5367	-0.801006
2	23.9489	0.941250

Cesium

<u>N</u>	<u>Expn.</u>	<u>Coef.</u>
2	0.0024	0.006272
2	0.0207	0.024091
2	0.0107	0.006142
2	0.0780	0.116074
2	2.3428	-7.197930
2	3.3439	14.154476
2	11.2220	-26.084212

Table II. Alkali one-electron effective potentials including the core polarization potential.

Lithium

	<u>N</u>	<u>Expn.</u>	<u>Coef.</u>	<u>SO Coef.</u>
s-p	2	0.7998	24.333699	
	2	0.7741	-20.666397	
	1	1.1943	-1.142892	
p	2	0.8078	-0.118667	0.000035
	2	2.5500	-1.217794	-0.000160
	1	7.2535	-1.375805	0.000869
	0	0.0072	-0.001920	
	0	0.0592	-0.009676	
	0	2.5296	-0.039715	
	0	11.4534	0.000094	
	0	4.7934	-0.004525	
	0	1.3799	0.083685	
	0	0.2485	-0.028873	

Potassium

	<u>N</u>	<u>Expn.</u>	<u>Coef.</u>	<u>SO Coef.</u>
s-d	2	0.5112	-37.835439	
	2	0.5772	120.886896	
	2	0.6951	-152.062672	
	2	0.8167	80.156594	
	2	3.3950	16.615307	
	1	6.5450	11.298329	
	0	11.3671	3.154872	
	p-d	2	0.5471	117.508418
2		0.6363	-260.313582	
2		0.8212	267.148680	

(Table II continued)

	2	1.1072	-195.109813	
	2	1.4439	91.069030	
	1	5.3317	19.952725	
	0	16.0573	4.577794	
d	2	0.0144	-0.001240	
	2	0.0725	-0.018390	
	2	0.2325	-0.305632	
	2	0.5425	-1.527033	
	2	1.3421	-5.092303	
	2	1.8821	4.116548	
	2	2.3429	-3.774148	
	2	3.2608	-8.264919	
	2	10.2460	-27.179525	
	1	28.3226	-11.778307	
<u>Rubidium</u>				
	<u>N</u>	<u>Expn.</u>	<u>Coef.</u>	<u>SO Coef.</u>
s-f	2	0.6363	65.054571	
	2	0.7570	-120.607511	
	2	1.0163	-106.893699	
	2	1.4185	-47.546889	
	2	2.8147	40.527653	
	1	7.8347	33.352080	
	0	23.2174	3.447365	
p-f	2	0.2673	2.683806	0.102068
	2	0.7757	-7.838162	-2.423131
	2	1.0540	24.629052	4.430870
	2	1.7352	-15.938484	-4.829433
	2	2.4849	20.646762	2.967709
	1	4.4073	22.009533	-0.250163

(Table II continued)

	0	10.5958	5.370101	0.011549
d-f	2	0.2843	-0.440185	-0.020579
	2	1.0028	-13.003515	1.172525
	2	1.4347	17.003515	-3.507962
	2	2.4644	-60.118998	5.303213
	1	3.4178	28.116669	-1.804485
	0	1.7479	9.119068	0.055949
f	2	0.3219	-0.600080	-0.005346
	2	0.8055	-4.441304	0.010683
	2	2.5355	-11.420121	-0.005607
	2	8.1193	-48.179546	-0.028517
	2	27.2052	-104.712637	0.708229
	2	101.8095	-271.802477	-1.860548
	1	394.5032	-32.685563	3.012352
	0	0.0389	-11.737376	
	0	0.0534	29.125907	
	0	0.1162	16.228309	
	0	0.0822	-33.296302	
	0	1.9098	-0.846857	
	0	2.9130	0.536722	
<u>Cesium</u>				
	<u>N</u>	<u>Expn.</u>	<u>Coef.</u>	<u>SO Coef.</u>
s-f	2	0.5122	81.182748	
	2	0.6096	-144.340705	
	2	0.8666	121.996481	
	2	1.4255	-122.022007	
	2	1.8741	106.424359	
	1	5.8450	32.688999	
	0	14.5177	6.534110	

(Table II continued)

p-f	2	0.2018	2.316408	0.075977
	2	0.7523	4.199852	-1.243771
	2	1.1348	9.988803	4.454973
	2	1.9013	-43.852012	-19.666637
	2	2.1044	61.806692	17.230669
	1	4.6455	26.566202	-0.211490
	0	10.6589	5.880648	0.022357
d-f	2	0.1915	-0.207906	-0.011402
	2	0.5525	-0.382707	0.034552
	2	1.3348	74.621288	2.342940
	2	1.6417	-142.833250	-4.817578
	2	2.1351	104.981921	2.490409
	1	5.6905	28.195932	-0.105891
	0	13.2946	7.479835	0.004243
f	2	0.2589	-0.749031	-0.010561
	2	0.6474	-4.514607	0.023957
	2	2.2653	-19.002832	-0.039558
	2	7.1287	-53.410594	0.081047
	2	25.4779	-141.616206	0.730629
	2	77.6688	-267.683874	-3.129600
	1	242.4565	-44.424984	2.825665
	2	0.0083	-0.001091	
	2	0.0434	-0.021671	
	2	0.1548	-0.223780	
	2	1.2688	-51.158585	
	2	1.0261	11.586544	
	2	0.5128	7.495693	

Table III. Spectroscopic constants for alkali dimer cations. Bond lengths are in angstroms, dissociation energies are in eV, and the others in cm^{-1} .

	R_e	D_e	ω_e	$\omega_e \chi_e$	β_e	α_e	
Li_2^+	3.10	1.290	264	1.8	0.503	0.0050	
	-----	1.298	262	1.7	0.496	0.0052	(Expt)
LiK^+	3.86	0.594	155	1.0	0.190	0.0018	
	3.87	0.596	154	0.94	0.189	0.0017	(Ref 1)
K_2^+	4.50	0.816	74	0.19	0.042	0.00016	
	4.51	0.817	74	0.20	0.042	0.00017	(Ref 1)
Rb_2^+	4.84	0.757	44				
		0.73(6)					(Expt)
CsRb^+	5.03	0.597	37		0.013		
Cs_2^+	5.24	0.705	33				
		0.68(5)					(Expt)

Table IV. Spectroscopic constants for alkali dimers. Bond lengths are in angstroms, dissociation energies are in eV, and the others in cm^{-1} .

	R_e	D_e	ω_e	$\omega_e \chi_e$	β_e	α_e	
K_2	3.94	0.52	90	0.33	0.055	0.0030	
	3.94	0.54	92	0.26	0.056	0.0024	(Ref 1)
Rb_2	4.21	0.47	56				
	4.21	0.45	58				(Expt)
$CsRb$	4.41	0.43	47				
	4.37	0.48					(Expt)
Cs_2	4.63	0.41	43				
	4.65	0.45	42				(Expt)

FINAL REPORT
RESEARCH INITIATION PROGRAM

1989

PREPARED BY
SUSAN COLLINS
DEPARTMENT OF CHEMISTRY
CALIFORNIA STATE UNIVERSITY, NORTHRIDGE
NORTHRIDGE, CALIFORNIA, 91330

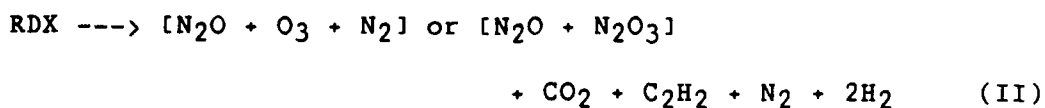
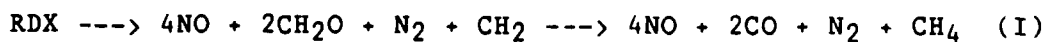
I. OBJECTIVES AND SUMMARY

During the last year, our work has been concerned with obtaining fluorescence spectra of matrix-isolated lithium. After obtaining the spectra of lithium using fluorescence, the intention was to use the same experimental conditions to deposit lithium, and to investigate the reactions of lithium with small organic molecules using FTIR spectroscopy. We experimented with several different knudsen ovens, but were not able to obtain decent fluorescence spectra. Students Terry Miles and Edmond Anderaissan worked on this for approximately six months. At present we have a new oven on order from Torrovap Industries in Canada, and the project will continue upon receipt of the new oven.

Another project, which stems from my Summer 1988 Faculty Research Program at Edwards Air Force Base, was to investigate the photoreactions of RDX in rare gas matrices at 10 K using FTIR spectroscopy. The photoproducts were compared to the known thermal decomposition products of RDX in the liquid, gas and molecular beam studies. Student Jeff Alix and I completed the project in one year and the report of this work follows.

II. ABSTRACT

The photochemistry of RDX was studied in argon matrices at 10 K and examined by FTIR spectroscopy. The spectra and kinetics of product growth indicate that there are two decomposition pathways:



The mechanism II nitrogen products can easily be rationalized for the chair configuration of RDX with axial NO_2 groups adjacent (C_s symmetry). When considering the carbon products of II, it may be necessary to postulate intermolecular reactions. Our studies gave no evidence of the symmetric triple fission path, which leads to N_2O and CH_2O , or the NO_2 stripping mechanism reported for the gas-phase thermal reactions, which leads to the formation of NO_2 and HCN . Rather, our findings were more consistent with the known condensed phase products. The production of CH_4 , C_2H_2 , N_2O_3 and O_3 are unique to the matrix study.

III. EXPERIMENTAL

The apparatus used for these experiments has been described recently (1). FTIR spectra were recorded on a Nicolet 20 DXB instrument with 1.0 cm^{-1} resolution. The RDX was deposited by heating it to approximately 200 C in a stainless steel vacuum line positioned in front of the CsI substrate window. Argon was passed over it at 1-2 mmole per hour for one hour. The argon stream entrained the RDX vapors and mixing occurred before deposition. The photolysis light source was an Oriel medium pressure xenon lamp. Broad band irradiation was used for all experiments.

RDX was kindly supplied to us by Dr. Steve Rodgers at the Edwards Air Force Base. Argon (Matheson, 99.995%) and occasionally nitrogen (Airco, 99.995%) were used as matrix gases, and they were used without further purification. No significant experimental differences were found when the reaction was carried out in argon or nitrogen matrices.

IV. INTRODUCTION

The technique of matrix isolation has proven to be extremely valuable for isolation of intermediates which are key steps in establishing chemical and photochemical mechanisms. 1,3,5-trinitrohexahydro-s-triazine, RDX, is known to decompose by several pathways. The products depend on the phase and temperature of the starting material. The condensed-phase decomposition occurs just above the melting point giving NO, N₂O, H₂, CO, CH₂O, and CO₂ (2). Another study showed that a primary deuterium kinetic isotope effect ($k_H/k_D = 1.5$) is associated with C-H breakage during the rate determining step under these conditions (3). When decomposition is studied at higher temperatures producing gas phase molecules, two other mechanisms predominate (2,4). The first involves the NO₂ stripping mechanism in which all three NO₂ groups are removed before the triazine fragment decomposes to form HCN and presumably H₂. The second pathway, which clearly has been seen in molecular beam studies, is the symmetric triple fission to form CH₂NNO₂ fragments which then further decompose to form CH₂O and N₂O (5). Our study was motivated by the possibility of trapping the CH₂NNO₂ fragment and obtaining its infrared spectrum, and to determine whether the mechanism in the matrix is similar to the gas or to the condensed phase mechanisms. We report here the matrix FTIR spectra of RDX and its photoproducts and their kinetic behavior at 10 K.

V. RESULTS

The present section will describe the infrared absorptions of the photochemical products and intermediates at in Ar at 10 K.

The infrared spectra of RDX in argon at 10 K is shown in figure 1A. Photolysis of RDX is 80% complete in 40 minutes resulting in the product spectrum shown in figure 1B. After continued irradiation for eleven hours, there is complete disappearance of the RDX bands and evidence of secondary photochemical reactions. Figure 1C shows the photolysis bands after eleven hours. Of the three spectra, only the 40 min spectrum contains RDX and products together as positive bands. The product bands in 1B and 1C are indicated by dark shading. Table I gives the frequencies and relative intensities of the product bands, normalized to the most intense band of its kind, at three different photolysis times. The molecule assignments associated with the listed bands will be discussed in the next section.

Figure 2 illustrates the kinetics of the product bands. Three distinct behavior patterns, types A, B, and C, are illustrated in 3A, 3B, and 3C. Type A behavior is characterized by simple first-order kinetics and by a fast rise at early photolysis times. Type B behavior also is first order, but these bands rise more slowly. At long photolysis times, some bands from types A and B disappear with a concomitant rise of Type C bands. Thus at least two examples of consecutive reaction kinetics are seen.

VI. DISCUSSION

We will discuss the assignment of the product bands and develop a mechanism for the reactions in terms of the kinetic behavior. All of the product molecules are known molecules, and in all cases, matrix literature spectra are available.

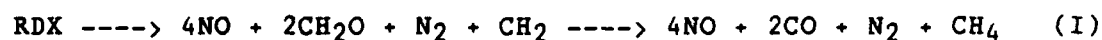
MECHANISM I

NO. The bands at 1851.0 and 1777.5 cm^{-1} are assigned as NO and the $(\text{NO})_2$ dimer. They follow type A kinetics. These bands appear in a unique portion of the IR spectrum and they compare very well with the literature argon matrix spectra of NO and $(\text{NO})_2$ (6). After eleven hours of photolysis, there appears to be some degradation of both the monomer and dimer.

CO. The band at 2140.0 cm^{-1} follows type C kinetics and is assigned to CO. This band is also very well known and appears in many matrix photochemical studies (e.g., ref. 2).

CH_2O , CH_4 , HCO, CH_2 . The bands at 1740.0 and 1498.1 cm^{-1} appear at early photolysis times with type A kinetics. Consistent with these band frequencies is the molecule formaldehyde (7). The kinetics support the assignment since formaldehyde is known to photolyse in the matrix (8). CO is expected to be a photoproduct, and indeed, the band at 2140.0 cm^{-1} assigned to CO exhibits type C kinetics. Other bands appearing with type C kinetics due to the decomposition of formaldehyde appear at 1300.0 and 2085.0 cm^{-1} .

We assign these bands as CH₄ and HCO (9,10). The methane would account for the uptake of hydrogen from the formaldehyde photolysis, conceivably by the reaction of CH₂ with excited CH₂O. For this, the formation of methylene also must be postulated as a product. To date, there are no literature reports of a matrix spectrum of CH₂. All attempts to stabilize methylene under matrix conditions have failed due to its extreme reactivity (11). The band at 2085.0 cm⁻¹ is assigned to formyl. This is tentative at best and at least consistent with the photochemical breakdown of formaldehyde. Another possibility is HCN, but this is ruled out since the known band for the CH bend at 717 cm⁻¹ is not seen in our experiments. Thus we postulate that one of the decomposition mechanisms of RDX results in NO, CH₂O, and CH₂ which later react to form NO, CO, and CH₄. In order to balance the reaction, the production of N₂ must be postulated to give the overall balanced reaction as:



The CH₄ band at 1300.0 cm⁻¹ seems intense relative to the CO band at 2140.0 cm⁻¹ in figure 1B, and it is not clear whether some absorption of the parent RDX overlaps in that region. Otherwise it may be necessary to postulate extra hydrogen from other sources, i.e., impurities, to react with methylene. Also one should note that a weak absorbance at 1740.0 cm⁻¹ due to formaldehyde still remains in figure 1B.

MECHANISM II

N_2O . The second decomposition reaction is characterized by type B, slower rise, kinetics. The bands at 2227.5, 2218.9, 1283.0, and 586.3 cm^{-1} are due to N_2O (12). These bands all follow type B kinetics. An authentic matrix sample of N_2O in argon (M/R = 1/100) gave an identical spectrum.

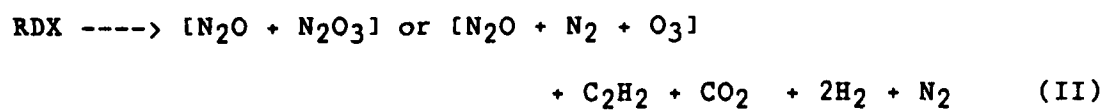
N_2O_3 . The very broad band at 1693.2 cm^{-1} has type B growth behavior. This band is assigned as symmetric N_2O_3 which has an absorption band at 1690.6 cm^{-1} in the literature (13). It is known to be a product of the reaction of $NO + O_2$ or $NO + O_3$ in argon matrices. It is not necessary to postulate these reactions, however, since it can form directly from RDX. One could easily envision its formation from RDX in the chair conformation with the axial NO_2 groups adjacent to each other (C_s symmetry).

O_3 . A type B band which exhibits consecutive reaction kinetics is at 1045.3 cm^{-1} . The assignment of O_3 is consistent with the IR spectrum, but one may easily question its formation, when there are so many other possible product molecules which would be more stable (14). Nevertheless, such an intermediate as ozone certainly would be trapped at 10 K. Furthermore it is known to decompose under matrix photolysis conditions (15). Again, considering the C_s -symmetry chair configuration known for solid phase RDX, the two NO_2 groups are adjacent and they could easily react to form N_2O , O_3 , and N_2 (16).

C_2H_2 . The next set of type B bands are at 733.3 and 3291.2 cm^{-1} . These bands also are well known and are easily assigned to acetylene (17). One could easily envision the reaction of two adjacent methylene groups in the chair configuration of RDX. The reaction of two methylene groups is known in the matrix to produce highly vibrationally excited ethylene which immediately decomposes to form acetylene and hydrogen (18). As in mechanism I, the presence of another methylene group could conceivably result in the rapid formation of methane.

CO_2 , H_2O . Comparison of the band at 2340.8 cm^{-1} in figures 1A, 1B, and 1C shows that CO_2 is present in the deposition spectrum as a consequence of our deposition method. There is only a slight increase during the initial 40 minutes of irradiation, but there is a dramatic increase during the eleven hour photolysis. This is much more than we normally see in this period of time when the background pressure is 10^{-6} torr. Thus, CO_2 certainly is a product associated with mechanism II. Matrix water at 1625.0 and 1597.6 cm^{-1} are seen in our experiments and are very well known to other researchers (e.g., ref. 13). We see normal amounts in the eleven hour spectrum compared to CO_2 absorbances in the 40 minute spectrum, Therefore we conclude that water is not a photoproduct of RDX.

If we consider one RDX molecule leading to products, then N_2 and H_2 must be postulated to balance the reaction:



This reaction would involve considerable movement of the atoms in forming the carbon products from one RDX molecule. Alternatively, more than one RDX molecule may participate in the formation of the carbon products.

VII. CONCLUSIONS

Reactions I and II are consistent with the condensed phase thermal chemistry and inconsistent with the gas phase chemistry. The formation of methylene, ethylene, methane, N_2O_3 , and ozone in our studies seems at first to be different from the known condensed phase chemistry. These differences may be unique to the matrix environment, the cryogenic temperature, and possibly the photochemical process. A weakness of our study was the absence of true isolation. Our postulated mechanisms assumed a unimolecular process, but participation from other RDX molecules or fragments could not be ruled out. In the limit that there are useful comparisons between matrix photochemical studies and high temperature condensed phase chemistry, then the matrix study shows that there must be two pathways leading to the higher temperature results.

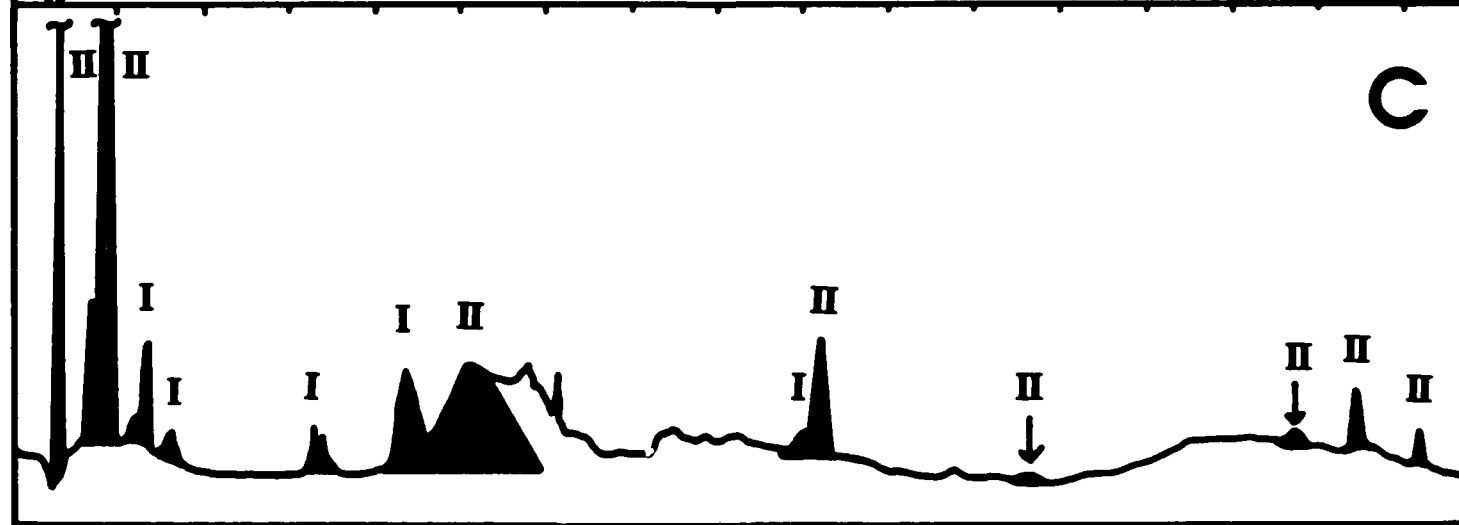
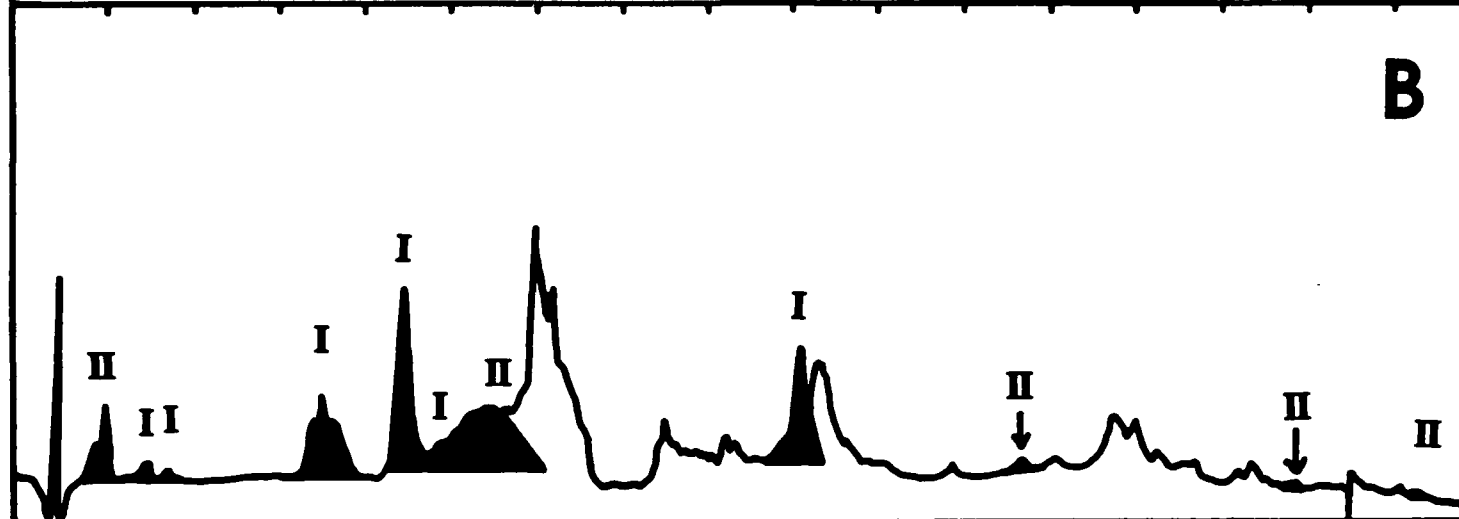
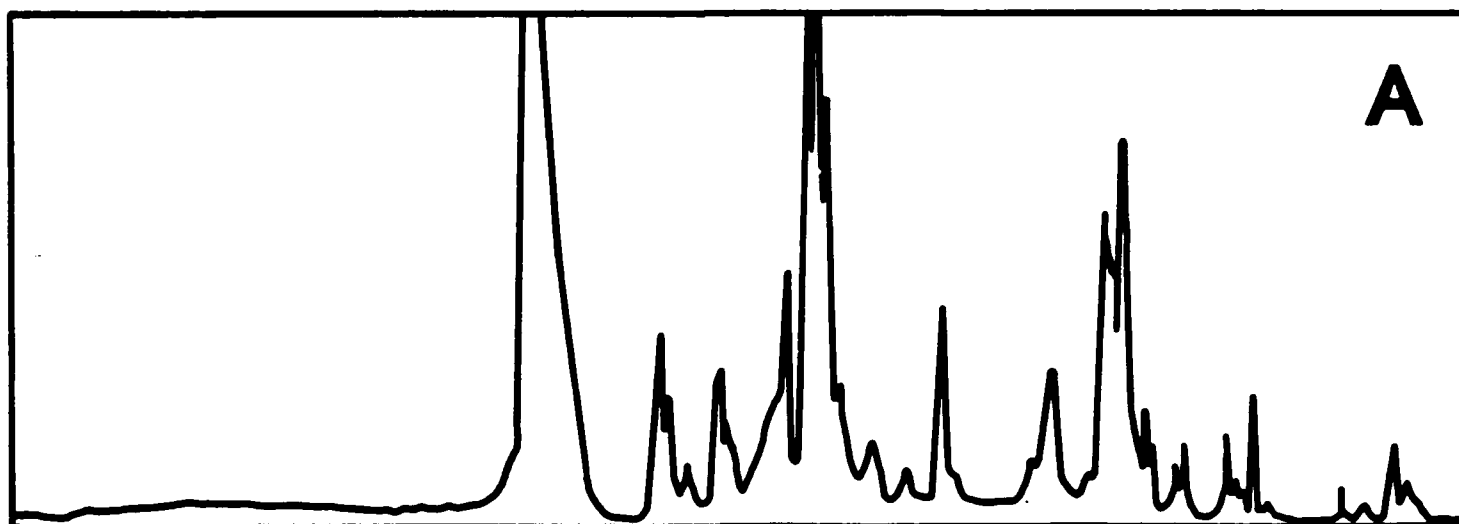
The conformation of the RDX in the solid phase is known to be the chair configuration with C_3 symmetry. A consequence of the C_3 symmetry is that the NO_2 groups are axial and adjacent. This structure could easily explain mechanisms I and II since the no geometric rearrangement of RDX is necessary for product formation except perhaps the carbon products in mechanism II. Furthermore the C_{3v} averaged configuration has the nitro groups pointing away from each other in the equatorial positions. This structure could more easily explain the stripping NO_2 mechanism and the symmetric triple fission processes seen in the gas-phase studies.

VIII. REFERENCES

1. W. Moran and S. Collins, *J. Mol. Struct.*, in press
2. M. Farber and R. Srivastava, *Chem. Phys. Lett.*, 1979, 64, 307.
3. S. Bulusu, D. Weinstein, J. Autura, and R. Veliky, *J. Phys. Chem.*, 1986, 90, 4121.
4. C. Capellos, S. Lee, S. Bulusu, and L. Gamss, "Advances in Chemical Reaction Dynamics" 1986, 398-404, D. Reidel Publ.
5. X. Zhao, E. Hintsä, and Y. T. Lee, *J. Chem. Phys.*, 1988, 88, 801.
6. W. GUillory and C. Hunter, *J. Chem. Phys.*, 1969, 50, 3516.
7. H. Khoshkhoo and E. Nixon, *Spectrochim. Acta*, 1973, 29A, 603.
8. J. Sodeau and E. Lee, *Chem. Phys. Lett.*, 1978, 57, 71
9. S. Collins, *J. Phys. Chem.*, in press
10. G. Ewing, A. Thompson, G. C. Pimentel, 1960, 32, 927.
11. C.B. Moore, T.D. Goldfarb, and G.C. Pimentel, *J. Chem. Phys.*, 1965, 43, 63.
13. S. Bhatia and J. Hall, *J. Phys. Chem.*, 1980, 84, 3255.
14. L. Andrews and R. Spiker Jr., *J. Phys. Chem.*, 1972, 76, 3208.
15. D. Lucas and G. Pimentel, *J. Phys. Chem.*, 31, 204, (1959
16. R. Karpowicz and T. Brill, *J. Phys. Chem.*, 1984, 88, 348.
17. A. Engdahl and B. Nelander, *Chem. Phys. Lett.*, 1983, 100, 129.
18. Y.P. Lee and G.C. Pimentel, *J. Chem. Phys.* 1981, 75, 4241.

IX. TABLE I

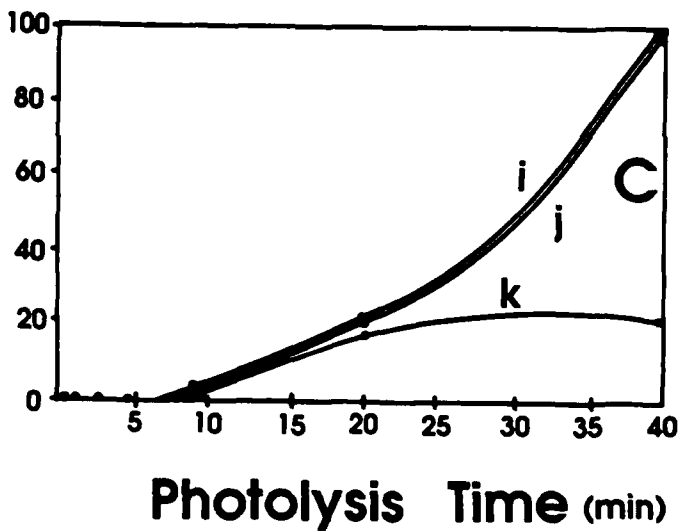
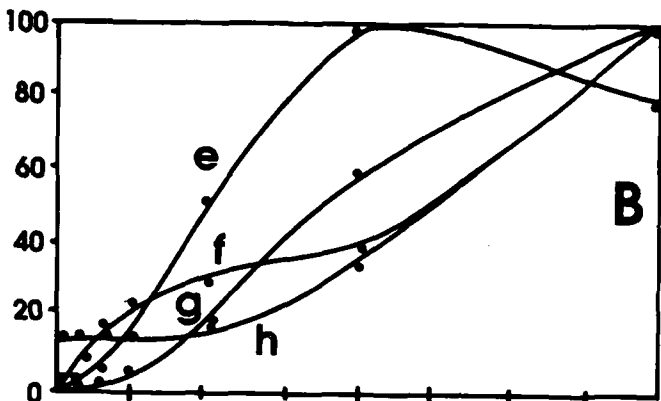
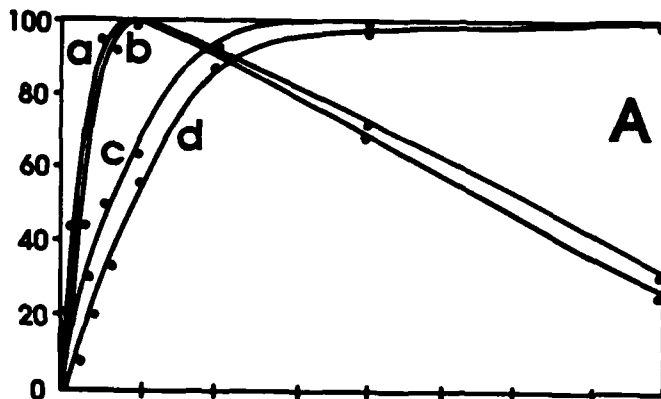
<u>FREQ.</u> <u>(CM⁻¹)</u>	<u>2 MIN</u>	<u>40 MIN</u>	<u>11 HRS</u>	<u>BAND IN</u> <u>TABLE I</u>	<u>KINETICS</u> <u>TYPE</u>	<u>ASSIGN-</u> <u>MENT</u>
3291.2	0	100	70	-	B	C ₂ H ₂
2227.5	2	20	100	-	B	N ₂ O
2218.9	2	25	100	f	B	N ₂ O
2140.0	0	18	100	i	C	CO
2085.0	0	31	100	k	C	CHO
1851.0	0	100	46	c	A	NO
1777.5	0	100	53	d	A	(NO) ₂
1740.0	20	42	0	a	A	CH ₂ O
1693.2	10	50	100	h	B	N ₂ O ₃
1498.1	20	45	0	b	A	CH ₂ O
1300.0	0	23	100	j	C	CH ₄
1283.0	2	20	100	-	B	N ₂ O
1045.3	4	96	90	e	B	O ₃
733.3	0	100	62	g	B	C ₂ H ₂
586.3	4	20	100	-	B	N ₂ O



400 2200 1900 1700 1500 1300 1100 900 700

WAVENUMBERS (cm^{-1})

Normalized Intensity



X. FIGURE CAPTIONS

1. FTIR absorption bands A.) of RDX in Ar at 10 K, B.) after 40 min photolysis and C.) after eleven hours photolysis. Bands with dark shading are product bands. Bands marked I and II are associated with mechanisms I and II, respectively.

2. Normalized FTIR product band intensities versus time. Curves marked a-k are from bands with the following frequencies: a. 1740.0, b. 1498.1, c. 1851.0, d. 1777.5, e. 1045.3, f. 2218.9, g. 733.3, h. 1693.2, i. 2140.0, j. 1300.0, k. 2085.0

XI. RECOMMENDATIONS

The lithium project will resume after the purchase of the new oven. The RDX project was completed.

XII. ACKNOWLEDGEMENTS

I would like to thank Dr. Steve Rodgers from the Edwards Air Force Base for suggesting these projects, and for his help and support during the summer 1988 faculty research program. I also would like to thank Pat Carrick, Walter Lauderdale and Wayne Roe for their support.

**FINAL REPORT NUMBER 20
CALIBRATION OF COMPOSITE-EMBEDDED
FIBER-OPTIC STRAIN SEMSORS
PENDING APPROVAL
Dr. David W. Jensen
210-9MG-052**

ENERGY- AND TIME-RESOLVED PHOTOPHYSICS AND
PHOTOCHEMISTRY OF HIGH ENERGY CRYOGENIC METAL-CONTAINING
ROCKET FUELS

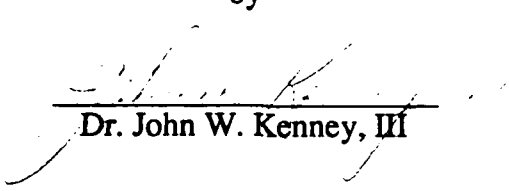
UES/AFOSR Contract No.
F 49620-85-C-00131 SB5651-0360 P.O. S-760-7MG-019
January 1988-April 1989

FINAL REPORT

submitted to

RESEARCH INITIATION PROGRAM
Universal Energy System, Inc.
4401 Dayton-Xenia Road
Dayton, Ohio 45432

by


Dr. John W. Kenney, III

Assistant Professor of Chemistry
Department of Physical Sciences--Chemistry
Eastern New Mexico University
Portales, New Mexico 88130

1987 UES/AFOSR Summer Faculty Research Fellow
Applied Research in Energy Storage Program
Air Force Astronautics Laboratory
Edwards Air Force Base, California 93523

April 27, 1989

Technical Focal Point: Dr. Stephen Rodgers, AFAL/CX
(805) 275-5413

University Focal Point: Dr. Everett Frost
Research Dean, ENMU
(505) 562-2147

INTRODUCTION

The focal point of our research effort in the High Energy Density Materials (HEDM) area was a detailed investigation of the photophysical properties of a series of bent titanium(IV) d^0 metallocene complexes. Also studied were a series of d^6 sandwich type metallocenes which included ferrocene, ruthenocene and many of their ring-substituted analogues. Selected organometallic complexes within these series have attracted attention as potential burn rate modifiers and fuel additives in propulsion applications. The basic metallocene structure--aromatic carbon containing rings providing stability to metals in energetic oxidation states via ring π /metal d orbital interactions--offers intriguing possibilities for energy storage as outlined in our UES/AFOSR RIP proposal for 1988. Our metal-ammonia research project, delayed owing to a cryogenic cell fabrication delay, will be initiated during the fall of 1989.

SUMMARY OF RESEARCH RESULTS

A. Bent Titanium(IV) Metallocenes

We carried out a detailed electronic spectroscopic study of a series of bent titanium(IV) metallocenes of the type Cp_2TiX_2 where Cp = cyclopentadienyl ($C_5H_5^-$) and X = halogen (F, Cl, Br, I) or phenyl in an effort to understand the energetics of these interesting molecules. We investigated solvent shifts in the ultraviolet-visible absorption spectra of these systems and we obtained the first reported solid state and solution glass photoluminescence spectra on the series. Our luminescence band maxima show small progressive shifts as we move down the periodic table in the halo series. A molecular orbital electronic model consistent with these spectral characteristics suggests that the lowest excited electronic state from which emission originates is a triplet charge transfer state involving the Cp π orbitals. Our luminescence results also show that for the X = I system there is also participation from non-bonding π orbitals of the I ligand. The very bright emissions observed in these complexes are consistent with their comparatively long luminescence lifetimes (as measured relative to a 10 μs standard). This is highly attractive for energy storage in rocket propulsion applications. Quantitative lifetime measurements will be carried out in the near future.

B. Iron Group Sandwich Metallocenes

Early literature references to the uses of metallocenes in propulsion cite ferrocene as the specific example. Our research effort has focused on obtaining high resolution luminescence spectra of

ferrocene and a large series of ferrocene analogues at cryogenic temperatures with a specific emphasis on resolving vibronic fine structure based upon the metal sandwich breathing mode. Such a spectrum has been obtained for solid ferrocene at 12 K. New luminescence spectra were measured for several substituted ferrocenes. These studies have helped to clarify the role of ring substitutions on the energy storage capacities of these systems. The vibronic fine structure in the electronic spectra of metallocenes provides a unique window through which to monitor the effects of high pressure perturbations (1-10 GPa) on the electronic environments of these systems leading ultimately to the possibility pressure-stabilized excited electronic states.

C. Metal Ammonia Solutions

Preliminary studies of a series of alkali metal/amine cryogenic solutions were undertaken. It was decided to focus the primary spectroscopic effort on metallocene systems while awaiting fabrication of a special matrix deposition cell for the study of cryogenic matrices of metal/amine systems. This special cell, a copy of one designed by us for use at AFAL during the summer of 1987, was delivered from AFAL in February 1989. It will be used in spectroscopic studies on these systems to be initiated in the Fall of 1989.

RESEARCH PRESENTATIONS/PUBLICATIONS

Low-Lying Charge Transfer Excited States of Bis(cyclopentadienyl)titanium Dichloride. D.R. Striplin, J.W. Kenney, III, M.I.S. Kenney, Inorganic Chemistry Paper 376, presented at the 196th National Meeting of the American Chemical Society, Los Angeles, California, September 1988.

Specific Impulse Enhancement Via Pressure Stabilized Excited Electronic States of High Energy Density Propellants. John W. Kenney, III, presented at the High Energy Density Materials Contractors Conference, New Orleans, Louisiana, March 1989.

Electronic Models of Bent Titanium(IV) Metallocenes. D.R. Striplin, J.W. Kenney, III, M.I.S. Kenney, Inorganic Chemistry Poster Paper 177, presented at the 197th National Meeting of the American Chemical Society, Dallas, Texas, April 1989.

Electronic States of Bent Titanium(IV) Metallocenes. D.R. Striplin, J.W. Kenney, III, M.I.S. Kenney, to be submitted to *Organometallics*, May 1989.

UNDERGRADUATE STUDENT RESEARCH SUPPORT

Five high ability undergraduate students were supported as research assistants in the Chemical Physics Laboratory through this UES/AFOSR RIP grant in carrying out the work described above. Mr. Durwin Striplin, an outstanding graduating senior chemistry major who will be entering the Ph.D. program in Chemical Physics at Washington State University in September 1989, did the major portion of the titanium research and initiated the ferrocene research. Mr. Striplin has received much praise and recognition for his outstanding original work on metallocene photophysics.

MAJOR EQUIPMENT ACQUISITIONS

A Hewlett-Packard (HP) digital storage oscilloscope, Hewlett Packard A/D converter components, and series of laser accessories as outlined in the original grant budget were the major equipment acquisitions. These equipment items were used to carry out the metallocene photophysical studies. A standard calibration lamp system was developed for a fraction of the cost estimated in the original budget allowing a greater budget allocation to be made for supplies, chemicals, and student salaries.

1989 USAF-UES RESEARCH INITIATION PROGRAM

Sponsored by the
AIR FORCE OFFICE OF SCIENTIFIC RESEARCH

Conducted by
Universal Energy Systems, Inc.

FINAL REPORT

Experimental Verification and Development of Structural
Identification Techniques on a Grid

Prepared by: Steven P. Kahn
Academic Rank: Graduate Student
Department: Engineering Science and Mechanics
University: Virginia Tech
Major Advisor: Dr. Mark Norris
Date: December 18, 1989
Contract No.: 4 - 35770

1.0 Abstract

The work that is reported herein deals with system identification methods for large flexible structures. Primarily we are interested in identifying vibrational parameters of the system including natural frequencies and mode shapes, commonly known as modal identification. Sometimes it is of interest to estimate or update the mass, damping, and/or stiffness properties of a structure, which is referred to as parameter identification. The motivation for this work comes from the area of control. Proposed plans for the future include the deployment of space structures, e.g., NASA's space station. These structures must be controlled to suppress unwanted vibration and to maneuver the structure to desired locations. Before controlling any structure, it is necessary to have an accurate model which includes knowing the natural frequencies and mode shapes. System identification is an important process that leads to system control.

As the control requirements on systems become more stringent, it will become necessary to improve the identification results and it will be necessary to implement these algorithms on-orbit for space systems. Hence, not only must the identified values be accurate, but the efficiency in obtaining them is vital to their potential application. This work attempts to study, investigate, and

improve existing identification algorithms to determine their properties, improve their efficiency, and comment on their applicability to the identification problem in a space environment.

2.0 Acknowledgements

I would like to take this opportunity to express my gratitude to various individuals who were a help to me in completing this research. First of all, much thanks and appreciation are due to my major advisor on this work, Dr. Mark A. Norris. His guidance and leadership throughout this year have been immeasurable. Also, I would like to thank Dr. Alok Das of the Astronautics Laboratory at Edwards Air Force Base for his ideas and support. In addition, I find it necessary to express my gratitude to Waid Schlaegel, also at the Astronautics Lab, for all the help he has provided me. Finally, I would like to thank my wife, Buff, for her support, understanding, and encouragement. Without her I'm not sure if I would have made it.

3.0 Introduction

In recent years the study of large space structures has become increasingly important. As a result, hundreds of technical papers have been written dealing with this subject. The dynamical properties of large space structures can be described by lightly-damped, nearly self-adjoint distributed systems. In order to control these systems on-orbit, it is necessary to first obtain a mathematical model that will adequately describe the system's response.

Identification methods are either carried out in the frequency domain or the time domain. Early schemes were implemented in the frequency domain, but problems often occurred in identifying repeated or closely spaced frequencies. Ibrahim developed an effective time domain algorithm [1]. Juang and Pappa introduced the Eigensystem Realization Algorithm (ERA) [2,3] which uses the singular value decomposition of a generalized Hankel matrix. Multiple data sets can be used to identify repeated frequencies. Several papers have been written by Montgomery and others [4-6] that use Autoregressive Moving-Average (ARMA) models to identify control effectiveness parameters of distributed structures. These methods use a linear least-squares approach. Norris and Silverberg [7,8] have introduced a method that uses the temporal correlation properties exhibited between combinations of sensor measurements to reduce

the differential eigenvalue problem to an algebraic one.

The previous methods are concerned with modal identification. Martinez [9,10] has developed a frequency domain method for parameter identification that uses the iterative Extended Kalman Filter equations. The problem can be formulated in different ways depending on what quantities are to be estimated. Meirovitch and Norris [11,12] have introduced parameter identification methods based on the finite element method using both the time and frequency domain. Norris has recently shown that a constrained version of the ERA exists for the modal identification of lightly-damped systems [13].

An important aspect of identification is spillover. Because of practical limitations, structures must be modeled by discrete systems. In other words, only a subset of the modes of the structure are used in the modeling process. The effect of the residual (unmodeled) modes on the identified values is known as identification spillover. Since practical applications give rise to this phenomenon, it is of interest and importance to investigate its properties for various algorithms.

4.0 Objectives

Control of large flexible structures requires the accurate knowledge of the system parameters, e.g. natural frequencies and mode shapes, along with mass, damping, and stiffness properties. In the case in which ground-based testing of the fully deployed structure is not possible, a robust, computationally-efficient identification algorithm must be implemented on-orbit. To test and evaluate the identification techniques, ground tests must be performed to determine their practicality, performance, and robustness.

The objective of the research was to experimentally verify, compare, and improve existing structural identification techniques, focusing on those which are suitable for ground-based testing and on-orbit application. The intent of the work is to develop a computationally-efficient identification algorithm suitable for space applications. In addition, the efficiency of the algorithms will be enhanced by considering the structures to be lightly damped. The identification techniques will be tested by using a ground-based experiment, namely the Astronautics Laboratory (AL) Grid structure.

We mainly consider two identification algorithms: (1) the Temporal Correlation Method (TCM) [8] and (2) the Eigensystem Realization Algorithm [2]. The TCM uses the temporal correlation properties of lightly-damped distrib-

uted systems to show that approximations to the natural frequencies and mode shapes can be obtained directly from the solution of an algebraic eigenvalue problem. The matrices in the eigenvalue problem can be formed by correlating sensor measurements. The ERA begins by forming the generalized Hankel matrix consisting of free response measurements. The singular values of the Hankel matrix are used to obtain a minimum order realization of the system. We note that the ERA is implemented in the state space. In the ERA, the order of the model is twice the order of the model for the TCM as the TCM is implemented in the configuration space.

We show how the TCM reduces to a constrained version of the ERA in cases of light damping. This is significant because it effectively reduces the order of the ERA model by a factor of two. Since we are interested in large space structures, the condition of light damping is easily met.

Other identification methods that were investigated to various degrees include the Autoregressive Moving-Average (ARMA) models and the Extended Kalman Filter (EKF). It was found to be more beneficial to concentrate on the TCM and the ERA, but some work was accomplished with the other routines.

5.0 The Temporal Correlation Method

5.1 Equations of Motion

The governing equation of motion of a lightly-damped distributed structure is given by the partial differential equation (pde)

$$\mathcal{L}u(P,t) + \xi \dot{u}(P,t) + m(P)\ddot{u}(P,t) = f(P,t), P \in D \quad (1)$$

where $u(P,t)$ is the displacement at the spatial position P at time t , \mathcal{L} is a linear self-adjoint differential operator of order $2p$ representing the system stiffness, ξ is a viscous damping operator, $m(P)$ is the system mass distribution, and $f(P,t)$ is the external force density. We concern ourselves with the case of light damping, or where the term $\xi \dot{u}(P,t)$ is of at least one order of magnitude smaller than the remaining terms in Eq.(1). The associated boundary conditions are given by

$$B_i u(P,t) = 0, \quad i=1,2,\dots,p, \quad P \in S \quad (2)$$

where B_i are linear differential operators of order 0 to $2p-1$. The boundary conditions can either be geometric, in which case the order of B_i is no greater than p , or natural, in which case the order of B_i is greater than p . Functions satisfying the geometric boundary conditions are called admissible functions whereas functions satisfying

all boundary the conditions are called comparison functions.

for the case of free vibration, consider the eigenvalue problem associated with Eq.(1)

$$\Delta \phi_r(P) = \lambda_r m(P) \phi_r(P), \quad r=1,2,\dots \quad (3)$$

where $\phi_r(P)$ are functions that satisfy the boundary conditions

$$B_i \phi_r(P) = 0, \quad i=1,2,\dots,p, \quad r=1,2,\dots \quad (4)$$

The solution to Eqs.(3) and (4) consists of a denumerably infinite set of real, non-negative eigenvalues and associated real eigenfunctions $\phi_r(P)$. The eigenvalues are related to the undamped natural frequencies of the system by $\lambda_r = \omega_r^2$ ($r=1,2,\dots$). For convenience, we order the eigenvalues so that $\lambda_1 \leq \lambda_2 \leq \dots$.

The eigenfunctions obey the following orthonormality conditions:

$$\int_0 m(P) \phi_r(P) \phi_s(P) dD = \delta_{rs}, \quad r,s = 1,2,\dots \quad (5)$$

and

$$\int_0 \phi_r(P) \Delta \phi_s(P) dD = \lambda_r \delta_{rs}, \quad r,s = 1,2,\dots \quad (6)$$

where δ_{rs} is the Kronecker delta function. From the expansion theorem [14], we can express the displacement as

$$u(p,t) = \sum_{r=1}^{\infty} \phi_r(p) u_r(t) \quad (7)$$

where $u_r(t)$ are generalized coordinates and are modal coordinates for the undamped structure. Substituting Eq.(7) into Eq.(1), multiplying the result by $\phi_s(p)$, and integrating over the domain gives

$$\ddot{u}_r(t) + \sum_{r,s=1}^{\infty} c_{rs} \dot{u}_r(t) + \omega_r^2 u_r(t) = f_r(t), \quad r,s=1,2,\dots \quad (8)$$

where

$$c_{rs} = \int_D \phi_r(p) \xi \phi_s(p) dD, \quad r,s=1,2,\dots \quad (9)$$

are small viscous damping coefficients and

$$f_r(t) = \int_D \phi_r(p) f(p,t) dD, \quad r=1,2,\dots \quad (10)$$

are modal control forces.

Equations (8) represent an infinite set of ordinary differential equations that govern the response of lightly-damped, nearly self-adjoint distributed structures. In the presence of high damping, the decoupling nature is destroyed, the structure can no longer be classified as nearly self-adjoint, and the following development is invalid. In the case of light levels of damping, however, the self-adjointness property is preserved, and the generalized coordinates can be regarded as modal coordinates.

5.2 Correlation of the Modes of Vibration

Consider the case where the distributed structure is lightly-damped so that the system can be considered self-adjoint. The orthonormality conditions, Eqs.(5) and (6), hold which means that the modes of vibration are spatially orthogonal. It can be shown that the modes of vibration are uncorrelated in time as well [8]. In particular, the correlation condition between modal coordinates is given by

$$\left\langle \frac{d^n u_r(t)}{dt^n}, \frac{d^n u_s(t-T_0)}{dt^n} \right\rangle = \frac{1}{\alpha_r} (\alpha_r + \omega_r)^{2n} |A_r|^2 e^{\alpha_r T_0} \cos \omega_r T_0 \delta_{rs} \quad (11)$$

where α_r is the r^{th} modal decay rate, ω_r is the r^{th} natural frequency of oscillation, A_r is the r^{th} modal amplitude, and T_0 is a time offset. Recall that $u_r(t)$ is the r^{th} modal coordinate. Also, the temporal inner product $\langle \cdot, \cdot \rangle$ between any two generalized coordinates $q_r(t)$ and $q_s(t)$ is given by [8]

$$\langle q_r(t), q_s(t) \rangle = \lim_{T \rightarrow \infty} \frac{1}{T} \int_0^T q_r(t) q_s(t) dt \quad (12)$$

Note from Eq.(11) that the temporal correlation of different modes is identically zero. Hence, the modes of vibration are uncorrelated in time.

5.3 Discretization

In general, closed-form solutions to Eq.(1) do not exist, so that we must consider an approximate solution. Commonly used techniques for obtaining approximate solutions are discretization techniques such as the finite element, the Rayleigh-Ritz, and the Galerkin methods. The techniques approximate the pde given by Eq.(1) by expressing the solution as a discrete linear combination of test functions multiplied by generalized coordinates. The Galerkin method is applicable to non-self-adjoint systems, in which the test functions must satisfy all the boundary conditions [14]. The finite element and Rayleigh-Ritz methods are applicable to self-adjoint systems, where the former can be regarded as a variant of the latter [14]. The finite element and Rayleigh-Ritz methods are based on a variational principle, in which test functions need only be admissible functions and guarantee convergence to the exact solution of the pde.

Consider the admissible functions $\psi_r(P)$ ($r=1,2,\dots,n$) and express the displacement $u(P,t)$ as a linear combination of the functions $\psi_r(P)$ multiplied by time-dependent generalized coordinates $q_r(t)$ as follows:

$$u^{(n)}(P,t) = \sum_{r=1}^n \psi_r(P) q_r(t) = \underline{\Psi}^T(P) \underline{q}_n(t) \quad (13)$$

where $u^{(n)}(P,t)$ is the n^{th} -order approximation of $u(P,t)$, $\underline{\Psi}(P) = [\psi_1(P) \cdot \cdot \cdot \psi_n(P)]^T$ is an n -vector of admissible func-

tions, and $\underline{q}_n(t)$ is an n-vector of generalized coordinates. The n-degree-of-freedom discretized model can be obtained using the finite series expansion given by Eq.(13) and has the form [14]

$$M^{(n)} \ddot{\underline{q}}_n(t) + C^{(n)} \dot{\underline{q}}_n(t) + K^{(n)} \underline{q}_n(t) = \underline{F}^{(n)}(t) \quad (14)$$

where

$$M^{(n)} = \int_0^D m(p) \underline{\Psi}(p) \underline{\Psi}^T(p) dD \quad (15a)$$

$$C^{(n)} = \int_0^D \underline{\Psi}(p) [\xi \underline{\Psi}(p)]^T dD \quad (15b)$$

$$K^{(n)} = [\underline{\Psi}(p), \underline{\Psi}^T(p)] \quad (15c)$$

are n x n mass, damping, and stiffness matrices respectively, and

$$\underline{F}^{(n)}(t) = \int_0^D \underline{\Psi}(p) F(p,t) dD \quad (16)$$

is an n-dimensional generalized force vector. In addition, [,] is an energy inner product [14] obtained through integration by parts of $\int_0^D \underline{\Psi}(p) (\mathcal{L} \underline{\Psi}(p))^T dD$, and hence, is symmetric because \mathcal{L} is self-adjoint. The energy inner product [u,u] is proportional to the potential energy of the system [14]. Since the structure is lightly-damped, the term $C^{(n)} \dot{\underline{q}}_n(t)$ is of at least one order of magnitude

smaller than the remaining terms in Eq.(14). We consider the undamped n-degree-of-freedom discrete model of the distributed structure. Unlike other discretization techniques, an attractive feature of the Rayleigh-Ritz method is that by increasing the number of degrees of freedom n, the previously calculated mass and stiffness coefficients do not change, so that one need only calculate an additional row (or column) to obtain the updated mass and stiffness matrices. For an (n+1)-degree-of-freedom discrete model, the mass and stiffness matrices have the form

$$M^{(n+1)} = \begin{bmatrix} M^{(n)} & X \\ X & X \end{bmatrix}, \quad K^{(n+1)} = \begin{bmatrix} K^{(n)} & X \\ X & X \end{bmatrix} \quad (17)$$

The eigenvalue problems associated with the discrete models are given by

$$\lambda_r^{(n)} M \underline{x}_r^{(n)} = K \underline{x}_r^{(n)}, \quad r=1,2,\dots,n \quad (18)$$

and

$$\lambda_r^{(n+1)} M \underline{x}_r^{(n+1)} = K \underline{x}_r^{(n+1)}, \quad r=1,2,\dots,n+1 \quad (19)$$

The inclusion principle [14] requires the eigenvalues of the n-degree-of-freedom model and the eigenvalues of the (n+1)-degree of-freedom model to obey the relationship

$$\lambda_1^{(n+1)} \leq \lambda_1^{(n)} \leq \lambda_2^{(n+1)} \leq \lambda_2^{(n)} \leq \dots \leq \lambda_n^{(n)} \leq \lambda_{n+1}^{(n+1)} \quad (20)$$

As the number of degrees of freedom n in the discrete model is increased, the approximate eigenvalues decrease monoton-

ically and approach the actual eigenvalues of the system asymptotically from above [14].

5.4 Modal Identification of Lightly-Damped Structures

We wish to use free response measurements to obtain estimates of the system's natural frequencies and mode shapes. Due to the discretization procedure, only approximations to the modes of vibration can be obtained. It will be shown that the identified eigenvalues obey the inclusion principle as was the case for the Rayleigh-Ritz method. In addition, the identified eigenvalues approach the system eigenvalues monotonically from above as the order of the model is increased. Consider correlating the derivatives of the generalized coordinates $\underline{q}_n(t)$ and define

$$A^{(n)} = \left\langle \frac{d^m}{dt^m} \underline{q}_n(t), \frac{d^m}{dt^m} \underline{q}_n(t) \right\rangle \quad (21)$$

and

$$B^{(n)} = \left\langle \frac{d^k}{dt^k} \underline{q}_n(t), \frac{d^k}{dt^k} \underline{q}_n(t-T_c) \right\rangle \quad (22)$$

The generalized coordinates can be written as a linear combination of the eigenvectors \underline{x}_r ($r=1,2,\dots,n$) multiplied by the modal coordinates, or

$$\underline{q}_n(t) = \sum_{r=1}^n \underline{x}_r^{(n)} u_r(t) \quad (23)$$

Substituting Eq.(23) into Eqs.(21) and (22), we arrive at the following

$$A^{(m)} = \sum_{r=1}^n \sum_{s=1}^n \tilde{x}_r^{(n)} \tilde{x}_s^{(n)T} \left\langle \frac{d^m u_r(t)}{dt^m}, \frac{d^m u_s(t)}{dt^m} \right\rangle \quad (24)$$

and

$$B^{(n)} = \sum_{r=1}^n \sum_{s=1}^n \tilde{x}_r^{(n)} \tilde{x}_s^{(n)T} \left\langle \frac{d^k u_r(t)}{dt^k}, \frac{d^k u_s(t-T_0)}{dt^k} \right\rangle \quad (25)$$

Now consider the algebraic eigenvalue problem

$$\lambda_r^{(n)} A^{(n)} \underline{v}_r^{(n)} = B^{(n)} \underline{v}_r^{(n)} \quad (26)$$

By using Eq.(11) in Eqs.(24) and (25) and substituting the result into Eq.(26) gives

$$\lambda_r^{(n)} \sum_{s=1}^n \frac{1}{\alpha_s} (\alpha_s + \omega_s)^{2m} |A_s|^2 \tilde{x}_s^{(n)} \tilde{x}_s^{(n)T} \underline{v}_r^{(n)} = \sum_{s=1}^n \frac{1}{\alpha_s} (\alpha_s + \omega_s)^{2k} |A_s|^2 \tilde{x}_s^{(n)} \tilde{x}_s^{(n)T} e^{\alpha_s T_0} \cos \omega_s T_0 \underline{v}_r^{(n)} \quad (27)$$

It can be shown by using the orthonormality conditions of Eq.(18) that the solution to Eq.(27) is given by

$$\underline{v}_r^{(n)} = M^{(n)} \tilde{x}_r^{(n)} \quad (28)$$

and

$$\lambda_r^{(n)} = (\alpha_r + \omega_r)^{2(k-m)} e^{\alpha_r T_0} \cos \omega_r T_0 \quad (29)$$

The modal identification procedure is as follows: First, the matrices $A^{(n)}$ and $B^{(n)}$ are computed by correlating the generalized coordinates $\underline{q}_A(t)$. In practice the generalized coordinates can be replaced by actual sensor

measurements, i.e. accelerations, velocities, angular rates, etc.. Then, the eigenvalue problem of Eq.(26) is solved to obtain $\lambda_r^{(n)}$ and $v_r^{(n)}$. Finally, Eqs.(28) and (29) provide the relationship between the eigenvalues and eigenvectors of Eq.(26) to produce identified natural frequencies and mode shapes of the system.

Consider the case where we let $k=m$ in Eqs.(21) and (22). With the light damping restriction $\alpha_r \approx 0$, we obtain

$$\omega_r = \frac{1}{T_0} \cos^{-1} \lambda_r^{(n)} \quad (30)$$

Now consider the case where we let $k=2$, $m=1$, and $T=0$. This gives us

$$\omega_r = \sqrt{\lambda_r} \quad (31)$$

The first case suggests that we use the same type of sensor measurement in computing both $A^{(n)}$ and $B^{(n)}$, the only difference between the two being the time offset T_0 . In the second case, we use velocities for the correlation in Eq.(21) and accelerations in Eq.(22) which implies that the time offset be identically zero [8].

In summary, the sensor measurements are correlated to obtain two $n \times n$ matrices $A^{(n)}$ and $B^{(n)}$. An eigenvalue problem is solved involving these two matrices, and its eigenvalues and eigenvectors are directly related to the

identified natural frequencies and mode shapes of the system. Because of the way in which $A^{(n)}$ and $B^{(n)}$ are computed, the eigenvalues of Eq.(26) obey the inclusion principle. Specifically, since the higher order models have similar structure to Eq.(17) in that they are formed by adding rows and columns to the existing $A^{(n)}$ and $B^{(n)}$, the $(n+1)$ -degree-of-freedom model eigenvalues obey the inclusion principle given by Eq.(20).

6.0 The Eigensystem Realization Algorithm

6.1 Equations of Motion

For the Eigensystem Realization Algorithm (ERA), we consider the state space model of a finite dimensional, discrete-time, linear, time-invariant dynamical system given by

$$\underline{x}(k+1) = A \underline{x}(k) + B \underline{u}(k) \quad (32)$$

and

$$\underline{y}(k) = C \underline{x}(k) \quad (33)$$

where \underline{x} is an n-dimensional state vector, \underline{u} is an m-dimensional input vector, and \underline{y} is a p-dimensional output vector. The dynamical properties (i.e. mass, stiffness, etc.) of the system are contained within the matrix A. Our goal is to extract the modal parameters from the free or impulse response measurements. A realization is obtained by finding matrices [A, B, C] that satisfy Eqs.(32) and (33) so that the outputs of the discrete model match those of the actual system while considering the noise in the sensor measurements.

6.2 The Hankel Matrix

The foundation of the ERA lies in the formation of the generalized Hankel matrix. It is composed of impulse

response sensor measurements. The Hankel matrix is actually an $r \times s$ block matrix with each individual block having dimension $l \times m$ where l is the number of sensors used in the analysis and m is the number of sets of impulse response data. The use of multiple impulse response records is particularly useful in identifying repeated eigenvalues. The overall dimension of the generalized Hankel matrix is $(lr) \times (ms)$ and has the form

$$H(k-1) = \begin{bmatrix} Y(k) & Y(k+1) & \dots & Y(k+S-1) \\ Y(k+1) & Y(k+2) & & \\ \vdots & & \ddots & \\ Y(k+H-1) & & & Y(k+H-2) \end{bmatrix} \quad (34)$$

Actually, the more general form of the algorithm allows for arbitrary integer increments in the Hankel matrix [2] opposed to the unity increments considered here.

6.3 The Singular Value Decomposition

After forming the generalized Hankel matrix $H(k)$, a singular value decomposition is performed using $H(0)$, the value of the Hankel matrix at time zero. In the remainder of this section we show a method for obtaining the singular values of a rectangular matrix that uniquely defines its singular value decomposition. Consider the decomposition of $H(0)$ and $H(0)$

$$H(0) = USV^T \quad (35)$$

and

$$H^T(0) = VS^T U^T \quad (36)$$

where the $(lr) \times (lr)$ matrix U and the $(ms) \times (ms)$ matrix V are isometric so that $UU^T = I$ and $VV^T = I$. Also note that S is diagonal and has dimension $(lr) \times (ms)$, the same dimension as $H(0)$. Now

$$H^T(0)H(0)V = VS^2 \quad (37)$$

and

$$H(0)H^T(0)U = US^2 \quad (38)$$

where S^2 is a square diagonal matrix. Now consider the two eigenvalue problems

$$G\underline{v}_i = \underline{v}_i \lambda_i \quad (39)$$

and

$$G^T \underline{u}_i = \underline{u}_i \lambda_i \quad (40)$$

where $G = H^T(0)H(0)$. Note that the eigenvalues of Eqs. (39) and (40) are simply the square roots of the singular values of $H(k)$. Also, the eigenvectors \underline{v}_i and \underline{u}_i are the columns of the matrices V and Q respectively.

6.4 Minimum Order Realization

The matrices U , S , and V are partitioned such that $H(s) = PDQ^T$ where P has dimension $(lr) \times n$, D has dimension $n \times n$, and Q has dimension $(ms) \times n$. The matrices P , D , and Q are further partitioned by retaining only the singular values pertaining to the system modes. Using this partitioned decomposition, it can be shown [2] through a series of matrix manipulations that the minimum order realization, the triple $[A,B,C]$, is given by

$$[A,B,C] = [D^{-1/2} P^T H(s) Q D^{-1/2}, D^{1/2} Q^T E_m, E_p^T P D^{1/2}] \quad (4)$$

where $E_m = [I_m, 0_m, \dots, 0_m]$ is an $m \times (ms)$ matrix and $E_p = [I_p, 0_p, \dots, 0_p]$ is an $l \times (lr)$ matrix.

6.5 Modal Parameter Identification

The generalized Hankel matrix has dimension $(lr) \times (ms)$ as was mentioned before. The number of singular values will be equal to the greater of the row and column dimension. For n modes participating in the system response, all but $2n$ of these singular values will be zero for the case of no noise in the output measurements. Since in practical applications there is always some noise present, these singular values are not zero but are very small. Also in practice we do not know how many modes are participating in the response. Therefore, the procedure is

to put the singular values in descending order, establish a criterion for determining which of these are due to the response and which are due to noise, and partition D, P, and Q [2].

The next step in the process is to solve the eigenvalue problem

$$A\psi_r = \psi_r z_r, \quad r=1, 2, \dots, 2n \quad (42)$$

where A is the realized A-matrix of Eq.(41) given by

$$A = D^{-1/2} P^T H(1) Q D^{-1/2} \quad (43)$$

The identified eigenvalues obtained from the solution of Eq.(42) are in the z-plane, as the original formulation was in discrete time. The eigenvalues can be transformed to the s-plane using the relationship

$$s_r = (\ln z_r \pm i 2j\pi) / \Delta\tau \quad (44)$$

where j is an integer usually taken to be zero and $\Delta\tau$ is the sampling interval. In general the identified eigenvalues are complex in which the real parts represent the identified modal damping rates and the imaginary parts represent the identified damped natural frequencies of the structure. In addition, the mode shapes are contained in the matrix

$$M = E_p^T P D^{1/2} \Psi \quad (45)$$

where M is the identified eigenvector matrix or the modal participation matrix.

6.6 Modal Amplitude Coherence: An Accuracy Indicator

In real applications the number of modes participating in the response is not known a priori and measurement noise degrades the results of the identification in which "noise modes" are identified. An accuracy indicator used to quantify the degree to which a particular mode is likely to be a system mode was developed by J. N. Juang and R. S. Pappa [2]. The indicator determines the coherence between the predicted modal amplitude history using the actual data and an ideal one based on the identified eigenvalue and eigenvector of each identified mode. The coherence is appropriately named the modal amplitude coherence and symbolized by γ .

We can summarize the procedure for modal identification in the ERA as follows: (1) construct the generalized Hankel matrix from free response data, (2) perform the singular value decomposition as given by Eq.(35) and obtain the matrices P , D , and Q through partitioning, (3) inspect

the singular values and determine the order of the system, (4) partition P , D , and Q further based on the system order, (5) identify the eigenvalues and mode shapes by solving the eigenvalue problem of Eq.(42), and (6) calculate the modal amplitude coherence for each identified mode.

7.0 Demonstration of the Methods

In this section we provide several cases to demonstrate how the TCM and the ERA work. We consider situations in which there is (1) no damping in the system and no noise in the sensor measurements, (2) damping without noise, (3) noise without damping, and (4) damping with noise. For all four cases we consider a simply supported beam with the three lowest modes participating in the response. The beam has uniform properties with length $L = 5\text{m}$, bending rigidity $EI = 30 \text{ N m}$, and mass density $m = 1 \text{ kg/m}$. With these values, the eigenvalue problem of Eq.(3) has the closed-formed solution [14] $\omega_r = \sqrt{30} \left(\frac{r\pi}{5}\right)^2$ ($r=1,2,\dots$) and $\phi_r(x) = \sqrt{\frac{2}{5}} \sin\left(\frac{r\pi x}{5}\right)$ ($r=1,2,\dots$). For each case, six acceleration sensors were used at positions $x_i = iL/7$. Also, for the TCM, we use velocities in the correlation of Eq.(21) and accelerations in the correlation of Eq.(22) so that the identified eigenvalues and eigenvectors are obtained from Eqs.(26) and (31).

The identified natural frequencies for case (1) are illustrated in Table 1. Both methods give good results for no damping and no noise, however the ERA identifies the natural frequencies exactly, while for TCM there is a small error. This is attributed to the truncation of the temporal inner products given by Eqs.(21) and (22). The identified mode shapes for the TCM and the ERA are also consistent with the first three mode shapes of a simply supported beam

as shown in Figs. 1 and 2.

TABLE 1-Identified frequencies

r	ω_r -actual	ω_r -TCM	ω_r -ERA
1	2.1623	2.1496	2.1623
2	8.6493	8.6527	8.6493
3	19.4609	19.4500	19.4609

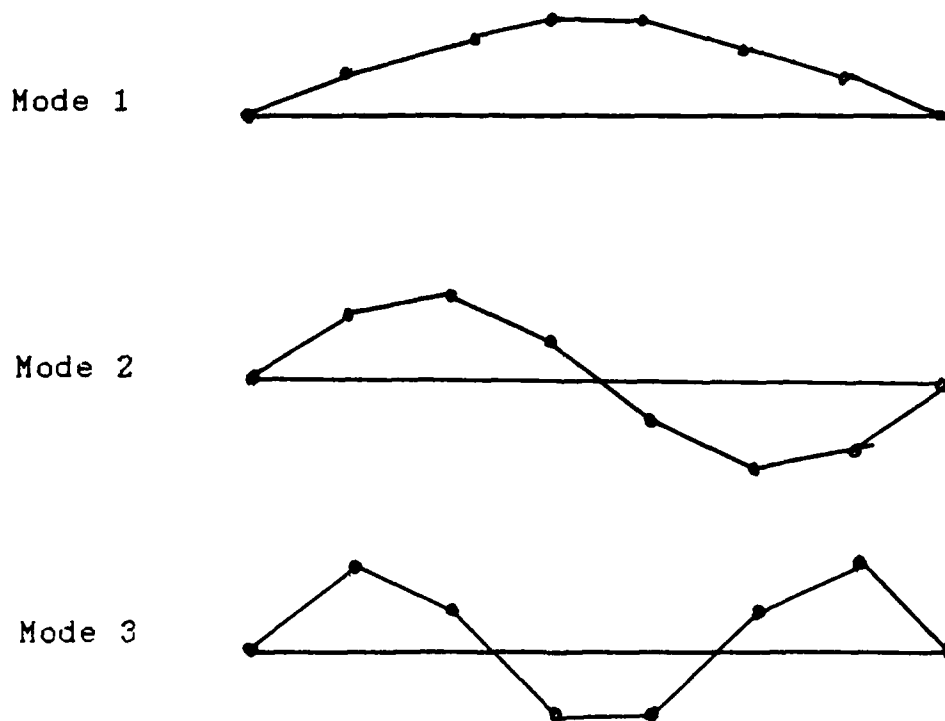


Figure 1: Identified mode shapes of a simply supported beam using the TCM with no damping and no noise.

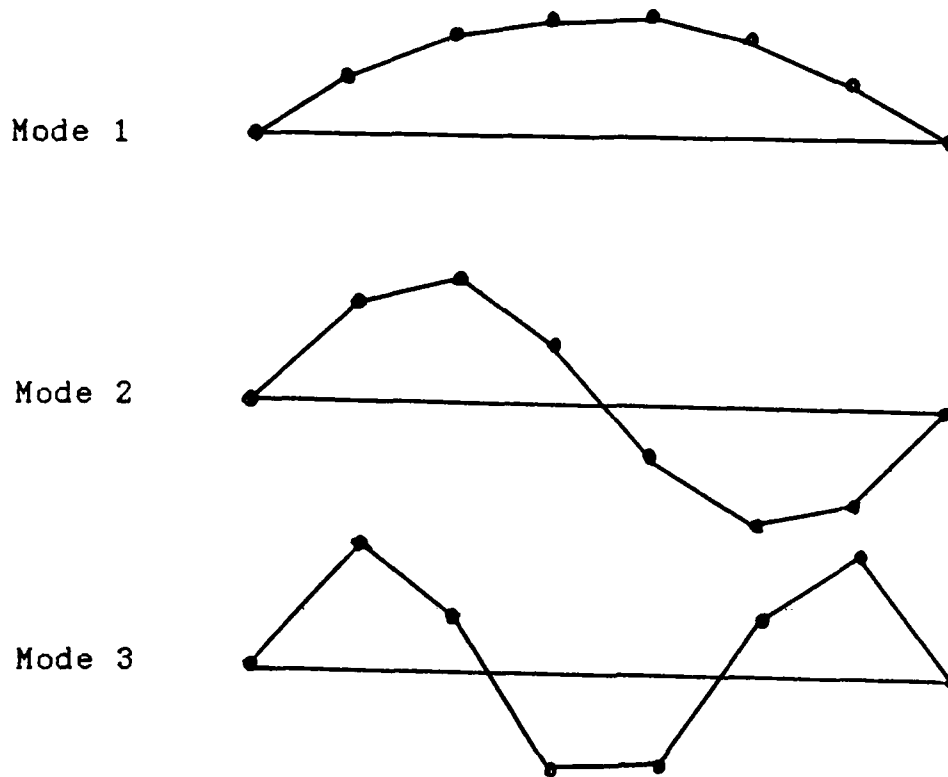


Figure 2: Identified mode shapes of a simply supported beam using the ERA with no damping and no noise.

Now we look at the case where we include damping in the response. Of course, in real applications there is always some level of damping present. Here we consider a damping coefficient of $\zeta = .1$. This is consistent with the light damping restriction imposed by the TCM. The identified natural frequencies are shown in Table 2.

Table 2-Identified frequencies

r	ω_r -actual	ω_r -TCM	ω_r -ERA
1	2.1623	2.1926	2.1623
2	8.6493	8.6466	8.6493
3	19.4609	19.0556	19.4609

Notice that the identified natural frequencies for both methods are still quite good for this case. In fact, the ERA provides exact results. It is interesting to note that each of the identified natural frequencies for the TCM are effected by different amounts by the damping. The mode shapes for ERA in the case of damping do not change. They are not effected at all by the addition of damping. Conversely, the mode shapes identified by the TCM do undergo some change from the undamped case. These changes caused by damping are slight, however, and the mode shapes are similar to those shown in Fig. 2.

Next we consider the case where Gaussian noise is added to the sensor outputs such that at one standard deviation, the noise added is 10% of the measurement, denoted by $\eta = 10\%$. In addition, there is no damping. The identified natural frequencies are given in Table 3. Notice that the ERA gives much better results for this

example. In fact, the TCM is roughly 100% off for the fundamental frequency, but better for the remaining ones. In the next section we shall investigate more in depth the effect of noise on the two methods.

Table 3-Identified frequencies

r	ω_r - actual	ω_r - TCM	ω_r - ERA
1	2.1623	5.5821	2.2053
2	8.6493	10.6527	8.6388
3	19.4609	18.6960	19.4584

The mode shapes for this case are not shown. Both methods identify eigenvectors that are consistent with the actual mode shapes. The largest deviation from any element in the normalized identified eigenvectors in the case with no noise is about 3% for the TCM while it is about 30% for the ERA. On average, however, the deviation is less than 5% for the ERA and less than 2% for the TCM. Hence, the presence of 10% noise is not detrimental to the identified results of the eigenvectors for both methods.

Finally, we include both damping and noise with values $\xi = .05$ and $\eta = 5\%$. Table 4 contains the identified natural frequencies for the two methods. The ERA once again gives the more accurate estimates. However, the

identified frequencies for the TCM are much better than they were for case three. It is apparent that noise effects, at least for the case of linear, light damping considered here, are much more a cause for error in the identified natural frequencies than are damping effects.

Table 4-Identified frequencies

r	ω_r - actual	ω_r -TCM	ω_r -ERA
1	2.1623	2.7842	2.2053
2	8.6493	8.0946	8.6349
3	19.4609	18.1804	19.4389

The identified eigenvectors for the two methods are in close agreement with the actual mode shapes. We do not show them here, but we note that there is not a great difference between the results for the two methods.

8.0 Comparison of Noise Effects

We wish to investigate the effect of adding noise to simulated data to the identified eigenvalues or natural frequencies for both the TCM and the ERA. In particular, we compare the performance of the two methods when the amount of noise added is increased. This type of study provides some insight into how to interpret identified results in actual applications in addition to determining if either method can be considered superior in the area of noise.

Plots of the signal-to-noise ratio (snr) versus the average percent error ρ in the identified natural frequencies for the first three modes of a simply supported beam are shown in Figs. 3, 4, and 5 respectively. Because of the randomness introduced by the added noise, two consecutive runs will produce different results. Hence, the plots shown here correspond to average values obtained after ten runs. Three acceleration sensors were used at intervals $x_i = iL/4$.

As can be seen, in all cases the identified values converge to the actual values as the signal-to-noise ratio approaches infinity. There are, however, many differences in the rates of convergence. In particular, it seems as though for lower levels of noise the ERA method provides better results. However, we notice that the TCM yields better results for the first two modes when the snr has

decreased beyond a certain value.

It has been noticed throughout the research that the ERA is more sensitive to noise in the response than is the TCM. However, we must recall that more powerful methods of dealing with this problem have been introduced by Jaung and Pappa [3], so that it is likely that ERA performs better than would be indicated here. It was also noted throughout the research that the first mode identified by ERA was often the only one that was adversely affected by the noise. Therefore, the relative performance of the methods depends on: (1) the level of noise, (2) the particular mode considered, and (3) the physical system.

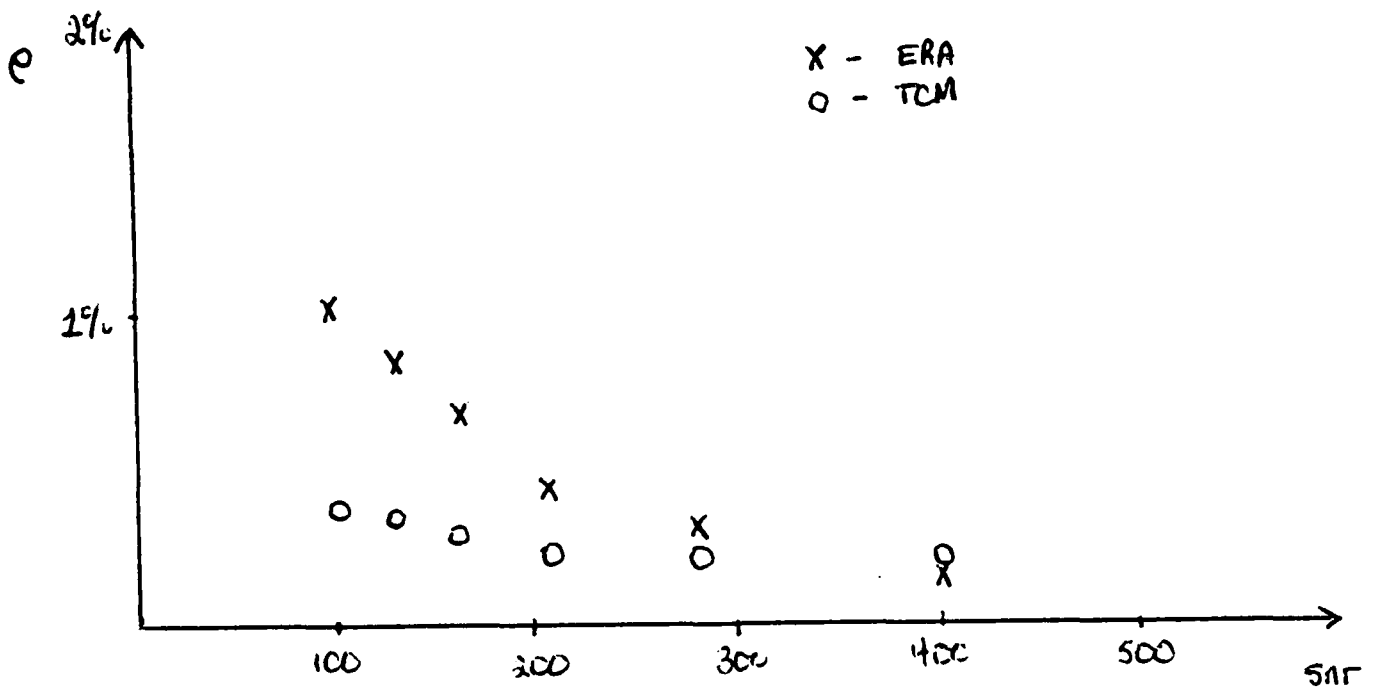


Figure 3: Effect of noise on 1st natural frequency

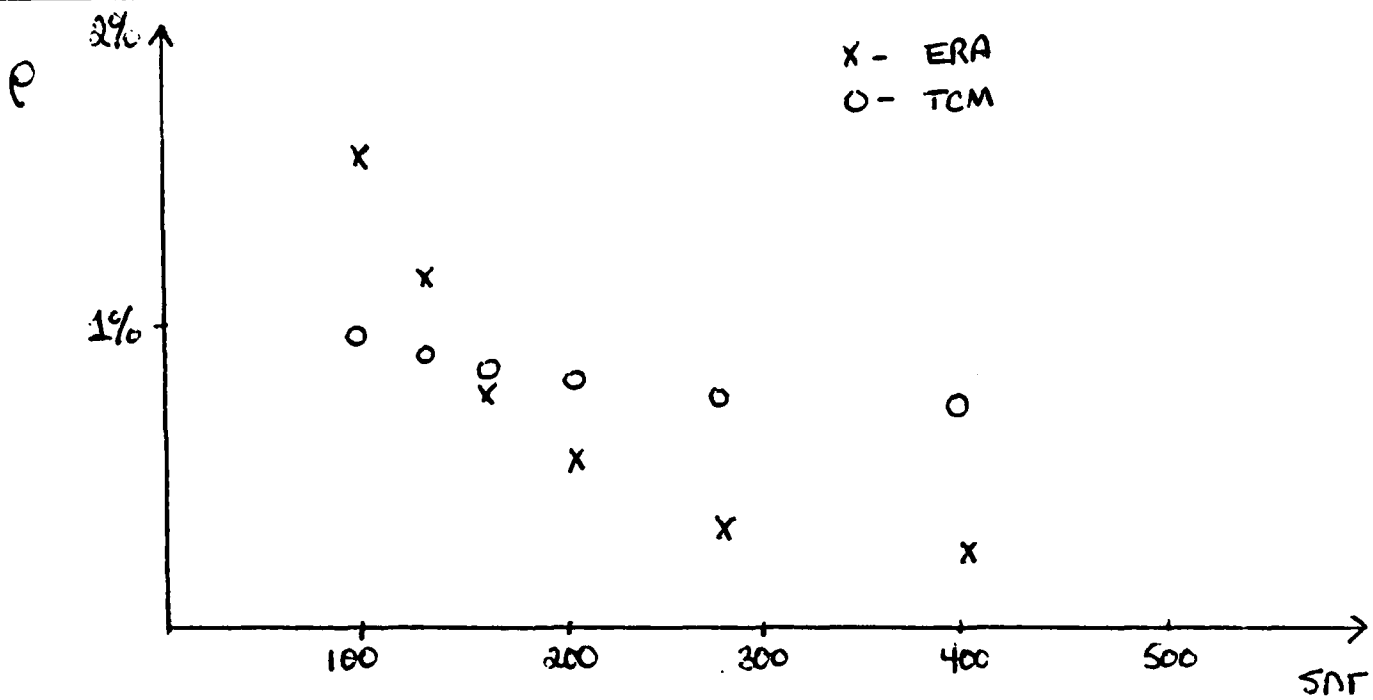


Figure 4: Effect of noise on 2nd natural frequency

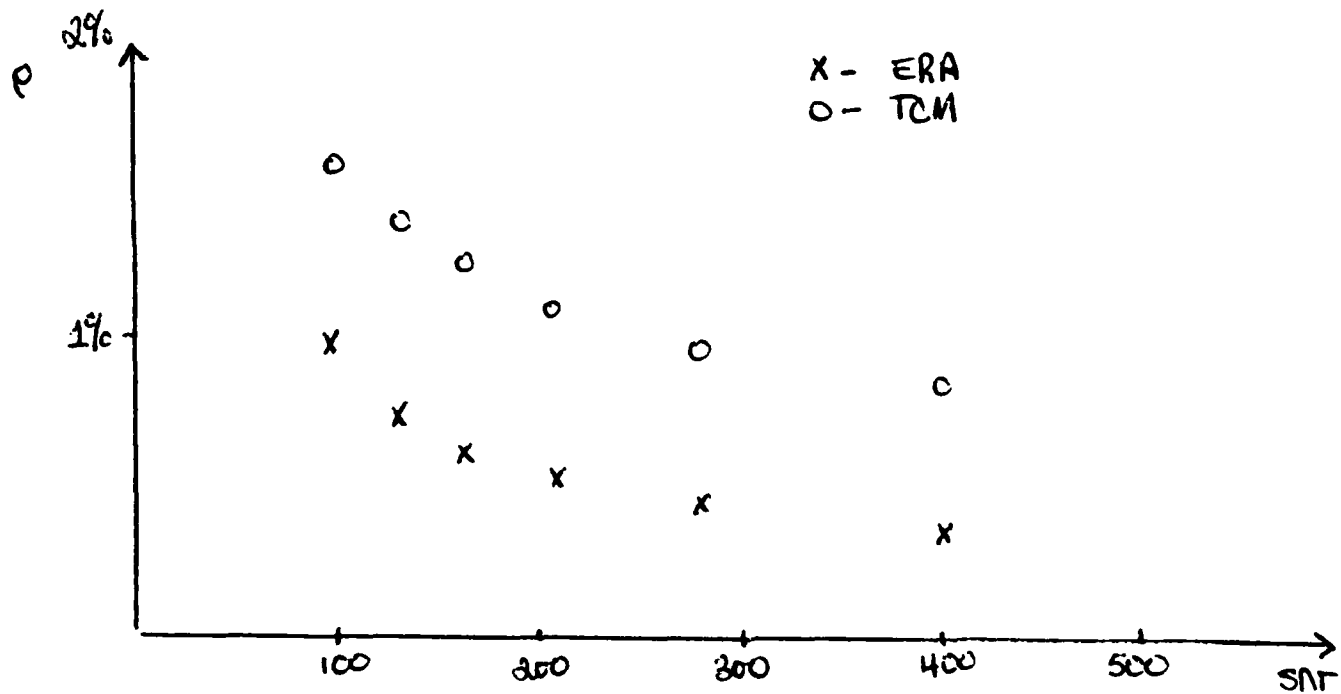


Figure 5: Effect of noise on third natural frequency

9.0 Identification Spillover

Practical limitations dictate that the control of distributed structures be designed and implemented using finite order models, whereby only a subset of the modes of the structure may be actively controlled. The controlled modes may represent a reduced-order model of the realized structural model. The excitation of the residual (uncontrolled) modes caused by the controller is known as control spillover and can degrade the system performance. An analogous effect exists in the identification of modal parameters in distributed structures. Because distributed structures must be modeled by discrete systems, the contamination from the residual (unmodeled) modes leads to identification spillover, which tends to degrade the identification results [14].

The identified eigenvalues for the TCM obey the inclusion principle. As the order of the model is increased, the identified eigenvalues approach the actual ones monotonically from above. To illustrate this and to investigate the behavior of the identified eigenvalues of the ERA, we consider once again a simply supported beam example. For this case we let the first six modes participate in the response. We implement the two methods four times, increasing the number of modes to be identified from three to six and monitor the identified frequencies.

The results for the TCM and the ERA are presented in

Tables 5 and 6 respectively. It is clear that the identified natural frequencies, and hence the eigenvalues, obey the inclusion principle for the TCM. Indeed, the first natural frequency for the case of three modes identified lies between the first and second identified frequencies for the case of four modes identified, and so on. This is not the case for those natural frequencies identified by the ERA, although the inclusion principle is nearly obeyed for the ERA in this example. Note that identification spillover was examined for the ERA by retaining $2m$ singular values.

An important result to point out is that for the ERA the lowest mode is significantly affected by the identification spillover. Also, when we try to identify only three of the six modes participating in the response, the natural frequencies identified are good approximations to the fourth through sixth natural frequencies of the system. This would seem to indicate that the ERA is better suited to identify the higher modes. This type of phenomenon is not characteristic of the results of the TCM. In fact, when identifying three modes the values show no resemblance to the actual frequencies of the structure.

Therefore, it would seem as though both methods have their own advantages with respect to identification spillover. On the one hand, the TCM natural frequencies obey the inclusion principle so that the identified eigenvalues approach the actual ones monotonically from above. Hence,

the TCM can be used to indicate how many modes participate in the response. On the other hand, the ERA provides information on the higher natural frequencies when only a subset are modeled. In other words, the higher modes that are identified are not adversely affected by the residual modes.

Table 5-Identified frequencies for the TCM

m =	3	4	5	6	actual
	12.14	7.85	5.43	2.79	2.79
	40.02	25.79	17.87	11.18	11.17
	84.33	54.33	37.57	25.13	25.12
		93.05	64.58	44.67	44.67
			98.35	69.80	69.79
				100.50	100.50

Table 6-Identified frequencies for the ERA

m =	3	4	5	6	actual
	40.21	23.46	8.43	2.79	2.79
	68.21	44.14	25.17	11.17	11.17
	99.92	69.81	44.51	25.12	25.12
		100.51	69.79	44.67	44.67
			100.49	69.79	69.79
				100.50	100.50

The results presented here to illustrate identification spillover and the inclusion principle used simulated data. Experimental verification of these phenomena for the TCM will be discussed in Section 11.

10.0 TCM: A Constrained Version of ERA

A primary objective of this research was to determine the relationship between the TCM and the ERA. It was highly desired to closely tie together the two methods and show exactly any correspondence between them. To this end, it was discovered that the TCM is a constrained version of the ERA for lightly-damped structures. This result has important implications. By constraining the ERA, it can be shown that the modal identification is less sensitive to sensor noise [13]. Furthermore, the number of computations can be drastically reduced as the TCM works in the configuration space which has half the dimension of the state-space.

Consider a constrained generalized Hankel matrix which has only a single row of block matrices given by Eq.(34). Hence, the constrained Hankel matrix has dimension $1 \times (ms)$. The matrices $A^{(n)}$ and $B^{(n)}$ in Eqs.(21) and (22) can be written as [13]

$$A^{(n)} = H(k)H^T(k) \quad (46)$$

and

$$B^{(n)} = H(k+1)H^T(k) \quad (47)$$

in which the derivatives in the two inner products are of the same order and the time offset, T_0 , is equal to the sampling interval. Note that the column dimension of the

Hankel matrix must be large enough to sufficiently correlate the sensor measurements as is required by the TCM. Recall that for the restrictions given, the identified natural frequencies are found from Eq.(30) where the λ_r are obtained from the solution to the eigenvalue problem given by Eq.(26).

Equations (46) and (47) express the correlation matrices used in the TCM in terms of the generalized Hankel matrix used in the ERA. This is the fundamental step in the development of the constrained ERA (CERA). Substituting Eqs.(46) and (47) into the eigenvalue problem of Eq.(26) gives

$$\lambda_r H(k) H^T(k) \underline{v}_r = H(k+1) H^T(k) \underline{v}_r \quad (48)$$

where the superscripts have been dropped for convenience.

Using the singular value decomposition of $H(k)$, Eq.(48) becomes

$$\lambda_r P D Q^T Q D^T P^T \underline{v}_r = H(k+1) Q D^T P^T \underline{v}_r \quad (49)$$

or

$$\lambda_r P D^2 P^T \underline{v}_r = H(k+1) Q D^T P^T \underline{v}_r \quad (50)$$

where we have made use of $Q Q^T = I$ and $D = D^T$. Now we define a vector $\underline{w}_r = D P^T \underline{v}_r$. Then, Eq.(50) can be written

$$\lambda_i P D^{1/2} \underline{w}_i = H(K+1) Q D^{-1/2} \underline{w}_i \quad (51)$$

Premultiplying Eq.(51) by $D^{-1/2} P^T$ gives us the following

$$\lambda_i \underline{w}_i = D^{-1/2} P^T H(K+1) Q D^{-1/2} \underline{w}_i \quad (52)$$

Comparing Eq.(52) to the eigenvalue problem we encountered in the ERA formulation, Eqs.(42) and (43), we see that they are identical except for one important aspect. In the ERA formulation the order of the eigenvalue problem is $2n$, while Eq.(52) represents an eigenvalue problem of order n . Hence, for the case of light-damping, the TCM reduces to a constrained version of the ERA. The constrained Hankel matrix contains only a single row of Markov parameters. The procedure in the CERA is the same as proposed by the ERA, with the exception that one-half the number of singular values are retained in the system realization and that the eigenvalue problem for modal identification is performed in the configuration space. To summarize, in the presence of light damping, we can reformulate the ERA so that the system the realization retains n singular values (n is the number of realized modes) and the size of the eigenvalue problem is n . After constructing the Hankel matrix from one row of sensor measurements and a sufficient number of columns required for convergence, the eigenvalue problem given by Eq.(52) is solved for n real eigenvalues, opposed to $2n$ complex eigenvalues in the gen-

eral form of the ERA. The identified natural frequencies are found from Eq. (30) where T_0 is the sampling interval.

Like the ERA, the CERA identifies natural frequencies and mode shapes for lightly-damped systems. The CERA does not identify modal damping directly as in the ERA. Damping tends to be more sensitive to sensor measurement noise so that, in practice, it is quite difficult to obtain accurate estimates of the damping. Recent developments, however, show that the CERA in conjunction with modal filters does provide improved damping estimates [13].

Let us consider an example of the CERA and illustrate how it relates to the TCM. Consider a simply supported beam of uniform properties undergoing bending vibration. We let the beam have the following properties: $L = 10\text{m}$, $EI = 20 \text{ N m}$, and $m = 1 \text{ kg/m}$. The natural frequencies are

$$\omega_r = \sqrt{20} \left(\frac{r\pi}{10} \right)^2 \quad (53)$$

and the normalized mode shapes are

$$\phi_r(x) = \sqrt{\frac{1}{5}} \sin\left(\frac{r\pi x}{10}\right) \quad (54)$$

Consider the case in which the three lowest modes participate in the response, and we wish to identify the eigenvalues corresponding to these modes. Six acceleration measurements are used at the measurement stations $x_i = iL/7$

($i=1,2,\dots,6$) for this example. The response of the beam is obtained using an initial modal displacement and an initial modal velocity for the first three modes. We compare the identified eigenvalues for the ERA, the TCM, and the CERA. The number of sample points in correlating the measurements in the TCM is much greater than that used for the CERA. This is due to the lengthy amount of time needed to perform the singular value decomposition on large matrices. Because of this, results for the TCM are better than those for the CERA.

Table 7 contains the results for the case of no damping in the response and no noise added to the outputs. We can see that the results for all three methods are in close agreement with the actual values. Table 8 contains the results for the case of damping at $\xi = .02$ for all three modes and no noise. In this case the identified values for the CERA begin to deviate from the actual values. This method is highly sensitive to the level of damping. In fact, when we take $\xi = .05$, the percent error is as high as forty percent. Finally, Table 9 contains the results for $\xi = .02$ and Gaussian noise added to the sensor outputs such that at one standard deviation, the noise added is 2%. We notice that both the ERA and the TCM still give very good results for all three modes, with the largest deviation being seven percent. Also, the identified natural frequencies given by the ERA are better than those obtained by the TCM. Focusing our attention now on the results obtained by

the CERA, we see that the first identified natural frequency is considerably inaccurate. However, the method still gives good results for the second and third identified frequencies.

Table 7-Identified frequencies

r	ω_r - actual	ω_r - ERA	ω_r - TCM	ω_r - C-ERA
1	.4414	.4414	.4419	.4220
2	1.766	1.766	1.767	1.710
3	3.972	3.972	3.973	3.941

Table 8-Identified frequencies

r	ω_r - actual	ω_r - ERA	ω_r - TCM	ω_r - C-ERA
1	.4414	.4414	.4414	.4908
2	1.766	1.766	1.760	1.843
3	3.972	3.972	3.941	3.920

Table 9-Identified frequencies

r	ω_r - actual	ω_r - ERA	ω_r -TCM	ω_r - C-ERA
1	.4414	.4400	.4755	.6359
2	1.766	1.764	1.693	1.854
3	3.972	3.971	3.944	3.921

Norris [13] has performed a more extensive development of the CERA and has given results for more examples including a membrane problem. His results show a better performance for the CERA than has been depicted here. An important distinction to be made is that the TCM uses both accelerations and velocities in its formulation, while the ERA and the CERA use only accelerations. For simulated cases we can normally use exact velocity profiles. However, in real applications the acceleration profile may have to be integrated to obtain the velocity profile. This could be a source of additional error in experimental results.

11.0 Identification of a Flexible Grid

To this point, the results presented have used numerical simulations only. In this section, the TCM and the ERA will be implemented using experimental data from an actual system. In particular, we consider a flexible grid consisting of nine thin aluminum strips as depicted in Fig. 6. The grid is cantilevered at the top to an I-beam that is mounted to a large, highly-stiff concrete slab. The experimental setup is located at the Astronautics Laboratory, Edwards Air Force Base.

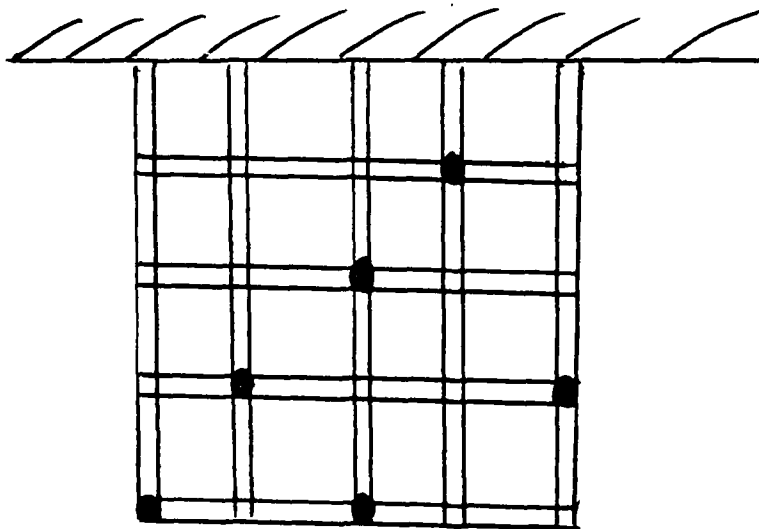


Figure 6: The AFAL Grid

The aluminum grid was one of several elements that comprised the system. In order to measure the response of the grid, piezoelectric accelerometers (Endevco Model 7751-500) were mounted to the grid at various locations. Due to the nature of these accelerometers, these locations were limited to places on the grid where the strips overlapped. A total of eleven accelerometers were available for use. In addition the system consisted of a MAX_100 central computer for data storage, a VT220 computer terminal that provided a link to MATRIXx software, and various electrical connectors. The grid was initially excited by manually shaking it by hand. Because this often produced noise and excited the higher modes, it was usually necessary to wait ten seconds before measuring the response. In all cases the sampling frequency used was 200 Hz.

Many sets of data were taken, each one differing in the way it was shaken, where the accelerometers were located, how many samples were taken, or how much time passed between the excitation and the data collection, which we call the collection lag. In theory, the greater the collection lag the better the results will be for both the TCM and the ERA. Note that the higher modes damp out more quickly, leaving only the lower modes to participate in the response, so that the effect of identification spillover is lessened.

The frequency response plots of the different sets of data can be viewed to determine which set was the "cleanest". It was found that this data set was characterized by 4096 samples at 200 Hz giving a total sampling interval of $T = 20.48$ s. In addition, the accelerometers were placed at points located by Fig. 6.

Table 10 contains the identified frequencies corresponding to the first four modes of the grid for both the TCM and the ERA. The size of the Hankel matrix for ERA is defined by the parameters $r=36$, $l=4$, $s=100$, and $m=1$ in Eq. (34). Actual raw data was used, meaning that no filtering was performed. In addition, Table 10 contains the estimated values of the first four frequencies of the grid which were obtained by inspection of the frequency response plots of the accelerometer outputs. We note that the results for the TCM on the first, second, and fourth modes are good, while the result for the third mode is in error. Also, the ERA results are not accurate, except that the second and third identified frequencies correspond well to the third and fourth estimated frequencies.

Table 10-Identified frequencies

r	ω_r -estimated (Hz)	ω_r -TCM	ω_r - ERA
1	.83	.93	1.38
2	1.76	2.01	4.44
3	4.35	3.32	6.54
4	6.49	6.36	13.14

In order to improve the results for the two methods, it was necessary to filter the data. The process consisted of performing a Fast Fourier Transform (FFT) of the accelerometer outputs, setting to zero all terms past a selected frequency, and performing an inverse FFT to return to the time domain. Table 11 displays the estimates of the first four natural frequencies using the TCM and the ERA after the acceleration data had been filtered with a cutoff frequency of 10 Hz.

Table 11-Identified frequencies

r	ω_r -estimated (Hz)	ω_r - TCM	ω_r - ERA
1	.83	.86	.78
2	1.76	1.79	2.46
3	4.35	2.52	4.34
4	6.49	5.98	6.55

We can see that the results for both methods have improved drastically. Both methods identify the fundamental frequency, often the one of greatest interest, extremely well. It is also evident, however, that the TCM has trouble with the higher two modes, while the ERA has trouble with the second mode only. To improve the results for the ERA even further, we consider using several data sets. This is done by splitting up the set of data used previously into three subintervals, and by taking each subinterval as an independent data set with different initial conditions.

Table 12 compares the actual frequencies with those obtained by ERA using the parameters $r=36$, $l=4$, $s=100$, $m=1$ and with those obtained by ERA using the parameters $r=36$, $l=4$, $s=100$, $m=3$. The first two identified frequencies show an improvement from the addition of multiple data sets. Conversely, the third and fourth identified frequencies

either degenerate or remain unchanged. Overall, however, it appears that improved results are obtained by including multiple data sets. It should be noted that the improved results are not without cost. Using multiple data sets, more computer time is required in both constructing the Hankel matrix and performing the singular value decomposition.

Table 12-Identified frequencies

r	ω_r - estimated (Hz)	ω_r - TCM	ω_r - ERA
1	.83	.78	.84
2	1.76	2.46	1.96
3	4.35	4.43	4.34
4	6.49	6.55	6.55

In section 7.0 we investigated the effect of identification spillover on the identified natural frequencies for both the TCM and the ERA. It was found that the identified frequencies for the TCM obey the inclusion principle and that the higher modes for the ERA are not greatly affected. These conclusions were based on a simulated example of a simply supported beam. Now consider identification spillover for these two methods using accelerometer data from the grid. The data is filtered at 10 Hz so that four modes participate in the response.

Table 13 contains the results for identifying two, three, and four modes using the TCM. Note that the number of sensors used is equal to the number of modes to be identified. Once again it is clear that the identified natural frequencies obey the inclusion principle. For the simulated case, the first identified frequency deviated significantly from the actual value as the number of modes identified decreased. For the actual data, this was not the case. Note that even when two modes are identified, the first identified frequency is a good estimate of the actual fundamental frequency. In comparison with the simulated data in Section 9, more modes are participating in the response for the simulated case so that the effect of identification spillover is more pronounced.

Table 14 shows similar information for the identified frequencies using the ERA. The parameters used were $r=48$, $l=4$, $s=150$, and $m=1$. As was the case for the simulated case, only the lowest mode seems to be adversely affected by the residual modes.

Table 13-Identified frequencies for the TCM

m =	2	3	4	estimated
	.93	.87	.86	.83
	2.29	2.22	1.79	1.76
		4.99	2.52	4.35
			5.98	6.49

Table 14-Identified frequencies for the ERA

m =	2	3	4	estimated
	1.36	.97	.78	.83
	4.55	4.42	1.92	1.76
		6.58	4.46	4.35
			6.61	6.49

In summary, the TCM seems to be better suited to identify the lower modes, while the ERA may be better suited to identify the higher modes. In particular, it seems that noise and residual modes affect the higher frequencies identified by the TCM the greatest, while they affect the lower frequencies identified by the ERA the greatest. It should be noted that as the size of the Hankel matrix for the ERA was varied, the lower identified frequencies changed the most.

12.0 Additional Results

The research proposal discussed several other parameter and modal identification algorithms. These included the Autoregressive Moving-Average (ARMA) models and the Extended Kalman Filter (EKF). Work on these topics was somewhat limited. This section describes these methods and gives any results, conclusions, or comments that might be valuable.

12.1 Autoregressive Moving-Average (ARMA) models

Consider the n-degree-of-freedom model given by [4]

$$M\ddot{\underline{x}} + K\underline{x} = \underline{F} \quad (55)$$

Using an orthogonal transformation, the discrete model has the form given by

$$\ddot{u}_i + \omega_i^2 u_i = f_i, \quad i = 1, 2, \dots, n \quad (56)$$

where u_i are the modal coordinates and f_i are the modal control vectors. Considering a single mode with empirically determined modal damping, we have the state-space formulation

$$\dot{\underline{x}} = \begin{bmatrix} 0 & 1 \\ -\omega^2 & -2\zeta\omega \end{bmatrix} \underline{x} + \begin{bmatrix} 0 \\ b_f \end{bmatrix} \underline{F} \quad (57)$$

where $\underline{x} = \{ u, \dot{u} \}$ and b_f is the actuator control effectiveness parameter that we wish to identify. Using the z-transform, we obtain the following difference equation for the modal amplitudes

$$u_k = a_1 u_{k-1} + a_2 u_{k-2} + b_1 f_{k-1} + b_2 f_{k-2} \quad (58)$$

where a_1 , a_2 , b_1 , and b_2 are the difference equation coefficients. The procedure uses free-decay tests to identify the coefficients a_1 and a_2 via linear least-squares estimation [5]. The additional coefficients b_1 and b_2 are then identified using the forced response [4].

The research and testing of this method for identifying the control effectiveness parameters has just begun. At this time only simple simulated cases have been performed for the identification of a_1 and a_2 using the free-response. No simulated cases have been performed for the identification of b_1 and b_2 using the forced response.

12.2 The Extended Kalman Filter

The identification methods discussed thus far have been based in the time domain. At this point we consider an Extended Kalman Filter (EKF) algorithm which utilizes the frequency domain. Consider the following model

$$M\ddot{\underline{x}} + C\dot{\underline{x}} + K\underline{x} = \underline{f}(t) \quad (59)$$

To obtain the frequency response functions, consider differentiating Eq.(59) twice with respect to time to obtain

$$M\ddot{\underline{\ddot{x}}} + C\ddot{\underline{\dot{x}}} + K\ddot{\underline{x}} = \ddot{\underline{f}}(t) \quad (60)$$

Now we take the Fourier transforms (FT) of the individual terms in Eq.(60) and use $FT [\ddot{x}] = i\omega FT [\dot{x}]$. This gives us the following expression in the frequency domain:

$$[-\omega^2 M + i\omega C + K] \ddot{\underline{x}}(\omega) = -\omega^2 \underline{F}(\omega) \quad (61)$$

where $\underline{x}(\omega) = FT [x]$. We can rearrange Eq.(61) to give us the admittance matrix function. We write

$$\ddot{\underline{x}}(\omega) = -\omega^2 [K - \omega^2 M + i\omega C]^{-1} \underline{F}(\omega) \quad (62)$$

or

$$\ddot{\underline{x}}(\omega) = H_{F-A}(\omega) \underline{F}(\omega) \quad (63)$$

Consider the state equation described by [10]

$$\frac{d\underline{a}}{d\omega} = \underline{g}_a \quad (64)$$

where \underline{a} is the parameter vector to be estimated, and \underline{g}_a is the process noise. The statistical characteristics of the process noise and the initial estimate of the unknown par-

ameter vector are given by

$$\underline{q}_a \sim \mathcal{N}[\underline{0}, Q^*(\omega)], \quad \underline{a}_0 \sim \mathcal{N}[\hat{\underline{a}}_0, P_{a_0}] \quad (65)$$

implying that \underline{q}_a is a Gaussian random variable with zero mean and covariance matrix $Q^*(\omega)$. The measurement equation is [10]

$$z(\omega_{k+1}) = h(\omega_{k+1}; \underline{a}_{k+1}) + v(\omega_{k+1}) \quad (66)$$

where $h(\omega_{k+1}; \underline{a}_{k+1})$ is a nonlinear function of frequency and $v(\omega_{k+1})$ is the measurement noise with statistical properties given as $v \sim \mathcal{N}[\bar{v}, R(\omega)]$. Using a standard modal identification package, we obtain the magnitude of the admittance matrix function given by

$$Z(\omega) = \left| H_{F-A} \right|_{\alpha\beta} + V(\omega) \quad (67)$$

where the subscripts $\alpha\beta$ denote a particular frequency response function in the admittance matrix.

Using $Z(\omega)$ the Kalman Filter equations [10] are implemented with a linearized version of the nonlinear state and measurement equations. The equations are linearized about a nominal parameter state at each iteration in the algorithm. As estimates become available, they are used to improve the accuracy of the model.

Although at first glance this procedure may seem

straight forward, there are many intricacies that make the task quite difficult. First, in the Extended Kalman Filter equations partial derivatives of $h(\omega_{k+1}; \alpha_{k+1})$ with respect to the parameters to be estimated are required at each step. The acquisition of these derivatives can pose problems. Second, it is required that the statistical properties of the process and measurement noise be known. This presents another challenging obstacle. D. Martinez [10] gives a thorough development on how these quantities, means and covariances, are computed. Finally, it was not clear on what type of excitation should be used to obtain the frequency response function. It was desired to use a signal generator that provided a sine-wave of sweeping frequency. Unfortunately, the sweep generator at the Astronautics Laboratory at Edwards Air Force Base was not functioning. Therefore, individual tests at different frequencies would have to be conducted to get enough points.

13.0 Recommendations

The research conducted was primarily concerned with the comparison, testing, and improvement of the Eigensystem Realization Algorithm and the Temporal Correlation Method. The methods were compared on their behavior in the presence of measurement noise. It was found that such factors as the level of noise, the particular mode considered, and the physical system can determine which method will work best. Also, both methods were used to identify natural frequencies of a grid structure at Edwards Air Force Base.

The most valuable development was showing how the TCM reduces to a constrained version of the ERA for light damping. The constraint that the Hankel matrix contain only one row of sensor outputs reduces the order of the eigenvalue problem to be solved in the ERA by an order of two. Hence, the computational efficiency of the ERA is improved in this respect. Other methods of modal and parameter identification were also discussed, namely, the Autoregressive Moving-Average (ARMA) models and the Extended Kalman Filter.

Both the TCM and the ERA were implemented using experimental data from the AFAL Grid structure. It would be of interest to investigate the performance of the CERA for the experimental data as well. In addition, the CERA should be tested more exhaustively for its properties concerning damping, noise, and identification spillover.

It should be pointed out that for on-orbit applications it would not be possible to perform the type of filtering described in Sec. 11. Other types, specifically those that can be implemented on-line, might be of use however. In general it would be most convenient if no filtering were required, as this would certainly be most efficient. Whether or not this is possible given the accuracy needed, is yet to be determined and would be a subject of interest. Also of interest is a topic concerning sensor locations and how they affect the identified results. This is synonymous with actuator placement and how it affects control results. Other areas of further research might include investigating identification spillover for the ERA to a greater extent, finding ways to reduce the effect of measurement noise on the identified values, and continued development of the CERA.

The problems encountered when implementing the Extended Kalman Filter algorithm on the Grid Experiment were posed to D. Martinez of Sandia National Laboratories. His belief was that for our application and goals, other methods of parameter estimation would be more suitable. He suggested that using frequency response functions as data works good for simulated data, but experimental data might give bad results if the fidelity of the model is not good. It should be noted that the method was tested on simulated data with good results.

Time did not permit the investigation of the Direct

Physical Parameter Identification method. Unlike the EKF algorithm, the parameters are updated using the structures time domain response. The technique is based on a finite element model of the structure, and the goal is to identify average values of mass, damping, and stiffness over each finite element. The implementation of this method along with the ARMA models would also be an interest of further study.

This research proved to be both valuable and interesting. The process of modeling and identification are very broad subjects and can be applied to many disciplines.

14.0 References

1. Ibrahim, S.R., 'A Method for the Direct Identification of Vibration Parameters from the Free Response,' The Shock and Vibration Bulletin, Vol. 47, Pt. 4 , 1977, pp. 183-198.
2. Juang, J.N. and Pappa, R.S., 'An Eigensystem Realization Algorithm for Modal Parameter Identification and Modal Reduction,' Journal of Guidance, Control, and Dynamics, Vol. 8, No. 5, Sept. - Oct. 1985, pp. 620-627.
3. Juang, J.N. and Pappa, R.S., 'Effects of Noise on Modal Parameters Identified by the Eigensystem Realization Algorithm,' Journal of Guidance, Control, and Dynamics, Vol. 9, No. 3, May-June 1986, pp. 294-303.
4. Montgomery, R.C., Williams, J.P., Lazarus, T.L., and Nelson, P.E., 'Control Effectiveness Characterization for State Estimation and Control on a Highly Flexible Grid,' Proceedings of the AIAA Guidance, Navigation and Control Conference, Williamsburg, VA, August 18-20, 1986.

5. Montgomery, R.C., Shenhar, J., and Williams, J.P., 'On-Line Identification and Attitude Control for SCOLE,' Proceedings of the AIAA Guidance, Navigation and Control Conference, Monterey, CA, August 17-19, 1987.

6. Montgomery, R.C., and Lazurus, T.L., 'Recent Developments in the Experimental Identification of the Dynamics of a Highly Flexible Grid,' Proceedings of the 1987 ASME Winter Annual Meeting, Boston, MA, December 6-11, 1987.

7. Norris, M.A., and Silverberg, L.M., 'Modal Identification of Self-Adjoint Distributed-Parameter Systems,' 23rd Annual Technical Meeting Society of Engineering Science, University of Buffalo, Buffalo, NY, August 25-27, 1986, also appeared in the Journal of Earthquake Engineering and Structural Dynamics. Vol. 18, 1989, pp. 633-642.

8. Norris, M.A., Silverberg, L.M., Kahn, S.P., and Hedgecock, C.E., 'The Temporal Correlation Method for Modal Identification of Lightly-Damped Structures,' Proceedings of the 7th VPI&SU/AIAA Symposium on Dynamics and Control of Large Structures, Blacksburg, VA, May 8-10, 1989: Submitted for publication in the Journal of Sound and Vibration.

9. Martinez, D.R., 'Estimation Theory Applied to Improving Dynamic Structural Models,' Sandia Report No. SAND 82-0572, Sandia National Laboratories, Albuquerque, NM, November 1984.
10. Martinez, D.R., 'Parameter Estimation in Structural Dynamics Models,' SAND80-0135, Sandia National Laboratories, Albuquerque, NM, March 1981, also Dissertation in Engineering, Mechanics, and Structures Department, University of California, Los Angeles, 1979.
11. Meirovitch, L. and Norris, M.A., 'Parameter Identification in Distributed Spacecraft Structures,' Journal of the Astronautical Sciences, Vol. 32, No. 4, Nov. - Dec. 1986, pp. 341-353.
12. Meirovitch, L. and Norris, M.A., 'A Perturbation Technique for Parameter Identification in Distributed Structures,' Applied Mathematical Modelling, Vol. 12, April 1988, pp. 167-174.
13. Norris, M.A., "A Constrained Eigensystem Realization Algorithm for Lightly-Damped Distributed Structures," seminar presented at the Advanced Radiation Controls Development Branch, Kirtland Air Force Base, September 1989; to be submitted for publication in the Journal of Guidance, Control, and Dynamics.

14. Meirovitch, L., Computational Methods in Structural Dynamics, Sijthoff & Noordhoff, The Netherlands, 1980.

**FINAL REPORT NUMBER 23
REPORT NOT AVAILABLE AT THIS TIME
Dr. Rameshwar P. Sharma
210-9MG-103**

EXPERIMENTAL INVESTIGATION OF THE STABILITY OF JETS NEAR THE CRITICAL POINT

D. L. GRAHAM and S. H. SOHRAB
Department of Mechanical Engineering
Northwestern University, Evanston Illinois 60208

ABSTRACT

The physical characteristics and stability of CO₂ jets injected into pressurized stagnant nitrogen environment are experimentally investigated. In particular, the transition from laminar to turbulent flow of CO₂ jets is studied as the critical pressure of CO₂ is being gradually approached. The maximum flow rates at transition, defined as the onset of fluctuating and wavy flow at a fixed distance from the nozzle rim, are measured at different fixed pressures. It is found that the maximum velocity at transition steadily decreases as the critical pressure of CO₂ is being approached. The critical Reynolds numbers at transition however remain nearly constant. The experimental results are found to be consistent with a cascade model of turbulence. In addition to single jets, the behavior of two impinging CO₂ jets under increasing chamber pressures is also studied using laser shadowgraph photography. Potential application of the vanishingly small surface tensions under supercritical state to the atomization of liquid jets and the production of fine sprays is discussed.

For presentation in the Central States Section Meeting of the Combustion Institute, Dearborn, Michigan, April 30, 1989.

INTRODUCTION

Studies on the stability of jets of fluid under supercritical state are important to the understanding of fuel injection/atomization as well as combustion processes in liquid rocket and diesel engines among other important applications. The analytical and experimental studies of droplet and spray combustion have primarily considered low pressure subcritical conditions for the fuel and its oxidizing environment. However, because of the substantial modifications of physico-chemical properties of reactants as the critical point is exceeded, the extension of the results from subcritical studies to actual engine performance is quite complex if not altogether impossible. Experimental study of jets and the associated stability, atomization and combustion processes at high pressures would help to bridge such gaps.

An analytical model of droplet combustion under supercritical state was first introduced by Spalding(1959). This work considered the droplet as a point source of fuel which is represented by a puff of vapor when the critical pressure and temperature (P_c , T_c) are exceeded. Subsequently, Rosner and Chang(1973) extended the model by considering a distributed source for the droplet. More recent literature on supercritical droplet burning have been discussed (Williams,1985; Farrell and Peters,1986). The pioneering experimental and theoretical investigations by Faeth et al.,(1963) Lazara and Faeth(1971), and Canada and Faeth (1975) greatly contributed to the understanding of high pressure droplet combustion when suspended droplets undergo free fall. The resulting data for combustion of octane and decane droplets were found to be in good qualitative agreement with the more recent theoretical study of Sanchez-Tarifa et al. (1972). However, more recent experiments by Kadota and Hiroyasu (1981) under pressures slightly above P_c are not consistent with the earlier experimental and theoretical findings.

In most of the experimental investigations, combustion of stationary suspended droplets in the absence of external convective fields have been considered. Obviously, in the turbulent spray combustion within rocket motors, the role of hydrodynamics in transient droplet/flow/flame interactions(Chen, et al.,1988) will be significant. The impact of the convective effects such as hydrodynamic stretching are expected to be aggravated under supercritical states because of the

vanishing surface tension (Sohrab, 1986). The influence of convection on droplet combustion at high pressures was experimentally studied by Natarajan and Bruzustowski (1970). However, the strong emission from soot particles prevented the visualization of the physical geometry of the burning droplets. Clearly, more experiments are needed to further illuminate the important role of convection in atomization/combustion processes.

In view of the above considerations, the understanding of high pressure reactive flows requires improved knowledge concerning the hydrodynamics of nonreactive jets at elevated pressures. In the present experimental investigation, the hydrodynamic stability of jets of CO₂ is experimentally studied as the critical pressure is being approached. In particular, we consider transition from laminar to turbulent flow when the jets of CO₂ flow into a stagnant nitrogen environment. In addition, the nature of hydrodynamic interactions between two impinging CO₂ jets under increasing pressures is examined. Such studies may improve our understanding of the nozzle performance in liquid rocket engines.

In the sequel, the description of the experimental system and procedures are presented. Next, the critical velocities at transition as a function of pressure as well as direct photographs for single CO₂ jets are presented and discussed, and are followed by the results for two impinging jets. Our experimental results are then described using a multi-scale cascade model of turbulence. A summary of our principal findings is presented in the concluding remarks.

EXPERIMENTAL SYSTEM AND METHODOLOGY

A schematic of the high pressure chamber, constructed at the Air Force Astronautics Laboratory, is shown in Fig.1. The volume of the chamber is about 2.46×10^4 cm³, such that the modification of the chamber environment due to the small CO₂ flow during testing is negligible. The system was tested under maximum hydrostatic pressure of 2000 psi. An automatic 1800 psi pressure release valve was used for protection against accidental over-pressurization. The assembled system weighed about 227 kg and required construction of a special heavy table. The excellent stability of this heavy table proved to be valuable, since the jets were observed to be

sensitive to small laboratory perturbations.

Three circular quartz windows allowed direct visualization of the jet. An enlarged shadowgraph image of the jet was projected on a screen (see Fig. 1) using an expanded and collimated beam from argon-ion laser. The visible length of the jet was limited by the 2.54 cm (1") window openings, such that only the first 1.9 cm (3/4") of the jet could be seen. The shadowgraph projection was enlarged about 6 times to a 10.2 cm (4") diameter such that many small details of the flow could be detected. Direct photographs were taken using a 35 mm camera and ISO 400 speed Ektachrome daylight slide film (over-exposed 3 stops). The nozzles were fabricated by drilling 0.24 cm (3/32") holes in a 0.635 cm (1/4") Swagelock tubing caps and silver soldering 1.9 cm (3/4") length of 0.24 cm (3/32") diameter thin-walled smooth tubing to the end of the cap. The nozzle length/diameter ratio represents typical value used in rocket motors. Pure CO₂ was used from a bottle at room temperature and the corresponding saturated vapor pressure of about 850 psi. Because of the very small flow rates, needle-type metering valves with 0.635 cm (1/4") fittings were used. Thermocouples were installed both within the tank and through a T-fitting, into the CO₂ stream. A heating system (Fig. 1) for varying the temperature of the jet fluid was constructed using 127 cm (50') of 0.48 cm (3/16") copper tubing immersed in an electrically heated water bath. However, this system proved to be largely ineffective, in spite of the long residence time, about two minutes, of the jet fluid, and was not used for these experiments. Not shown in Fig. 1 are 1.27 cm (1/2") thick plexiglass safety shields enclosing the all of the pressurized components.

For the straight jet, transition to turbulence is defined as the onset of wavy and fluctuating flow at one particular location of the jet projected image, about three nozzle diameters downstream of the nozzle rim. As the mean jet velocity V was increased, a region of fluctuation first began at the downstream end of otherwise laminar visible jet and steadily moved toward the nozzle rim. Thus, the transition velocity V_c was defined as the velocity at which the upstream edge of the turbulent fluctuating region has reached the assigned position within the observable domain. For impinging jets, transition was identified as the flow rate that allowed the jets to arrive at the

impingement plane as laminar jets while producing intense turbulent flow after collision.

The orifice meter originally intended to measure the CO₂ flow, was ineffective since the flow rates were too small for the pressure gradient to be measurable. Therefore, the following, somewhat unusual procedure was used for measuring high pressure flows while using low pressure glass-tube instruments. First, the jet flow is set at transition point using micro-metering valve #2(Fig.1) and the jet is photographed, with the micro-metering valve #3 closed. The pressure on the gauge upstream of the orifice is then noted. The jet flow is then stopped using the shut-off valve #1. Next, the micro-metering valve #3 is opened until the pressure gauge reads the same value as in the earlier step.

The above procedure essentially "tricks" the flow into believing that it is being injected into the tank since the pressure drop across the metering valve is kept the same. The flow rates could then be measured by monitoring either the position of the float of the rotameter and/or the time for a bubble to traverse a known volume. Since the pressure drop across metering valve #2 was large, about 50 psi, the flow measurements were fairly accurate and repeatable to within 5%. The pressure drop across the orifice for these low flow rates was only a few psi, and the drop from the nozzle to the tank was a small fraction of a psi.

RESULTS AND DISCUSSION

A series of direct photographs of CO₂ jets for various pressures in the range 50 to 500 psig are presented in Figure 2. Typical appearance of the jets before and after transition are shown in Figure 3 for 100 and 300 psi. According to the photographs (Fig.2), the characteristic size of the turbulent fluctuations steadily increases with pressure. Because of the weak shadowgraph image under atmospheric pressure, no photograph of the jet could be obtained for this condition. In the photographs, the locations of maximum density gradient, CO₂-N₂ interfaces, showed the highest degree of luminosity. Therefore, the variations in the laser light intensity indirectly reveal the nature of the mixing between the jet and its environment. Indeed, the shadowgraph method may be utilized for future exploration of the opalescence phenomenon when the interface between the

liquid and gas phase vanishes as the critical point is approached.

The measured maximum velocities at transition V_c are found to decrease with pressure as shown in Fig.4. At pressures beyond 600 psig, almost all velocities of the jet, however small, are observed to result in unstable wavy flows. Such tendencies are to be expected in view of the substantial reduction in kinematic viscosity and hence reduced dissipation of the system perturbations. In other words, the high pressure jets cannot readily dissipate velocity fluctuations and are thus more susceptible to instabilities.

A most interesting aspect of the experimental observations is the approximate constancy of the transition Reynolds number as a function of pressure. The calculated values of

$$Re_c = \frac{d V_c}{\nu} \approx 525 \quad (1)$$

based on the jet diameter d , the kinematic viscosity ν , and transition velocity V_c are shown in Fig.5. Thus, the variation of V_c and ν with pressure appear to compensate each other resulting in nearly constant values of Re_c . In the following section, a phenomenological description of these observations will be presented within a general scheme of hydrodynamic interactions in turbulent combustion discussed elsewhere (Sheu and Sohrab, 1988).

The characteristic hydrodynamic length for diffusion of momentum in the jet is defined as

$$l_H = \frac{\nu}{V} \quad (2)$$

based on the kinematic viscosity ν . The Reynolds number for the laboratory scale $Re_L = d/l_H$ is thus an expression for the non-dimensional length scale of the problem. That is, the ratio of the characteristic laboratory scale to that for the diffusion of momentum. In view of the definition of ν from the kinetic theory of gases, $\nu = l_m v_m / 3$ we have

$$Re_L = \frac{d}{l_H} = \frac{dV}{\frac{1}{3} l_m v_m} \quad (3)$$

with l_m and v_m referring to the mean free path and mean thermal speed of the molecules, respectively. Hence, in view of Eq.(1), the ratio of the products of the length and velocity for the diverse laboratory versus molecular scales remains invariant with pressure and relates to the transition Reynolds number

$$\frac{dV_c}{l_m v_m} \approx \frac{525}{3} \quad (4)$$

Because of the constant values of both d and the temperature of the gas, hence v_m , Eq. (4) suggests that the ratio $V_c l_m$, remains invariant under increasing pressures. Also, the constancy of Re_c suggests that the critical diffusion length scale at transition

$$l_{Hc} = \frac{v}{V_c} \quad (5)$$

does not vary with pressure. Under a cascade model of turbulence (i.e. Sheu and Sohrab, 1988) a multiplicity of intermediate scales (l_i, v_i) may be considered between the largest, laboratory scale (d, V), and the smallest, i.e. molecular scale (l_m, v_m).

Among the entire spectrum of scales just described, some particular value of length and velocity scale (l_i, v_i) would correspond to the transition from laminar (stable) to turbulent (unstable) flow conditions. The turbulent Reynolds number is defined as

$$Re_t = \frac{l_t v_t}{l_m v_m} \quad (6)$$

where l_t and v_t are the correlation scale i.e. integral scale, and the turbulent fluctuating velocity, respectively. Thus, the turbulent length scale of typical eddies l_t are expected to relate to l_m

through Re_t . Strong correlation between l_t and l_m in spite of their diverse differences is not surprising in view of the result in Eq.(4) suggesting such a correlation between d and l_m . In fact, the invariance of Re_c may suggest constancy of Re_t with pressure, thus requiring $l_t v_t$ to be related to $l_m v_m$ and hence decrease with pressure. Thus a cascade of momentum diffusivities may then be expressed as

$$\dots dV \gg l_t v_t \gg l_i v_i \gg l_k v_k \gg l_m v_m \gg \dots \quad (7)$$

where l_k and v_k refer to the Kolmogorov, dissipation, length and velocity scales (Batchelor,1953). The ratios between successive elements of this cascade define a series of Reynolds numbers

$$Re_n = \frac{l_n v_n}{l_{n-1} v_{n-1}} \quad (8)$$

where n denotes the element of the cascade. In other words, for each statistically independent scale, the transport of momentum occurs through the motion of the element of fluid with the characteristic size l_i and velocity v_i . With lower kinematic viscosity, the turbulent length scale l_t is expected to increase with pressure in qualitative agreement with our observations (Fig.2) even though $l_t v_t$ decreases with pressure.

The correlation between laboratory and molecular scales discussed above are consistent with Reynolds (1895) original observations concerning approximate invariance of Re at transition for flow of different fluids in different tubes. However, the critical value of Re at transition is known to be non-unique and dependent on the tube surface properties as well as upstream perturbations. Therefore, no universally unique values could be associated with either the Re or the system perturbation size at the transition point. Thus, Eq.(7) is an expression of cascade of momentum from large scale motions to the smaller scales and the eventual fading of the observable motions into non-observable background thermal motion of the molecules. This is indeed the description of turbulence as was originally stated by Reynolds(1895):

"...That such change of energy of mean-motion to energy of heat motion may be properly called transformation becomes apparent when it is remembered that neither mean-motion nor relative-motion have any separate existence, but are only abstract quantities, determined by the particular process of abstraction, cause transformation of the abstract energy of the one abstract-motion, to abstract energy of the other abstract motion. ..."

To further explore the role of molecular-scale quantities (l_m, v_m), some preliminary tests with helium were performed. For helium at the same temperature as CO_2 , both v_m and l_m are expected to be higher with $(l_m v_m)_{\text{He}} = 10(l_m v_m)_{\text{CO}_2}$. From the examination of photographs of helium jets the size of typical flow fluctuations, l_t were found to be smaller than the corresponding lengths observed for CO_2 jets. This tendency is expected based on the slightly larger values of V_c as well as the higher viscous dissipations of the helium jet. However, the exact role of viscous effects for He versus CO_2 requires further future exploration.

The nature of hydrodynamic interactions as a function of pressure was also explored by performing some preliminary tests on two impinging CO_2 jets. The direct photographs of the jets, impinging at 90° angle, under chamber pressures $P = 50, 100$ psig for laminar, transition, and fully turbulent flow conditions are shown in Figure 6. Because of the inevitable asymmetries, as the flow rate through the identical nozzles increased, one jet becomes turbulent while the other remains laminar. In the absence of a better criteria, this condition was chosen to correspond to the transition point. The measured transition velocities as a function of pressure are shown in Figure 7.

Some preliminary observations were also made on two impinging water jets. Such flow configuration, which have practical application to rocket injector/atomizer design, may be modeled by tilting the conventional opposed finite-jet flows (Lin and Sohrab, 1989). As is to be expected, the jets produce a sheet of fluid perpendicular to the collision plane illustrated in Figure 8. The thickness of this liquid sheet is an indirect measure of the characteristic hydrodynamic interaction length of the system. In the limit as Re approaches infinity, this sheet is expected to have infinite extent but zero thickness. Of course, in actual jets, transition to turbulence and eventual formation of shock waves are expected as Re is indefinitely increased. However, impinging jets at higher pressures and hence lower values of v , would produce thinner liquid sheets. The instability of

such thin sheets are expected to be enhanced because of the vanishingly small surface tensions near the critical point. The potentials for production of smaller droplets by atomization near the critical point requires further exploration.

CONCLUDING REMARKS

The onset of instability of CO₂ jets flowing into stagnant nitrogen environment under increasing pressures was visualized using the laser shadowgraph technique. It was found that the transition Reynolds numbers remained nearly independent of pressure. However, the maximum velocity at transition decreased as the critical pressure was being approached at a constant temperature. The transition was defined as the onset of instability two diameters downstream of the nozzle rim. In addition, some preliminary observations on the behavior of two impinging CO₂ jets at high pressure were made.

The experimental results were found to be consistent with a cascade model of turbulent length and velocity scales. Also, the relevance of the study to the atomization process under supercritical states was discussed.

ACKNOWLEDGEMENTS

This research is sponsored by the AFOSR/UES, Contract No. F49620-85-C-0013. The support of AFAL personnel is kindly appreciated.

REFERENCES

1. Abromovich, G. N. (1963) **The Theory Of Turbulent Jets**, MIT Press, Cambridge.
2. Batchelor, G. K. (1953). **The Theory of Homogeneous Turbulence**, Cambridge Univrsity Press, Cambridge.
3. Canada, G. S. and Faeth, G. M. (1975) Combustion of liquid fuels in a flowing combustion gas environment at high pressures, **15th Symposium (Int.) On Combustion**, The Combustion Institute.
4. Chen, Z. H., Lin, T. H. and Sohrab, S. H. (1988) Combustion of liquid fuel sprays in stagnation-point flow, **Combust. Sci. and Tech.** 60, p. 63.
5. Faeth, G. M., Dominics, D. P., Tulpinsky, J. F. and Olson, D. R. (1970) Supercritical bipropellant droplet combustion, **12th Symposium (Int.) on Combustion**, The Combustion Institute, p. 9.
6. Farrell, P. V. and Peters, B. D. (1986) Droplet vaporization in supercritical pressure environments, **Acta Astronautica** 13, p. 673.
7. Kadota, T. and Hiroyasu, T. A. (1981) Combustion of fuel droplet in supercritical gaseous environments, **18th Symposium (Int.) on Combustion**, The Combustion Institute.
8. Lazara, R. S. and Faeth, G. M. (1971) Bipropellant droplet combustion in the vicinity of the critical point, **13th Symposium (Int.) on Combustion**, The Combustion Institute, p. 9.
9. Lin, T. H. and Sohrab, S. H. (1989) Finite Jets with/without rigid-body rotation, **J. Fluid Mech.**, to appear.
10. Natajan, R. and Bruzutowski, T. A. (1970) Some new observations combustion of hydrocarbon droplet at high pressures, **Combust.Sci. and Tech.** 2, p. 259.
11. Reid, R. C., Prausnitz, M. J. and Poling, E. B. (1987) **The Properties of Gases and Liquids**, McGraw Hill, New York, p. 418.
12. Reynolds, O.(1895) On dynamic theory of incompressible viscous fluids and the determination of the criterion, **Phil. Trans. Roy. Soc.A** 186,123.
13. Rosner, D. E. and Chang, W. S. (1973) Transient evaporation and combustion of a droplet near the critical temperature, **Combust. Sci. and Tech.** 9, p. 145.
14. Sanchez-Tarifa, C., Crespo, A. and Fraga, E. (1972) Theoretical model for the combustion of droplets in supercritical conditions and gas pockets, **Acta Astronautica** 17, p. 685.
15. Sheu, W. J. and Sohrab, S. H. (1989) On upstream interactions between flamelets in turbulent premixed flames, **Combust. Sci. and Tech.**, to appear.
16. Sohrab, S. H. (1986) Combustion under supercritical states and influence of radiation on droplet combustion, **AFOSR Final Report**, F49620-85-0013.
17. Spalding, D. B. (1959) Theory of particle combustion at high pressures, **ARS J.**, p. 828.

18. Williams, F. A. (1985) **Combustion Theory**, 2nd ed. Benjamin Cummins: Palo Alto, California.

LIST OF FIGURES

- Figure 1 Schematic of the experimental apparatus.
- Figure 2. Direct photograph of the CO₂ jet shadowgraphs at the transition point with rising pressures.
- Figure 3 Direct photograph of the CO₂ jet shadowgraphs
(a) $p = 100$ psig, $V=5.1$ cm/s, (b) $p = 300$ psig, $V=5$ cm/s, (c) $p = 100$ psig, $V=20$.cm/s, (d) $p = 300$ psig, $V=20$ cm/s.
- Figure 4. Transition velocity as a function of chamber pressure for single CO₂ jet.
- Figure 5. Transition Reynolds number as a function of chamber pressure for single CO₂ jet.
- Figure 6. Two impinging CO₂ jets (a) $p = 50$ laminar, (b) $p = 100$ laminar, (c) $p = 50$ transitions, (d) $p = 100$ transtion, (e) $p = 50$ turbulent, (f) $p = 100$ turbulent.
- Figure 7 Velocity as a function of chamber pressure for impinging CO₂ jets under laminar, transition, turbulent conditions.
- Figure 8 Formation of liquid sheet by two impingingwater jets.

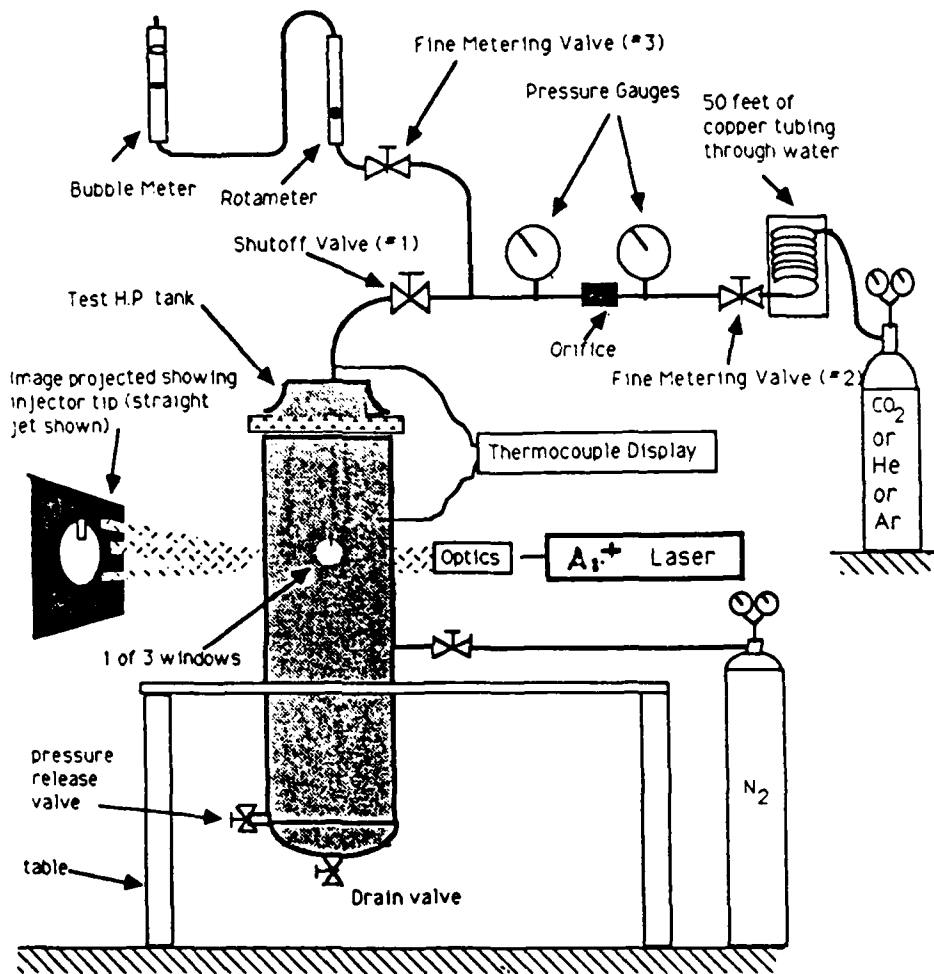
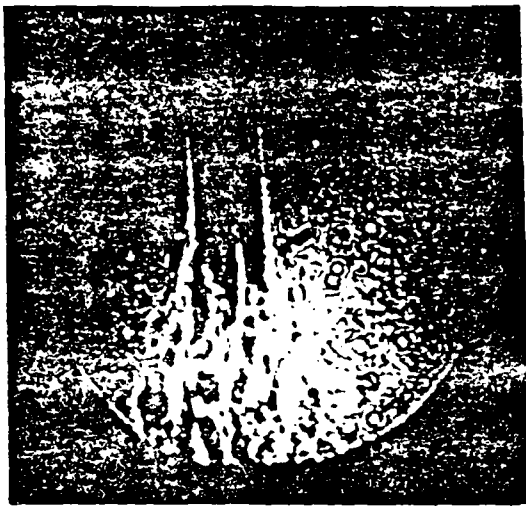
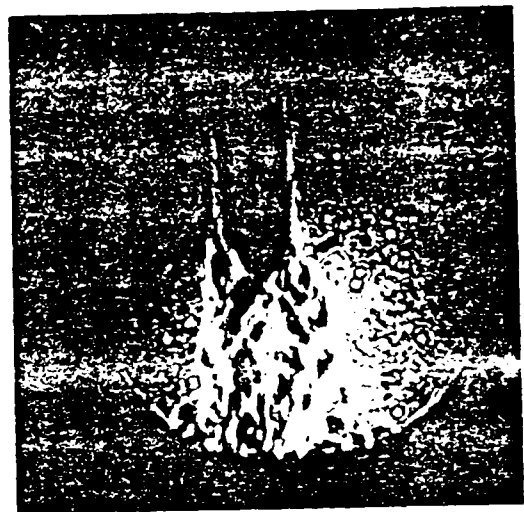


Figure 1



(a) 50 psi



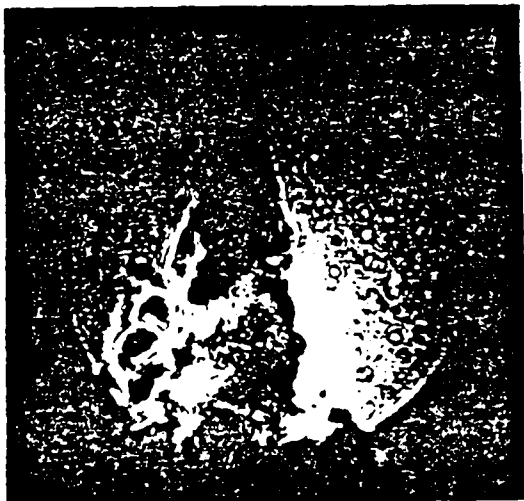
(b) 100 psi



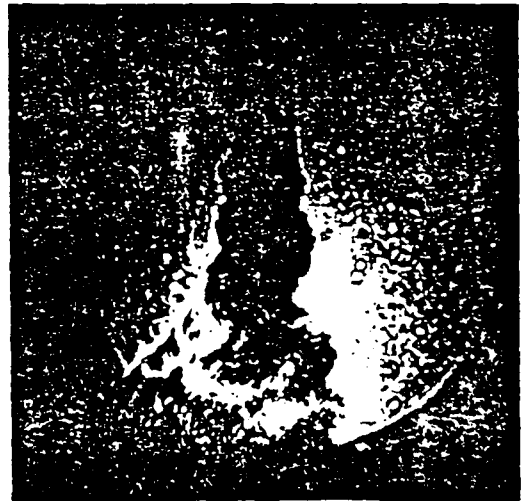
(c) 200 psi



(d) 300 psi

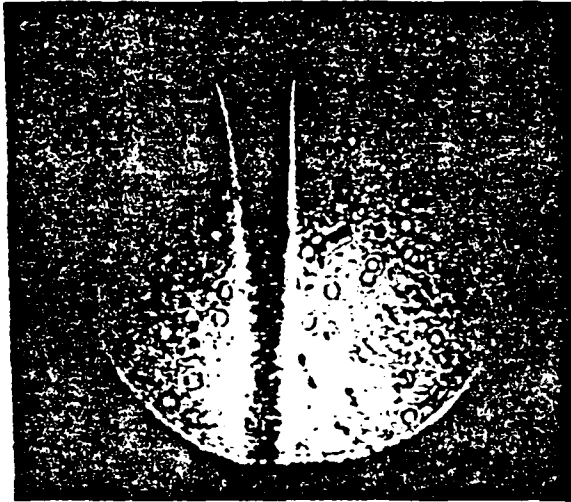


(e) 400 psi

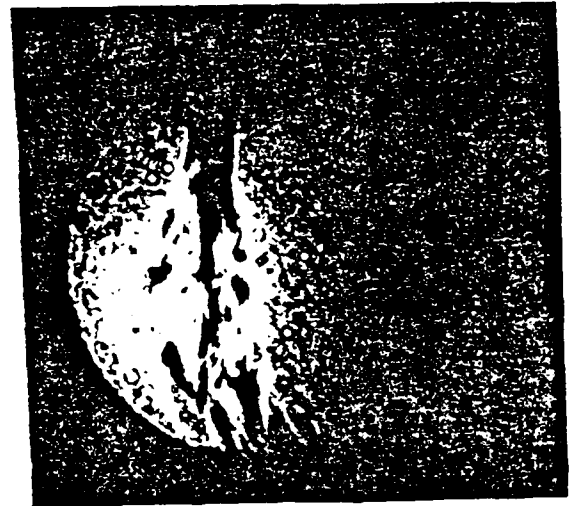


(f) 500 psi

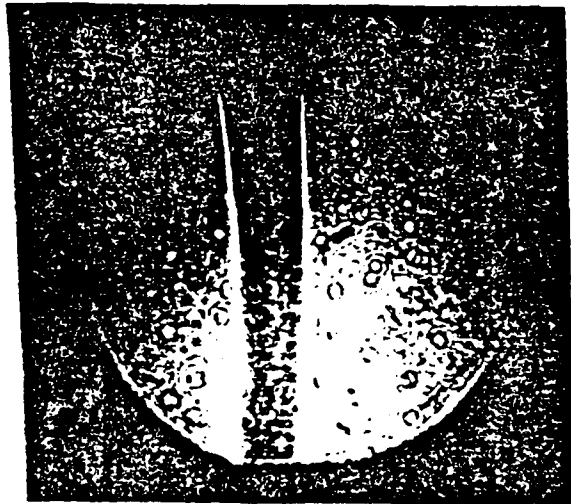
Figure 2



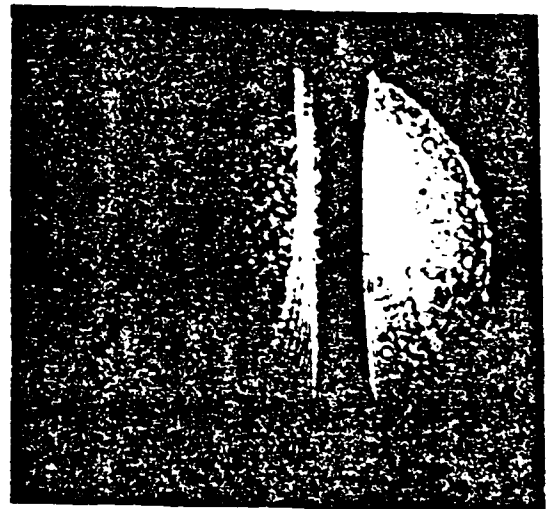
(a)



(b)



(c)



(d)

Figure 3

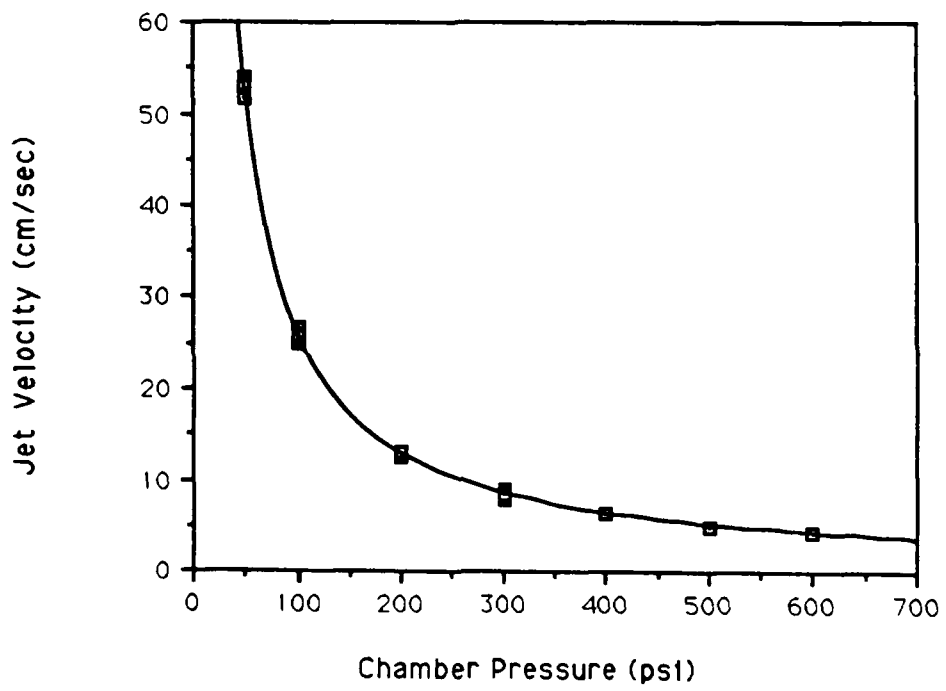


Figure 4

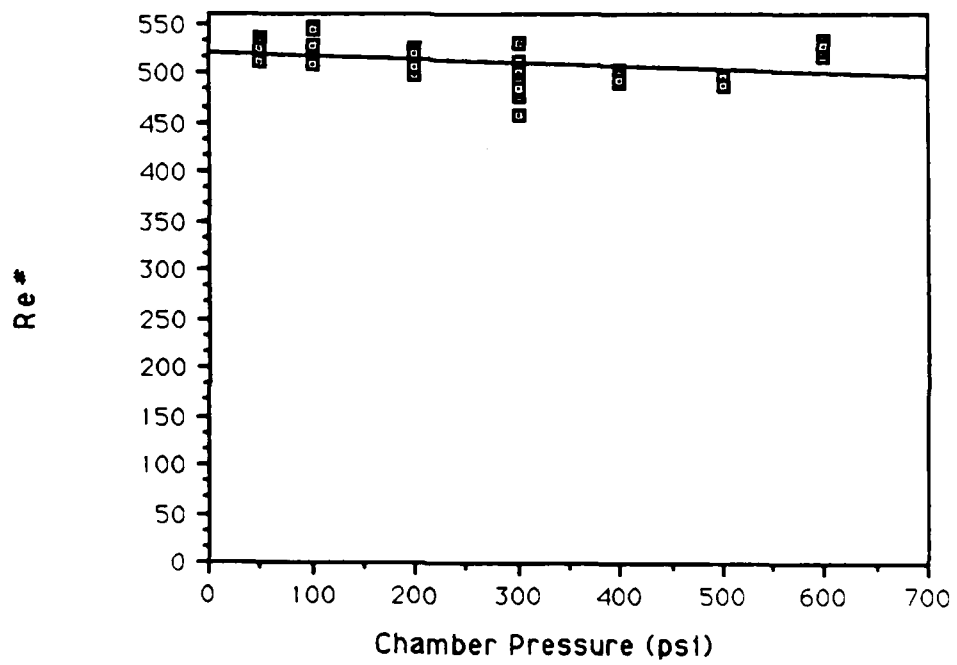
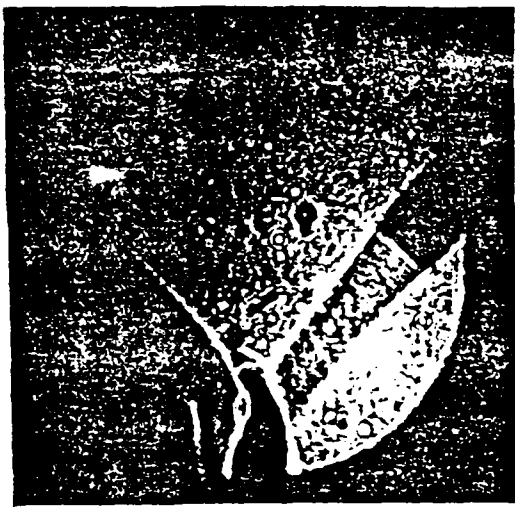
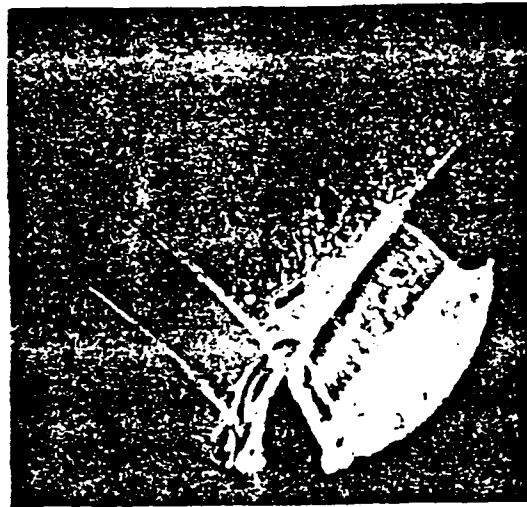


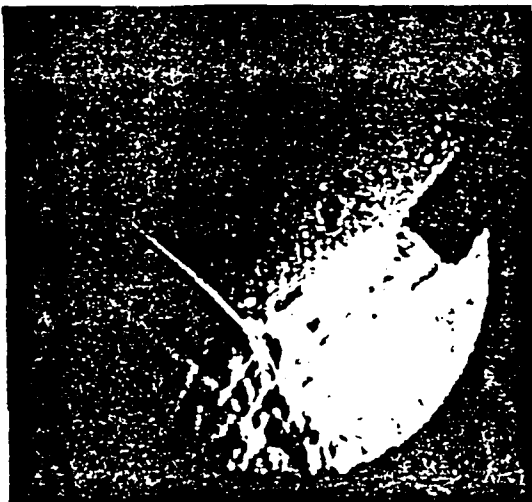
Figure 5



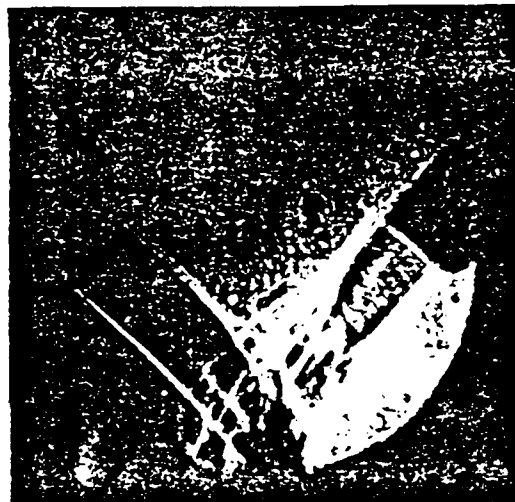
(a)



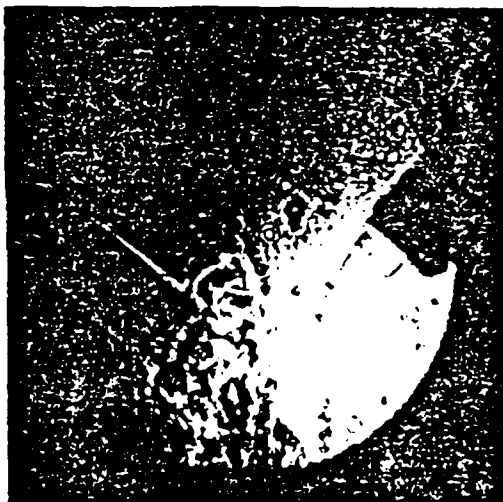
(b)



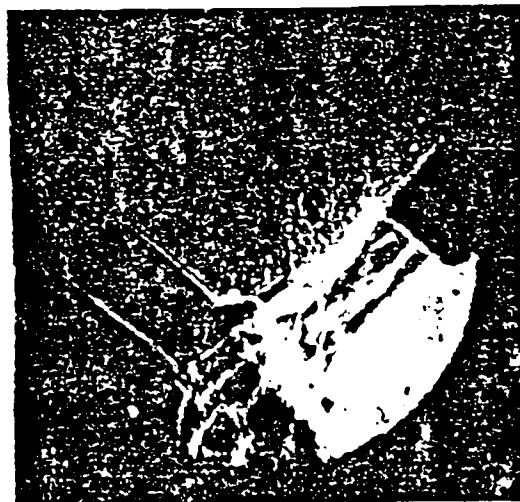
(c)



(d)



(e)



(f)

Figure 6

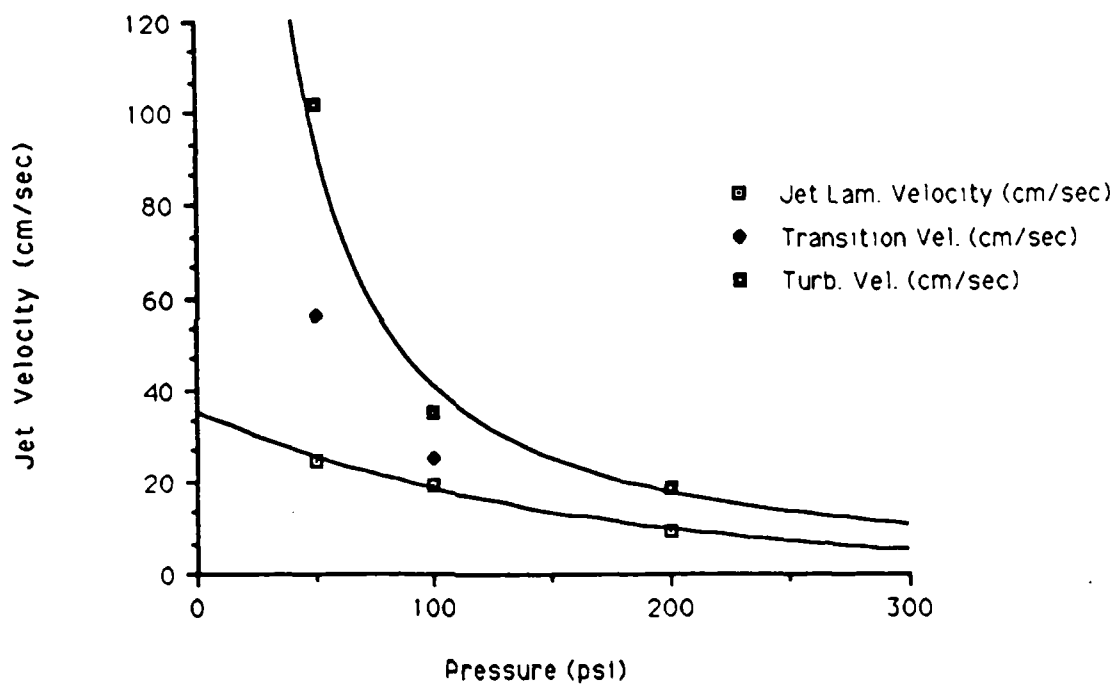


Figure 7

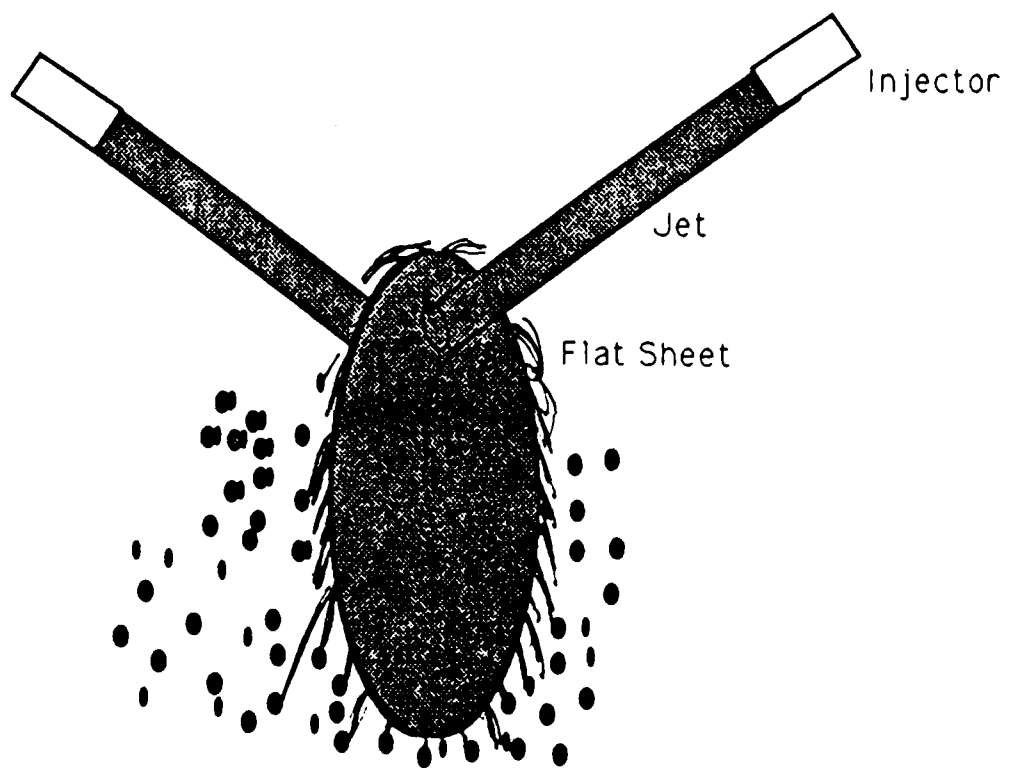


Figure 8

HF NETWORK EVALUATION
FINAL REPORT
contract #F49620-88-C-0053/SB5881-0378
George N. Bratton
March 25, 1989

The Alaskan HF project was designed to demonstrate and evaluate the performance of computer controlled high frequency radios in a network. Descriptions of the project can be found in the final report of my summer faculty research project and the proposal that I submitted for the RIP funding.

Research Initiation Program funding was requested for 1989 for two purposes. To continue the data analysis work that I had performed during the summer of 1988 and to broaden the investigations of the actual network performance in relation to the predictions made in a computer simulation.

Neither of these two activities was continued during 1989 for several reasons beyond my control. First, due to hardware problems in the Alaskan network the amount of data being received in Boston steadily declined from the summer of 1988. The network was not actually restored to operational status until early in December. Second, from the summer of 1988 until the present time four different Air Force officers have been in charge of the project. This lack of continuity has led to the stagnation of the project. Finally, the primary civilian contractor has chosen not to accommodate my efforts, knowing that I would not work on the project after 1989.

I made several attempts to continue the work that was begun in 1988. In early March of 1989 I traveled to Boston to meet with Major Tom Bird, the project officer at that time and Dr. John Dalphin, another RIP faculty researcher on this project. During this visit we also spent two hours discussing the status of the Alaskan network with Mitre Corporation personnel, since Mitre was the primary civilian contractor. From these meetings I learned that the network was currently not operational and would not be operational until sometime during the summer. Both Major Bird and the Mitre group indicated that they would like Dr. Dalphin and I to work on another networking project, this one based in western Europe. However, after I returned from Boston, this never materialized.

During the summer of 1989 Major Bird retired and another major, whose name I never learned assumed the responsibility for the Alaskan HF project. In the fall, when I was to again work on the project, I made two unsuccessful attempts to contact the appropriate person before I made contact with Lt. Jampoler and Major Guillen, the current project officers, in early October. Another trip to Boston followed. This time Dr. Dalphin and I learned of Major Guillen's plans to go to Alaska in November to attempt to resolve the difficulties in person. He told us then that if he did not get guarantees of better cooperation from the Alaskan Air Command that the project would be terminated. We proposed to Major Guillen at that time that

we would each continue to work on the project, but would require funding for salary and modest travel. He accepted written proposals but decided not to fund them.

Consequently, I have not been sent any data to analyze because no data has been collected during the year that I had time set aside to work on the project. The attempts that I made to participate in other activities were thwarted by the reluctance of Mitre Corporation to cooperate with our requests.

The software written by Dr. Dalphin and I, the instructions for its use, and all supporting materials have been given to Lt. Jampoler. Earlier copies of these items seem to have disappeared in the personnel shuffle. I think that this fact further illustrates the deterioration of this project.

FINAL REPORT NUMBER 26
REPORT NOT AVAILABLE AT THIS TIME
Dr. John F. Dalphin
210-9MG-023

FINAL REPORT NUMBER 27
RELIABILITY IN SATELLITE COMMUNICATION NETWORKS
Dr. Stephan Kolitz
PENDING APPROVAL
760-6MG-094

HIGH INTENSITY COMPRESSIVE
STRESS WAVE PROPAGATION
THROUGH UNSATURATED SANDS

FINAL REPORT

Prepared by

Geotechnical Engineering Program
Colorado State University
Fort Collins, Colorado 80523

Authors

S.J. Pierce and W.A. Charlie

Principal Investigator

Wayne A. Charlie, Ph.D., P.E.

Prepared for

Universal Energy Systems, Inc.
4401 Dayton-Xenia Road
Dayton, Ohio 45432

Funded by

Air Force Office of Scientific Research
Bolling AFB, DC

November, 1989

ACKNOWLEDGEMENT

The research was funded by a grant from the Air Force Office of Scientific Research, Bolling AFB, DC, under the Research Initiation Program(Contract F49620-87-0004 and S-210-9MG-075 with UES,Inc. of Dayton, Ohio). Dr. C. Allen Ross, AFOSR University Resident Research Professor at Tyndall AFB, Florida, provided considerable help, insight and encouragement. Steven T. Kuennen, 2Lt, USAF, provided considerable help with conducting the laboratory tests. Drs. Deanna Durnford and Donald Doehring of Colorado State University reviewed the report.

ABSTRACT

HIGH INTENSITY COMPRESSIVE STRESS WAVE PROPAGATION THROUGH UNSATURATED SANDS

High amplitude split-Hopkinson pressure bar laboratory tests were performed on confined specimens of 20-30 Ottawa and Eglin sands. Triaxial confining stresses of zero and 310 kPa were used, and the samples were subjected to a constant incident stress. Samples were compacted dry, then saturated, then desaturated by use of the pressure plate method. For saturation levels increasing from zero to 80 percent, the compressive wave velocity and stress transmission ratio values decreased slightly for both confining stresses. Quasi-static constrained modulus was found to vary in a similar manner. Previous researchers have shown that for specimens compacted moist, the values of wave velocity, stress transmission ratio and quasi-static constrained modulus increase as the saturation level increases from zero to approximately 30 percent, and then decreases with any further increase in saturation. Several specimens were compacted moist in this research and the results show similar trends. The difference in trends is directly related to the moisture content of the sand during compaction.

Civil Engineering Department
Colorado State University
Fort Collins, CO 80523

LIST OF SYMBOLS AND UNITS

- A - cylindrical explosive in Hopkinson bar schematic
- B - time piece in Hopkinson bar schematic
- B - bulk modulus (kPa)
- cm - centimeter
- C - incident bar in Hopkinson bar schematic
- C_c - coefficient of curvature
- C_t - compressibility of soil structure with respect to change in $(\sigma - u_a)$ (1/kPa)
- C_u - coefficient of uniformity
- C_w - compressibility of soil structure with respect to change in capillary pressure (1/kPa)
- d - diameter of cylindrical material (m)
- d_x - effective grain size diameter; x% of soil has size finer than this value (mm)
- D - constrained modulus (kPa)
- D - momentum trap in Hopkinson bar schematic
- D_s - constrained modulus of mineral skeleton (kPa)
- e - void ratio
- E - Young's modulus (kPa)
- ft - feet
- g - acceleration due to gravity (9.81 m/sec^2)

G_s - specific gravity of mineral particle
 G_o - shear modulus (kPa)
kg - kilogram
kPa - kilo Pascals
K - aggregate bulk modulus (kPa)
 K_o - coefficient of lateral stress under static conditions
l - total length of material (m)
m - mass
m - meter
mm - millimeter
n - porosity
N - Newton
psi - pounds per square inch
psf - pounds per square foot
 P_d - displacement pressure (kPa)
P - hydrostatic pressure (kPa)
 P_c - capillary pressure (kPa)
 R^2 - coefficient of determination
 r_m - radius of meniscus (m)
s - second
s - standard deviation
S - saturation level (%)
SHPB - Split-Hopkinson Pressure Bar

S_r - residual saturation (%)
 t - time
 T - surface tension (kPa)
 u_a - pore air pressure (kPa)
 u_w - pore water pressure (kPa)
 V_c - compressional wave velocity (m/sec)
 w - water content (%)
 x - variable length (m)
 \bar{x} - mean
 z - variable length in vertical direction (m)
 ϵ - strain (longitudinal)
 ϵ_r - radial strain
 ϵ_v - volumetric strain
 ϵ_z - strain in z direction
 μs - microsecond (10^{-6} seconds)
 ρ - density of material (kg/m^3)
 ρ_t - total density of soil (kg/m^3)
 ρ_w - density of water (kg/m^3)
 ρV_c - acoustic impedance ($kg/m^2 \cdot sec$)
 σ - total stress (kPa)
 σ' - effective stress (kPa)

- σ_1 - stress due to the incident stress wave (kPa)
- σ_2 - stress due to the reflected stress wave (kPa)
- σ_D - average dynamic stress applied by SHPB (kPa)
- σ_I - stress in incident material due to incident stress wave (kPa)
- σ_o - isotropic confining stress (kPa)
- σ_r - radial stress (kPa)
- σ_R - stress in incident material due to reflected stress wave (kPa)
- σ_T - stress in transmitting material due to transmitted stress wave (kPa)
- σ'_T - stress transmitted into a third medium (kPa)
- σ_z - total stress in z direction (kPa)
- γ_d - dry unit weight (N/m^3)
- χ - saturation parameter

I. INTRODUCTION

A. STATEMENT OF PROBLEM

Compressive stress wave propagation through soils is of considerable interest to the armed forces, mining industry and in the area of geophysical investigations. Research on high amplitude, short duration compressive loadings is particularly important in understanding the soil-structure response of buried structures subjected to explosive-induced stress waves. Because the response of a structure is highly dependent on the dynamic properties of the soil, changes in the characteristics of the soil during construction and over time could greatly affect the behavior of the structure.

A substantial amount of research has been conducted in the area of compressive wave propagation and compressibility of dry or saturated sand. However, little has been done for unsaturated sands. This lack of research is especially evident for high amplitude loading conditions.

Previous studies and wave propagation theory have shown that there is a link between the saturation level and stiffness of soil. The soil stiffness is reflected in the values of compressive wave propagation velocity and the magnitude of the stress wave being transmitted through the soil. Currently there are no methods

available for predicting these parameters under large amplitude compressive stress wave loading conditions.

For two sands compacted in a similar manner to the same void ratio, but at different moisture contents, the static and dynamic properties of the sands will be different. It has been shown previously that the liquefaction potential, cyclic shear strength and permeability of sands are affected when different specimen compaction procedures are used. Therefore, before the compressive stress wave propagation parameters can be evaluated, an understanding of the effects of sample preparation technique is required.

B. OBJECTIVES OF THIS INVESTIGATION

The objective of this research is to determine how moisture content during compaction, saturation level and confining stress affect the values of wave velocity, stress transmission ratio and quasi-static constrained modulus for 20-30 Ottawa (ASTM C190) and Eglin sands. In order to achieve this objective, a split-Hopkinson pressure bar, located at Tyndall Air Force Base, Florida was utilized to subject the sands to high amplitude, short duration compressive loadings. Quasi-static stiffness tests were performed to determine the relationship between the quasi-static and dynamic parameters of the two sands.

In this investigation saturation level and confining stress were varied. Samples were compacted dry to a constant void ratio, and the applied dynamic stress was held constant for both of the sands used.

During testing, samples were allowed to strain one-dimensionally under triaxial confining stresses of zero and 310 kPa.

The results obtained in this investigation have been compared to tests performed on the same two sands by Ross et al. (1988). Ross et al. used the same split-Hopkinson pressure bar, the same void ratio and range of saturation levels, and subjected the sands to identical dynamic stress and confining conditions as in this investigation. The only difference between the research performed by Ross et al. and the current investigation is that Ross et al. compacted the sand samples moist, while in this investigation, the samples were compacted dry, saturated, then desaturated by use of the pressure plate method. The results have also been compared to experimental results obtained by other investigators, and compared with several mathematical models developed for the determination of compressive wave velocities through soils.

II. LITERATURE REVIEW

This chapter consists of five sections in which previous research has been reviewed and cited for its relevance and usefulness in the current investigation. The first section is a review of the wave propagation equations which are used in this study. The second section is a history of the evolution of the split-Hopkinson pressure bar. The third section is a brief review of the current state of knowledge in the area of capillarity and unsaturated soil mechanics. Section four is a summary of the most recent work in the area of compaction, and its effects on lateral stress and fabric development in sands. The final section is a review of compressibility and wave propagation research performed on unsaturated, cohesionless soils within the saturation ranges used in this investigation.

A. WAVE PROPAGATION THEORY

The velocity of a wave as it propagates through a material can be theoretically determined from Newton's Second Law of Motion and elasticity theory if the applied stress is within the elastic limits of the material. Depending on the strain conditions allowed, one of the following equations can be used to determine the compression wave propagation velocity (Kolsky, 1963):

$$v_c = \left\{ \frac{E}{\rho} \right\}^{0.5} \quad (2.1)$$

$$v_c = \left\{ \frac{B}{\rho} \right\}^{0.5} \quad (2.2)$$

$$v_c = \left\{ \frac{D}{\rho} \right\}^{0.5} \quad (2.3)$$

where E is Young's Modulus, B is the Bulk modulus, and D is the constrained modulus. Equations 2.1 through 2.3 state that the compressive wave velocity is only a function of the stiffness and the density of the material. Total density is used in these equations when determining the propagation velocity through soils.

When a propagating wave comes to a boundary with a material of different acoustic impedance, a portion of the wave will be reflected back into the bar, and a portion will be transmitted into the second medium. Acoustic impedance is defined as the wave propagation velocity multiplied by the mass density of the material. Rinehart (1975) shows that the amount of stress reflected back into the first material can be determined by:

$$\sigma_R = \frac{\rho_2 v_{c_2} - \rho_1 v_{c_1}}{(\rho_2 v_{c_2} + \rho_1 v_{c_1})} \sigma_I \quad (2.4)$$

where σ_I and σ_R are the incident and reflected stresses, and the subscripts 1 and 2 denote the two mediums being considered. The values in the form ρv_c are the acoustic impedances of the two materials. The amount of stress being transmitted into the second medium can be determined from:

$$\sigma_{T_2} = \frac{2\rho_2 V c_2}{(\rho_2 V c_2 + \rho_1 V c_1)} \sigma_{I_1} \quad (2.5)$$

where σ_T is the transmitted stress.

If several materials are in contact, such as Figure 2.1, the stress at each interface can be determined. Using equation 2.5 for the stress transmitted into material 2, and assuming no wave attenuation occurs through material 2, then the magnitude of the stress transmitted into the third medium can be determined by replacing the incident stress with the stress transmitted into medium 2 and changing the values for the acoustic impedances in equation 2.5:

$$\sigma'_{T_3} = \frac{2\rho_3 V c_3}{(\rho_2 V c_2 + \rho_3 V c_3)} \sigma_{T_2} \quad (2.6).$$

σ'_T is the stress transmitted into the third medium. This process can be continued for any number of boundary conditions which are of interest.

If the special case occurs where the first and third mediums of Figure 2.1 are the same, but different than the second, a relationship between the incident pulse and the pulse transmitted into the third medium can be determined. If equations 2.5 and 2.6 are combined for this condition, the following equation is obtained:

$$\frac{\sigma'_{T_1}}{\sigma_{I_1}} = 4 \frac{\rho_1 V c_1 \rho_2 V c_2}{(\rho_2 V c_2 + \rho_1 V c_1)^2} \quad (2.7).$$

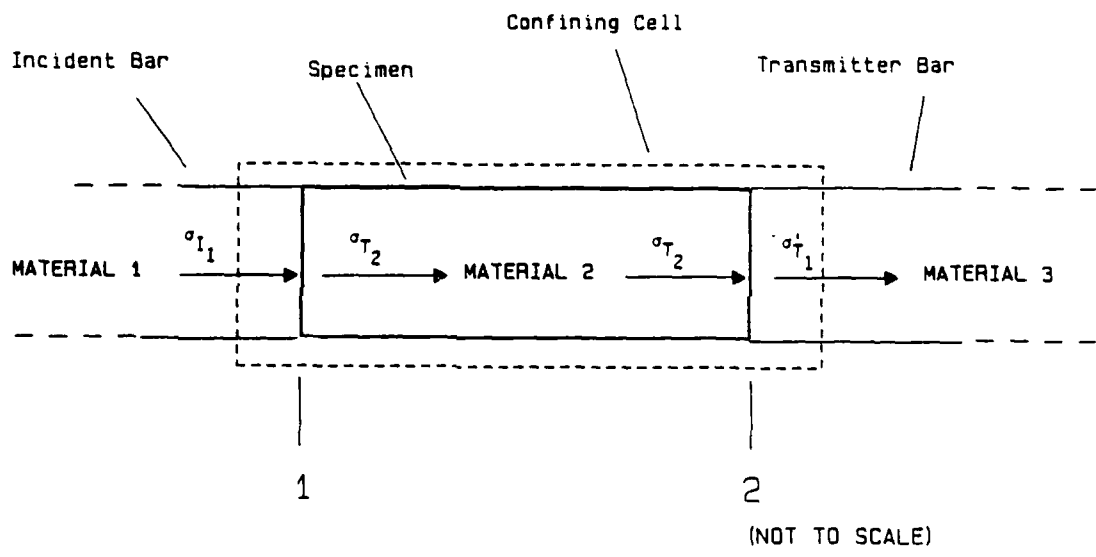


Figure 2.1 Stress Wave Propagating Through Three Materials

The value in equation 2.7 is referred to as the stress transmission ratio. Comparing equations 2.5 and 2.7, the magnitude of the stress transmitted into the third medium is approximately two times the magnitude of the stress in the second medium if the acoustic impedance of the second medium is considerably smaller than the first and third. This relationship is of particular importance in an investigation utilizing a split-Hopkinson pressure bar. In this investigation, a soil sample (medium 2) is placed between two steel bars (mediums 1 and 3).

B. SPLIT-HOPKINSON PRESSURE BAR DEVELOPMENT

The split-Hopkinson pressure bar (SHPB) was developed through the need for a better understanding of the behavior of materials at high strain rates. As strain rates change, the stress-strain properties of the material may also change. Bar impact methods such as the split-Hopkinson pressure bar, apply strain rates to materials from 5×10^1 to 10^4 per second with loading rise times from approximately 10^{-4} to 10^{-6} seconds.

The split-Hopkinson pressure bar has evolved as a method to measure the stress-strain properties of materials at high strain rates. Only recently, the bar has been used in measuring dynamic properties of soils. Recently the device was used to measure strain rate properties of soils (Felice, 1986), while in this investigation and the investigation by Ross et al. (1988) have used the SHPB to measure the effects of propagating a single transient pulse through a soil sample.

1. The Hopkinson Bar

Hopkinson (1914) developed a laboratory apparatus for measuring the maximum pressure developed and loading duration for an explosive impact in the laboratory. Hopkinson's schematic of the device is shown in Figure 2.2. A compressive stress pulse was generated by firing a cylindrical explosive, marked "A" in the figure, at the end of a steel bar (marked "C" in the schematic). At the other end of the bar a "time piece" (shown as "B" in the figure) was magnetically attached. This time piece was a section of steel with the same diameter as the incident bar, but of variable length. When the compressive pulse passed through the time piece, the wave was reflected off the end, which created a tensile pulse in the opposite direction. When the tensile wave met the joint between the time piece and bar, the magnetic joint could not transmit the tensile wave causing the time piece to accelerate away from the bar into a ballistic pendulum, which is shown as "D" in the schematic. The pendulum was used to measure the momentum of the time piece. If the time piece was of a length such that the entire pulse was trapped within it, the incident bar would not move once the time piece separated. The duration of the pulse was then twice the length of the time piece multiplied by the wave velocity of the material.

From this apparatus, the maximum stress applied to the bar could be determined from the momentum trap, and the duration of the pulse (the wavelength) could be determined. Because of limitations in

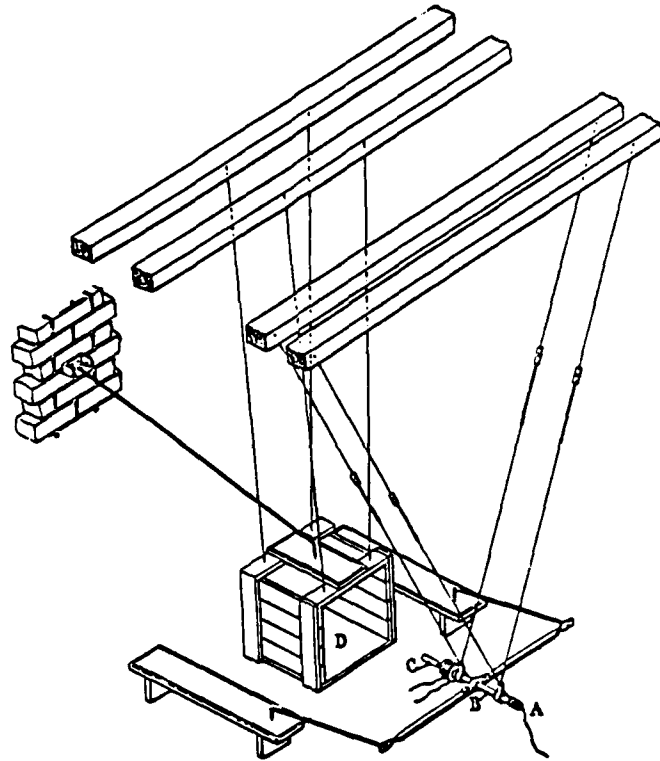


Figure 2.2 Apparatus Developed by Hopkinson (Hopkinson, 1914)

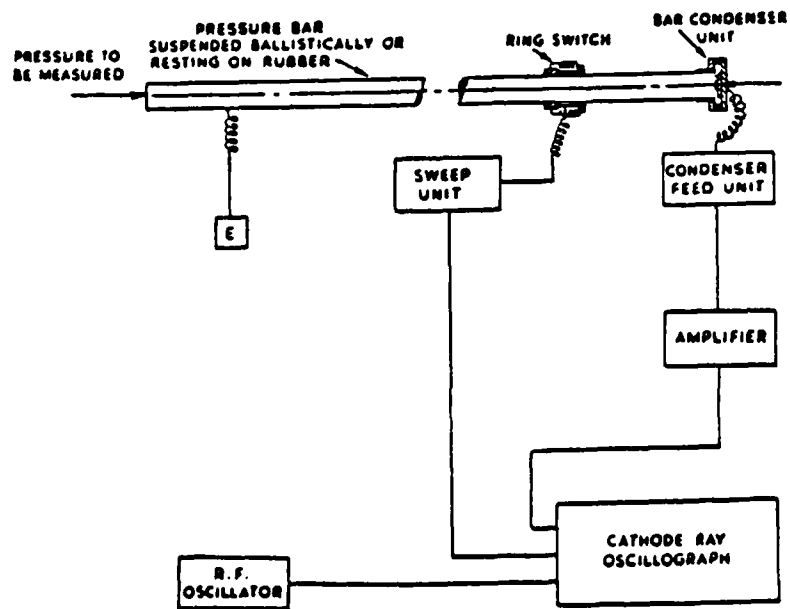


Figure 2.3 Apparatus Developed by Davies (Davies, 1948)

the equipment, the pressure-time history of the pulse as it travelled through the bar could not be determined.

2. The Davies Bar

R.M. Davies (1948) updated the Hopkinson apparatus by replacing the time piece with a bar condensor unit to measure displacements at the end of the bar. Figure 2.3 shows the bar condensor unit as it fit over the free end of the incident bar. This configuration allowed the incident bar to be one face of a parallel plate condensor, while the bar condensor was used as the other face.

Davies used the relationship between compressive stress and particle velocity to relate the displacement at the end of the bar to the stress-time history developed by the compressive wave. Stress is related to particle velocity by:

$$\sigma = \rho v_c \frac{du}{dt} \quad (2.8)$$

where the particle velocity is du/dt . As a compressive stress pulse travels down the bar to the free end, the particle velocity doubles giving:

$$\sigma = 1/2 \rho v_c \frac{du}{dt} \quad (2.9)$$

or

$$\frac{du}{dt} = \frac{2\sigma}{\rho v_c} \quad (2.10).$$

By utilizing the bar condensor unit, the Davies bar gave the displacement-time history of the pulse, which was then differentiated

and used in equation 2.10 to find the pressure time history of the pulse.

3. The Kolsky Device (Split-Hopkinson Pressure Bar)

Kolsky (1949) modified the Davies bar to allow for the determination of the dynamic stress-strain properties of materials. As shown in Figure 2.4, the modifications consisted of separating the bar into two pieces (the incident and transmitter bars) to allow for the placement of a thin specimen of metal, rubber, or other material between the bars. The apparatus utilized the same type of bar condensor unit at the end of the transmitter bar used by Davies to determine the displacement of the end of the bar, while using a cylindrical condensor to determine the radial displacement of the incident bar.

Kolsky (1948, 1963) has shown that the relationship between the incident and transmitter bar displacements can be used to determine the stress-strain relationship for the thin specimens. The thin specimens allow for multiple reflections to occur within the samples in order to create a uniform stress throughout the specimen.

Fletcher and Poorooshasb (1968) determined the stress-strain relationship for clay samples using a SHPB under saturated conditions. The magnitude of the stress through the soil were varied from zero to 830 kPa. Felice, Gaffney, Brown and Olsen (1987) utilized the SHPB to measure the stress-strain properties of compacted sands. In both of these investigations, thin specimens were used which had a length to diameter ratio of 0.1.

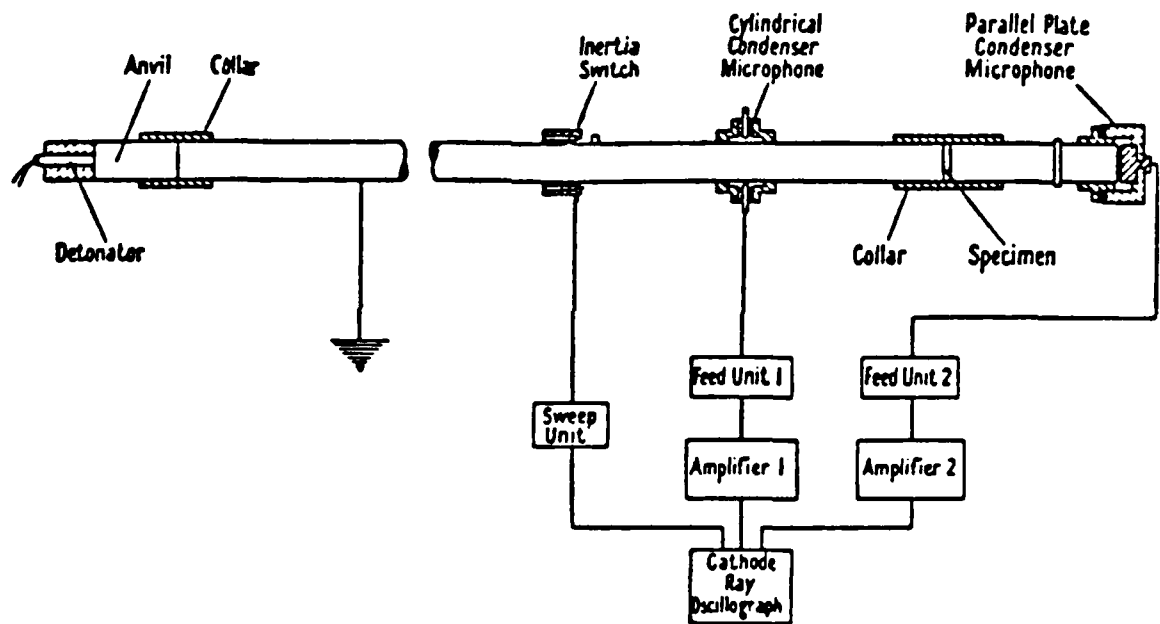


Figure 2.4 Kolsky Apparatus (Kolsky, 1963)

C. CAPILLARITY AND UNSATURATED SOIL MECHANICS

1. Capillarity

Capillarity is a phenomena that occurs in soils due to the surface tension of water in contact with air. Figure 2.5 shows the relationship between capillary menisci and individual soil particles. Holtz and Kovacs (1981) explain that the surface tension of the water increases the intergranular stress between the two soil particles. Lambe and Whitman (1969) show that capillary forces cause sand grains to resist rearrangement at low water contents. This behavior is referred to as bulking and is shown in Figure 2.6.

McWhorter and Sunada (1977) show that the capillary pressure is a function of surface tension and pore size radius. This relationship is expressed by:

$$P_c = u_a - u_w - \frac{2T}{r_m} \quad (2.11)$$

where u_a is the pore air pressure, u_w is the pore water pressure, T is the surface tension and r_m is the radius of the air-water interface. The value r_w depends on soil type, grain size and shape, gradation, and packing.

Equation 2.11 shows that the capillary pressure and therefore, the use of water due to capillarity, are function sof the radius of the air-water interface. For the capillary rise to increase, the pore space that the water occupies must become increasingly smaller. As a

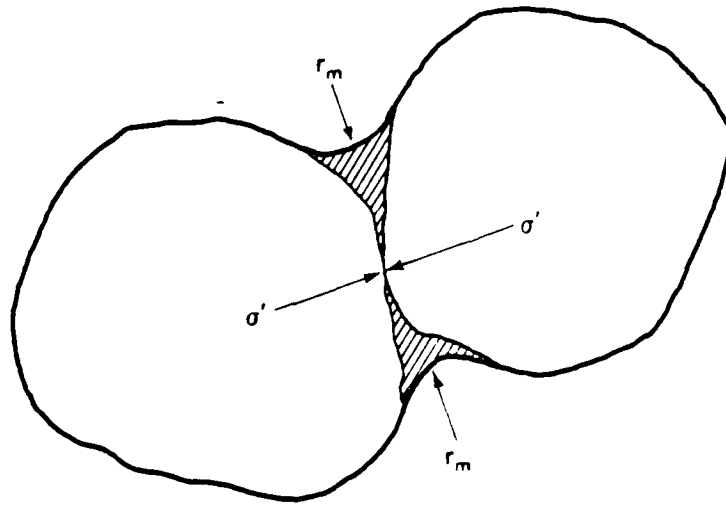


Figure 2.5 Sand Grains Held Together Due to Capillarity (Holtz and Kovacs, 1981)

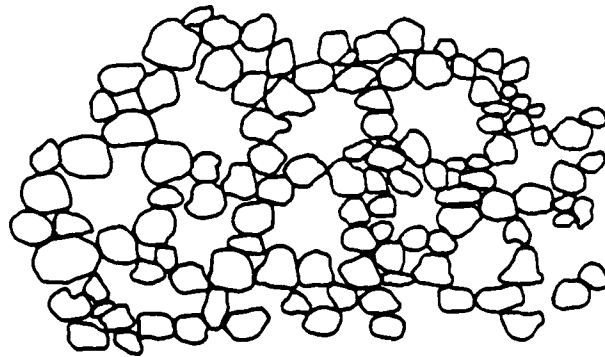


Figure 2.6 Bulking in Sand (Holtz and Kovacs, 1981)

result, a relationship exists between the capillary pressure and saturation level of the soil at a particular point above the groundwater table. This relationship can be expressed by a capillary pressure-desaturation curve as shown in Figure 2.7.

Corey (1986) states that the relationship between capillary pressure and saturation is not unique, but depends on the saturation history. The drainage curve in Figure 2.7 is obtained by starting with a water saturation of 100 percent, and increasing the capillary pressure to obtain the relationship as shown. The wetting curve is obtained by starting with a moist soil and allowing the soil to imbibe water. The two curves are different due to a hysteresis effect, and in general, soils in the field have capillary pressure-saturation distributions somewhere between the wetting and drying curves.

Corey (1986) states that the hysteresis may be due to several effects. One effect is due to wettability changes which depend on which phase (air or water) first comes in contact with the soil particles. A second effect is illustrated in Figure 2.8 which shows the results of drainage or imbibition on capillary tubes with irregular cross-sections. Because of the increase in pore radius, the imbibition capillary is unable to attain the same capillary pressure (or capillary rise) as the capillary which was initially saturated and allowed to drain and equilibrate.

The value of S_r shown in Figure 2.7 is referred to as the residual saturation. This minimum saturation only occurs due to drainage by gravity. Soils can reach a lower saturation level by evaporation, plant uptake of soil moisture, and variations in

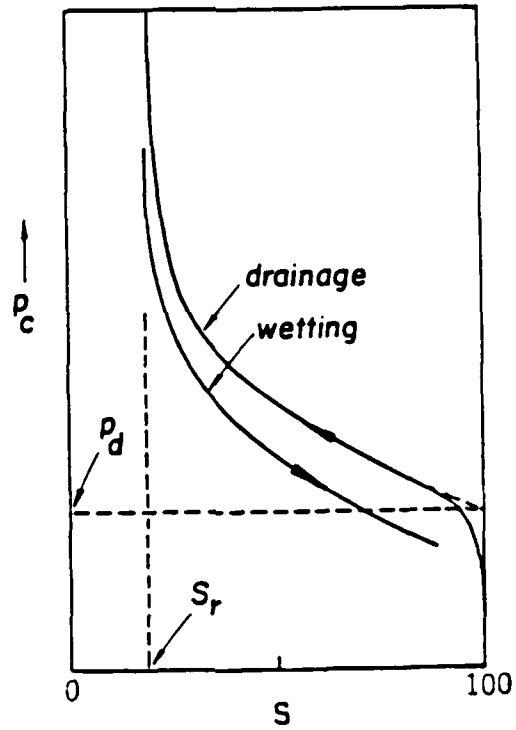


Figure 2.7 Capillary Pressure-Desaturation Curves (Corey, 1986)

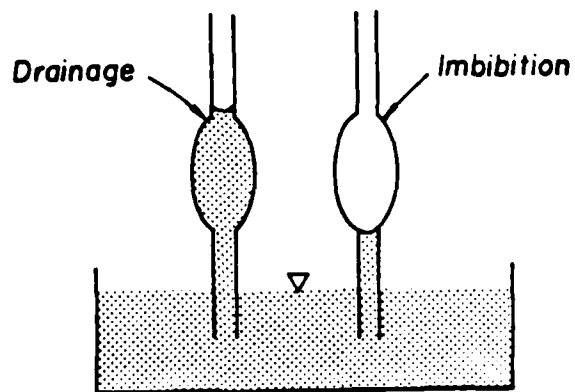


Figure 2.8 Drainage Versus Imbibition Schematic (Corey, 1986)

temperature. This saturation level is considered to be constant for large values of P_c . The value P_d shown in the same figure is called the displacement pressure of the soil. For values of $P_c < P_d$, the water is still saturated, which makes it within the zone of the "capillary fringe". Once the displacement pressure is reached, desaturation of the wetting cycle begins to occur.

The capillary pressure-desaturation curves can be determined by the use of a pressure plate apparatus (Klute, 1986). The apparatus applies positive air pressure to moist soil samples while the water within the samples remains at atmospheric pressure. The water within the samples is allowed to drain and come into equilibrium with the air pressure. The saturation level of the soil is then measured, and higher air pressures are applied to obtain points on the wetting curve as shown in Figure 2.7. Imbibition curves are generated by allowing water to flow into the soil samples which are initially under high air pressures. The air pressure is reduced successively for each point on the wetting curve.

As explained previously, under field conditions the pore air pressure is usually atmospheric, while the pore water pressure is negative (gage). With the pressure plate apparatus, the pore air pressure is positive while the pore water pressure remains atmospheric. In both cases, the capillary pressure ($u_a - u_w$) is constant. Therefore, the pressure-saturation relationship is the same in the field and when using the pressure plate, which is independent of the individual values of u_a and u_w . Because of this relationship,

large capillary pressures can be applied to soil samples in the laboratory.

2. Unsaturated Soil Mechanics

Bishop et al. (1960) presented an equation for the determination of the effective stress in an unsaturated soil based on Terzaghi's theory of effective stress for saturated soils. The equation takes the form:

$$\sigma' = (\sigma - u_a) + \chi (u_a - u_w) \quad (2.12)$$

where σ' is the effective stress, σ the total stress, u_a the air pressure, u_w the water pressure. χ is a parameter which is thought to depend mainly on saturation and to a lesser extent soil type, the cycle of wetting and drying, and stress change. For saturated conditions $\chi = 1$, while in dry conditions $\chi = 0$, which allows for transition to Terzaghi's effective stress equation.

Jennings and Burland (1962) have determined that the parameter χ varies with changes in saturation for various soil types. In fact, it has been shown that χ is unique for a specific soil, and that the value of χ may vary, depending on the saturation level of the soil. This, in effect shows that the principle for effective stress for unsaturated soils presented by Bishop et al. is not sufficient for determining the volume change and shear strength characteristics of unsaturated soil.

Based on the results obtained by Jennings and Burland (1962), Bishop and Blight (1963) have modified the theory by showing that

volume change and shear strength relationships of soil are not only based upon the effective stress, but also on the stress paths of the two components $(\sigma - u_a)$ and $(u_a - u_w)$.

Matyas and Radhakrishna (1968) have proposed that the relationship between soil properties (shear strength and volume change) may be related to the two stress parameters $(\sigma - u_a)$ and $(u_a - u_w)$ rather than trying to correlate them to a single value of effective stress.

Based on this proposal, Matyas and Radhakrishna have related void ratio and saturation directly to the two independent stress components $(\sigma - u_a)$ and $(u_a - u_w)$. From this, predictions can be made for changes in void ratio and saturation under field conditions.

In all of the theories for unsaturated soil mechanics discussed up to this point the soil is considered to consist of three independent phases, solid, liquid and gas. Fredlund and Morgenstern (1977) have proposed a fourth independent phase which is the air-water interface, or contractile skin. They have shown that the contractile skin has unique properties that cause it to behave more as a solid than a liquid. Based on this theory, they have presented a four phase system for unsaturated soil mechanics in which two of the phases come into equilibrium under applied stress (soil particles and contractile skin) and two phases which flow under applied stress (air and water).

Due to the creation of a four phase system, force equilibrium equations were developed for each phase of the unsaturated soil based on multiphase continuum mechanics. From this, one of the following

three normal stress variable combinations can be used to define the stress state of the unsaturated soil. The stress variables are:

$$(\sigma - u_a) \text{ and } (u_a - u_w)$$

$$(\sigma - u_w) \text{ and } (u_a - u_w)$$

$$(\sigma - u_a) \text{ and } (\sigma - u_w).$$

Fredlund (1979) recommends that the first combination be used because the effects of changes in total stress and pore pressure can be separated.

The stress variables $(\sigma - u_a)$ and $(u_a - u_w)$ yield a smooth transition from unsaturated to saturated conditions. As saturation approaches 100 percent, the pore air pressure approaches the pore water pressure. The capillary pressure $(u_a - u_w)$ then goes to zero and the pore air pressure term in the first variable becomes the pore water pressure.

Constitutive relationships for volume change and consolidation theory have been presented by Fredlund and Morgenstern (1976), Fredlund and Hasan (1979), Fredlund et al. (1980) and Fredlund (1986). Based on the constitutive relations for volume change presented by Fredlund and Morgenstern (1976), the constitutive equation for volumetric strain of the soil structure, ϵ_v , can be written:

$$\epsilon_v = C_t d(\sigma - u_a) + C_w d(u_a - u_w) \quad (2.13)$$

where C_t is the compressibility of the soil structure with respect to a change in $(\sigma - u_a)$, and C_w is the compressibility of the soil structure with respect to a change in $(u_a - u_w)$. In Figure 2.9 this

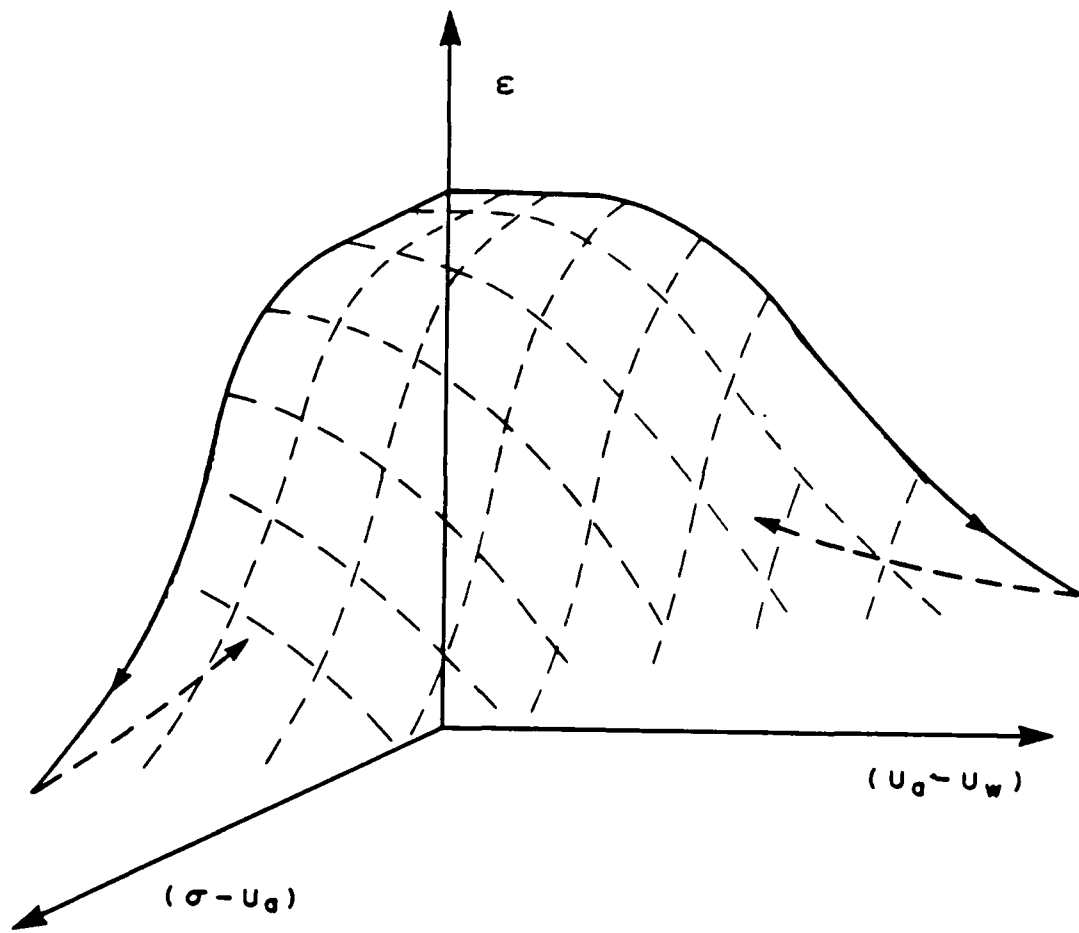


Figure 2.9 Stress State Variables Versus Strain (Fredlund, 1986)

relationship can be presented in a three dimensional plot of void ratio versus $(\sigma - u_a)$ and $(u_a - u_w)$.

The soil structure constitutive relationship is not sufficient to completely describe the state of the unsaturated soil. The stress history of the soil, and air or water constitutive relationships must also be evaluated (see Fredlund and Morgenstern, 1977).

D. COMPACTION OF UNSATURATED COHESIONLESS SOILS

Comparing wave propagation velocities obtained in this investigation with previously published results, it will be shown that the method of sample compaction is of considerable importance. A sample compacted moist will often give different results than a sample compacted dry, then saturated and desaturated to the same moisture content and dry density. These differences may be attributed to variations in lateral stress and fabric developed during the compaction process.

For cohesionless materials compacted by a dynamic compaction technique, the relationship between dry density and moisture content takes the form of Figure 2.10. Foster (1962) states that this type of compaction curve will occur when the material is permeable enough to impede the development of positive pore pressures during compaction. Lambe and Whitman (1969) attribute the low densities at lower water contents to bulking; a phenomena which occurs when the capillary forces of the soil resist particle rearrangement.

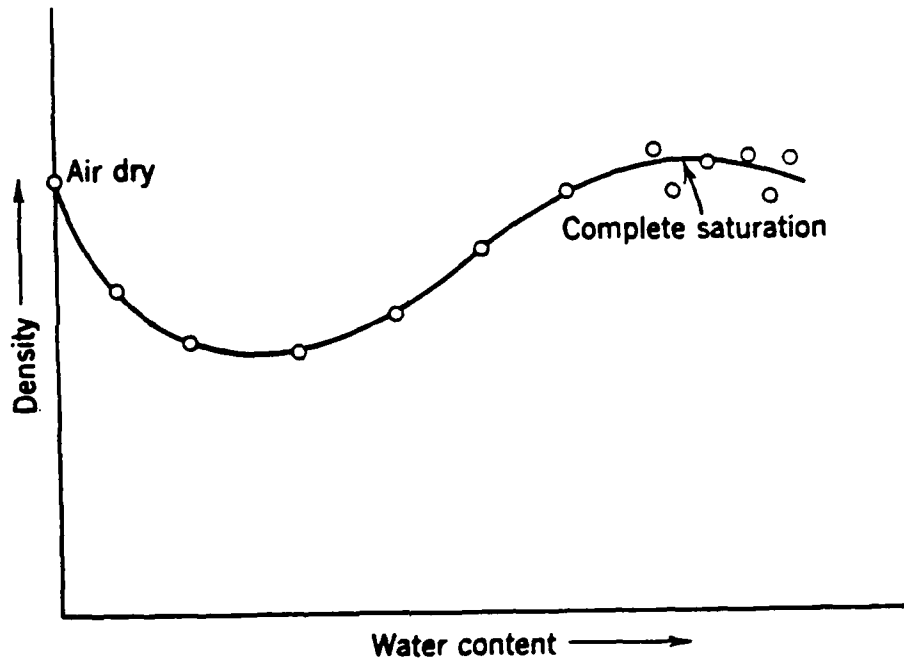


Figure 2.10 Compaction Curve for Cohesionless Soils (Foster, 1962)
"Constant Energy"

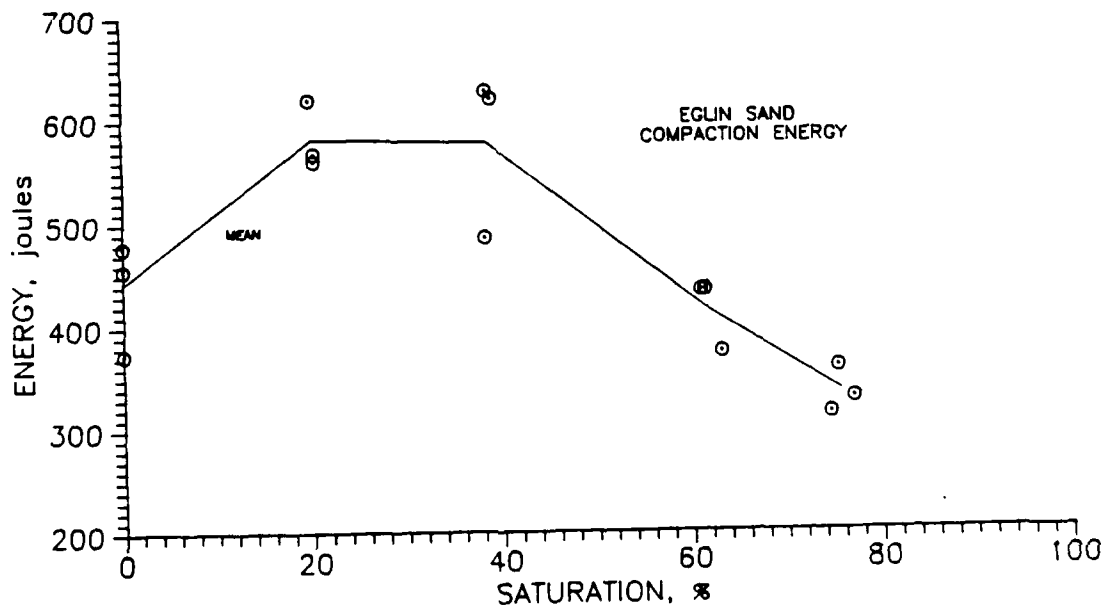


Figure 2.11 Compaction Energy Versus Saturation (Ross, 1989)
"Constant Dry Density"

In order to determine the relationships between saturation and compaction energy, Ross (1989) developed a compaction energy apparatus. Eglin sand was mixed at a particular moisture content and loosely placed within a sample container which did not permit lateral deformation. A 24.5 N hammer was dropped on the sample from a height of 30.5 cm. The number of hammer drops required to compact the sample to a dry density of 1760 kg/m^3 was recorded. Subsequent tests were performed on samples with different saturation levels. Figure 2.11 shows the relationship between saturation and the amount of energy required to compact Eglin sand to a constant dry density. The amount of energy required to compact the sand increases by approximately 22 percent, then decreases with any further increase in saturation. It appears that at intermediate saturation levels, the capillary stress between the sand particles increases the stiffness of the sand. As a result, more energy is required to break the capillary bonds and compact the sample.

Very little research has been performed in determining the influence of saturation on changes in lateral stress under conditions of cyclic loading. Such loading occurs in the dynamic compaction process. For dry sands, Lambe and Whitman (1969) have shown that under confined compression conditions, an increase in lateral stress occurs during cycles of loading and unloading. The vertical force applied to the soil causes the individual soil particles to compress and slide in the vertical direction. Upon unloading, the particles regain their original shape. This causes reverse sliding on the grain-grain contacts, causing the horizontal stress to increase. Youd

and Craven (1975) have shown that for dry 20-30 Ottawa sand, the amount of increase in lateral stress was greatest during the first cycle of loading and unloading, and diminished with each cycle thereafter. D'Appolonia et al. (1969) have shown that when a vibratory roller is used, the static horizontal stress was found to increase slightly with each roller pass. They also show that if two samples are prepared having the same dry density, but different values of K_0 (the ratio of horizontal to vertical stress under static conditions), the sample with the higher K_0 will be less compressible. They conclude that the compaction process is similar to preloading.

Drnevich et al. (1967) have shown that the effects of cyclic preloading on a dry 20-30 Ottawa sand specimen increases the shear modulus of the sample even if the sand density remains constant. Once the maximum increase in modulus occurs, any further prestraining begins to reduce the effects.

Hendron et al. (1969) measured the maximum horizontal and lateral stresses developed during their studies on the effects of saturation on soil compressability. For a sample of sandy silt compacted moist, the ratio of lateral stress to maximum axial stress (K_0) increases up to a particular intermediate saturation level, then decreases with a further increase in saturation. The results are for static loading, but it may be assumed that the trend also exists once the vertical load is removed.

Various investigators have shown that differences in fabric or pore size distributions result from sands being compacted by different techniques and moisture contents. Specifically, Mulilis et al. (1977)

have shown that various compaction techniques and water contents will affect the liquefaction potential of sands. Based on their tests using eleven different compaction techniques on dry and moist sand, they conclude that the differences in liquefaction potential are due to differences in the orientation of contacts between sand grains and the uniformity of packing.

Ladd (1977) performed cyclic triaxial strength tests on sands compacted by various methods and with different moisture contents. It has been found that the method of compaction of the sand is of secondary importance to the moisture content of the soil when explaining the differences in cyclic behavior that was observed. Ladd has hypothesized that sand specimens compacted moist tend to have a more random fabric than those prepared by dry methods because the capillary stress tended to impede particle movement. As a result, sands with a random fabric tend to have a greater stiffness than sands with more oriented fabric.

Juang and Holtz (1986) studied the pore size distributions of sandy soils compacted to a constant dry density but at different moisture contents. They have determined that as the moisture content increases to the optimum amount, the pore size goes from a condition of two dominant pore sizes to one dominant pore size. As a result of increasing the moisture content, the larger pore mode tends to decrease for the same compactive effort. As a result, the permeability of the soil compacted dry is higher than that compacted moist. Similar results were obtained by Nimmo and Akstin (1988), who concluded that compaction primarily affects the large pore mode, while leaving the small pore mode relatively unchanged.

E. COMPRESSIBILITY AND WAVE PROPAGATION THROUGH CONFINED SOILS

1. Compressibility

a. Dry Sands

From elasticity theory, a relationship was derived which links the propagation velocity of a wave to the stiffness of the soil. For a compressional wave the relationship is as follows:

$$v_c = \left\{ \frac{D}{\rho} \right\}^{0.5} \quad (2.3).$$

This equation, derived from elastic theory, is only true within the elastic limits of the material. For conditions where the stress applied is outside of the material's elastic range, equation 2.3 is only approximately correct. Whitman et al. (1960) state that one of the differences between the propagation of a wave through soils and through an ideal elastic medium is that the soil is an assemblage of discrete particles.

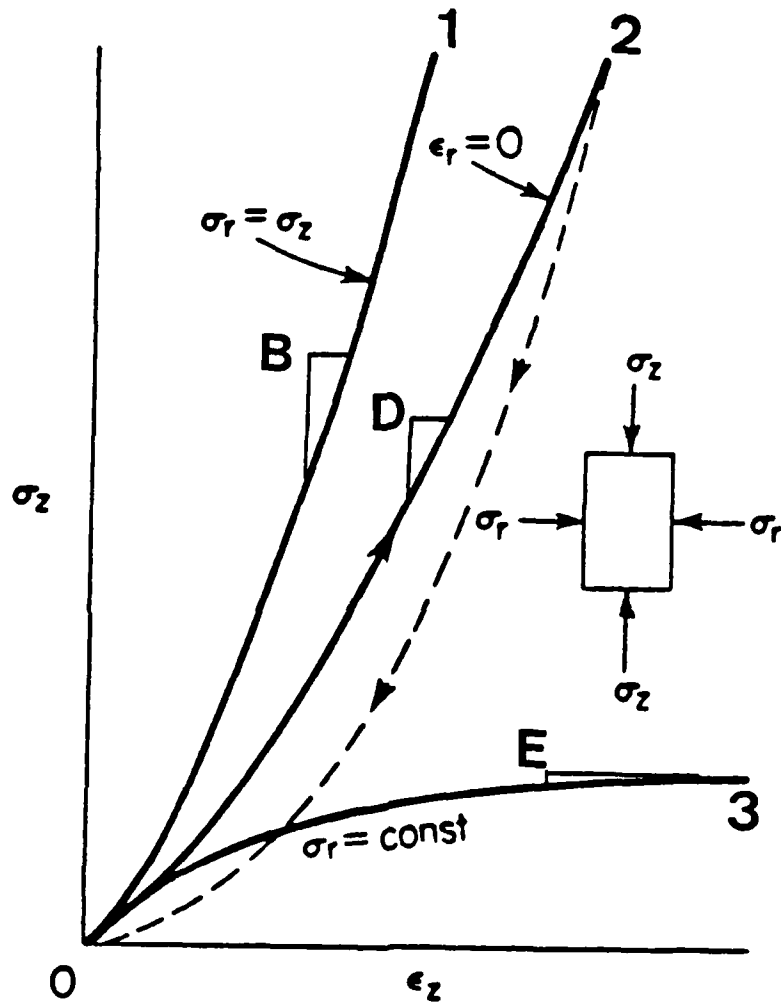
If the mineral skeleton is observed at a microscopic level it can be seen that when a soil is loaded, the stress is transmitted across the small particle contacts. Because these contacts gain their strength from cementation, friction or capillarity, they are weak in compression when compared to a material such as steel. As a result it takes very little energy to break these bonds and cause compression or strain. Whitman et al. (1960) states that the deformation of the soil mass is brought about largely by distortion of the points of contact between the particles. The resistance of a soil mass to deformation

is determined largely by the distortion resistance of these contact points.

Under all loading conditions, the soil will rearrange its structure elastically and plastically to come into equilibrium with the applied load. If the applied load is small, the majority of the structure will deform in an elastic manner. Once the load is removed only a small portion of the deformation will be irreversible (linear stress-strain behavior). Once the loading becomes larger than the elastic limit of the soil, the particles will permanently rearrange themselves in order to equilibrate with the applied load (nonlinear stress-strain behavior).

The shape of the stress-strain curve which exhibits nonlinear behavior is a function of the boundary conditions imposed on the soil. Richart et al. (1970) explain that curve 1 in Figure 2.12 is created when the lateral strain is equal to the vertical strain under hydrostatic loading. Curve 2 represents the behavior of "strain hardening" which occurs when the lateral strain is equal to zero. For the condition where there is no restriction on the amount of lateral strain, a curve such as 3 is developed.

Whitman et al. (1964) have hypothesized that under conditions of zero lateral strain (confined compression) the stress-strain curve is s-shaped. When the load is initially applied the grains undergo elastic deformations. As the stress is increased the contact points between particles slip, causing displacement of the grains. This results in a decrease in modulus. Slippage causes the grains to roll past one another into a more compact, dense condition. As the particles move into the more compact condition, the modulus increases.



1. Isotropic Compression
2. Confined Compression
3. Triaxial Compression ($\sigma_2 = \sigma_2 = \sigma_r$)

Figure 2.12 Theoretical Stress-Strain Curves for Different Lateral Confinement (Richart et al., 1970)

Once the stress is large enough to cause grain crushing, the modulus decreases until a more compact particle arrangement is formed.

Hendron (1963) performed one-dimensional compression tests on four different sands utilizing a high pressure one-dimensional compression apparatus. This compression device imposes stresses of up to 22,100 kPa to the soil samples. All tests were performed on dry sands under very low loading rates. The test results show that as the stress is increased, the shape of the stress-strain curves behave similarly to that found by Whitman et al (1964). He notes that significant grain crushing did not occur below stresses of 20,700 kPa. Hendron has also found that for the sands tested, the constrained modulus is proportional to the vertical applied stress to the one third power.

b. Unsaturated Sands

Under unsaturated conditions the behavior of the soil is much more complicated than the dry or fully saturated conditions. For small stress changes the compressibility of the soil is governed by the mineral skeleton. At larger values of stress, the strain will be large enough to cause the soil to saturate, which will reduce the soils compressibility considerably.

Hendron et al. (1969) performed high pressure (0 to 138,000 kPa) static, one-dimensional compression tests on samples of sandy silt. Samples were computed moist to various dry densities in consolidation rings by use of a Harvard miniature type compactor. Figure 2.13 shows the results obtained . The figure indicates that at

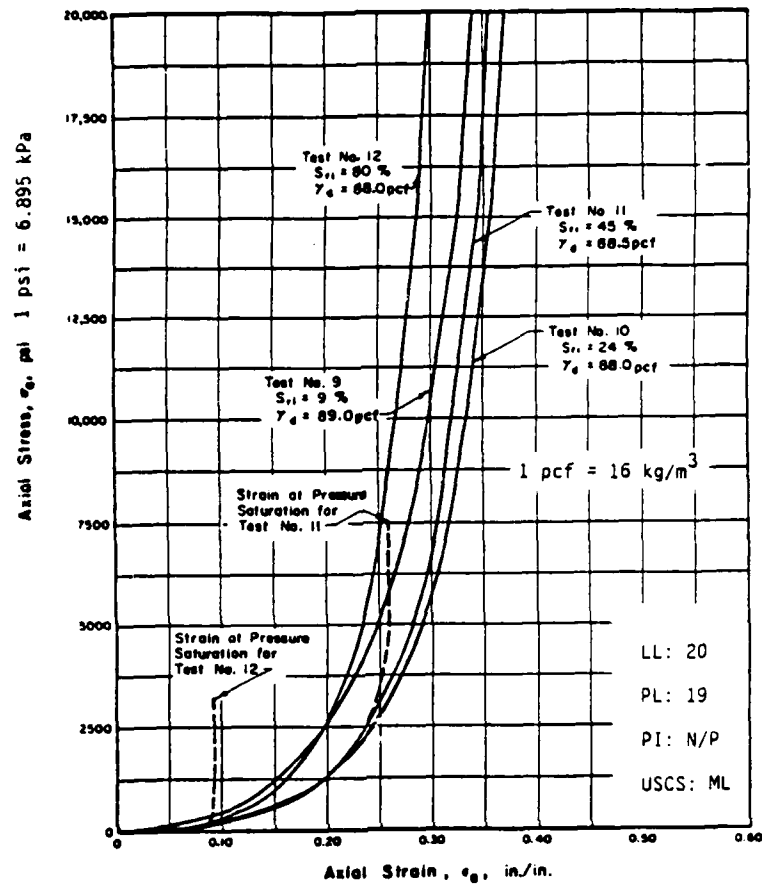


Figure 2.13 Stress-Strain Curves For Sandy Silty at Various Saturation Levels (Hendron, et al., 1969)

- Spheres $\frac{1}{8} \pm 10 \times 10^{-6}$ in. diameter
- △ Spheres $\frac{1}{8} \pm 50 \times 10^{-6}$ in. diameter

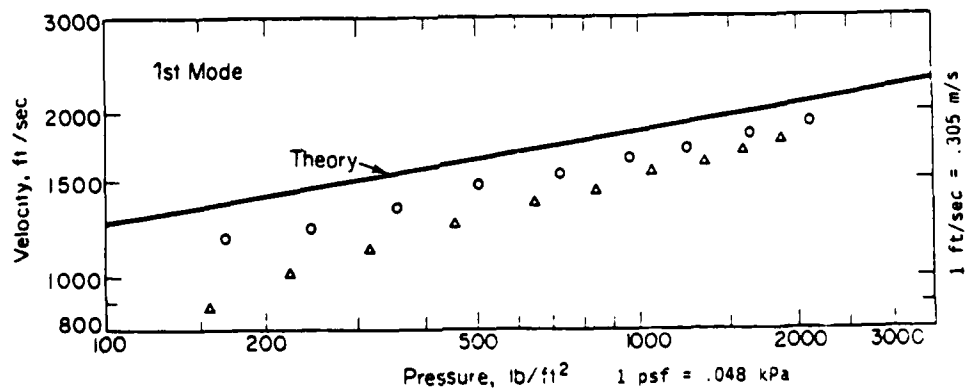


Figure 2.14 Variation of Compression Wave Velocity with Confining Stress for Steel Spheres (Duffy and Mindlin, 1957)

lower stress levels the more saturated samples are more compressible. As the stress level increases the wetter samples reach full saturation before dryer samples. As a result the increase in stiffness due to saturation occurs at lower stress levels for wetter samples. Based on the test results, it has been concluded by the authors that the most important variables governing one-dimensional stress-strain relations are void ratio and saturation level.

Based on their experimental results, Hendron et al. (1969) present an equation for the determination of the secant constrained modulus for stress levels above 21,000 kPa. The equation is valid for unsaturated soils which are either remolded or undisturbed, as the results of their analysis show that the modulus will be the same for stresses over 21,000 kPa.

Balakrishna Rao (1975) has attempted to develop a method for predicting stress-strain curves for a given soil under varying degrees of saturation. An oedometer was used for the testing which allowed for stresses ranging from zero to 4800 kPa, and loading rates from 3 to 30 milliseconds. Two sands were tested, a 20-30 Ottawa sand and concrete sand, which were compacted moist to a constant dry density of 1680 kg/m^3 to obtain a particular saturation level. The method of compaction used was not given in the report. Balakrishna Rao has concluded that for saturation levels between zero and 60 percent, the water has little influence on the stress-strain relationships for either sand studied.

c. Loading Rate Affects

Whitman (1970) concluded that time dependent effects on the value of constrained modulus can be ignored for dry granular soils subjected to loadings having millisecond or larger rise times. It is noted that time effects may become important when the duration of the stress pulse is below approximately one millisecond, but further research is required to verify the findings.

Jackson et al. (1980) performed tests on three dry sands under dynamic loadings. The loading rate does not effect the value of constrained modulus for rise times above 1 millisecond. For rise times between 0.1 and 1 millisecond, the constrained modulus increases by an order of magnitude. No theory has been developed to why this effect occurs.

2. Wave Propagation

Various studies have been performed to determine the relationship between stress wave propagation and soil parameters including void ratio, confining stress, soil type, grain shape, grain size distribution, saturation and soil type. Most of the research has been performed on dry or saturated soils, while little has been done in the area of compressive wave propagation through unsaturated soils.

a. Low Intensity Waves

.. . .

Duffy and Mindlin (1957) proposed one of the earliest theories relating the stress wave velocity with stress-strain properties of a dry granular medium has been proposed by Duffy and Midlin (1957). Their theory is based on the elastic properties of a face-centered cubic array of spheres and the theory of elastic bodies in contact (including normal and tangential forces). From the theory of the elastic behavior of spheres in contact, the longitudinal (and bulk) modulus vary with confining stress to the one-third power. From the relationship between wave velocity and modulus (equation 2.1) they anticipated that the wave velocity would vary with confining stress to the one-sixth power.

A portion of the experimental results obtained are shown in Figure 2.14. Wave velocities predicted by the theory are higher than those resulting from experimentation, though the differences decrease as the confining stress is increased.

Whitman, Roberts and Mao (1960) analyzed soniscope tests (used for field esting of concrete by a pulsing technique) performed by Martin (1957) on Vicksburg loess to study the effects of moisture content on sonic propagation velocity. Figure 2.15 presents the results obtained by Martin for the relationship between dry density and compressional wave velocity, with water content for various compaction energies. Whitman et al. (1960) observed from Figure 2.15 that the wave velocity drops as the molding water content is increased above the optimum level. Since a soil can have the same dry density above and below the optimum moisture content, they conclude that other

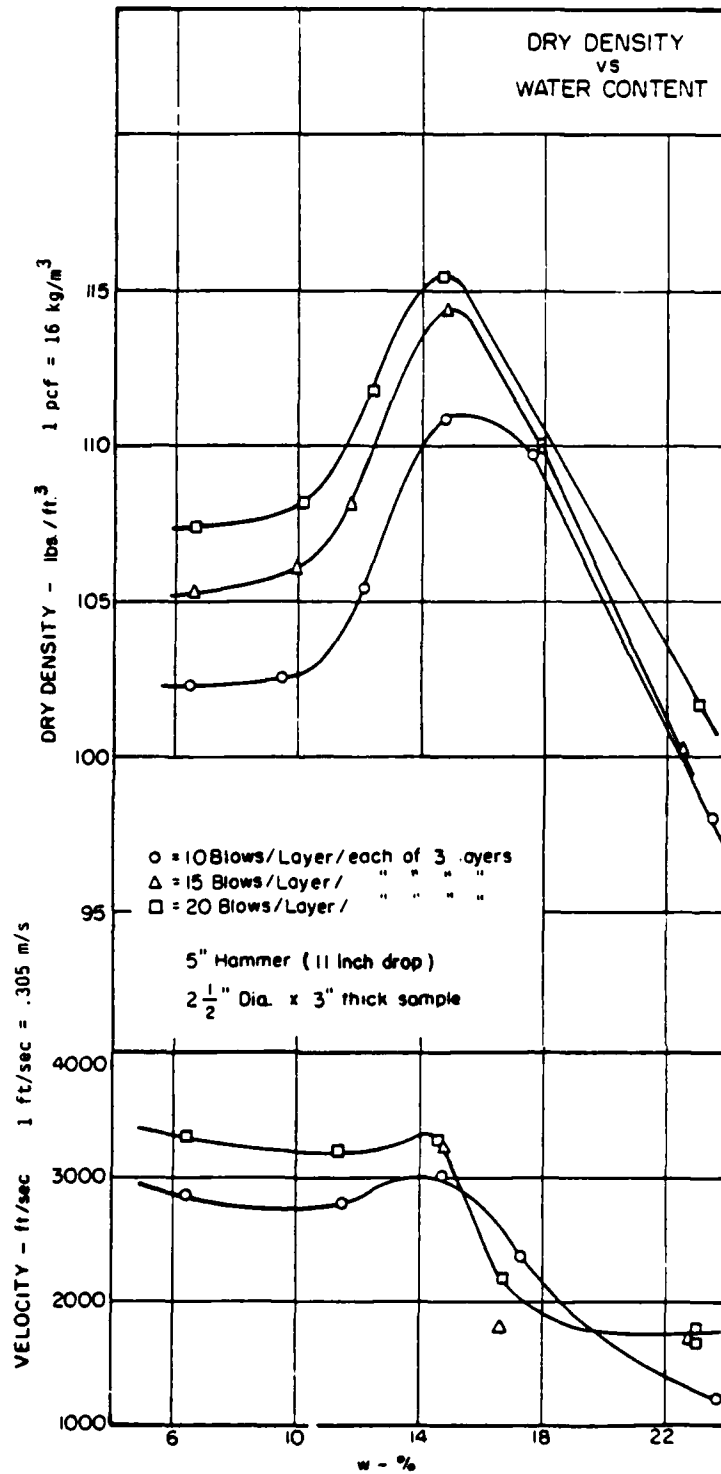


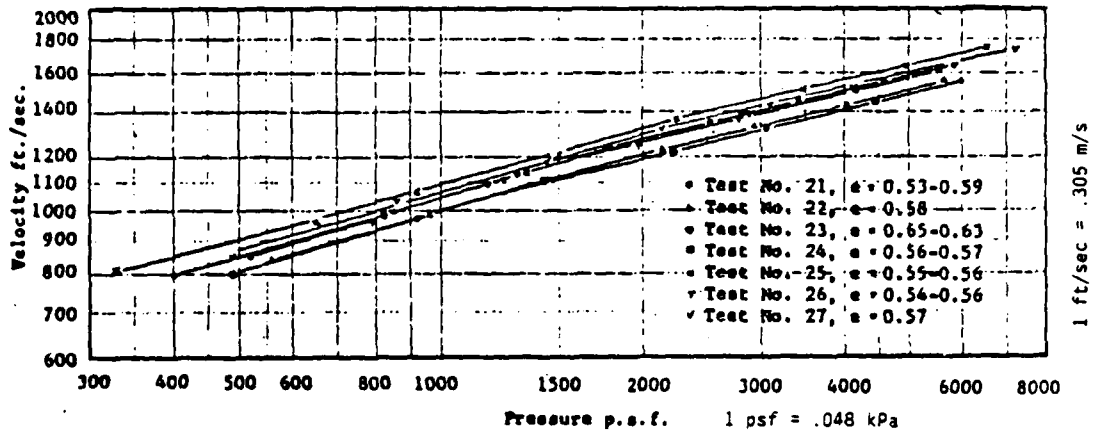
Figure 2.15 Variation of Dry Density with Compactive Effort and Moisture Content for Vicksburg Loess (Martin, 1957)

factors than dry density must affect the wave velocity. No explanation is given as to what the effect is.

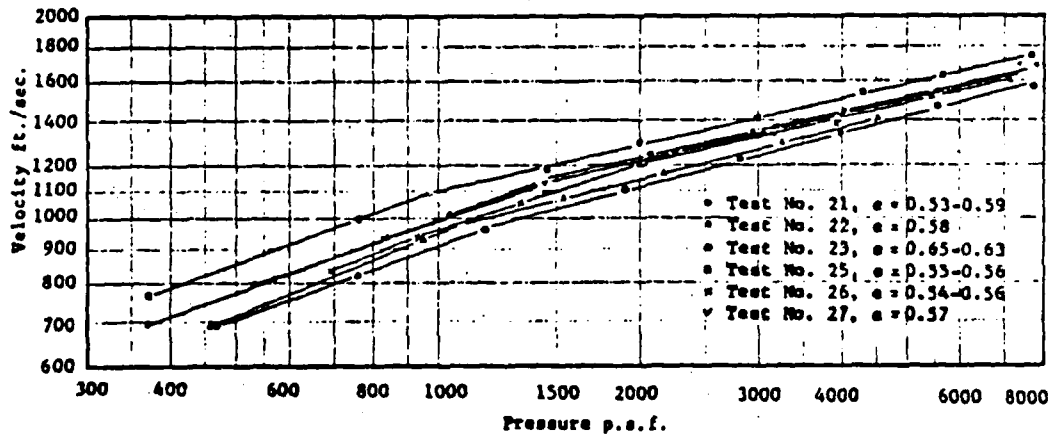
Hardin (1961) utilized an early resonant column device to determine the relationship between elastic compressional and shear wave velocities, with confining stress, void ratio and sand type for dry, saturated and drained samples. The drained samples had an average moisture content of 1.4 percent. Hardin has found that as the confining stress is increased, the wave velocity increases, and as the void ratio is increased, the wave velocity generally decreases. Some of the results for dry Ottawa sand are presented in Figure 2.16. The wave velocity through the saturated samples was generally less than either the drained or dry samples. He attributed this to the drag of the water in the pore spaces, though it should be noted that from equation 2.3, the increase in density of a saturated specimen will also reduce the wave velocity.

Based on all of the experimental results, Hardin concluded that for dry, saturated or drained specimens under a confining stress of between 13,800 and 55,200 kPa, an exponent of $1/4$ should be applied to the confining stress when relating it to wave velocity. For a confining stress below 13,800 kPa, the exponent varies between $1/2$ and $1/4$ depending on moisture content and grain angularity.

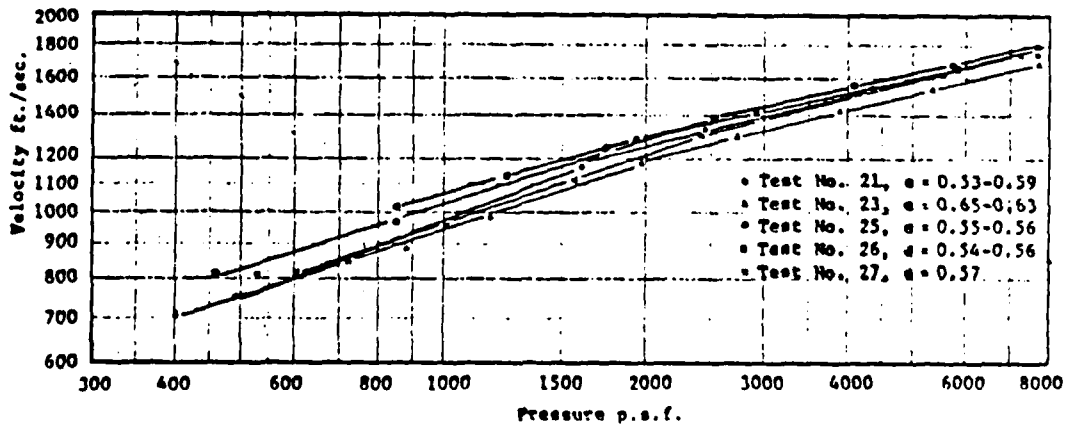
Whitman (1970) theorizes that at high saturation levels, the pore phase of a soil is much less compressible than the mineral skeleton. This allows the compression wave to travel primarily through the pore phase. At lower saturation levels, the mineral



a. Dry



b. Saturated



c. Moist

Figure 2.16 Variations of Wave Velocity with Confining Stress
a. Dry, b. Saturated, c. Moist (Hardin, 1961)

skeleton is less compressible than the pore phase, allowing the majority of the wave to travel through the skeleton.

Whitman (1970) presents a mathematical model which relates saturation to wave velocity through the equation:

$$v_c = \left\{ \frac{\frac{u'_a}{n(1-S)} + D_s}{((1-n)G_s + S n)\rho_w} \right\}^{1/2} \quad (2.14)$$

where u'_a is the absolute air pressure, n is the porosity, S the saturation level, D_s the constrained modulus of the mineral skeleton and G_s the specific gravity. This relationship is based on a modified rule of mixtures. When the saturation approaches 100 percent, the wave velocity increases dramatically. Whitman states that on the basis of this model, the threshold value of saturation is unity. For any value of saturation less than 100 percent, the compressional wave velocity is controlled by the mineral skeleton.

A model has been presented by Anderson and Hampton (1980) for determining the sound velocity in a gassy sediment. The model is based on the acoustical properties of the gassy sediment and an equation for simple mixtures. The equation takes the form:

$$v_c = \left\{ \frac{K}{\rho} \right\}^{0.5} \quad (2.15).$$

K is the aggregate bulk modulus which is based on a parallel spring assumption for the contributions of stiffness due to the soil solids, water and air. The soil density, ρ , is based on a modified rule of mixtures which is an extension of the equation presented by Wood (1930). Richart et al. (1970) presents a similar model for estimating the compression wave velocity in an unsaturated soil.

b. High Intensity Waves

Stoll and Ebeido (1965) have performed shock wave propagation tests on dry 20-30 Ottawa sand under conditions of limited radial strain. An input pressure pulse of 552 kPa and a rise time of 20 microseconds was used under a confining vacuum which varied from 5.8 to 95.8 kPa. The results obtained are shown in Figure 2.17. Also plotted are results obtained by Hardin (1961). The tests performed at high amplitudes and loading rates (Stoll and Ebeido) result in higher wave velocities than obtained under elastic conditions (Hardin, 1961). Because the samples were laterally confined in this analysis, the stress-strain curve is concave to the stress axis. As the applied stress increases, the modulus increases under this condition. As a result, equation 2.3 would predict that the wave velocities should be higher under this condition than when soils are tested under elastic conditions, or when there is no lateral confining stress. Stoll and Ebeido also show that as the rise time decreases, the wave velocity increases. This would indicate that the rate of loading changes the modulus.

Ross et al. (1988) have utilized a split-Hopkinson pressure bar to test the effects of varying moisture content on wave velocity and stress transmission for four different sands. All tests have been performed under confined compression conditions, with an incident stress of 177 kPa and a rise time of 15 microseconds. All sand samples were mixed with a particular amount of water then compacted moist to a constant dry density. Figures 2.18 through 2.21 show the results obtained by Ross et al. for the 20-30 Ottawa and Eglin sands.

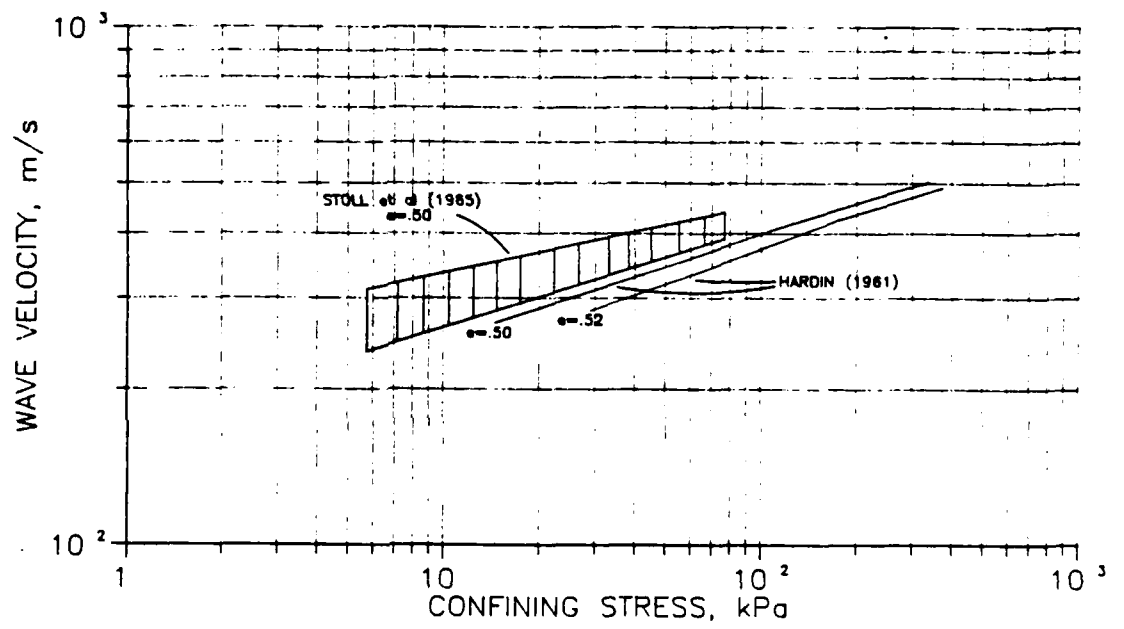


Figure 2.17 Variations of Wave Velocity with Confining Stress (Hardin, 1961; Stoll and Ebeido, 1965)

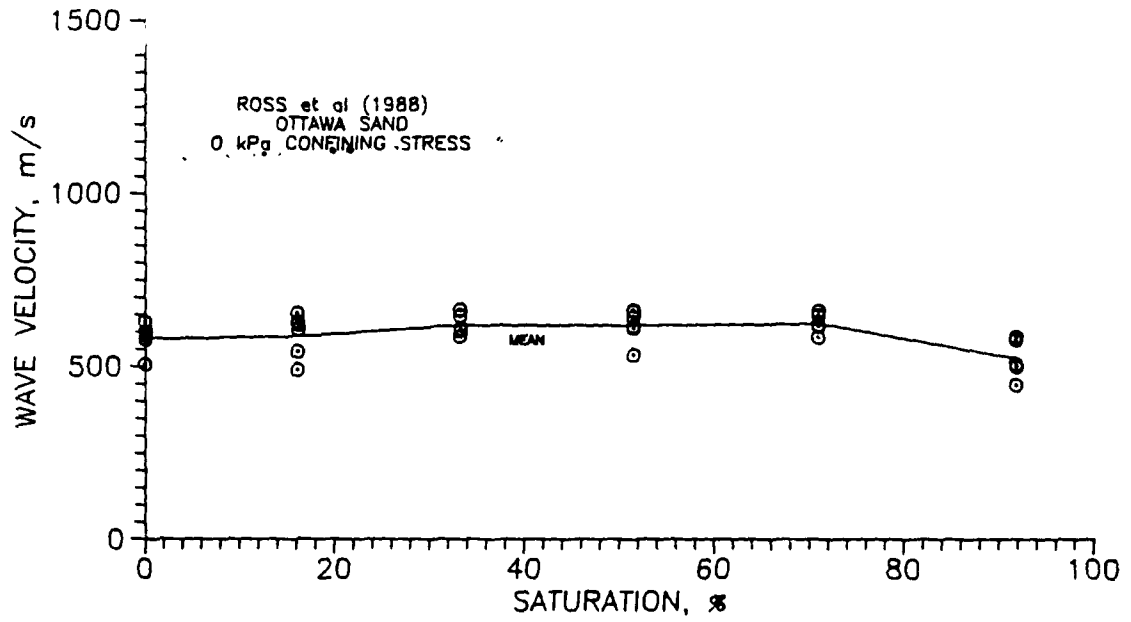


Figure 2.18 Wave Velocity Versus Saturation for 20-30 Ottawa Sand (Ross et al., 1988)

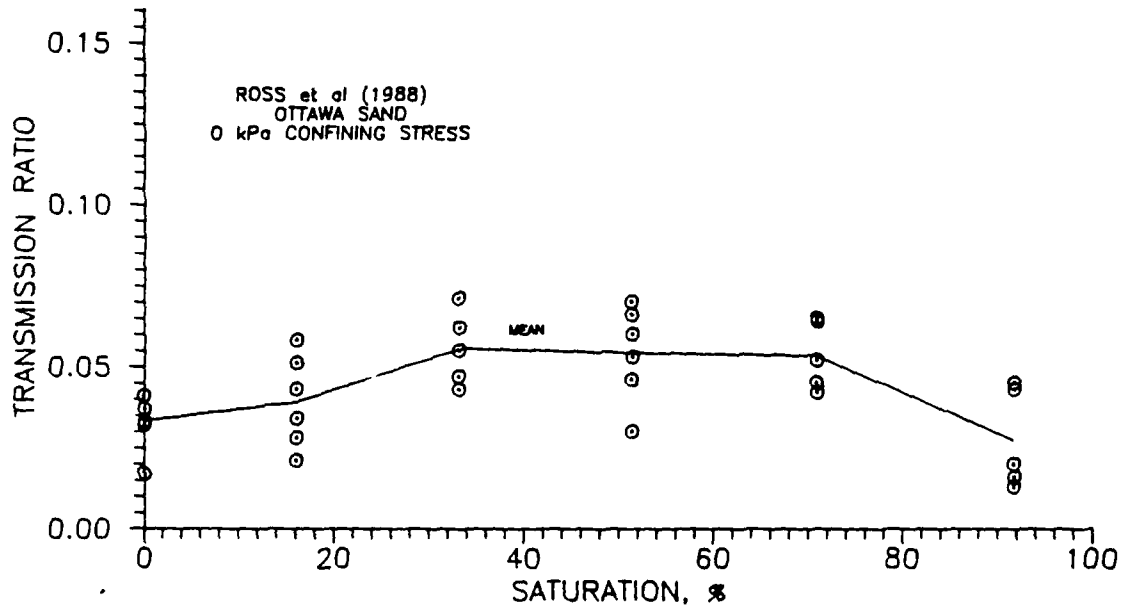


Figure 2.19 Transmission Ratio Versus Saturation for 20-30 Ottawa Sand (Ross et al., 1988)

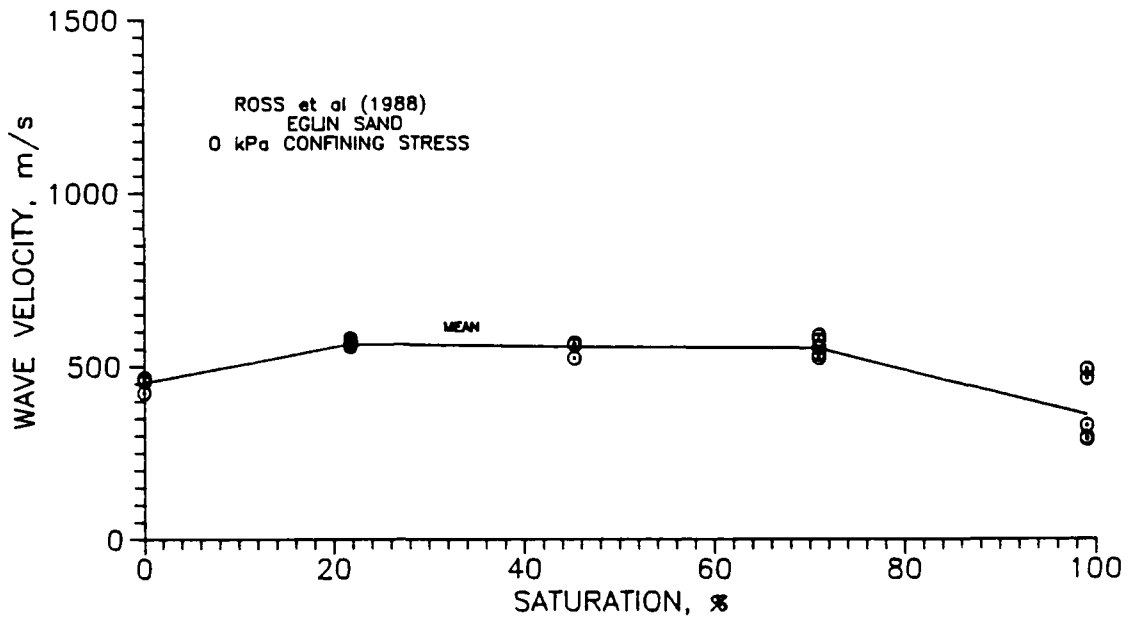


Figure 2.20 Wave Velocity Versus Saturation for Eglin Sand (Ross et al., 1988)

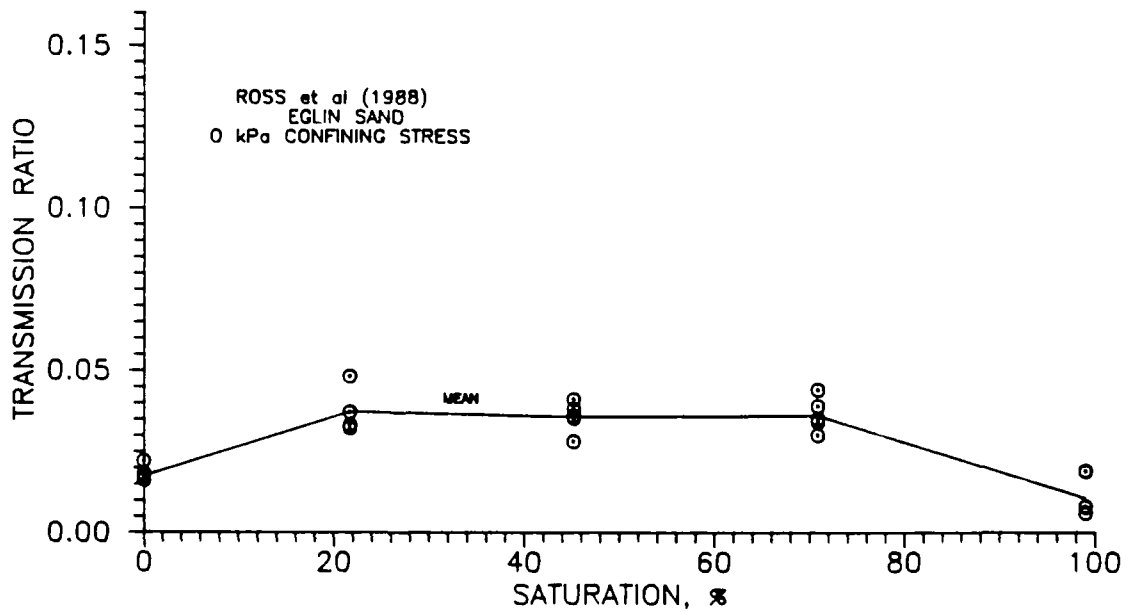


Figure 2.21 Transmission Ratio Versus Saturation for Eglin Sand (Ross et al., 1988)

The wave velocity and stress transmission values increase as the saturation level increases from 0 to approximately 40 percent, then decrease with any further increases in saturation. Quasi-static stiffness tests show similar results as shown in Figure 2.22.

The authors show that the trends obtained may be explained by the effects that saturation and capillary stress have on effective stress. In order to quantify this relationship, they utilize equation 2.12 and assume that the parameter χ is equivalent to the saturation level of the sand. The increase in effective stress due to saturation is presented in Figures 2.23 and 2.24 for both the Eglin and Ottawa sands. These figures show similar trends to those for wave velocity, stress transmission and stiffness, though the magnitudes of the increase in effective stress due to capillarity are small.

Ross et al. (1988) concluded that the increase in effective stress can be attributed to the effects of capillarity. But, the increase in stress transmission ratio at intermediate saturations is approximately two to three times the dry or near saturated values, while the increase in effective stress due to capillarity is very small. As a result of the small increase in effective stress due to capillarity, the effective stress equation by Bishop et al. (1960) may not be adequate to explain the trends observed. They also state that the energy required to compact the specimens may affect the results.

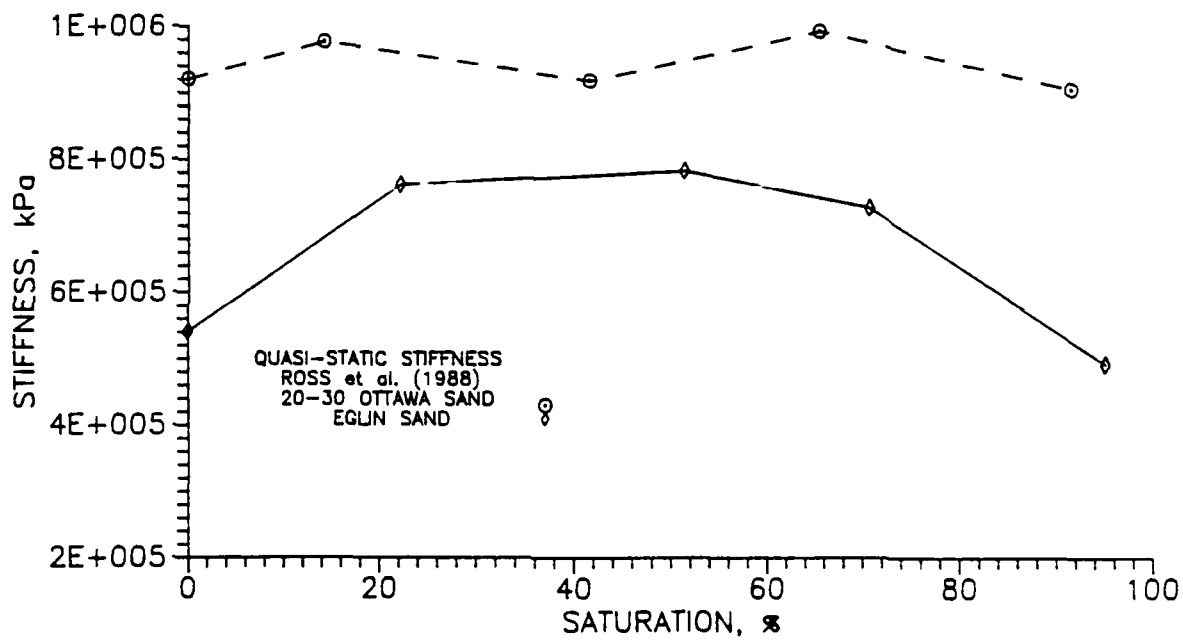


Figure 2.22 Quasi-Static Stiffness Results for 20-30 Ottawa and Eglin Sands (Ross et al., 1988)

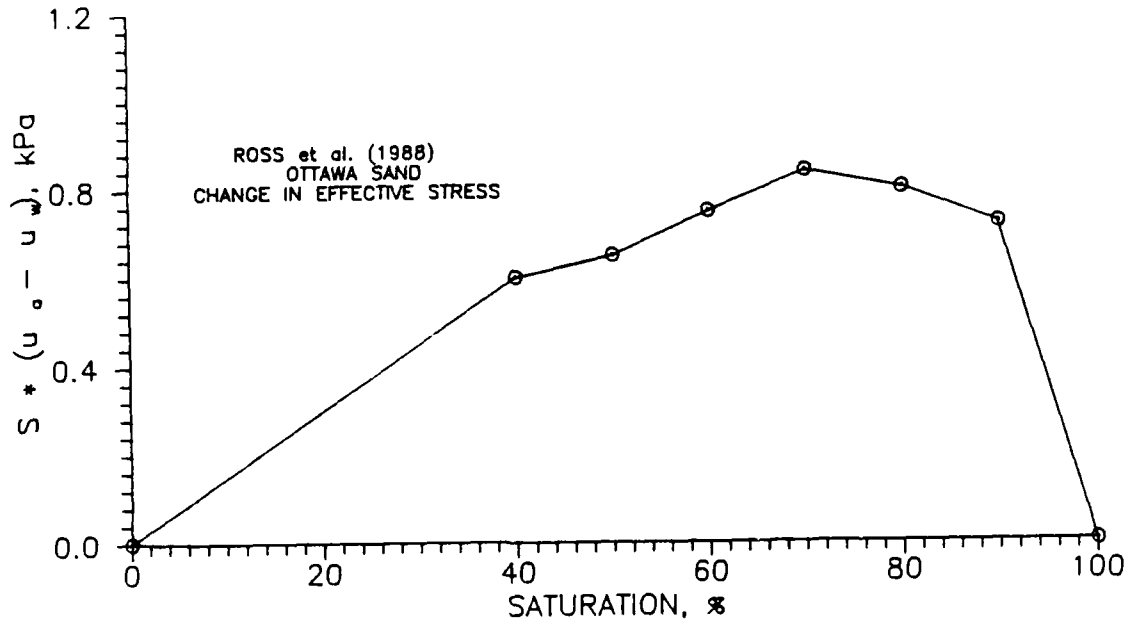


Figure 2.23 Increase in Effective Stress Due To Capillarity for 20-30 Ottawa sand (Ross et al., 1988)

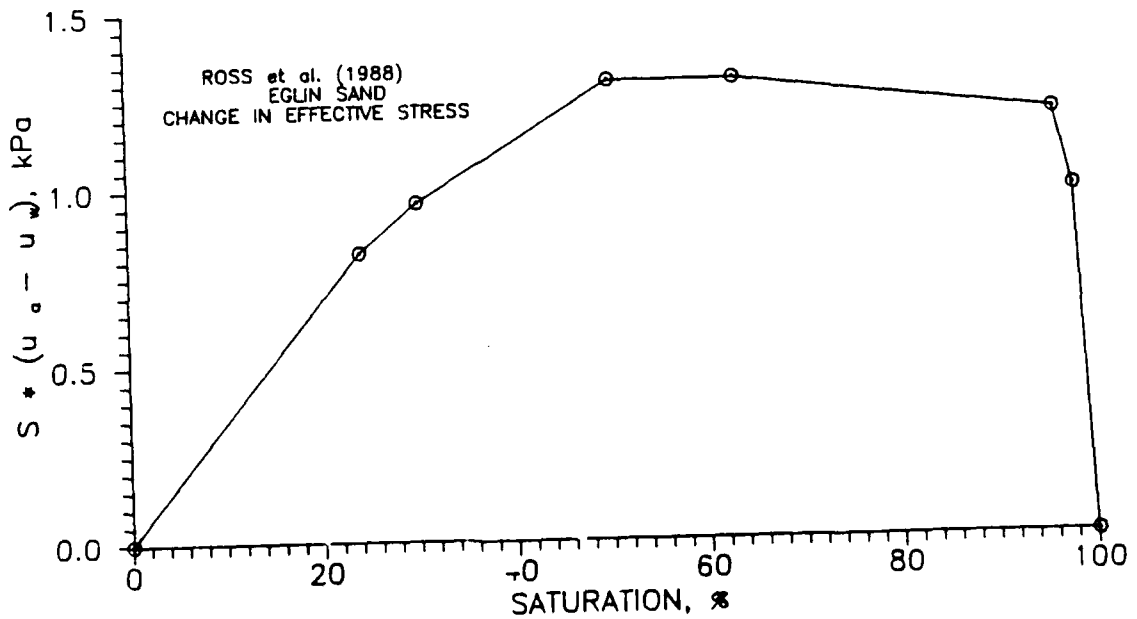


Figure 2.24 Increase in Effective Stress Due to Capillarity for Eglin Sand (Ross et al., 1988)

3. Comparisons between Compressibility and Wave Velocity

Moore (1963) performed static and dynamic one-dimensional compression tests and compressive wave propagation tests on dry Monterey sand to determine the relationship between the experimental constrained modulus and that determined from the wave propagation velocity through equation 2.3. A resonant column device which has the ability to confine the specimens laterally was used to determine the wave velocities. The confining stress magnitudes were varied between 103 and 2069 kPa, and the soil was compacted to a dry density of 1600 kg/m³. Dynamic compression tests were performed utilizing several different devices.

An example of the results obtained are shown in Figure 2.25. The wave propagation velocity values have been corrected for dispersion that was shown to occur during testing. Moore has concluded that in general the static and dynamic moduli are the same as the modulus based on wave velocity at low and high stress levels, while they diverge at intermediate levels. A considerable amount of scatter occurred in the data which could be a result of stress history effects or experimental error.

Calhoun and Kraft (1966) performed high stress (5,500 kPa) laterally confined compression tests on unsaturated silt in order to develop a mathematical model to determine the compressive wave velocity and attenuation based on the stress-strain relationships determined at high stresses. The model developed is based on a model by Weidlinger and Matthews (1964) which defines one-dimensional shock

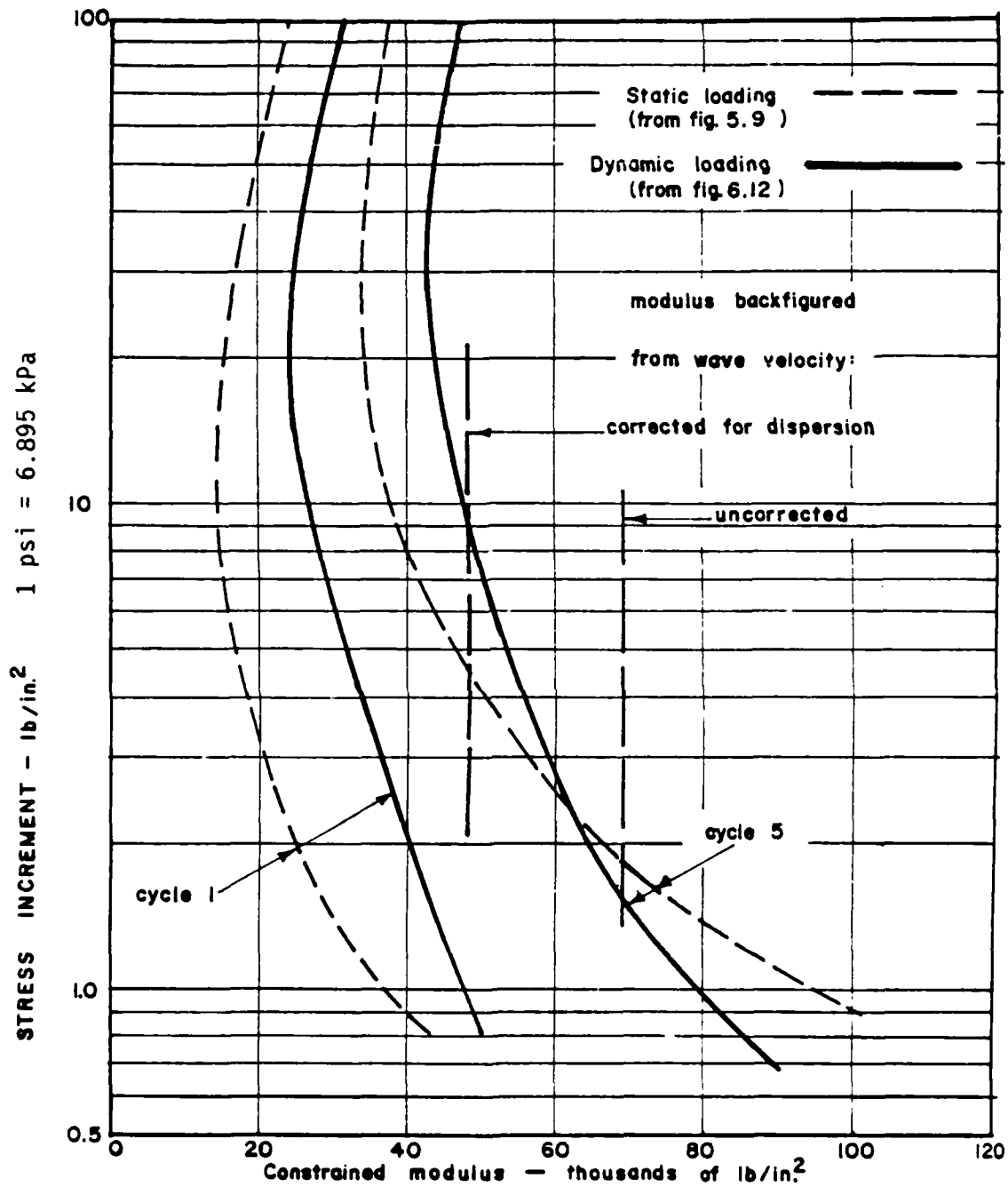


Figure 2.25 Variations of Wave Velocity with Confining Stress for Monterey Sand Due to Static, Dynamic and Wave Propagation Methods (Moore, 1963)

wave phenomena in a nonlinear, locking medium. Combining this model with the equation for momentum and a governing shock equation, equations for predicting stress wave propagation and attenuation with depth have been developed. From these equations, Calhoun and Kraft found that wave propagation and attenuation are functions of only the initial static surcharge (confining stress) when the soil saturation is below 90 percent. Above 90 percent, the increase in modulus due to water becomes important. The results are based on silt samples which were compacted moist by use of a Harvard miniature compactor prior to confined compression testing.

F. ADDITIONAL USEFUL UNSATURATED SOIL RESEARCH

Wu et al. (1984) have performed resonant column tests on fine grained cohesionless soils to determine the influence of saturation on shear modulus. The relationship between wave velocity and shear modulus is similar to equations 2.1 through 2.3. Samples were compacted moist in a standard mold (3.6 cm in diameter and 8 cm high), and confining stresses were varied from 25 to 98 kPa.

The gradations of the soils tested are shown in Figure 2.26, and an example of the variation in shear modulus with saturation and confining stress is shown in Figure 2.27. A trend is developed with changes in saturation which is similar to that obtained by Ross et al. (1988). The maximum values of shear modulus for each soil type and confining stress used are shown in Table 2.1. It should also be noted that as the confining stress is increased, the wave velocity

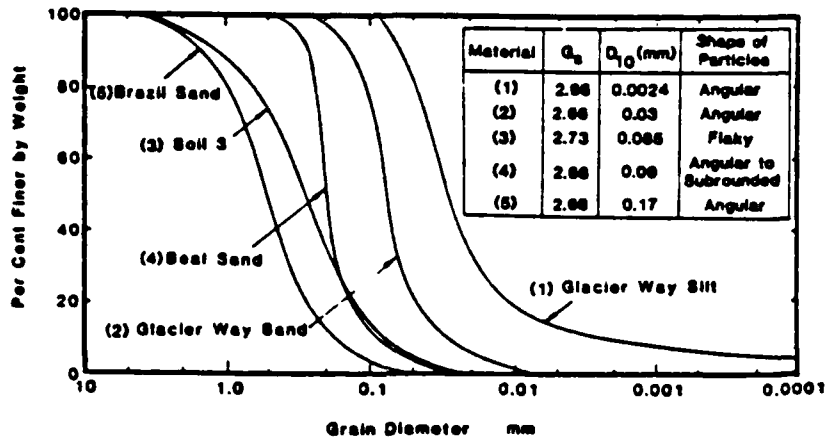


Figure 2.26 Gradations for Soil Types Used by Wu et al., (1984)

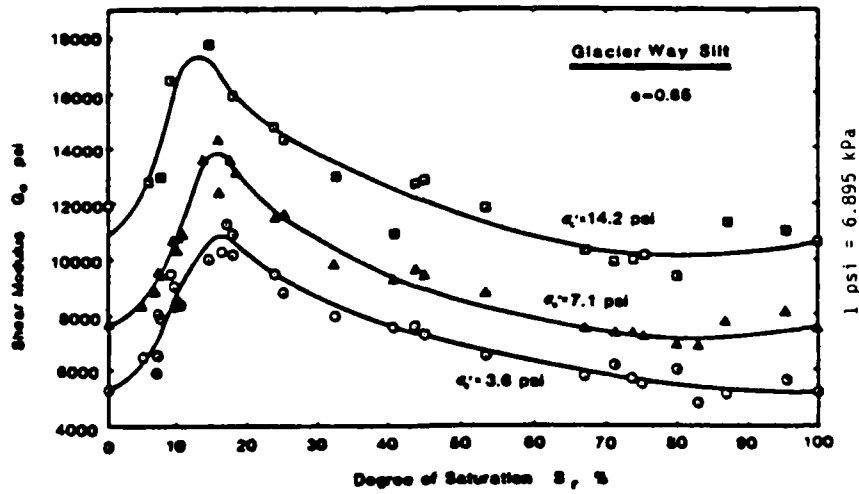


Figure 2.27 Variations of Shear Modulus with Saturation Under Several Confining Stresses for Glacier Way Silt (Wu et al., 1984)

Table 2.1 Maximum Variation in Shear Modulus with Changes in Saturation and Confining Stress (Wu et al., 1984)

Material tested (1)	G_s (G_s in the moist condition) ^a			$(S_s)_{opt.}$, as a percentage (5)
	$G_{s(dry)}$ (G_s in the dry condition)			
	$\sigma'_c = 3.6$ psi (2)	$\sigma'_c = 7.1$ psi (3)	$\sigma'_c = 14.1$ psi (4)	
Glacier Way Silt	2.05	1.78	1.66	17.5
Glacier Way Sand	1.62	1.44	1.37	10.0
Soil 3	1.84	1.65	1.56	9.0
Beal Sand	1.54	1.38	1.34	7.5
Brazil Sand	1.27	1.13	—	5.0

^aHerein the ratio of $G_s/G_{s(dry)}$ is specifically denoted as the *maximum* value of the ratio and $(S_s)_{opt.}$ is the optimum degree of saturation corresponding to this maximum value.

increases, but the trend obtained for the variations in shear modulus with saturation becomes less distinct.

In order to assess the influence of capillarity on the shear modulus, the effective stress equation 2.12 has been utilized by Wu et al. The results obtained are similar to those presented by Ross et al. (1988). Wu et al. found that the capillary influence is greatest in soils having a small effective grain diameter, d_{10} , and a low confining stress. An empirical relationship has also been presented relating shear modulus at any moisture content to the saturation level and dry shear modulus.

Hryciw and Dowding (1987) completed a laboratory study of the effects of saturation on cone penetration resistance. Samples were prepared at different saturation levels through a unique procedure. Samples were saturated, then vibrated to a particular relative density. Under pressure, carbon dioxide was then allowed to enter the

system. Once completed, the pressure was slowly reduced to allow the dissolved carbon dioxide to come out of solution. The amount of displaced water could then be measured to determine the degree of saturation. The results obtained are very similar to those presented by Wu et al. (1984) and Ross et al. (1988).

G. SUMMARY OF PREVIOUS RESEARCH

Literature pertinent to this investigation has been reviewed in this chapter. The sections on capillarity, unsaturated soil mechanics, compressibility, and wave propagation properties of unsaturated sands have shown that there has been little research performed in determining high intensity stress wave propagation parameters for unsaturated soils. The section on the effects of compaction procedures has shown that while there are documented cases of compaction effects on values of liquefaction potential, cyclic strength and permeability, little theory or experimental data has been developed to determine how and why it occurs.

Currently, there are no theoretical models to explain the results obtained by Martin (1957), Wu et al. (1984) and Ross et al. (1989). The theory of effective stress for unsaturated soils proposed by Bishop et al. (1960) may help in understanding how capillarity affects stress wave parameters. The theories presented by Fredlund (1986) have yet to be used in dynamic soil problems. Neither of the two models proposed for predicting the wave velocity in an unsaturated soil (Whitman, 1970; Anderson and Hampton, 1980) produce trends which are similar to those obtained for soils compacted moist.

There have been no detailed studies performed to determine if and how moisture in the compaction process effects the stiffness of sands under static and dynamic loading conditions. The trends obtained by Ross et al. (1988) do not behave in a manner predicted by any of the conventional unsaturated soil mechanics theories because the method of compaction could control the stiffness of the soil. Currently, there has not been enough research performed in the area of high intensity stress wave propagation to conclude whether the compaction technique is an important factor to consider.

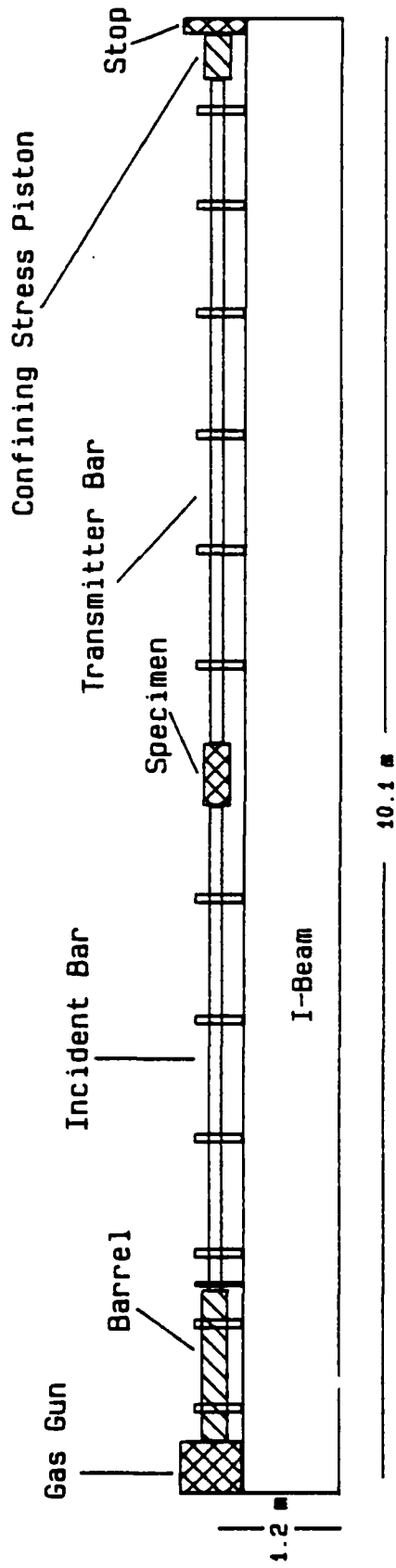
III. EXPERIMENTAL PROCEDURES

A. EQUIPMENT UTILIZED

1. Description of Split-Hopkinson Pressure Bar

The apparatus which was used to measure the propagation of compression waves through unsaturated sand specimens is the split-Hopkinson pressure bar (SHPB) located at the Engineering and Services Center, Tyndall Air Force Base, Florida. The apparatus is the same as that used by Ross et al. (1986, 1988). This device has been designed to accommodate long specimen samples which have an aspect ratio (length / diameter of specimen) greater than one. This particular SHPB has been used in testing high strain properties of soil, concrete and mortar. The SHPB and electronic equipment are briefly discussed here. For a more complete discussion of the SHPB design, refer to Ross et al. (1986).

A schematic of the SHPB used is shown in Figure 3.1. A gas gun located at the left end of the I-beam is used to accelerate a striker bar through the barrel and impact the incident bar. This impact produces a stress pulse which travels down the incident bar. A portion of the wave will be transmitted through the sand sample, and into the transmitter bar according to the wave propagation theory presented in Chapter 2.



(NOT TO SCALE)

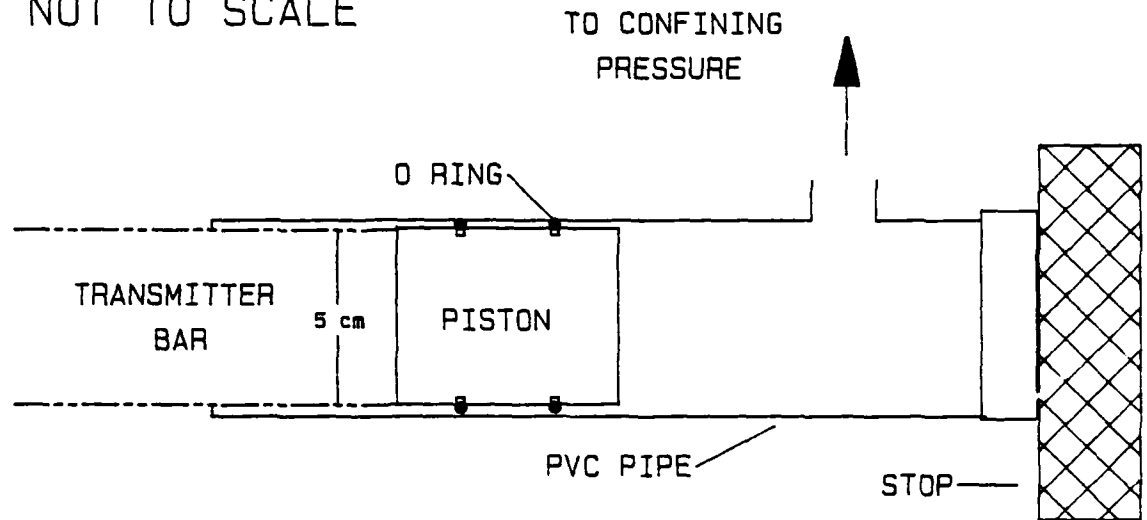
Figure 3.1 Schematic of Split-Hopkinson Pressure Bar

The gas gun launcher consists of two chambers and utilizes compressed nitrogen with a fast acting pressure relief piston. In this investigation a constant striker bar length of 20.32 cm was used, while the pressure within the outer chamber of the gas gun was kept at 172 kPa. This resulted in a striker bar velocity of approximately 13 meters per second for all tests performed. The impact of a steel striker bar of this length and velocity against a steel bar of the same diameter results in a stress pulse with a rise time of 15 microseconds, a pulse length of 80 microseconds, and a magnitude of approximately 290,000 kPa traveling through the incident bar.

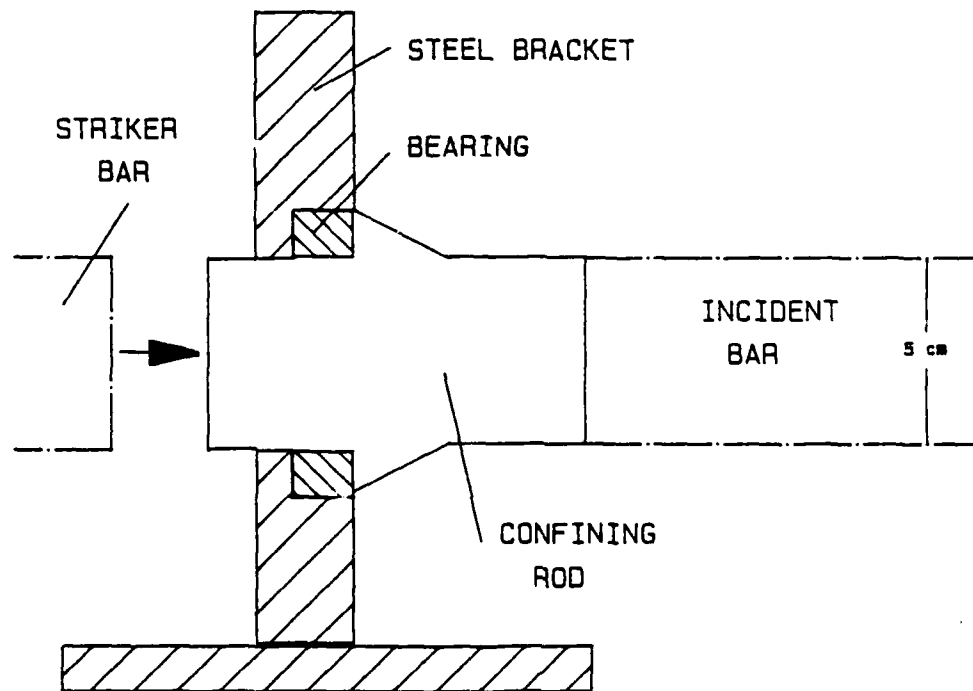
The pressure bars used in the SHPB are composed of 5.08 cm diameter PH 13-8 Mo stainless steel rods. The incident bar was 3.66 m long, the transmitter bar 3.35 m long and the striker bar was 20.32 cm long. The pressure bars are held in place by Dodge Journal bearings spaced approximately 0.9 meters apart on top of the I-beam.

In order to create triaxial confining stress, confining pressure was required along the incident and transmitter bars. In order to accomplish this, axial confining pressure was applied through the pressure bars from a confining stress piston placed on the "free" end of the transmitter bar. Figure 3.2a is a schematic of the piston. In order to prevent the pressure bars and sample container from moving into the gas gun barrel upon application of the axial confining stress, a bracket was designed and placed between the incident bar-striker bar interface. As shown in Figure 3.2b a 10.2 cm long piece of stainless steel was machined to allow for the incident pulse to be transmitted from the striker bar to the incident bar while containing

NOT TO SCALE



(a)



(b)

Figure 3.2 Schematic of Axial Confining Stress Components
a. Confining Piston, b. Confining Bracket

the axial confining stress. A bearing was placed within the bracket to allow for some movement of the confining rod during wave propagation.

The source of confining pressure for the lateral and axial confinement was a 830 kPa air compressor. In order to have the same pressure in the sample container and along the pressure bars, a single line of confining pressure connected to both the sample container and the confining piston was built as shown in Figure 3.3. Since the chosen confining fluid for the sample container was water, an air-water interface was placed between the air compressor and sample container.

2. Specimen Container

A schematic of the sample container used in this investigation is shown in Figure 3.4. The container was designed to allow for the application of variable confining stress around the sample, while preventing any lateral strain from developing while the compressive wave propagated through the specimen. The outer cylinder of the container is composed of 0.635 cm thick stainless steel. The cylinder has an inside diameter of 5.40 cm and a length of 15.24 cm.

In order to apply a confining pressure to the sand sample, a 1 mm thick membrane was used to line the inside of the steel cylinder. Two valves were connected to the cylinder to allow for the application of confining stress and vacuum between the steel cylinder and membrane

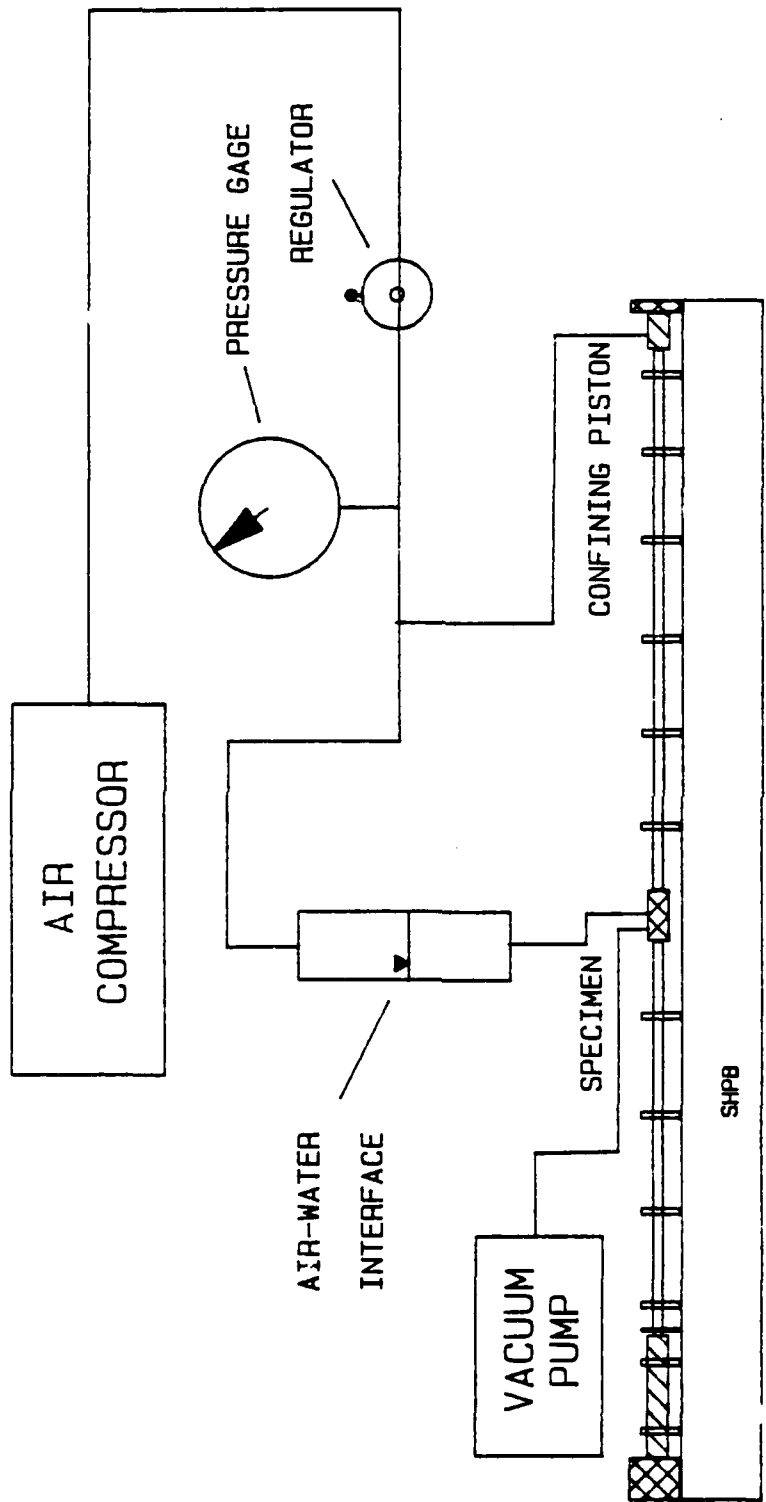


Figure 3.3 Schematic of Confining Pressure Apparatus

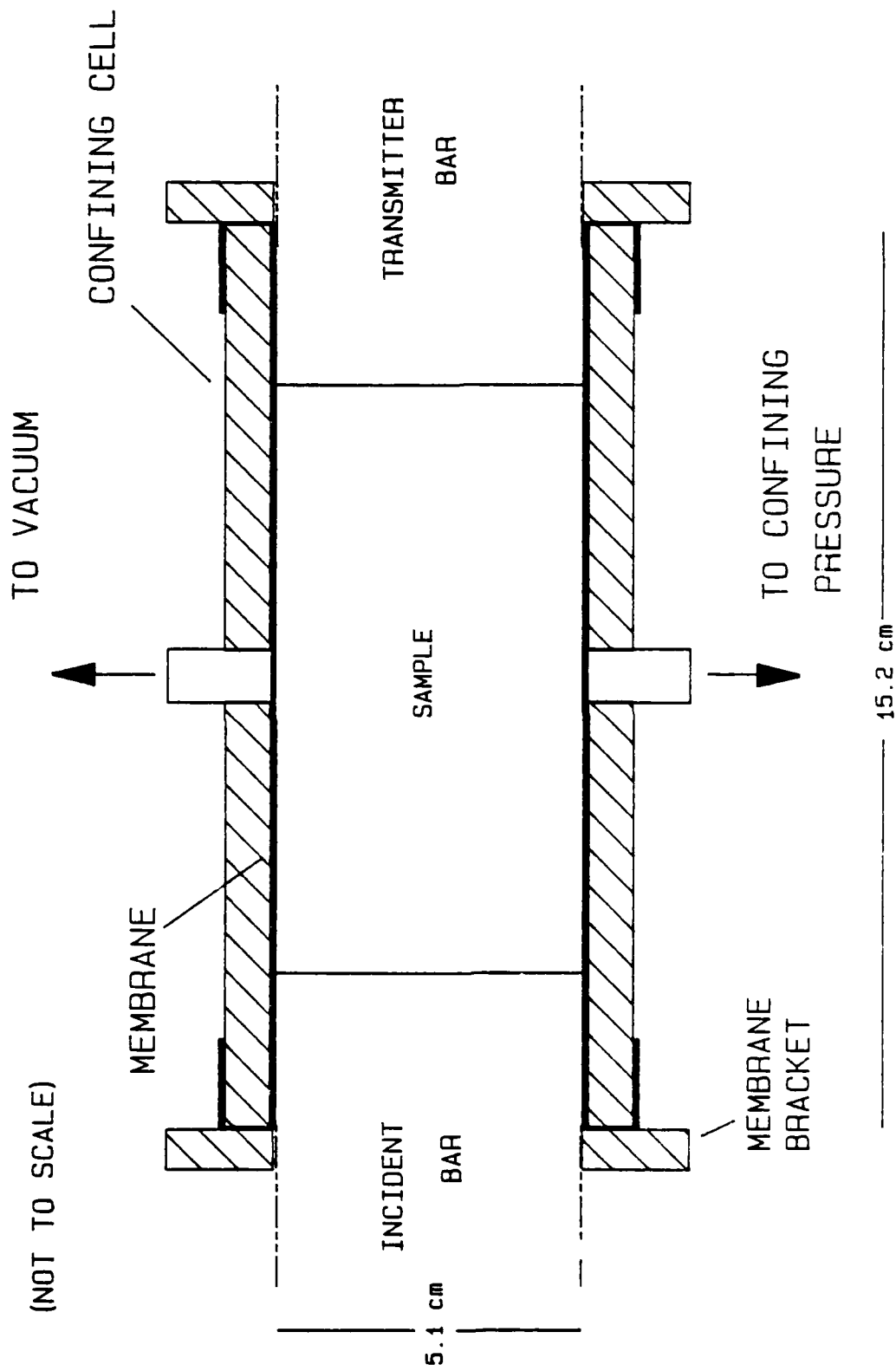


Figure 3.4 Schematic of Sample Container

membrane. Water was chosen as the confining fluid because its stiffness is sufficient to resist lateral expansion of the sand specimen.

3. Data Recording System

A schematic of the data acquisition system used in conjunction with the SHPB is shown in Figure 3.5. In order to measure the velocity of the striker bar before impact into the incident bar, an infrared emitter and sensor circuit was placed at the end of the barrel. The distance between the ends of the circuit was fixed, and a counter-timer unit was connected to the circuit allowing for the striker bar velocity to be calculated.

Two diametrically opposed strain gages were placed on both of the pressure bars to measure the properties of the propagating wave. Both sets of gages were located an equal distance from the specimen container. When the gages were triggered, the information received in each gage was sent through an amplifier to a two channel digital oscilloscope. The results obtained from the oscilloscope were digitized and stored on a floppy disk. The results could then be analysed on a personal computer. Figure 3.6 is a photograph of the oscilloscope and amplifiers used.

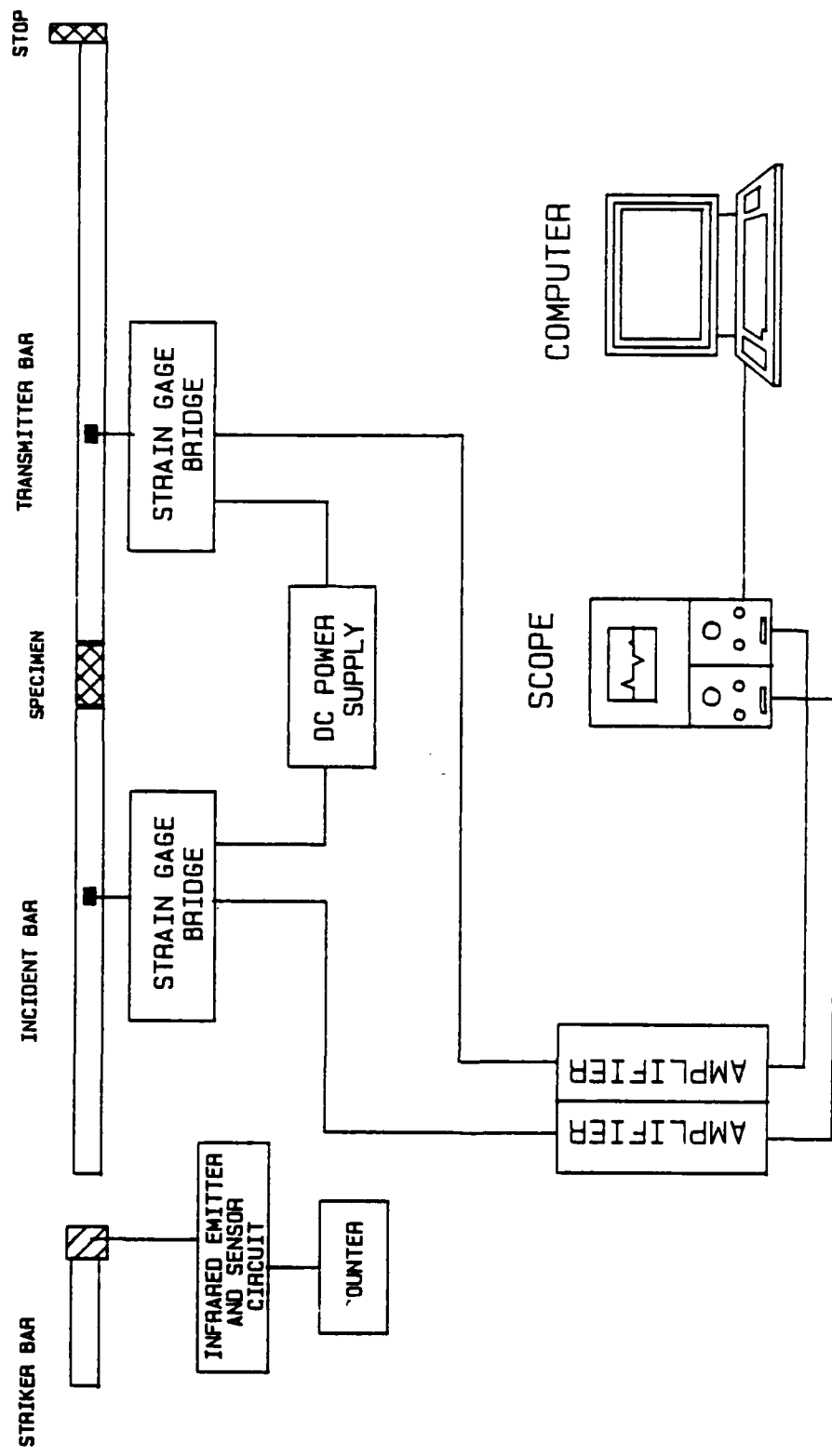


Figure 3.5 Schematic of SHPB Data Recording System

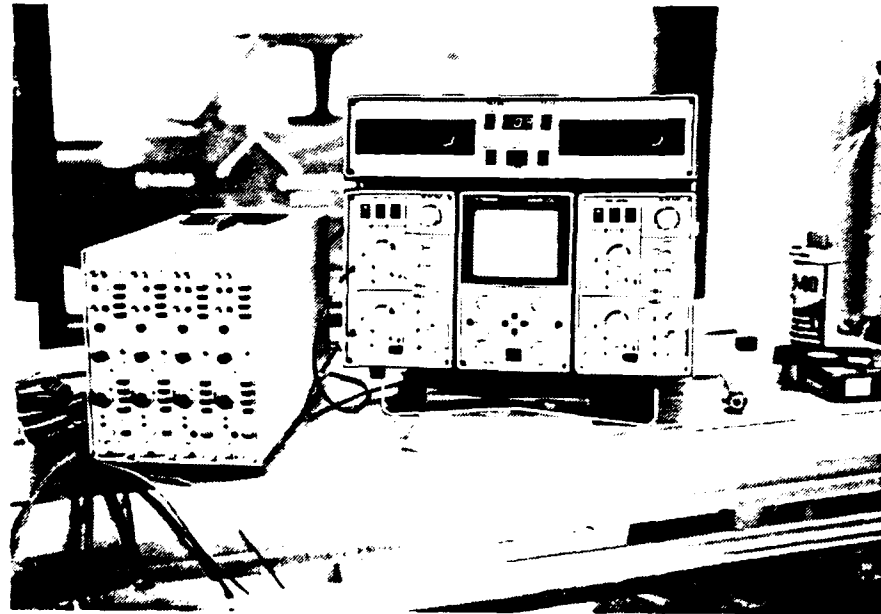


Figure 3.6 Oscilloscope and Amplifiers Used in Conjunction with SHPB Data Recording System

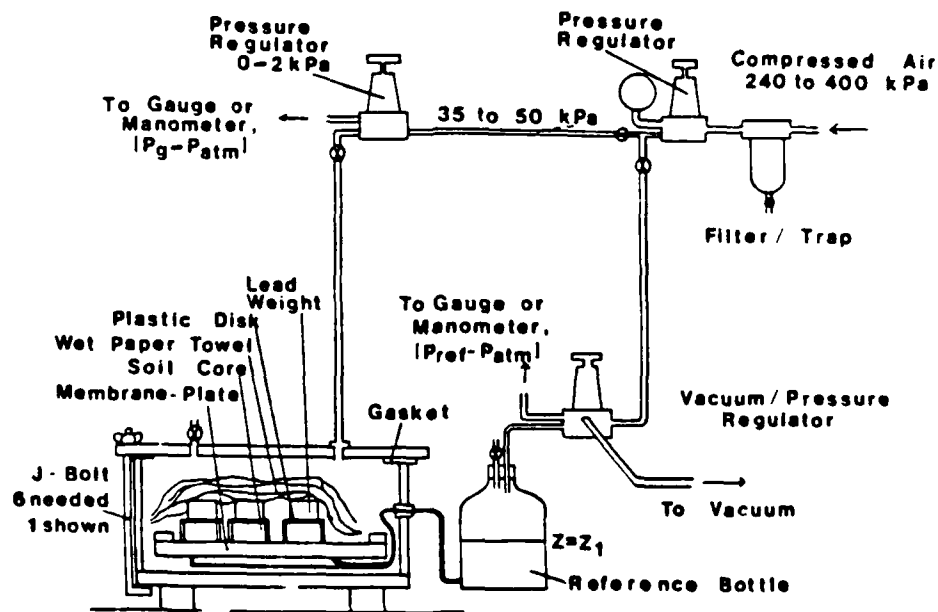


Figure 3.7 Standard Pressure Plate Apparatus

4. Soil Saturation - Desaturation Equipment

For the samples compacted dry in this investigation, they were brought to the required saturation level by saturating the samples, then desaturating them by use of a pressure plate apparatus. All samples were compacted within the sample container described previously to a constant dry density of 1760 kg/m^3 .

Once the samples were compacted they were placed in a saturation chamber. Vacuum was applied to the chamber to remove all of the air from the specimens, then water was allowed to slowly enter the system until the samples were saturated. Specimens were then transferred to a pressure plate apparatus for desaturation to a particular saturation level.

The pressure plate apparatus consists of a pressure chamber and saturated porous ceramic plate. A complete description of the pressure plate apparatus is given by Klute (1986). Figure 3.7 is a schematic of a standard pressure plate apparatus. The procedures used in this investigation generally followed the procedures outlined in ASTM D2325.

5. Quasi-Static Confined Compression Apparatus

Quasi-static confined compression tests were performed to determine the relationship between saturation and constrained modulus under small strain rates. Samples were tested in the same specimen containers as used in the SHPB tests.

Figure 3.8a shows the specimen and loading apparatus utilized. Figure 3.8b is a photograph of the strip-chart recorder used to record the load-time curves of the specimens under one-dimensional compression and strain at a strain rate of 10^{-1} per second.

B. PROCEDURES

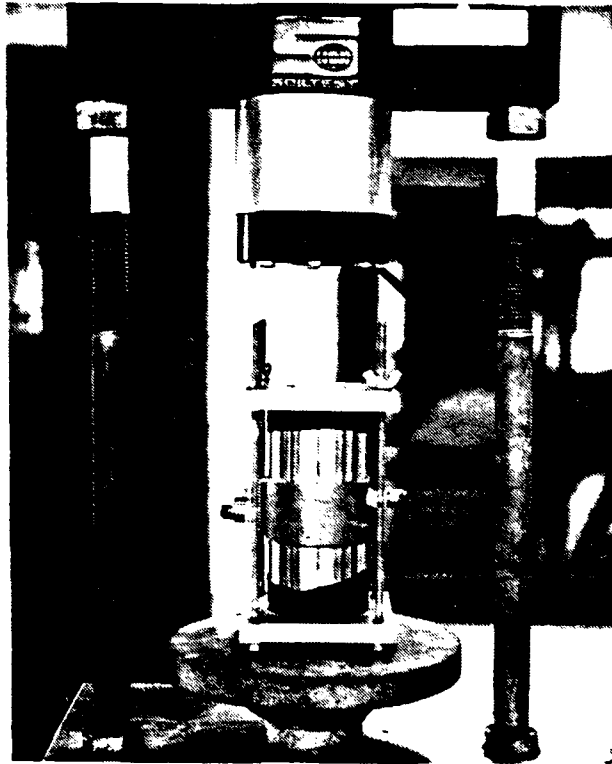
1. Sample Preparation

Both the Ottawa and Eglin sands were compacted in the same manner to a void ratio of 0.51. In order to obtain consistency, three samples were prepared simultaneously in three separate sample containers. Two of the samples were used in SHPB testing, while one sample was prepared for quasi-static compression testing.

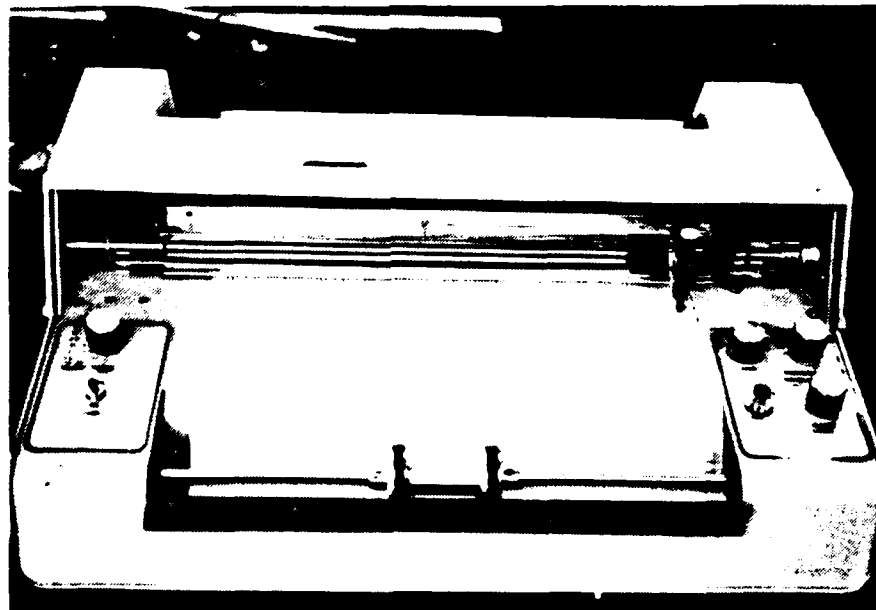
Each sample was compacted dry in four 2.54 cm lifts. One fourth of the sand by weight was poured into the container, then a 5.1 cm diameter steel rod was placed on top of the soil. The soil lift was then compacted dynamically by striking the top of the steel rod with a rubber mallet. Once the sand sample was compacted to a height of 2.54 cm, the next portion of the sand was added. The process was continued until the sample was compacted to a height of 10.16 cm.

2. Sample Saturation and Desaturation

Once the three duplicate samples were compacted, they were fully saturated by use of a saturation chamber, then desaturated to a particular level by use of the pressure plate apparatus. Due to the



a.



b.

Figure 3.8 Quasi-Static Confined Compression Apparatus, a. Load Cell and Sample Container, b. Strip-Chart Recorder

large sample height, equilibration would usually take eight hours or more. For higher pressures the samples were allowed to equilibrate for twelve or more hours. Once the specimens equilibrated, the pressure was reduced and the samples were removed and prepared for testing.

3. Split-Hopkinson Pressure Bar Tests

For triaxially confined tests, the confining stress piston was placed at the end of the transmitter bar prior to testing. If tests were to be run with zero confining stress, the piston was removed and the transmitter bar was placed directly against the stop.

The samples were removed from the pressure plate as needed for testing. Vacuum was then applied to the sample container in order to make it easier to place the sample between the pressure bars. Vacuum was also applied to remove any air from between the membrane and steel cylinder in preparation for applying the confining pressure. The sample container was then put in place between the pressure bars and a line for the confining stress was attached to the other valve on the sample container. The pressure bars were then pushed against the sample, and calipers were used to measure the position of the bars in relation to the sample. The vacuum was then turned off and water was pushed into the specimen container interface under slightly positive pressure. The valve to the vacuum was opened periodically to allow any trapped air to flow out of the interface. Figure 3.9 shows a specimen container in place between the pressure bars.

The specimen was now in position for testing. A confining stress of zero or 310.5 kPa was applied to the sample, and the amplifiers and digital oscilloscope were reset. A sampling rate of 0.5 microseconds was used for all SHPB tests. Once the test was performed, the data was immediately transferred to a floppy disk, and the sample was removed and its moisture content was determined according to ASTM D2216.

4. Quasi-Static Compression Tests

The specimens for quasi-static testing were prepared in the same manner as those for SHPB testing. No confining stress was applied to any of the samples that were tested quasi-statically. Prior to placement on the load machine, a 5.08 cm steel bar was placed on both ends of the sample to allow for the application of the load. The sample container was then oriented vertically in the load machine. The test was performed and the load-time history was recorded using the strip-chart recorder. Once the test was complete, the moisture content was determined using the procedures of ASTM D2216.

5. Capillary Pressure-Desaturation Curves

Capillary pressure-desaturation curves were generated for both sand types following the procedures described in ASTM D2325. Small sample containers were used to contain the samples on the pressure plate, and a piece of cheesecloth was placed over the bottom of each sample to hold the sand in place and allow sufficient contact between

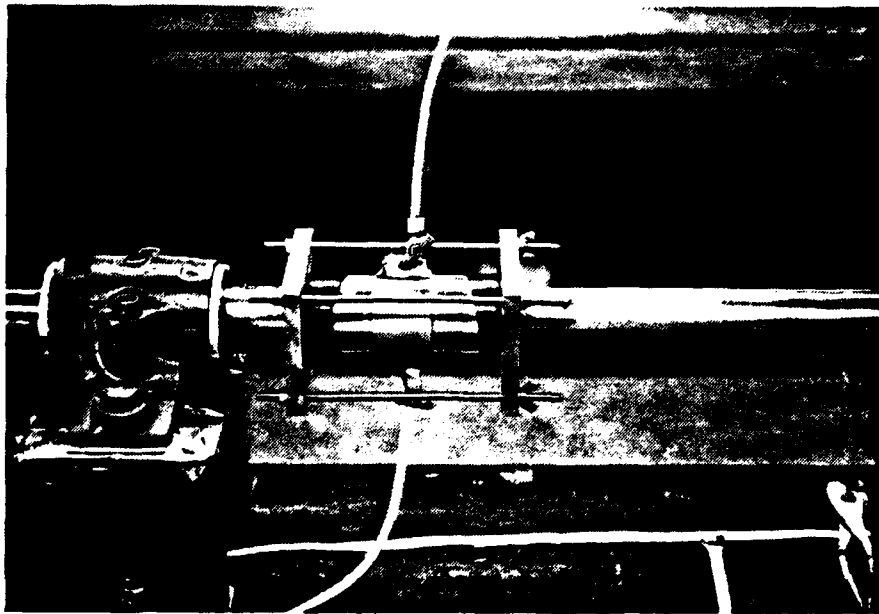


Figure 3.9 Specimen Container in Place Between Pressure Bars

the sand and the ceramic plate during desaturation. The sands were compacted to a void ratio of 0.51, the same as in all other testing.

For each saturation level, three samples of each sand type were desaturated. Once equilibrium was attained, the samples were removed, weighed, and then replaced for the next pressure increment. After the samples equilibrated under the largest pressure applied, the samples were removed, weighed, and then oven dried for moisture content determination. Pressures were applied from zero to approximately 82.7 kPa. For each pressure an average saturation level was obtained for each soil type and used for the capillary pressure-desaturation curves.

IV. EXPERIMENTAL RESULTS

A. PHYSICAL PROPERTIES OF SOILS

Two different sands were used in this research. A .22 kN bag of 20-30 Ottawa sand (ASTM C190) was obtained from the U. S. Silica Company, Ottawa, Illinois. A 300 N bag of the second sand, designated Eglin sand, was collected from Eglin Air Force Base, Florida. Both sands were thoroughly mixed with a sample splitter and the organics removed prior to use. The sands were then stored in covered containers, and samples were removed in a random fashion as needed.

A summary of the physical properties pertinent to this investigation are shown in Tables 4.1 and 4.2. Basic physical properties of each sand were evaluated according to standard laboratory procedures presented by the American Society of Testing and Materials. The test results given in this section are for the 20-30 Ottawa and Eglin sands which were compacted dry to 1760 kg/m^3 , saturated, then desaturated to the required saturation by use of a pressure plate apparatus.

Grain size distributions for the 20-30 Ottawa and Eglin sands are shown in Figure 4.1. Based on the grain size distributions, the 20-30 Ottawa sand is classified as SP, while the Eglin sand is

Table 4.1 Physical Properties of 20-30 Ottawa Sand

Unified Soil Classification	SP
Specific Gravity	2.65
Particle Size Data:	
d_{10}	0.61 mm
d_{30}	0.67 mm
d_{50}	0.70 mm
d_{60}	0.71 mm
% passing #200 sieve	0%
ρ_d maximum	1,566 kg/m ³
ρ_d minimum	1,532 kg/m ³
(Kolbuszewki, 1948)	
Description of Soil	Poorly graded sand. Individual particles are subrounded to rounded in shape.

Table 4.2 Physical Properties of Eglin Sand

Unified Soil Classification	SP-SM
Specific Gravity	2.65
Particle Size Data:	
d_{10}	0.09 mm
d_{30}	0.19 mm
d_{50}	0.26 mm
d_{60}	0.31 mm
% passing #200 sieve	7.3%
ρ_d maximum	1,626 kg/m ³
ρ_d minimum	1,558 kg/m ³
(Kolbuszewki, 1948)	
Description of Soil	Poorly graded sand with silt. Individual particles are subangular to subrounded in shape.

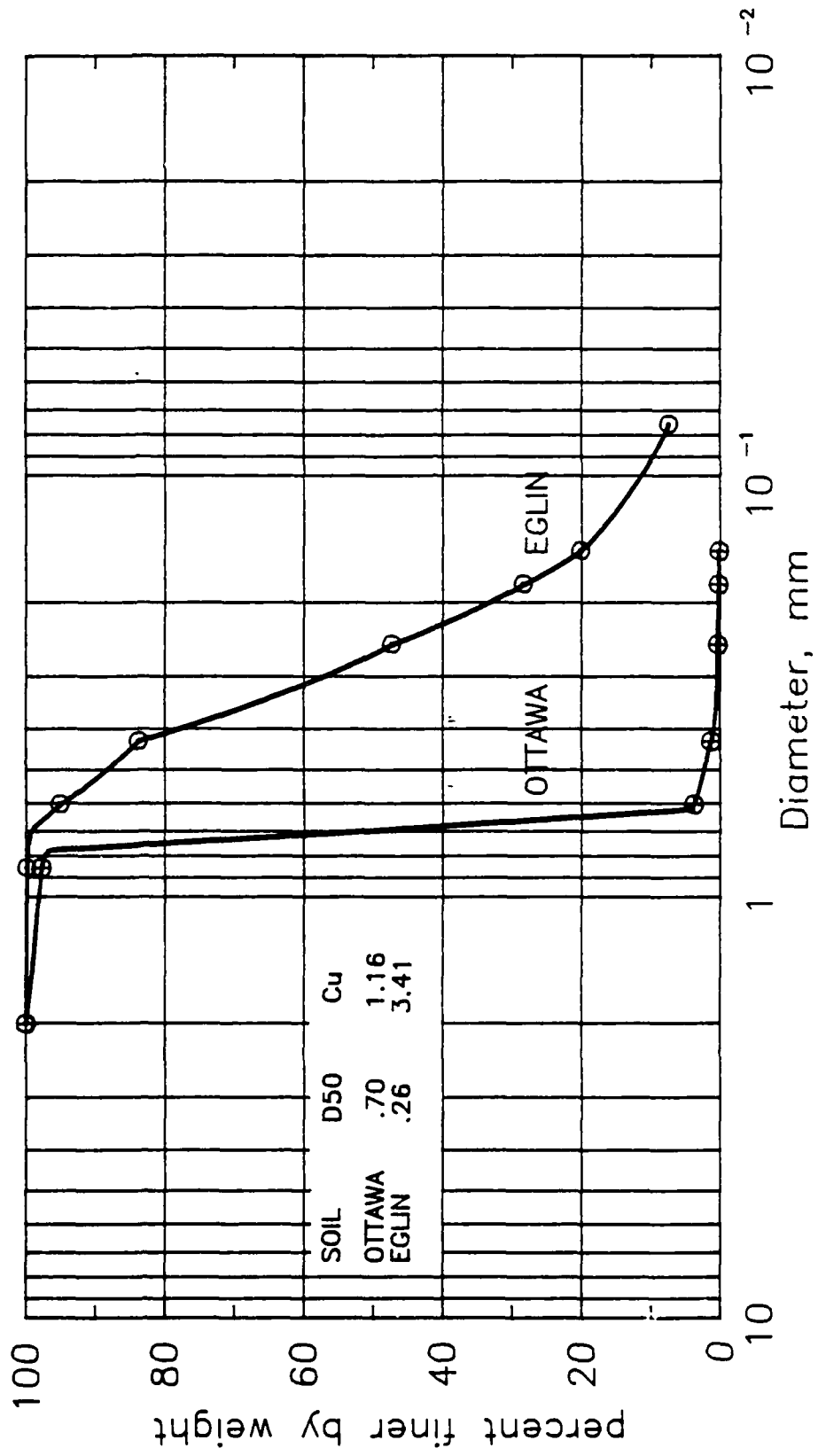


Figure 4.1 Grain Size Distributions for 20-30 Ottawa and Eglin Sands

classified as SP-SM according to the Unified Soil Classification System.

B. SPLIT-HOPKINSON PRESSURE BAR TEST RESULTS

High strain wave propagation tests were performed on both sands to determine the relationship between wave velocity and stress transmission with variations in saturation level and confining stress. A typical oscilloscope trace is shown in Figure 4.2. The signal obtained from the strain gage mounted on the incident bar is represented as a solid line, while the dashed line shows the signal obtained from the transmitter bar strain gage. For this figure, compressive waves are considered negative, while tensile waves are positive.

Figure 4.2 shows that the magnitude of the incident pulse (-2.9×10^5 kPa) is much greater than that of the transmitted pulse (-1.8×10^4 kPa). This is due to the difference in acoustic impedance of the steel pressure bars and the sand specimen. The difference is so large that the transmitted pulse was multiplied by ten in the figure for the purpose of presentation.

Based on wave propagation theory, a compressive wave traveling in a material of high acoustical impedance (steel bars) will transmit a portion of the compressive wave into a material of lower impedance (sand), while a portion of the pulse will be reflected back along the incident material in the form of a tensile wave. Figure 4.2 shows this relationship. It should be noted from equations 2.4 through 2.7

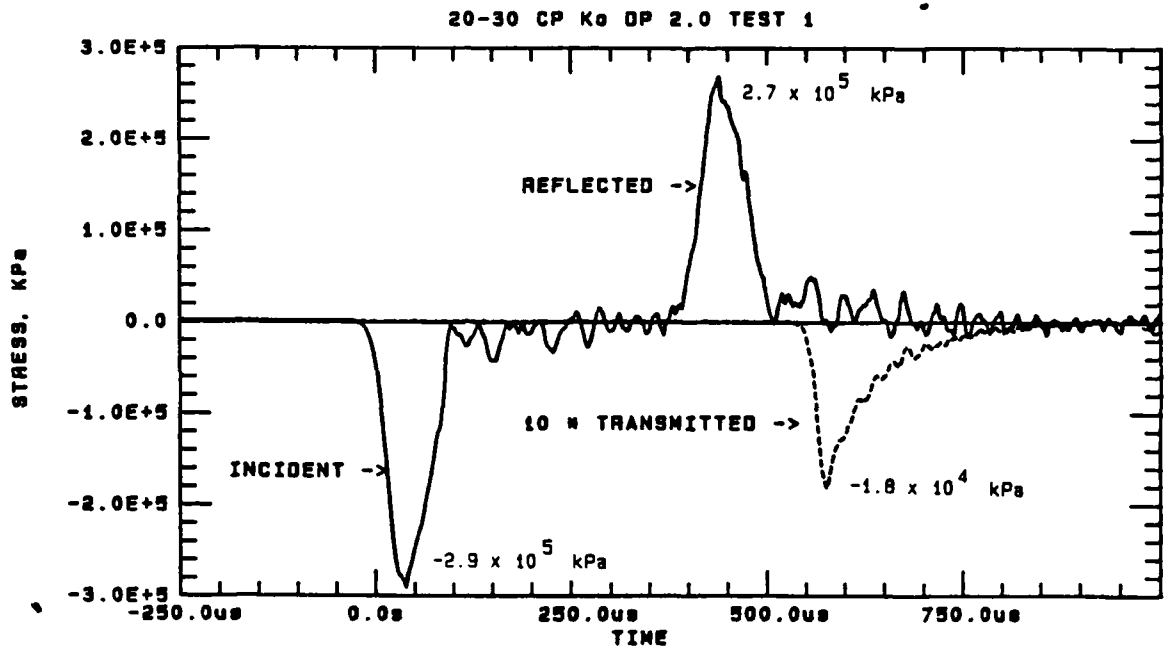


Figure 4.2 Typical Oscilloscope Trace of Compression Wave as Recorded by Pressure Bar Strain Gages

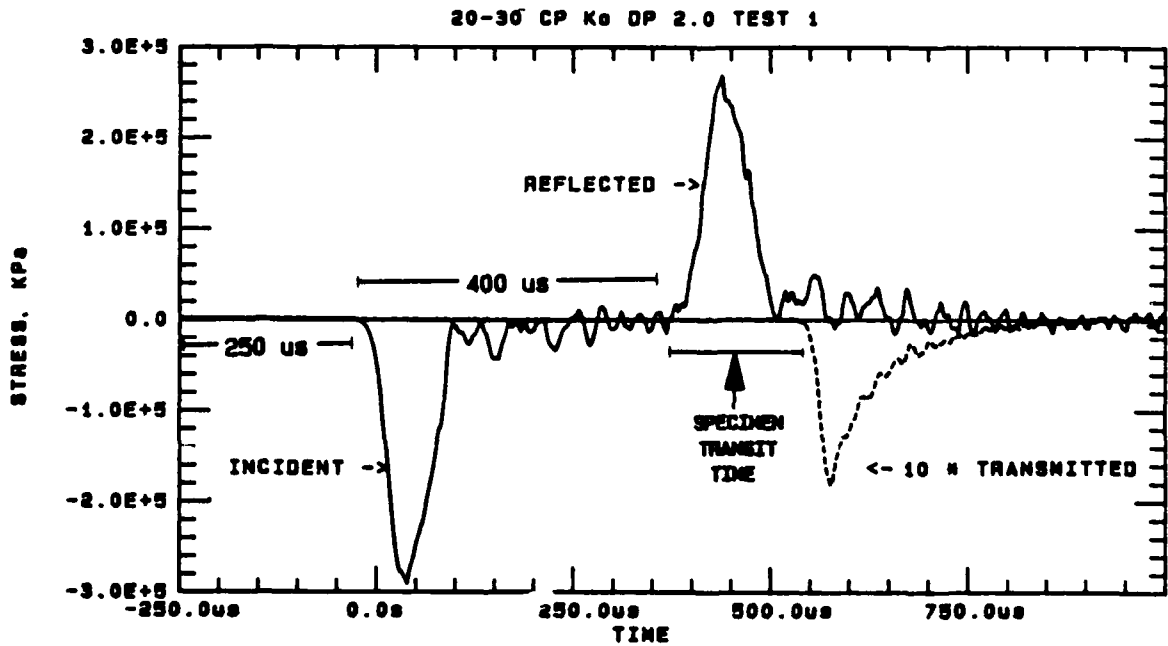


Figure 4.3 Typical Oscilloscope Trace with Wave Transit Times

that the maximum stress within the soil sample is approximately half the value in the transmitter bar.

The average wave velocity through the sample was determined by measuring the time required for the wave to travel between the incident and transmitter bar strain gages. For this particular SHPB a compressive wave travels at a rate of 1.97 microseconds per centimeter. Since the incident and transmitter bar strain gages are each 101.6 cm away from the end of each bar, a compressive wave would take 400 microseconds to travel from the incident strain gage to the transmitter strain gage if the pressure bars were in contact. To find the transit time across the specimen, 400 microseconds was subtracted from the time measured for the wave to travel between the pressure bar strain gages. The length of the specimen was known, allowing for the determination of the wave velocity. Figure 4.3 shows the specimen transit time determination on an oscilloscope plot. It should be noted that the velocity determined is an average velocity. No corrections were made to account for the attenuation of the wave due to damping as it passed through the sand specimen.

The maximum incident and transmitted stress was determined to be the peak stresses recorded on the oscilloscope by the incident and transmitter bar strain gages. Though the gages were mounted 101.6 cm away from the sample, no significant attenuation of the wave occurs in the steel bars between the strain gages and sample.

The data obtained for each test is shown in Tables 4.3 through 4.6. Values for peak incident, reflected and transmitted stresses, and wave velocities are given. The ratio of the incident to the transmitted

Table 4.3 SHPB Test Results for 20-30 Ottawa Sand Under Zero Confining Stress

SAMPLE NUMBER	SATURATION (%)	SAMPLE LENGTH (cm)	VOID RATIO	INCIDENT PEAK STRESS (kPa)	REFLECTED PEAK STRESS (kPa)	TRANSMITTED PEAK STRESS (kPa)	STRESS TRANSMISSION RATIO	WAVE SPEED (m/s)
Ko-0-1	0.0	10.16	0.51	-292596	267054	-18163	0.0621	574.0
Ko-0-2	0.0	10.24	0.53	-292596	263081	-3689	0.0126	564.2
Ko-0-3	0.0	10.24	0.53	-296285	266770	-9238	0.0312	550.5
Ko-0-4	0.0	10.16	0.51	-293731	264784	-19383	0.0660	612.0
Ko-0-5	0.0	10.16	0.51	-288623	256554	-17752	0.0615	601.2
Ko-0-6	0.0	10.16	0.51	-285501	265919	-22732	0.0796	637.0
Ko-1.5-1	5.3	10.16	0.51	-303380	265068	-11423	0.0377	547.7
Ko-1-1	5.4	10.16	0.51	-302813	261946	-15112	0.0499	572.4
Ko-1-2	7.3	10.16	0.51	-286069	263932	-13140	0.0459	561.3
Ko-1.5-2	8.4	10.16	0.51	-304799	268757	-13055	0.0428	572.4
Ko-2.0-1	12.8	10.16	0.51	-291745	269041	-18191	0.0624	625.2
Ko-2.0-2	16.1	10.16	0.51	-304232	263081	-5974	0.0196	546.2
Ko-4.5-1	16.4	10.08	0.50	-294583	253148	-12147	0.0412	580.6
Ko-4.5-2	25.4	10.16	0.51	-290326	251729	-8117	0.0280	564.5
Ko-4-2	29.8	10.16	0.51	-278974	252580	-16290	0.0584	603.0
Ko-3.7-2	33.0	10.16	0.51	-291461	255986	-8471	0.0291	566.0
Ko-2.5-1	33.3	10.16	0.51	-291745	267054	-7223	0.0248	570.8
Ko-3.7-1	34.3	10.08	0.50	-291745	258256	-15538	0.0533	626.1
Ko-2.5-2	37.3	10.16	0.51	-297704	263081	-14318	0.0481	585.6
Ko-2.9-3	39.9	10.16	0.51	-315016	274433	-6854	0.0218	541.8
Ko-2.9-2	42.9	10.16	0.51	-290893	264500	-13197	0.0454	580.6
Ko-2.9-4	44.5	10.16	0.51	-294583	257973	-10827	0.0368	552.2
Ko-2.9-1	61.9	10.16	0.51	-309340	284366	-3689	0.0119	523.7
Ko-3.0-2	70.7	10.31	0.54	-294866	262797	-8145	0.0276	522.5
Ko-3.0-1	81.5	10.31	0.54	-293447	264216	-9521	0.0324	570.1
MEAN		10.172	0.513	-295082				
ST. DEV.		0.051	0.010	7731				

Table 4.4 SHPB Test Results for 20-30 Ottawa Sand Under 310 kPa Confining Stress

SAMPLE NUMBER	SATURATION (%)	SAMPLE LENGTH (cm)	VOID RATIO	INCIDENT PEAK STRESS (kPa)	REFLECTED PEAK STRESS (kPa)	TRANSMITTED PEAK STRESS (kPa)	STRESS TRANSMISSION RATIO	WAVE SPEED (m/s)
45-0-1	0.0	10.24	0.53	-311610	273298	-28323	0.0909	682.6
45-0-2	0.0	10.16	0.52	-305083	255986	-27387	0.0898	666.2
45-4.4-1	4.8	10.16	0.51	-315867	274433	-25826	0.0818	659.7
45-4.4-2	5.2	10.16	0.51	-293164	268473	-27216	0.0928	691.2
45-1.5-4	7.4	10.24	0.53	-302245	268757	-31360	0.1038	689.5
45-1.5-5	7.5	10.16	0.51	-318138	265919	-30111	0.0946	686.5
45-3-3	13.6	10.16	0.51	-285501	260527	-23995	0.0840	686.5
45-3-4	20.2	10.16	0.51	-280393	267906	-23470	0.0837	651.3
45-2.9-3	31.1	10.16	0.51	-307070	273865	-29174	0.0950	710.5
45-3-2	41.0	10.16	0.51	-300542	269041	-28011	0.0932	659.7
45-2.9-1	44.7	10.3	0.54	-304799	285785	-16687	0.0547	631.1
45-1.5-3	51.5	10.31	0.54	-301110	280109	-19696	0.0654	614.2
45-1.5-2	54.6	10.31	0.54	-300826	286069	-23612	0.0785	637.0
45-3-1	61.3	10.16	0.51	-294015	260243	-30310	0.1031	679.6
45-2.9-2	64.5	10.39	0.55	-299975	275852	-27273	0.0909	700.2
45-2.9-4	73.6	10.16	0.51	-316151	260243	-27330	0.0864	651.3
45-1.5-1	78.3	10.31	0.54	-307353	282095	-21597	0.0703	653.4
45-2.9-5	81.3	10.16	0.51	-309056	270743	-21285	0.0689	668.4
45-0-1 (sat)	100.0	10.16	0.51	-300258	255702	-46330	0.1543	1421.0
MEAN		10.212	0.521	-302798				
ST. DEV.		0.074	0.014	9589				

Table 4.5 SHPB Test Results for Eglin Sand Under Zero Confining Stress

SAMPLE NUMBER	SATURATION (%)	SAMPLE LENGTH (cm)	VOID RATIO	INCIDENT PEAK STRESS (kPa)	REFLECTED PEAK STRESS (kPa)	TRANSMITTED PEAK STRESS (kPa)	STRESS TRANSMISSION RATIO	WAVE SPEED (m/s)
Ko-0-1	0.0	10.16	0.51	-283231	270176	-8627	0.0305	506.7
Ko-0-2	0.0	10.16	0.51	-286920	281244	-5747	0.0200	452.6
Ko-0-3	0.0	10.16	0.51	-282947	285217	-7762	0.0274	511.9
Ko-8.8-1	23.4	10.16	0.51	-290609	269041	-4285	0.0147	444.6
Ko-8.8-2	23.5	10.16	0.51	-277838	272446	-3888	0.0140	427.8
Ko-5.9-1	24.8	10.16	0.51	-290326	277555	-5491	0.0189	453.6
Ko-5.9-2	25.1	10.16	0.51	-293447	271595	-3916	0.0133	404.0
Ko-4.4-1	25.6	10.16	0.51	-287204	276419	-4285	0.0149	429.6
Ko-4.4-2	28.7	10.16	0.51	-290326	275000	-3377	0.0116	416.4
Ko-3.7-2	29.6	10.16	0.51	-285217	276987	-2341	0.0082	392.3
Ko-3.7-1	32.6	10.16	0.51	-288623	263365	-6357	0.0220	454.6
Ko-2.2-2	45.2	10.16	0.51	-286069	270176	-3136	0.0110	415.5
Ko-2.9-2	45.6	10.16	0.51	-287771	264784	-3732	0.0130	397.6
Ko-2.2-1	47.0	10.16	0.51	-282947	267338	-5506	0.0195	457.7
Ko-2.9-1	54.4	10.16	0.51	-349923	302529	-2824	0.0081	404.0
Ko-1.5-2	79.7	10.16	0.51	-301394	275852	-4285	0.0142	456.5
Ko-1.5-1	81.8	10.16	0.51	-297137	269608	-4498	0.0151	483.8
MEAN		10.16	0.51	-291878				
ST. DEV.		0.000	0.000	15491				

Table 4.6 SHPB Test Results for Eglin Sand Under 310 Confining Stress

SAMPLE NUMBER	SATURATION (%)	SAMPLE LENGTH (cm)	VOID RATIO	INCIDENT PEAK STRESS (kPa)	REFLECTED PEAK STRESS (kPa)	TRANSMITTED PEAK STRESS (kPa)	STRESS TRANSMISSION RATIO	WAVE SPEED (m/s)
45-0-1	0.0	10.16	0.51	-284082	271027	-11196	0.0394	546.2
45-0-2	0.0	10.16	0.51	-286069	269608	-10997	0.0384	537.6
45-2.9-1	25.5	10.16	0.51	-282663	260243	-9748	0.0345	549.3
45-2.9-2	27.2	10.16	0.51	-282663	276419	-9692	0.0343	587.3
45-4.4-1	28.5	10.16	0.51	-285217	268189	-10884	0.0382	539.0
45-4.4-2	32.0	10.16	0.51	-284650	269041	-6343	0.0223	485.0
45-3.7-1	35.9	10.16	0.51	-300542	284933	-8230	0.0274	536.1
45-2.2-2	41.1	10.16	0.51	-296002	267054	-8571	0.0290	521.0
45-2.2-1	41.4	10.16	0.51	-283514	273014	-5988	0.0211	486.1
45-1.5-1	72.9	10.08	0.50	-289474	276987	-8443	0.0292	529.2
45-1.5-2	79.0	10.16	0.51	-286920	274717	-9053	0.0316	499.3
MEAN		10.15	0.5090	-287435				
ST. DEV.		0.021	0.0028	5529.4				

peak stress has also been calculated for each test and is included in the tables.

The relationship between saturation and wave velocity under the two confining pressures is given in Figures 4.4 through 4.7 for the 20-30 Ottawa and Eglin sands. Transmission ratio versus saturation is presented in Figures 4.8 through 4.11 for both sand types and confining stresses.

In order to show that the differences in trends obtained by Ross et al. on the same sands compacted moist to the same void ratio was not due to the use of different sample containers, several samples were compacted moist in the sample container used in this investigation, and tested on the SHPB. Figure 4.12 shows wave velocity and stress transmission results for the Eglin sand obtained by Ross et al. and in the current investigation.

In an attempt to determine the role of the moisture during the compaction process, several samples of Eglin sand were compacted moist in the sample container used by Ross et al. (1988). The specimen and container was then placed in an oven for a period of 24 hours to remove all moisture in the sample, then the sample was then tested dynamically on the SHPB. Figure 4.13 shows the results obtained.

C. QUASI-STATIC STIFFNESS TESTS

Quasi-static stiffness tests were performed to determine the relationship between stiffness and saturation level under quasi-static loading rate conditions. The results obtained were used to predict the wave velocity using equation 2.3 based on the quasi-static

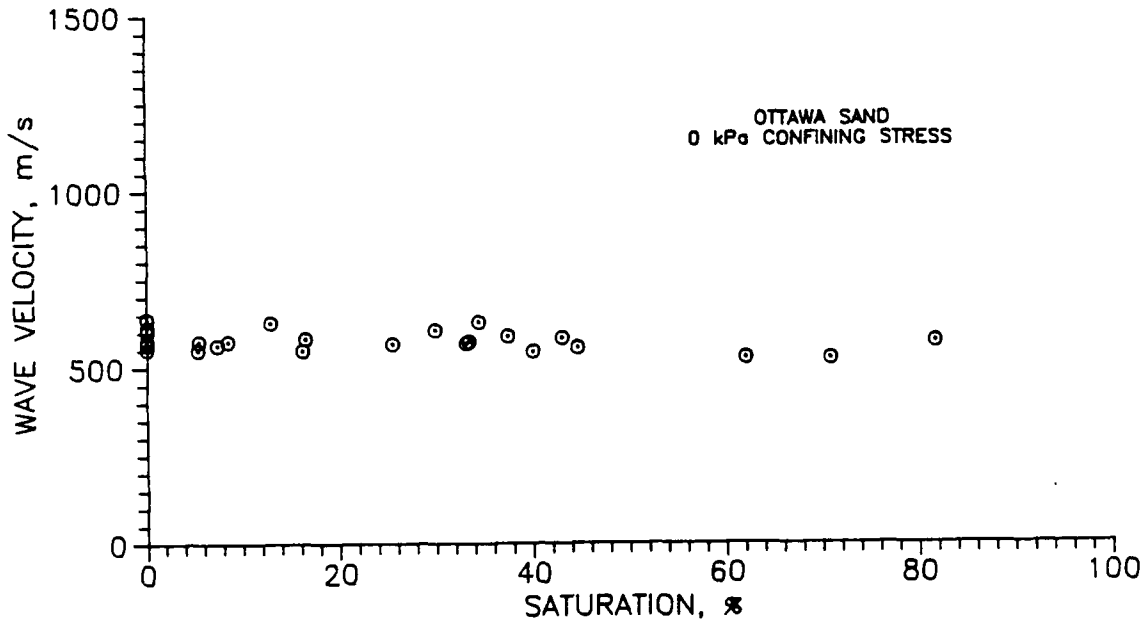


Figure 4.4 Wave Velocity Versus Saturation for 20-30 Ottawa Sand Under Zero Confining Stress

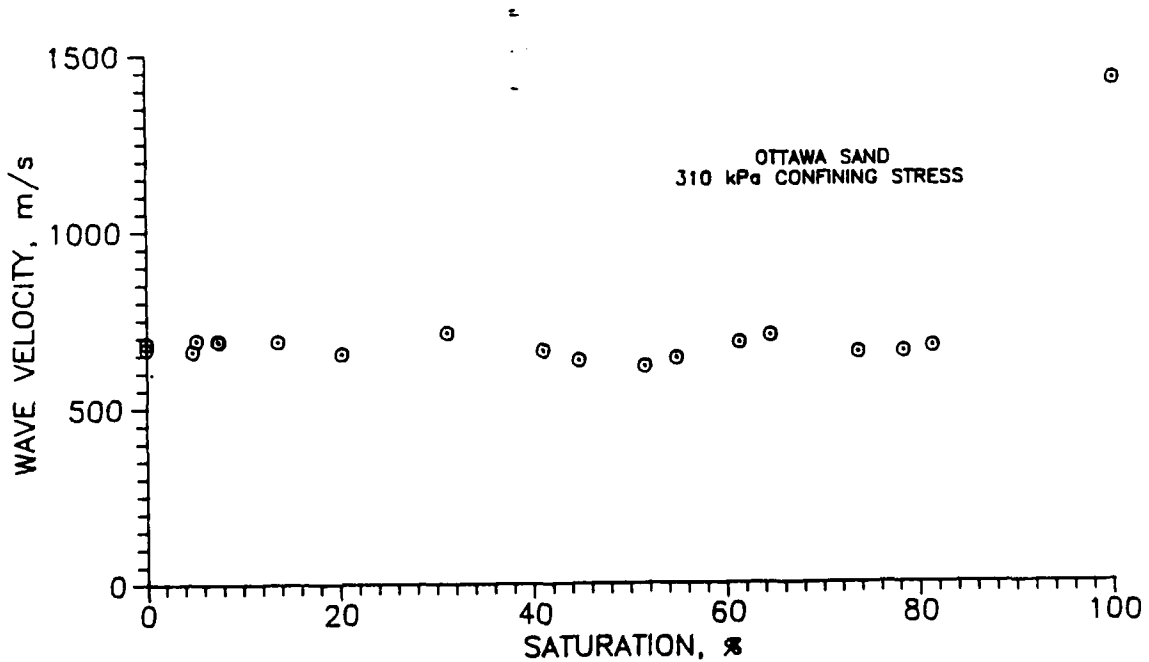


Figure 4.5 Wave Velocity Versus Saturation for 20-30 Ottawa Sand Under 310 kPa Confining Stress

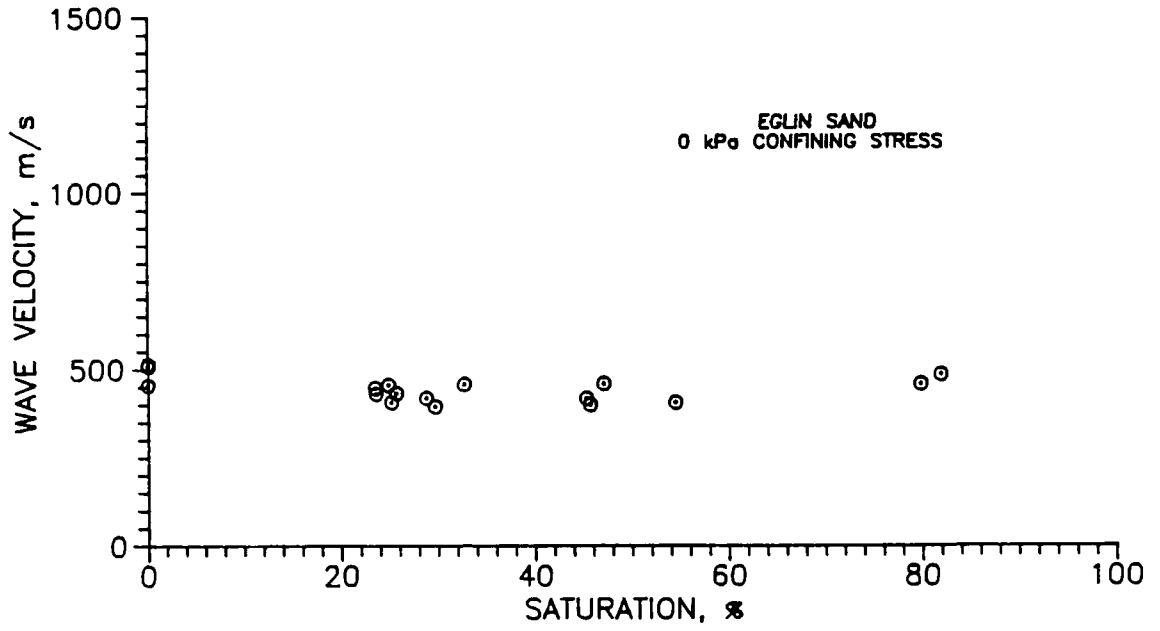


Figure 4.6 Wave Velocity Versus Saturation for Eglin Sand Under Zero Confining Stress

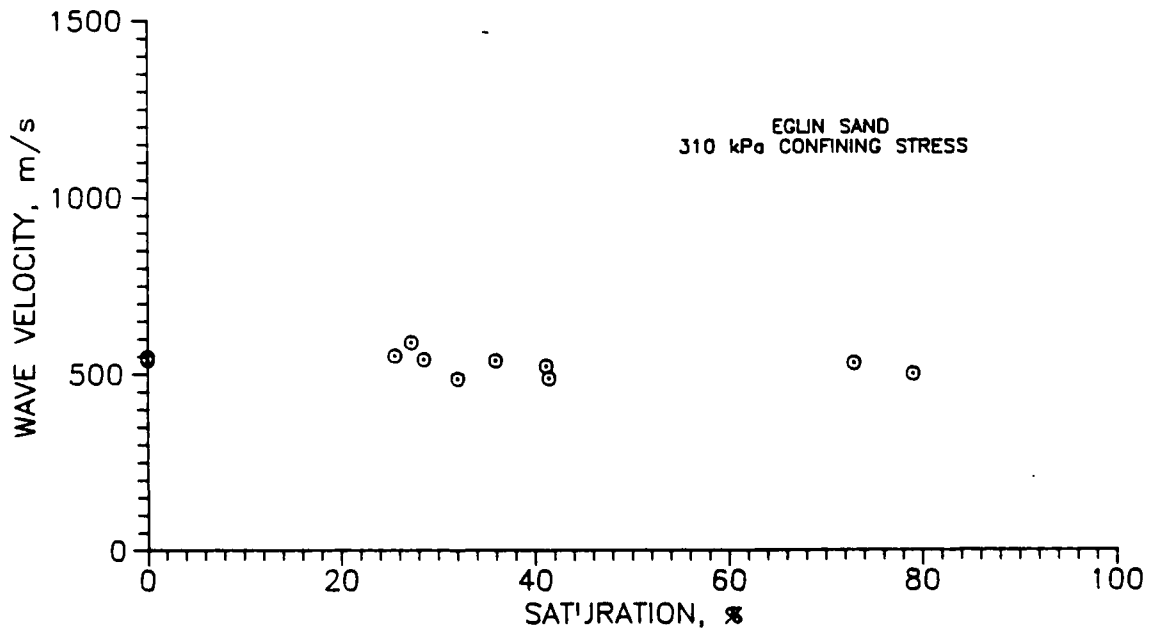


Figure 4.7 Wave Velocity Versus Saturation for Eglin Sand Under 310 kPa Confining Stress

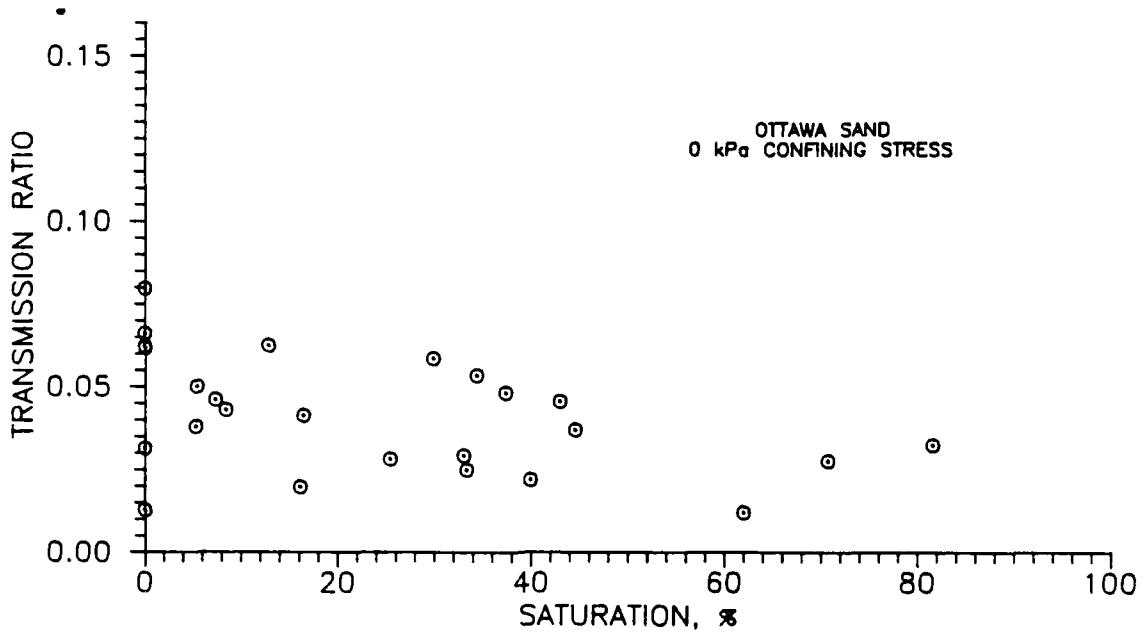


Figure 4.8 Transmission Ratio Versus Saturation for 20-30 Ottawa Sand Under Zero Confining Stress

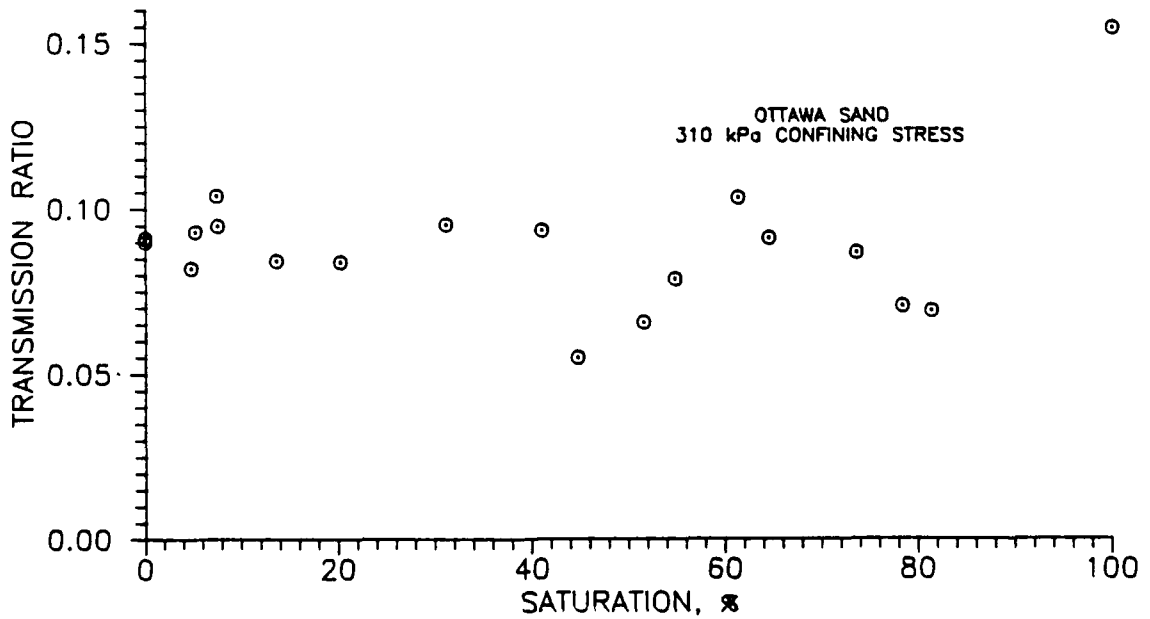


Figure 4.9 Transmission Ratio Versus Saturation for 20-30 Ottawa Sand Under 310 kPa Confining Stress

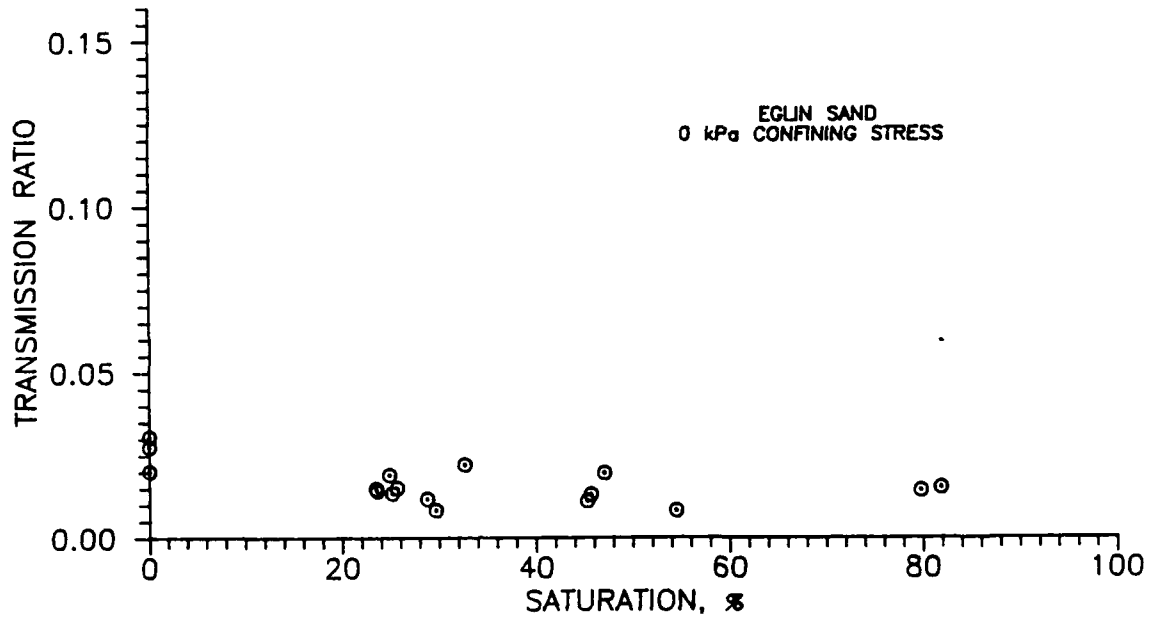


Figure 4.10 Transmission Ratio Versus Saturation for Eglin Sand Under Zero Confining Stress

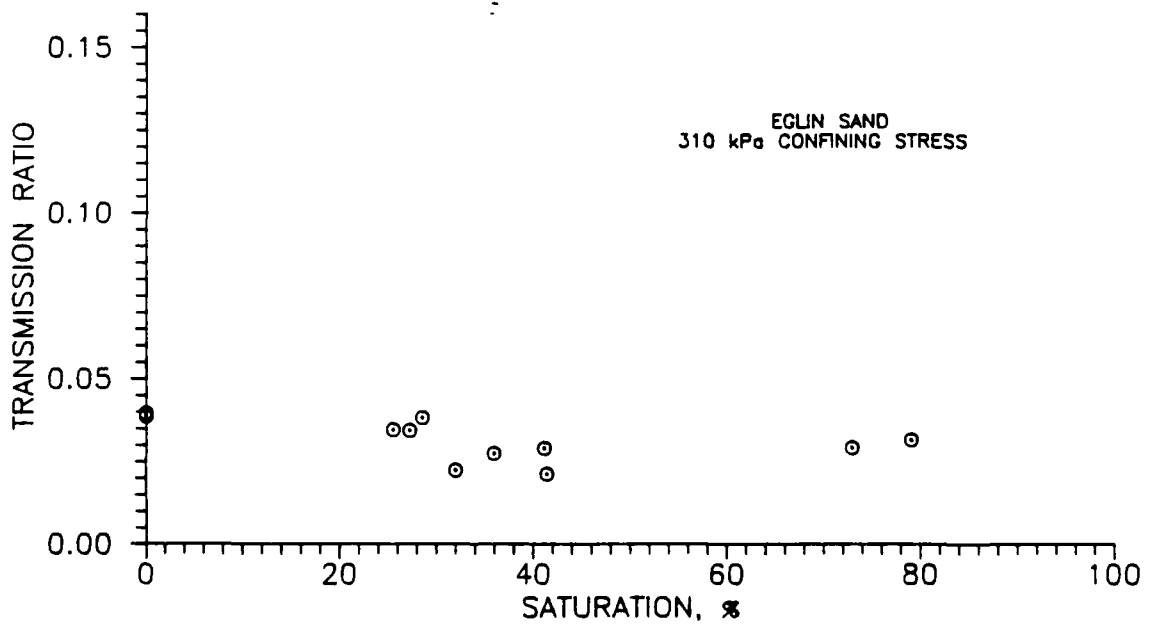
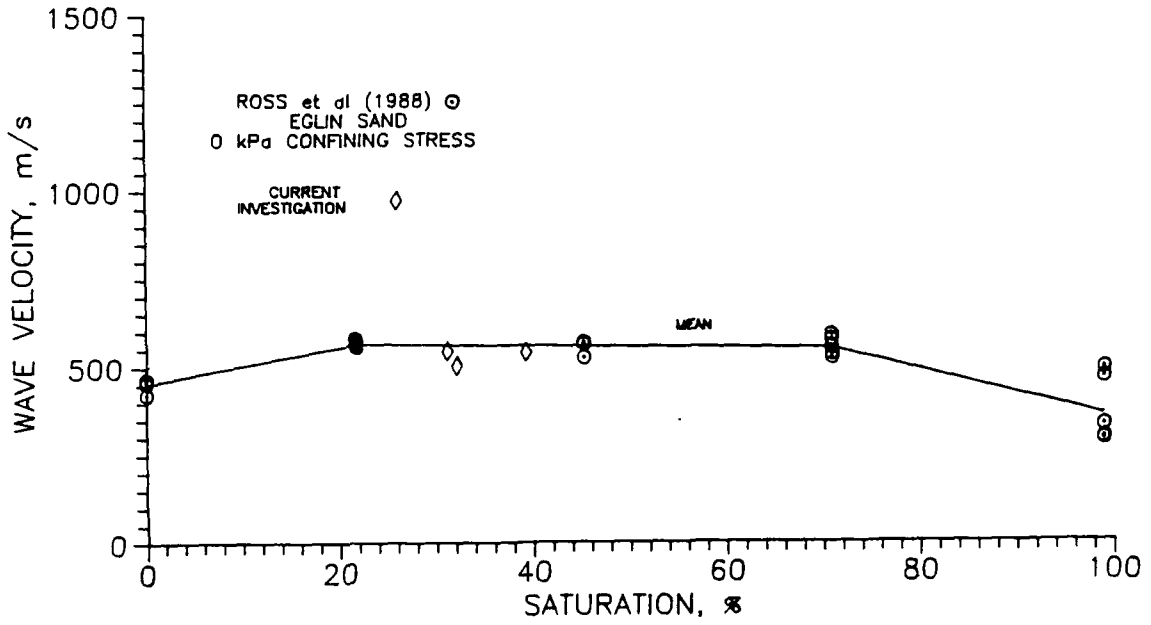
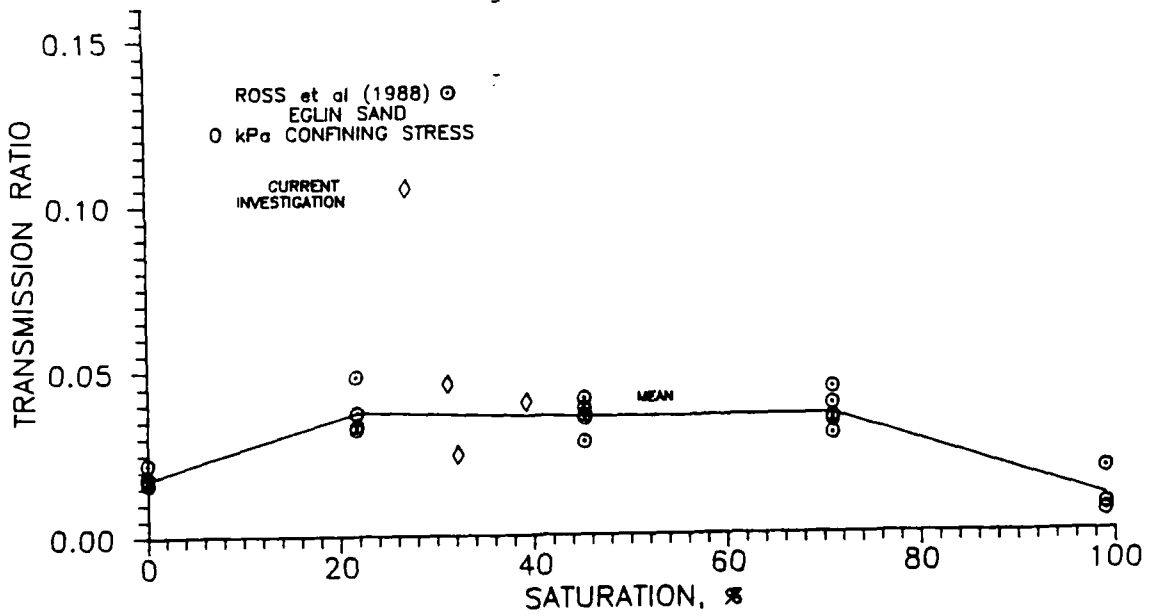


Figure 4.11 Transmission Ratio Versus Saturation for Eglin Sand Under 310 kPa Confining Stress



a.



b.

Figure 4.12 Results For Eglin Sand Obtained by Ross et al. (1988) and Results for Samples Compacted Moist Using Sample Container in Current Investigation a. Wave Velocity, b. Transmission Ratio

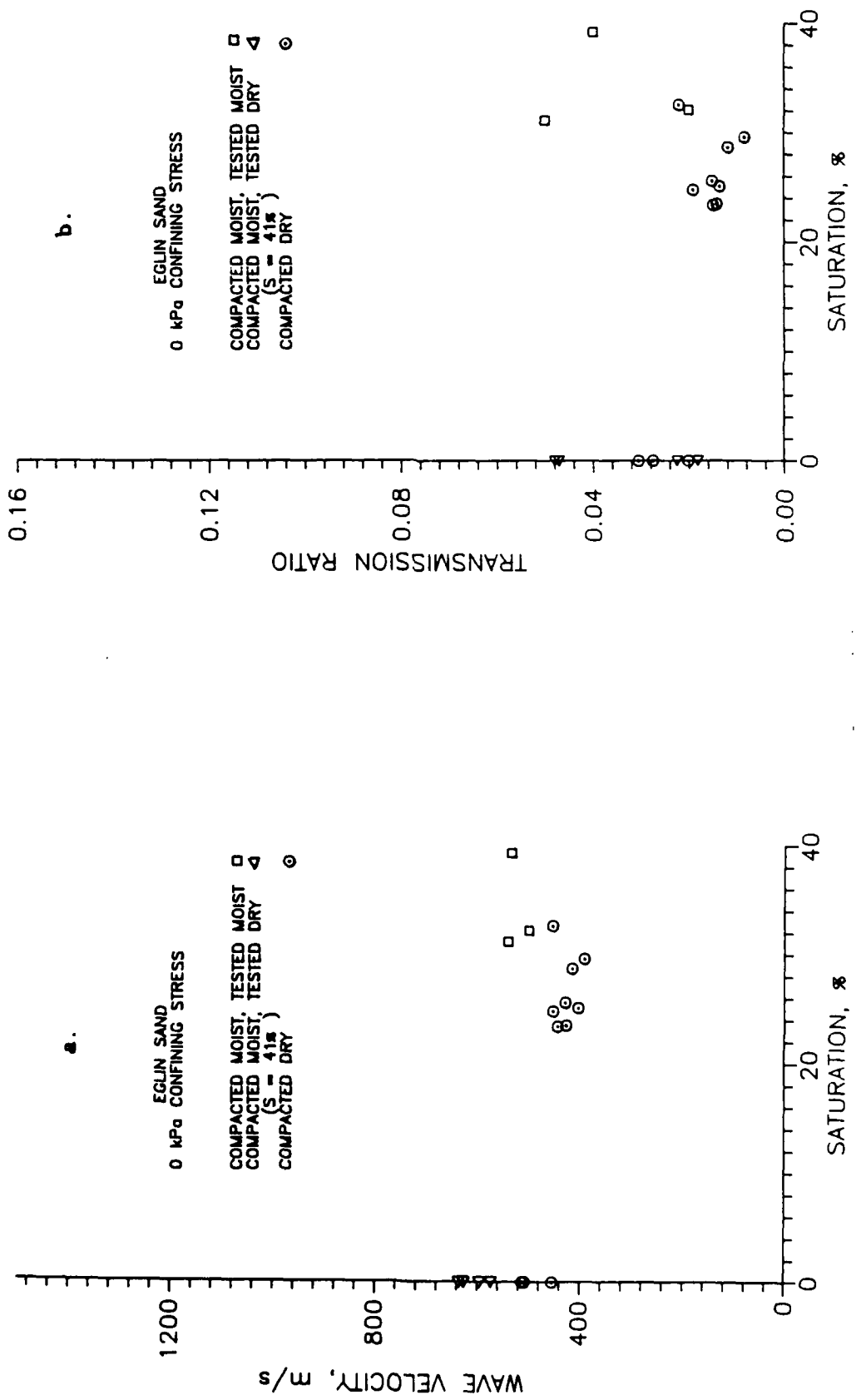


Figure 4.13 Comparison of Egline Sand Samples Compacted and Tested Both Moist and Dry a. Wave Velocity, b. Transmission Ratio

constrained modulus. These predictions were then compared with the wave velocities obtained from the SHPB tests.

A typical strip-chart recorder stress-time history is shown in Figure 4.14. The secant constrained modulus was determined for the tests by measuring the displacement between axial loads of 4.45kN (2,200 kPa) and 31.14 kN (15,000 kPa) divided by the sample strain.

Tables 4.7 and 4.8 list the values of constrained modulus for initial loading and reloading conditions for various saturation levels. The relationships between constrained modulus and saturation are presented in Figure 4.15 for the Ottawa sand, and Figure 4.16 for the Eglin sand.

D. CAPILLARY PRESSURE-DESATURATION CURVES

Capillary pressure-desaturation curves were determined for each sand according to ASTM D2325. The results are presented in Figures 4.17 and 4.18 for the Ottawa and Eglin sands.

Both sands desaturate with a small increase in capillary pressure (less than 2 kPa), making it difficult to determine the displacement pressure. The moisture in the 20-30 Ottawa sand displaces at a very low capillary pressure due to the uniformity of the grain size distribution. The Eglin sand has a higher percentage of finer grained particles, making the displacement pressure somewhat higher (less than 7 kPa). The residual saturation level for the 20-30 Ottawa sand is approximately 2 percent, while the Eglin sand has a residual saturation level of approximately 16 percent.

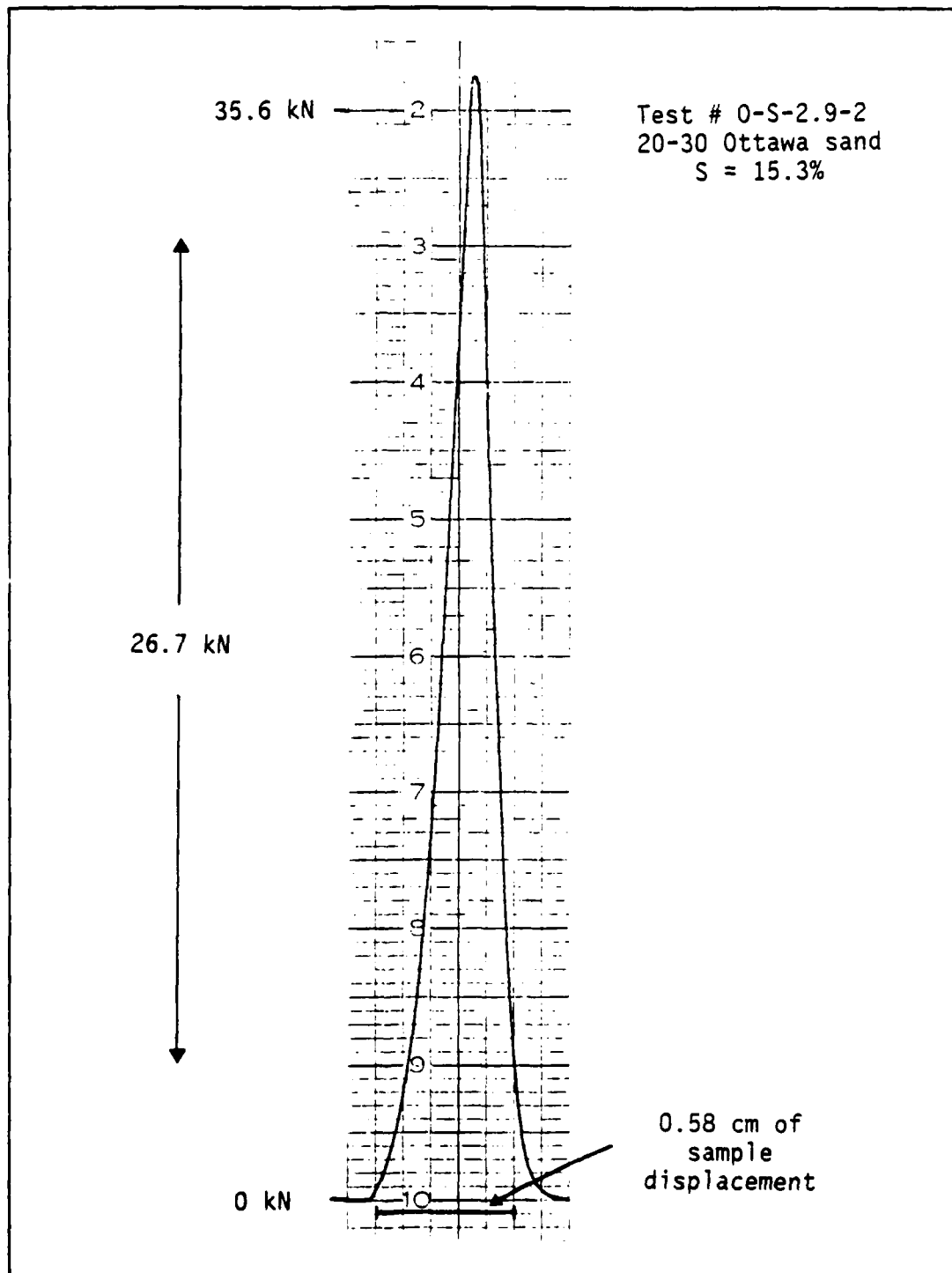


Figure 4.14 Typical Strip-Chart Recorder Load-Time History for Quasi-Static Tests

Table 4.7 Quasi-Static Constrained Modulus Values for 20-30 Ottawa Sand at Various Saturation Levels

SAMPLE NUMBER	SATURATION (%)	VOID RATIO	D INITIAL (kPa)	D RELOAD (kPa)
0-1	0.0	0.51	611531	698891
0-2	0.0	0.51	627211	698891
4.5-1	7.9	0.51	582407	764414
2-1	11.4	0.51	611531	698891
3-1	14.0	0.51	555937	679475
2.9-2	15.3	0.51	611531	741247
3.7-1	19.1	0.51	596611	723706
2.9-1	39.8	0.51	509609	_____

Table 4.8 Quasi-Static Constrained Modulus Values for Eglin Sand at Various Saturation Levels

SAMPLE NUMBER	SATURATION (%)	VOID RATIO	D INITIAL (kPa)	D RELOAD (kPa)
0-1	0.0	0.51	436805	661113
0-2	0.0	0.51	394532	643717
5.9-1	23.8	0.51	317680	543581
8.8-1	25.9	0.51	370627	596611
4.4-1	26.0	0.51	370627	568865
2.9-2	27.6	0.51	407688	627211
4.4-2	29.8	0.51	376329	611531
2.2-2	44.6	0.51	339737	543581
2.9-1	46.8	0.51	344522	568865
2.2-1	52.7	0.51	354506	568865
1.5-1	76.2	0.51	344522	555937
1.5-2	76.4	0.51	382204	643717

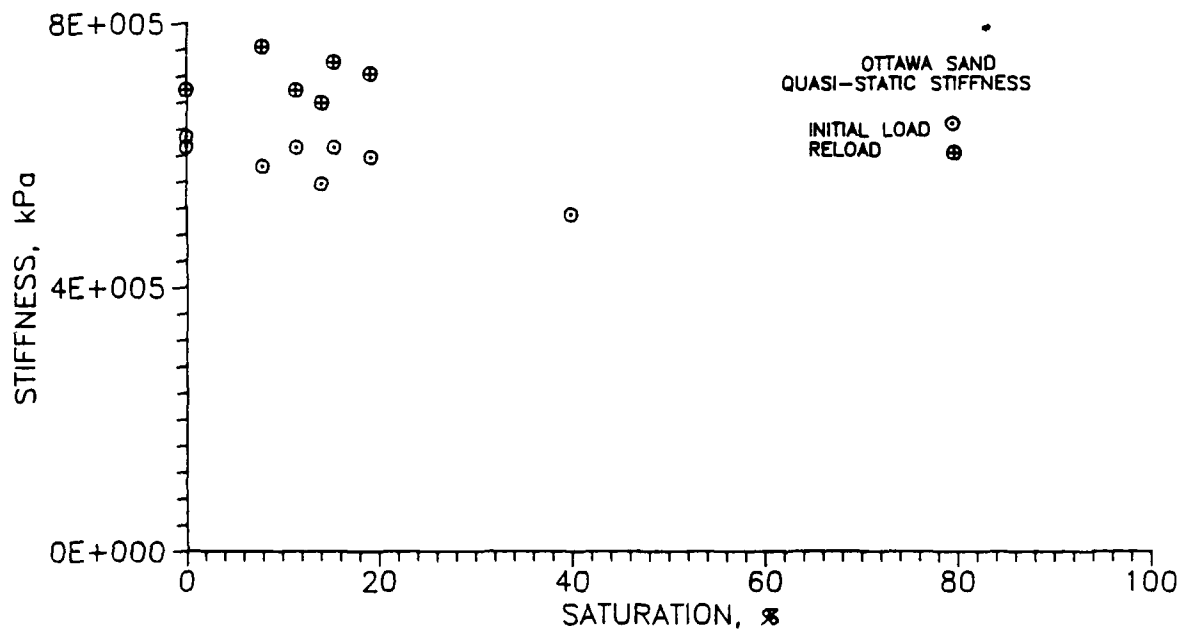


Figure 4.15 Quasi-Static Constrained Modulus Versus Saturation for 20-30 Ottawa Sand

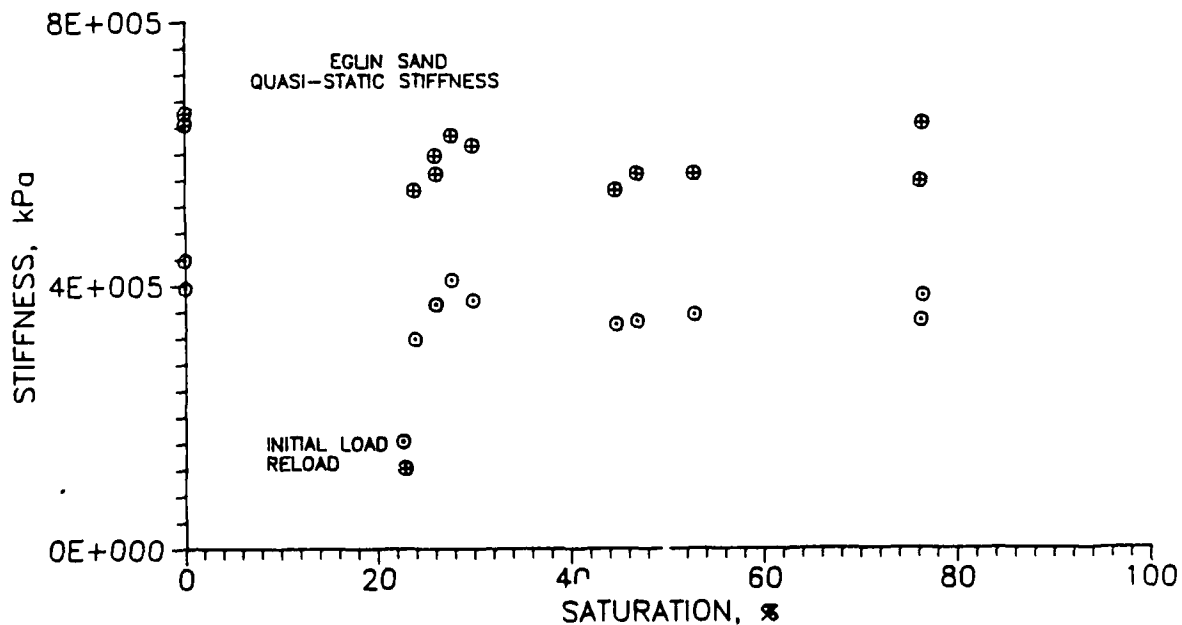


Figure 4.16 Quasi-Static Constrained Modulus Versus Saturation for Eglin Sand

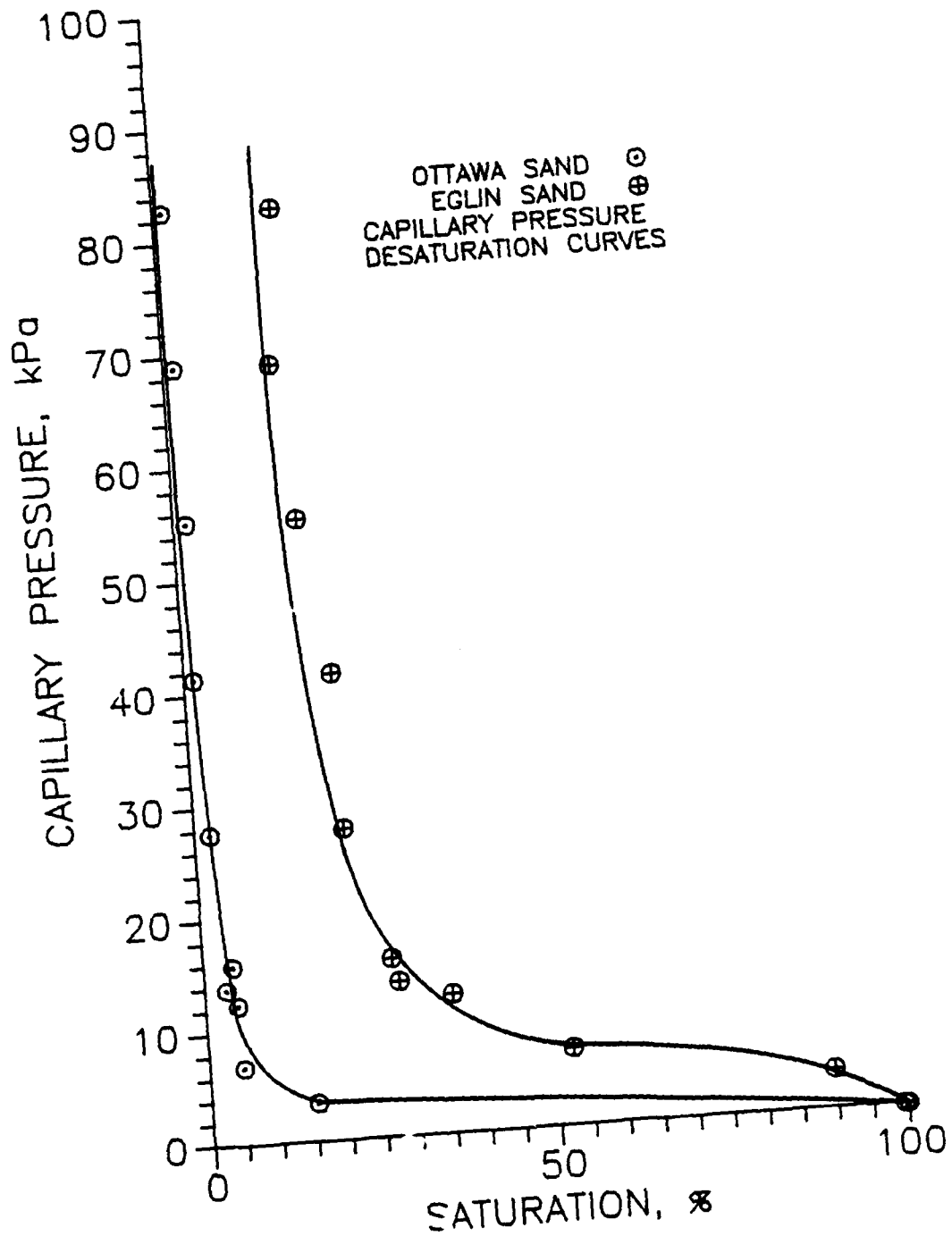


Figure 4.17 Capillary Pressure-Desaturation Curve for 20-30 Ottawa and Eglin sands

V. ANALYSIS OF RESULTS

A. PRESENT INVESTIGATION

1. General Observations

The wave velocity, stress transmission and quasi-static confined compression tests all seem to show the same trend as saturation is increased. In general, the values of wave velocity, stress transmission and quasi-static constrained modulus decrease slightly as the saturation level increases up to approximately 80 percent. Above this saturation level the dynamic test results show an increase in wave velocity and stress transmission. This may occur because the compressive wave front begins to travel through the water phase as saturation is increased during the high strain testing. This effect was theorized by Whitman (1970) and discussed in Chapter 2. Quasi-static stiffness tests on both sands have shown that the constrained modulus also decreases with increasing saturation. The variation in stiffness which occurred with changes in saturation was as much as 20 percent.

Comparing the dynamic tests results performed under different triaxial confining stresses shown in Figures 4.4 through 4.11, it appears that the confining stress increases the wave velocity and stress transmission. At high confining stresses, the wave velocity and transmission ratio still decreases with increasing saturation

levels. Therefore, confining stress has shifted the results without affecting the general trends observed. Based on the two confining stresses used, wave velocity varies with the total applied stress (confining and dynamic stress) based on the following equations for the 20-30 Ottawa and Eglin sands, respectively:

$$V_c = 47.3 \sigma^{0.5} \quad (R^2 = 0.85) \quad (5.1)$$

$$V_c = 5.7 \sigma^{0.3} \quad (R^2 = 0.94) \quad (5.2)$$

There is no definitive reason for the scatter obtained in this investigation, though several conclusions can be drawn. Since it occurs in both the dynamic and quasi-static test results the scatter is not a function of the strain rate. Comparing tests performed with 310 kPa confining stress with tests performed with zero confining stress, it appears that there is no variation in the scatter recorded. Sand type also has little effect as similar amounts of scatter occur for both the Ottawa and Eglin sands. Based on the above observations, the amount of scatter obtained may be due to sample preparation differences, interparticle variations within the compacted sand specimens or end effects between the pressure bars and the sand sample. Nimmo and Akstin (1988) express their concern that changes in humidity or temperature in the room where compaction takes place may affect the particle arrangement of sand specimens. From Figures 2.18 through 2.22, similar scatter was recorded by Ross et al. (1988).

Sample preparation errors were minimized by compacting, saturating and desaturating several samples simultaneously through the course of this investigation. Sample preparation was closely

controlled, resulting in a mean void ratio of 0.514, and a standard deviation of 0.010 for all specimens prepared.

It should be noted that there were no tests performed on the Eglin sand between saturation levels of zero and 23 percent. The residual saturation level as shown in Figure 4.17 prevented the Eglin sand from being desaturated below this value.

2. Prediction of Wave Velocity based on Quasi-Static Modulus

Compressive stress wave velocity can be predicted through equation 2.3 if the constrained modulus and total density of the soil are known. In order to determine if there are any strain rate effects in loading the Ottawa and Eglin sands, quasi-static moduli were used to predict the wave propagation velocities for each sand at various saturation levels. Because there was no data obtained under any other condition, this analysis is limited to dynamic tests performed at zero confining stress.

Figures 5.1 and 5.2 show the relationship between the wave velocities and transmission ratios determined from SHPB testing and those predicted by quasi-static modulus for 20-30 Ottawa sand. Figures 5.3 and 5.4 show the same relationships for the Eglin sand. The predicted values for transmission ratio were determined by equation 2.7 using the acoustic impedance of the steel and soil. The

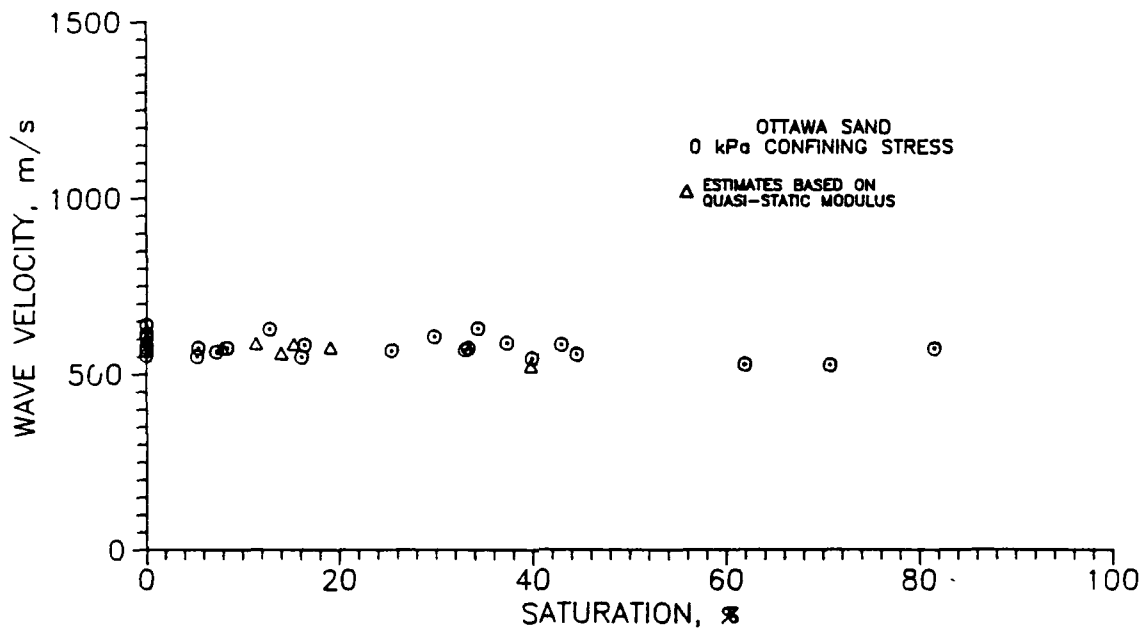


Figure 5.1 Wave Velocity Versus Saturation Results with Values Based on Quasi-Static Modulus for 20-30 Ottawa Sand Under Zero Confining Stress (Compacted Dry)

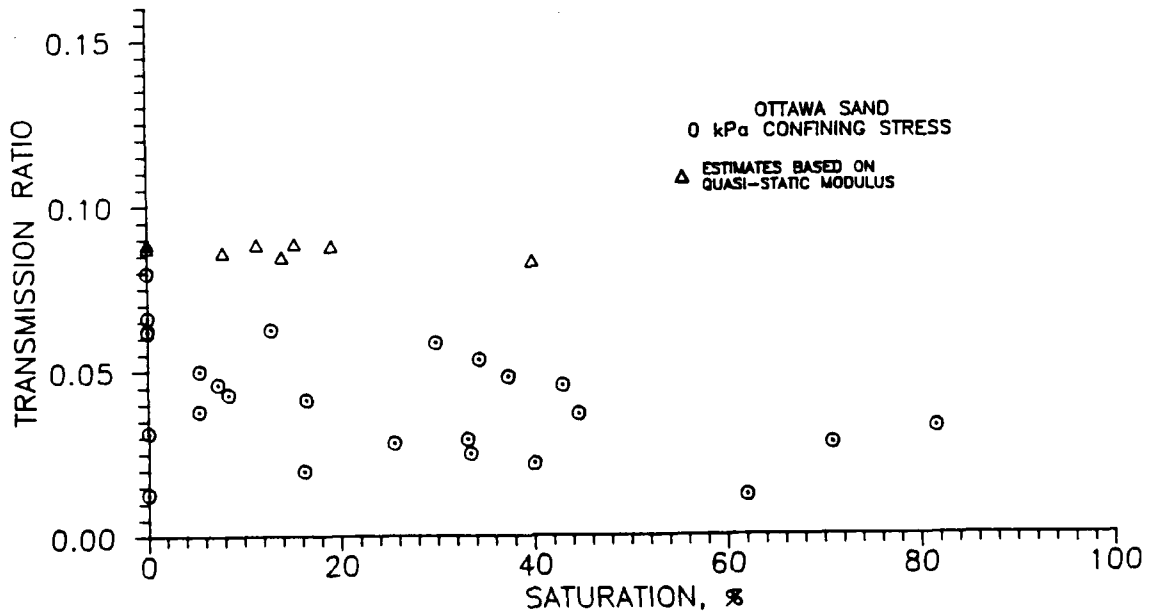


Figure 5.2 Transmission Ratio Versus Saturation Results with Values Based on Quasi-Static Modulus for 20-30 Ottawa Sand Under Zero Confining Stress (Compacted Dry)

acoustic impedance of the soil was calculated based on the predicted wave velocity and total density for each test.

The wave velocity values predicted from the quasi-static modulus are very similar to the experimentally determined dynamic values for both the Ottawa and Eglin sands. This would seem to show that the rate of loading does not affect the constrained modulus for either of the sands.

The predicted values of transmission ratio for both the Ottawa and Eglin sands are two to three times larger than the actual values obtained from SHPB testing. Equation 2.7, used to predict the transmission ratio values, is based on the assumption that no attenuation of the compressive wave occurs as it passes through the soil. The experimental results in Figures 5.2 and 5.4 show that a significant amount of attenuation occurs through the two sands.

3. Prediction of Wave Velocity based on Constant Modulus

If the capillarity of an unsaturated sand contributes to an increase in intergranular stress within the sand, an increase in wave propagation velocity would be expected due to the increase in modulus. If there is little contribution due to capillarity, a simple model can be developed to predict the wave velocity. The dry dynamic modulus (or as explained in the previous section, the dry quasi-static modulus) and the total density of the sand at a particular saturation level can be used in equation 2.3 to predict the wave velocity at any saturation level. Figures 5.5 through 5.8 show the wave velocity results obtained from the SHPB for each sand under the two confining

stresses. Also placed on the figures are the predicted wave velocities based on the average dry dynamic modulus for each sand and confining stress determined from equation 2.3. For the saturation levels used in this investigation, the model predicts the experimental results satisfactorily. Equation 2.3 shows that the water phase has little influence on the modulus of the soil, but influences the wave velocity through an increase in total density.

The transmission ratio can also be estimated from this model in the same manner described in the previous section. But it is of little use since equation 2.7 does not take attenuation effects into consideration.

4. Constrained Modulus in Terms of $(\sigma - u_a)$ and $(u_a - u_w)$

Fredlund and Morgenstern (1976) presented equation 2.13, discussed in Chapter 2, which relates the volumetric strain of the soil structure, ϵ_v , to the normal strain components. This is expressed by:

$$\epsilon_v = C_t d(\sigma - u_a) + C_w d(u_a - u_w) \quad (2.13).$$

This equation demonstrates that the strain is related to the stress components $(\sigma - u_a)$ and $(u_a - u_w)$ through the compressibility of the soil due to the solid and water phases.

A similar relationship can be determined between the stress components and the wave velocity of a compression wave propagating through soil. From equation 2.3 the compressive wave velocity is a function of the constrained modulus and the total density of the soil

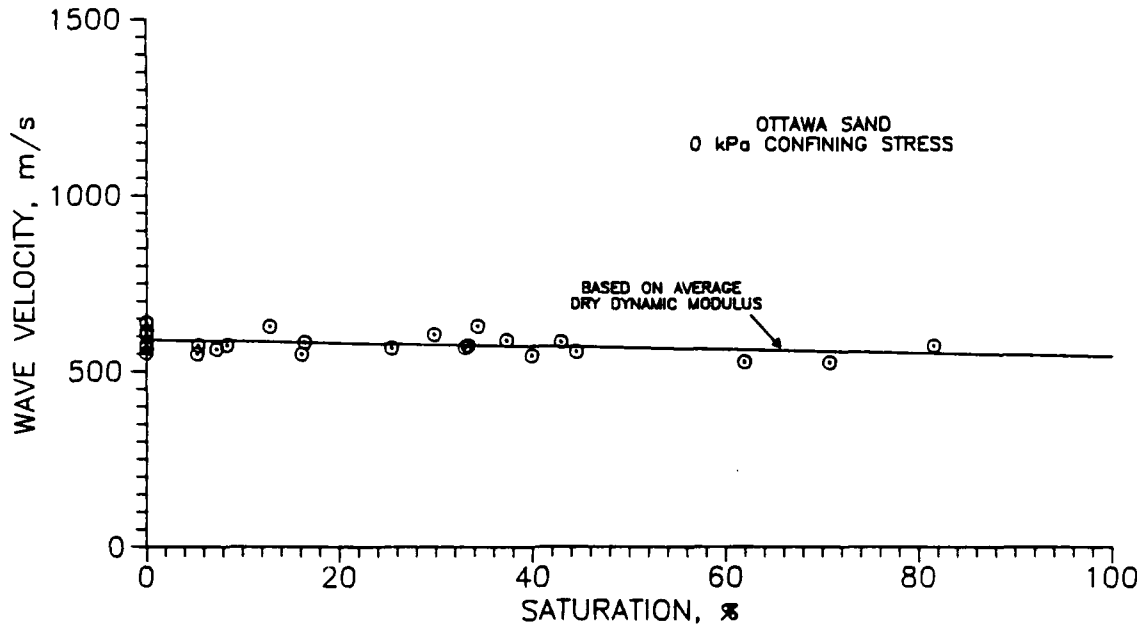


Figure 5.5 Wave Velocity Versus Saturation Model Based on Constant Modulus for 20-30 Ottawa Sand under Zero Confining Stress (Compacted Dry)

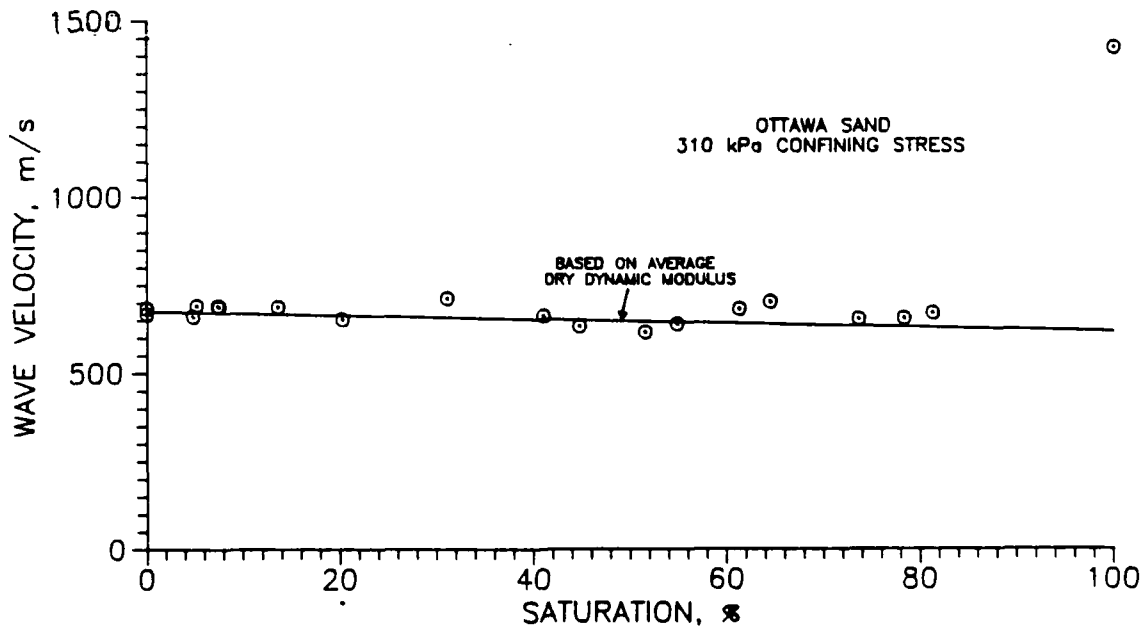


Figure 5.6 Wave Velocity Versus Saturation Model Based on Constant Modulus for 20-30 Ottawa Sand under 310 kPa Confining Stress (Compacted Dry)

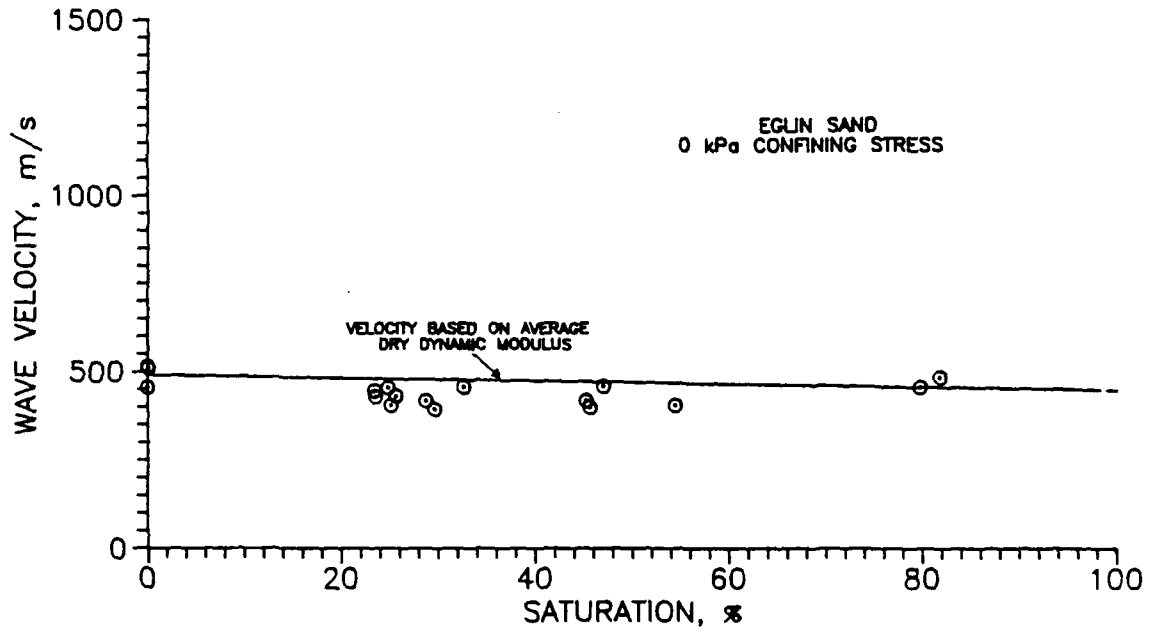


Figure 5.7 Wave Velocity Versus Saturation Model Based on Constant Modulus for Eglin Sand Under Zero Confining Stress (Compacted Dry)

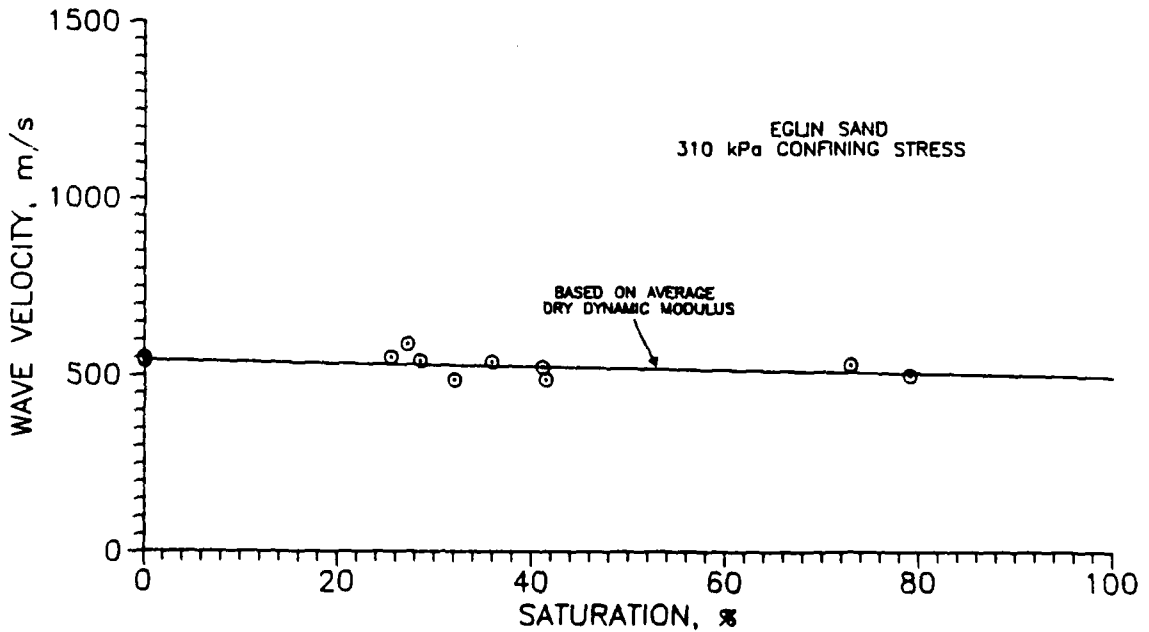


Figure 5.8 Wave Velocity Versus Saturation Model Based on Constant Modulus for Eglin Sand Under 310 kPa Confining Stress (Compacted Dry)

under confined compression. From equation 2.13 above, the modulus is a function of stress and strain, therefore the wave velocity squared multiplied by the total density ($V_c^2 \rho_t$) is a function of the stress and strain within the soil. The relationship between wave velocity and stress is not a constitutive equation, but it is useful in relating the wave velocity to the stress components ($\sigma - u_a$) and ($u_a - u_w$).

Figures 5.9 and 5.10 present the constrained modulus ($V_c^2 \rho_t$) (in kPa) as a function of the two stress components for both the Ottawa and Eglin sands. The total stress used in this analysis, σ , is the sum of the confining stress, σ_o , and dynamic stress, σ_D . The dynamic stress component is the average stress within the sample due to the dynamic loading. This value was calculated based on the SHPB incident and transmitted stress and the acoustic impedance of the steel and sand. The capillary pressure values used in the figures were based on the saturation levels of the sands prior to testing, and capillary pressure-desaturation curves given in Figure 4.17. The constrained modulus was determined from the average wave velocity through the sample and the total soil density.

Based on a linear regression analysis, the outline of the best-fit planes through the data is also presented. These best-fit planes can be used in predicting the modulus of the sand based on the applied stress and pore pressure conditions of the soil. Table 5.1 contains the equations for both of the best-fit planes presented.

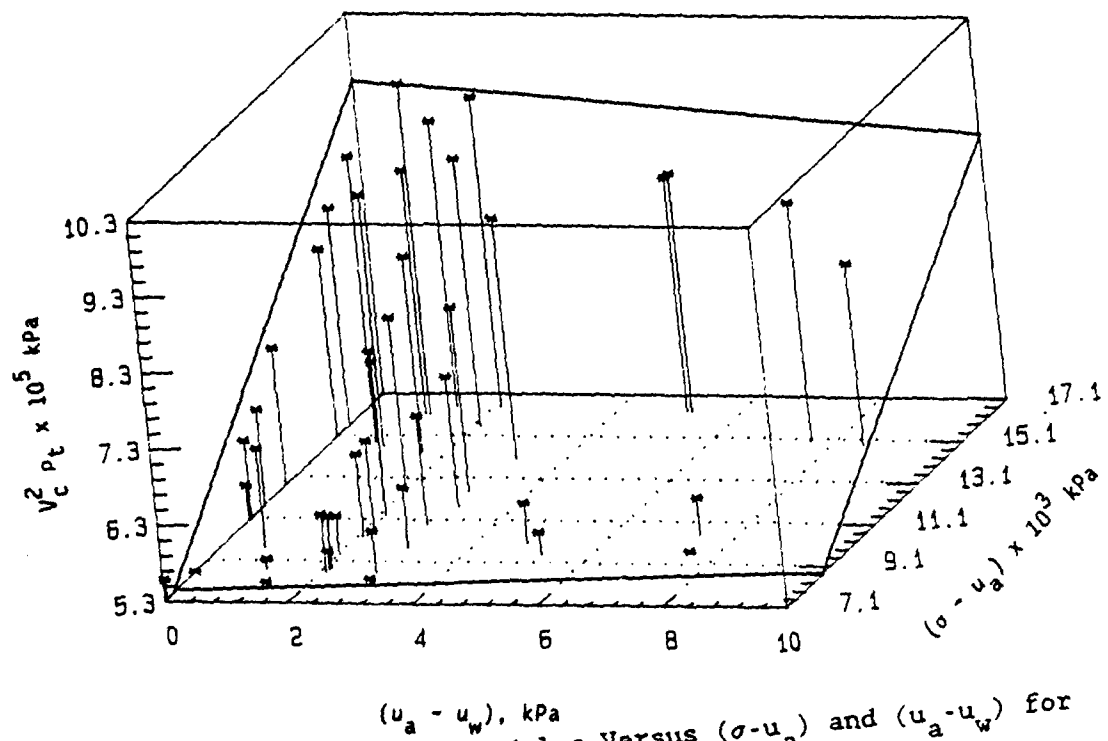


Figure 5.9 Constrained Modulus Versus $(\sigma - u_a)$ and $(u_a - u_w)$ for 20-30 Ottawa Sand (Compacted Dry)

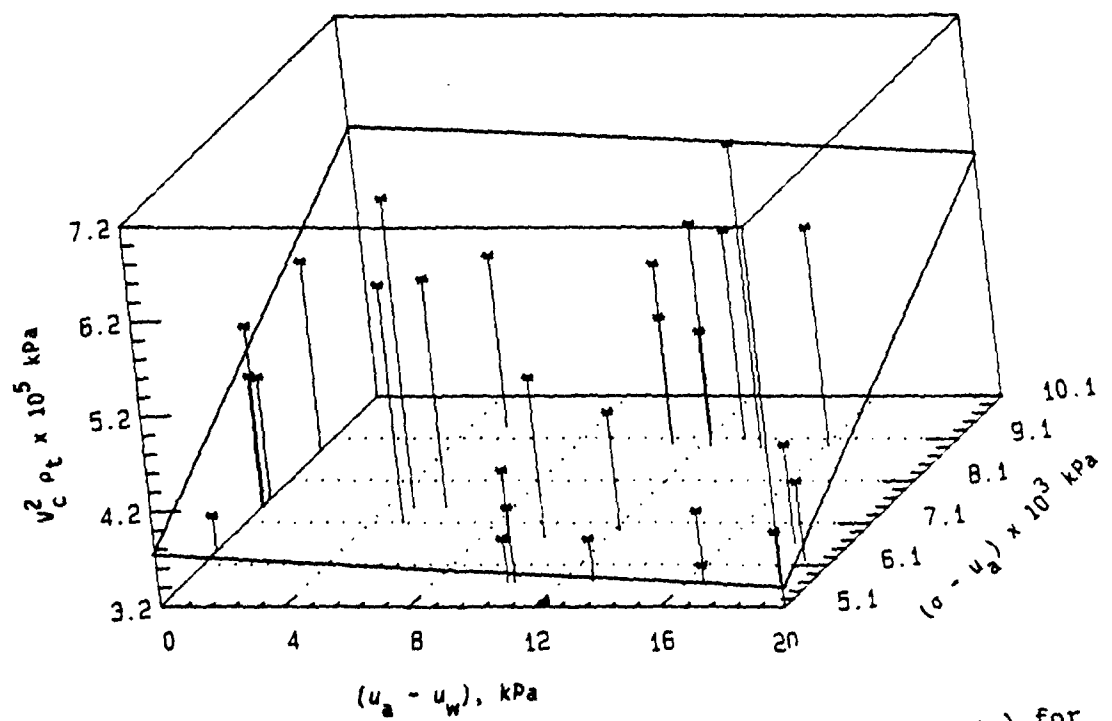


Figure 5.10 Constrained Modulus Versus $(\sigma - u_a)$ and $(u_a - u_w)$ for Eglin Sand (Compacted Dry)

Table 5.1 Equations for Multiple Regression Analysis Planes for Ottawa and Eglin Sands Based on Total Peak Applied Stress, Pore Pressure and Constrained Modulus

20-30 Ottawa Sand:

$$V_c^2 \rho_t = (2.024 - 0.056 * (u_a - u_w) + 0.0004 * (\sigma - u_a)) \times 10^5$$

$$R^2 = 0.901 \qquad s = 0.42$$

Eglin Sand:

$$V_c^2 \rho_t = (1.510 - 0.016 * (u_a - u_w) + 0.0004 * (\sigma - u_a)) \times 10^5$$

$$R^2 = 0.522 \qquad s = 0.63$$

From the slopes of the best fit lines in Figures 5.9 and 5.10, it appears that the pore pressure component, $(u_a - u_w)$ has little influence on the value of constrained modulus. When the pore water pressure is altered due to a change in saturation, the constrained modulus appears to be relatively unaffected. As the total stress, $(\sigma - u_a)$ increases, the constrained modulus generally increases, which is in agreement with the theory for stress-strain conditions under confined compression (see Figure 2.12). When the samples are compacted dry, Fredlund's theory supports the conclusion that the pore water has little influence in changing the values of constrained modulus for the ranges of saturation used in this investigation.

B. COMPARISON WITH THE RESULTS OBTAINED FROM PREVIOUS INVESTIGATIONS

1. Effects of Confining Stress

Figure 5.11 shows the results obtained by Hardin (1961) and Stoll and Ebeido (1965). Also shown are the results obtained in this investigation for dry 20-30 Ottawa sand under a confining stress of

310 kPa. The results obtained by Stoll and Ebeido show a considerable amount of scatter, but the wave velocities are greater than those obtained by Hardin. This follows theoretical predictions that a soil with some lateral constraint will have a higher modulus at higher stress levels resulting in higher wave velocities. The results obtained in this investigation have higher wave velocities than either of the other two sets of data. This was expected because the samples in this investigation were not allowed to strain laterally, and were subjected to larger dynamic stresses.

Using high stress, confined compression tests, Hendron (1963) determined that the constrained modulus varies with confining stress to the one-third power. From equation 2.3, the wave velocity would then be expected to be proportional to confining stress to the one-sixth power. This result is the same as that predicted by Duffy and Mindlin (1957) and Richart et al. (1970), based on a theoretical packing of spheres. Based on this relationship, the predicted wave velocities are lower than that obtained in the current investigation. There are several reasons for this difference. First, Hendron did not use 20-30 Ottawa or Eglin sands in his investigation. Differences in sand type may be responsible for the difference between the wave velocities obtained in this investigation and that based on Hendron's work. Also, equation 2.3 was developed for determining the wave velocity for a material which is within its elastic range.

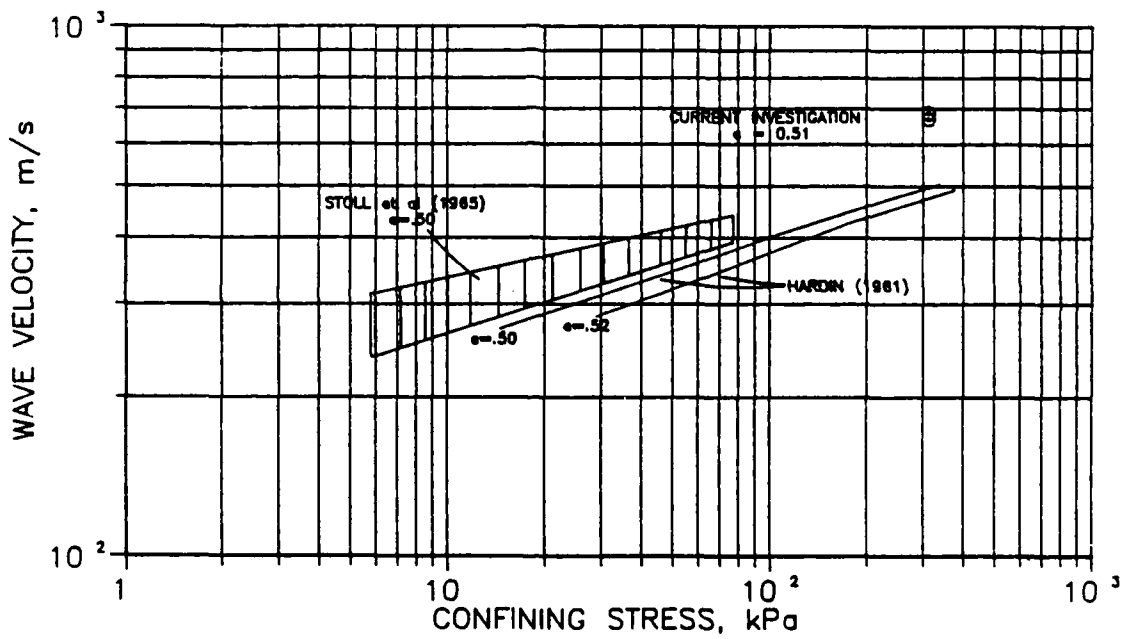


Figure 5.11 Confining Stress Versus Wave Velocity for Results Obtained by Hardin (1961), Stoll et al. (1965), and the Current Investigation for 20-30 Ottawa Sand (Compacted Dry)

2. Effects of Saturation

In this investigation it was found that the saturation levels between zero and 80 percent do not greatly influence the values of wave propagation velocity, transmission ratio or quasi-static stiffness for 20-30 Ottawa and Eglin sands compacted dry. If compacting a sample at different moisture contents is influential in determining the wave velocity parameters and static stiffness, the results obtained by Calhoun and Kraft (1966), Hendron et al. (1969), Wu et al. (1984), and Ross et al. (1988) should be similar because all samples were compacted moist to a particular saturation level prior to testing. Because the samples were compacted dry in this investigation, the results obtained would be expected to be different. As discussed in Chapter 2, the results obtained by Ross et al. (for constrained modulus) and Wu et al. (for shear modulus) show the greatest increase in stiffness occurs at intermediate saturation levels. The results obtained by Calhoun and Kraft, and Hendron et al. are very different. Soil type may be influential in the trends observed, but Wu et al. performed shear wave propagation tests on both sandy and silty soils and obtained similar trends. From the summary given in Chapter 2, all of the these researchers have compacted their samples by different methods. Based on the study by Mulilis et al. (1977), the method of sample compaction is a consideration which is as important as the amount of moisture used during compaction. The disparity in results obtained by the previous researchers may be attributed to both variations in sample preparation, and the types of testing apparatus used. The results obtained in this investigation

may also be attributed to the sample compaction process. It is apparent that before the variations in saturation levels can be evaluated, the method of compaction must first be considered.

3. Effects of Loading Rate

Whitman (1970) and Jackson et al. (1980) have concluded that loading rate effects in dry granular soils are an important consideration for rise times of less than one millisecond. The data obtained in this research shows that for the Ottawa and Eglin sands, compacted dry, then saturated, then desaturated, there are no rate effects occurring between samples loaded quasi-statically and those loaded with rise times of 15 microseconds (see Figures 5.1 through 5.3). The differences in results may be a function of the types of sand used and the high dry densities used in this investigation.

4. Model Comparisons

a. Whitman (1970)

Equation 2.14 presented by Whitman (1970) relates the compressive wave velocity to the dry soil modulus, specific gravity and saturation level. Wave velocities have been computed from this equation based on the dry moduli of the Ottawa and Eglin sands under both confining stresses. The results are presented along with the experimental data from this investigation in Figures 5.12 through 5.15. As shown in the figures, the model proposed by Whitman

accurately describes the experimental data. Figure 5.13 shows that the model is still accurate at almost complete saturation.

Whitman's model shows that at lower saturation levels there is little contribution by the water phase in changing the modulus of the soil. Whitman's model takes into account the increase in wave velocity as saturation levels approach 100 percent, which is an improvement over the previous model at higher saturation levels. It is interesting to note that at lower saturation levels, the results of this model are almost identical to the previously described model, which is based on constant dry modulus.

b. Anderson and Hampton (1980)

The model presented by Anderson and Hampton (1980) was developed to determine the compressive wave velocities through gassy sediments. Presented in Figures 5.16 and 5.17 are results based on the model along with the data obtained in this investigation for the Ottawa and Eglin sands under zero confining stress. The velocity data is presented as a ratio of the moist wave velocity divided by the average dry wave velocity for each sand.

Figures 5.16 and 5.17 show that the model does not accurately represent the data obtained in this investigation. The model predicts the wave velocity results to be much lower than those determined experimentally.

This model is based on a modified rule of mixtures for soil particles suspended in a fluid and was developed for the determination of wave velocities in soft ocean sediments. The accuracy of the model

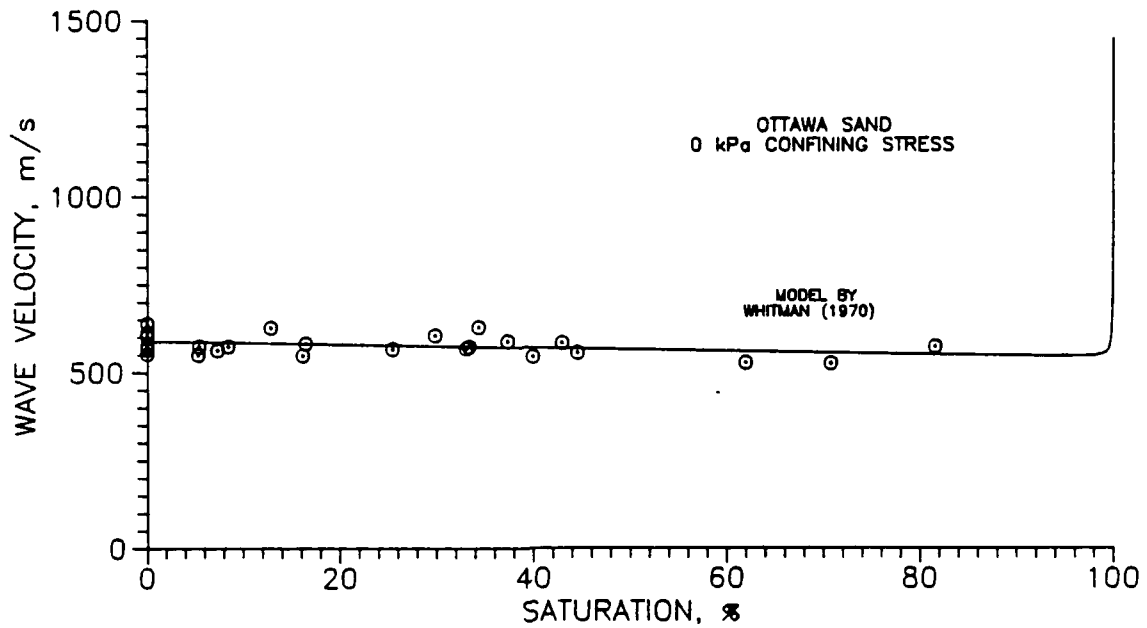


Figure 5.12 Wave Velocity Versus Saturation Results with Model Proposed by Whitman (1970) for 20-30 Ottawa Sand Under Zero Confining Stress (Compacted Dry)

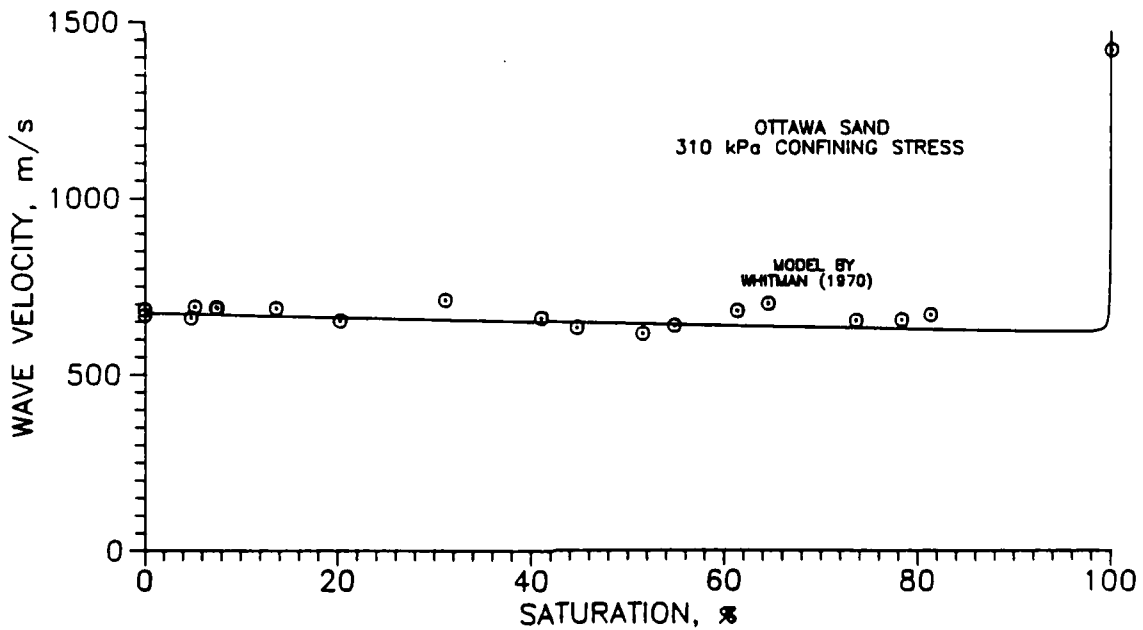


Figure 5.13 Wave Velocity Versus Saturation Results with Model Proposed by Whitman (1970) for 20-30 Ottawa Sand Under 310 kPa Confining Stress (Compacted Dry)

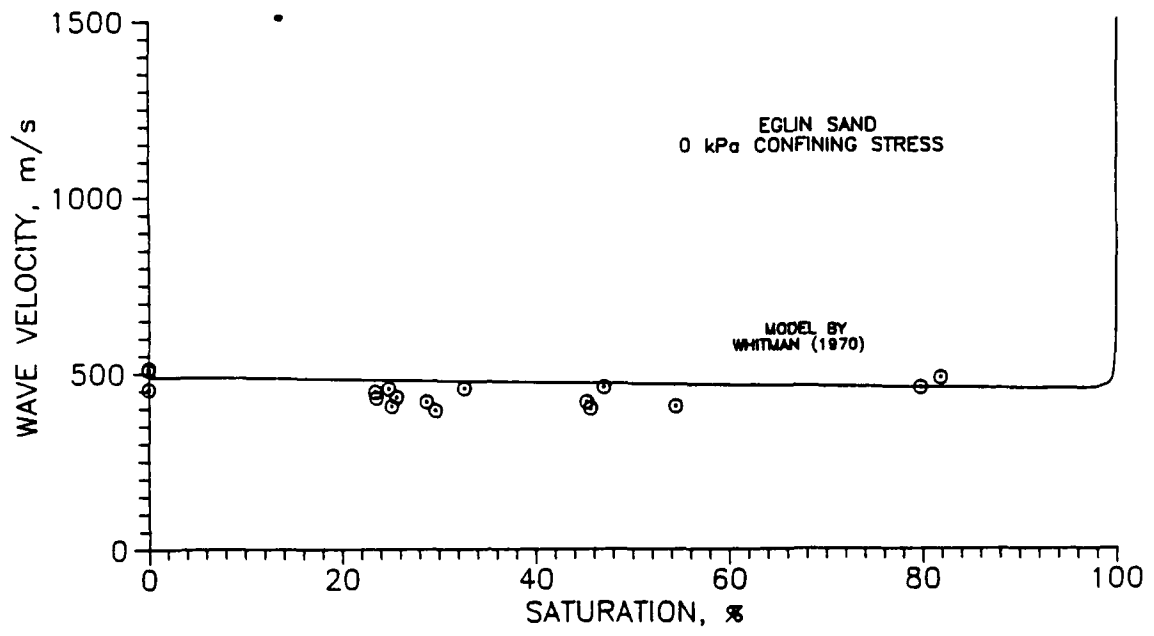


Figure 5.14 Wave Velocity Versus Saturation Results with Model Proposed by Whitman (1970) for Eglin Sand Under Zero Confining Stress (Compacted Dry)

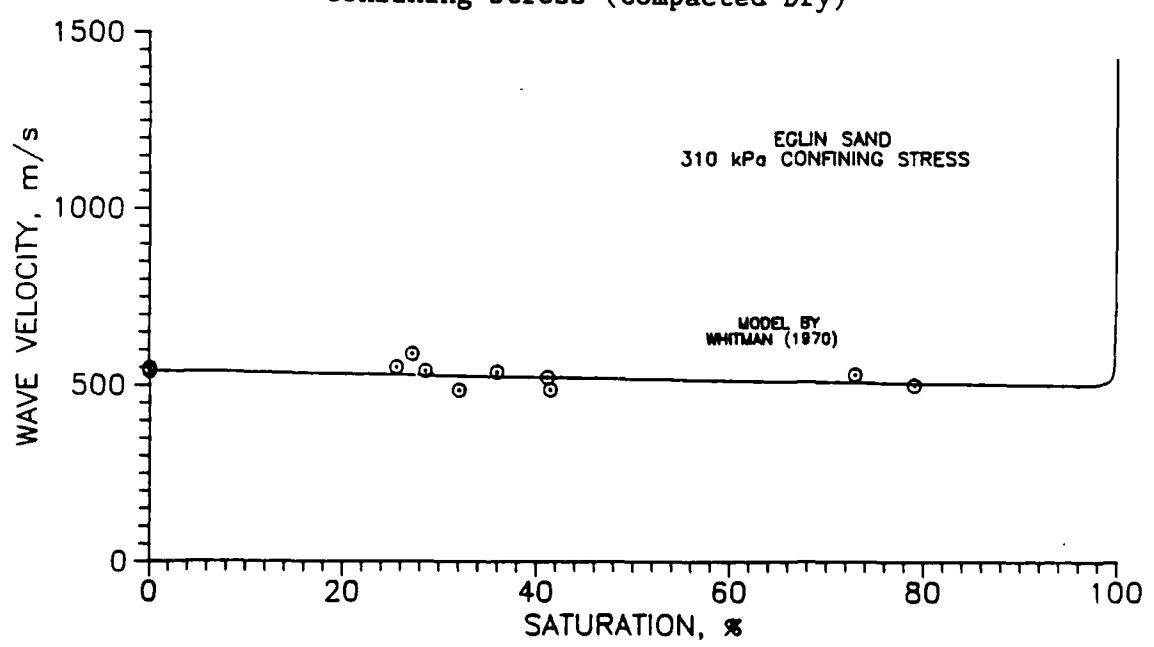


Figure 5.15 Wave Velocity Versus Saturation Results with Model Proposed by Whitman (1970) for Eglin Sand Under 310 kPa Confining Stress (Compacted Dry)

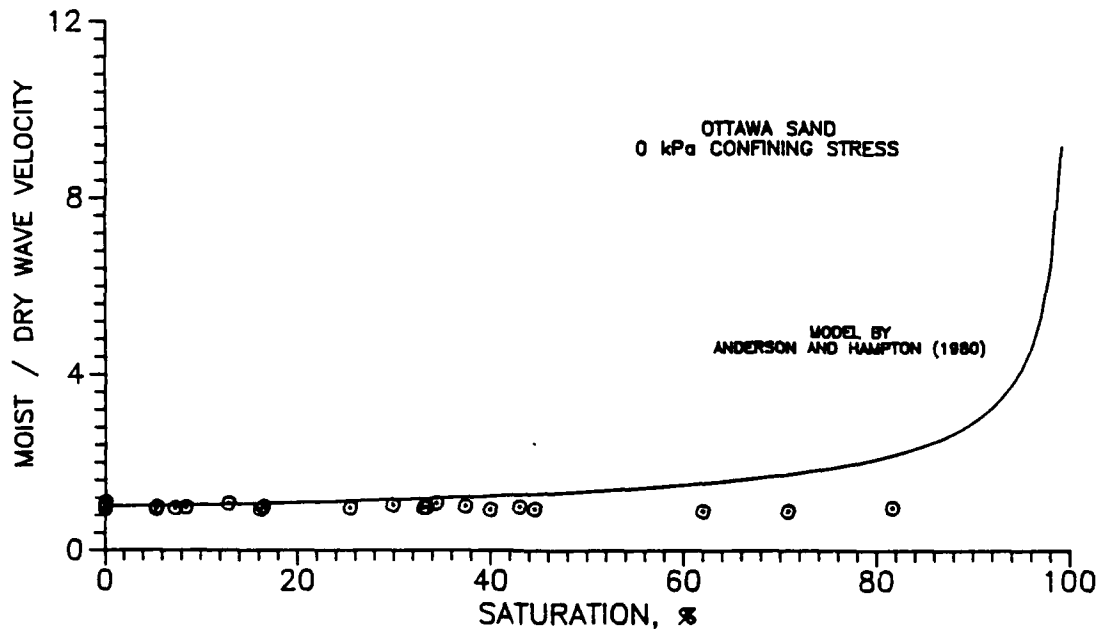


Figure 5.16 Wave Velocity Versus Saturation Results with Model Proposed by Anderson and Hampton (1980) for 20-30 Ottawa Sand Under Zero Confining Stress (Compacted Dry)

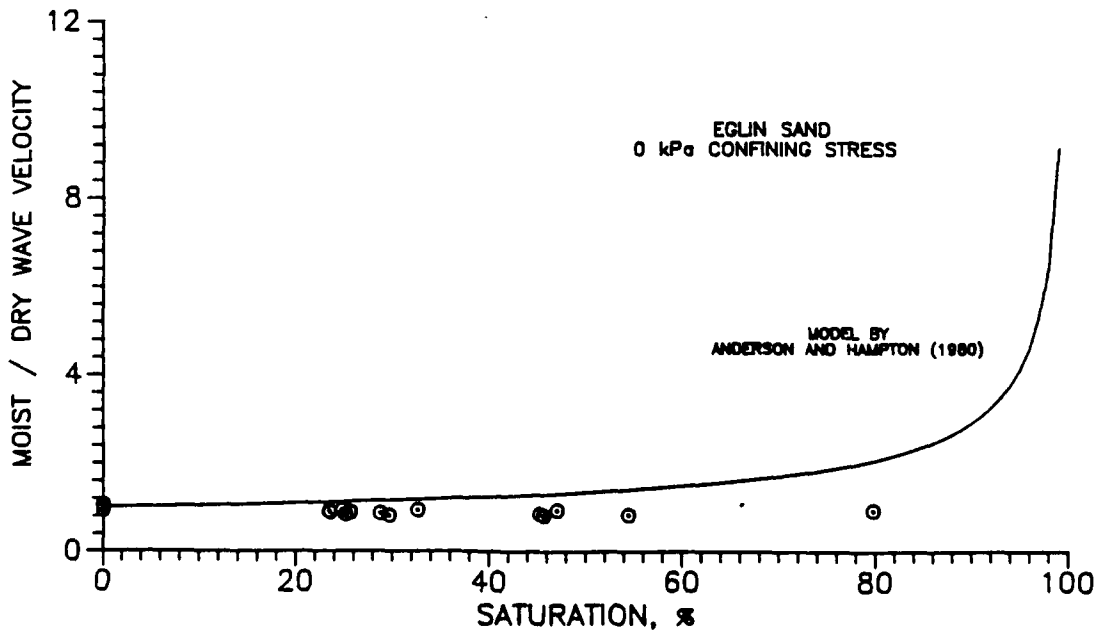


Figure 5.17 Wave Velocity Versus Saturation Results with Model Proposed by Anderson and Hampton (1980) for Eglin Sand Under Zero Confining Stress (Compacted Dry)

increases as the saturation levels approach 100 percent. The differences at lower saturation levels occur because the compressibility of the dry soil in the model is dependent on the compressibility of air. This combined compressibility will be very low, therefore the predicted wave velocities are very low. Since the saturation levels used in this investigation are well below 100 percent, this model does not fit the data with sufficient accuracy.

5. Results obtained by Ross et al. (1988)

All testing performed by Ross et al. (1988) and that performed in this investigation utilized the same SHPB, soil types, saturation ranges, and dry densities. The general trends for wave velocity, stress transmission and quasi-static modulus tests performed by Ross et al. (given in Figures 2.18 through 2.22), are considerably different than those obtained in this investigation. Figures 5.18 and 5.19 show the values of wave velocity and stress transmission ratio obtained for Eglin sand by Ross et al. Also on the figures are the results obtained in this investigation. A similar relationship occurs with quasi-static modulus. The difference in results could be due to differences in the sample containers used, or the moisture content of the sand during compaction. All other factors were consistent in both investigations.

The sample container used by Ross et al. was a thick-walled steel specimen container designed to prevent lateral expansion. Figures 4.12a and b show that when samples were compacted moist in the specimen cell used in this investigation, the wave velocities are

similar to those obtained by Ross et al., and are markedly higher than those obtained in this investigation when the samples were compacted dry, then brought to the same saturation level. The results obtained by both investigations for dry compacted samples show similar results and scatter for values of wave propagation velocity and stress transmission ratio. This would seem to rule out any possibility for differences in sample containers being responsible for the differences in trends observed.

Based on the above discussion, the only differences in sample preparation techniques which could account for the difference in trends is that Ross et al. compacted the samples moist, while in this investigation they were compacted dry then brought to the same saturation level. It appears that there is something inherent in the compaction process which is causing differences to occur when relating velocity, transmission ratio and quasi-static constrained modulus to saturation level using different compaction techniques.

From the discussion in Chapter 2, several investigators have concluded that sample compaction procedures create differences in the behavior of the soil during testing. Changes in liquefaction potential (Mulilis et al., 1977), cyclic stability (Ladd, 1977) and permeability (Juang and Holtz, 1986; Nimmo and Askin, 1988), have been attributed to variations in the sand fabric or grain orientations created during the compaction process.

The energy compaction curve presented by Ross (1989) shown in Figure 2.11 shows that variations in saturation level of moist sands during compaction will affect the energy required to compact a sample

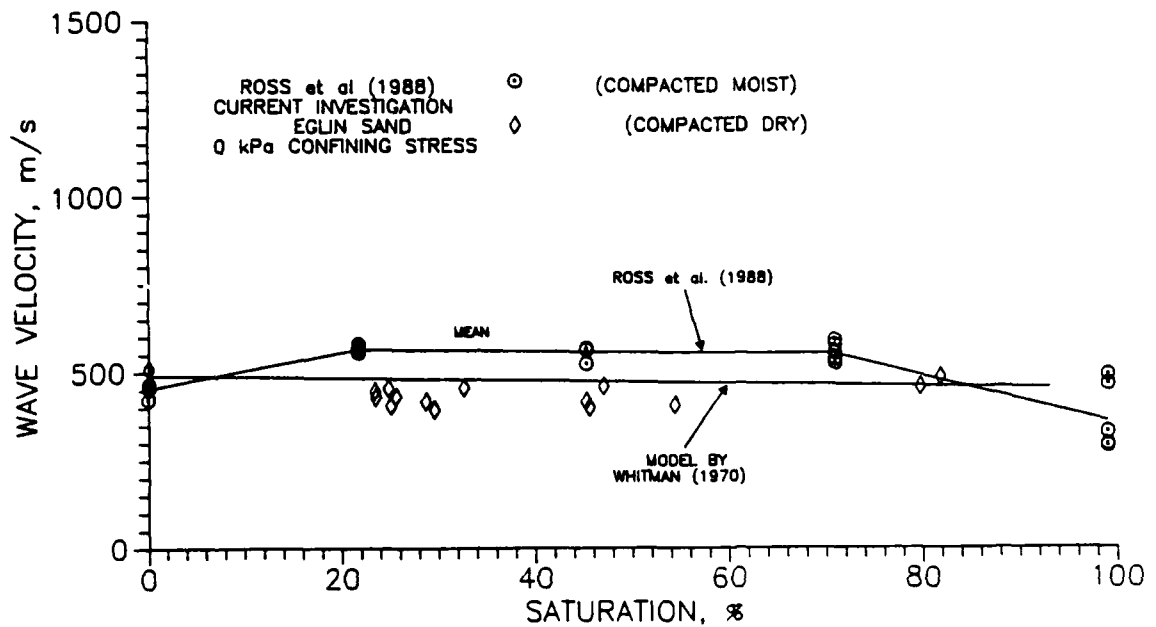


Figure 5.18 Wave Velocity Values Obtained by Ross et al. (1988) and in the Current Investigation for Eglin Sand Under Zero Confining Stress

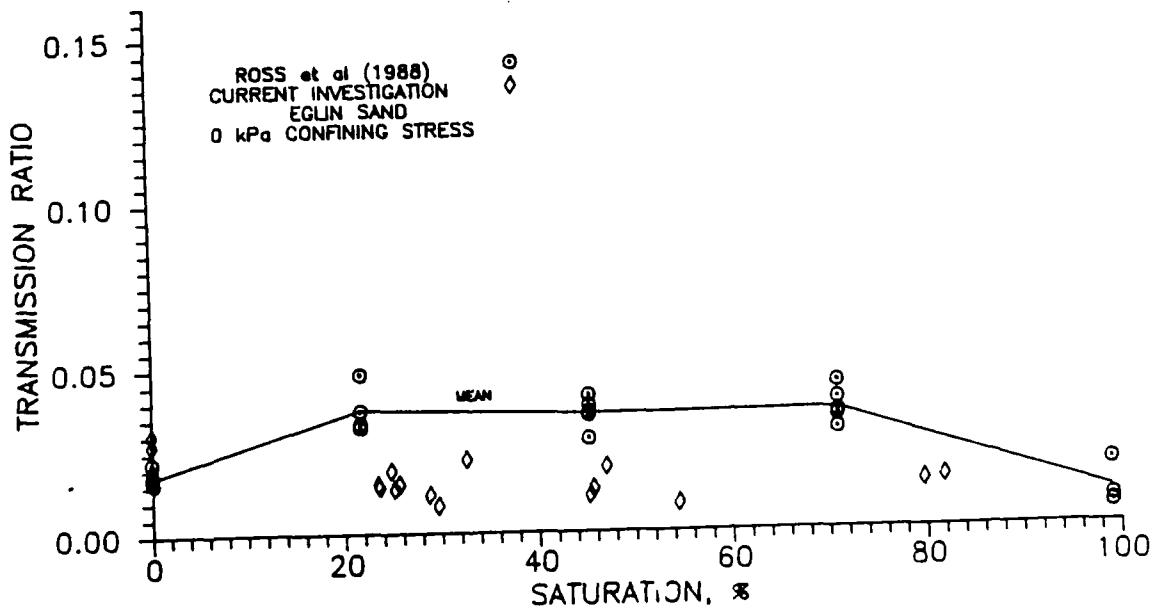


Figure 5.19 Stress Transmission Ratio Results Obtained by Ross et al. (1988) and in the Current Investigation for Eglin Sand Under Zero Confining Stress

to a constant dry density. If this energy variation is due to capillary forces between the sand particles, the theory by Ladd (1977) would predict that the most random fabric should occur during compaction when the capillary stress is a maximum. From Figure 2.11, this occurs between saturation levels of 20 to 40 percent. From the results presented by Ross et al. (Figures 2.18 through 2.24), the maximum wave velocity, stress transmission and constrained modulus values occur when the capillary stress in the soil is high. It may be concluded that the more random fabric creates higher values of wave propagation velocity, stress transmission and quasi-static constrained modulus.

Based on the studies by Juang and Holtz (1986) and Nimmo and Askin (1988), sands compacted dry have a larger range of pore sizes than sands compacted moist. For sands compacted moist to the same void ratio, the distribution of pore sizes is more uniform and generally smaller than when compacted dry. Based on the results obtained by Ross et al. (1988) this uniform distribution of pore sizes makes the sand less compressible under quasi-static and dynamic loading conditions.

For the samples of Eglin sand compacted moist, oven dried, then tested on the SHPB, Figure 4.13a shows the values of wave velocity are somewhat higher than the average values obtained for specimens compacted and tested dry. The transmission ratio results did not appear to be effected as much by the procedure as shown in Figure 4.13b. If the wave velocity results are correct, there may be a difference in fabric between samples compacted moist and dry, and

once the fabric is formed, it will not change once the moisture is removed.

It is also possible that sands compacted under various moisture contents will have different amounts of lateral (or confining) stress "locked in", that is, the sand is being overconsolidated by different amounts depending on the molding water content. This will effectively increase the stress within the sample. As discussed in Chapter 2, cyclic loading has been shown to change the value of K_0 for sands and silts (Drnevich et al., 1967; D'Appolonia et al., 1969; Lambe and Whitman, 1969; Youd and Craven, 1975). There is also a small amount of data suggesting values of K_0 vary under static confined compression for samples molded under different water contents (Hendron et al., 1969).

From this investigation it has been found that total applied stress varies with wave velocity to the second or third power, depending on sand type. Hardin (1961) has shown that based on his experimentation, confining stress is proportional to wave velocity to the fourth power, while Duffy and Mindlin (1957) and Richart et al. (1970) show that confining stress is proportional to wave velocity to the sixth power when based on the theoretical packing of spheres. From these relationships, a small increase in confining stress will cause a very large increase in wave velocity. If the amount of lateral confining stress stored in a sand is dependent on moisture content during compaction, a small change will cause large changes in wave velocity and transmission ratio.

Figure 5.20 shows the results obtained in this investigation for the Eglin sand under both zero and 310 kPa confining stress. Also in the figure are the results obtained by Ross et al. (1988) for Eglin sand under zero confining stress. It may be concluded that at intermediate saturation levels, the samples prepared by Ross et al. contain an "equivalent" confining stress locked in the soil with a value near 310 kPa. In order to quantify the actual values of equivalent confining stress, controlled tests must be performed to measure the change in confining stress during the compaction process.

One of the objectives on this investigation was to determine how fluctuations in saturation level will affect compressive stress wave velocity and stress transmission. It appears that based on the study performed by Ross et al. (1988), and the current investigation, the moisture content during compaction is very important in determining the dynamic properties of an unsaturated sand. From this investigation it was found that capillarity in itself does not appear to greatly affect the dynamic or static stiffness of sands. Therefore, when sands are compacted dry, variations within the saturation ranges used in this study will not greatly effect soil stiffness under static or dynamic conditions. It is the moisture content at which a sand is compacted that appears to influence the fabric and grain orientation of a sand, or change it's stress state. Based on a limited amount of data, the grain orientations or the stress state will remain within the sand, independent of changes in saturation level over time.

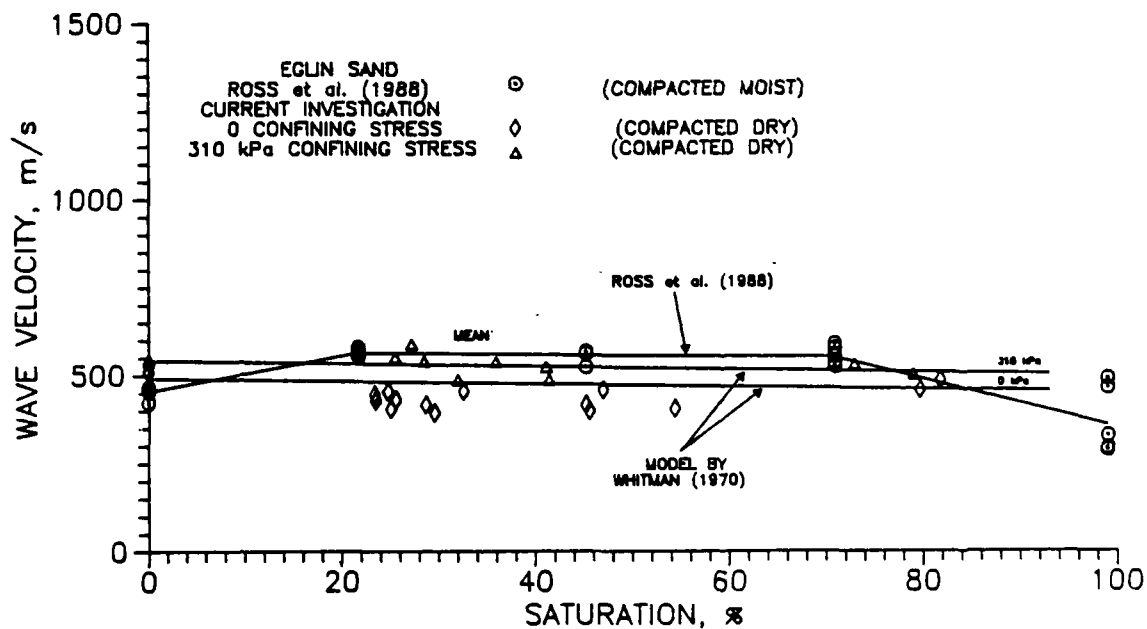


Figure 5.20 Wave Velocity Values Obtained by Ross et al. (1988) and in the Current Investigation for Eglin Sand Under Zero and 310 kPa Confining Stress

VI. SUMMARY, CONCLUSIONS AND RECOMMENDATIONS

A. SUMMARY

This investigation has studied the effects of saturation level and compaction technique on the parameters of compressive stress wave propagation in sands. Many soils in the field are in an unsaturated state, so research in this area is useful in understanding soil-structure interaction due to blast or impact loadings.

Dynamic wave propagation tests were performed utilizing a split-Hopkinson pressure bar, which applied high strain, short duration compressive loadings to the sand specimens. Values of wave propagation velocity and stress transmission ratio were measured for two sand types. Samples were prepared by compacting the sand dry to a constant density, then saturating, and then desaturating the samples by use of a pressure plate apparatus. Saturation levels were varied from zero to 82 percent. During testing, specimens were allowed to strain one-dimensionally under triaxial confining stress of either zero or 310 kPa. Quasi-static compression tests were also performed to determine the relationship between the results obtained dynamically and under quasi-static conditions.

For the range of saturation studied, the test results show that the values of wave velocity and stress transmission ratio decrease slightly with an increase in saturation for both confining

stresses used. Values of quasi-static constrained modulus vary in a similar manner. The results obtained for wave propagation velocity are closely predicted by Whitman's (1970) model given in equation 2.14.

The trends obtained in this investigation are much different than that presented by Ross et al. (1988) for the same soil types and dry densities. Their tests were performed on the same apparatus as in this investigation, but the samples were compacted moist to the required saturation levels. Changes in liquefaction potential (Mulilis et al., 1977), cyclic strength (Ladd, 1977), and permeability (Juang and Holtz, 1986; Nimmo and Askin, 1988) have been attributed to variations in compaction technique. Research also suggests that the method of sample compaction may also effect the amount of lateral or confining stress stored within the sand structure (Drnevich et al., 1967; D'Appolonia et al., 1969; Lambe and Whitman, 1969; Youd and Craven, 1975). It appears from the current investigation that the moisture content of the sand during compaction is very influential in determining the values of wave velocity, transmission ratio and quasi-static constrained modulus for sands. In particular, compacting samples at different moisture contents may influence the fabric and grain orientation of the sand or change the stress state in the sand.

B. CONCLUSIONS

The objective of this study is to determine how moisture content during compaction, saturation level, and confining stress affect the values of wave velocity, stress transmission ratio and

quasi-static constrained modulus. From this experimental laboratory investigation performed on 20-30 Ottawa and Eglin sands, several conclusions can be made.

The most significant conclusion reached is that the sand compaction process is very influential in determining the values of wave velocity, stress transmission, and quasi-static constrained modulus. Ross et al. (1988) determined that sands which are compacted moist at intermediate saturation levels have values of wave velocity, stress transmission, and stiffness which can be as much as 20 percent higher than those compacted dry or very wet. When the 20-30 Ottawa and Eglin sands were compacted dry, then saturated, then desaturated in this investigation, the saturation level appeared to have little influence on the compressive stress wave parameters and quasi-static stiffness. It appears that when the sand is compacted dry, fluctuations in saturation level will not greatly effect the dynamic wave propagation parameters or quasi-static stiffness.

From this investigation and that performed by previous researchers, there are at least two possible reasons why compaction technique affects the static and dynamic parameters of sands. First, compacting sands at different saturation levels may effect the fabric and grain orientation of the sand particles. Secondly, it is also possible that variable amounts of lateral stress is stored within the sand during the compaction process, depending on the quantity of moisture in the sand during compaction. Even with these possible explanations, no definitive conclusions can be drawn from this investigation as to why the static and dynamic properties of the sands used in this investigation are affected by the compaction process.

Sand samples were compacted dry in this investigation to show the influence of moisture on the compaction process. Though it is not common practice to compact sands in the field in this manner, the results obtained based on this compaction method, and that performed by Ross et al. (1988) has shown that the stiffness of the soil is very dependent on the moisture content used. This infers that conventional field compaction methods of adding water during compaction will affect the stiffness of the sand. When laboratory data is used to predict the behavior of a sandy soil, it is very important that the samples be compacted in the same manner, and at the same moisture content as will be used in the field.

Increasing the confining stress around the sand increases the values of compressive wave velocity and stress transmission ratio. The wave velocity varies with confining stress to the one-third power for 20-30 Ottawa sand and to the one-half power for Eglin sand at the particular dry densities used in this study. For both confining stresses used, wave velocity and stress transmission decrease slightly with increasing saturation for samples compacted dry, saturated, then desaturated by use of the pressure plate method.

The theory presented by Fredlund (1986) accurately predicted that the capillary pressures developed in the sands which were compacted dry, then saturated, then desaturated would have little influence on the stiffness. The equation proposed by Bishop et al. (1960) for determining the change in effective stress in an unsaturated soil did not predict the variations in wave velocity, stress transmission and quasi-static stiffness for sands compacted in the same manner. The theory for effective stress presented by Bishop

et al. does predict the trends obtained by Ross et al. (1988). It should be noted though that this investigation has shown that trends obtained by Ross et al. (1988) are largely due to the compaction process.

C. RECOMMENDATIONS

From the results of this investigation and a review of the pertinent literature, the following recommendations for further research on wave propagation in moist sands are made.

- Study how sand grain fabric is affected by changes in moisture content and the compaction process.
- Determine the relationship between changes in lateral and axial stress with changes in moisture content during compaction.
- Perform wave propagation tests on sands compacted by several different methods to determine how wave velocity and stress transmission ratio results change.
- Develop an analytical or empirical method for predicting wave velocity and stress transmission ratio for different compaction techniques and saturation levels.

VII. REFERENCES

- ASTM (1987). Annual Book of ASTM Standards. American Society for Testing and Materials, Philadelphia, PA.
- Anderson, A. L. and Hampton, L. D. (1980). "Acoustics of Gas-Bearing Sediments, I. Background, and II. Measurements and Models." Journal of the Acoustic Society of America, Vol. 67, No. 6, 1865-1903.
- Balakrishna Rao, H. A. (1975). "One-Dimensional Compression of Partially Saturated Soils." Report No. AFWL-TR-73-177, Air Force Weapons Laboratory, Kirtland AFB, NM.
- Bishop, A. W., Alpan, I., Blight, G. E., and Donald, I. B. (1960). "Factors Controlling the Strength of Partially Saturated Cohesive Soils." Conference on Shear Strength of Cohesive Soils, ASCE, 503-532.
- Bishop, A. W. and Blight, G. E. (1963). "Some Aspects of Effective Stress in Saturated and Partially Saturated Soils." Geotechnique, Vol. 13, No. 3, 177-197.
- Calhoun, D. E., and Kraft, D. C. (1966). "An Investigation of the Dynamic Behavior of a Partially Saturated Silt with Applications to Shock-Wave Propagation." Technical Report No. AFWL-TR-65-176, Air Force Weapons Laboratory, Kirtland AFB, NM.
- Corey, A. T. (1986). Mechanics of Immiscible Fluids, 2nd Ed. Water Resources Publications, Littleton, CO.
- D'Appolonia, D. J., Whitman, R. V., and D'Appolonia, E. (1969). "Sand Compaction with Vibratory Rollers." Journal of the Soil Mechanics and Foundation Engineering Division, ASCE, Vol. 95, No. SM1, 263-284.
- Davies, R. M. (1948). "A Critical Study of the Hopkinson Pressure Bar." Philosophical Transactions of the Royal Society of London, Series A, Vol. 240, 375-457.
- Dowding, C. H. (1985). Blast Vibration Monitoring and Control. Prentice-Hall, Inc., Englewood Cliffs, N.J.
- Drnevich, V. P., Hall, J. R., Jr., and Richart, F. E., Jr. (1967). "Large Amplitude Vibration Effects on the Shear Modulus of Sand." Contract Report No. DA-22-079-eng-340 NWER Subtask 13.009, U.S. Army Engineer Waterways Experiment Station, CE, Vicksburg, MS.
- Duffy, J., and Mindlin, R. D. (1957). "Stress-Strain Relations and Vibrations of a Granular Medium." Applied Mechanics Division, ASME, Vol. 24, 585-593.

Felice, C. W. (1986). "The Response of Soil to Impulse Loads Using the Split-Hopkinson Pressure Bar Technique." AFWL-TR-85-92, Air Force Weapons Laboratory, Air Force Systems Command and Kirtland Air Force Base, NM.

Felice, C. W., Gaffney, E. S., Brown, J. A., and Olsen, J. M. (1987). "Dynamic High Stress Experiments on Soil." Geotechnical Testing Journal, GTJODJ, Vol. 10, 192-202.

Fletcher, E. B. and Poorooshasb, H. B. (1968). "Response of a Clay to Low Magnitude Loads Applied at a High Rate." Proceedings of the International Symposium on Wave Propagation and Dynamic Properties of Earth Material, Univ. of New Mexico, 781-786.

Foster, C. R. (1962). "Field Problem: Compaction." Foundation Engineering, G.A. Leonards (ed), McGraw-Hill, New York, NY, 1000-1024.

Fredlund, D. G. (1979). "Appropriate Concepts and Technology for Unsaturated Soils." Second Canadian Geotechnical Colloquium, Canadian Geotechnical Journal, Vol. 16, No. 1, 121-139.

Fredlund, D. G. (1986). "Soil Mechanics Principles that Embrace Unsaturated Soils." Proceedings of the Eleventh ICSMFE, San Francisco, Vol. 2, 465-472.

Fredlund, D. G., and Hasan, J. U. (1979). "One-Dimensional Consolidation Theory: Unsaturated Soils." Canadian Geotechnical Journal, Vol. 1, No. 3, 521-531.

Fredlund, D. G., Hasan, J. U., and Filson, H. L. (1980). "The Prediction of Total Heave." Fourth International Conference on Expansive Soils, Denver, CO, 1-17.

Fredlund, D. G., and Morgenstern, N. R. (1976). "Constitutive Relations for Volume Change in Unsaturated Soils." Canadian Geotechnical Journal, Vol. 13, No. 3, 261-276.

Fredlund, D. G., and Morgenstern, N. R. (1977). "Stress State Variables for Unsaturated Soils." Journal of Geotechnical Engineering, ASCE, Vol. 103, No. GT5, 447-466.

Hardin B. O. (1961). "Study of Elastic Wave Propagation and Damping in Granular Materials." Presented to the University of Florida, Gainesville, Fl, in partial fulfillment of the requirements for the degree of Doctor of Philosophy.

Hardin B. O., and Richart, F. E., Jr (1963). "Elastic Wave Velocities in Granular Soils." Journal of the Soil Mechanics and Foundation Engineering Division, ASCE, Vol. 89, No. SM1, 33-65.

Hendron, A. J. (1963). "The Behavior of Sand in One-Dimensional Compression." Thesis presented to the University of Illinois, Urbana,

IL, in partial fulfillment of the requirements for the degree of Doctor of Philosophy.

Hendron, A. J., Davisson, M. T., and Parolola, J. F. (1969). "Effect of Degree of Saturation on Compressibility of Soils from the Defence Research Establishment, Suffield." P.O. No. WESBPJ-68-67, U.S. Engineer Waterways Experiment Station, CE, Vicksburg, MS.

Holtz, R. D., and Kovacs, W. D. (1981). An Introduction to Geotechnical Engineering. Prentice-Hall, Englewood Cliffs, NJ.

Hopkinson, B. (1914). "A Method of Measuring the Pressure Produced in the Detonation of High Explosives or by the Impact of Bullets." Philosophical Transactions of the Royal Society of London, Series A, Vol. 213, 437-456.

Hryciw, R. D., and Dowding, C. H. (1987). "Cone Penetration of Partially Saturated Sands." Geotechnical Testing Journal, GTJODJ, Vol. 10, No. 3, 135-141.

Jackson, J. G., Jr., Ehrgott, J. Q., and Rohani, B. (1980). "Loading Rate Effects on Compressibility of Sand." Journal of Geotechnical Engineering, ASCE, Vol. 106, No. GT8, 839-852.

Jennings, J. E. B., and Burland, J. B. (1962). "Limitations to the Use of Effective Stresses in Partially Saturated Soils." Geotechnique, Vol. 12, No. 2, 125-144.

Juang, C. H., and Holtz, R. D. (1986). "Fabric, Pore Size Distribution, and Permeability of Sandy Soils." Journal of Geotechnical Engineering, ASCE, Vol. 112, No. 9, 855-868.

Klute, A. (1986). "Water Retention: Laboratory Methods." Methods of Soil Analysis, Part I. Physical and Mineralogical Methods. 2nd Ed. Soil Science Society of America, Publishers, Madison, WS, 635-661.

Kolbuszewski, J.J. (1948). "An Experimental Study of Maximum and Minimum Porosities of Sands." Proceedings of the Fourth International Conference for Soil Mechanics and Foundation Engineering, Rotterdam, Netherlands, Vol. 2, pp. 158-165.

Kolsky, H. (1949). "An Investigation of the Mechanical Properties of Materials at Very High Rates of Loading." Proceedings of the Physical Society, Section B, Vol. 62, 676-700.

Kolsky, H. (1963). Stress Waves in Solids. Dover Publications, Inc., New York, NY.

Ladd, R. S. (1977). "Specimen Preparation and Cyclic Stability of Sands." Journal of Geotechnical Engineering, ASCE, Vol. 103, No. GT6, 535-547.

Lambe, T. W., and Whitman, R. V. (1969). Soil Mechanics. John Wiley and Sons, New York, NY.

Lindholm, U. S. (1971). Techniques in Metals Research, R. F. Bunshah (ed), Vol. 5 Part I. Interscience, New York, NY.

Martin, J. W. (1957). "Correlation of Sonic Engineering Properties of Soils through Use of the Soniscope." Presented to M.I.T. in partial fulfillment of the requirements for the degree of Master of Science.

Matyas, E. H., and Radhakrishna, H. S. (1968). "Volume Change Characteristics of Partially Saturated Soils." Geotechnique, Vol. 18 No. 4, 432-448.

McWhorter, D., and Sunada, D. K. (1977). Groundwater Hydrology and Hydraulics. Water Resources Publications, Littleton, CO.

Moore, P. J. (1963). "Report No. 21: One-Dimensional Compression and Wave Propagation." Contract No. DA-22-079-eng-224, U.S. Army Engineer Waterways Experiment Station, CE, Vicksburg, MS.

Mulilis, J. P., Seed, H. B., Chan, C. K., Mitchell, J. K., and Arulanandan, K. (1977). "Effects of Sample Preparation Technique on Sand Liquefaction." Journal of Geotechnical Engineering, ASCE, Vol. 103, No. GT2, 91-108.

Nicholas, T. (1982). Impact Dynamics, Zukas, J. A., Nicholas, T., Swift, H. F., Greszczuk, L. B., Curran, D. R. (eds). John Wiley and Sons, New York, NY.

Nimmo, J. R., and Akstin, K. C. (1988). "Hydraulic Conductivity of a Sandy Soil at Low Water Content After Compaction by Various Methods." Journal of the Soil Society of America, Vol. 52, 303-310.

Richart, F. E., Jr., Hall, J. R., Jr., and Woods, R. D. (1970). Vibrations of Soils and Foundations. Prentice-Hall, Inc., Englewood Cliffs, NJ.

Rinehart, J. S. (1975). Stress Transients in Solids. HyperDynamics, Santa Fe, NM.

Ross, C. A. (1989). Unpublished Data. Engineering and Services Laboratory, AF Engineering and Services Center, Tyndall AFB, FL.

Ross, C. A., Nash, P. T., and Friesenhahn, C. J. (1986). "Pressure Waves in Soils Using a Split-Hopkinson Pressure Bar." ESL-TR-86-29 Engineering and Services Laboratory, AF Engineering and Services Center, Tyndall AFB, FL.

Ross, C. A., Thompson, P. Y., and Charlie, W. A. (1988). "Moisture Effects on Wave Propagation in Soils." ASCE/EMD Specialty Conference, Blacksburg, VA.

Stoll, R. D., and Ebeido, I. A. (1965). "Shock Waves in Granular Soil." Journal of the Soil Mechanics and Foundation Engineering Division, ASCE, Vol. 91, No. SM4, 107-125.

Weidlinger, P., and Matthews, A. T. (1964). "Shock and Reflection Phenomena in a Nonlinear Medium." Paper presented at the ASCE Structural Engineering Conference, New York, NY.

Whitman, R. V. (1970). "The Response of Soils to Dynamic Loadings." Contract No. DA-22-079-eng-224, U.S. Army Engineer Waterways Experiment Station, CE, Vicksburg, MS.

Whitman R. V., Miller, E. T., and Moore, P. J. (1964). "Yielding and Locking of Confined Sand." Journal of the Soil Mechanics and Foundation Engineering Division, ASCE, Vol. 90, No. SM4, 57-84.

Whitman, R. V., Roberts, J. E., and Mao, S. (1960). "Report 4: One-Dimensional Compression and Wave Velocity Tests." Contract No. DA-22-079-eng-224, U.S. Army Engineer Waterways Experiment Station, CE, Vicksburg, MS.

Wood, A. B. (1930). A Textbook of Sound. McGraw Hill, New York, NY.

Wu, S., Gray, D. H., and Richart, F. E. (1984). "Capillary Effects on Dynamic Modulus of Sands and Silts." Journal of Geotechnical Engineering, ASCE, Vol. 110, No. 9, 1188-1203.

Youd, T. L., and Craven, T. N. (1975). "Lateral Stress in Sands During Cyclic Loading." Journal of Geotechnical Engineering, ASCE, Vol. 101, No. GT2, 217-221.

**FINAL REPORT NUMBER 29
DECONTAMINATION AND ELISA ANALYSIS OF BLOOD
GROUP SUBSTANCES FROM HUMAN TISSUE
PENDING APPROVAL
Dr. David H. DeHeer
210-9MG-112**

ESTIMATION OF JET FUEL CONTAMINATION IN SOILS

by

Deanna S. Durnford
Douglas R. Hansen
Judith A. Billica
John A. Brookman

Agricultural and Chemical Engineering Department
Civil Engineering Department
Colorado State University
Fort Collins, Colorado 80523

Contract No.
F49620-88-C-0053/SB5881-0378
Contract Dates: 1 Dec., 1989-30 Nov., 1989

January, 1990

DISCLAIMER

This report has not been reviewed by the Air Force Office of Scientific Research or the Environics Laboratory at Tyndall AFB. The opinions expressed are solely those of the authors. Mention of any trade names of commercial products does not constitute endorsement or recommendation for use.

ACKNOWLEDGEMENTS

We wish to thank the Air Force Office of Scientific Research, Bolling AFB, DC for sponsoring this research. We would also like to acknowledge the staff at the Environics Laboratory, Tyndall AFB. Mr. Jack Milligan was instrumental in setting up the field portion of this work. He and many other staff members contributed their ideas and we found working at Tyndall to be a very rewarding experience. The project would not have been possible without the support of Colonel Hokanson and Colonel Lubozinski. Their support is sincerely appreciated.

ESTIMATION OF JET FUEL CONTAMINATION IN SOILS

CONTENTS

DISCLAIMER.....	
ACKNOWLEDGEMENTS.....	
FIGURES.....	
TABLES.....	
ABSTRACT.....	
1.0 INTRODUCTION.....	
2.0 BACKGROUND INFORMATION.....	
2.1 Location of LNAPL in the Vertical Profile.....	
2.2 Review of Field Monitoring Techniques.....	
2.3 Mechanisms of Entrapment.....	
3.0 LABORATORY INVESTIGATION.....	
3.1 Objective.....	
3.2 Experimental Methodology.....	
3.3 Preliminary Results.....	
4.0 FIELD INVESTIGATION.....	
4.1 Introduction.....	
4.2 Site Description.....	
4.3 Sampling Procedure.....	
4.4 Prototype Cryogenic Sampler.....	
4.5 Laboratory Analysis.....	
4.6 Results.....	
5.0 SUMMARY, CONCLUSIONS AND RECOMMENDATIONS.....	
5.1 Summary.....	
5.2 Conclusions.....	
5.3 Recommendations for Future Research.....	
6.0 REFERENCES.....	

LIST OF FIGURES

<u>Figure</u>	<u>Page</u>
2.1	Distribution of LNAPL in the subsurface environment....
2.2	Equilibrium saturation distributions of water, air, and LNAPL in a typical soil.....
2.3	Typical relative permeability curves for LNAPL and water in a sandy soil.....
2.4	Notation used in equations that relate LNAPL thickness in a monitoring well to LNAPL thickness in an aquifer..
2.5	Schematic of pore doublet with a) no trapping in conventional pore doublet, b) trapping of non-wetting phase in pore with bulge.....
2.6	An example of the snap-off process.....
2.7	Triangular pore throat with wetting phase pathways.....
2.8	Residual hydrocarbon saturation ratio, relating final residual saturation S_{or} to initial residual S^*_{or} as a function of capillary number, N_c
3.1	Diagram of laboratory column used in residual work.....
3.2	Photos of styrene movement resulting from water table being raised.....
3.3	Change in viscosity of initiated styrene with time.....
3.4	Comparison of ERDAS-measured styrene residual with original digitized image.....
3.5	Styrene residual for 2.68 mm sand using Oil Blue N dye.
3.6	Styrene residual for 2.03 mm sand using Oil Blue N dye.
3.7	Styrene residual for 2.68 mm sand using Sudan IV dye...
3.8	Styrene residual for layered system of 0.72 mm sand over 2.68 mm sand.....
4.1	A schematic showing the location of fuel tanks in the field study area.....
4.2	Particle size distribution for Tyndall AFB sand.....
4.3	Location of sampling points
4.4	The total hydrocarbon content measured at point #1.....
4.5	The total hydrocarbon content measured at point #2.....
4.6	The total hydrocarbon content measured at point #3.....
4.7	The total hydrocarbon content measured at point #4.....
4.8	The total hydrocarbon content measured at point #5.....
4.9	The total hydrocarbon content measured at point #6.....
4.10	Composited total hydrocarbon content
4.11	Averaged composited hydrocarbon content.....
4.12	LNAPL content for each point above and below the water table for a bulk density = 1110 kg/m^2
4.13	LNAPL content for each point above and below the water table for a bulk density = 1630 kg/m^2
4.14	LNAPL saturations determined from direct sampling.....
4.15	Baildown test data, July 13 test.....
4.16	Baildown test data, July 13 test.....

LIST OF FIGURES - CONT.

<u>Figure</u>	<u>Page</u>
4.17 Product thickness, Baildown test, July 13.....	
4.18 Baildown test data, August 2 test.....	
4.19 Depth-to-Product, Baildown test, August 2.....	
4.20 Water characteristic curve for Tyndall AFB sand.....	
4.21 Capillary pressure-saturation curves for water/air, water/LNAPL and LNAPL/air fluid pairs.....	
4.22 Equilibrium distributions of LNAPL, air and water.....	
5.1 LNAPL saturations determined from direct sampling.....	
5.2 LNAPL saturations predicted from baildown tests and equilibrium theory.....	

LIST OF TABLES

<u>Table</u>	<u>Page</u>
2.1 Equations used to relate LNAPL thickness in wells to LNAPL thickness in an aquifer.....	
3.1 Properties of fluids often used in residual work.....	
3.2 Sand size designation used in residual tests.....	
3.3 Surface and interfacial tension measurements for fluid pairs used in tests.....	
4.1 Elevations and product thicknesses at field site.....	
4.2 Precision of laboratory method.....	
4.3 Estimation of recovery factor in laboratory.....	
4.4 Comparison of measured total LNAPL with predicted volume from baildown tests.....	
4.5 Surface tensions for clean and contaminated fluids.....	

ABSTRACT

This report documents the results of a study of jet fuel contamination in soils and includes (1) a review of literature on field methods used to quantify LNAPL (Light Non-Aqueous Phase Liquid) volumes and distributions in soils, (2) a summary of a laboratory investigation evaluating LNAPL entrapped in the saturated soil zone, and (3) results of a field study conducted at a contaminated site at Tyndall AFB, FL.

Early in this project, the importance of LNAPL entrapped in the saturated zone became apparent. Whereas considerable research effort has been devoted to estimating LNAPL product at and above the water table, there has been very little work on LNAPL entrapped in the saturated region below the water table. Entrapped LNAPL is recognized as a significant source of contamination as constituents of the LNAPL continue to dissolve into the bulk groundwater. However, the hysteretic nature of the capillary pressure-saturation relationships that control entrapment, coupled with the difficulty in obtaining quantitative field data from below the ground water table, have prevented significant inroads into this area of research. Current efforts are generally limited to laboratory column studies that concentrate on the dissolution processes with the quantity of LNAPL entrapped predetermined. Therefore, a major part of the research reported in this paper was devoted to determining the quantity and distribution of product

entrapped below the water table in a sandy soil, and developing laboratory and field techniques to study this aspect.

Results from the laboratory investigation indicate that about 10% of the pore space would be filled with entrapped LNAPL in a sandy soil. This value is dependent on fluid and soil properties. Methods to generalize our results are ongoing.

Results from the field study indicated that over 70% of the total LNAPL in the soil was entrapped below the water table, although less than 10% of the pore space was filled with LNAPL. Obviously, both regulatory considerations and remediation strategies would be seriously in error if entrapped LNAPL were ignored. Additionally, an adequate risk analysis of a site would depend on an accurate assessment of both quantity and distribution of the product in the formation. The field study also emphasized the importance of spatial and temporal variability of the LNAPL distribution.

Conclusions from this study include: (1) LNAPL entrapped in the saturated zone can be very significant in some cases and should be evaluated in a site characterization, (2) a cryogenic sampler can be successfully used to determine LNAPL distribution in the saturated zone of a sandy soil, (3) currently available field methods, other than direct sampling, have serious shortcomings when used to determine LNAPL

distribution in a sandy soil under fluctuating water table conditions.

CHAPTER 1.0

INTRODUCTION

This report summarizes the results of a study to quantify the volume and distribution of LNAPL (Light Non-Aqueous Phase Liquid) contamination in soils. The study includes complimentary laboratory and field investigations. Early in the project, it became apparent that the volume of LNAPL entrapped below the water table was significant in many field cases and was generally neglected in past research. There are several probable reasons why this is true. First, much of our current understanding of immiscible flow physics was originally developed for the petroleum industry. There is no equivalent to a fluctuating water table condition in petroleum recovery, since liquid and gas pressures are very high in petroleum reservoirs. Secondly, the hysteretic, transient nature of the entrapment process is a theoretically formidable problem and accurate determination of the required inputs for such a theory is extremely difficult. Finally, field sampling of a saturated soil, especially a sandy soil, is difficult when both the fluids and soil must be extracted intact for accurate analysis. Therefore, although product both above and below the water table was evaluated in this project, our emphasis has been on determining the distribution of product below the water table. This has included development of the laboratory and field techniques to study this aspect of the problem.

Chapter 2.0 of this report provides background discussions of the location of LNAPL in the vertical profile. In addition, a review of the literature on field monitoring techniques is presented, along with a discussion of the shortcomings of current methods. A discussion of the mechanisms of entrapment is also included in Chapter 2.0.

Chapter 3.0 describes the laboratory experimental methodology and preliminary results. The objective of the laboratory study was to establish relationships between soil and fluid properties and the quantity of entrapped LNAPL.

Chapter 4.0 reports results from a field study conducted at Tyndall AFB, FL. The primary objective of the field study was to determine the vertical distribution of LNAPL, particularly the quantity entrapped below the water table. A prototype cryogenic sampler was developed during this study to extract intact samples from below a water table in sandy soils. This sampler is described in Chapter 4.0. The results of the soil sampling are also presented and compared to results obtained from baildown test data and from interpretation of monitoring well data using equilibrium theory.

Chapter 5.0 is a summary of the project and discussion of the conclusions that can be drawn. Recommendations for future research are also included.

The terms LNAPL, product, oil and hydrocarbon are used somewhat interchangeably in this report, although the choice

of which term is used reflects either the source of information or the degree of generality implied. For example, when the results of the direct sampling are presented, the term hydrocarbon is used since the chemistry lab procedure determines total hydrocarbon. When references to research associated with the petroleum industry are made, the terms oil or hydrocarbon are used. When generalities are discussed that imply any immiscible, lighter than water fluid, the terms LNAPL or product are used.

CHAPTER 2.0

BACKGROUND INFORMATION

2.1 Location of LNAPL in the Vertical Profile

A Light Non-Aqueous Phase Liquid (LNAPL) such as jet fuel will exist as a separate, immiscible fluid after it leaks or spills into the soil environment. The movement of immiscible fluids in soil and aquifer systems is governed by the physics of multiphase flow where the three phases - air, LNAPL, and water - occupy varying proportions of the pore space. Depending on the total volume of LNAPL that has leaked or spilled, the LNAPL can ultimately be distributed in three zones: (1) as a discontinuous phase in the vadose zone, (2) as a continuous phase at the water table, and (3) entrapped as a discontinuous phase below the water table (Figure 2.1). It is important to know both the total volume and distribution of LNAPL in the subsurface environment in order to design appropriate cleanup measures or develop an accurate risk assessment.

LNAPL that has spilled or leaked into the soil environment will move primarily downward. Driving forces are due to capillary pressure gradients and gravity. As the LNAPL moves toward a water table, a certain fraction of the product will remain behind in the vadose zone. LNAPL in the vadose zone is discontinuous, immobile and comprises a relatively small fraction of the total pore space. It exists at negative fluid pressures (negative relative to atmospheric pressure).

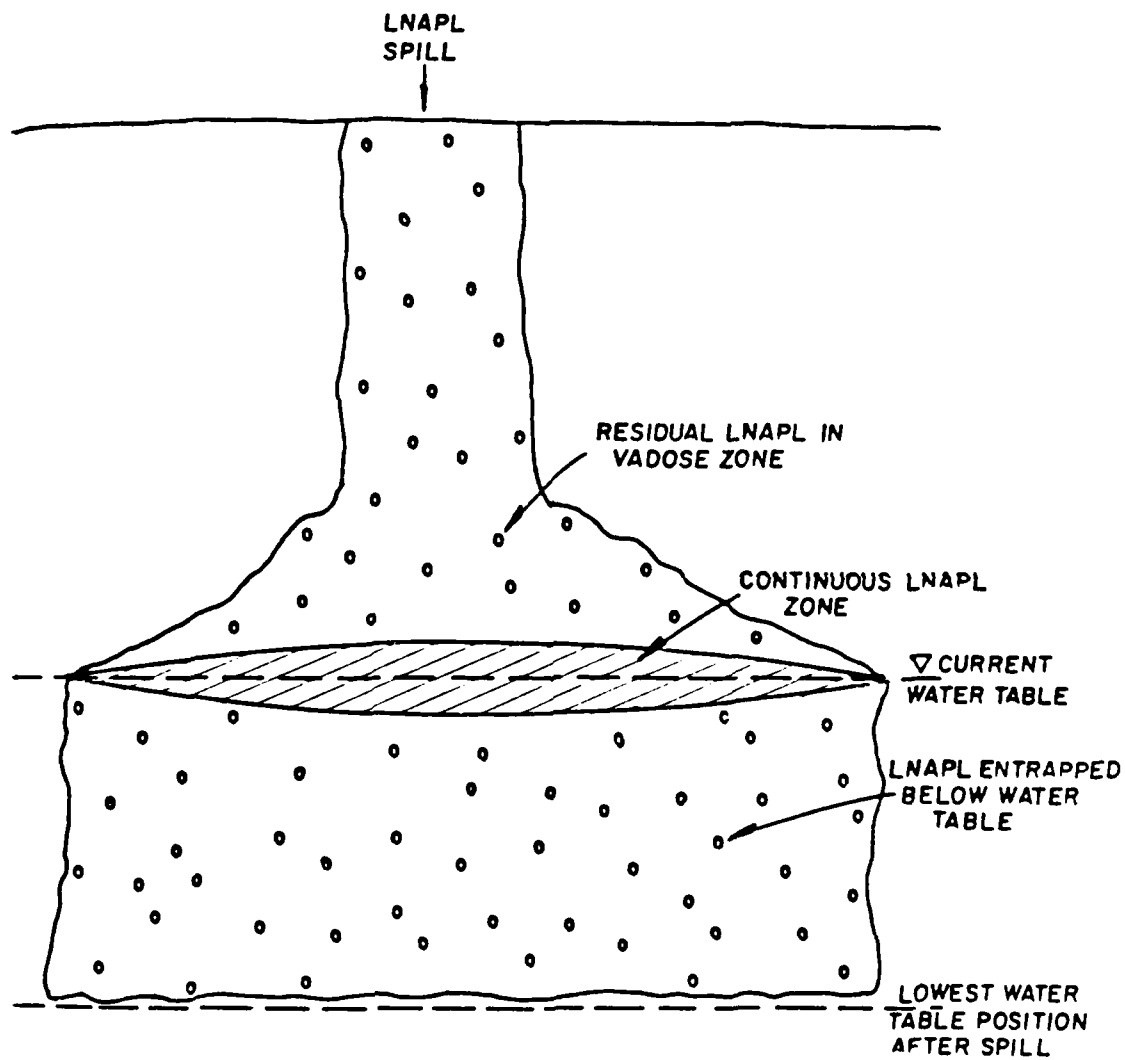


Figure 2.1 Distribution of LNAPL in the subsurface environment.

Laboratory work indicates that, in some cases, up to 10 percent of the pore volume in the unsaturated soil zone can consist of residual LNAPL (Wilson et al, 1988). The presence of LNAPL in this zone can be detected through bulk soil and soil vapor analyses. In addition, several in situ remediation technologies are being developed to remove LNAPLs from unsaturated soils, including volatilization, biodegradation, soil washing with or without surfactants, and soil heating using radio or microwaves.

As the water table is approached, LNAPLs will spread laterally due to the increased resistance to flow that occurs upon reaching higher water contents. Below some critical spill volume, the product that spreads laterally will still exist at negative pressures and will not flow into a monitoring well. Above the critical spill volume, some of the LNAPL would also exist at positive pressures. LNAPL at positive pressure can flow into a monitoring well and is sometimes referred to as "mobile" product. Although monitoring wells are used to detect the presence of LNAPLs in the vicinity of a water table, their usefulness is limited because there is no simple relationship between the amount of product observed in the well and the amount and distribution of product that actually exists in the aquifer (Hampton and Miller, 1988; Abdul et al, 1989). However, monitoring wells are routinely used to estimate the amount of LNAPL present in

the aquifer and the amount of free product recovery that should be expected during cleanup.

Water tables generally fluctuate on a seasonal, annual or daily basis as a result of rainfall infiltration, tidal influences, irrigation, or pumping. Water table fluctuations cause the LNAPL to be spread in a vertical direction . In addition, they can cause discontinuous, immobile blobs of LNAPL to be entrapped below the water table as the water table rises. Entrapped LNAPL is a continuous source of dissolved contaminants for water flowing through the aquifer. Laboratory investigations indicate that entrapped LNAPL can occupy from 15 to 40 percent of the pore space in an LNAPL-water system (Wilson and Conrad, 1984; Wilson et al, 1988). LNAPLs have a potentially greater residual saturation below a water table than above it in the vadose zone. However, currently available field methods do not allow for the detection and monitoring of product that may be entrapped below a water table.

The distribution of LNAPL saturations and pressures in the subsurface environment have important implications in terms of designing appropriate clean-up procedures. For example, if a monitoring well contains a layer of LNAPL, it is often assumed that a "layer" of mobile LNAPL also exists in the aquifer, such that 100 percent of the pore volume in this layer is occupied by product. However, such an LNAPL-saturated zone generally does not exist. Instead, the pore space consists of

varying proportions of water, LNAPL, and air (Figure 2.2). Some of this LNAPL could exist at positive pressures and could theoretically be removed with trenches or extraction pumps. However, since the LNAPL only occupies some fraction of the pore space, its relative permeability will only be a fraction of the saturated permeability. This will significantly effect its ability to flow into a well or trench.

Typical relative permeability curves for a water-LNAPL system are shown in Figure 2.3. The actual permeability of the LNAPL at a particular saturation is calculated by multiplying the permeability at 100 percent LNAPL saturation by the relative permeability value. At low LNAPL saturations, the actual permeability of the LNAPL may be so low that it is essentially immobile, even though it exists at positive pressures. Because of this, extraction wells and trenches can only be expected to remove some portion of the LNAPL having positive pressures. An EPA report (EPA, 1988) reviewed four case studies where different methods were used to recover free product. The review indicated an average product recovery of only 29 percent. If the saturation distribution of the LNAPL was known, a better estimate of recoverable LNAPL could have been made and a more appropriate cleanup system designed.

2.2 Review of Field Monitoring Techniques

Conceptual and theoretical analyses of LNAPL movement in soil and ground-water systems have been presented by a number

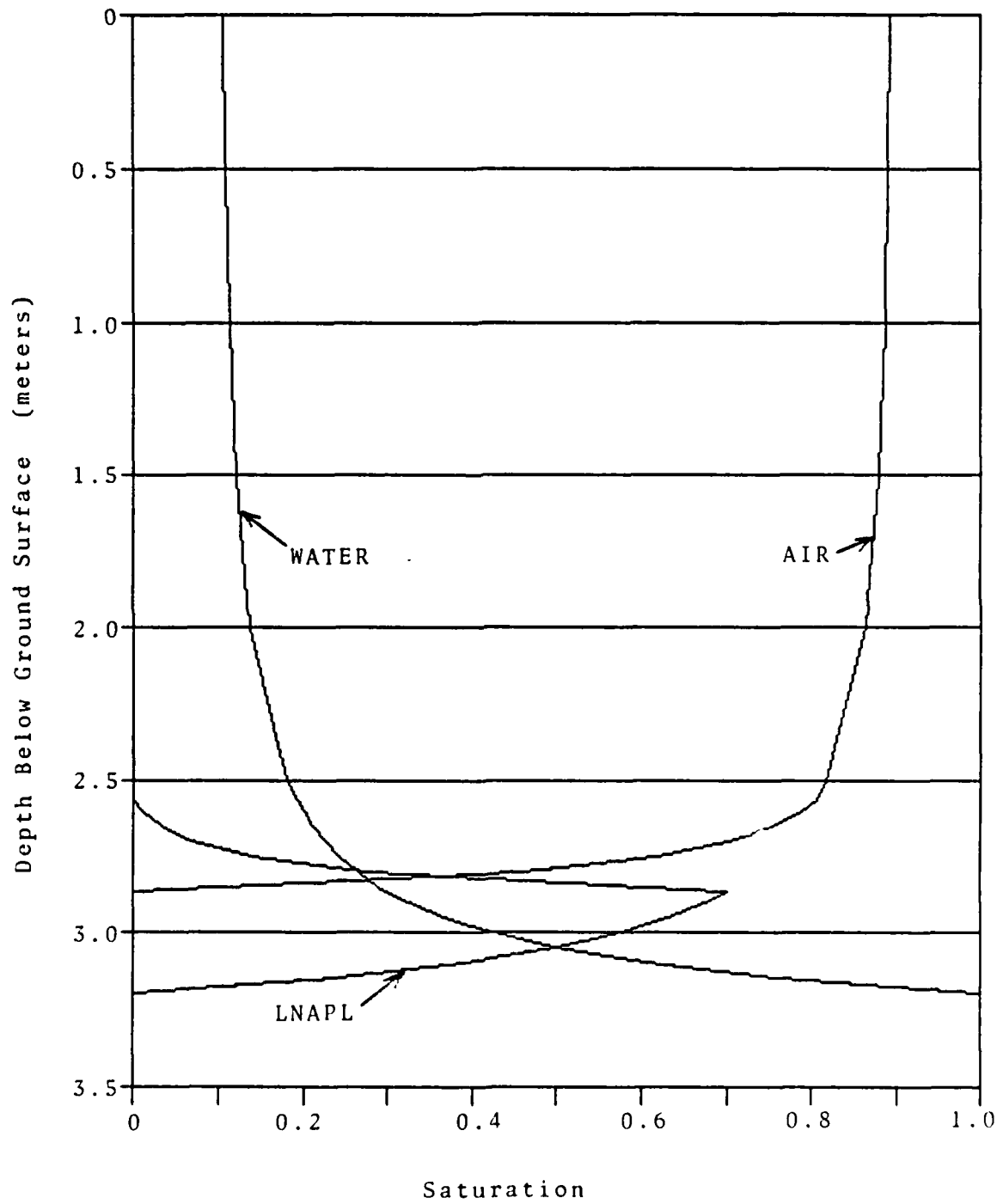


Figure 2.2 Equilibrium saturation distributions of water, air, and LNAPL in a typical soil.

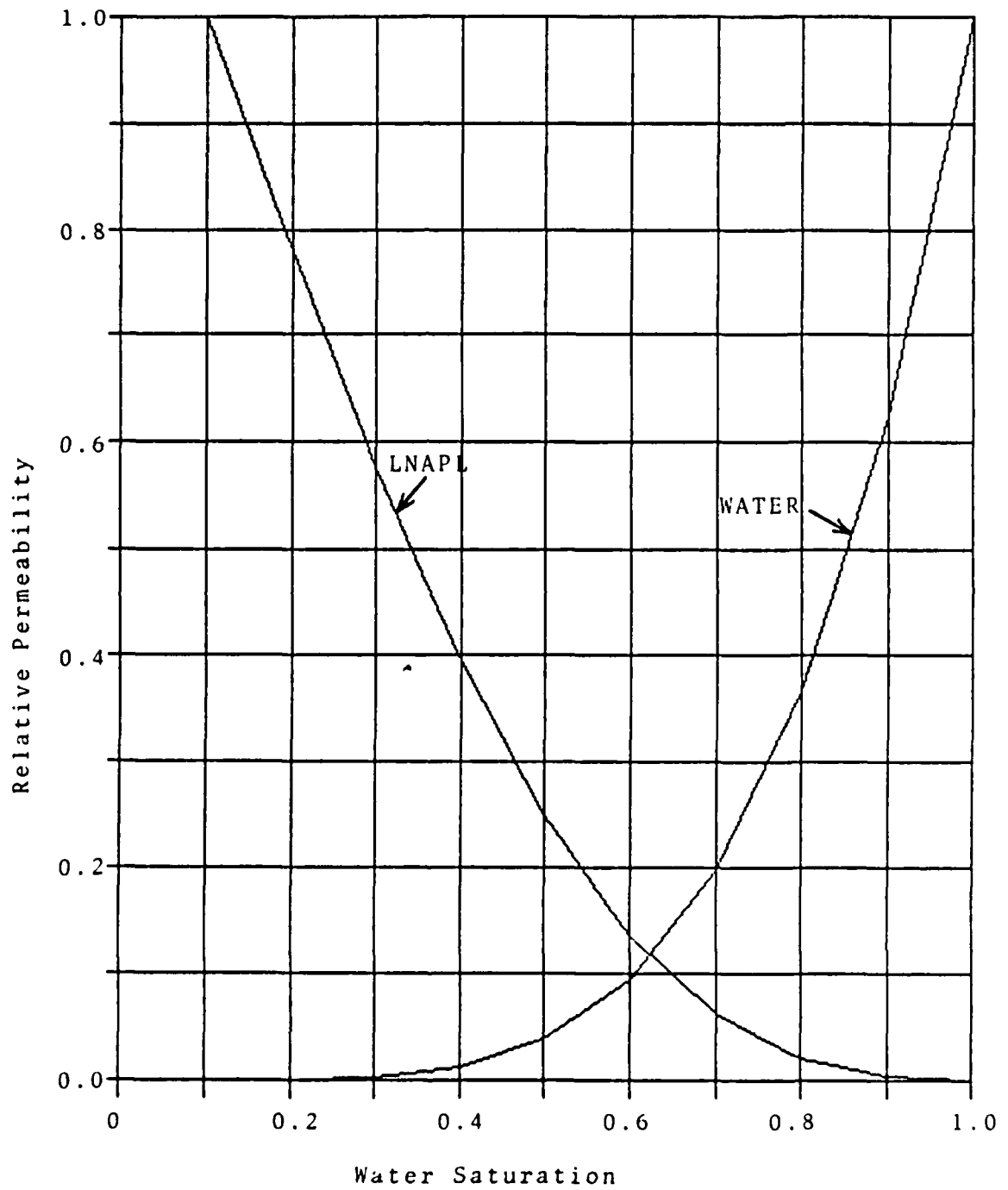


Figure 2.3 Typical relative permeability curves for LNAPL and water in a sandy soil

of investigators (van Dam, 1967; Schwille, 1967; Hassanizadeh and Gray, 1979a, 1979b, 1980; Schwille, 1984; Schiegg, 1985; CONCAWE, 1979). This section presents a review of field methods relevant to determining the movement, distribution and volume of LNAPLs that have spilled or leaked into soil and ground-water systems. The review has indicated that additional investigations are required to provide workable theories and practical field methods for determining LNAPL distributions and volumes in aquifers.

Monitoring wells are routinely used to estimate the amount of LNAPL present in an aquifer. A number of relationships have been developed to relate the thickness of LNAPL observed in a monitoring well to the actual thickness of the LNAPL contaminated zone in the aquifer (Zilliox and Muntzer, 1975; CONCAWE, 1979; Hall et al, 1984; Schiegg, 1985). Other relationships have been developed that relate LNAPL thickness in a monitoring well to LNAPL volume per unit area in the aquifer (Durnford, 1988; Lenhard and Parker, 1989; Farr et al, 1989). Some of the relationships are presented in Table 2.1, with variables as defined on Figure 2.4. The simplest and perhaps the most widely used relationship is the 4:1 ratio developed by CONCAWE where the actual LNAPL thickness in the aquifer is assumed to be one-fourth the thickness of the LNAPL in the well. Other methods account for fluid and porous media properties to varying degrees.

TABLE 2.1

EQUATIONS TO RELATE LNAPL THICKNESS IN A MONITORING WELL
TO LNAPL IN AN AQUIFER

EQUATION (1)	SOURCE
a. $H = D + A - B$	Zilliox and Muntzer, 1975
b. $H = D/4$	CONCAWE, 1979
c. $H = D - (\text{Formation Factor})$	Hall et al, 1984
d. $H = D - 2h_c$	Schiegg, 1985
<p>where h_c = mean capillary height of the air-water saturation drainage curve</p>	
<p>e. $\frac{V_o}{A\phi} = (D + A - B) + \frac{A}{\alpha} \left(\left(\frac{D_w^{so}}{A} \right)^\alpha - 1 \right) - \frac{B}{\alpha} \left(\left(\frac{D_w^{ow}}{B} \right)^\alpha - 1 \right)$</p>	Durnford, 1988

where α, A, B = capillary pressure curve parameters
 ϕ = porosity
 λ = pore size distribution index
 $\alpha = \lambda - 1$

(1) Common variables are defined on Figure 4.

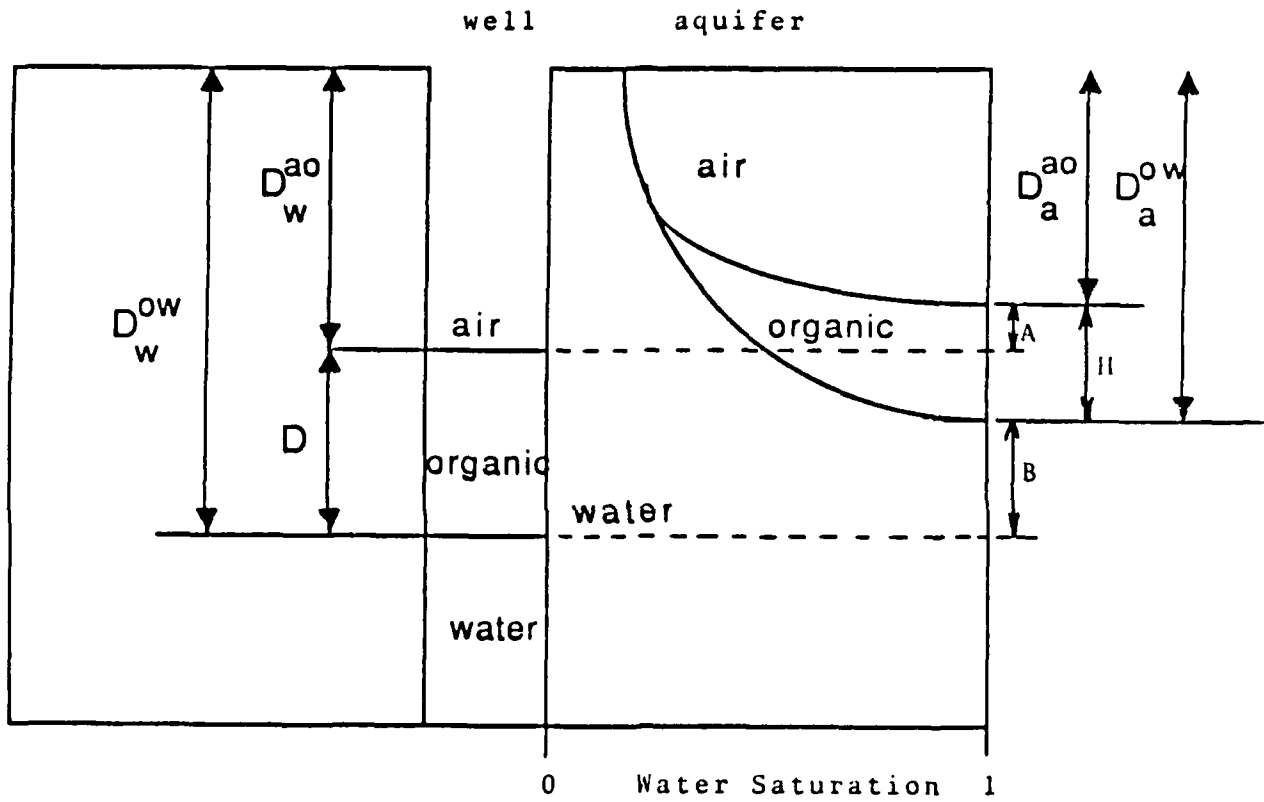


Figure 2.4 Notation used in equations that relate LNAPL thickness in an aquifer

All of the relationships presented in Table 2.1 have several limitations. Some of these limitations include:

1. None of the equations directly account for discontinuous LNAPL that may be entrapped below the water table. As the volume of entrapped LNAPL changes over time due to fluctuating water tables, the thickness of LNAPL observed in the monitoring well will also change (Yaniga, 1984), even if the total LNAPL in the aquifer remains constant. Each time the LNAPL layer in the monitoring well is measured, a different 'actual' thickness in the aquifer can potentially be calculated.

2. The equations that are based on soil and fluid properties require laboratory measurements of capillary pressure-saturation curves. These curves are difficult to obtain in practice and may not even be representative of actual field conditions.

3. None of the methods account for the spatial variability in hydrogeologic parameters.

4. None of the methods account for the hysteretic nature of multiphase flow.

Due to these limitations, it seems prudent to use some other method to determine the actual volume of LNAPL in an aquifer. Gruszczenski (1987) developed a field baildown test to determine a realistic estimate of the thickness of the free-product zone (the zone where LNAPL has positive pressures) in an aquifer. The test is similar to a rising

head slug test. LNAPL is first bailed from the monitoring well. Then, the rise in the LNAPL-water interface in the well is recorded over time. A graph of the water and LNAPL levels versus time is interpreted to obtain an actual free product thickness in the aquifer (i.e. where LNAPL pressures are positive). Data collected during field tests show that during recharge to the well, water levels will first rise then begin to fall. The LNAPL thickness at the time when the water level begins to fall is interpreted to be the actual product thickness.

The baildown test is a widely used field method to evaluate the true thickness of free LNAPL in an aquifer, although the procedure remains unproven (Testa and Paczkowski, 1989). In addition, the method has a number of problems associated with it, including measurement errors, bailing of ground water in addition to LNAPL, and data interpretation. Data interpretation assumes that there is a layer in the aquifer that is 100% saturated with LNAPL. Although this assumption may be reasonable for aquifers consisting of very coarse grained materials, in most soils the free LNAPL will only occupy some fraction of the total pore space. Finally, this method does not account for LNAPL that is entrapped below the water table.

Hughes et al (1988) present two field techniques designed to provide a more accurate estimate of the true LNAPL thickness in a sandy, unconfined aquifer: well tests and

continuous coring through the zone of interest. Two well tests are presented. The first is a recharge test that involves pumping the LNAPL from the well until steady state conditions have been reached, then shutting the pump off and measuring the top of the LNAPL surface in the well as the LNAPL recharges. The second method is a baildown test similar to that presented by Gruszczenski (1987), although the data interpretation is different. Hughes et al state that the recharge test is more accurate than the baildown test since LNAPL is removed from the aquifer during the recharge test. However, both of these well tests suffer from the same limitations previously presented for the Gruszczenski baildown test.

The second field technique described by Hughes et al (1988) involves coring through the contaminated zone, allowing for a determination of the vertical extent of contamination. Depth discrete samples are taken through the zone of interest with a split spoon sampler using a dry coring method (augers or air rotary). A UV light is used to detect the presence of LNAPL in the core samples if their presence cannot be detected under normal light. Although a UV light is only a qualitative tool, the 100 percent LNAPL-saturated samples will glow the brightest compared to the other samples. However, such qualitative information does not provide values for fluid saturations and pressures.

Keech (1988) is developing a portable dielectric logging system to determine the LNAPL thickness in a formation and the depth interval at which it resides. The dielectric properties of the formation are measured by transmitting an electromagnetic wave into the formation and then receiving it after it has passed through a portion of the formation. The thickness of the LNAPL layer is determined by detecting differences in the dielectric characteristics of the air-saturated, LNAPL-saturated, and water-saturated zones. In practice, one or more dielectric logging wells would be installed adjacent to standard monitoring wells. Measurements of the LNAPL thickness made by the dielectric logging system would be used to establish a calibration factor to correct LNAPL thicknesses measured in the standard monitoring wells.

The direct sampling of aquifer material with its pore fluids intact appears to be the most promising method for determining the distribution and quantity of LNAPL at and below the water table. However, most existing core sampling techniques are inadequate for retrieving both the core fluid and the solids from saturated porous media. Existing techniques usually result in the mechanical disturbance of samples, the loss of pore fluid, and the contamination of the sample by drilling fluid or by fluid adjacent to the sample location. A piston sampler reported by Zapico et al (1987) and a piston sampler currently under development by Starr and Ingleton (1989) both address some of these problems.

2.3 Mechanisms of Entrapment

Entrapped LNAPL is LNAPL that has become immobilized and discontinuous within the porous media. Entrapped LNAPL is also referred to as residual saturation, and is commonly represented as the volume of LNAPL trapped in the pores relative to the total volume of the pores (Wilson and Conrad, 1984). LNAPL entrapped in the vadose zone is described by McKee et al (1972) as pellicular and by Wilson and Conrad (1984) as pendular rings. LNAPL entrapped within the saturated zone is in the form of discontinuous, single-pore blobs or as multi-pore ganglia. The term blob is normally used to designate LNAPL occupying a single pore space, while the term ganglion refers to LNAPL that occupies an interconnecting set of pore bodies (Ng et al, 1978).

The trapping of LNAPL in a porous media is a very complex process. Several factors influence the amount of entrapped LNAPL, including (1) pore network and geometry, as determined by the size, shape, and distribution of soil particles, (2) solid/fluid properties such as wettability and adsorption, (3) fluid/fluid interactions such as interfacial tension, density differences, and viscous forces, and (4) the applied pressure gradient and gravity. Three phases, air, LNAPL and water, are all present in a rising water table situation. Interaction between these fluids and the soil particles influence the entrapment process. In most systems, the water preferentially wets the solid phase. The LNAPL phase is assumed to have

intermediate wetting properties between the nonwetting air and the wetting water.

Once LNAPL becomes entrapped, capillary forces will hold it in place. For LNAPL that becomes entrapped below a water table, there is a difference in pressure across an LNAPL-water interface. This difference in pressure across an interface between two fluids is called the capillary pressure and is described by the LaPlace equation (Larson et al, 1977):

$$P_{LNAPL} - P_{water} = \frac{2 \sigma \cos \theta}{r}$$

The capillary pressure is directly related to the interfacial tension, σ , and inversely related to the equivalent radius of curvature of the interface, r . Once the LNAPL becomes entrapped, it is very difficult to displace due to capillary forces (Dias and Payatakes, 1986). Abrams (1975) found that a 100 to 500-fold increase in the rate of injection of the wetting phase was required to displace LNAPL that had detached from the main body of oil.

LNAPL is trapped in the porous media by either or both of two mechanisms: by-passing and snap-off (Wilson and Conrad, 1984). In by-passing, the LNAPL will be trapped in the larger arm of a pore doublet as a result of the capillary pressure difference between the two arms (Abrams, 1975). However, the pore that traps the LNAPL must have the bulge configuration shown in Figure 2.5, as the conventional pore doublet will result in complete displacement of the non-wetting phase

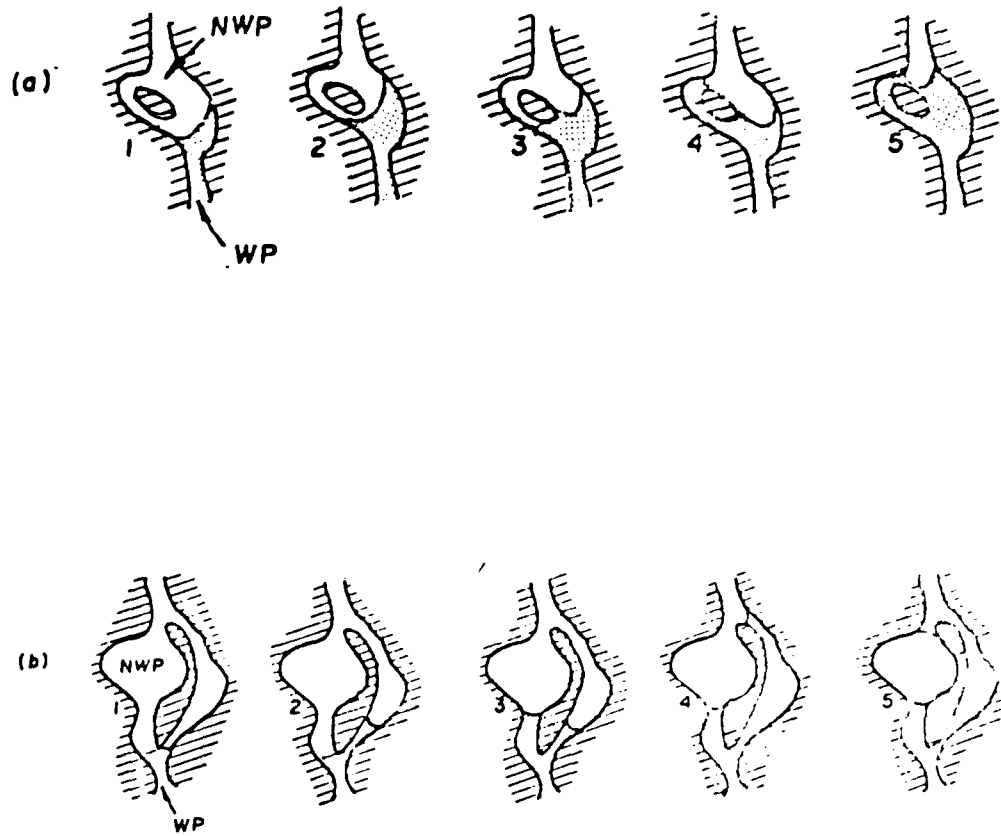


Figure 2.5 Schematic of pore doublet with a) no trapping in conventional pore doublet, b) trapping of non-wetting phase in pore with bulge. (Chatzis and Dullien, 1983)

(Chatzis and Dullien, 1983). The wetting phase will fill the smaller pore first, and if the proper pore geometry is present, bypass to the downstream pore prior to the displacement of the non-wetting phase from the larger pore. Thus, trapping of oil is expected to occur primarily in the larger bulge pores. By-passing is an important entrapment process in soils having a high degree of heterogeneity.

Snap-off is the dominant process for soils having a high aspect ratio, where the pore throats are much smaller than the pore bodies. A simplified example of the snap-off process is shown in Figure 2.6. In extensive studies of the snap-off process, Roof (1970) observed the formation of a collar of water just downstream of the pore throat. As the collar grows in size, it proceeds to choke the flowing oil until finally an unstable condition is reached, and the neck of oil in the collar begins to pulsate. After three to six pulsations, the collar chokes off the thread of oil, and the snap-off is complete.

The collar of water is required for the snap-off process to occur, and will form easily in a natural soil since any pore throat will have some acute angle formed by the soil particles that can function as the pathway for the wetting phase. In laboratory investigations where a constriction in a round glass tube was used to represent the pore throat, minimum entrapment was observed prior to the cutting of a small groove in the inside wall of the constriction (Roof,

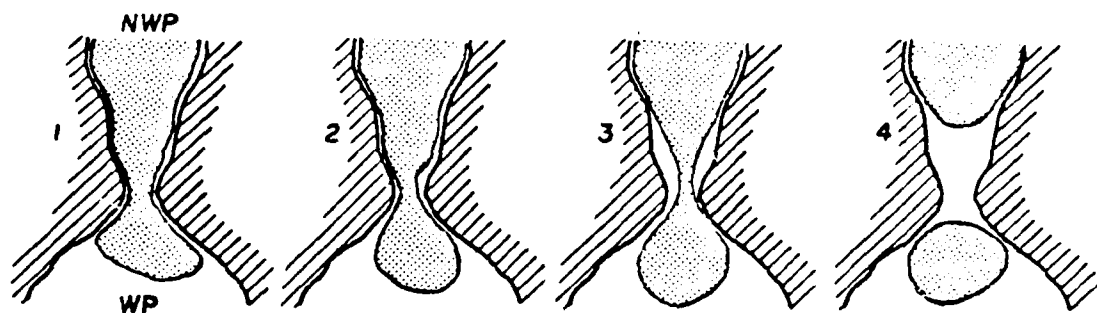


Figure 2.6 An example of the snap-off process (as described by Roof, 1970).

1970). Without this groove, it was very difficult to form the collar and initiate the choking-off process in the pore throat. In experiments using a tube with a throat of square cross-section, Arriola et al (1983) measured oil velocities slightly less than the average water velocity, again indicating that by-passing of some water occurred around the oil droplet through the triangular channels in the corners of the tube. Figure 2.7 shows this corner concept for a triangular pore throat.

In the displacement of oil by water, two formulas are commonly used to characterize the conditions that control the amount of residual entrapped oil in the soil. Capillary number (N_{CA}) is a dimensionless ratio of viscous to capillary forces and can be defined as (McKellar and Wardlaw, 1988):

$$N_{CA} = \frac{\mu v}{\sigma}$$

where: μ = displacing phase (water) viscosity
 v = Darcy velocity
 σ = interfacial tension

Increasing the wetting phase velocity will increase the capillary number and result in a corresponding decrease in the amount of residual deposited in the soil. Many researchers, primarily those interested in petroleum recovery, have made measurements to estimate the capillary number at which the hydrocarbon residual is at a maximum and no longer affected by the hydraulic gradient of the wetting phase (Chatzis et al, 1984, Hinkley et al, 1987, Ng et al, 1978, Wilson and Conrad,

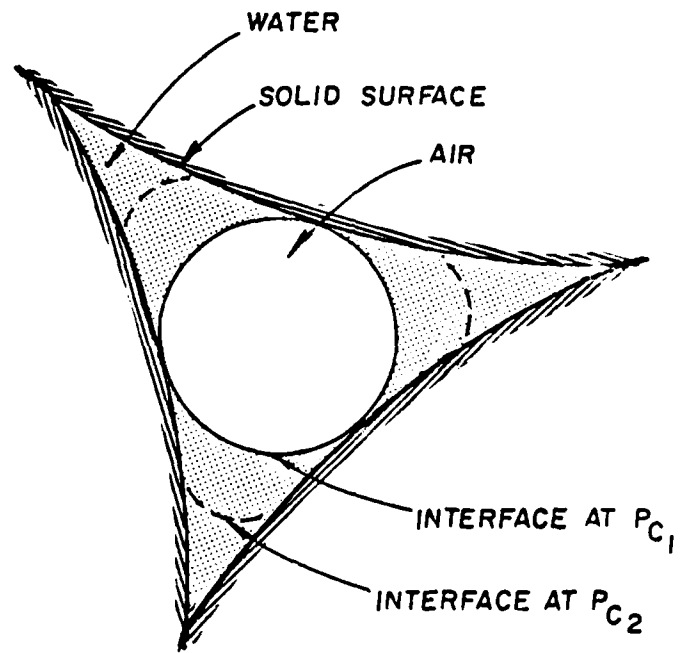


Figure 2.7 Triangular porethroat with wetting phase pathways.

1984, and others). Since the capillary number is a fundamental property of the soil and fluids used (Taber, 1969), it is difficult to extrapolate from other work, but a capillary number of $N_{CA} = 10^{-3}$ seems to be the critical value above which residual hydrocarbon is reduced for a pack of round glass beads. For sandstones, the critical capillary number is about $N_{CA} = 10^{-5}$. The relationship between residual and capillary number is shown in Figure 2.8. Above these critical levels, capillary forces no longer completely determine the manner in which the fluids are distributed, and the degree of displacement of oil from the larger pores increases as a result of a greater influence of the viscous forces relative to capillary forces.

The bond number is also used to characterize the potential for residual hydrocarbon. Bond number is the ratio of capillary to buoyancy forces, and is defined as (Ng et al, 1978):

$$N_B = \frac{k \Delta\rho g}{\sigma}$$

where: k = intrinsic permeability of the soil
 $\Delta\rho$ = density difference of fluids
 g = gravitational acceleration
 σ = interfacial tension

In the absence of flow, there is a critical condition in which buoyancy is just able to overcome capillarity and mobilize the entrapped LNAPL vertically. For a given pair of fluids, the ability of the buoyancy force to mobilize an

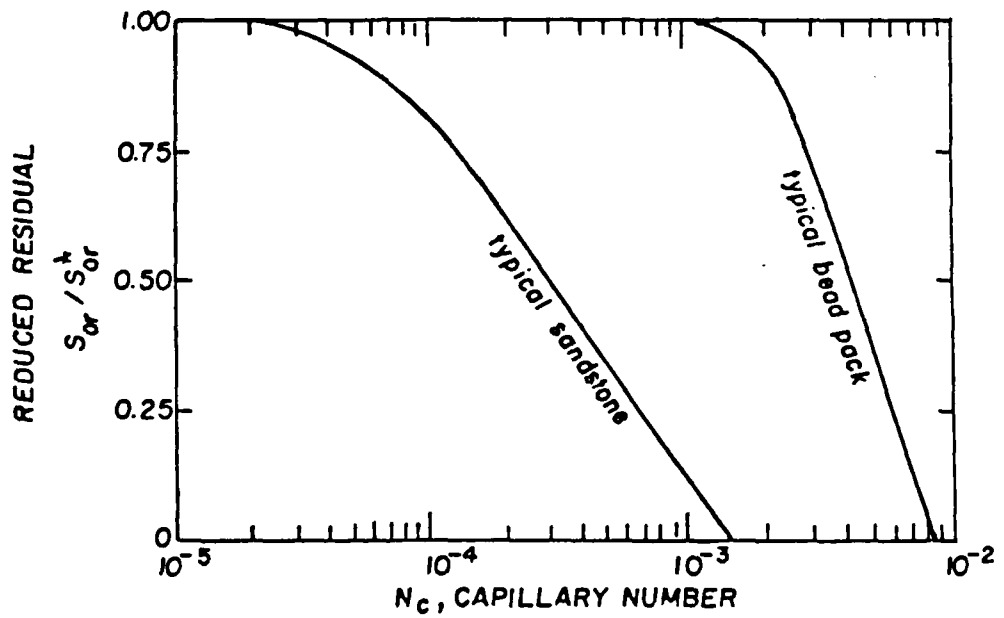


Figure 2.8 Residual hydrocarbon saturation ratio, relating final residual saturation S_{or} to initial residual S_{or}^* , as a function of capillary number, N_c (Wilson and Conrad, 1984).

individual LNAPL residual is a direct function of the length of the ganglia. For vertical displacement with the water flow in the same direction as the buoyancy force, the effects of the capillary number and bond number are additive.

CHAPTER 3.0

LABORATORY INVESTIGATION

3.1 Objective

The objective of the laboratory investigation was to determine the relationships between soil and fluid properties and the total LNAPL entrapped in the saturated zone under fluctuating water table conditions. Results reported here are preliminary. It is expected that this part of the project will be completed by May, 1990 and available as an M.S. thesis.

3.2 Experimental Methodology

A column of soil was packed, saturated with distilled water and then allowed to drain to residual water content. An LNAPL, a styrene that subsequently solidifies, was then injected in the residual water zone and the water table raised slowly, entrapping the LNAPL. After entrapment of the LNAPL was complete, the styrene was solidified and the water phase was replaced by an epoxy. This allows sectioning and digitizing of the column for analysis. The technique of using a non-wetting phase (representing the LNAPL) that can be solidified and later analyzed has been used by several research groups in oil displacement work (Chatzis et al, 1984; McKellar and Wardlaw, 1988; Wilson et al, 1989; Yadav et al, 1987; and others). The method was modified in this project to apply to fluctuating water table conditions.

Fluids used: The fluid pair that has been used most commonly in past research has been a styrene monomer to represent the non-wetting phase, and a 2% CaCl brine to represent the wetting phase. For work simulating LNAPL entrapment in shallow aquifer systems, the styrene monomer is better paired with distilled water rather than the calcium chloride solution, since most shallow aquifers contain water of relatively high quality compared to that normally found in the region of oil production. The properties of the three fluids most commonly used are shown in Table 3.1 (Wilson et al, 1989).

Styrene preparation: Styrene monomer is normally sold containing an inhibitor to prevent polymerization during transport and storage. This inhibitor can be removed by a fairly lengthy distillation procedure, or more commonly with the use of inhibitor removal columns available from chemical supply companies. Single-use inhibitor removal columns were prepared from 6 mm ID glass tubing and used for this work.

Following removal of the inhibitor, benzyl peroxide was added as an initiator for the polymerization process. This particular initiator is used because it maintains the water-wetness of the soil sample (Chatzis et al, 1984).

Column Preparation: The sample column was constructed from a three inch diameter, ten inch long glass cylinder. Machined aluminum plates were used to cap the ends of the

liquid	specific gravity	density (g/cm ³)	kinematic viscosity (cst)	dynamic viscosity (cp)	interfacial tension with 0.3% CaCl ₂ soln (dynes/cm)	surface tension (dynes/cm)
aqueous phase	1.003	1.000	0.98	0.98	NA	72.0
styrene	0.906	0.903	0.89	0.81	35.3	31.9
Tracon 2114 epoxy resin	1.096 (factory)	1.072 (factory)	545 (factory)	597 (factory)	<2	40.9

Table 3.1 Properties of fluids used in LNAPL visualization experiments. All measurements were taken at 23°C (Wilson et al, 1989)

column (Figure 3.1). Three 1/4 inch threaded rods clamped the glass cylinder between the aluminum end plates.

A single port with a valve was installed on the top plate to allow for attachment of a vacuum during the saturation procedure, and also to allow for pressure equalization during the time the water table was raised. The base contained two ports. One was used in conjunction with a rubber septum to inject the styrene at the top of the capillary fringe immediately prior to initiating the movement of the water table. The second port was equipped with a valve, and attached to the pump during the water table movement. An 1/8 inch rubber gasket was used to seal between the glass and the aluminum plates. The top set of plates sandwiched an O-ring that served to seal that junction. All threaded connections were sealed with teflon thread tape.

The column was packed with sand by dropping the sand as discrete particles through a PVC pipe from a height of five feet. This method allows for the sand to reach terminal velocity and results in a maximum density of sand in the column. Observation of the sand pack through the glass detected no layering or preferential deposition of the sand.

The packed column of sand was prepared for the test by vacuum saturating with water. The column was then drained for 24 hours to develop a stable water distribution throughout the column. By adjusting the height of the water table (i.e. the

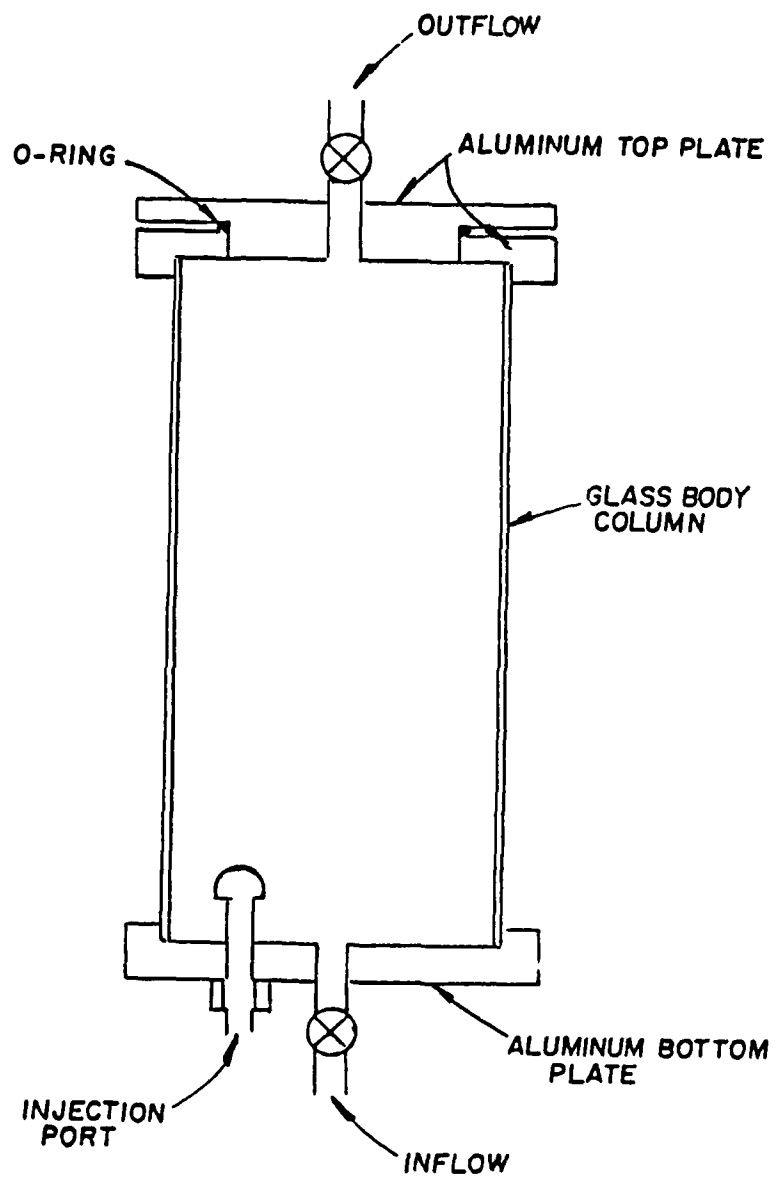


Figure 3.1 Diagram of laboratory column used in residual work.

drain tube), the top of the capillary fringe was established approximately three centimeters from the base of the column.

Styrene Solidification: Fifty milliliters of the initiated styrene was placed on top of the capillary fringe by injecting the styrene with a large hypodermic needle through the injection port on the base of the column. Using this volume of styrene resulted in a floating layer approximately 5 centimeters thick. An oil based dye (Oil Blue N) was added to the styrene prior to injection. This dye eventually changes from a blue to a red color due to the presence of benzyl peroxide.

The water table was raised in the column by pumping water via a peristaltic pump into the bottom of the column. Figure 3.2 shows a series of photos that illustrate the movement of the styrene when the water table is raised. A rate of 40 milliliters per hour was used and results in conditions such that the capillary number is well within the limits for maximum residual established previously in this report. As shown in Figure 3.3, the viscosity of the initiated styrene increases with time, so the water table fluctuation must be completed within approximately 12 hours. Once the final equilibrium was reached, the column was placed in a 85°C oven for 40 hours to polymerize the styrene.

Epoxy Solidification: Following the solidification of the styrene, the water was flushed from the column with isopropyl alcohol and the column was again dried. An epoxy

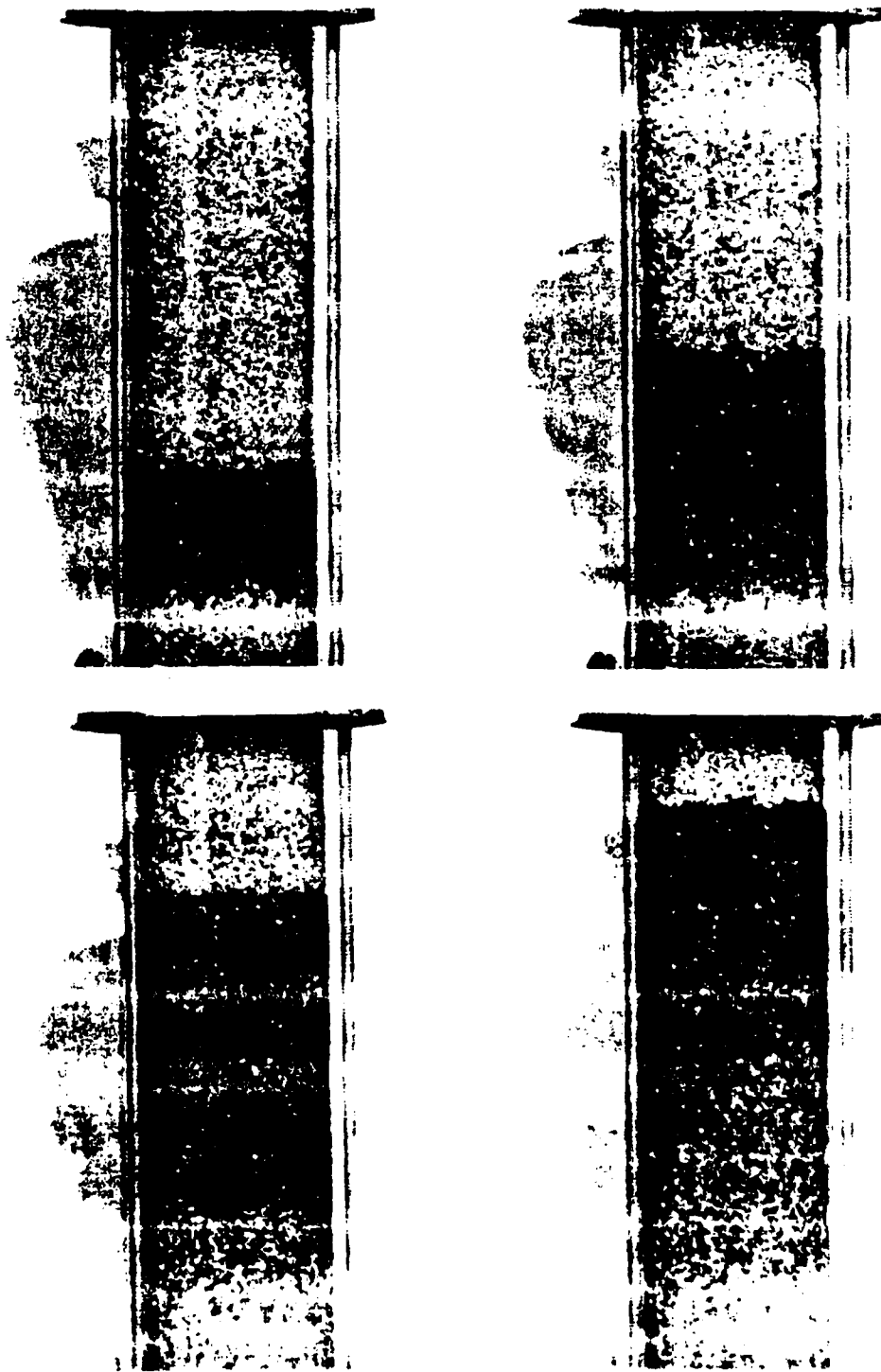


Figure 3.2. Photos of styrene movement resulting from water table being raised.

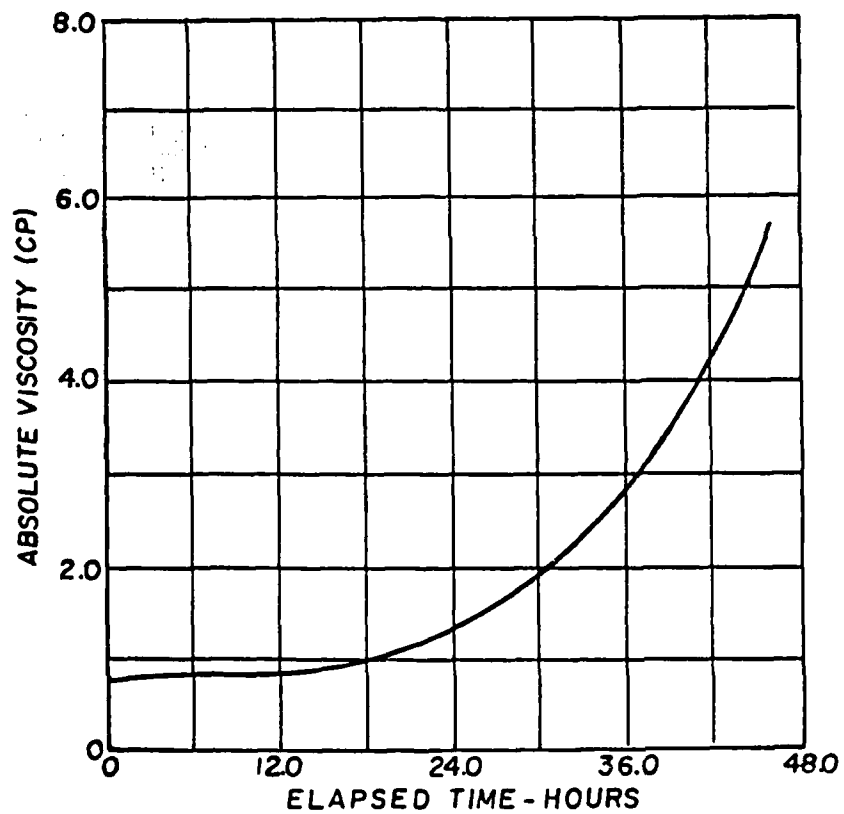


Figure 3.3 Change in viscosity of initiated styrene with time.
(Wilson et al, 1989)

resin was injected under vacuum to fill the pore space previously occupied by the water. The epoxy generally hardens enough to prevent flow within one hour, so this step must be completed quickly. The same dye used to color the styrene was also used in the epoxy. However, the dye remains a blue color, providing a contrast between the red solidified styrene and whitish sand grains. Twenty-four hours was allowed for the epoxy to properly cure.

Sectioning: After epoxy injection and curing, the column is a solid consisting of the porous media, styrene, and epoxy. The column was sacrificed for observation of serial cross-sections by sectioning the column into approximately 2 mm disks with a diamond blade rock saw.

Digitizing: The amount of solidified styrene in each cross-section is measured with a video camera and a digitizing software produced by ERDAS (ERDAS, 1988). The greatest contrast between the styrene and the epoxy was achieved by placing the thin sample disk on an unlit photographic slide viewing table, and using a reflected light source at a relatively shallow angle of about 30 degrees. Lighting the sample in this manner allowed for a true two-dimensional measurement of the styrene present on the surface of each disk.

The digitizing process is complex, and requires a familiarization period before accurate measurements can be made. Figure 3.4 shows the final comparison between the

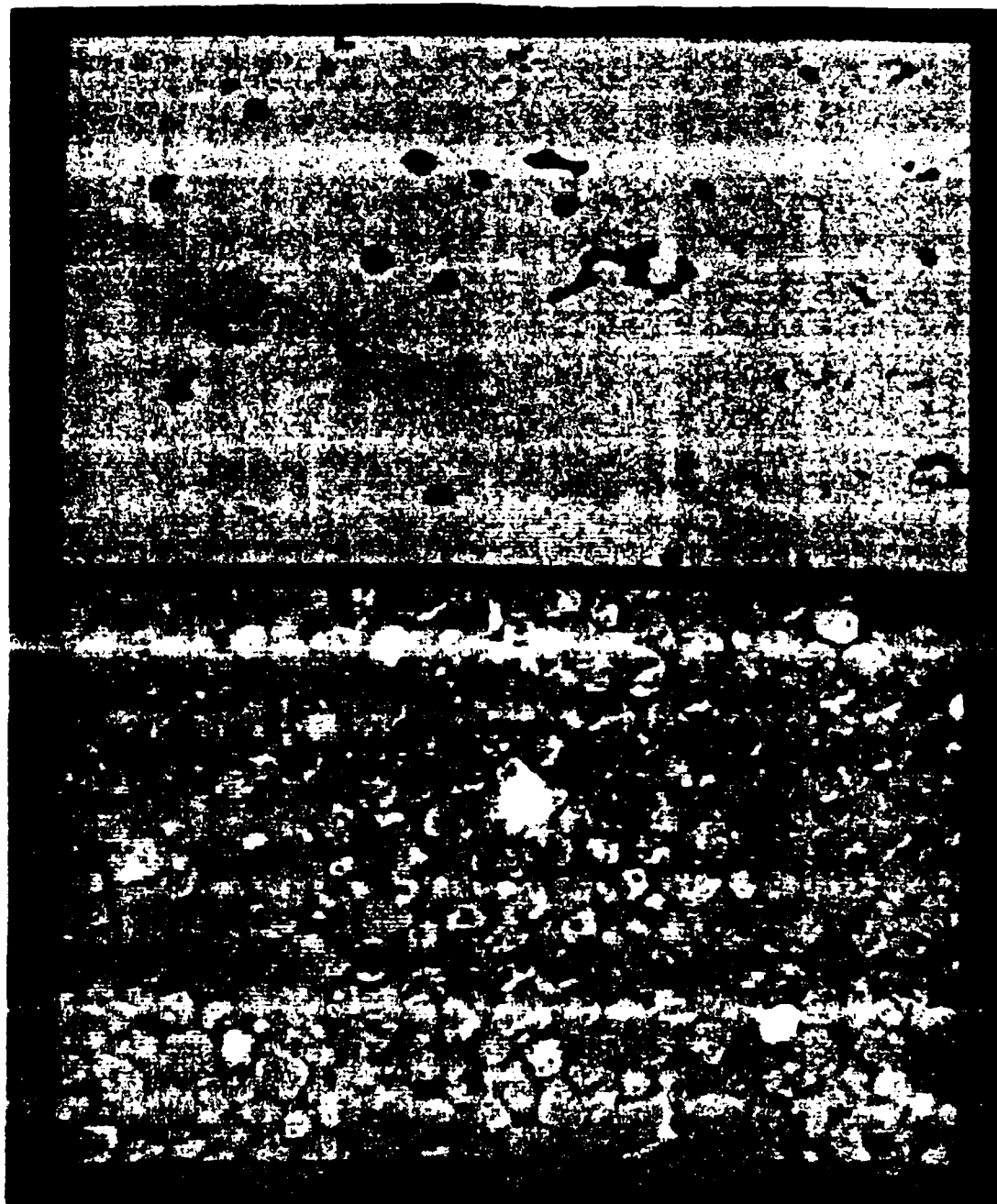


Figure 3.4 Comparison of WEDM-measured styrene content (top) with original digitized image (bottom).

initial digitized image (bottom) and the styrene vs sand and epoxy classified image (top). The styrene appears as the white area in the classified image.

3.3 Preliminary Results

A silica sand purchased from Colorado Silica Sand, Inc. near Colorado Springs, Colorado was used for the residual tests. All the sizes contained about 98% SiO₂. The sand was relatively round, and varied in size from 0.25 to 3.35 mm. The size characteristics associated with each size classification are shown in Table 3.2. For convenience, the average grain diameter was used to designate the different sizes of sands used in the testing. All sand was cleaned under running water on a sieve of the smaller size limit to remove any fractured sand grains and to remove any silt or clay adhered to the sand grains.

The first series of tests were performed to measure the styrene residuals in a range of uniform sand sizes. The characteristics of the fluids were kept constant for these tests. For the cross sections which held a uniform distribution of LNAPL, residuals were measured as occupying an average of 10 to 12% of the available pore volume. Although it is difficult to draw general conclusions from the limited data available, the lack of sensitivity to grain size in a uniform soil is consistent with the saturated zone measurements made by Wilson and Conrad (1984) on different

Table 3.2. Sand size designation used in residual tests.

U.S. Sieve Series Designation (mesh)	Size Range (mm)	Assumed Average Size (mm)
6-10	2.00 - 3.35	2.68
8-12	1.70 - 2.36	2.03
10-16	1.18 - 2.00	1.59
16-20	0.85 - 1.18	1.02
20-30	0.60 - 0.85	0.72

sizes of glass beads. Their residual was slightly higher at 14%, but the difference could be the result of an increased interfacial tension due to a different dye in the styrene. The glass beads should also have a more perfect wetting condition than the natural sand, which according to the Laplace equation would increase the effective tension on the fluid/fluid interface. Wilson and Conrad (1984) also had different initial saturation conditions, which would influence the final residual concentration (Pickell et al 1966).

As seen in Figures 3.5 and 3.6, the styrene residuals were not constant with respect to height in the column. For both these sands, residual LNAPL increased with column height. Only slices corresponding to two column levels could be measured for the 2.03 mm sand test. Above 7 cm from the initial styrene/water interface, styrene was observed only in the region of sand located near the edge of the glass column, with the main body of the column void of styrene. The smaller sand sizes tested, 1.59 and 1.02 mm, resulted in sample slices that contained styrene only in the region near the outer glass wall.

The authors are not aware of any reports of residual saturation varying with distance traveled by the LNAPL-water interface through a homogenous system. The use of short columns in other tests may not allow for a significant difference in LNAPL residual concentration over the length of the column. Also, each of the short columns are often treated

2.68 mm DIAMETER SAND

OIL BLUE N DYE

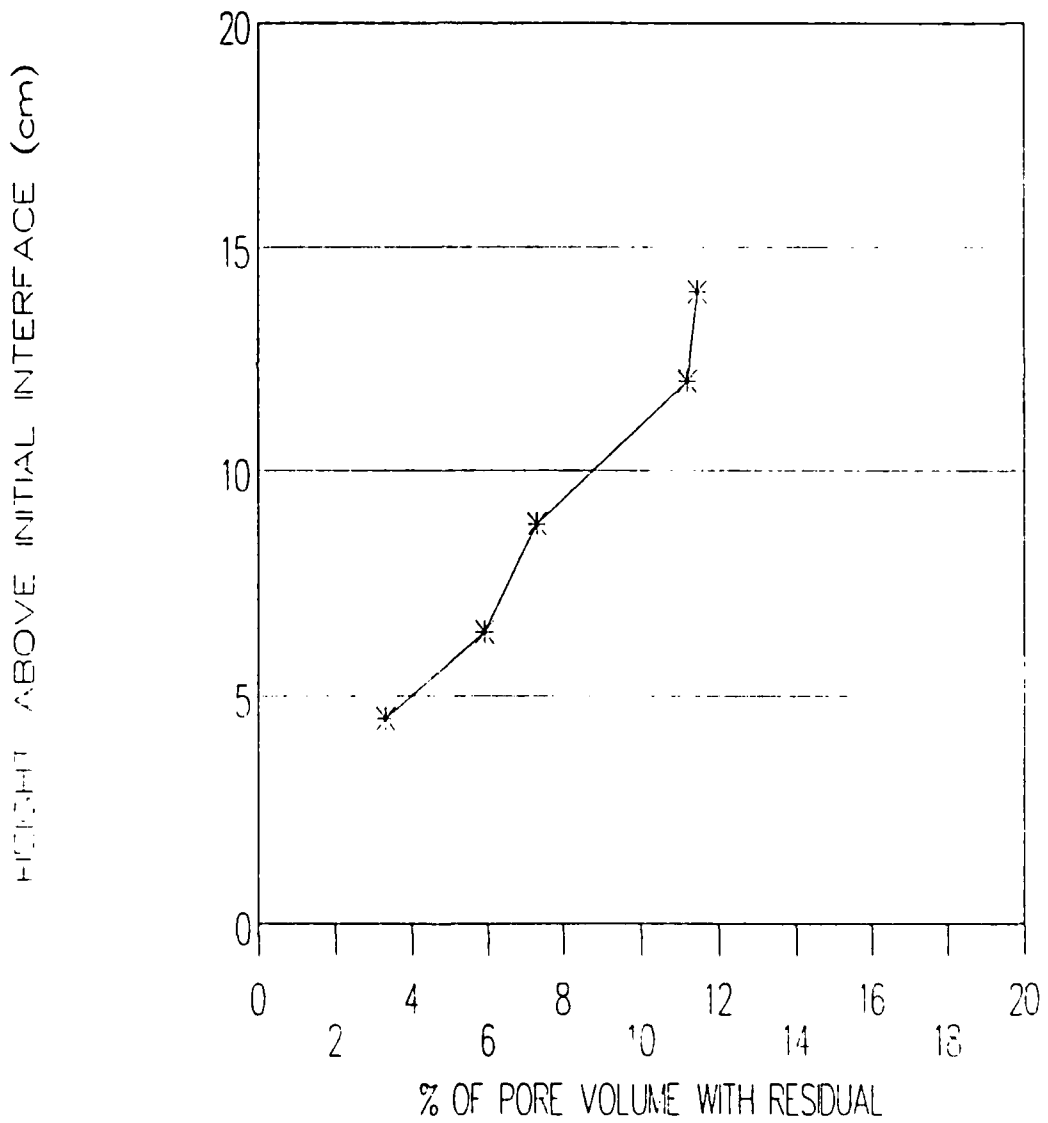


Figure 3.5 Styrene residual for 2.68 mm sand using Oil Blue N dye.

2.03 mm DIAMETER SAND

OIL BLUE N DYE

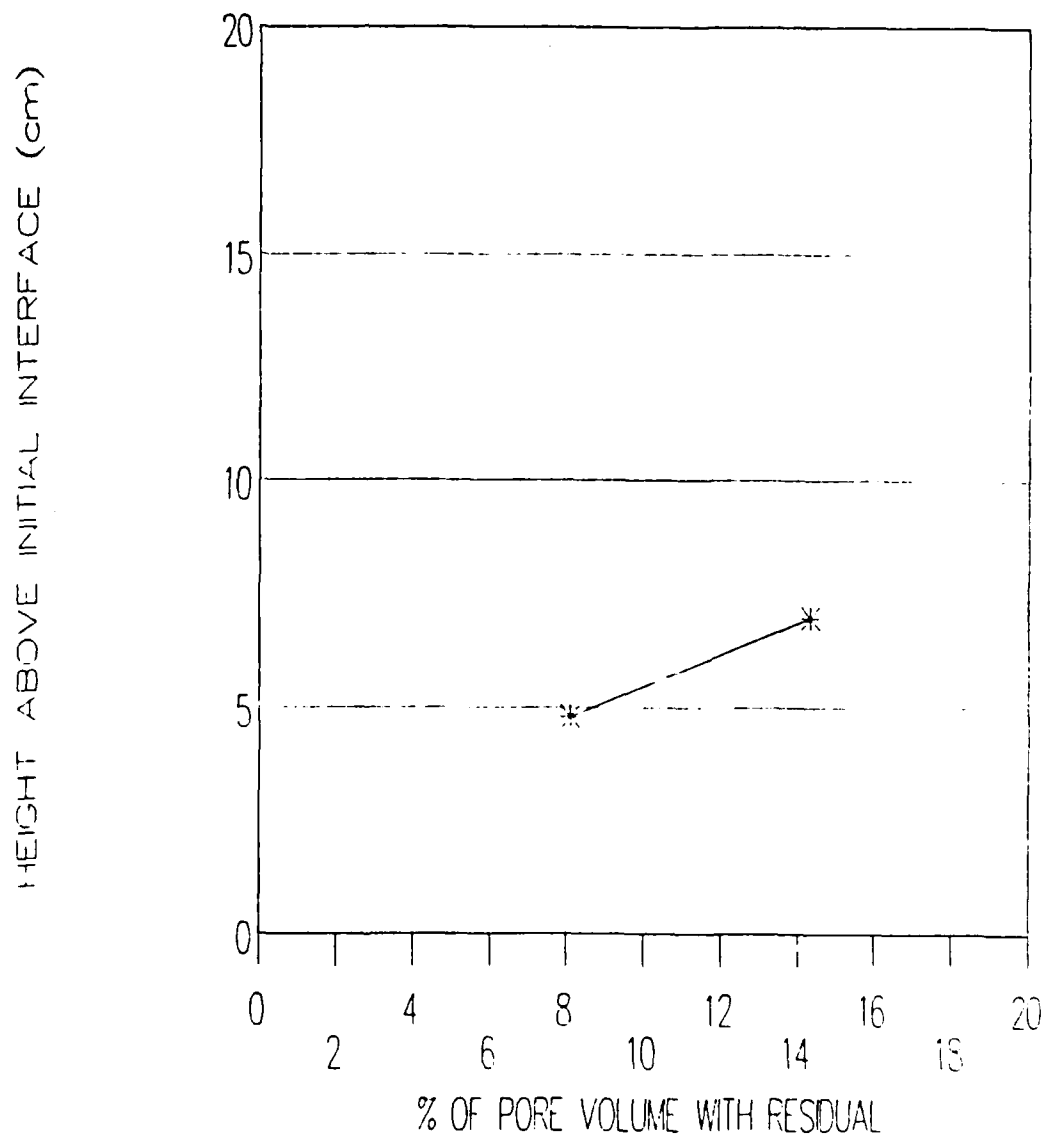


Figure 3.6 Styrene residual for 2.03 mm sand using Oil Blue N dye.

in a uniform manner prior to the displacement of the LNAPL by the wetting fluid, which may not allow for the evidence of the effect of distance traveled by the interface.

To test the effect of interfacial tension on LNAPL residual, a different dye was used to color the styrene. Sudan IV dye colored the styrene red, and resulted in an interfacial tension approximately twice that of the Oil Blue N dye. Table 3.3 summarizes the surface and interfacial tensions measured for styrene colored with these two dyes.

As seen in Figure 3.7, Sudan IV dye gave higher styrene residuals than the Oil Blue N dye for the same 2.68 mm sand size. The LNAPL residual was also fairly consistent over the first 13 cm that the styrene/water interface traveled. Above that level, residual styrene increased in a similar manner to the case with the Oil Blue N dye. Although doubling the interfacial tension between the styrene and the water did not result in a doubling of the measured residual, the increase in stability of the measured residual is in itself significant. When a higher interfacial tension exists between the wetting and the nonwetting phase, the system appears to be more resistant to the entrapment process that caused the increase in styrene residual with travel distance mentioned previously. Since interfacial tensions for gasoline and JP4 jet fuel are approximately 25 dynes/cm, the conditions of the test using Sudan IV dye in the styrene may better approximate a "natural" fuel spill than does the styrene and Oil Blue N test. More

Table 3.3. Surface and interfacial tension measurements for fluid pairs used in residual tests. All measurements are in dynes/cm.

	<u>air</u>	<u>water</u>
styrene with Oil Blue N dye	35.1	10
styrene with Sudan IV dye	34.5	21

2.68 mm DIAMETER SAND

SUDAN IV DYE

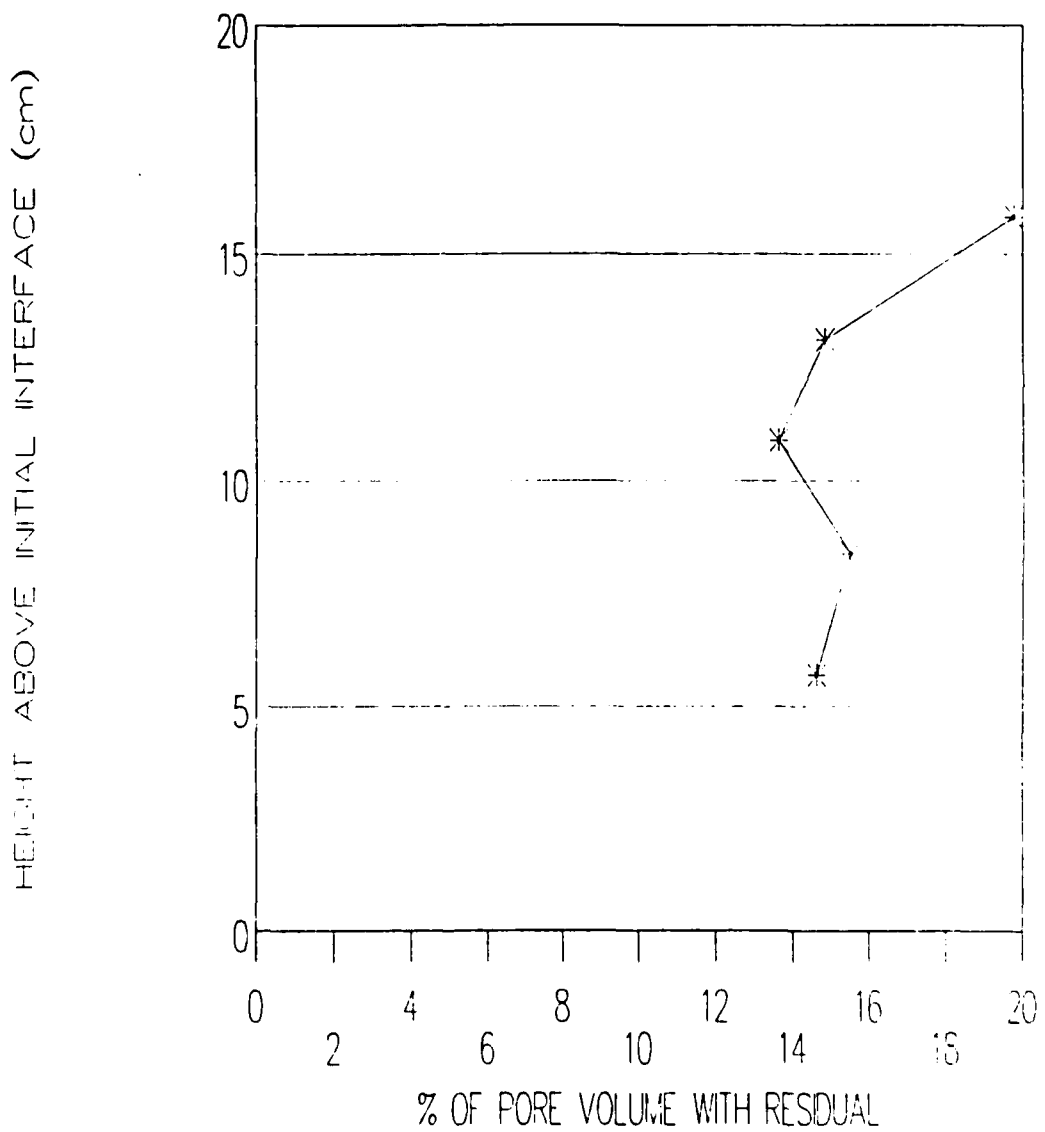


Figure 3.7 Styrene residual for 2.68 mm sand using Sudan IV dye.

tests are needed to determine the exact solution to this problem.

The change in styrene residuals with height in the column is not the result of increasing interfacial tension, as measurements made over the length of time of a test revealed only very minor changes for both surface (styrene-air) and interfacial (water-styrene) tension. Two other possibilities exist that might explain this anomaly. Schiegg and McBride (1987) have measured an edge effect of the container wall on the sand pack that extends four to five grain diameters from the edge. This edge effect results in a higher porosity, and thus slightly larger pores in that region. It is suspected that the smaller sands gave conditions that were more sensitive to these non-homogeneities in the column.

Larger pores would be the first to be occupied by the non- or intermediate-wetting phase during the imbibition process. As a result of the dependence of flow on saturation level, these conditions could result in regions of self-perpetuating preferential flow conditions in the column. If the water was able to move in the smaller pores found in the middle region of the column, with the styrene preferentially restricted to the larger pores along the core boundary, the water could bypass the floating styrene layer to the sand at residual water content above. The styrene which had initially been floating would become immobile once water occupied the region above the styrene. This is consistent with the

findings of Dias and Payatakes (1986), who demonstrated that a ganglia surrounded by water is extremely stable due to the reversal of the capillary forces from the initial air-LNAPL-water system.

In a natural aquifer system, the sands making up the aquifer substrate would generally contain more heterogeneities than the laboratory columns. As a result, the entrapment of a LNAPL due to bypassing and preferential flow in a natural system should be even more pronounced than in the controlled laboratory environment.

Another possible explanation of the styrene residuals increasing with height in the column might be the result of interstitial water being displaced by the LNAPL front. As this water moves ahead of the invading styrene, it could also form a continuous band. Once the styrene is "capped" by the water, small areas of styrene will be isolated from the main body of styrene. Small entrapped pockets of LNAPL would not have the volume to supply the buoyancy necessary to move them vertically, and will thus remain entrapped. A higher interfacial tension between the two fluids would delay the conditions that result in the styrene residual being isolated by the water.

The smaller sands will have a higher water content at a given capillary pressure than will the large sands. This larger volume of interstitial water could result in the

smaller sands being more sensitive to the process that results in isolated areas of styrene.

A second system, using a horizontally layered system, was also tested. This column contained a 2.68 mm sand in the lower half, and a 0.72 mm sand in the upper half of the cylinder. Upon initiating the water table movement, the LNAPL layer seemed to move as had been observed previously with that size sand. However, when the styrene layer contacted the smaller sand, movement ceased, and water bypassed the styrene to the smaller sand above. Figure 3.8 shows the results of this test. The measured residuals were influenced by the smaller sand layer for all the heights measured, but especially for the sand located immediately below the small sand, where the styrene residual occupied nearly 72% of the available pore volume. Possibly a minimum thickness of floating hydrocarbon is required to provide the buoyancy force necessary to exceed the displacement pressure of the small sand, however, this hypothesis has not been tested. This test shows the dramatic effect on entrapment and trapping of a LNAPL if stratification is present in an aquifer system.

0.72 mm/2.68 mm - WETTED SAND

OIL BLUE N DYE

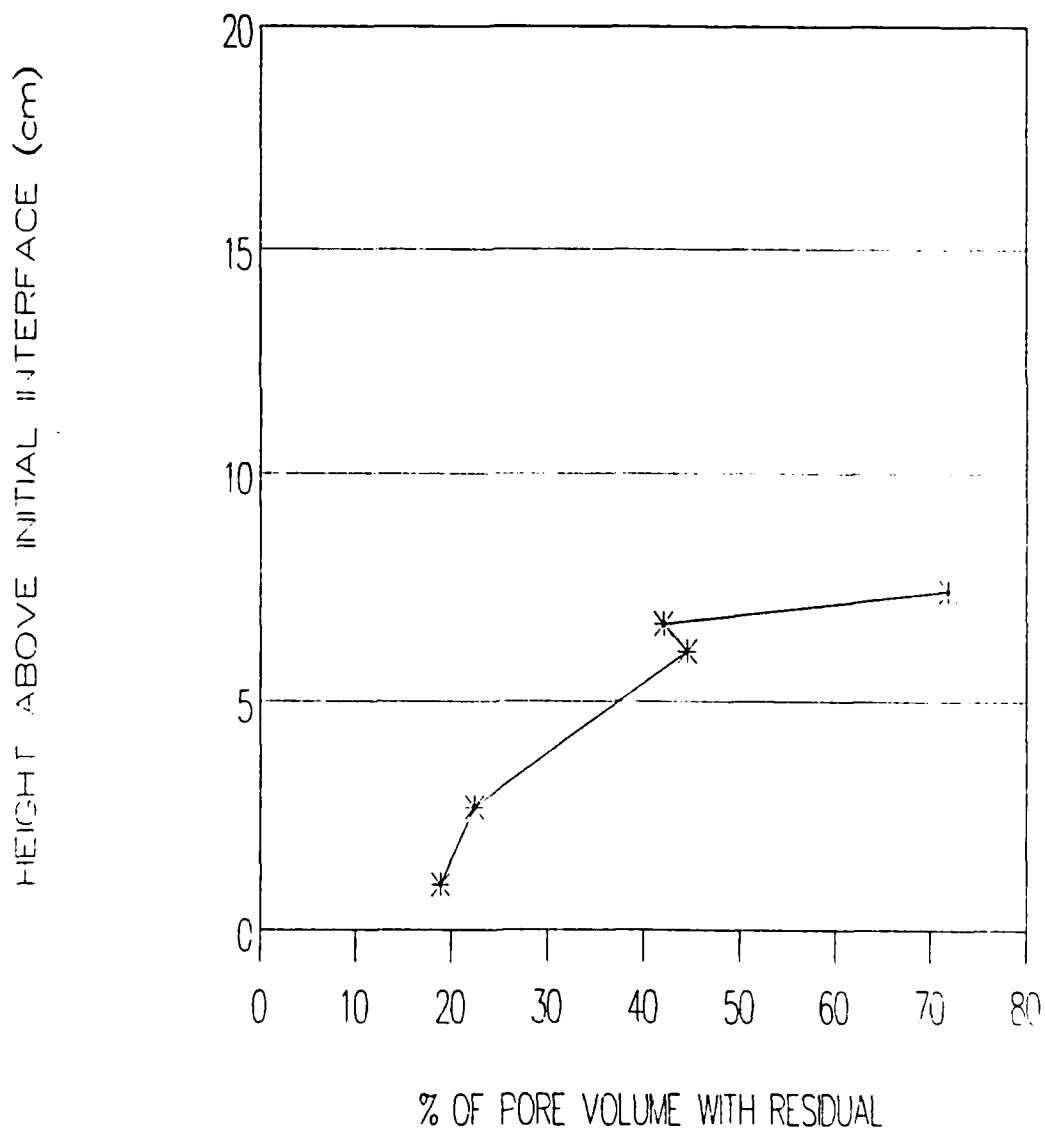


Figure 3.8 Styrene residual for layered system of 0.72 mm sand over 2.68 mm sand.

CHAPTER 4.0

FIELD INVESTIGATION

4.1 Introduction

The primary objective of the field investigation was to determine the vertical distribution of an LNAPL at a field site and verify our laboratory results that indicate a significant percentage of the total LNAPL volume contaminating an aquifer could be entrapped below the water table under fluctuating water table conditions. Two secondary objectives were included in this part of the project. The first was to field test a prototype cryogenic sampler designed to extract intact samples of fluids and solids from below a water table in sandy soils. The second was to evaluate the usefulness of baildown tests and monitoring well data to predict total product volume.

4.2 Site Description

POL Area "B" at Tyndall Air Force Base, Florida was the site used for the field investigation. The area is in the flight line area of the base and is a former fuel storage area that contained jet fuel and diesel in underground tanks. A schematic of the location of the fuel tanks is shown in Figure 4.1. The tanks were removed a few years ago and the area was backfilled with local sand, concrete block, and other material including wood. Figure 4.2 shows the particle size distribution for the Tyndall base soil, a poorly graded sand.

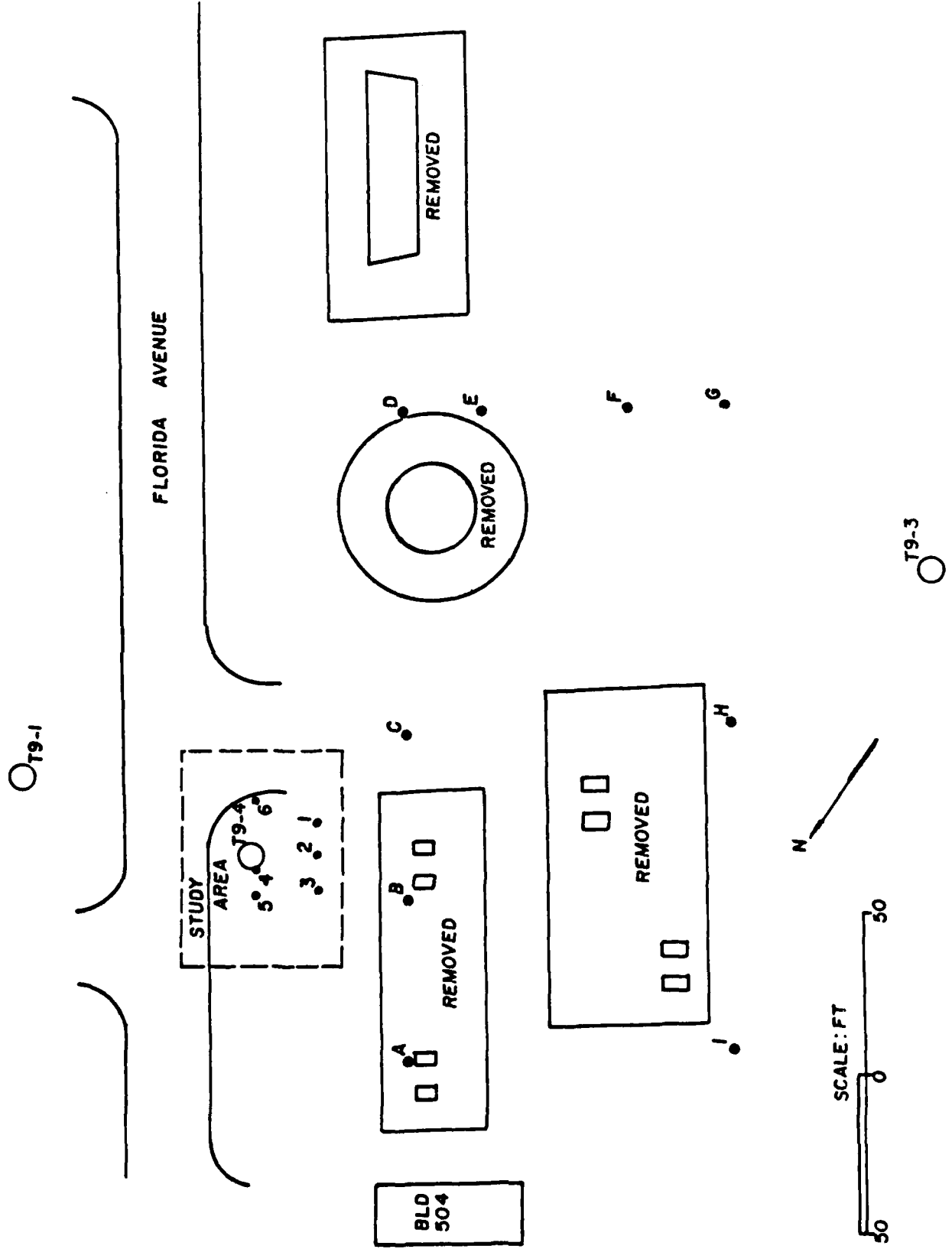


Figure 4.1 A schematic showing the location of fuel tanks in the field study area.

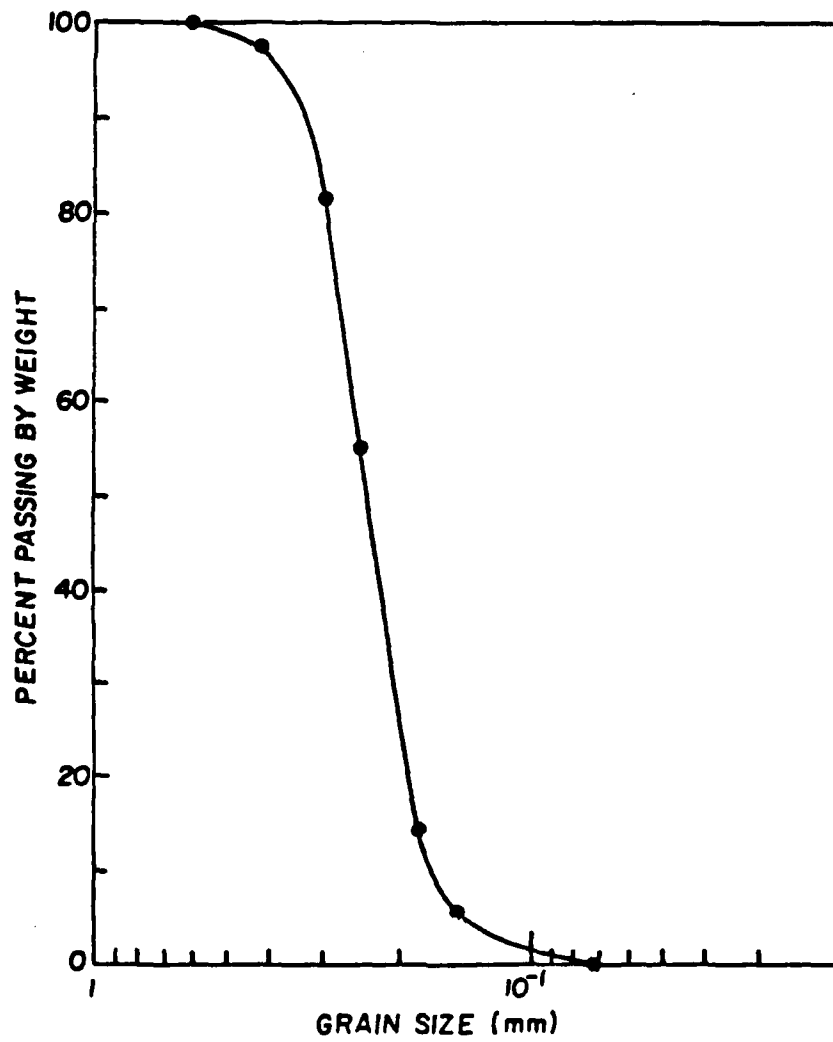


Figure 4.2 Particle size distribution for Tyndall AFB sand.

The water table at the site slopes from southwest to northeast. Ground water levels range from about 1 foot to 10 feet below the ground surface. Because the soil is sandy, the water table rises quickly following periods of heavy rainfall and then declines during dry periods. Tyndall AFB has an average annual rainfall of 140 cm (55.2 inches) occurring in approximately 125 precipitation days (Environmental Science and Engineering, 1988). At the time of the field study, the water table was 4 to 5 feet below the ground surface.

Figure 4.3 shows the location of the sampling points and observation wells. For each point, ground surface elevations, water table elevations and product thickness in wells at the time of the investigation are shown in Table 4.1. About 12.5 cm (0.41 feet) of product was found in Well T9-4. This well was monitored to evaluate the range of fluctuations that could be expected during the field study. Product thickness varied from 8.8 cm (0.29 feet) to 17 cm (0.56 feet) during the three week evaluation period. The product thickness was measured with a oil/water interface probe and, therefore, does not provide a continuous record of product thickness. No attempt was made to measure diurnal fluctuations. Product was also found in hole 6, located 16 feet from T9-4. Wells A and D contained product in a lesser amount. Product was not found in the other wells at the site, including hole 5 which is located just four feet from T9-4.

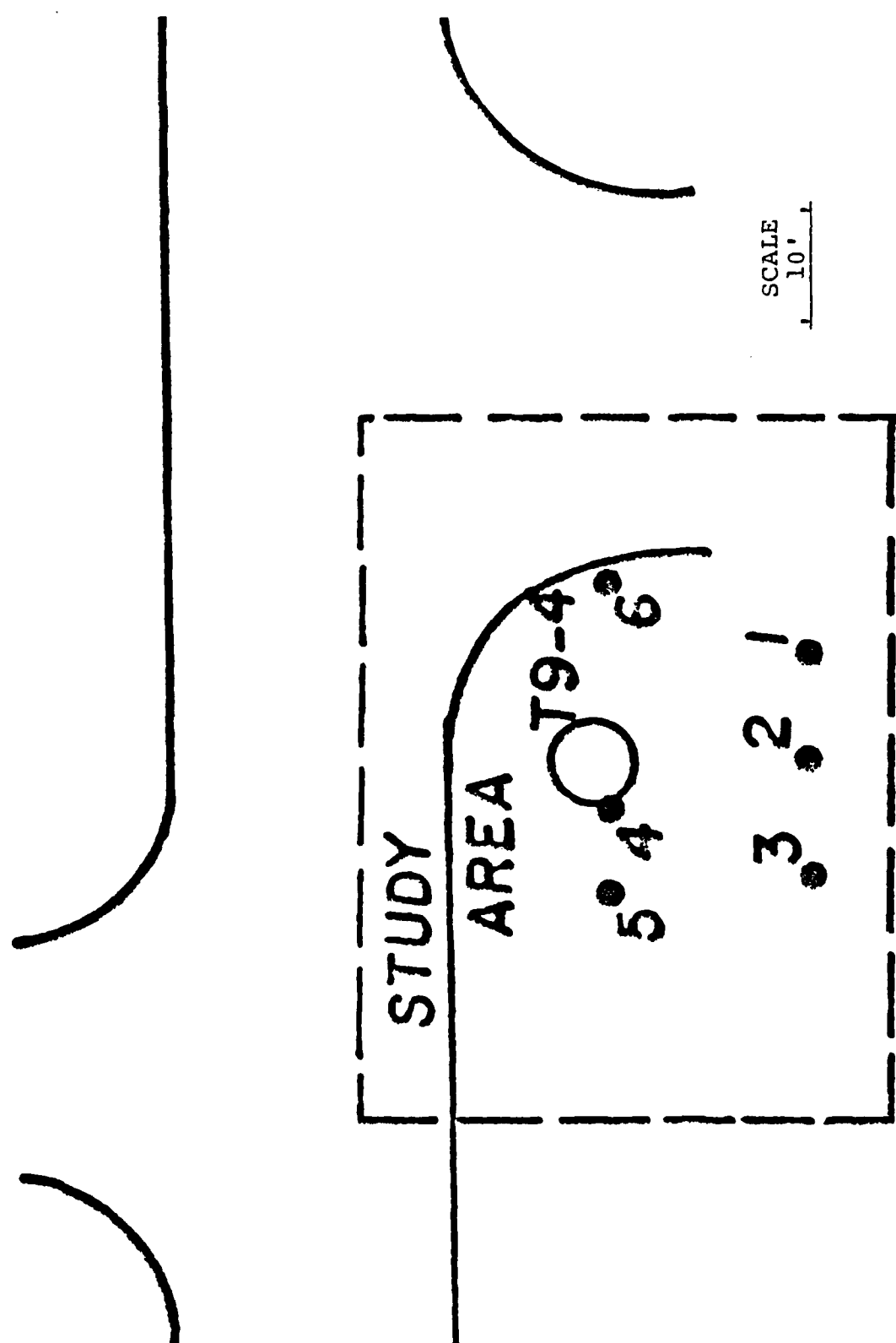


Figure 4.3 Location of sampling points.

Table 4.1 Elevations and Product Thicknesses at Field Site

FIELD ID	GROUND ELEVATION (FT MSL)	WATER TABLE ELEVATION (FT MSL)	PRODUCT THICKNESS (FT)	DEPTH TO WATER TABLE (FT)
T9-4	22.1	17.5	0.41	4.6
T9-3	26.1	21.8	0	4.3
1	22.6	----	----	----
2	22.4	----	----	----
3	22.5	18.3	0	4.2
4	22.5	18.3	0	4.2
5	22.1	17.7	0	4.4
6	22.2	17.4	>0.25	4.8
A	22.6	18.7	0.1	3.9
B	22.5	18.7	0	3.8
C	22.3	19.0	0	3.3
D	22.4	18.7	0.1	3.7
E	22.7	18.1	0	4.6
F	23.3	21.0	0	2.3
G	23.7	21.3	0	2.4
H	24.4	21.4	0	3.0
I	24.3	----	----	----
J	24.6	----	----	----
K	25.3	17.5	0	7.8
L	23.6	18.8	0	4.8

---- INDICATES NO MEASUREMENTS TAKEN
 DATE OF SURVEY: JULY 14, 1989

4.3 Sampling Procedure

Samples were taken near Well T9-4 at locations 1 through 6 shown on Figure 4.3. Holes were hand augered through the unsaturated zone, a depth to about four feet below ground surface. Samples taken from within two feet of the ground surface were not saved for laboratory analysis because they appeared relatively clean. Soil below two feet was noticeably darker and was obviously contaminated. At about 4 feet, the soil was saturated and augering or using a conventional core sampler would result in loss of sand and fluid when the soil core was removed. To address this problem, a prototype cryogenic sampler was developed. This sampler is described in the next section. The cryogenic sampler allowed us to retrieve intact samples to a depth of 8 feet. The full depth was not sampled in some cases because we hit concrete or wood rubble. Several other holes were attempted but rubble limited the depth; holes with shallow samples only were not included in the analysis.

Extracted soil-fluid samples were placed in glass jars that were sealed, protected from sunlight, and packed in dry ice in the field immediately following coring. However, temperatures were over 90°F during the field testing so some volatilization undoubtedly occurred. Samples were transferred to a laboratory freezer each day and shipped frozen within three days to the chemistry laboratory for analysis.

4.3 Prototype Cryogenic Sampler

The sampler developed for this study is a solid body drive type sampler that incorporates an oversize cutting head, interchangeable internal sampling sleeves, and a gas expansion chamber for rapid cooling/freezing of the lower section of a soil core. The sampler is pushed into the soil medium to a pre-determined depth. CO₂ gas or liquid is introduced through a feed tube into the expansion chamber at a determined pressure and for a time interval sufficient to cool the liquid in the soil sample at the lowest end of the sampler to below freezing. The sampler is withdrawn from the soil, the drive head is removed and the sleeves containing the sample are removed from the top of the sample core barrel and separated into segments. Each segment is stored for analysis.

The sampler used in this study is a prototype. Although the concept has been shown to be valid, there are several changes that should be investigated to make the sampler easier to use and to characterize its usefulness under a variety of field conditions. Consideration should be given to designing only a cutting head that could be fitted to a standard split spoon sampler. Alternatively, the sampler core barrel could be redesigned to open like the clam shell split spoon. Protection of the gas/liquid lines, insulation of the lines and/or barrel and sampler diameter are aspects of the sampler that should receive further evaluation.

4.5 Laboratory Analysis

Analysis for total fuel volume was performed at the Tennessee Valley Authority Environmental Chemistry Laboratory in Chattanooga, Tennessee. The method used is a modification of EPA Method 418.1 (American Petroleum Institute, 1987). Freon is used to extract volatile and nonvolatile petroleum hydrocarbons from the soil prior to determining the total hydrocarbon via infrared analysis. Calibration is accomplished using prepared standards of a known hydrocarbon. The standard chosen should resemble the scan of the unknown in the region of interest. Results are given in units of milligrams of hydrocarbon per kilogram of wet soil. The laboratory also measured percent dry weight for each sample by oven drying.

Percent Recovery is estimated in the API manual for gasoline on a fine grained clayey loam, gasoline on a medium sand, and No. 2 fuel oil on a medium sand. These values are 82%, 87% and 95%, respectively. To assess the recovery and precision of the analysis in this study, 15 samples were analyzed in duplicate, and 22 spiked samples (both soil and blank samples) were analyzed by the laboratory. The blank samples were prepared samples of freon, water and a reference oil. Of the 22 spiked samples analyzed, 16 were spiked by the chemistry laboratory and 6 were blind spikes sent with the soil samples. The blind spikes were prepared at Tyndall AFB using clean JP4.

The results of the quality control program to determine precision and recovery are shown in Tables 4.2 and 4.3. The precision of the method was satisfactory with an average standard deviation of 13%. Mean recovery was calculated as 70% with a standard deviation of 33%. Blank spikes tended to have a high recovery of 92%, whereas the spiked soil had a mean recovery of 64%. The spiked soil recovery value corresponds to the percent recovered from soil and, thus, includes the loss of hydrocarbon during the laboratory extraction procedure. This recovery value of 64% will be used in the subsequent analysis. None of the values given in Table 4.3 include field losses due to handling or losses that could occur during the storage time between the field test and the laboratory analysis. Additionally, the samples were spiked with either clean JP4 or a laboratory reference oil. It is expected that recovery values of a contaminated fluid may be significantly different than values obtained for clean fluids.

4.6 Results

The total hydrocarbon content in milliliters of hydrocarbon/kilogram of dry soil is given for each location sampled in Figures 4.4 through 4.9. To provide a reference, the relative ground surface and water table elevations are shown on each figure. A recovery factor of 0.64 and a fluid specific gravity of 0.77 were assumed to convert the raw lab data to the data shown in these figures.

Table 4.2 Precision of laboratory method

ID	VALUE #1	VALUE #2	RSD
1-6	9400	8100	17.0
1-10	1300	1200	7.1
2-1	200	<200	-
2-5	1700	1600	5.4
2-6	<200	340	-
2-7	2300	2800	17.0
2-8	930	830	10.0
2-2	140	150	6.1
2-11	320	420	24.0
2-14	8800	7300	17.0
1-8	3400	4600	27.0
2-12	1000	1000	0.0
5-8	50	<30	-
6-6	670	970	33.0
1-2	3800	4200	8.9
1-4	4200	4300	2.1
2-9	1000	1000	0.0
2-17	260	300	13.0
MEAN RSD			N = 13 = 13.

Table 4.3 Estimation of Recovery Factor in Laboratory

ID	OBS. (PPM)	BKG. (PPM)	RECOV. (PPM)	ADDED (PPM)	%RECOV.	
1-6	9380	8755	625	625	100%	
2-1	3000	200	2800	5700	49%	
2-6	3090	270	2820	7350	38%	
2-11	1940	370	1570	6940	23%	
1-10	2830	1250	1580	6020	26%	
5-5	310	240	70	250	28%	
5-11	230	30	200	250	80%	
2-8	3580	880	2700	3920	69%	
5-9	4400	30	4370	7580	58%	
2-17	2370	280	2090	2630	79%	
6-6	4930	820	4110	6670	62%	
				MEAN	56%	
				S.D.	25%	
2-7	17500	2550	14950	12500	120%	JET FUEL SPIKE
---	281	0	281	250	112%	BLANK SPIKE
---	260		260	250	104%	BLANK SPIKE
6-11	11000	5400	5600	12500	45%	JET FUEL SPIKE
---	10000	0	10000	12500	80%	BLANK JET FUEL SPIKE
				MEAN	92%	
				S.D.	30%	
A	4300	0	4300	15100	28%	
B	48000	0	48000	51300	94%	
C	130000	0	130000	185600	70%	
D	200000	0	200000	189600	105%	
E	190000	0	190000	152500	125%	
F	13000	0	13000	34800	37%	
				MEAN	77%	
				S.D.	0.33	
			TOTAL	MEAN	70%	
				S.D.	33%	
			SPIKED SOIL ONLY	MEAN	64%	
				S.D.	31%	

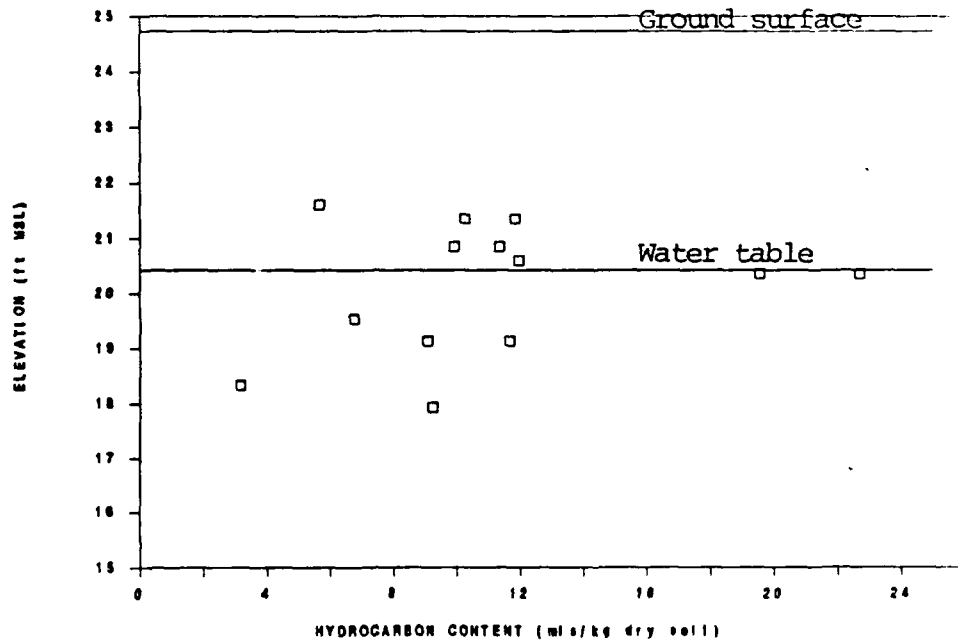


Figure 4.4 The total hydrocarbon content measured at point #1

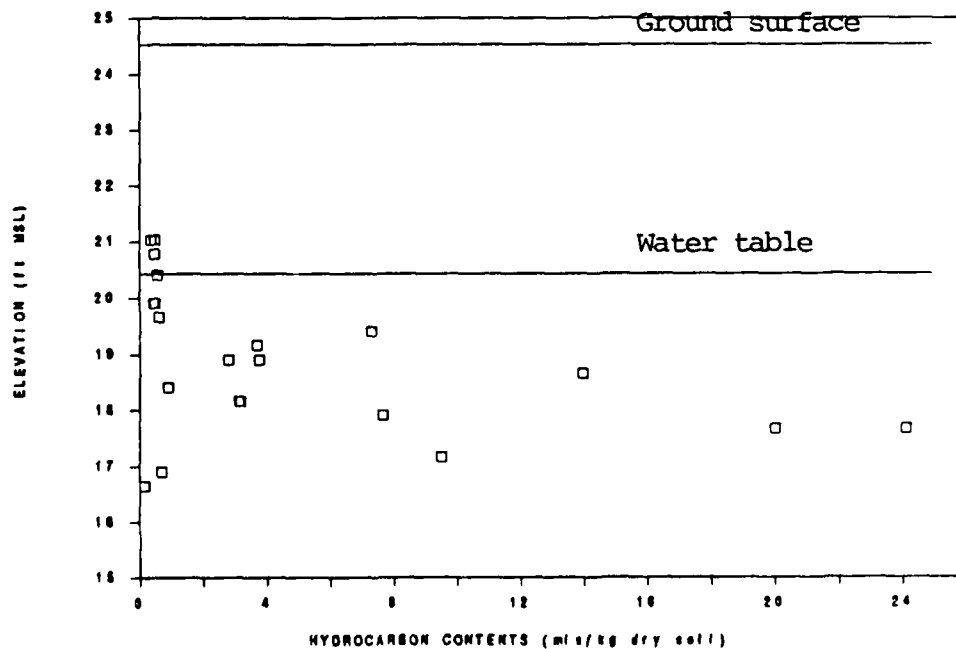


Figure 4.5 The total hydrocarbon content measured at point #2

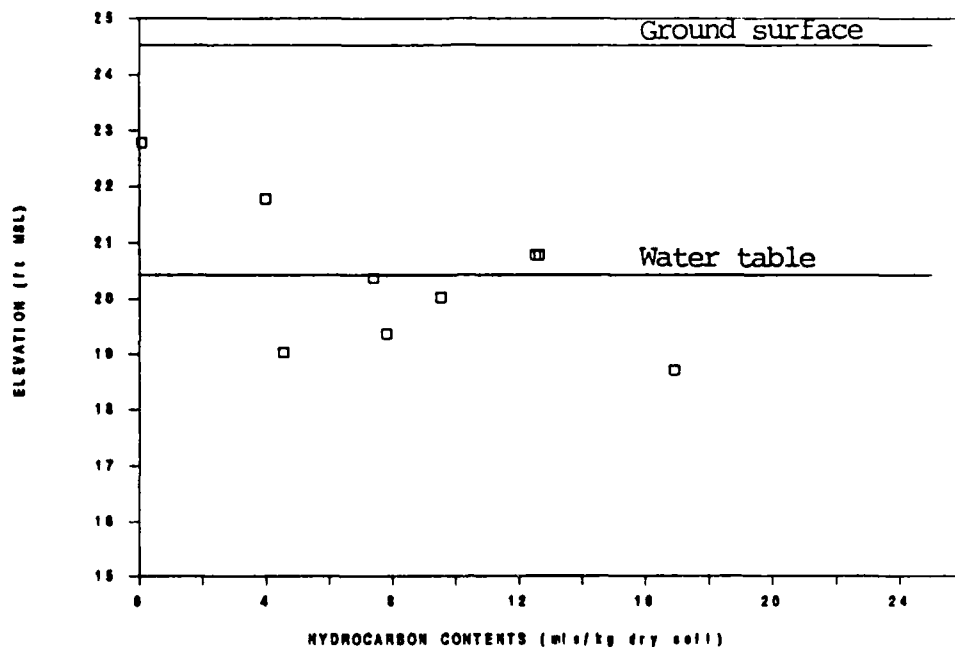


Figure 4.6 The total hydrocarbon content measured at point #3

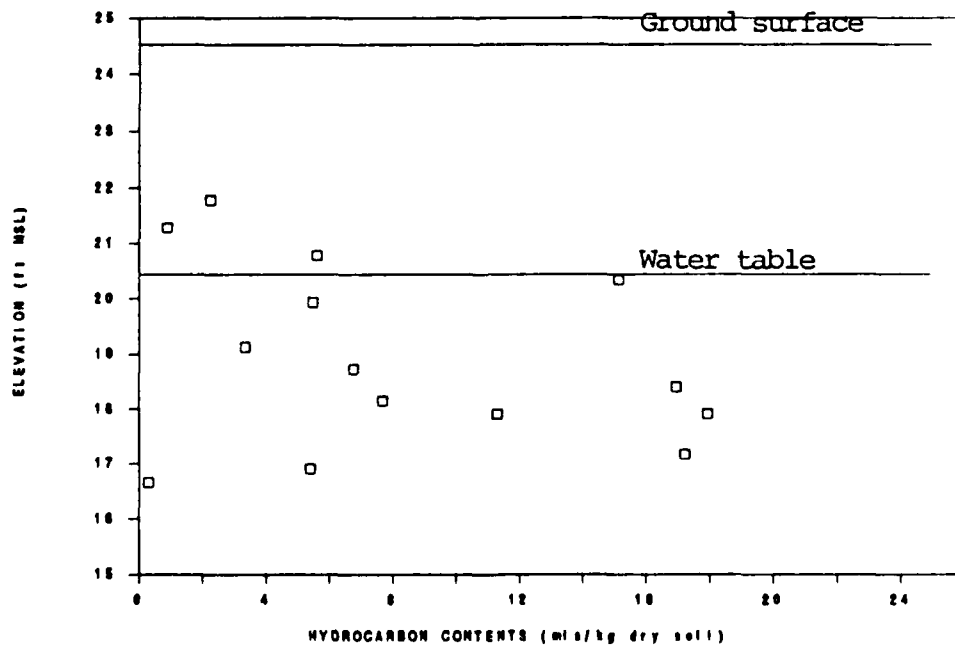


Figure 4.7 The total hydrocarbon content measured at point #4

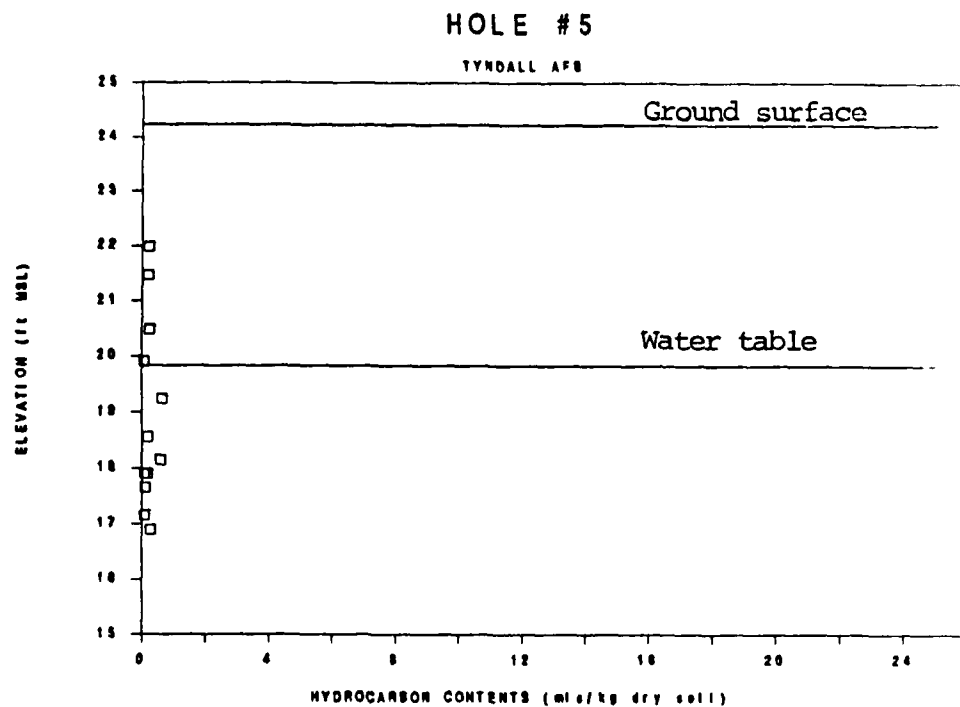


Figure 4.8 The total hydrocarbon content measured at point #5

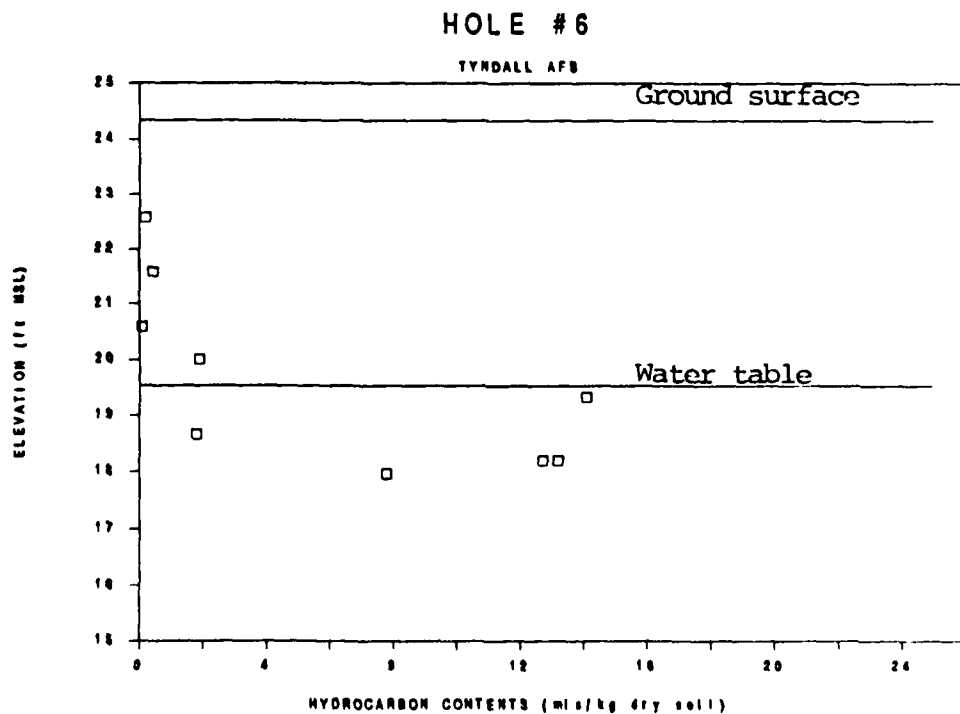


Figure 4.9 The total hydrocarbon content measured at point #6

The following sections present an evaluation of total jet fuel contamination of the study site based on results from (1) direct sampling, (2) baildown tests and (3) interpretation of well data.

Direct Sampling: Six holes were sampled during this filed project. The data obtained from these six holes show the significant spatial variability in aquifer characteristics across the study site. This spatial variability should be thoroughly characterized, but this was not possible during this study. As a first approximation, a simple averaging of the data was used to obtain an estimate of site contamination. However, it should be kept in mind that the site is very heterogeneous and that the values presented for jet fuel volume are only gross averages. One objective of this study is to evaluate the usefulness of the baildown test and monitoring well data. Data for these evaluations could only be obtained from well T9-4. Because of this, it is reasonable to use the averaged value obtained from direct sampling for comparison with the baildown test and monitoring data. Additionally, it was obvious during the analysis phase that neither the well data nor the baildown test correspond to data from Hole 5, the hole closest to the well. Because of the very low concentrations found at Hole 5, it was decided to exclude this data from the subsequent analysis. It is suspected that because of the close proximity of this hole to

the well, the area was significantly disturbed during installation and subsequent monitoring of the well.

All duplicate sample pairs presented in Figures 4.4 through 4.9 were averaged prior to further data analysis. Then, data from all holes were combined (excluding data from Hole 5) into one data set. Since the water table, as opposed to the ground surface, is the reference point for all of the analysis in this report, the data from all holes were combined with respect to position relative to the water table. The composite data set is graphed in Figure 4.10. Then, to smooth out the data, each data point in this composite set was weighted according to the depth interval it represents. Averaged composited values were determined for each 0.5 foot interval and are shown in Figure 4.11.

The higher fuel concentrations found near the water table are expected from equilibrium theory. Lower concentrations above the water table are probably due to volatilization, since this shallow unsaturated zone is close enough to the ground surface for gas exchange to freely occur. The peak in concentrations at about three feet below the water table is unexpected. However, it clearly occurred in holes 2, 3 and 4, and to some extent in holes 1 and 6. Without additional data on the soil, it is difficult to reach any conclusions as to the reason for this concentration. However, the existence of such a peak clearly shows the influence of soil heterogeneity,

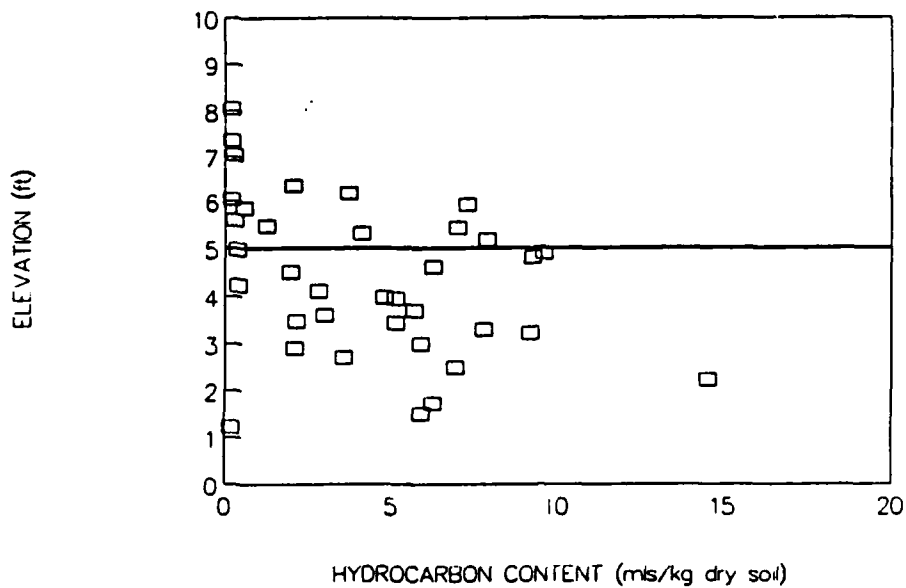


Figure 4.10 Composited total hydrocarbon content

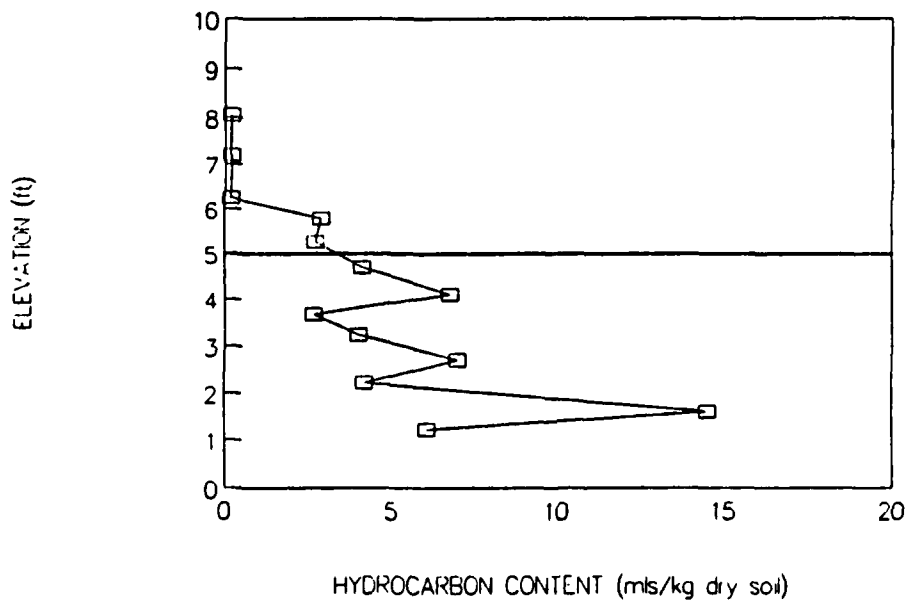


Figure 4.11 Averaged composited hydrocarbon content

the importance of considering the contamination below the water table, and the need for direct sampling.

Figure 4.12 shows LNAPL content for each hole above and below the water table in liters/square meter (and gallons/square foot) of surface area. The numbers were calculated using a soil dry bulk density of 1110 kg/m^3 and a recovery factor of 0.64. These correspond to the measured bulk density and a recovery factor based only on the spiked soil samples. The bulk density is low for a sandy soil. It would be expected to be closer to the maximum density for sands of 1630 kg/m^3 . Figure 4.13 shows calculated values if this maximum density is assumed. Note that the relative values of LNAPL above and below the water table are insensitive to bulk density but the total amount is directly related since the lab analysis determines mg of hydrocarbon per kg of soil. The recovery factor of 0.64 is discussed at the beginning of Section 4.6 of this report. This value reflects only losses after the sample reaches the lab. Any losses that occurred in extraction or handling of the sample in the field are not included. Therefore, numbers in Figures 4.12 and 4.13 are conservative. As shown in these figures, the total quantity of LNAPL below the water table is significantly more than above the water table. Analysis of the sampled data results in an averaged estimate of total fuel in the soil that varies from 10.6 L/m^2 ($0.26 \text{ gallons/ft}^2$) to 15.6 L/m^2 ($0.38 \text{ gallons/ft}^2$) depending on the bulk density assumed with 72% of

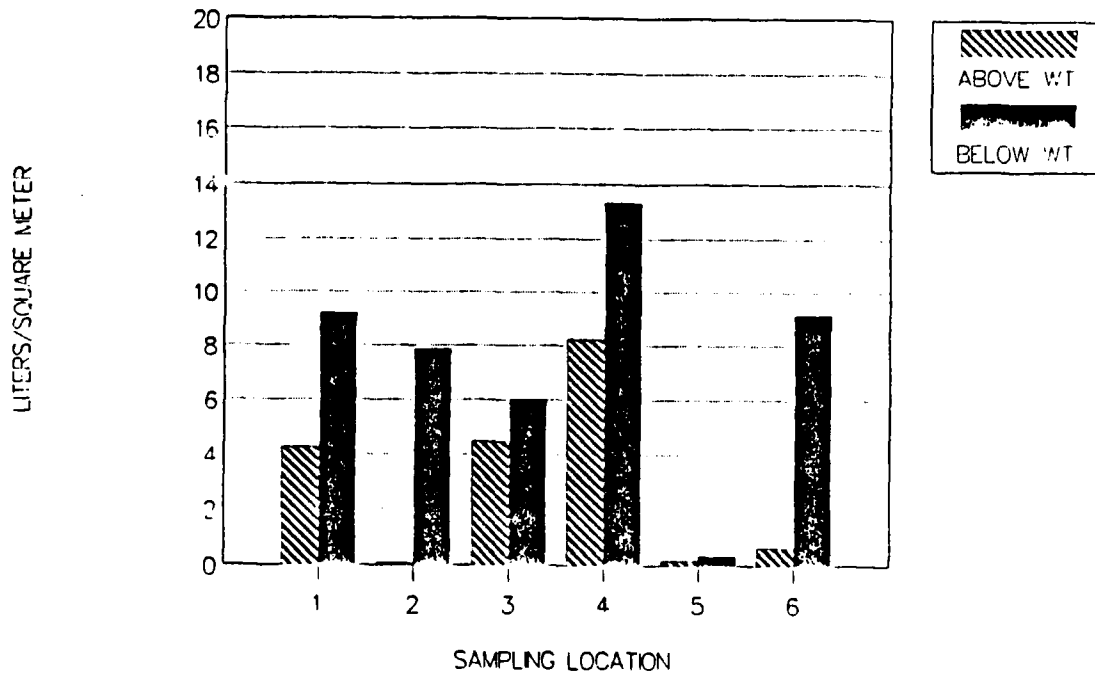


Figure 4.12 LNAPL content for each point above and below the water table for a bulk density = 1110 kg/m³

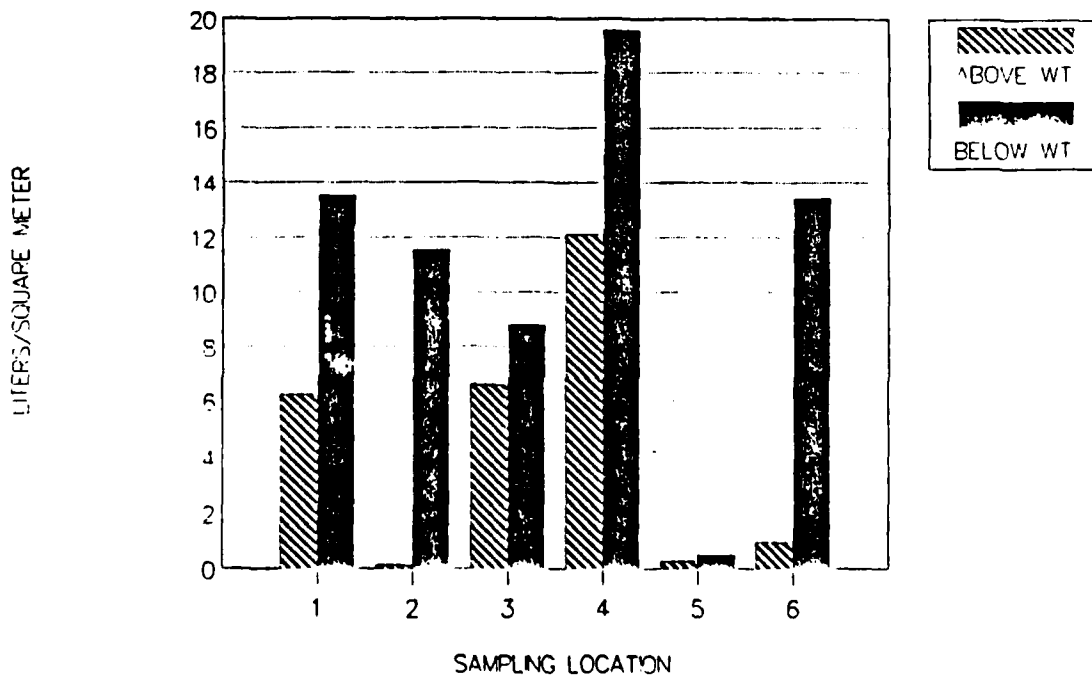


Figure 4.13 LNAPL content for each point above and below the water table for a bulk density = 1630 kg/m³

the total LNAPL located below the water table. Figure 4.14 shows LNAPL saturations above and below the water table.

Baildown tests: A baildown test to estimate "actual" product thickness of an LNAPL has been suggested by Gruszczenski (1987) and discussed further by Hughes (1988) and by Testa and Paczkowski (1989). These references should be consulted if the reader is interested in a more detailed explanation of the interpretation procedure. The baildown test is popular because of its ease of application and its familiarity to most groundwater engineers and hydrogeologists. Similar tests have been used for many years to evaluate permeability of aquifers to water. However, the theory upon which the data interpretation is based is questionable. Further, practical considerations such as the effect of the well casing and gravel pack are not adequately addressed. Other problems are discussed in the references.

One of the major assumptions of the baildown test is that there is a depth of soil that is 100% saturated with product. While this is never true, it is probably less in error when the aquifer material is a uniform sand such as Tyndall AFB sand. In this case, the residual water content is small and the pressure-saturation curve has a very sharp desaturation profile because of the uniform pore sizes. Therefore, the likelihood of good results from a baildown test is higher in this study than in the more usual case of well graded soils.

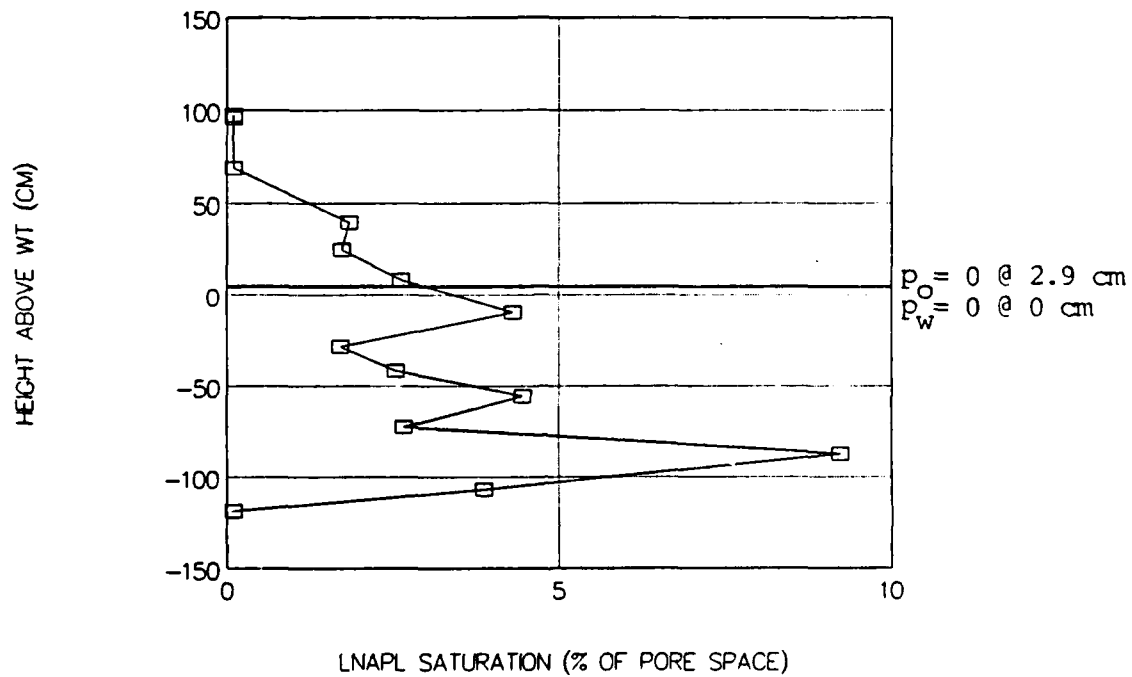


Figure 4.14 LNAPL saturations determined from direct sampling

Two baildown tests were performed at Well T9-4. In the first test, product and water were bailed from the well at time $t = 0$. The recovery of the well fluids was monitored for six hours using an interface probe. The second baildown test was performed in a similar manner. However, only product (no water) was initially bailed from the well.

In the discussion that follows, product thickness that is estimated using baildown tests refers to product thickness at positive pressures in the formation. This is different than the usual definition that refers to both product at positive pressures and product in the LNAPL-air capillary fringe. Baildown tests do not include the capillary fringe.

Figure 4.15 shows the results of the first baildown test. The top line on the figure is the top of product level in the well and the bottom line is the water/product interface level. Analysis of the first set of data follows the paper by Gruszczenski (1987). An inflection point is determined on the depth-to-fluid graph. The difference between the product line and the water/product interface line at the inflection point is interpreted to be the "actual product thickness" assumed by Gruszczenski to be saturated product thickness at positive pressures in the aquifer (again, this definition is different than the usual because the "actual product thickness" is only product at positive pressures). Figures 4.16 and 4.17 show the first 60 minutes of the data and the product thickness for this interval with the inflection point indicated on the

BAILDOWN TEST

JULY 13

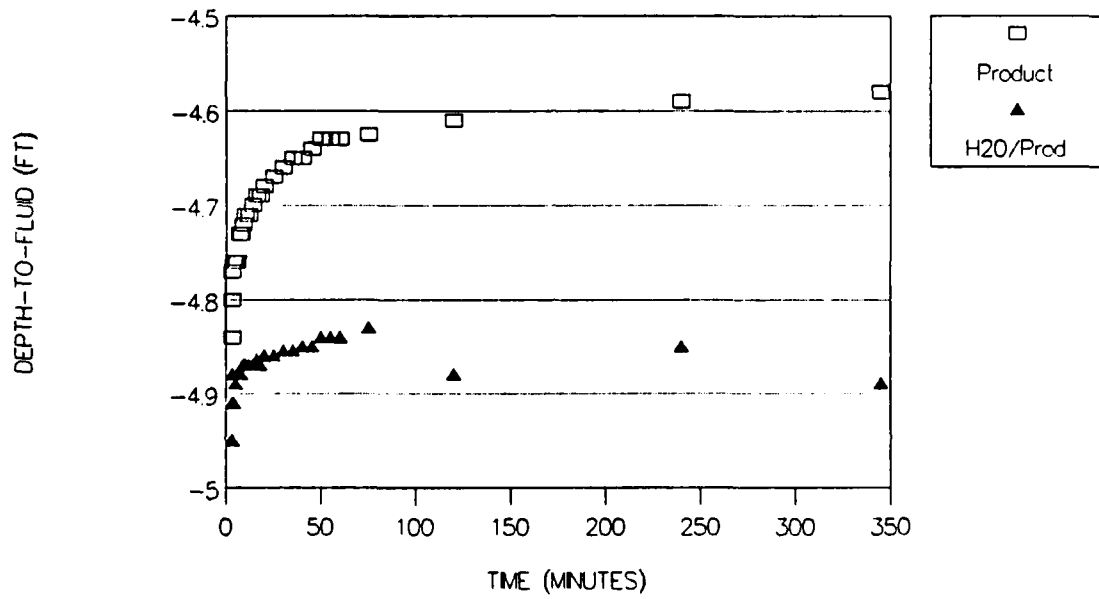


Figure 4.15 Baildown test data, July 13 test

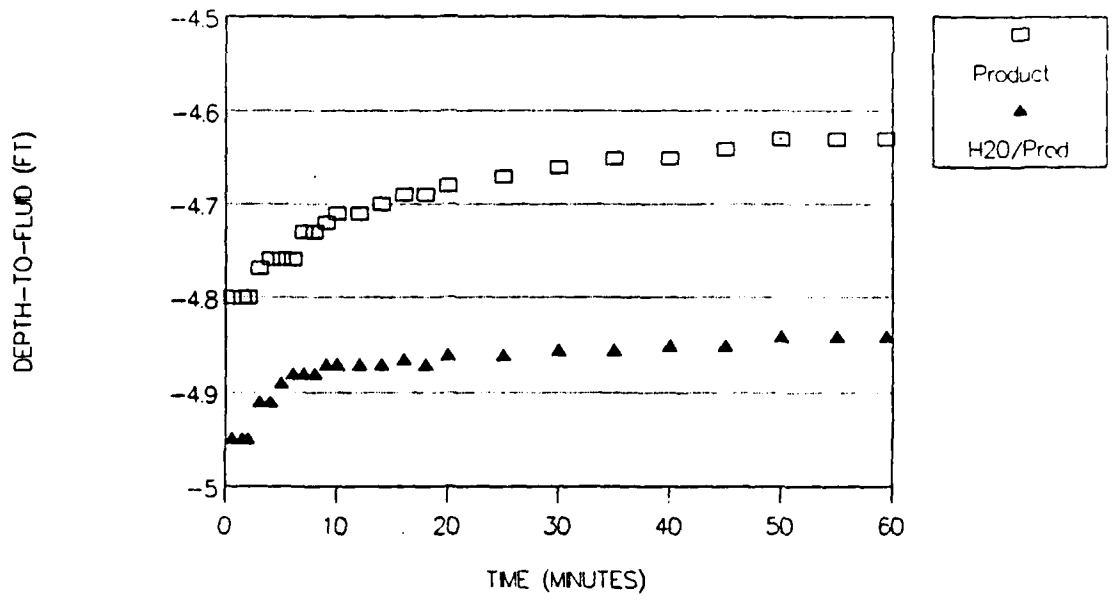


Figure 4.16 Baildown test data, July 13 test

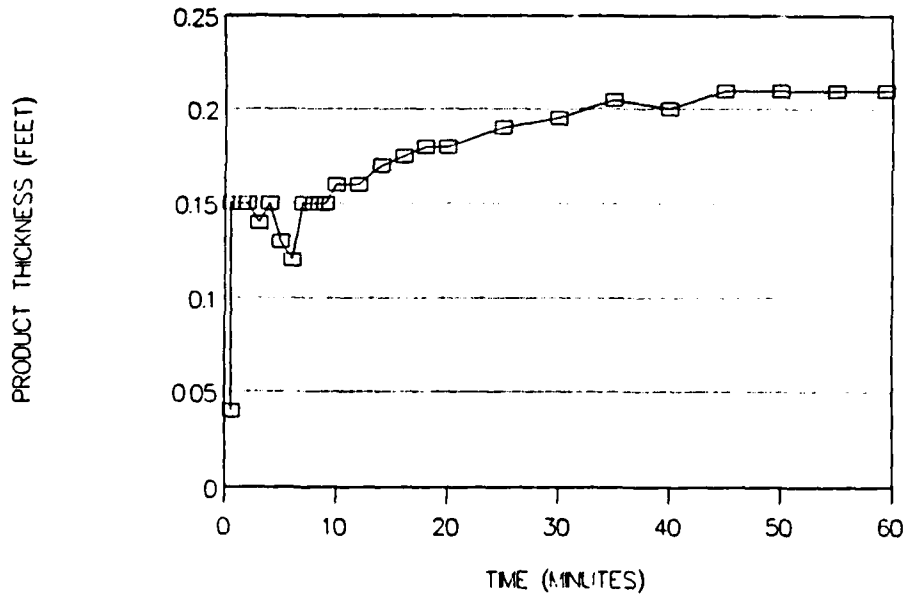


Figure 4.17 Product thickness, Baildown test, July 13

figures. Assuming a porosity of 40%, fully saturated with LNAPL, this method results in an estimate of "actual product thickness" of 0.046 m (0.15 feet) or a total volume of 18.3 L/m² (0.45 gallons/ft²) at positive pressure.

In the second baildown test, we attempted to bail only product from the well initially. Because of the very small product thickness, this was very difficult to do effectively. Measurement of the water/product interface level during recovery was also difficult because of the small thickness in the well. Figure 4.18 shows the depth-to-fluid curves for this second test. The depth-to-product levels seem reasonable but the water/product interface level shows considerable scatter. It is also difficult to determine an inflection point in the data. Gruszczenski refers to a curve where there is no inflection point as a Type A curve and suggests that there is a one to one correspondence between the measured and actual formation product thickness (product at positive pressures). Using this criteria and, again, assuming a 40% saturated porosity, free product would be estimated as 12.2 L/m² (0.3 gallons/ft²) corresponding to a product thickness of 0.03 m (0.1 feet). Testa and Paczkowski (1989) specify that when baildown tests do not conform to the theoretical response anticipated, maximum theoretical values can be determined by subtracting the static depth-to-product from the corrected depth-to-water. This thickness, according to Testa and Paczkowski will give a conservative value. Using this method

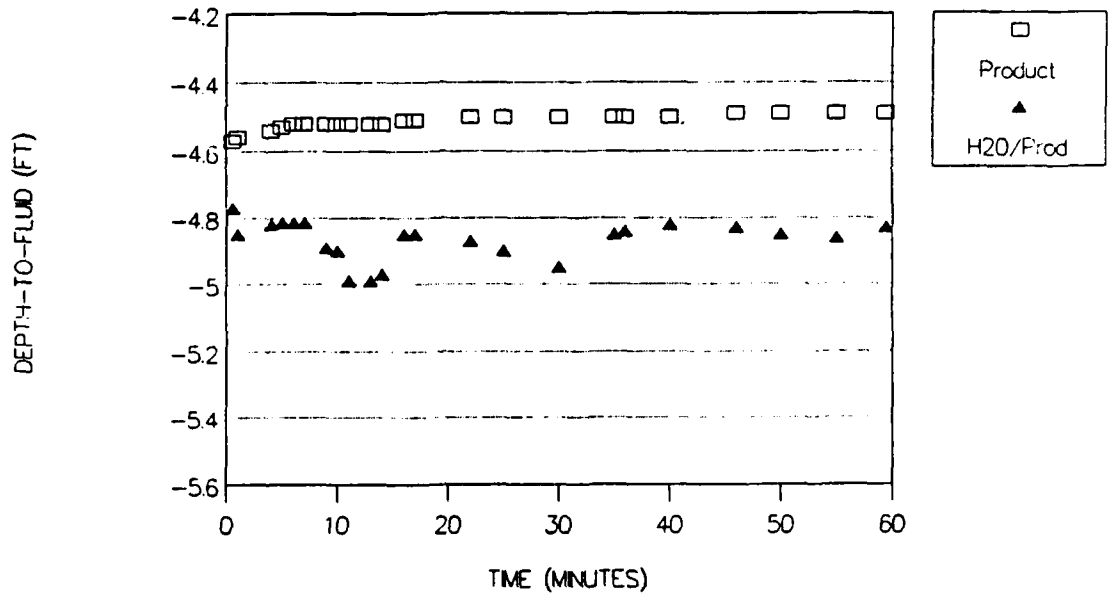


Figure 4.18 Baildown test data, August 2 test

of estimation, the actual product thickness is 0.0411 m (0.135 feet) and total product in the aquifer is 16.5 L/m² (0.4 gallons/ft²). Hughes et al (1988) also provide a method of interpretation for baildown tests. Their method is based on a graph of depth-to-product in the well as it recharges. This curve is shown for the second test in Figure 4.19. In their paper, they have three types of recharge curves for baildown tests. The first type has a distinct inflection point. In this case, it is assumed that the base of the hydrocarbon in the formation is above the potentiometric surface. The well recharges at a constant rate to the base of the hydrocarbon in the formation and then begins to recharge at a steadily decreasing rate. The inflection point represents the elevation of the base of the hydrocarbon layer in the formation. The second type of curve has a steadily decreasing rate of flow into the well from the beginning of the test. This curve does not yield any information that is useful for determining the thickness of free product. The third curve has a constant rate of recharge from the beginning of the test until the static level in the well is achieved. In this case, there is no free product in the aquifer, i.e. there is capillary hydrocarbon only. Figures 4.16 and 4.19 indicate that the data from both baildown tests would be classified as the first type of curve since there are inflection points evident in the product level lines in both tests. Interpretation of the figures using the criteria

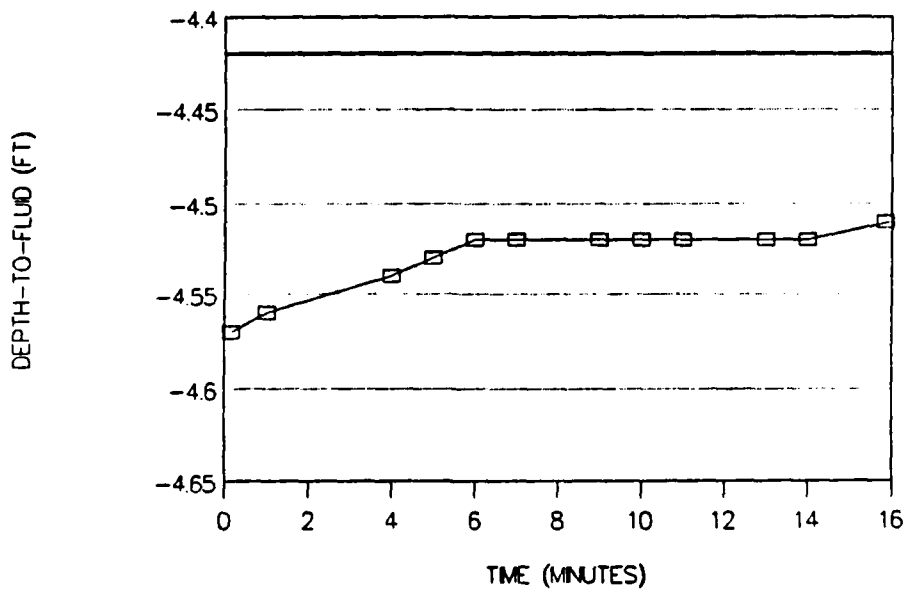


Figure 4.19 Depth-to-Product, Baildown test, August 2

suggested by Hughes et al (1988) yields a thickness of 0.05 m (0.18 feet) and 0.03 m (0.10 feet) for tests 1 and 2, respectively or a total product of 21.2 and 12.2 L/m² (0.5 and 0.3 gallons/ft²), respectively, for the first and second tests.

Comparison of the total volumes of LNAPL predicted from analysis of the baildown tests are summarized in Table 4.4. Although the total product calculated compares favorably with the total product sampled, the distribution in a vertical cross section is significantly in error.

Well Monitoring With Predictive Equations: Spatial and temporal variability of fuel contamination is an important consideration in a nonhomogeneous field case. Predictive equilibrium equations are based on soil properties that typically vary considerably spatially. In addition, the relationship between the capillary pressures and liquid saturations of LNAPL, water and air are hysteretic. Whereas only two path directions are possible in two-phase flow (imbibition and drainage), there are 12 primary paths possible in three-phase flow (IID, IDI, DII, IDD, DDI, DID, CDI, CID, ICD, DCI, IDC AND DIC where D, I and C designate drainage, imbibition and constant saturation, respectively) and an infinite number of intermediate scanning loops. As mentioned earlier in this report, temporal variability is also very important especially in a sandy aquifer material such as that found at Tyndall. These difficulties, combined with the

Table 4.4 Comparison of measured total LNAPL with predicted volume from baildown tests

Reference	Test	Product Thickness (cm)	Total Product (l/m ²)
Gruszczenski (1987)	Baildown #1	4.6	18.3
	Baildown #2	3.0	12.2
Testa and Paczkowski (1989)	Theoretical Maximum	2 to 4	8.14 to 15.7
Hughes et al (1989)	Baildown #1	5.5	21.2
	Baildown #2	3.0	12.2
Direct Sampling	Total product distributed over about 2.5 meters		10.6 to 15.6

inherent difficulty and expense of obtaining good capillary pressure-saturation relationships, make field based sampling methods an attractive alternative to predictive methods at this time. However, there are ongoing efforts by many researchers to relate easily obtained field data such as soil texture to capillary pressure-saturation relationships. These efforts generally assume that the pressure-saturation relationships directly correlate to pore size distributions and, hence, to particle size distributions. Although these methods are not sufficiently developed to use with any confidence at this time, it is expected that the large amount of effort directed toward developing these relationships will result in accepted methodologies in the near future. For some cases, especially sands, it is reasonable to expect that the predictions will be well within acceptable errors. Certainly, the difficulty of obtaining texture data is minimal when compared to the difficulty of obtaining accurate moisture characteristics. Therefore, the feasibility of using predictive equations, combined with an investigation of the spatial and temporal variability of the site, may be high.

Several equations have been published that relate the apparent thickness of LNAPL in a monitoring well to the actual volume of product in the formation. Some of these equations were reviewed in Section 2.2 of this report. In some cases, the relationship between the well product thickness and the aquifer contamination is simply a rule of thumb, such as the

Concawe factor (Concawe, 1979) that states the apparent product thickness, measured in the well, is about four times the average product thickness in soil near the well. Other more physically based equations assume equilibrium and homogeneous conditions. In these equations, equilibrium pressures determined from the well bore data are related to the equilibrium volumetric quantities of water, LNAPL and air in the soil. The procedure used to interpret well data has been discussed by Durnford (1988), Lenhard and Parker (1990), Farr et al (1990) and others and will not be repeated here. The reader is referred to these publications for details.

The drainage and imbibition water characteristic curves for the Tyndall Base Sand are shown in Figure 4.20. The data shown were determined in a laboratory using distilled water and clean sand packed to a maximum density. The LaPlace equation can be used to convert these curves to curves that more closely represent the fluid properties found in field conditions (Lenhard and Parker, 1987). Surface tensions and fluid densities were determined for a sample of contaminated water and contaminated LNAPL taken from well T9-4 and compared to values measured using distilled water and clean JP4. These data comparisons are given in Table 4.5. It is interesting to note that the LNAPL/air surface tension value did not change significantly but the water/air and water/LNAPL tensions were considerably different for the contaminated fluids when compared to values for the clean laboratory fluids. The

MEASURED WATER-AIR SATURATIONS

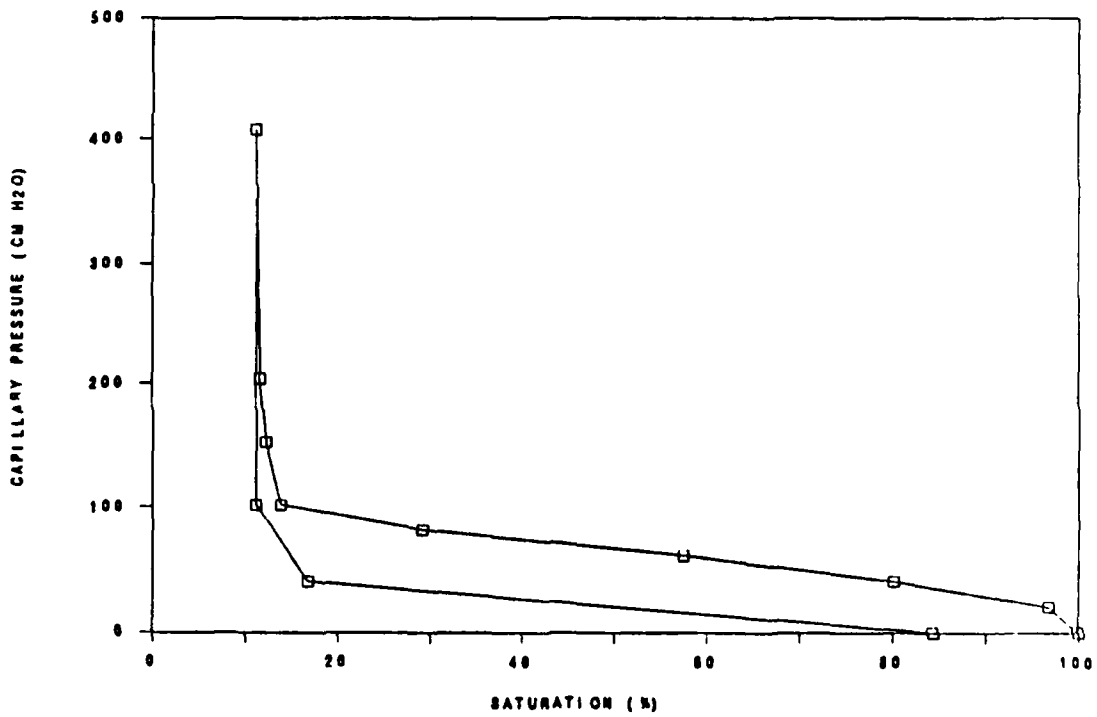


Figure 4.20 Water characteristic for Tyndall AFB sand

Table 4.5 Surface Tensions for Clean and Contaminated Fluids

SURFACE TENSION (DYNES/CM)	CLEAN FLUID PAIRS	FLUIDS FROM WELL T9-4
WATER/AIR	75.5	59.0
LNAPL/AIR	25.0	27.3
WATER/LNAPL	25.0	5.3

*JP4 used in the laboratory

Specific gravity of JP4 = 0.745

Specific gravity of well LNAPL = 0.769

surface tension between fluid pairs is a primary determinant of how much LNAPL is distributed in a porous medium. The fact that the water/LNAPL interfacial tension is 25 dynes/cm in a laboratory and only 5 dynes/cm using well fluids results in a significant difference between estimations of total volume based on clean fluids and estimations based on properties of the contaminated fluids. As discussed later in this section, accurate determination of the interfacial tensions is very critical.

Figure 4.21 shows Capillary Pressure-Saturation curves for water/air, water/LNAPL and LNAPL/air pairs. These curves were obtained by scaling the drainage water characteristic curve shown in Figure 4.20, using values of surface or interfacial tensions for the contaminated fluid pairs. The scaling procedure follows that suggested by Lenhard and Parker (1987). From these curves, LNAPL, air and water equilibrium distributions for Tyndall AFB sand are computed for a product thickness of 12.5 cm in the well. These distributions are shown in Figure 4.22. The datum for the abscissa on this figure is the water table. The ordinate axis is the percent of the pore space that would theoretically be filled with water, LNAPL and air above and below the water table. The LNAPL pressure equals zero at the same level as the top of product in the well, i.e. about 3 cm above the water table. Therefore, as Figure 4.22 shows, there is very little LNAPL under positive pressure. However, theoretically, about 80% of

CHARACTERISTICS CONTAMINATED FLUIDS

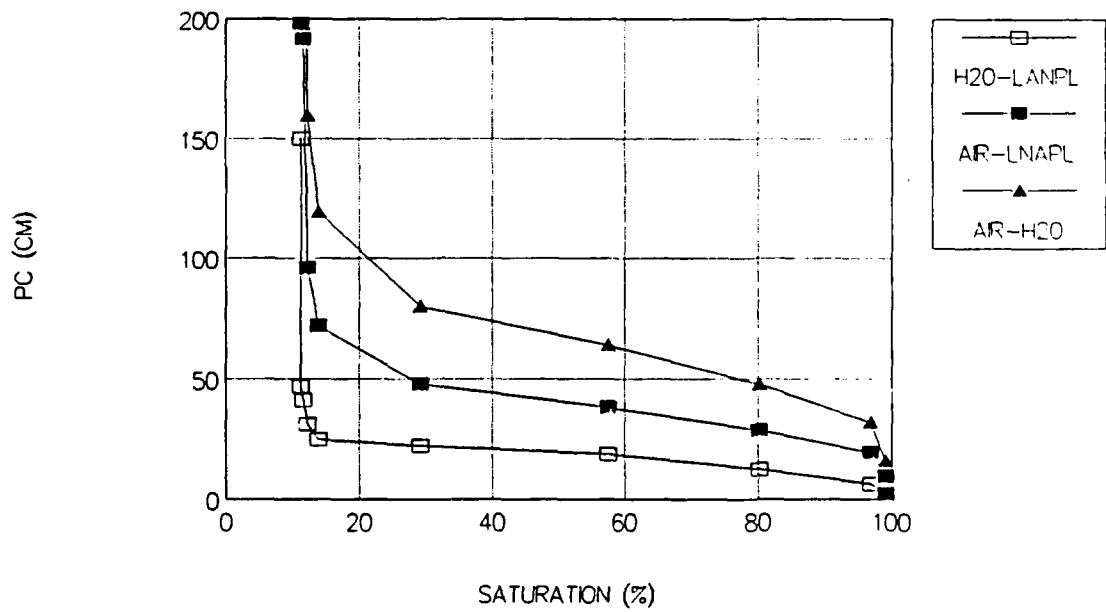


Figure 4.21 Capillary pressure-saturation curves for water/air, water/LNAPL and LNAPL/air fluid pairs

LNAPL DISTRIBUTION
EQUILIBRIUM ASSUMED

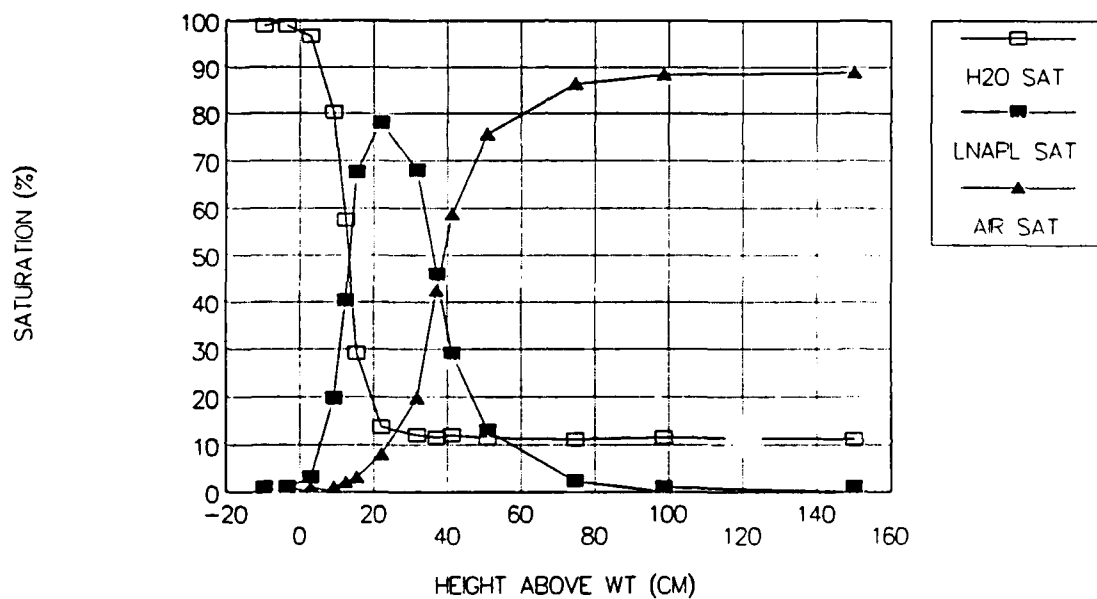


Figure 4.22 Equilibrium distributions of LNAPL, air and water

the pore space at an elevation of 20 cm would be filled with LNAPL.

An LNAPL volume estimation can be made by integration of the LNAPL saturation curve shown in Figure 4.22. This is equivalent to using Equation e in Table 2.1. The Brooks-Corey parameters needed, A, B and λ , were determined for the drainage water characteristic curve by linear regression. Values are a displacement pressure of 25 cm and a pore size distribution index, λ , of 1.22 ($r^2 = .8$). From these, values of A and B in equation e can be computed from fluid densities and interfacial tensions. Assuming interfacial tensions of 5.3 dynes/cm and 27.3 dynes/cm for water/LNAPL and LNAPL/air, respectively, the total LNAPL volume would be computed as 220 L/m². Note that this is about 10 times larger than the other estimates made in this report.

There are two possible explanations for the larger total volumes computed using equilibrium theory. One is that the value of the interfacial tension between water and JP4 is not known accurately. Although outside the scope of this report, it can be shown that by using a range of values from 5 to 25 for this parameter (corresponding to the difference measured between clean samples of fluids and contaminated samples taken from the well), a total volume estimate of LNAPL would vary from zero to 220 L/m². The value of zero product is calculated using the highest water/LNAPL value. Because of the higher water/LNAPL interfacial tension, the theory would

predict that, at the ground surface (137.5 cm above the top of product in the well), the soil would be 98% saturated with water. It can also be shown, however, that if the factor B in equation e is greater than 12.5 cm and a Brooks/Corey representation of the curves is applicable, that no product would be found in the well.

A second explanation for the overprediction of product volume using an equilibrium profile is that volatilization of the LNAPL is not accounted for in the theory. Since the water table is about 140 cm below the ground surface, volatilization of the LNAPL over time would be expected.

CHAPTER 5.0

SUMMARY, CONCLUSIONS AND RECOMMENDATIONS

5.1 SUMMARY

This project combines a literature review, laboratory studies, and field studies to investigate the volume and distribution of LNAPLs (Light Non-Aqueous Phase Liquids) in soil-aquifer systems. A review of literature on currently available field monitoring techniques was followed by a field study that evaluated the distribution of LNAPL in the vertical profile. A laboratory study is being conducted to determine the mechanisms and significant parameters involved in LNAPL entrapment. In this study, it is assumed that the movement and distribution of an LNAPL in a soil-aquifer system is governed by the physics of multi-phase flow. Depending on the volume leaked or spilled, LNAPL can exist as a discontinuous phase in the vadose zone, as a continuous phase at the water table, and as a discontinuous phase below the water table. Although LNAPL in the entire profile was evaluated, emphasis was placed on the entrapped phase below the water table.

In the laboratory investigation, a technique was developed to examine LNAPL entrapment on a microscale. This technique included procedures to simulate entrapment of LNAPL under fluctuating water table conditions in a laboratory column. The technique allowed subsequent sectioning of the column, digitization of column sections, and analysis of each cross section to accurately determine the location and

geometry of the entrapped LNAPL. Preliminary results indicate that about 10% of the pore space in a uniform sand would contain entrapped LNAPL. This value is dependent on fluid and soil properties but appears fairly consistent with other laboratory work and the field results. This laboratory work is ongoing.

The field study was conducted at a site at Tyndall AFB, FL that is a former fuel storage area. Approximately 12.5 cm (0.41 ft) of an immiscible, lighter than water, product was found in a monitoring well at the site. The objective of the field study was to estimate the total LNAPL in the soil and determine the distribution of the LNAPL in a vertical profile. Because the soil was a uniform sand, a prototype cryogenic sampler was developed to extract an intact fluid/soil sample from below the water table.

Results from direct sampling of the site indicate that the average total fuel in the soil is 10.6 L/m² to 15.6 L/m². On average, 72% of the total LNAPL in the soil was located below the water table. The LNAPL in the saturated zone was distributed through the sampling depth with less than 10% of the pore space filled with LNAPL. In the unsaturated zone, less than 5% of the pore space contained LNAPL. The free product was found to be negligible. Figure 5.1 shows the average LNAPL saturations determined by direct sampling.

The field investigation emphasized the need to define the spatial variability of a contaminated site, especially if the

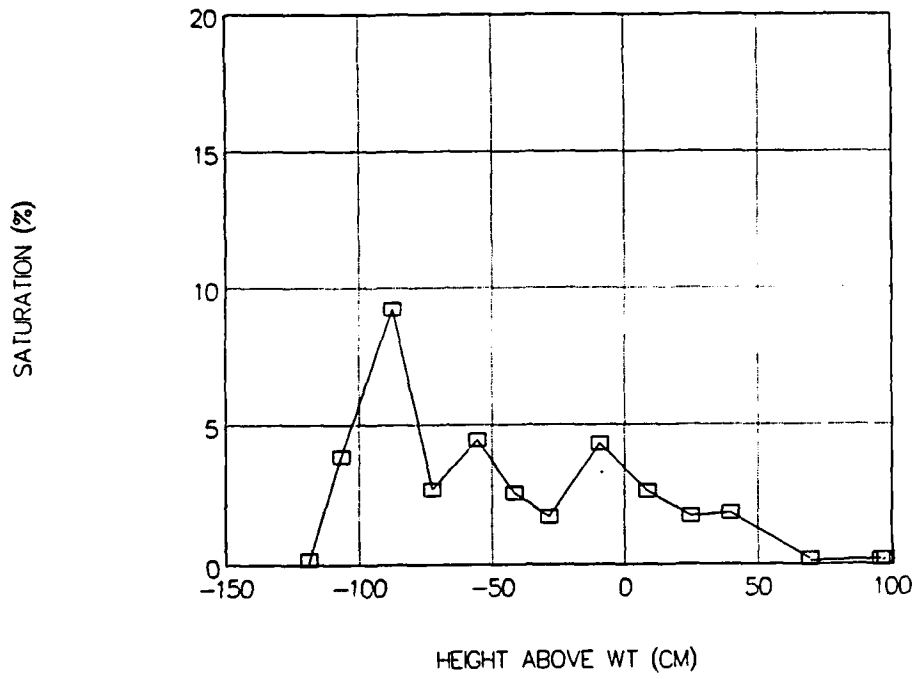


Figure 5.1 Average LNAPL saturations determined from direct sampling

site is a nonhomogeneous fill such as the site in this project.

Monitoring wells are routinely used to estimate the amount of LNAPL present in a soil. A number of relationships have been developed to relate product thickness in a well to total product in the soil. In addition, other field methods have been recently developed, including baildown tests, coring, and use of a dielectric logging system. All of these methods have serious limitations. In this project, interpretation of monitoring well data using equilibrium equations and baildown tests were compared to the results from direct sampling of the field site at Tyndall AFB. These were chosen as the most promising of the available techniques for estimating total LNAPL. However, neither the baildown tests or equilibrium theory adequately predicted the LNAPL distribution in the soil. Neither included entrapped product below the water table. The baildown tests significantly overpredicted the free product and ignored any product at negative pressure. The equilibrium equations accurately reflected negligible free product but significantly overpredicted total product because the quantity of LNAPL at negative pressure was significantly overpredicted.

Figure 5.2 shows the average of the LNAPL saturations predicted from baildown tests and the LNAPL saturation predicted using equilibrium theory. It is clear by comparing Figure 5.2 with Figure 5.1 that neither equilibrium theory nor

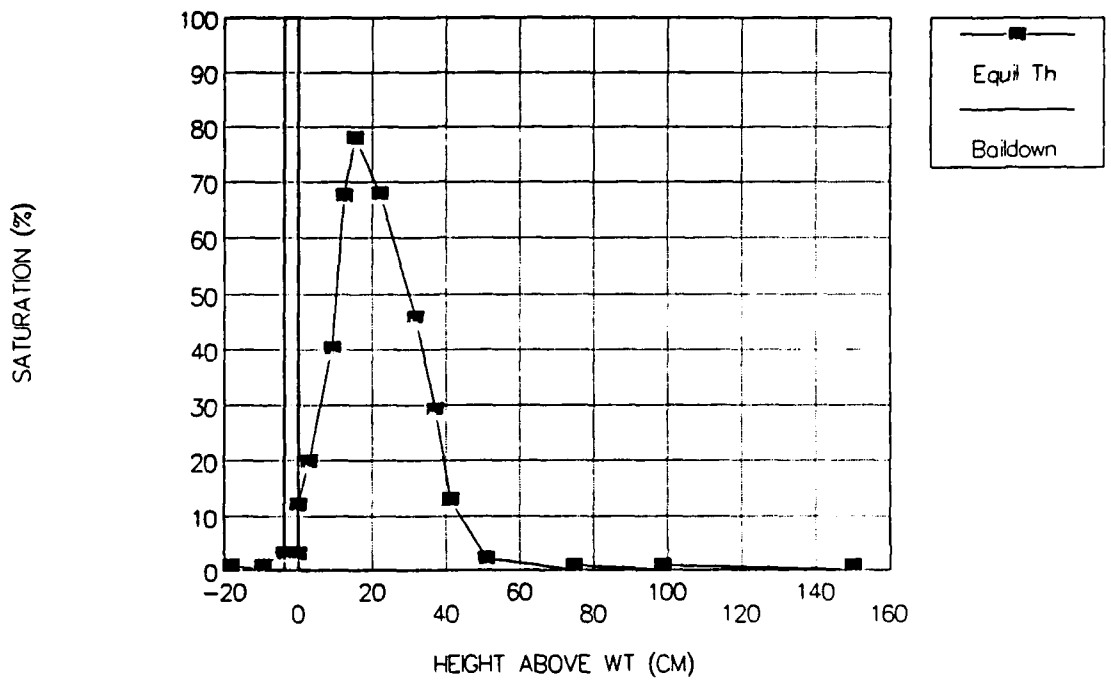


Figure 5.2 INAPL saturations from bardown tests and equilibrium theory

baieldown tests were adequate for this case.

5.2 CONCLUSIONS

An accurate assessment of the total quantity and vertical distribution of LNAPL is important for several reasons, including regulatory control, determination of remediation procedures, and risk assessment. A remediation strategy will be cost effective and efficient only if it is designed with the LNAPL distribution, properties and quantity in mind. An accurate estimation of the total LNAPL quantity is needed in order to assess the adequacy of the selected clean up program. Similarly, accurate risk assessment depends on an initial knowledge of the location and quantity of product at both the microscale and the macroscale. While these seem self-evident, current practice is more often based on trial and error than scientific evaluation.

From the results of this project, several conclusions can be drawn:

1. The best method currently available for determining LNAPL distribution at a field site appears to be direct sampling. Fluctuating water tables make interpretation of well data difficult since changes in LNAPL thickness in monitoring wells may not be due to extraction from or addition to the soil profile. Baieldown tests do not account for either product at negative pressures or entrapped LNAPL. Equilibrium equations do not include entrapped product and were found to

be very sensitive to interfacial tension, a parameter that is difficult to assess accurately in a field case. Other methods suggested in the literature do not account for the entrapped phase.

2. LNAPL entrapped below the water table can be a very significant percentage of the total product. About 72% of the total product was located below the water table at the field site studied in this project. This will change as the water table position changes. However, it is important to evaluate this component and to determine the vertical extent and saturation levels in this zone.

3. The prototype cryogenic sampler developed during this study has been shown to be useful for extracting intact fluid/soil samples from below the water table.

5.3 RECOMMENDATIONS FOR FUTURE RESEARCH

Based on the results from this study, the following should be considered for future work:

1. Future research efforts directed toward effective sampling should focus on development of a protocol that includes:

- a. guidelines for the number of samples required,
- b. criteria for the distribution of the samples,
- c. analysis of the laboratory techniques used

- to evaluate total product,
- d. analysis of methods used for extraction of the organic from the soil,
- e. a methodology for calculation of total LNAPL

One of the findings of this project was that spatial variability of the LNAPL distribution, both in the vertical and the horizontal, was important. A statistical protocol to define the spatial variability of the LNAPL and estimate total LNAPL within acceptable limits is needed. In addition, there were questions during the course of this project as to the adequacy of the chemistry laboratory techniques used for extraction of the hydrocarbon from the soil and estimation of total hydrocarbon. These methodologies deserve more evaluation. Finally, a methodology for calculation of total LNAPL should be developed based on the statistical criteria established.

2. The concept of freezing the lower portion of a saturated soil sample to allow intact extraction was shown to be valid in this project. However, more work is needed to make the developed sampler easier to use and more efficient. Redesign of the sampler should be undertaken and the usefulness of the sampler under a variety of field situations should be systematically evaluated.

3. A significant portion of the LNAPL at the field site studied was located below the water table, primarily as entrapped product. One area of future research would be to

develop cost effective, efficient methodologies to remove this entrapped phase.

4. In many field situations, much of the LNAPL entrapped in the saturated zone will not be removed and will become a continuing source of contamination as constituents dissolve into the bulk groundwater over time. Future research efforts directed toward evaluating the risk associated with this entrapped product should include:

- a. a study of the rates of chemical dissolution in soils,
- b. determination of the relationship between the location and geometry of the entrapped phase in a soil, the amount of contact between the entrapped phase and the bulk groundwater phase, and the dissolution process,
- c. analysis of the risk associated with LNAPL that is not removed.

CHAPTER 6.0

REFERENCES

Abdul, A.S., S.F. Kia, and T.L. Gibson. 1989. "Limitations of Monitoring Wells for the Detection and Quantification of Petroleum Products in Soils and Aquifers," Ground Water Monitoring Review, vol. 9, no. 2, pp 90-99.

Abrams, A. 1975. The Influence of Fluid Viscosity, Interfacial Tension, and Flow Velocity on Residual Oil Saturation Left by Waterflood, Society of Petroleum Engineers Journal, 15(5):437-447.

American Petroleum Institute. 1987. Sampling and Analytical Methods for Determining Petroleum Hydrocarbons in Ground Water and Soil, Method 4449.

Arriola, A., G. P. Willhite, and D. W. Green. 1983. Trapping of Oil Drops in a Noncircular Pore Throat and Mobilization Upon Contact With a Surfactant, Society of Petroleum Engineers Journal, 23(1):99-114.

Chatzis, I., M. S. Kuntamukkula, and N. R. Morrow. 1984. Blob-size Distribution as a Function of Capillary Number in Sandstones, SPE 13213, presented at the 59th Annual Technical Conference and Exhibition, Houston, TX, Sept. 16-19.

Chatzis, I. and F. A. L. Dullien. 1983. Dynamic Immiscible Displacement Mechanisms in Pore Doublets: Theory versus Experiment, Journal of Colloid and Interface Science, 91(1):199-222.

CONCAWE. 1979. "Protection of Ground Water from Oil Pollution," CONCAWE Report No. 3/79, The Hague.

Dias, M. M. and A. C. Payatakes. 1986. Network Models for Two-Phase Flow in Porous Media: Part 2. Motion of Oil Ganglia, Journal of Fluid Mechanics, 164:337-358.

Durnford, D. 1988. "Estimation of Jet Fuel Contamination in Soils," Final Report for AFOSR-UES SFRD, Contract No. F49620-87-0004.

Environmental Science and Engineering. 1988. Installation Restoration Program: Phase II - Confirmation/Quantification, Stage 2, Volume 1, Draft Report prepared for Tyndall Air Force Base, March, 1988, USAF Contract No. F33615-84-D-4401.

EPA. 1988. Cleanup of Releases from Petroleum USTs: Selected Technologies. Office of Underground Storage Tanks. EPA/530/UST-88/001.

ERDAS. 1988. Earth Resources Data Analysis System, Inc. Version 7.3 2801 Buford Highway, Suite 300, Atlanta, Georgia, 30329.

Farr, A.M., R.J. Houghtalen, and D.B. McWhorter. 1990. "Volume Estimation of Light Nonaqueous Phase Liquids in Aquifers from Observed Fluid Levels in Monitoring Wells," Ground Water, in review.

Gruszczenski, T.S. 1987. "Determination of a Realistic Estimate of the Actual Formation Product Thickness Using Monitoring Wells: A Field Bailout Test," In: Proceedings of Petroleum Hydrocarbons and Organic Chemicals in Ground Water-Prevention, Detection, and Restoration, NWWA, Houston, Texas, pp 235-253.

Hall, R.A., S.B. Blake and S.C. Champlin, Jr. 1984. "Determination of Hydrocarbon Thickness in Sediments using Borehole Data," In: Proceedings of the 4th National Symposium on Aquifer Restoration and Ground Water Monitoring, NWWA, p. 300-304.

Hampton, D.R. and P.D.G. Miller. 1988. "Laboratory Investigation of the Relationship Between Actual and Apparent Product Thickness in Sands," In: Proceedings of Petroleum Hydrocarbons and Organic Chemicals in Ground Water-Prevention, Detection, and Restoration, NWWA, Houston, Texas, pp 157-181.

Hassanizadeh, M. and W.G. Gray. 1979a. "General Conservation Equations for Multi-Phase Systems 1. Averaging Procedure," Adv. Water Resources, 2:131-144.

Hassanizadeh, M. and W.G. Gray. 1979b. "General Conservation Equations for Multi-Phase Systems 2. Mass, Momenta, Energy, and Entropy Equations," Adv. Water Resources, 2:191-203.

Hassanizadeh, M. and W.G. Gray. 1980. "General Conservation Equations for Multi-Phase Systems 3. Constitutive Theory for Porous Media Flow," Adv. Water Resources, 3:25-40.

Hinkley, R. E., M. M. Dias, A. C. Payatakes. 1987. On the Motion of Oil Ganglia in Porous Media, PhysicoChemical Hydrodynamics, 8(2):185-211.

Hughes, J.P., C.R. Sullivan, and R.E. Zinner. 1988. "Two Techniques for Determining the True Hydrocarbon Thickness in an Unconfined Sandy Aquifer," In: Proceedings of Petroleum

Hydrocarbons and Organic Chemicals in Ground Water-Prevention, Detection, and Restoration, Volume I, Houston, Texas, pp 291-314.

Keech, D.A. 1988. "Hydrocarbon Thickness on Groundwater by Dielectric Well Logging," In: Proceedings of Petroleum Hydrocarbons and Organic Chemicals in Ground Water - Prevention, Detection, and Restoration, Volume I, Houston, Texas, pp 275-289.

Larson, R. G., L. E. Scriven, and H. T. Davis. 1977. Percolation Theory of Residual Phases in Porous Media, Nature, 268(5619):409-413.

Lenhard, R.J. and J.C. Parker. 1990. "Estimation of Free Hydrocarbon Volume from Fluid Levels in Observation Wells," Ground Water, in review. ??

McKee, J. E., F. B. Laverty, and R. M. Hertel. 1972. Gasoline in Groundwater, Journal WPCF, 44(2):293-302.

McKellar, M. and N. C. Wardlaw. 1988. A Method of Viewing "Water" and "Oil" Distribution in Native-State and Restored-State Reservoir Core, The American Association of Petroleum Geologists Bulletin, 72(6):765-771.

Ng, K. M., H. T. Davis, and L. E. Scriven. 1978. Visualization of Bloch Mechanics in Flow Through Porous Media, Chemical Engineering Science, 33(8):1009-1017.

Roof, J. G. 1970. Snap-Off of Oil Droplets in Water-Wet Pores, Society of Petroleum Engineers Journal, 10(1):85-90.

Scheigg, H.O. 1985. "Considerations on Water, Oil, and Air in Porous Media," Water Science and Technology, 17:467-476.

Schwille, F. 1967. "Petroleum Contamination of the Subsoil- A Hydrological Problem," In: The Joint Problems of the Oil and Water Industries, ed. P. Hepple, The Institute of Petroleum, London, pp 23-54.

Schwille, F. 1984. "Migration of Organic Fluids Immiscible with Water in the Unsaturated Zone," In: Pollutants in Porous Media, Ecological Studies 47, eds. B. Yaron, G. Dagan, and J. Goldshmid, pp. 27-49, Springer-Verlag, Berlin.

Starr, R.C. and R.A. Ingleton. 1989. "A New Method for Collecting Core Samples Without a Drill Rig," submitted to Ground Water Monitoring Review.

Taber, J. J. 1969. Dynamic and Static Forces Required to Remove a Discontinuous Oil Phase from Porous Media Containing Both Oil and Water, Society of Petroleum Engineers Journal, 9(1):3-12.

Testa, S.M. and M.T. Paczkowski. 1989. "Volume Determination and Recoverability of Free Hydrocarbon," Ground Water Monitoring Review, vol. 9, no. 1, pp 120-128.

van Dam, J. 1967. "The Migration of Hydrocarbons in a Water Bearing Stratum," In: The Joint Problems of the Oil and Water Industries, ed. P. Hepple, pp 55-96, Inst. Petrol, London.

Wilson, J.L. and S.H. Conrad. 1984. "Is Physical Displacement of Residual Hydrocarbons a Realistic Possibility in Aquifer Restoration?", In: Proceedings of the NWWA/API Conference on Petroleum Hydrocarbons and Organic Chemicals in Ground Water-Prevention, Detection, and Restoration, Houston, Texas, pp 274-298.

Wilson, J.L., S.H. Conrad, E. Hagan, W. Mason, and W. Peplinski. 1988. "The Pore Level Spatial Distribution and Saturation of Organic Liquids in Porous Media," In: Proceedings of Petroleum Hydrocarbons and Organic Chemicals in Ground Water - Prevention, Detection, and Restoration, NWWA/API, Houston, Texas, pp 107-133.

Wilson, J. L., S. H. Conrad, W. R. Mason, W. Peplinski, and E. Hagan. 1989. Laboratory Investigation of Residual Liquid Organics: From Spills, Leaks, and the Disposal of Hazardous Wastes in Groundwater, Grant Number: EPA CR-813571-01-0.

Yadav, G. D., F. A. L. Dullien, I. Chatzis, I. F. MacDonald. 1987. Microscopic Distribution of Wetting and Nonwetting Phases in Sandstones During Immiscible Displacements, SPE Reservoir Engineering, 2(2):137-147.

Yaniga, P. M. 1984. Hydrocarbon Retrieval and Apparent Hydrocarbon Thickness: Interrelationships to Recharging/Discharging Aquifer Conditions, In: Proceedings of Petroleum Hydrocarbons and Organic Chemicals in Ground Water, NWWA, Houston, Texas, pp. 299-326.

Zapico, M.M., S. Vales, and J.A. Cherry. 1987. "A Wireless Piston Core Barrel for Sampling Cohesionless Sand and Gravel Below the Water Table," Ground Water Monitoring Review, Vol. 7, No. 3, pp. 74-82.

Zilliox, L. and P. Muntzer. 1975. "Effects of Hydrodynamic Processes on the Development of Ground-Water Pollution: Study on the Physical Models in a Saturated Porous Medium," Progress in Water Technology, vol. 7, pp. 561-568.

RESEARCH INITIATION PROGRAM

Sponsored by the
AIR FORCE OFFICE OF SCIENTIFIC RESEARCH

Conducted by
Universal Energy Systems, Inc.

FINAL REPORT

EXTRACTION OF VOLATILE ORGANIC CHEMICALS FROM UNSATURATED SOIL:
Experimental Results and Model Predictions

Prepared by: Neil J. Hutzler, Ph.D, P.E. and
David B. McKenzie

Academic Rank: Associate Professor and
M.S. Graduate Student

Department and University: Civil and Environmental Engineering
Michigan Technological University
Houghton, Michigan 49931

USAF Researcher: Dr. Thomas Stauffer
USAFESC/RDVW
Tyndall AFB, FL 32403

Date: March 9, 1990

Contract No: PO#5-210-9MG-059

ABSTRACT

A series of laboratory soil column experiments was performed to study the impacts of chemical volatility, soil structure, air flow rates, and soil moisture on the rate of removal of VOCs from porous media. Extraction rates are increased with increasing air-water partition coefficients and air flow rates. Extraction rates are generally faster in cohesionless material than in aggregated material. This is especially true when soil moisture is present. Extraction rates are increased with decreasing soil moisture. However, adsorption of chemical onto completely dry soils will slow the extraction process.

Results from the laboratory soil column experiments were successfully simulated and predicted with two dispersed air flow, diffusion into aggregates models using independently measured parameters. These soil column models include air advection, gas dispersion and diffusion, pore water diffusion, and air-water mass transfer as mass transfer mechanisms and adsorption and volatilization/dissolution are included as retardation mechanisms.

ACKNOWLEDGMENTS

We want to thank the Air Force Office of Scientific Research for the sponsorship of this project. We would also like to acknowledge Universal Energy Systems for their administrative support of the program. We would also like to thank the Air Force Engineering and Services Center at Tyndall Air Force Base for administrative and technical services at the beginning of the project. Dr. Tom Stauffer was invaluable in helping set up our initial experimental apparatus and offering technical advice.

We would like to acknowledge Dr. Joel Massmann, Dr. John Crittenden, and Dr. Jim Mihelcic for their review of this document. Lastly, we would like to say thanks to John Gierke, doctoral candidate in environmental engineering. We are grateful for the advise he gave on experimental design and for the development of the computer models used to interpret the results of the numerous experiments.

1. INTRODUCTION

1.1 Soil Vapor Extraction as a Remediation Alternative

Volatile organic chemicals (VOCs), whether spilled on the ground surface or leaked from underground storage tanks, can contaminate the subsurface environment. These contaminants may be held in the vadose zone and may slowly leach into groundwater aquifers as water infiltrates into the soil.

Soil vapor extraction is an in situ method of removing VOCs from the unsaturated soil zone before the chemical can leach into the groundwater aquifer. A typical soil vapor extraction system is presented in Figure 1.1.1. Air flow through unsaturated soils is induced by applying a vacuum at an extraction vent. Clean air is introduced to the contaminated soil from an inlet, injection vent, or from the ground surface. Volatilization of chemicals from the contaminated soil occurs, and the chemical is swept out with the induced air flow. Treatment of this contaminated soil can significantly reduce treatment time and costs involved in aquifer clean-up. Soil vapor extraction can be one of the most cost effective remediation methods of removing VOCs from unsaturated soils (Towers et al., 1989).

A comprehensive state of technology review which includes the description of typical soil vapor extraction systems, in addition to the description of many existing sites located around the country, is presented by Hutzler et al. (1989). Included in this comprehensive review is a list of important soil vapor extraction system variables which must be considered when designing an actual field system. These variables are classified as site conditions, soil properties, chemical properties, control variables, and response variables. These variables

are presented in Table 1.1:1.

Table 1.1.1 Soil vapor extraction system variables.

<u>Site Conditions</u>	<u>Control Variables</u>
Distribution of VOCs	Air withdrawal rate
Depth to groundwater	Well configuration
Infiltration rate	Extraction well spacing
Location of Heterogeneities	Vent well spacing
Temperature	Ground surface covering
Atmospheric pressure	Pumping duration
	Inlet air VOC concentration and moisture content
<u>Soil Properties</u>	<u>Response Variables</u>
Permeability (air and water)	Pressure gradients
Porosity	Final distribution of VOCs
Organic carbon content	Final moisture content
Soil structure	Extracted air concentration
Soil moisture characteristics	Extracted air moisture
Particle size distribution	Extracted air temperature
	Power usage
<u>Chemical Properties</u>	
Henry's constant	
Solubility	
Adsorption equilibrium	
Diffusivity (air and water)	
Density	
Viscosity	

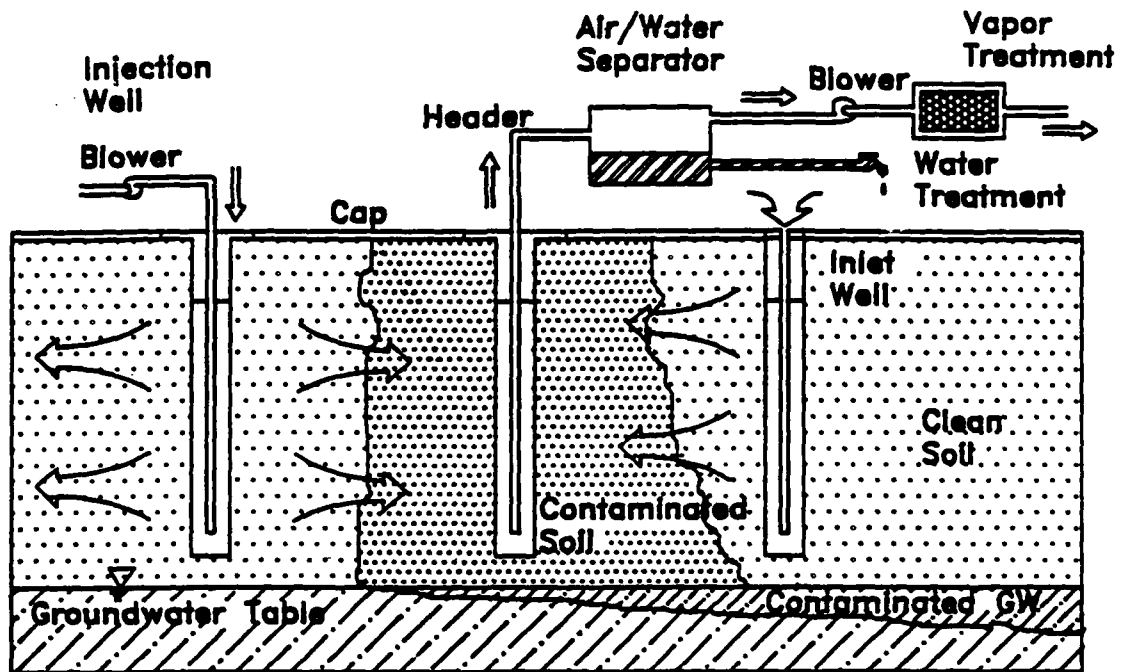


Figure 1.1.1 Schematic of a full scale soil vapor extraction system.

1.2 Objectives of the Study

The purpose of this study is to investigate some of the variables that affect the rate of soil vapor extraction. This was accomplished by performing a series of laboratory experiments and modeling exercises. Soil columns were used to simulate the extraction process in the laboratory. With the soil column procedure, the impacts of soil type and structure, chemical volatility, degree of saturation, and air flow rate were investigated through the completion of laboratory soil column experiments.

An Air Dispersed Flow Diffusion into Aggregates Model (Bednar, 1990) was validated with the results compiled from the laboratory soil

column experiments. This model incorporates air advection, gas dispersion and diffusion, pore diffusion, and air-water mass transfer as mass transfer mechanisms. Adsorption and volatilization/dissolution are retardation mechanisms included in the model. Mass transfer mechanisms affect the shape of the chemical front, while retardation mechanisms slow the front as it moves through the soil column.

The relative impacts of these mechanisms were investigated through the results of twelve experiments along with model predictions and simulations. The effects of dispersion were investigated through the results of a methane tracer study. Gas dispersion and adsorption were investigated in dry soil column experiments. Volatilization/dissolution was investigated from the results of moist soil column experiments. Both dispersion and pore diffusion become important mass transfer mechanisms in gas flow through aggregated materials.

2. EXPERIMENTAL APPROACH

A logical approach was taken in order to investigate the soil vapor extraction process in the laboratory. First, soil columns were used to study the impact of variables important in the transport of VOCs through porous media. Second, models were developed in order to extend the utility of the data which was collected from the laboratory experiments. Lastly, in order to completely validate the chemical transport models, independent experiments were performed and literature correlations were used to determine model parameter values.

2.1 Experimental Design

Column experiments were designed to simulate the process of soil vapor extraction under laboratory conditions. Four independent

variables; pumping rate (air velocity), soil structure, degree of saturation of soil, and chemical volatility; were investigated with respect to their effect on the removal of volatile organic chemicals (VOCs) from laboratory soil columns. These variables were chosen because of their importance in the soil vapor extraction process. In addition, any alteration of these variables could be readily verified or measured. The range of values for each variable is summarized in Table 2.1.1.

Table 2.1.1 Range of values of independent variables:

<u>Independent Variable</u>	<u>Range</u>
Air Velocity	0.001-0.085 cm/sec
Soil Structure	Cohesionless and Aggregated
Degree of Saturation	Dry, Moist, and Humidified
Chemical Volatility	0.24 and 0.64 (dimensionless H)

Air velocity was set such that low flow experiments generally had a velocity three times slower than those of the high flow experiments. Soil structure was investigated by using a cohesionless sand and a particle with high internal porosity which simulated an aggregated media.

Degree of saturation was investigated by performing soil column experiments under dry and moist conditions. Dry soil conditions were achieved by oven-drying the soil at 103 degrees Celsius for 2 to 3 hours before the soil columns were packed. Moist soil conditions were achieved by first wetting the soil with distilled, deionized water and

then allowing excess water to drain from the column by gravity. A uniform moisture content was achieved by pushing any residual water out with a siphon bulb. An additional moisture condition was also investigated. A dry soil column was humidified with water vapor. Volatile organic chemical was introduced through a water humidifier before entering the soil column. Elution air was fed through a non-contaminated humidifier.

Toluene and 1,1,1-Trichloroethane were used to investigate chemical volatility. These two chemicals differed in volatility by approximately a factor of three.

The primary dependent variable was the rate of VOC extraction as derived from effluent vapor concentration versus time.

2.2 Experimental Apparatus

In the soil column experiments, three apparatus configurations were used to demonstrate the soil vapor extraction process. Each successive apparatus was developed to eliminate possible flaws in the previous technique. Experimental apparatus included equipment that would be nonadsorbing of organics.

The first laboratory system is depicted in the schematic shown in Figure 2.2.1. Soil material was packed in plexiglas columns which were used in previous work at Michigan Technological University by Krause (1987). One of the two 10.8-cm diameter columns was packed with a cohesionless sand and was 29.9 cm in length, whereas the second was packed with porous particles and was 20.1 cm in length. Both plexiglas columns were modified for use in the soil vapor extraction experiments. The perimeter of the bottom flange was drilled and fitted with four pipe

thread fittings, and an air manifold was inserted for distribution of air at the bottom of the column. This manifold consisted of four short sections of 1/8"-diameter stainless steel tubing which were crimped at one end to block flow. Two 1/16"-diameter holes were drilled along each tube length to allow air to enter the column. These tubes could be gently tapped into the four fittings in the bottom flange of the column.

Air was drawn into the system by an FMI Lab pump (Fluid Metering, Inc., Oyster Bay, NY). This vacuum pump was able to withdraw between 1 and 40 mL/min of air from the soil columns. The pump first pulled laboratory air through a granular activated carbon (GAC) column and then through a water humidifier before the air entered the soil column. The GAC column removed organics that may have been present in the lab air. The water humidifier delivered air with 100 percent relative humidity to the soil column. This eliminated the possibility of the soil drying *during an experiment*. The humidifier also served as a visual check to determine if the system was leak tight. If bubbling occurred within the humidifier, no leaks were present in the apparatus. It was observed that the pump had a constant and reproducible flow rate as long as pressure on both the suction and discharge sides of the pump remained constant.

All vapor extracted from the column by the vacuum pump was passed through a sample loop contained in a gas sampling valve which was attached to a gas chromatograph (Perkin-Elmer Sigma 1000). An actuator valve would close at predesignated times, and a sample would be delivered by a nitrogen carrier gas to the gas chromatograph for analysis. A bubbler was installed after the vacuum pump to measure flow.

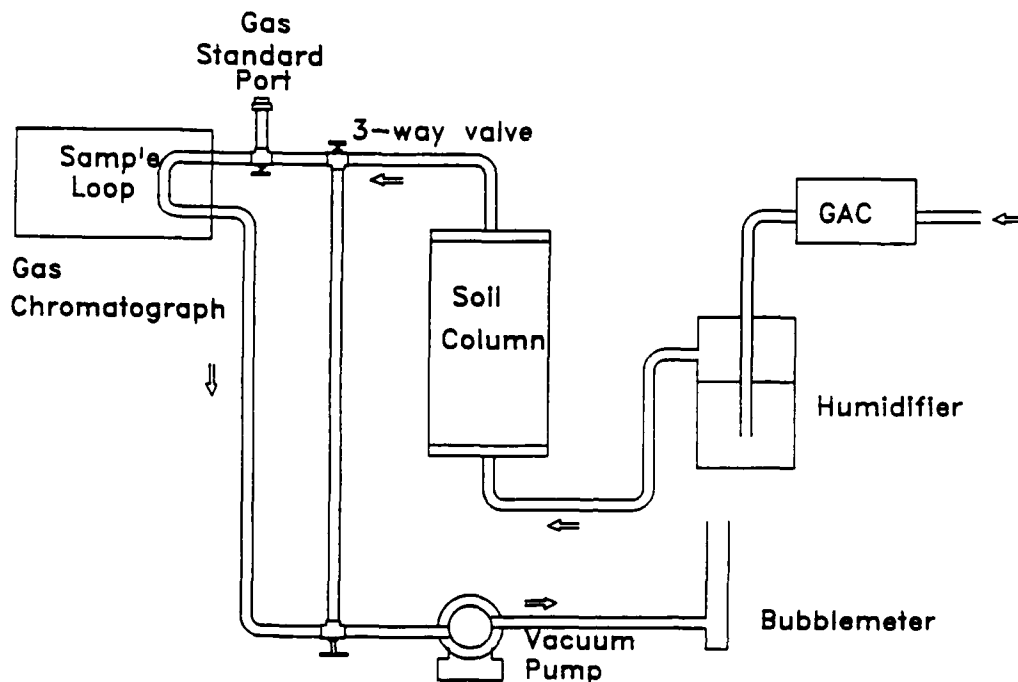


Figure 2.2.1. Laboratory apparatus used to investigate impact of chemical volatility and soil structure on soil vapor extraction.

Most tubing material consisted of stainless steel with small amounts of Teflon tubing used as needed. All stainless steel tubing was wrapped with heat tape in order to eliminate condensation of VOC onto the inner walls. To insure that the stainless steel tubing was clean, benzene, acetone, and finally, methanol was pumped through the stainless steel tubing to remove all oils and organics which may have been present. The tubing was then placed in a forced air oven for several hours to remove all solvents used in the cleaning process.

Volatile organic chemicals were introduced with water which was pumped into the soil column. When VOC was introduced to the plexiglas

soil column in this manner, the water phase concentrations could not be accurately measured. Because of this, it was difficult to accurately predict the mass of chemical contained in the soil column at the start of an experiment. Therefore, a complete mass balance, comparing chemical introduced to that extracted, could not be closed. It was suspected that some adsorption of VOC onto the plexiglas soil column had occurred. Nonetheless, the results using this set-up demonstrate the relative impacts of chemical volatility and soil structure on rate of soil vapor extraction.

To eliminate the mass balance problem, the apparatus and procedure were modified such that VOC was introduced to the column as a gas. Concentrations of volatile organic chemicals in gas could be measured during both introduction and elution of VOC from the soil column making mass balances easier to calculate. The apparatus was also changed to use glass soil columns instead of plexiglas.

A complete schematic of the second experimental apparatus with design changes is shown in Figure 2.2.2. This second apparatus was used to investigate the impacts of flow rate and degree of saturation on the soil vapor extraction process.

The glass soil column (Ace Glass, Inc., Vineland N.J.) measured 5 centimeters in diameter and 30.13 centimeters in length. End caps were threaded Teflon which were screwed into both ends of the glass column. The bottom end cap had a milled cavity which was filled with glass beads and enclosed with a stainless steel screen for flow distribution. The top end cap had a small diameter drill hole to collect flow. Before the top end cap was installed, a piece of Teflon mesh was placed on top of the sand to eliminate any shifting of sand which may occur during the

column wetting process. Total end cap volume contributing to column dead volume was 0.0112 liters or 1.9 percent of the total column volume.

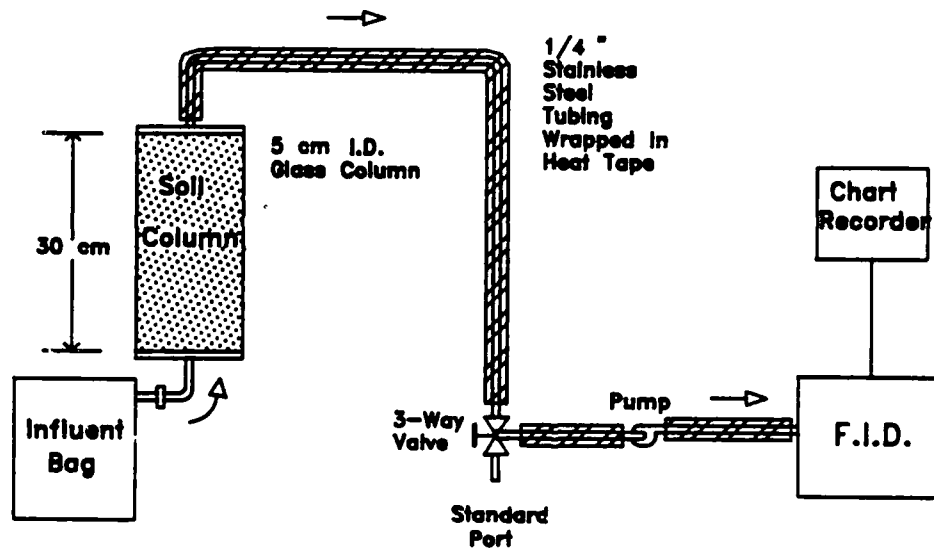


Figure 2.2.2 Laboratory apparatus used to investigate impacts of flow rate and degree of saturation on soil vapor extraction.

After packing, the soil column was attached to a nitrogen gas cylinder under approximately 10 psig pressure and submerged in water to observe for leaks. The end caps and fittings were tightened until all pressure leaks were eliminated.

The FMI Lab Pump that was used in the first experiments, was also

used as the vacuum source in this system. As in the previous apparatus, stainless steel tubing was cleaned and then wrapped with heat tape to eliminate condensation onto the inner walls. A flame ionization detector was installed in line with the system so that concentrations could be recorded continuously. This eliminated the need for a gas sampling valve. Since only single chemicals were introduced to the system at a time, a gas chromatograph was unnecessary also.

A final apparatus and procedure change was made to allow the introduction of chemical into the glass soil column from gas cylinders. This change was made because the vacuum pump used in the study delivered a pulsed flow resulting in an unsteady electronic signal from the chemical detector. This modification was also made so that an insoluble, non-adsorbing, highly volatile chemical (methane) could be used as an air tracer in dispersion experiments. The second modification of the experimental apparatus is shown in Figure 2.2.3.

Chemical was introduced into the glass soil column by connecting it to a pressurized gas cylinder containing the volatile organic chemical (Scott Speciality Gases, Troy, MI). The exit of the soil column was attached directly to the same flame ionization detector for chemical detection. The elution or extraction of chemical was performed by attaching a compressed breathing air cylinder in place of the VOC gas cylinder. A pressure regulator on both cylinders was set such that both cylinder pressures were as close to one another as possible. The pressures were set at approximately 2 psig. A needle valve (Whitey, Neenah, WI) was used to control air flow to the soil column. However, because pressures of both cylinders were not identical, the flow rate differed slightly from the introduction of chemical and its elution.

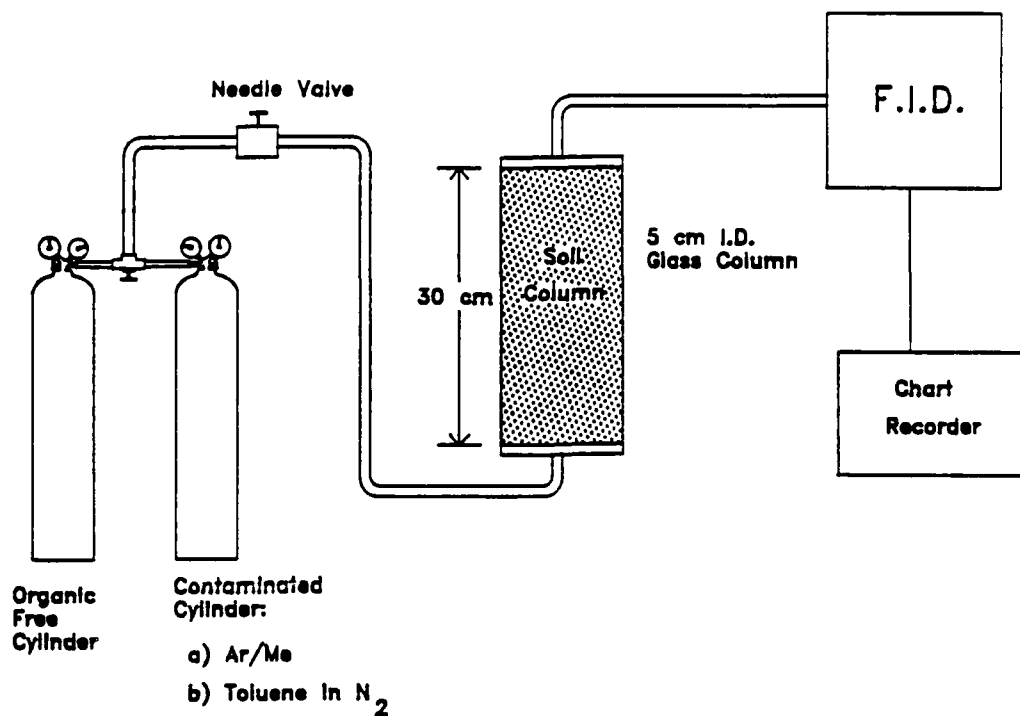


Figure 2.2.3. Apparatus used to investigate impacts of dispersion and soil moisture on soil vapor extraction process.

2.3 Chemical Detection

In the first apparatus presented in Figure 2.2.1, chemical concentrations were measured by gas chromatography (Perkin-Elmer Sigma 1000). A flame ionization detector (FID) was used to detect mass of chemical in each sample, and an integrator was used to convert this mass of chemical to area units which were presented graphically as integrator output. These reported area units were converted to concentrations by way of a standard calibration curve.

This gas chromatograph was linked to a computer aided data acquisition system. This system was set-up such that only an

experimental starting time and a sampling frequency was required as input. With this information programmed, all sampling was automated. Because of the ease in sampling, samples were taken every 30 minutes.

For the last two systems, a Dohrmann Envirotech Organic Analyzer (Santa Clara, CA) equipped with an FID was used to detect and to quantify VOC concentrations. It was found that the FID had good reproducibility at high concentrations and could be used to detect all organic chemicals used for this study. The Organic Analyzer was modified such that all gas flow was directed to the FID. No sampling valve and no gas chromatography column was used. Since all gas from the soil column was analyzed, a continuous analog signal was sent from the detector to a chart recorder. A Hewlett-Packard 680 strip chart recorder (Pasadena, CA) was used to convert the millivolt signal to a line plot. This line plot moved above baseline as concentrations increased and thus, peak heights could be converted to concentrations. This particular recorder was used because it allowed the incoming unsteady signal caused by pulsed flow to be dampened by using the gain adjustment. Because of the continuous analog signal, sampling was simplified.

The use of a photoionization detector (HNU Systems, Inc., Newton Highlands, MA) was also tried but was found to be sensitive to both concentration and pressure variations resulting in poor reproducibility at high concentrations and flow rates. Also, only chemicals with an ionization potential less than that of the ultraviolet lamp (10.7 eV) could be detected.

2.4 Standard Preparation

A set of standards was prepared for each experiment, from which, a

calibration curve was developed. Through this calibration curve, area units or peak heights were converted to concentration units. Each of these standards were prepared by injecting chemical into organic-free air in 10-liter Tedlar bags (SKC, Inc., Eighty-Four, PA).

In order to make a set of standards, it was necessary to clean the Tedlar bags. The bags were cleaned by replacing the punctured Teflon-lined butyl rubber septa with a new septa and evacuating any existing gas with a vacuum pump. Next, approximately 6 liters of compressed breathing air were added to each bag. After several minutes, this gas was evacuated from the bag with a vacuum pump. This filling and evacuation of the standard bags was an iterative process which cleaned the bags by diluting any remaining VOC contained in the bag. For quality control/quality assurance, several bags were filled with organic-free air and samples were analyzed to determine if any chemical remained in the bags after one flushing cycle. In all cases, no contaminant was detectable after one flushing.

After the bags were adequately cleaned, approximately 4 or 5 gas standards were prepared for each experiment. Gas standards were made such that the concentration range was 5 to 95 percent of the pure vapor concentration of the chemical of interest. Tedlar bags were filled with a measured volume of compressed breathing air, and a measured mass of pure chemical was injected to this volume. All gas measurement was made with a wet test meter (Precision Scientific Co., Chicago, IL). A gas-tight syringe was used for all chemical additions to the Tedlar bags. Before chemical addition to the Tedlar bag, the syringe was weighed full, and, after injection of chemical through the teflon-lined butyl rubber septum, the needle was wiped, and the syringe was again weighed.

The mass of VOC added was determined by difference. Standard concentration is calculated as follows:

$$\text{standard conc. (mg/L)} = [\text{mass added (mg)}][\text{vol. of air (L)}]^{-1} \quad (2.4.1)$$

Depending on the method of chemical detection, standards were injected into the G.C. or the Dohrmann FID and areas or peak heights were measured. These data were plotted and fit to a calibration curve. It was observed that most calibration data were best fit with a straight line through zero. A completed standard set with all data and best fit parameters including percent errors is shown in Appendix A.

Since standards could almost always be fit best with a straight line through zero, it was possible to determine a relative concentration by dividing each peak height by the maximum peak height registered while chemical was fed to the column. This eliminated the need for developing a complete set of standards for each experiment.

2.5 Media Characteristics

Three soils were used in the study -- a cohesionless sand, a fired, porous aggregate, and a sandy loam soil. The first soil to be used was Ottawa sand, a round, uniform, cohesionless, silica sand. Ottawa sand was used in previous work at Michigan Technological University and was observed to have no adsorption capacity under saturated or unsaturated conditions (Krause, 1987). Ottawa sand was packed dry to obtain a total porosity of 0.34 (± 0.02) and a bulk density of 1.75 g/cm³.

The second soil type was SCR Verilite, a very light-weight, fired porous aggregate. Verilite is used as an insulating material in the steel and iron production industry. Verilite was also used in previous

experimental work by Krause (1987). Because of its high internal porosity, verilite was used to simulate an aggregated material. A column packed with verilite has a total porosity of 0.68 (± 0.04), and particle porosity of 0.50 (Krause, 1987). The particle density was determined to be 1.51 g/cm³ (Krause, 1987) giving a bulk density of 0.48 g/cm³. This material is similar to ottawa sand in size and the amount of organic material present. It showed no adsorption of volatile organic chemical when saturated with water.

An additional soil, Keweenaw-7, was used in the study of gas dispersion. This is a field soil containing a much higher organic carbon content. A soil column containing K-7 had a porosity of 0.356. Keweenaw-7 soil has a particle density of 2.59 g/cm³. The characteristics of this soil are given by Hutzler et al. (1986).

The following table compares the important properties of the media used in this research.

Table 2.5.1 Media characteristics.

	Ottawa Sand	Verilite	K-7
Particle diameter (cm)	0.07	0.07	0.016
Bulk density (g/cm ³)	1.747	0.424	1.667
Particle density (g/cm ³)	2.65	1.51	2.59
Total Porosity	0.341	0.720	0.356
Microporosity	-	0.50	-
Macroporosity	0.341	0.44	0.356
Organic Carbon (%)	-	-	0.85

Before packing, all soils were first rinsed with distilled water and then placed in a convection oven at 103 degrees Celsius until dry. After drying, the soils were placed in glass bottles for storage.

The soil columns were packed by the following procedures with all calculations presented in Appendix B. A column was first weighed empty with both end caps attached to give the total mass of the empty column. The column was then filled with water and weighed again. This measurement minus the empty weight was used to calculate the total volume of the soil column. The column was then dried, packed with dry media, and weighed again. This weight minus the weight of the empty column gives mass of media packed in the column. The mass of dry sand divided by total column volume gives bulk density (ρ_b) of the media. The porosity can be determined from:

$$\epsilon = 1 - \rho_b/\rho_s \quad (2.5.1)$$

where ρ_b = bulk density, g/mL

ρ_s = particle density, g/mL

For the dry experiments, all porous media were packed dry into the soil column. Packing consisted of adding 1/4" layers of media (1/8" layers for K-7) and compacting each layer lightly with a 1" plug. To minimize stratification when packing K-7, the soil was added in small amounts through a long, narrow-tubed funnel. This process was continued until the soil column was full and the end cap rested tightly upon the soil. Before the end cap was installed, a Teflon screen was placed on top of the media. This eliminated any shifting of sand which might occur.

The same process was followed for experiments when water was

introduced into the columns. However, it was necessary to saturate verilite particles before packing. This was accomplished by adding several hundred grams of verilite to boiling, distilled, deionized water. Boiling reduced the surface tension of the water within the internal pores of the particles and also removed air from the water. Once the particles were saturated, they were then added to the soil column in the same procedure as stated above.

2.6 Chemical Characteristics

Three chemicals were used throughout this vapor extraction study -- toluene, 1,1,1-trichloroethane (Fisher Scientific, Chicago, IL), and methane (Scott Gases, Troy, MI). These three chemicals gave a wide range of volatility and solubility. Toluene and 1,1,1-TCA were used to investigate volatility effects on the rate of vapor extraction. Methane was used as a nonadsorbing chemical tracer to estimate soil column tortuosity. The properties of the three chemicals used during the study are given in the following table.

Table 2.6.1 Chemical properties (25 degrees Celsius).

	Toluene	1,1,1-TCA	Methane
Vapor Pressure (mm Hg)	28	125	205,000
Molecular Weight (g/mole)	92.1	133.4	16.0
Solubility (mg/L)	500	1245	-
Henry's Constant (dim.)	0.281	0.717	high
Density (g/mL)	0.866	1.35	0.656

2.7 Experimental Procedure

All experiments were performed at 23 degrees Celsius (± 3 degrees) in a temperature controlled room. Atmospheric pressure ranged from 740 to 770 mm Hg.

2.7.1 Soil Column Procedure

When using the first apparatus (Figure 2.2.1), the volatile organic chemical was introduced into the soil column by pumping several liters of distilled, deionized water spiked with the chemical upward through the column. The water flow was kept slow to ensure that as many air pores could be filled with the water solution as possible. After several pore volumes of spiked water were flushed through the column, the column was capped and allowed to equilibrate for several hours.

During the introduction of VOC, a saturated porous stone was in place at the bottom of the soil column to insure an even distribution of water over the entire cross section of the porous media. Also, while VOC was introduced to the soil column, the air distributors were removed and the air ports were capped.

Just prior to the start of the experiment, the column was uncapped and allowed to drain by gravity. During draining, several attempts were made to measure the liquid concentration. This measurement, along with the initial gas phase concentration, were to be used to estimate Henry's constant.

$$H = C_v/C_b \quad (2.7.1)$$

where C_v = gas phase concentration, mg/L

C_b = liquid phase concentration, mg/L

After draining, the column was inverted and the saturated porous stone

was removed and a plexiglas plate was inserted in its place. The air distributors were then tapped into place and the air ports were again capped for a period of time in order to allow equilibrium to be achieved. At this time, the soil column was weighed to measure the degree of saturation (s).

$$s = (\text{wet col. wt.} - \text{dry col. wt.}) (\rho_w)^{-1} (\text{column void vol.})^{-1} \quad (2.7.2)$$

At the start of the experiment, the air ports were uncapped and attached by teflon tubing to the the humidifier and GAC column. At this time, an initial gas concentration was measured, and samples were taken at regular intervals thereafter.

The experimental procedure was similar for the second apparatus (Figure 2.2.2). However, VOC was introduced into the soil column by pumping a gas from a Tedlar bag. Elution of the chemical was conducted by pumping organic-free air from a Tedlar bag through the soil column. Chemical concentrations were measured continuously, therefore, mass retained by the column as compared to mass recovered could be more easily computed. If an unsaturated experiment were to be performed, water had to be introduced to the column. This was accomplished by connecting the column to a Milli-Q (Millipore, Bedford, MA) water system. The Milli-Q water system delivers distilled, deionized, and organic-free water. This water was pumped upward through the column to remove as much air as possible. After several pore volumes of water were passed through the column, the water system was disconnected and the column was capped for a period of several hours.

Prior to the start of an experiment, the column was uncapped and the water was allowed to drain by gravity. To remove any large pockets

of water, a siphon bulb was used to push air downward through the soil column. This was continued until no more water exited the column. This insured a uniform water profile. The column was then weighed to measure the degree of saturation (Eq. 2.7.2).

An influent bag containing approximately 50 percent of the pure vapor concentration of toluene was prepared. After this was prepared, the experiment proceeded. This chemical-laden air was pumped through the soil column until the peak height registered by the recorder reached a maximum and became constant. Then, the influent bag was removed and a bag containing a measured volume of organic-free air was immediately attached to the bottom of the column. At the same time, the recorder output was marked as to the time that the breakthrough, that is, the entire time in which chemical is being introduced to the soil column, was complete and the elution was started. Elution of chemical was continued until the recorder output returned to the baseline. Once the elution was complete, the bag containing the organic-free air was attached to a wet test meter and the air was forced out. The volume used throughout the duration of the elution was determined by volume difference. The volume of air used during the elution divided by the time of elution gave the flow rate of air used throughout the experiment.

The time that air was in the dead volume of the column end caps and connected tubing was subtracted from the start time of both the breakthrough and the elution periods. The dead volume of the column and tubing was measured to be 33.3 mL or 5.6 percent of the total column volume. Dead volume divided by air flow rate gives the time correction which must be subtracted from both the breakthrough and the elution

data. The height of the breakthrough or elution curve from baseline was measured and converted to concentrations as previously described.

After concentrations and times were determined from the recorder plot, the data were written into a FORTRAN data file, and a program to calculate the mass retained by the column and the mass recovered from the column was run to compare the mass balance. The masses retained and removed were calculated through use of the trapezoidal rule of integration on the experimental data. An example showing the areas integrated to determine mass retained and mass removed is presented in Figure 2.7.1. Integration of region 1 gives mass retained, whereas, integration of region 2 gives mass removed.

Percent difference between mass retained and mass extracted can be determined by:

$$\% \text{ difference} = (\text{mass retained} - \text{mass removed}) / \text{mass retained} \quad (2.7.3)$$

Calculation of mass retained, mass recovered and the associated percent error between the two calculations gave an indication of the goodness of the experimental technique and procedure. Also, time to the center of mass of both the breakthrough and elution curves can be determined from the calculated mass which was retained and removed from the soil column (regions 1 and 2 from Figure 2.7.1, respectively) by dividing by the flow rate and maximum (influent) concentration of the experiment. This calculation of the time to the center of mass gives the average travel time for a molecule of chemical to travel through the soil column. Any amount of time exceeding the required time for one air pore volume to pass through the column denotes that retardation is occurring. An air pore volume fed is calculated as:

$$\text{Air Pore Volume Fed} = Q [A L \epsilon (1-s)]^{-1} \quad (2.7.4)$$

with Q = air flow rate, mL/hr

A = column cross-sectional area, cm^2

L = column length, cm

ϵ = column porosity

s = degree of saturation

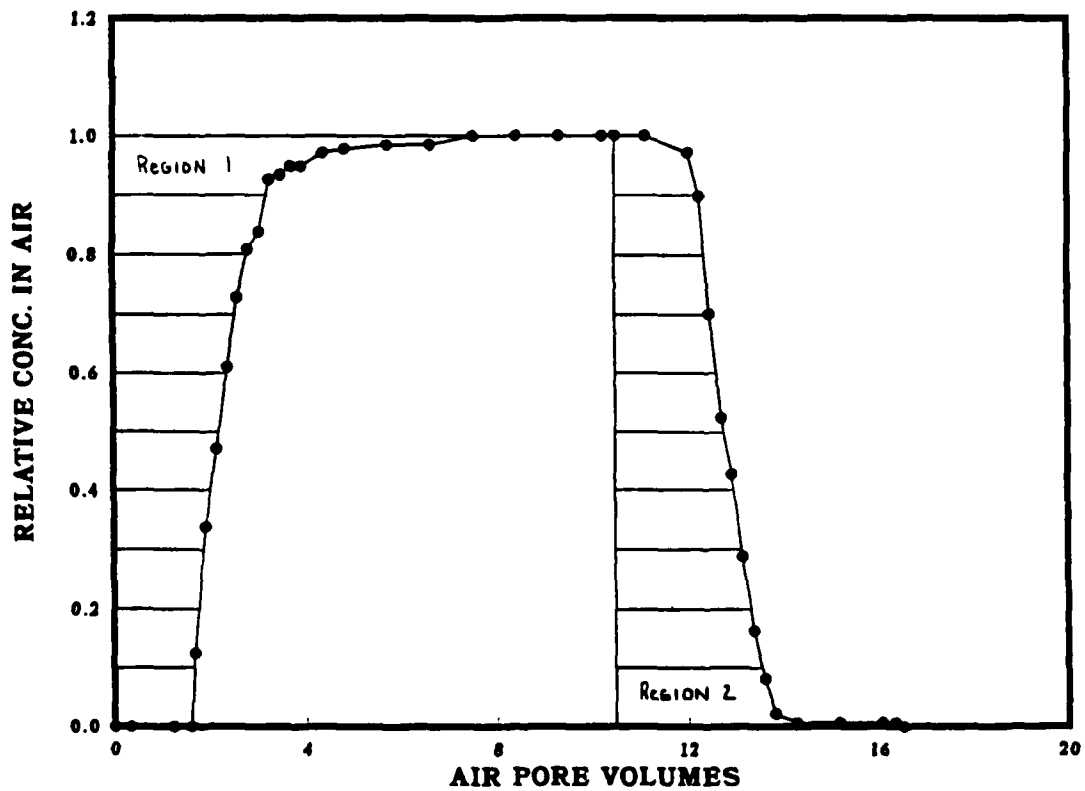


Figure 2.7.1 Example plot demonstrating integration to determine mass removed and mass recovered.

By using air pore volumes fed to represent time, experimental data from several experiments can be directly compared even if air flows or

degrees of saturation differ. Therefore, air pore volumes fed will be used in all discussions of experimental data and model simulations.

From the mass balance and center of mass calculations, parameters necessary to describe equilibrium inside the soil column can be estimated. Assuming equilibrium exists, adsorption onto dry media can be estimated from equation 2.7.5.

$$\begin{aligned}
 \text{Mass Retained in Column (M.R.)} &= \text{Mass in Air} + \text{Mass in Water} \\
 &+ \text{Mass Sorbed from Air} + \text{Mass Sorbed from Water} \\
 &= AL\epsilon(1-s)Cv_0 + AL\epsilon(s)(Cv_0/H) \\
 &\quad + AL(1-\epsilon)\rho_s(K_v)Cv_0 \\
 &\quad + AL(1-\epsilon)\rho_s(K/H)Cv_0 \qquad (2.7.5)
 \end{aligned}$$

where

- A = column cross sectional area, cm²
- L = column length, cm
- ε = soil column porosity
- s = degree of saturation
- Cv₀ = initial gas concentration, mg/L
- H = Henry's constant, dimensionless
- ρ_s = particle density, g/cm³
- K = Adsorption from water onto soil, mL/g
- K_v = adsorption from air onto soil, mL/g

Three assumptions of the above stated mathematical equation must be considered. Adsorption from vapor onto dry ottawa sand and verillite occurs, no adsorption onto moist ottawa sand occurs, and the concentration of the liquid present in the soil column can be related to the gas phase concentration through Henry's Law equilibrium.

Under dry column conditions, the adsorption potential of the soil

can be calculated as:

$$K_V = [M.R. - AL\epsilon C_{V0}][AL(1-\epsilon)\rho_S C_{V0}]^{-1} \quad (2.7.6)$$

2.7.2 Batch and Isotherm Procedures

Two additional experiments were conducted in addition to soil column experiments. The first was a bromide diffusion out of porous particles experiment which was adapted from Rao et al. (1982). This experiment was performed in order to estimate the interparticle tortuosity of verilite particles. To summarize the procedure, several hundred grams of verilite particles were saturated with a potassium bromide (KBr) solution. The exterior of the particles were dried by patting dry with Kimwipes (Kimberly-Clark, Roswell, GA). Before addition to a well-mixed batch reactor, the verilite particles were weighed. Wet weight minus the dry weight gave a volume of KBr contained within the particles. By knowing the concentration of the saturating solution allows the mass of bromide placed into the batch reactor to be calculated. The bromide concentration in the reactor was monitored with a specific ion electrode (Corning, Medfield, MA) and an Orion reference electrode (Cambridge, MA) over a period of sixty minutes until a constant bromide concentration was established.

The second experiment conducted was a gas phase isotherm which was to show the adsorption of toluene vapors onto dry sand particles. Four Tedlar bags were prepared by adding approximately 900 grams of sand to each bag. Each bag was then completely evacuated of all air with a vacuum pump. To each bag, 500 mL of compressed breathing air was added. Approximately 30 μ L of pure toluene was injected to make the concentration of the gas in each bag approximately 50 mg/L. A blank was

prepared in which 30 μ L of toluene were injected into 500 mL of compressed breathing air.

A 10-percent concentration change each bag was anticipated. However, small changes in concentration could not be directly attributed to chemical adsorption. Decreases in concentration could have been due to chemical diffusion out of the Tedlar bags or due to leakage of chemical from the bags. The findings of this isotherm were, therefore, inconclusive.

2.8 Soil Column Models

The laboratory soil column experiments previously described were designed in order to validate two laboratory soil column models. The model developments of the Combined Dispersed Flow Diffusion into Aggregates Model (CDFDAM) and the Air Dispersed Flow Diffusion into Aggregates Model (ADFDAM) are presented by Gierke (1986) and Bednar (1990), respectively. These soil column models describe the transport of VOCs through dry and unsaturated porous media.

Four mechanisms of chemical transport are considered by the soil column models. These mass transfer mechanisms include air advection, gas dispersion and diffusion, liquid (pore) diffusion, and air-water mass transfer. These mechanisms affect the shape of the chemical wave front as it travels through the soil column. If only advection occurs, the chemical front will move through the soil column as plug flow. Gas dispersion and diffusion, liquid diffusion and air-water mass transfer cause the wave front to spread as it travels through the soil column. Air-soil and water-soil equilibrium are established by Freundlich adsorption and air-water equilibrium is established by Henry's law. These equilibrium mechanisms retard the chemical wave front.

Sensitivity of the model to these mechanisms are discussed in Gierke et al. (1989).

Because the ADFDAM requires a nonzero degree of saturation to be input, the ADFDAM could only be used to model moist soil column experiments. The CDFDAM was used to model dry soil column experiments.

Several modeling assumptions are made and these assumptions must be considered when designing experiments. First, the model assumes that soil packing is homogeneous and soil aggregates can be modeled as uniformly sized spheres. Second, chemicals must be nondegradable and in dilute solution. Third, air flow is steady and one dimensional. Fourth, moisture content is uniform throughout the soil column. Lastly, sorption is instantaneous.

A third model was used to describe methane transport through ottawa sand. This model, the Dispersed Flow Local Equilibrium Model (DFLEM), assumes no mass transfer resistance and equilibrium between stationary and mobile phases (Crittenden et al., 1986). The solution of this model was given by Hashimoto et al. (1964). This model was used to determine dispersion in packed columns of dry ottawa sand and Keweenaw-7.

2.9 Parameter Estimation

Estimation of the values for parameters which are required for the chemical transport models can be obtained from direct measurement, literature correlations, laboratory experiments, or by fitting model solutions to concentration data that are obtained from soil column experiments. These models require soil column dimensions, experimental conditions, and soil and chemical properties as input parameters. To

prove the correctness of a mathematical model, it is imperative that each of these input parameters are determined independently.

Soil column dimensions required include length (L) and diameter (D). Experimental conditions include temperature (T), atmospheric pressure (P), air flow rate (Q), and degree of saturation (s). Soil properties include mobile porosity (ϵ), immobile saturation (s_f), particle density (ρ_s), and aggregate radius (R_a). Chemical properties include the air/water partition coefficient (H); influent chemical concentration (C_{vi}); film transfer (k_f), pore diffusion (D_p), and gas dispersion (E_v) coefficients; and isotherm capacity (K) and intensity ($1/n$).

Experimental conditions such as temperature, pressure, air flow rate, and degree of saturation and soil column dimensions such as length and diameter can be measured directly. Directly-measured soil properties include the mobile and immobile porosities, particle densities, and the aggregate radius. Influent chemical concentration is also a direct measurement.

Some parameters can be estimated from correlations present in the literature. For example, the film transfer coefficient can be calculated from a correlation by Wilson & Geankoplis (1966).

$$k_f = 1.09v[2Ra(v)\epsilon(s-s_f)/D_L]^{-0.667} \quad (2.9.1)$$

with v = interstitial velocity, cm/sec

R_a = aggregate radius, cm

ϵ = porosity

s = degree of saturation

s_f = immobile saturation

D_L = liquid diffusion coefficient, cm^2/sec

This correlation was developed for soil columns which had mobile and immobile water present. This correlation was applied to dry soil columns in which there were regions of mobile and immobile air. This parameter was found to be unimportant in gas transport modeling reported herein. Nonetheless, it is a required input for the CDFDAM computer program.

Both the CDFDAM and the ADFDAM computer programs require an overall mass transfer coefficient (K_L) between air and water to be input. This parameter can be calculated from a correlation presented by Treybal (1980):

$$K_L = 1[(1/k_l) + (1/Hk_g)]^{-1} \quad (2.9.2)$$

where k_l = local mass transfer in the water at the air/water interface, cm/sec

k_g = local mass transfer in the air at the air/water interface, cm/sec

H = Henry's constant, dimensionless

This parameter can be assumed to be unimportant when modeling chemical flow through dry soil columns. However, when moist soil columns were modeled, this parameter must be considered. The values of k_l and k_g can be determined from correlations by Shulman et al., (1955):

$$k_l = 12.6D_l Re_l^{0.45} Sc_l^{0.5} Ra^{-1} \quad (2.9.3)$$

where D_l = liquid diffusion coefficient, cm^2/sec (see Appendix C)

Re_l = Reynolds number based on interstitial water velocity

Sc_l = Schmidt number based on interstitial water velocity

$$k_g = 0.598D_G[1-\epsilon(1-s)]^{0.36}Re_g^{0.64}Sc_g^{0.33} \quad (2.9.4)$$

where D_G = gas diffusion coefficient, cm^2/sec (see Appendix C)

Re_g = Reynolds number based on interstitial gas velocity
 $= 2vR_a\rho_g/\mu_g$

Sc_g = Schmidt number based on interstitial gas velocity
 $= \mu_g D_G/\rho_g$

Since there is no mobile water in the soil vapor extraction experiments all mass transfer resistance can be assumed to be in the air phase.

Therefore, k_l can be ignored and Equation 2.9.2 can be rewritten as:

$$K_L = Hk_g \quad (2.9.5)$$

As was found with the film transfer coefficient, this parameter is unimportant in gas transport modeling. It is, however, a required input for both the CDFDAM and the ADFDAM computer programs.

The pore diffusion coefficient can be approximated by the free liquid diffusion coefficient divided by the interparticle tortuosity.

$$D_p = D_L / \tau_p \quad (2.9.6)$$

where D_p = pore diffusion coefficient, cm^2/sec

τ_p = interparticle tortuosity

Tortuosity equals the effective diffusion length divided by the straight line diffusion length. Tortuosity, by definition, must always be greater than one. Pore diffusion only becomes important when water is present in the soil column or in aggregated materials.

The gas dispersion coefficient can be estimated from a correlation adapted from Miyauchi & Kikuchi (1975).

$$E_v = D_G/1.4 + 2vR_a[(1-(1-e^{-2x})/2x)/x]/0.17 \quad (2.9.7)$$

$$x = 35 [Pe]^{-6/7} \quad \text{for } Pe > 10$$

$$x = 22 [Pe]^{-2/3} \quad \text{for } Pe < 10$$

$$Pe = v4R[e_f/(1-e_f)][3D_G]^{-1} \quad (2.9.8)$$

e_f = fraction of fluid volume that is fast moving

v = interstitial velocity, cm/sec

R_a = aggregate radius, cm

D_G = free gas diffusion coefficient, cm^2/sec

The second term of Equation 2.9.7 becomes negligible when gas flow is considered. Therefore, Equation 2.9.7 reduces to:

$$E_v = D_G / \tau_a \quad (2.9.9)$$

where τ_a = intraparticle tortuosity = 1.4

The value of 1.4 was given by Miyauchi & Kikuchi as the intraparticle tortuosity of packed beds. The tortuosity of a soil column can also be measured with a nonretarded chemical in a tracer study. Methane was used as a tracer chemical because it is nonadsorbing, is insoluble, and is detectable with a flame ionization detector.

The liquid and gas diffusion coefficients must be estimated for each chemical. The liquid diffusion coefficient is calculated from the Wilke-Chang correlation (Wilke & Chang, 1955) and the gas diffusion coefficient is determined from the Wilke-Lee empirical correlation (Wilke and Lee, 1955). Both correlations along with sample calculations are presented in Appendix C.

The air/water partition coefficient, or Henry's constant, was determined through the use of UNIFAC which is described in Reid et al., (1987). UNIFAC allows chemical properties to be estimated based on the

structural groups of the molecule of interest. A UNIFAC software package developed by Ashworth et al. (1988) allows Henry's constant, vapor pressure, and solubility data to be estimated for a list of organic chemicals at experimental temperatures.

The two remaining parameters, isotherm capacity (K) and intensity ($1/n$), should be determined in an independently performed gas-phase isotherm. As was mentioned previously, this was attempted but results were inconclusive.

3. EXPERIMENTAL RESULTS

Three sets of soil column experiments resulting in 31 separate runs were performed throughout this study. The experimental conditions, mass balances, and modeling parameter values are summarized in Appendix D. These experiments investigated the effects of soil type and structure, chemical characteristics, and two experimental conditions, including air flow rate (air velocity), and degree of saturation upon the soil vapor extraction process.

The effects of chemical volatility and soil structure were investigated with the use of the first apparatus (Figure 2.2.1). Chemical volatility was investigated with two chemicals -- toluene and TCA. The effects of soil structure were investigated with both a cohesionless soil (ottawa sand) and a soil simulating an aggregated material (verilite).

The effects of soil moisture and flow rate were investigated with the use of the second apparatus (Figure 2.2.2). Three degrees of moisture were introduced to the soil columns. Oven dry soils were used in dry experiments. Moist soil experiments were performed by first wetting and then draining all excess water from the soil columns. Soil was humidified by attaching a water humidifier to the bottom of the soil column and bubbling air through for a period of time. Air flow rates were investigated by adjusting flow of the vacuum pump.

3.1 Tortuosity Estimation

Tracer studies were conducted by introducing methane as the tracer chemical to soil columns packed with ottawa sand and Keweenaw-7. The results of the experiments allowed the calculation of the intraparticle

tortuosity for each of the porous media. With tortuosities so determined, gas dispersion coefficients can be calculated from Equation 2.9.9.

Four experiments were performed using the methane tracer. Experiments were performed at both high and low flow for both ottawa sand and Keweenaw-7. All experiments were performed under dry conditions. A complete listing of all experimental conditions is shown in Table 3.1.1

Table 3.1.1 Tracer study experimental data.

Parameter	Experiment No.			
	1	2	3	4
Chemical	Methane	Methane	Methane	Methane
Soil Type	ottawa sand	ottawa sand	Keweenaw-7	Keweenaw-7
Porosity	0.334	0.334	0.356	0.356
Deg of Sat.	0	0	0	0
Flow Rate (mL/min)	4.22 ^a 5.02 ^b	10.42 ^a 14.53 ^b	2.51 ^a 3.26 ^b	12.04 ^a 15.87 ^b
Velocity(cm/sec)	0.0107 ^a 0.0128 ^b	0.0265 ^a 0.0369 ^b	0.0600 ^a 0.0780 ^b	0.0287 ^a 0.0378 ^b
Temp(deg C)	23.5	23.0	23.5	22.0
Atm. Press(mm Hg)	746.0	747.0	746.0	750.0
a - breakthrough data b - elution data				

3.1.1 Ottawa Sand Tortuosity Estimation

These experiments were conducted under dry conditions. For the low

flow experiment, the breakthrough air flow rate was 4.2 mL/min, while the elution was 5.0 mL/min. This corresponds to interstitial velocities of 0.0107 cm/sec and 0.0128 cm/sec for the breakthrough and the elution, respectively. The high flow experiment had flows approximately 2 1/2 to 3 times higher. The breakthrough and elution flow rates were 10.4 and 14.5 mL/min, respectively, giving interstitial velocities of 0.0265 and 0.0369 cm/sec.

The experimental results along with two model predictions are shown in Figures 3.1.1 and 3.1.2. In all figures presented herein, concentration was normalized by dividing the effluent vapor concentration by the influent vapor concentration. The y-axis will be labeled as relative concentration in air. Time was normalized by dividing experimental run time by the hydraulic detention time of the soil column which gives air pore volumes fed. This calculation was presented in Equation 2.7.4.

The solid line CDFDAM prediction uses the Miyauchi and Kikuchi (1975) gas dispersion correlation (Eq 2.9.7). The dashed line was determined by fitting the DFLEM model to the experimental data with a least squares fitting routine to estimate a Peclet number.

$$Pe = vL/E_y \quad (3.1.2)$$

From the best fit Peclet number, a gas dispersion coefficient was calculated and from this, a best fit tortuosity was determined from Equation 2.9.9. The intraaggregate tortuosity for dry ottawa sand was calculated to be 1.8 for both the low and high flow experiments.

In viewing Figures 3.1.1 and 3.1.2, there is little difference between the estimated tortuosity of 1.4 and the best fit tortuosity of

1.8. Although there is little difference between the two model predictions, a tortuosity of 1.8 will be used in all gas dispersion calculations for ottawa sand herein since it was experimentally determined.

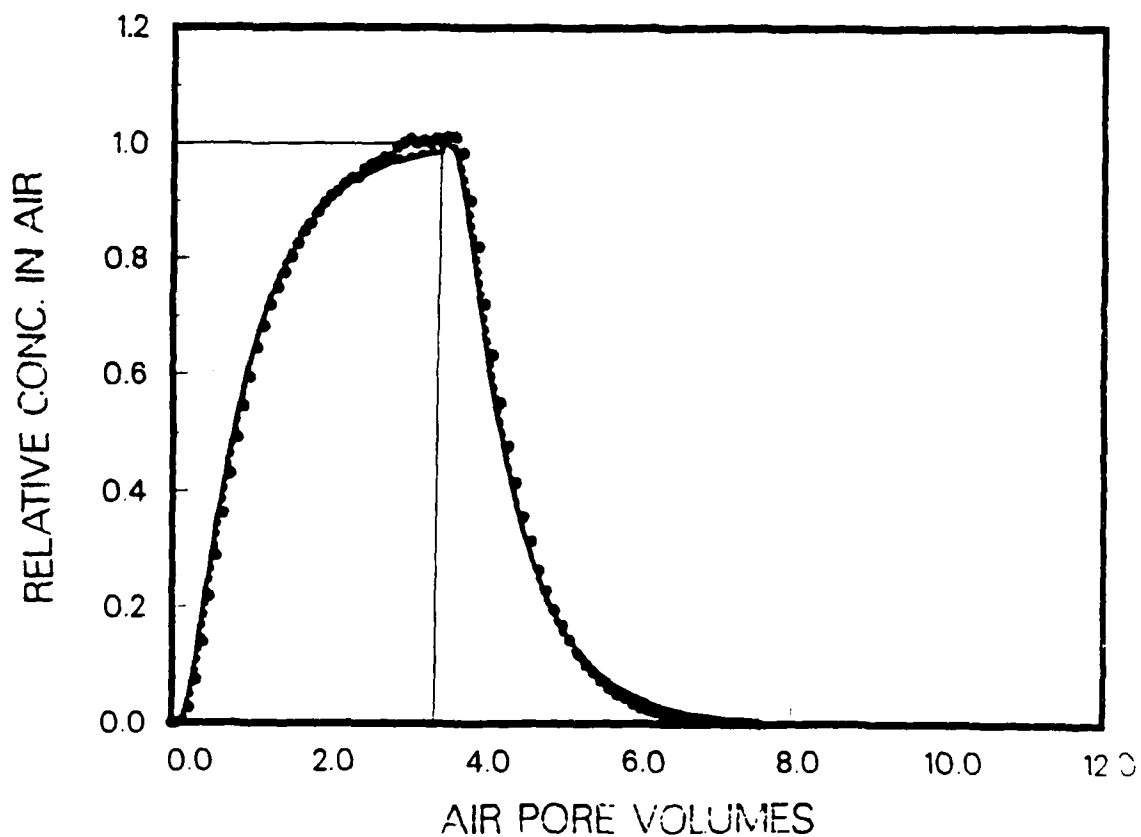


Figure 3.1.1. Breakthrough and elution of methane at low flow in a dry ottawa sand column. The solid line represents a CFDAM prediction using a tortuosity of 1.4 (Miyachi & Kikuchi, 1975). The dashed line fits the data to the DFLEM model. The best fit tortuosity is 1.8. The thin line is the influent chemical concentration history.

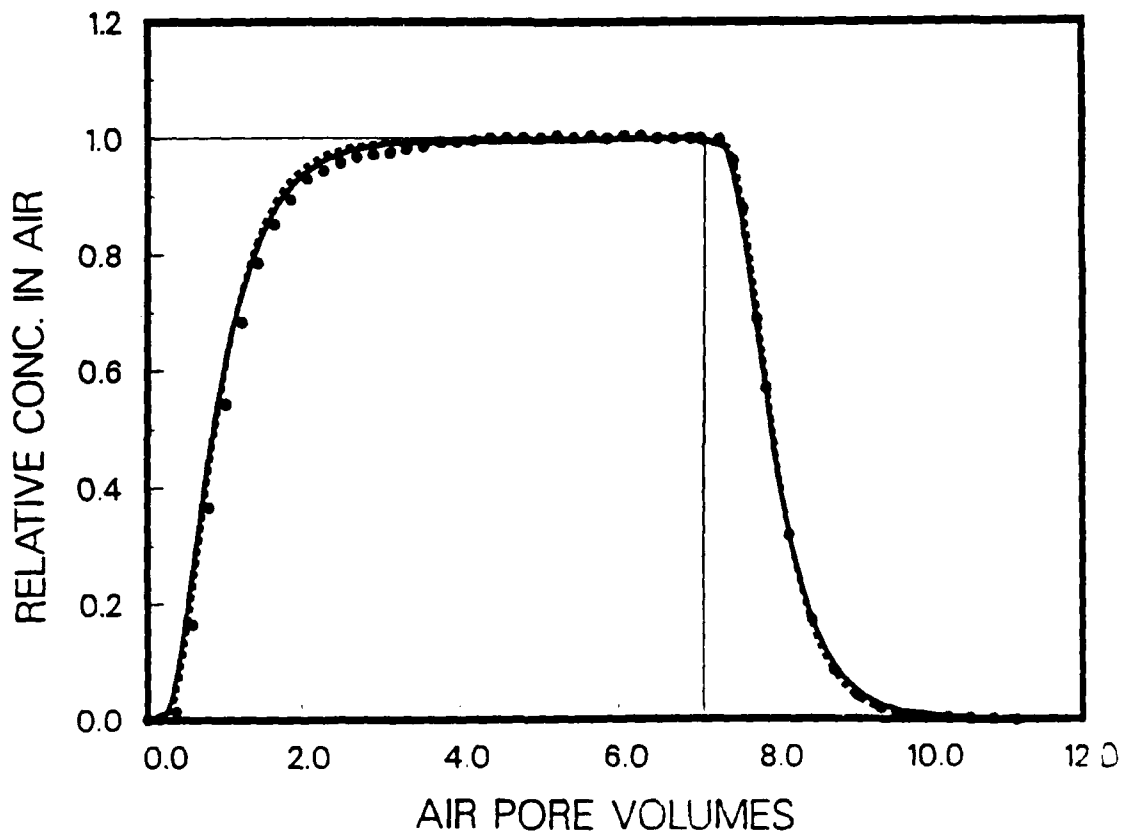


Figure 3.1.2. Breakthrough and elution of methane at high flow in a Ottawa sand column. The solid line shows the CFDAM model prediction using a tortuosity of 1.4. The dashed line is a CFDAM prediction uses a tortuosity of 1.8.

3.1.2 Keweenaw-7 Tortuosity Estimation

A similar procedure was used for a soil column packed with Keweenaw-7. The flows for the breakthrough and the elution of the low

flow experiment were 2.5 and 3.3 mL/min giving interstitial velocities of 0.0060 and 0.0078 cm/sec, respectively. For the high flow rate experiment, the flows were 12.0 and 15.9 mL/min or interstitial velocities of 0.0287 and 0.0378 cm/sec, respectively. The two model predictions shown as solid lines in Figures 3.1.3 and 3.1.4 represent a tortuosity of 1.4. The dashed line was determined by fitting the DFLEM to the experimental data with a least squares fitting routine in order to estimate a Peclet number. From the best fit Peclet number, a gas dispersion coefficient was calculated and from this a best fit tortuosity was determined. A best fit tortuosity of Keweenaw-7 for both high and low flow experiments was 3.0. As in the Ottawa sand tracer experiments, the model prediction using an intraaggregate tortuosity of 1.4 predicts the data nearly as well as the best fit tortuosity of 3. An increased tortuosity will decrease the calculated dispersion coefficient, thereby, increasing the Peclet number. The larger the Peclet number, the sharper the front of the breakthrough and elution curves of the experimental data. This is clearly shown by the two model simulations in Figures 3.1.3 and 3.1.4. As the porous media becomes nonuniform as is K-7, it becomes increasingly more important to measure the intraaggregate tortuosity through tracer studies if gas flow models are to describe experimental data adequately.

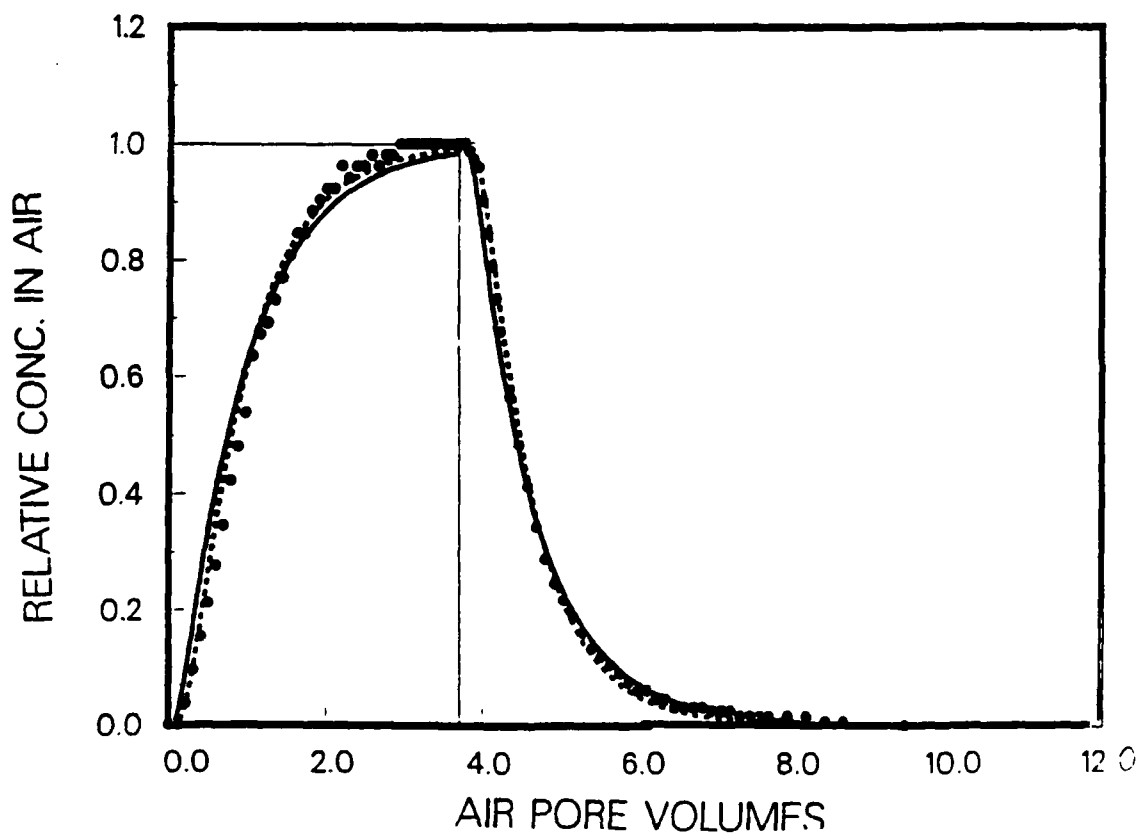


Figure 3.1.3. Breakthrough and elution of methane at low flow in a dry Keweenaw-7 soil column. The solid line represents a CFDAM prediction using a tortuosity of 1.4 (Miyachi & Kikuchi, 1975). The dashed line fits the data to the DFLEM and gives an intraaggregate tortuosity of 3.0.

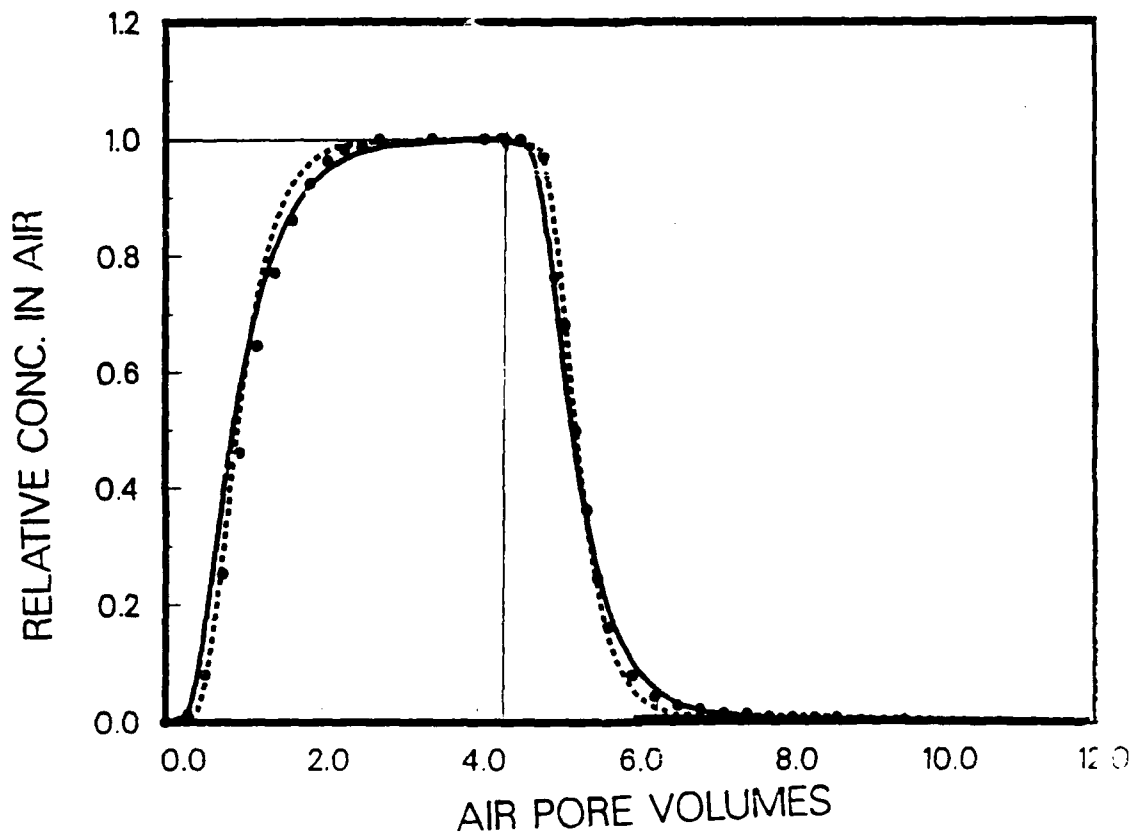


Figure 3.1.4. Breakthrough and elution of methane at high flow 7 in a Keweenaw-7 soil column. The solid line shows the CFDAM model prediction using a tortuosity of 1.4. The dashed line is a CFDAM prediction using a tortuosity of 3.0.

3.1.3 Verillite/Bromide Batch Experiment

Interaggregate pore diffusion was measured according to the procedure described in Section 2.7.2. The experimental data were fit to a diffusion-out-of-spheres model (Crank, 1980) by minimizing the sum of

the squares of the residuals between the measured values and the analytical solution (Gierke, personal communication). This best fit line along with the best fit parameters are presented in Figure 3.1.5. From this batch study, an aggregate tortuosity for the verillite particles was calculated to be 90.9. This value is extremely high, but after viewing the particles under electron scanning microscopy (Air Force Engineering and Services Center, Tyndall AFB, Florida) (see Figure 3.1.6), it was observed that the particle surface was impervious except at only a few locations. It can also be seen that many of the internal pores are not connected. Based on these pictures, an interparticle tortuosity of 90.9 seems to be a reasonable value.

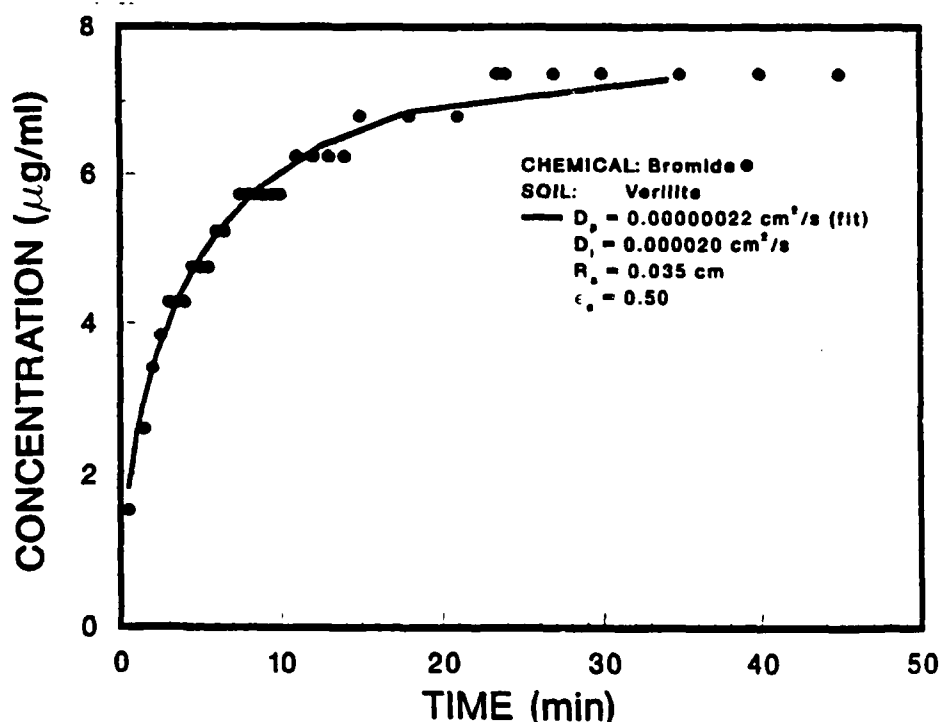


Figure 3.1.5. Diffusion of bromide from porous particles in a Batch Reactor. The solid line represents a best fit of a diffusion-out-of-porous spheres model developed by Crank (1980).

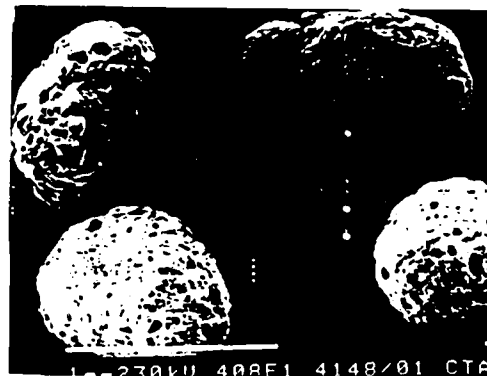


Figure 3.1.6. Electron microscopic photographs of a verilite particle showing surface and internal pores.

3.2 Chemical Volatility and Soil Structure Investigation

Four experiments using the apparatus shown in Figure 2.2.1 were performed at the U.S. Air Force Engineering and Services Center at Tyndall Air Force Base in Florida. During this initial study at Tyndall AFB, two system variables were investigated -- chemical volatility and soil structure. All other parameters including air flow rate and degree of saturation were held constant for each of the four experiments. Experimental conditions for the four experiments performed are presented

toluene.

While performing this study at Tyndall AFB, the impact of soil structure upon the removal of VOC's was also investigated. Ottawa sand is a cohesionless material, whereas, verilite has internal pore structure. Because the porous particles have immobile water within them, the process of pore diffusion becomes significant. The removal of both chemicals is much faster from ottawa sand than from verilite as shown in Figure 3.2.1. Liquid diffusion of chemical out of the immobile pore water requires more time, therefore, the removal time of chemical from the column packed with porous particles is much longer.

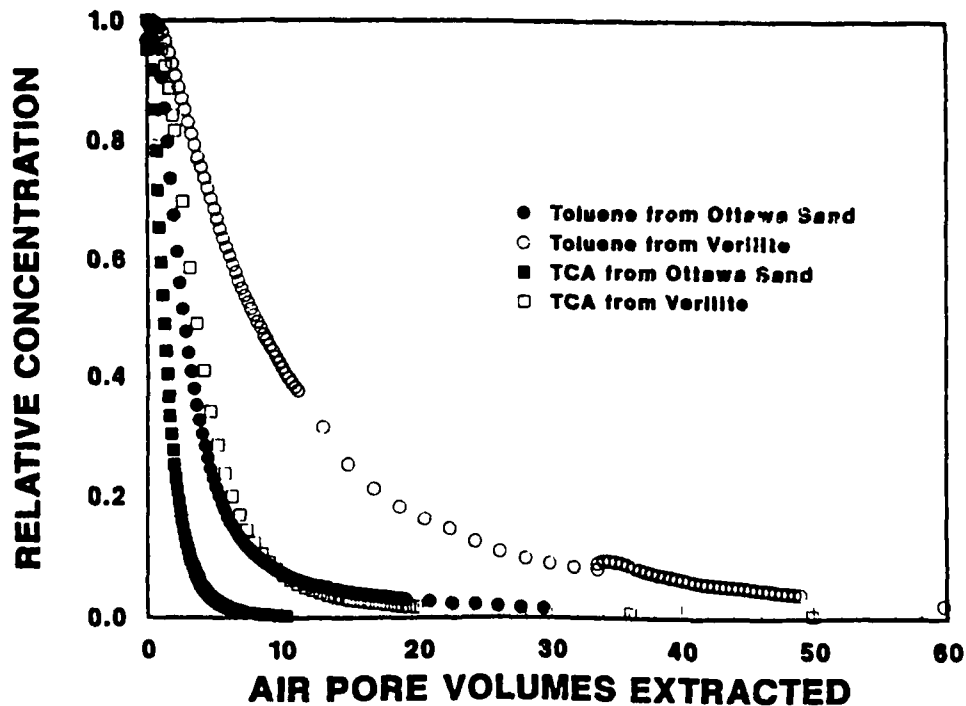


Figure 3.2.1. Extraction of toluene and 1,1,1-TCA from columns packed with ottawa sand and verilite.

On a percent mass removed basis, each of these four experiments showed between 115 and 135 percent mass removal if a UNIFAC H is used. More mass was removed than what was thought to be initially present in the soil column.

Greater than 100 percent mass removal can be explained by the inability to accurately determine the mass of chemical contained within the soil column at the start of the experiment. The mass retained by the column was estimated by measuring the initial gas-phase concentration and the degree of saturation of the soil column. UNIFAC Henry's constant was used to estimate the concentration of the water contained within the soil column, since air and water concentrations were assumed to be in equilibrium. No chemical was assumed to be sorbed to either soil or plexiglas. The initial mass calculation is shown in Equation 3.2.1.

Mass contained in the column =

$$\text{Mass in Air} + \text{Mass in Water} + \text{Mass Sorbed} \quad (3.2.1)$$

with: $\text{Mass in Air} = ALe(1-s)Cv_0$

$$\text{Mass in Water} = ALe(s)(Cv_0/H)$$

Mass sorbed assumed to be zero

The mass removed from the column was calculated by applying the trapezoidal rule of integration on the experimental data.

More mass being removed from the soil column than what was calculated to be contained in it could be explained by assuming adsorption of VOC onto plexiglas. Although Krause (1987) performed both saturated and unsaturated VOC transport experiments through plexiglas

soil columns and no problems were encountered, it is felt that some chemical may have adsorbed to the plexiglas during the soil vapor extraction experiments. From Brandup et al. (1975), it was found that most volatile organic chemicals including TCE, 1,1,1-TCA, and toluene are solvents which tend to dissolve plexiglas. One experiment was attempted in which toluene was introduced to the soil column as a gas and etching of the plexiglas cylinder was observed.

It may be concluded that the additional mass removed from the soil columns during these chemical volatility and soil structure investigations could be the result of adsorbed chemical onto the plexiglas and its slow desorption. It could also be due to slow diffusion from very small cracks in the plexiglas cylinder. Regardless of the reason, it was decided to eliminate the use of plexiglas in the laboratory studies.

The tailing in the elution curves could be the result of poor air distribution along the bottom of the soil column. If any of the air distributors had become blocked, sections of the column would have been subject to stagnation. This could result in large pockets of immobile water at the bottom of the column from which chemical would slowly diffuse.

In order to remedy these design problems, modifications of the laboratory apparatus were performed. These modifications included the use of glass soil columns with Teflon end caps, a simpler air distribution system, and gas phase contamination which would allow both chemical introduction and removal to be monitored.

3.3 Air Velocity and Degree of Saturation Investigation

The purpose of this set of experiments was to investigate the impact of soil structure, degree of saturation, and air flow rate (air velocity) on the soil vapor extraction process. Seven experiments were completed and experimental results will be presented along with modeling predictions and simulations. Values for experimental conditions are given in Table 3.3.1.

Table 3.3.1 Chemical volatility and flow rate investigation experimental conditions.

Parameter	Experiment No.						
	1	2	3	4	5	6	7
Chemical	Toluene	Toluene	Toluene	Toluene	Toluene	Toluene	Toluene
Inf. Conc. (mg/l)	60.0	63.0	60.5	60.0	60.0	58.9	61.0
Soil Type	Sand	Sand	Sand	Sand	Verilite	Verilite	Verilite
Porosity	0.341	0.341	0.341	0.341	0.720	0.720	0.720
Deg. of Sat.	0	0	0.265	0.267	0	0	0.621
Flow Rate (mL/min)	5.81	15.06	5.65	16.50	5.02	16.68	8.42
Velocity (cm/sec)	0.0145	0.0375	0.0191	0.0562	0.0097	0.0322	0.0260
Temp (deg C)	20.5	25.0	25.0	23.0	22.0	24.0	22.5
Atm. Press (mm Hg)	748.5	745.0	744.3	745.8	743.3	748.0	745.0

3.3.1 Dry Ottawa Sand; Low Flow

No water was introduced into the soil column for this first experiment. The gas flow was set at 5.81 mL/min, giving an interstitial gas velocity of 0.0145 cm/sec. The influent gas concentration was approximately 60 mg/L. The experimental data along with one model

prediction and one model simulation are presented in Figure 3.3.1.

The solid line represents a CDFDAM prediction assuming no chemical adsorption onto Ottawa sand. This assumption was made based on the conclusion of Krause (1987) who showed no adsorption of VOC onto Ottawa sand under saturated conditions. No adsorption of toluene onto Ottawa sand under dry conditions was expected either, since Ottawa sand contains no organic carbon. If there were no retardation, the center of mass of both the breakthrough and elution wave fronts would appear at 1 pore volume of air fed as is shown by the solid line. This model prediction verifies that this assumption is not acceptable when describing the transport of VOCs through dry Ottawa sand. Roy and Griffin (1987) have shown that as soil humidity decreases, nonpolar chemical adsorption from the gas phase onto soil particles increases. From their finding, and as shown in this experiment, it can be concluded that as soil moisture decreases to zero, adsorption onto soil becomes significant.

The dashed line CDFDAM simulation incorporates the relative adsorption determined through Equation 2.7.6 for this set of experimental data. The adsorption capacity was calculated to be 0.085 mL air/g soil. Since the air concentration was 60 mg/L, it can be calculated that 5.4 mg of toluene had adsorbed to the soil particles. It is assumed that the soil exhibits linear adsorption ($1/n = 1$).

The experimental data and both CDFDAM predictions show a similar amount of spreading as chemical is introduced to and eluted from the soil column. An intraaggregate tortuosity of 1.8, which was determined in the methane tracer experiments, was used to calculate the gas dispersion coefficient. Since no water was present in the soil column,

air advection and gas dispersion are the only mass transfer mechanisms found to be important. No adjustment of this parameter was necessary to accurately describe the data. The results of model calculations for all experiments are presented in Table 3.3.2.

Table 3.3.2 Model parameters for chemical volatility and flow rate investigations.

Parameter	Experiment No.						
	1	2	3	4	5	6	7
H	NN	NN	0.28	0.27	NN	NN	0.26
K(cm ³ /g)	0.085	0.085	NN	NN	0.797	0.797	0.48
Dp(cm ² /s)	4.58E-2	4.58E-2	6.25E-6	6.25E-6	9.08E-4	9.08E-4	1.24E-7
Ev(cm ² /s)	4.58E-2	4.58E-2	4.58E-2	4.58E-2	4.58E-2	4.58E-2	4.58E-2

H = UNIFAC Henry's Constant at experimental temperature
 NN = not necessary

To add confidence to the experimental data, mass retained by the soil column as chemical was introduced, was compared to the mass which was removed as chemical was eluted. Slightly more mass was retained by the soil column than was removed; 17.2 milligrams of toluene were retained, whereas, only 15.8 milligrams were removed giving a mass balance error of about 8 percent. The centers of mass for the breakthrough and elution have been calculated to be at 1.40 and 1.29 pore volumes, respectively. This slight difference between the centers of mass of the two curves corresponds to 3.8 minutes of run time from a total run time of over 300 minutes. The results of the mass balance calculations for all experiments are presented in Table 3.3.3.

Table 3.3.3 Mass retained versus mass removed data.

Parameter	Experiment No.						
	1	2	3	4	5	6	7
Mass Retained (mg)	17.2	18.2	31.6	0.350*	37.5	39.3	2.0*
Mass Removed (mg)	15.8	17.9	31.1	0.344*	36.4	36.3	1.6*
% Difference	8.1	1.6	1.6	1.7	2.9	7.6	20.0
Centers of Mass							
Breakthrough (pv)	1.40	1.38	2.63	2.33	1.46	1.54	12.4
Elution (pv)	1.29	1.40	2.66	2.21	1.44	1.41	9.58
Difference (minutes)	3.8	-0.3	-0.8	1.1	1.7	3.3	54.1

* dimensionless mass units
pv = pore volumes

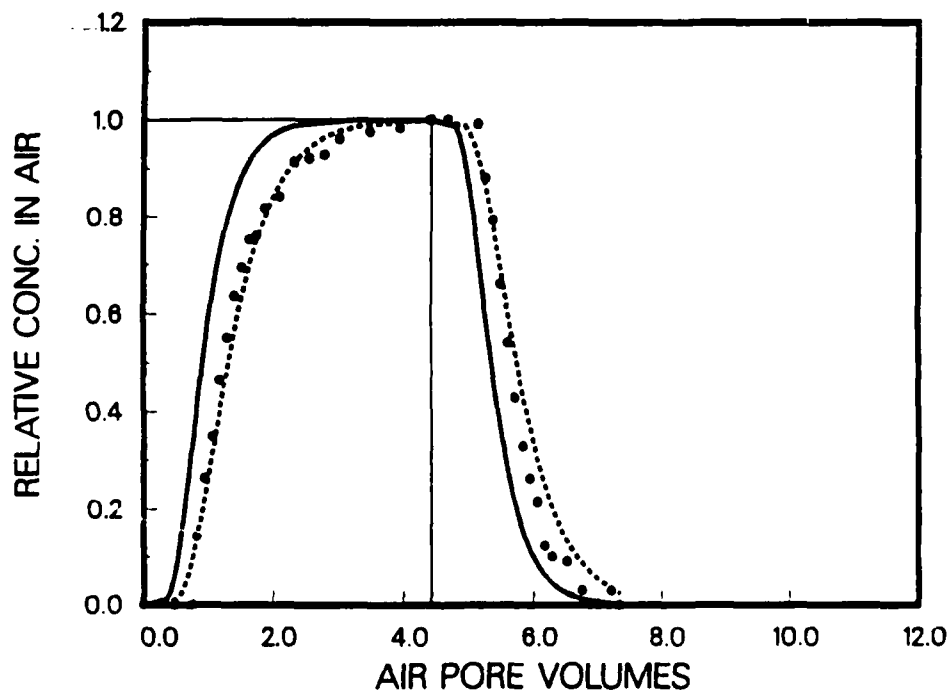


Figure 3.3.1. Breakthrough and elution of toluene at low flow in dry ottawa sand. The solid line CFDAM prediction assumes no adsorption of chemical onto the sand grains. The dashed line model prediction is based on an adsorption capacity of 0.085 mL/g. For both model simulations, the intraaggregate tortuosity of the soil column is 1.8 as determined in the methane tracer study.

3.3.2 Dry Ottawa Sand; High Flow

This experiment was performed in order to investigate the predictive ability of the CDFDAM. To accomplish this, the dry Ottawa sand experiment was reproduced in order to determine if the mass transfer and equilibrium parameters used to fit the low flow data could be used to describe this data set. One experimental variable was changed, however. The flow rate was increased almost three fold to 15.06 mL/min which corresponds to an interstitial velocity of 0.0375 cm/sec. The influent concentration was 63 mg/L. The experimental data along with the model prediction are presented in Figure 3.3.2. This figure demonstrates a complete prediction of experimental data by the CDFDAM.

Since the packing of the soil column was unaltered for this experiment, the same adsorption potential exists. It is shown that the CDFDAM accurately predicts the correct retardation of the chemical fronts when the adsorption potential determined in the low flow experiment ($K = 0.085$ mL/g) is used in the model calculations. Also, the spreading of both the breakthrough and elution wave fronts are described closely by the model prediction. This suggests that the mass transfer parameters used in the model calculations are correct.

To check the goodness of the experimental data, mass retained by the column was compared to that which was removed. A total of 18.2 milligrams of toluene were retained by the soil column and 17.9 milligrams were removed resulting in only a 1.6 percent mass balance error. The centers of mass of the breakthrough and elution curves were calculated to be at 1.38 and 1.40 pore volumes, respectively, differing by only 0.3 minutes from a total of over 80 minutes of run time.

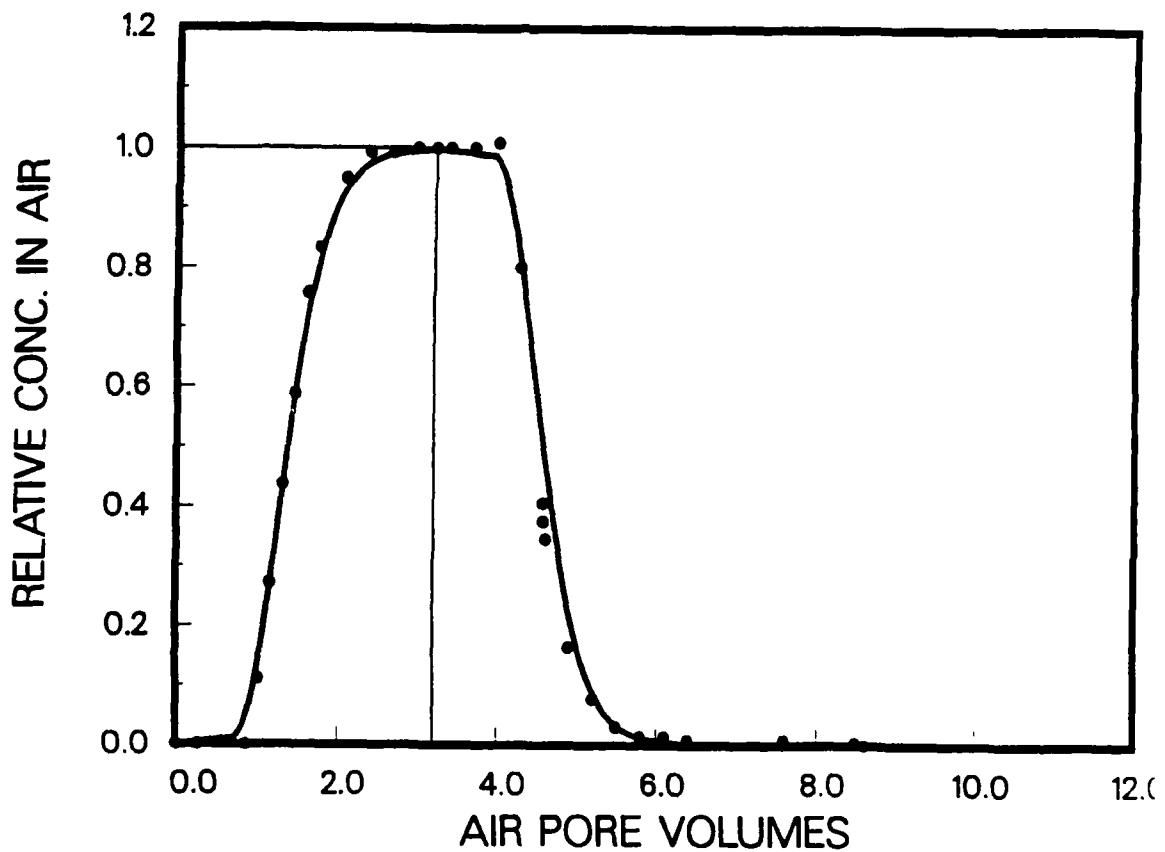


Figure 3.3.2. Breakthrough and elution of toluene at high flow in dry Ottawa sand. The solid line CFDAM prediction incorporates the same mass transfer and equilibrium parameters determined in the low flow Ottawa sand experiment.

3.3.3. Moist Ottawa Sand; Low Flow

To increase the complexity of the modeling exercise, water was introduced to the Ottawa sand soil column. Three mass transfer mechanisms, gas dispersion, pore diffusion and air-water mass transfer, may have an effect upon the shape of the chemical wave fronts. Air and water equilibrium within the column can be described by Henry's Law and

affects the location (retardation) of the chemical fronts. Because of the findings of Krause (1987) and Roy and Griffin (1987), adsorption is assumed to be nonexistent in the moist ottawa sand column.

A degree of saturation of 0.265 was present in the soil column. In other words, 26.5 percent of the void volumes contained water. The air flow rate for this experiment was 5.65 mL/min giving an interstitial air velocity of 0.0191 cm/sec. The influent gas concentration was approximately 60 mg/L.

The experimental results along with a model prediction are presented in Figure 3.3.3. The experimental temperature was 25 degrees Celcius and at this temperature a dimensionless Henry's constant of 0.28 was reported by UNIFAC. This value of Henry's constant predicts the center of mass of the experimental data well, however, the data is shifted slightly right of the model prediction. One explanation for this small rightward shift could be due to an error in measuring or recording the temperature at which the experiment was performed. A two degree decrease in temperature would effect Henry's constant by approximately 5 percent and would give an even better model prediction of the experimental data.

The spreading of the breakthrough and elution chemical fronts are described equally well with this model prediction. The same gas dispersion coefficient was used as was used in the dry ottawa sand experiments. A pore diffusion coefficient was estimated by calculating a liquid diffusion coefficient from the Wilke-Lee method (Appendix C) and adjusting by the intraaggregate tortuosity. Even though liquid diffusion is slow compared to gas diffusion, gas dispersion and diffusion are still the predominant mass transfer mechanisms to consider

in order to describe the shape of the breakthrough and elution curves through moist ottawa sand.

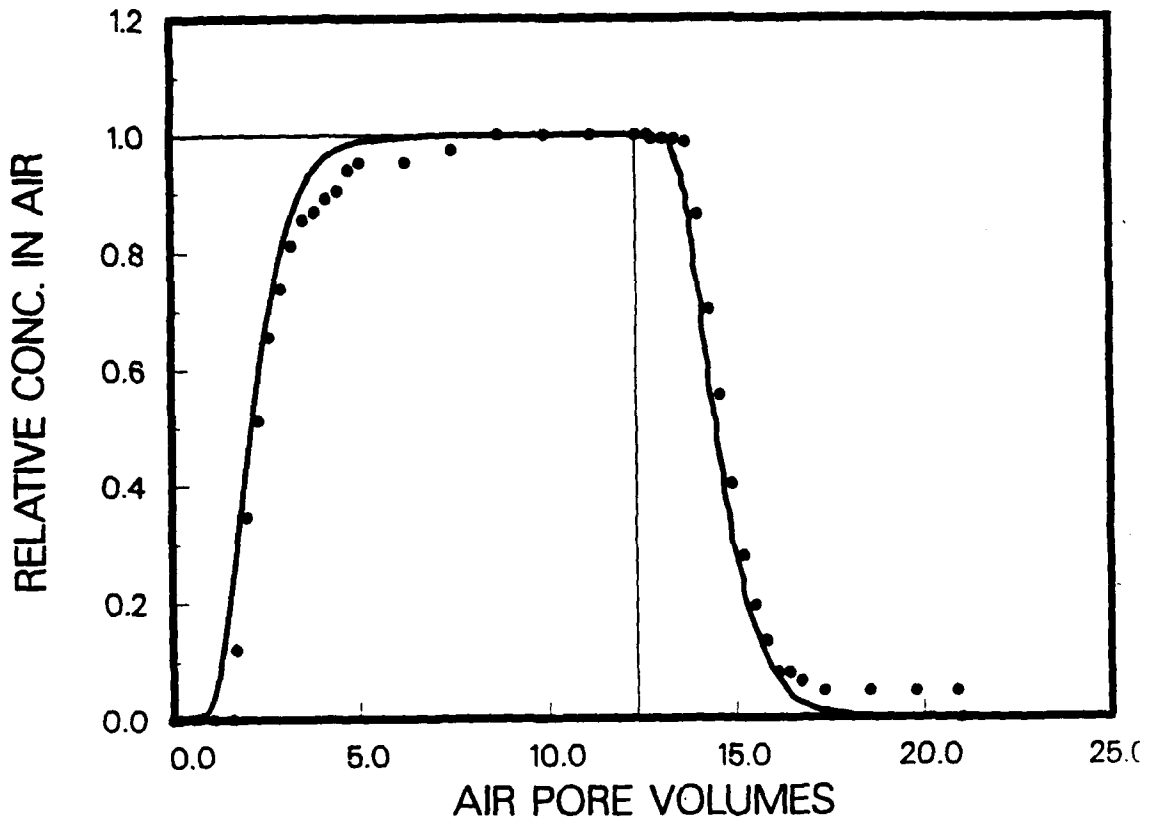


Figure 3.3.3 Breakthrough and elution of toluene at low flow in a moist ottawa sand column. The ADFDAM prediction describes equilibrium through Henry's constant with a value of 0.281 (UNIFAC). Gas dispersion and diffusion are the predominant mass transfer mechanisms.

In order to determine the goodness of the experimental data, mass retained by the column was compared to that which was removed. A total of 31.6 mg of toluene were retained by the column and 31.1 mg were removed giving a 1.6 percent mass balance error. The center of mass of

both the breakthrough and elution was 2.63 and 2.66 pore volumes, respectively. This corresponded to a difference of 0.8 minutes of run time. The shift in the center of mass of the breakthrough and the elution curves as compared to the dry column experiments is a result of immobile water contained in the soil column.

3.3.4. Moist Ottawa Sand; High Flow

This experiment was performed in a similar manner as experiment 3. All experimental variables remained the same, except the air flow rate, which was increased to 16.50 mL/min. This corresponds to an interstitial velocity of 0.0562 cm/sec. This experiment was conducted with a degree of saturation of 0.267 or 26.7 percent of the void volumes were filled with water. The influent gas concentration was 60 mg toluene/L. The experimental results along with the model prediction of the data are presented in Figure 3.3.4.

Since moisture was present in the soil column as in the previously described experiment, there was assumed to be no adsorption of chemical onto the sand particles. All retardation of VOC would be described by Henry's Law equilibrium. The ADFDAM prediction uses the UNIFAC Henry's constant of 0.263 which was determined for the temperature at which the experiment was performed. The model very accurately describes the location of the chemical fronts as well as the shape of the curves. Therefore, mass transfer and equilibrium are predicted accurately by the model.

On a dimensionless mass basis, there were 0.350 mass units retained in the column and 0.344 mass units recovered. This corresponds to 1.7 percent relative error. The center of masses for both the breakthrough and elution data correspond to 2.33 and 2.21 pore volumes, respectively.

The centers of mass differ by 1.1 minute of run time.

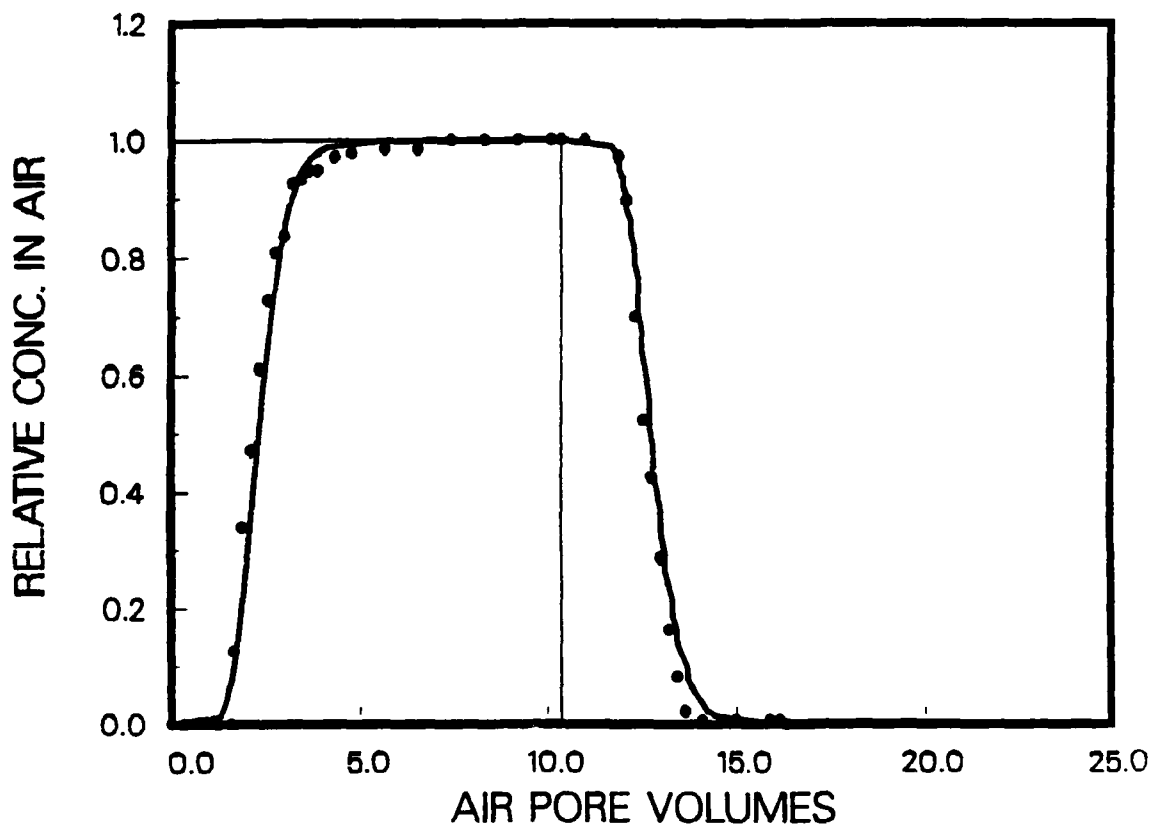


Figure 3.3.4 Breakthrough and elution of toluene at high flow in a moist ottawa sand column. The ADFDAM prediction describes equilibrium through Henry's constant with a value of 0.263 (UNIFAC). The predominant mass transfer mechanisms are gas dispersion and diffusion.

On a dimensionless mass basis, there were 0.350 mass units retained in the column and 0.344 mass units recovered. This corresponds to 1.7% relative error. The center of masses for both the breakthrough and elution data correspond to 2.33 and 2.21 pore volumes, respectively. The centers of mass differ by 1.1 minute of run time.

3.3.5 Dry Verilite; Low Flow

The experiments on dry verilite were performed in the same manner as those with dry ottawa sand. The flow rate of gas through the soil column was 5.02 mL/min for the first verilite experiment. This resulted in an interstitial velocity of 0.0097 cm/sec. The influent concentration was approximately 60 mg of toluene/L. The low flow, dry verilite experimental data with one model prediction and one model simulation are presented in Figure 3.3.5.

Krause (1987) showed no adsorption of TCE onto verilite under saturated conditions, therefore, no adsorption of toluene vapors onto dry verilite was anticipated. If no retardation of chemical occurs, the center of mass of the chemical wave front should exit the soil column after one pore volume of air fed. This is shown by the solid line CDFDAM prediction which assumes no adsorption of VOC as it travels through a column of dry, packed verilite. As with dry ottawa sand, the experimental data shows a rightward shift from the model prediction, clearly illustrating that adsorption is occurring.

The dashed line CDFDAM simulation describes the data well when an adsorption potential is included. The value of this adsorption potential for a column of verilite, calculated from Equation 2.7.6, is 0.797 mL/g.

Both model simulations describe the spreading of the experimental data. This illustrates that the mass transfer parameters are correct. Air advection and gas dispersion are the controlling mass transfer mechanisms, as in the ottawa sand experiments. An intraaggregate tortuosity of 1.8 was used to estimate the gas dispersion coefficient.

An interaggregate tortuosity of 90.9, which was determined in the bromide diffusion batch experiment, was used to calculate the pore diffusion coefficient. However, since no water was present in the verilite soil column, the effects of pore diffusion on gas transport of VOCs is unimportant.

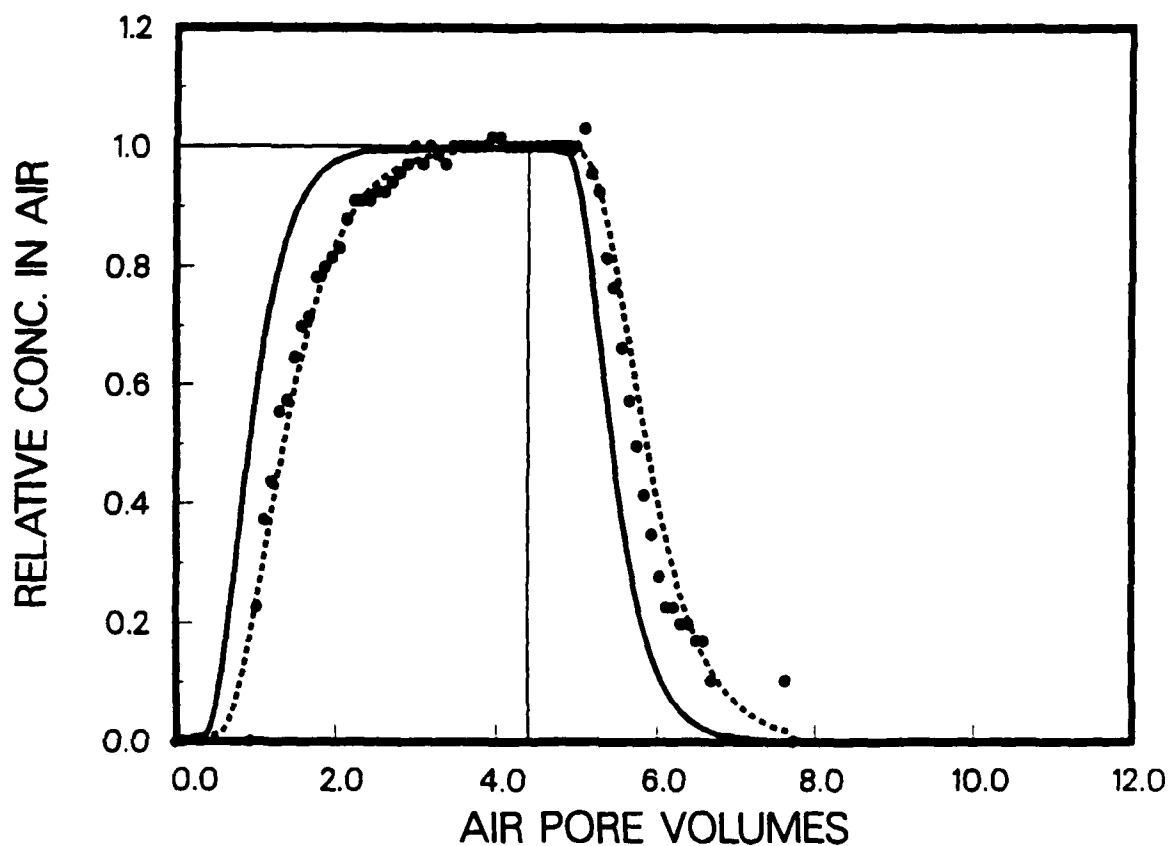


Figure 3.3.5 Breakthrough and elution of toluene at low flow in dry verilite. The solid line CFDAM prediction assumes no adsorption of chemical onto the porous particles. The dashed line CFDAM simulation is based on an adsorption potential of 0.797 mL/g. For both model simulations, the intraaggregate tortuosity was assumed to be 3. The interaggregate tortuosity was 90.9 as determined in the bromide diffusion batch experiment.

The adsorption potential is significantly higher for verillite than it is for ottawa sand. Because verillite particles have internal pore volume, there is a large amount of surface area inside the particle which may serve as active adsorption sites. A larger value of this adsorption potential is due to the decreased particle density of verillite and the difference in total porosity of the two soils. Ottawa sand has a particle density of 2.65 g/mL and a total porosity of 0.34, whereas verillite has a particle density of 1.51 g/mL and a total porosity of 0.72.

To demonstrate the goodness of the experimental data, mass retained by the soil column as chemical was introduced was compared to the mass which was removed during the elution of the soil column. This mass balance reported that 37.5 milligrams of toluene were retained in the column and 36.4 milligrams were recovered giving a 2.9 percent mass balance error.

3.3.6. Dry Verillite; High Flow

This experiment was performed in order to investigate the predictive ability of the gas transport model. To accomplish this, the previous dry verillite experiment was reproduced to determine if the values of the equilibrium and mass transfer parameters used to fit the low flow data can be used to predict this data. One experimental variable was altered, however. The gas flow rate was increased to 16.68 mL/min giving an interstitial velocity of 0.032 cm/sec. The experimental data along with the model prediction are presented in Figure 3.3.6. This figure illustrates a complete prediction by the CDFDAM.

Since the packing of the soil column was unaltered, the adsorption potential should be the same as determined in the low flow, dry verilite experiment. The CFDAM predicts the experimental data well when the adsorption potential determined in the low flow, dry verilite experiment ($K_v = 0.797 \text{ mL/g}$) is used. The spreading of the chemical wave front is also described well by the model prediction. As in the previous dry verilite experiment, air advection and gas dispersion are the predominant mass transfer mechanisms.

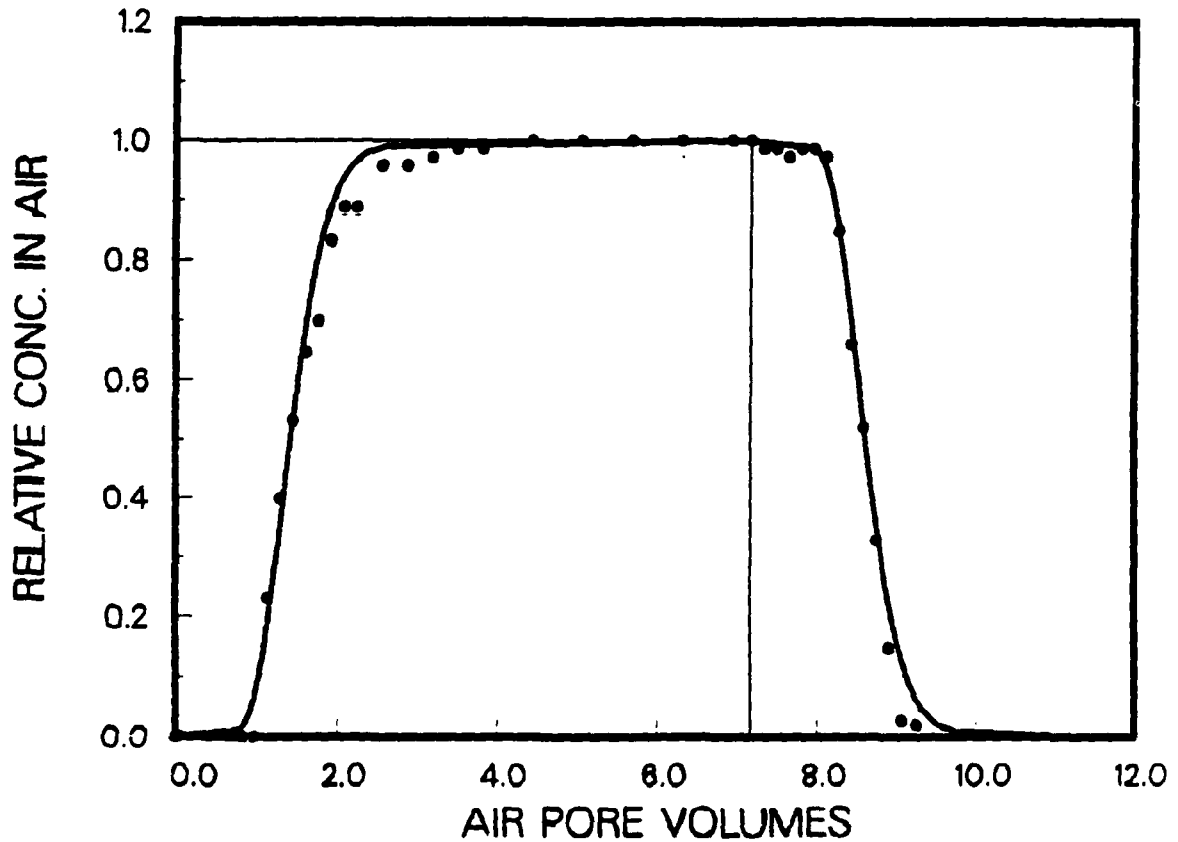


Figure 3.3.6. Breakthrough and elution of toluene at high flow in dry verilite. The CFDAM prediction assumes the same equilibrium and mass transfer parameters as determined in the previous low flow, dry verilite experiment.

The mass balance performed on the experimental data showed that 39.3 mg of toluene were retained in the soil column and 36.3 mg were recovered. This gives a difference of 7.6%.

3.3.7. Moist Verilite

The experiment was performed in order to investigate the impacts of all mass transfer mechanisms. Gas dispersion and diffusion, pore diffusion and air-water mass transfer could be important in this modeling exercise.

This moist verilite experiment was performed with an air flow rate of 8.42 mL/min giving an interstitial velocity of 0.0260 cm/sec. The porosity of the soil column was 0.72 as it was in the dry verilite experiments. The degree of saturation was 0.621 or 62.1 percent of the void volumes were filled with water. The experimental data along with one model prediction and one model simulation is presented in Figure 3.3.7.

Since the soil column is moist, an initial assumption was made in which no adsorption would occur. This assumption was made because ottawa sand showed no adsorption under moist conditions. Equilibrium within the column would be described by Henry's law, and this would account for retardation of the chemical fronts. The solid line model prediction assumes no chemical adsorption and a Henry's constant of 0.259 determined from UNIFAC at the experimental temperature. The experimental data show a rightward shift and are not described well by this initial model prediction. The center of mass of the chemical fronts could be fit by the model if either Henry's constant was decreased or chemical adsorption onto the verilite particles is occurring.

Henry's constant is directly proportional to temperature; Henry's constant decreases as temperature decreases. The experimental temperature would need to be decreased approximately 15 degrees in order for air-water equilibrium to describe the data. This 15 degree temperature difference is an impossibility, therefore, air-soil and water-soil equilibrium must be considered.

From the electron microscope photographs shown in Figure 3.1.6, a large amount of surface area is available inside the porous particles. It may be possible that all surfaces were not wetted by water and these dry surfaces allowed adsorption of toluene to occur. With the use of Equation 2.7.5, an adsorption potential of 0.48 mL/g was determined and used to fit the experimental data. This model fit of the experimental data is shown by the dashed line in Figure 3.3.7.

Although equilibrium is not predicted well by the model, the shape of the curve is described closely by the model prediction. Pore diffusion and gas dispersion are both important mass transfer mechanisms. Liquid diffusion from the immobile pore water inside the particles produces some spreading of the data. As in the other experiments, air-water mass transfer resistance is small. Therefore, this mechanism can be ignored.

A mass balance performed on the breakthrough and the elution data showed 2.0 mass units retained and 1.6 mass units recovered resulting in a 20 percent relative error. A 20 percent mass balance error causes concern to the goodness of the experimental data. This mass balance error may contribute to the inability of the model to fit the data well.

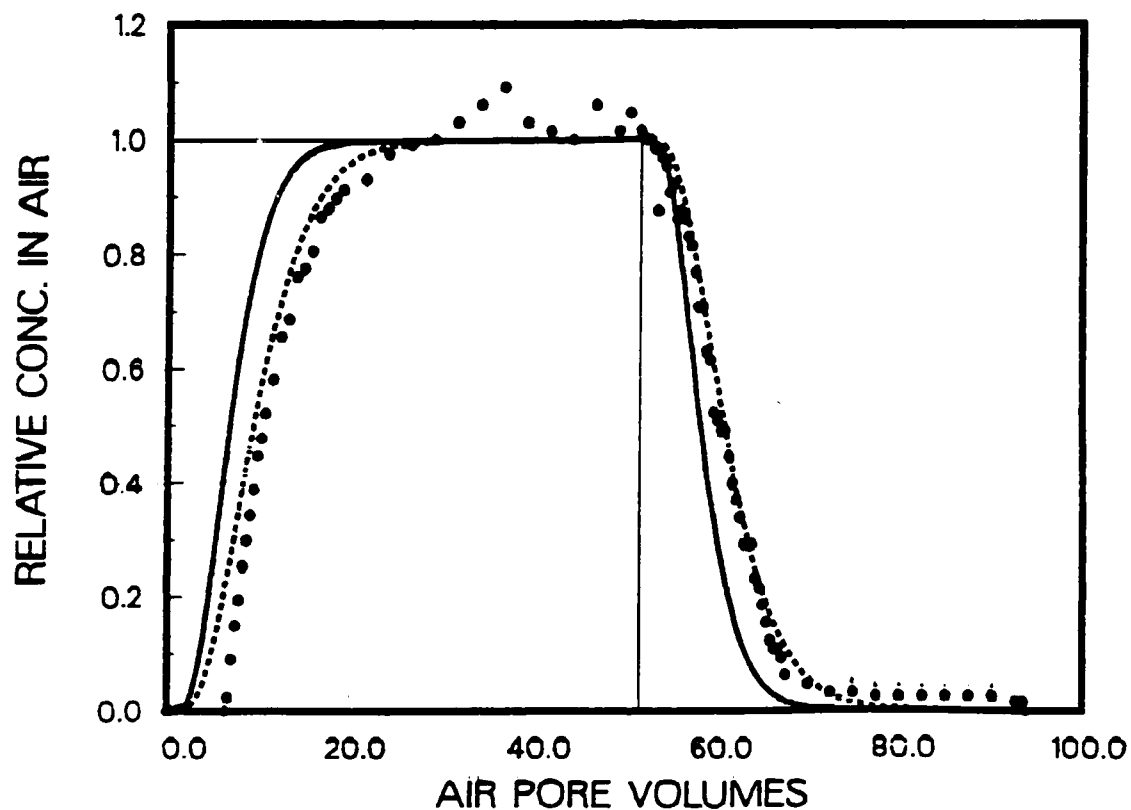


Figure 3.3.7 Breakthrough and elution of toluene in a moist verillite column. The solid line ADFDAM prediction describes equilibrium assuming no adsorption and a UNIFAC Henry's constant of 0.259. The dashed line ADFDAM prediction assumes an adsorption potential of 0.48 ml/g for the moist soil column. A intraaggregate tortuosity of 3 and an interaggregate tortuosity of 90.9 were used for both model simulations.

3.4 Soil Humidity Impact

The presence of water clearly has an effect upon the gas transport of volatile organic chemicals through a porous medium as observed in the dry versus moist experiments. A series of four additional experiments were conducted to investigate the impact of humidity on chemical

retardation. Each experiment was performed with glass columns packed with ottawa sand having a porosity of 0.34 (± 0.01). The gas flow rate of toluene vapor ranged between 15 and 22 ml/min for each experiment. The experimental conditions are summarized in Table 3.4.1.

Table 3.4.1. Experimental conditions for humidity impact investigation.

Parameter	Experiment No.			
	1	2	3	4
Soil	Sand	Sand	Sand	Sand
Soil Condition	Dry	Moist	Humidified	Dry
Porosity	0.341	0.341	0.334	0.334
Deg of Sat.	0	0.267	0	0
Flow Rate (mL/min)	15.06	16.50	14.78 ^a 16.65 ^b	22.22 ^a 21.02 ^b
Velocity (cm/sec)	3.75×10^{-2}	5.62×10^{-2}	3.76×10^{-2a} 1.41×10^{-2b}	5.65×10^{-2a} 5.34×10^{-2b}
Chemical	Toluene	Toluene	Toluene	Toluene
Inf. Gas Make-up	air with Water Vapor	air with Water Vapor	N ₂ with Water Vapor	N ₂
Temp (deg C)	25	23	21	25
Atm. press (mm Hg)	745	745.8	745	748

a breakthrough flow rate

b elution flow rate

The four experiments were conducted with four degrees of soil humidity. The first experiment was performed with oven dry soil. The influent gas was prepared by injecting pure toluene into a Tedlar bag.

The humidity inside the bag was the result of gas measurement by a wet test meter. The second experiment was conducted under moist soil conditions. The soil vapors were assumed to contain 100 percent humidity. The influent gas was prepared the same as in experiment one. The third experiment was performed with a dry packed soil column, and throughout the duration of the experiment, water vapor was introduced to the soil column by bubbling influent gas through a humidifier. A toluene in N₂ gas cylinder was used to feed chemical to the column. Prior to the start of the experiment, the toluene gas was bubbled through the humidifier for a period of time to saturate the water contained within it with toluene. Organic-free elution gas was bubbled through a noncontaminated humidifier before it entered the column. The fourth experiment was performed under dry soil conditions. No water was introduced; toluene in N₂ influent gas was fed to the soil column directly.

Figures 3.4.1 and 3.4.2 shows the relative retardation of each of the four degrees of humidity contained within the soil column. In each case, where water was present either due to moist soil or associated with the influent vapor, chemical adsorption onto the sand particles was small or nonexistent. However, when VOC's were introduced with no water present in any form, nonlinear adsorption is occurring. A sharpening of the breakthrough front and a spreading of the elution curve can be seen in Figures 3.4.1 and 3.4.2. This sharpening and spreading phenomena occurs when the isotherm intensity is less than 1 (Crittenden et al., 1986).

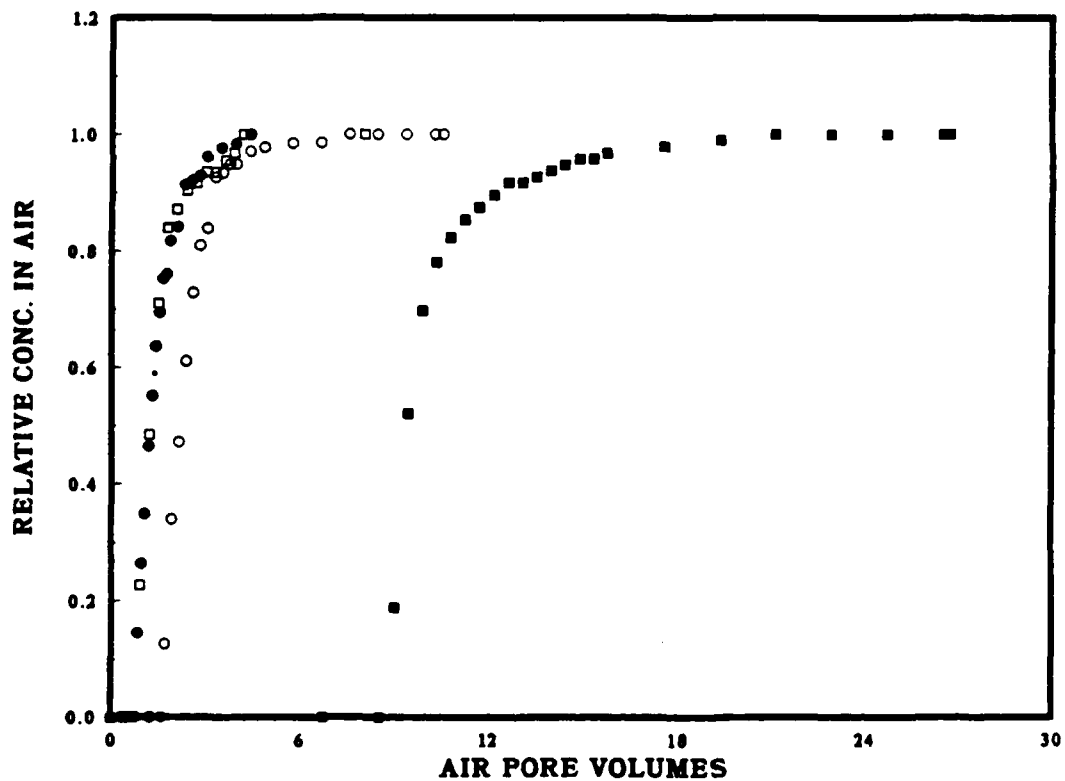


Figure 3.4.1 Experimental breakthrough data showing four degrees of humidity. The closed circle represents toluene vapor transport through dry sand. The influent gas contained water vapor. The open circle represent toluene vapor transport through moist sand. The influent gas contained water vapor. The open square represents toluene vapor transport through humidified soil. Influent gas was introduced to a water humidifier prior to entering the soil column. The closed square represents toluene vapor transport through dry soil. No water was present in the influent gas.

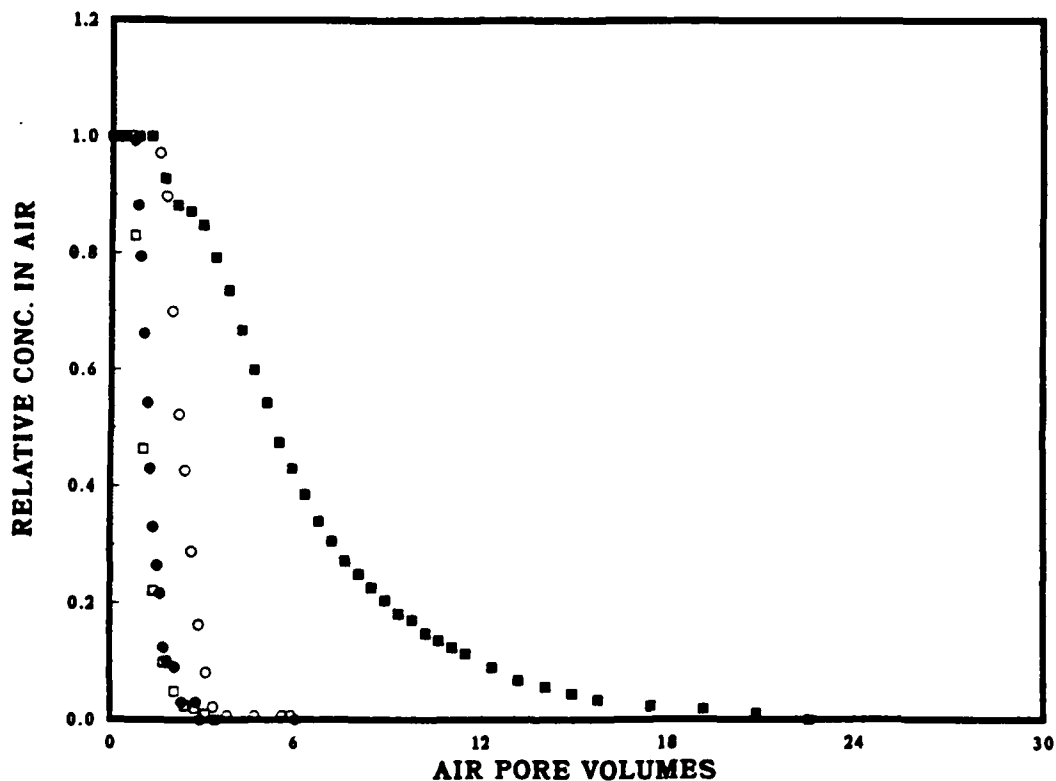


Figure 3.4.2 Experimental elution data showing four degrees of humidity. The closed circle represents toluene vapor transport through dry sand. The elution gas contained water vapor. The open circle represent toluene vapor transport through moist sand. The elution gas contained water vapor. The open square represents toluene vapor transport through humidified soil. Elution gas was introduced to a water humidifier prior to entering the soil column. The closed square represents toluene vapor transport through dry soil. No water was present in the elution gas.

To verify whether or not nonlinear adsorption is occurring, an ADFDAM simulation was performed and was compared to the experimental elution data. The model simulation and experimental data are presented

in Figure 3.4.3. Values of the mass transfer parameters used to describe the data in the dry ottawa sand experiments (Section 3.3.1 and Section 3.3.2) were used to describe the spreading of the chemical wave front. In order to predict the equilibrium between air and soil, an adsorption capacity of $1.07 \mu\text{g/g}(\text{mL}/\mu\text{g})^{1/n}$ was calculated by applying equation 2.7.5 to the elution data. An isotherm intensity (1/n) of 0.6 was fit to the data. All important model parameters used to describe the data are presented in the following table.

Table 3.4.2 Model parameters to transport of VOC's through sand with no water present.

	Breakthrough	Elution
E_v (cm^2/sec)	0.0458	0.0458
D_p (cm^2/sec)	0.0458	0.0458
K ($\mu\text{g/g}(\text{mL}/\mu\text{g})^{1/n}$)	1.07	1.07
1/n	0.6	0.6

Mass retained by the column did not coincide well with the mass removed from the column for this experiment. On a dimensionless mass basis, 2.0 mass units were retained by the soil column whereas, only 1.26 mass units were removed giving a mass balance error of 37 percent. This error can be attributed to possible error in flow measurement, since the flows for breakthrough and elution were different for this experiment. Because of this error in experimental data, the centers of mass of both curves did not correspond well.

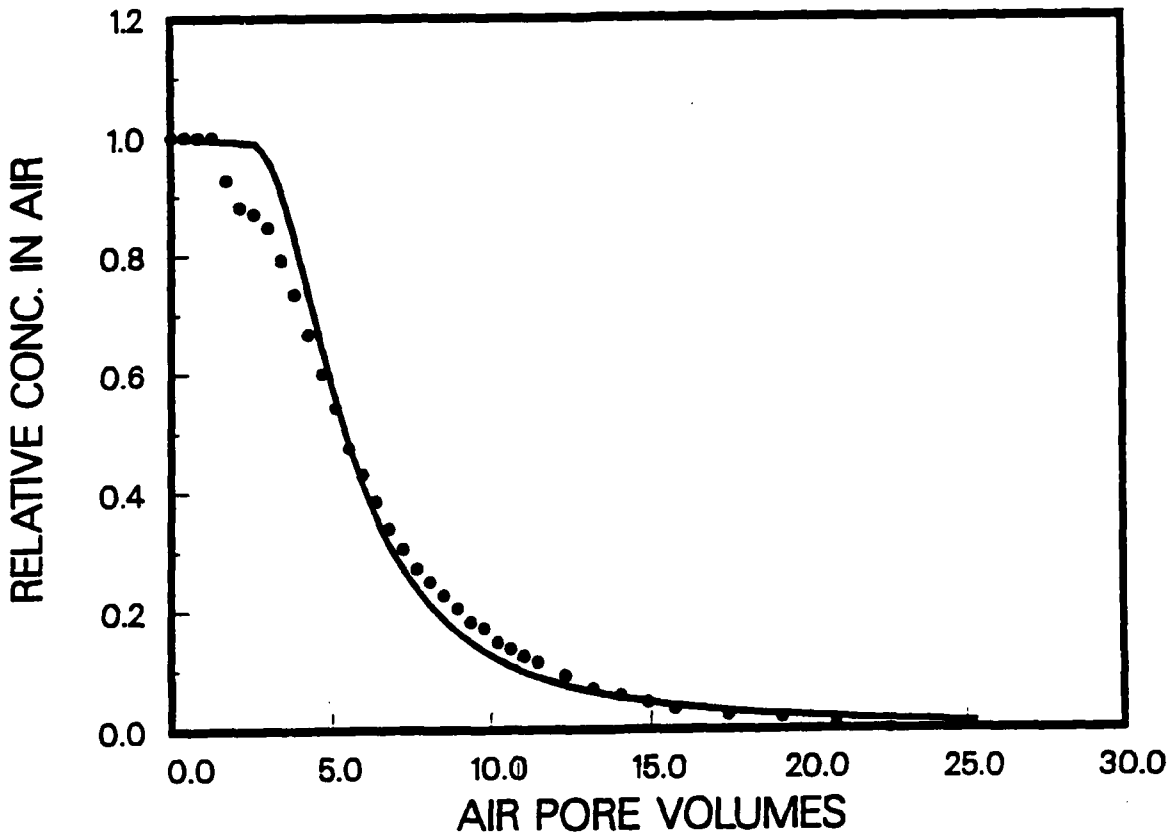


Figure 3.4.3 Elution of toluene in N_2 through dry Ottawa sand. CDFDAM simulation represents nonlinear sorption ($1/n = 0.6$).

The model parameters used to fit the elution data were used to predict the breakthrough data. This is shown in figure 3.4.4. As was expected due to more mass fed to the soil column than was removed, the retardation of the model prediction is low compared to that which is shown by the data. Regardless of the mass balance error, the shape of the chemical front is described well when an isotherm intensity of 0.6 is used. From this, it can be concluded that, in the absence of water, nonlinear adsorption will occur in soils.

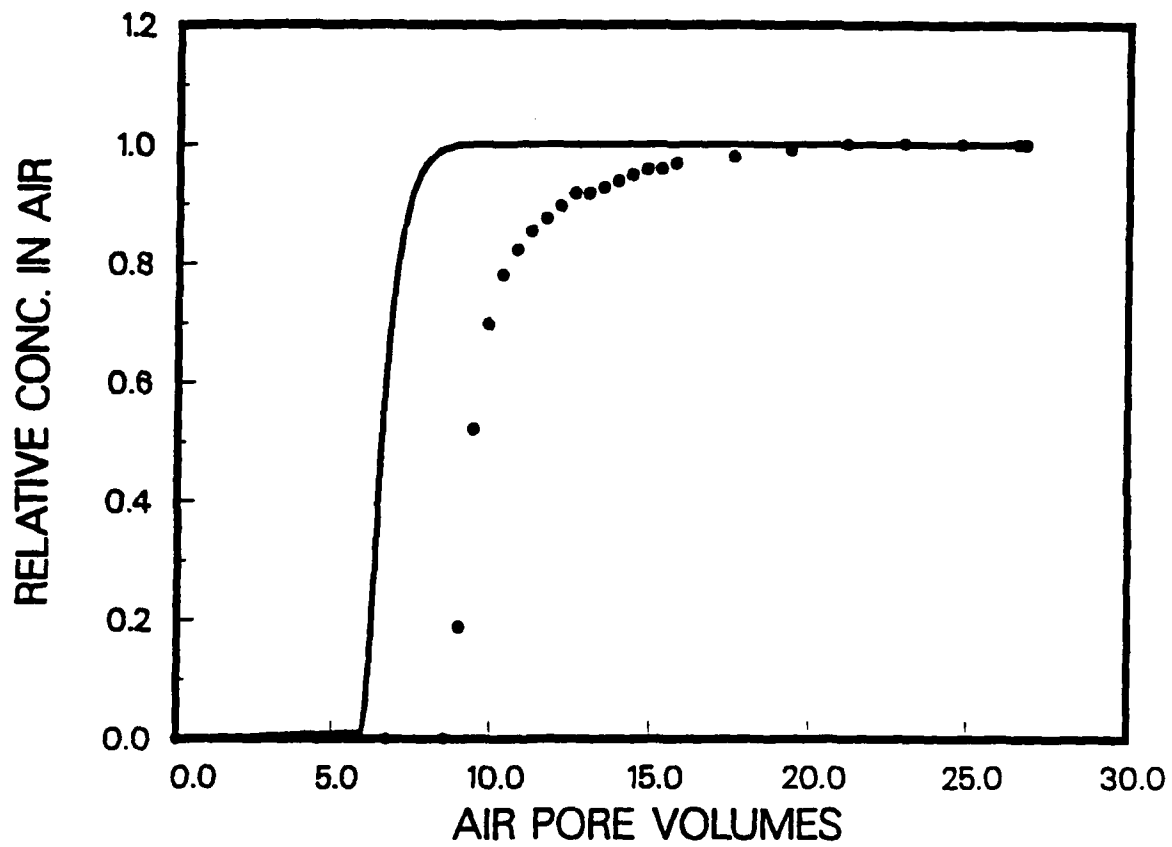


Figure 3.4.4 Breakthrough of toluene in N_2 through dry Ottawa sand. CFDAM prediction shows nonlinear sorption estimated from the elution data.

4. SUMMARY AND CONCLUSIONS

Soil column experiments were designed and performed to determine the relative impacts of chemical volatility, soil structure, air velocity and soil moisture on the soil vapor extraction process. The results compiled from these experiments were used to validate models developed by Gierke (1986) and Bednar (1990). This chemical transport model includes air advection, gas dispersion and diffusion, pore diffusion, and air-water mass transfer as mass transfer mechanisms. Retardation mechanisms include adsorption and volatilization/dissolution. The mass transfer mechanisms produce spreading of the chemical front as it travels through the soil column. Retardation decreases the velocity of the chemical front. The relative importance of these mechanisms was investigated by designing and performing experiments with different different chemicals, soil conditions, and air flow rates.

Three experimental apparatuses were used. The first apparatus and procedure consisted of plexiglas soil columns and chemical analysis by gas chromatography. Flow rate was induced by a vacuum pump. Although the experimental data could not be modeled, relative impacts of chemical volatility and soil structure could be observed.

1. It was found that extraction rates increase as chemical volatility increases.
2. Removal rates are also greatly affected by soil structure. A reduced extraction rate was shown from an aggregated material containing water than from a cohesionless sand.

The second apparatus was designed such that chemical was introduced

to the soil column in a gas phase. The amount of mass contained within the soil column before extraction could be better estimated through this procedure. Also, glass soil columns were used to reduce adsorption of VOC onto the experimental apparatus. A flame ionization detector was used to monitor chemical concentrations of soil column effluent. Seventeen soil column experiments were performed using this procedure with mass balance errors of generally less than 10 percent.

Three experimental variables were investigated using the second apparatus and procedure. These variables included soil structure, soil moisture, and air flow rate. The experimental results from seven soil column experiments were presented. These results were compared to model simulations and predictions in order to validate the soil column model.

1. Dry ottawa sand: Two experiments were performed demonstrating toluene flow through dry sand. The first experiment was conducted at low flow (0.0145 cm/sec). The shape of the breakthrough and elution curve fit well to the model prediction which assumed only air advection and gas dispersion as the active mass transfer mechanisms. However, adsorption of toluene onto the dry sand was observed. An adsorption potential of 0.085 mL/g was estimated from the mass balance and applied to the experimental data, and a second model simulation was made. This second model simulation closely described the data.

A second dry ottawa sand experiment was performed with toluene introduced to the column at a higher air flow (0.0375 cm/sec). Again, advection and dispersion were the only mass transfer mechanisms of importance. The adsorption potential determined in the low flow dry experiment was used to describe the equilibrium of the soil column. The experimental data were described well with the model prediction.

2. Moist ottawa sand: Two experiments were performed demonstrating toluene flow through moist sand. The first experiment was conducted at low flow (0.0191 cm/sec). By incorporating a Henry's constant of 0.28 determined with UNIFAC and the same dispersion coefficients used in the dry experiments, the model described both the shape and retardation of the experimental data. Slightly more retardation was observed than was described by the model. This could be attributed to an inaccurate temperature measurement.

A second moist experiment was performed with the toluene flow increased (0.0562 cm/sec). As in the low flow experiment, the model described the experimental data well. No adjustment of model parameters was necessary.

3. Dry verilite: Two experiments were performed demonstrating toluene flow through dry verilite. The first was conducted at low flow (0.0097 cm/sec). As was observed with dry ottawa sand, adsorption onto dry verilite occurred. The model predicted the shape of the breakthrough and elution wave fronts, and, when an adsorption potential of 0.797 mL/g (calculated from the experimental data) was incorporated, the model described the data well. No adjusting of dispersion parameters was necessary.

A second dry verilite experiment was performed with the flow increased to 0.0322 cm/sec. The same adsorption potential determined in the low flow experiment was used to predict the data. A good description of the experimental data was observed.

4. Moist verilite: A moist verilite experiment was performed with

toluene flow of 0.0260 cm/sec. Pore diffusion and gas dispersion were both important mass transfer mechanisms. The model prediction underestimated the retardation observed from the experimental data. It was assumed that some adsorption of toluene vapors was occurring under moist conditions. A retardation of 0.48 mL/g was determined from the experimental data and used in the model to fit the data reasonably well. A 20 percent relative error between the mass retained by the column and the mass removed from the column could be a reason for the discrepancy between data and model simulation.

A third experimental apparatus and procedure was designed such that air flow was induced by a gas cylinder. A flame ionization detector was used for chemical detection. Methane was used as a tracer gas in order to determine axial dispersion of two porous media -- ottawa sand and Keweenaw-7. Both high and low flow experiments were performed with each soil. The experimental data were fit to the DFLEM model by minimizing the sum of the squares of the residuals. From this fit, a Peclet number was estimated from which a dispersion coefficient was estimated. From this dispersion coefficient, an intraaggregate tortuosity for each soil was calculated. A intraaggregate tortuosity of 1.8 was estimated for ottawa sand and 3.0 was estimated for Keweenaw-7. Two conclusions can be made.

1. High tortuosities will sharpen the chemical front because gas diffusion will become negligible due to limited diffusion paths.
2. Measurement of soil tortuosities becomes increasingly more important as the soil becomes less homogeneous.

In addition to the tracer studies, the third apparatus and procedure was used to investigate the effects of soil moisture on the soil vapor extraction process. Four degrees of soil moisture were investigated, dry sand with water vapor introduced in the influent gas, moist sand with water vapor introduced with the influent gas, an oven-dry sand to which humidity was introduced by bubbling influent gas through a water humidifier, and an oven-dry soil through which chemical was fed from a toluene in N₂ gas cylinder with no water vapor.

As was shown by Roy and Griffin (1987), adsorption increased as soil humidity decreased. Moist ottawa sand showed no adsorption, whereas completely dry sand with no water present in the influent gas showed nonlinear adsorption. Nonlinear adsorption was verified by fitting the experimental data with the CDFDAM using an isotherm intensity (1/n) of 0.6. This exponent described the shape of both the breakthrough and elution wave fronts. The breakthrough curve showed sharpening whereas the elution curve showed spreading.

Two additional experiments were performed in order to independently determine parameters required by the soil column models.

1. A gas phase isotherm was performed in order to determine the adsorption potential of ottawa sand with no success.

2. A batch rate study was performed (Rao et al., 1982) in order to determine the interaggregate tortuosity of verilite particles. This value was found to be 91.

5. RECOMMENDATIONS FOR FUTURE WORK

Based on the conclusions of the experimental work performed, the following discussions should be investigated further:

1. Additional experiments should be performed with moist verillite to better determine the effects of pore diffusion on the soil vapor extraction process. Adaptations of the soil column model should be made which allow the impact of intermittent air flow upon the soil vapor extraction process to be investigated. In conjunction with this model adaptation, additional experiments should be designed and performed in which intermittent air flow is investigated in order to validate a pulsed-flow model.

2. An experimental procedure should be developed in order to perform gas phase isotherms on dry soils which contain no organic carbon. This would allow for the independent determination of adsorption parameters for these soils.

3. Design and perform laboratory soil column experiments investigating the removal of VOC's from natural field soils under various moisture conditions with several air flow rates. Comparisons between model simulations and experimental data should be made in order to determine which mass transfer mechanisms are important.

6. REFERENCES

- Ashworth, R. A., G. B. Howe, M. E. Mullins, and T. N. Rogers, Air-water partitioning coefficients of organics in dilute aqueous solutions, J. Haz. Mat., 18, 25-36, 1988.
- Bednar, M. L., Modeling Intermittent Operation of Laboratory-Scale Vapor Extraction Systems, M.S. Thesis, Dept. of Chem. Eng., Mich. Tech. Univ., Houghton, in preparation, 1990.
- Brandup J., Immergut E. H., Polymer Handbook, 2nd ed., IV Solution Properties, Wiley, New York, NY, 1975.
- Cooper C. D., Alley F. C., Air Pollution - A Design Approach 630pp. PWS Publishers, Boston, MA, 1986.
- Crank, J., The Mathematics of Diffusion, 2nd. ed., Oxford Univ. Press, Great Britain, 414 pp., 1980.
- Crittenden, J. C., N. J. Hutzler, D. G. Geyer, J. L. Oravitz, and G. Friedman. Transport of organic compounds with saturated groundwater flow: model development and parameter sensitivity, Water Resources Research, 22(3), 271-284, 1986.
- Gierke, J.S., Modeling the Movement of Volatile Organic Chemicals Through Homogeneous, Isotropic, Unsaturated Soils With Cocurrent Air and Water Flow, MSCE Thesis, University Microfilms, Ann Arbor, Michigan, 1986.
- Gierke, J.S., N.J. Hutzler, and J.C. Crittenden, "Modeling the Movement of Volatile Organic Chemicals in Columns of Unsaturated Soil," Water Resources Research, accepted for publication, 1989.
- Hashimoto, I., K. B. Deshpande, and H. C. Thomas, Peclet numbers and retardation factors for ion exchange columns, Ind. Eng. Chem. Fund., 3(3), 213-218, 1964.
- Hutzler, N. J., J. C. Crittenden, J. S. Gierke, and A. M. Johnson, Transport of organic compounds with saturated groundwater flow: experimental results, Water Resources Research, 22(3), 285-295, 1986
- Hutzler, N.J., J.S. Gierke, and L.C. Krause, "Movement of Volatile Organic Chemicals in Soils," in Reactions and Movement of Organic Chemicals in Soils, B.L. Sawhney and K. Brown, eds., Chapter 15, 373-404, Special Pub. No. 22, Soil Sci. Soc. of Amer., Madison, Wisconsin, 1989.
- Hutzler, N.J., B.E. Murphy, and J.S. Gierke, "State of Technology Review: Soil Vapor Extraction Systems," EPA 600/2-89-024, 87 pp., 1989.

Krause, L. C., Modeling the transport of volatile organic chemicals in unsaturated media: Experimental results, M.S. Civil Eng. thesis, Michigan Tech. Univ., Houghton, Univ. Microfilms, Ann Arbor, Mich., 1987.

LeBas, The Molecular Volumes of Liquid Chemical Compounds, Longmans Green, London, 1915.

Miyauchi, T., and T. Kikuchi, Axial dispersion in packed beds, Chem. Eng. Sci., 30, 343-348, 1975.

Rao, P. S. C., R. E. Jessup, and T. M. Addiscott, Experimental and theoretical aspects of solute diffusion in spherical and nonspherical aggregates, Soil Sci., 133, 342-349, 1982. .cp3

Reid, R. C., J. M. Prausnitz, and T. K. Sherwood, The Properties of Gases and Liquids, 4th ed., 731 pp., McGraw-Hill, New York, 1987.

Roy, W. R., and R. A. Griffin, Vapor-phase movement of organic solvents in the unsaturated zone, Open File Report No. 16, 37 pp., Environ. Inst. for Waste Mgmt. Studies, Univ. of Alabama, Tuscaloosa, June 1987.

Shulman, H.L., CF. Ulrich, A. Proulx, and J.O. Zimmerman, AIChE J., 1, 247-253, 1955.

Towers, D., Dent, M. J., Van Arnam, D. G., Part 1: Choosing a treatment for VHO-contaminated soil, Haz. Mat. Control, 2(2), 8-12+, 1989

Treybal, R. E., Mass Transfer Operations, 784 pp., McGraw-Hill, New York, 1980.

Weast, R. C., CRC Handbook of Chemistry and Physics, 61st ed., CRC Press, Boca Raton, Florida, 1981.

Wilke, C. R., and C. Y. Lee., Estimation of diffusion coefficients for gases and vapors, Ind. Eng. Chem., 47(6), 1253-1257, 1955.

Wilke, C. R., and Chang, P., Correlation of diffusion coefficients in dilute solution, AIChE J., 1: ,264-270, 1955.

Wilson, E. J., and Geankoplis, C. J., Liquid mass transfer at very low Reynold's numbers in packed beds, Ind. Eng. Chem. Fundam., 5(1), 9-14, 1966.

APPENDIX A -- Standard Preparation and Analysis

STANDARD CALIBRATION

STANDARD	SYRINGE WT.		MASS ADDED	VOLUME	CONC.	% E	
#	<u>before</u>	<u>after</u>	<u>grams</u>	<u>L</u>	<u>mg/L</u>	<u>linear</u>	<u>power</u>
1	17.28967	16.85100	0.43867	5.5	79.8	1.2	-2.1
2	17.26892	16.85015	0.41877	7.0	59.8	3.0	4.1
3	17.21131	16.85032	0.36099	9.0	40.1	-2.0	5.1
4	17.03490	16.85051	0.18439	9.0	20.5	-30.0	-17.2
5	14.16984	14.10176	0.06808	9.0	7.6	-44.1	-23.4

The calibration curves resulting from this set of standards are:

$$\text{conc} = \text{peak height} / 0.094131$$

$$\text{conc} = (19.65428)^{-1} * \text{peak height}^{1/1.14790}$$

APPENDIX B -- Media Packing Measurements

Ottawa Sand Packing Data

weight of glass column w/ end caps	1157.5 g
weight of glass column w/ end caps and fittings.	1208.0 g
weight of column and water	1810.8 g
end cap volume	11.2 ml
weight of column w/ sand	2190.8 g

Volume of Column

mass of column and water.	1799.6 g
(end cap volume eliminated)	
mass of column w/ end caps and fittings (dry)	<u>1208.0 g</u>
therefore, VOLUME OF COLUMN	591.6 mL

Mass of Sand

mass of column w/ sand	2190.8 g
mass of column w/ end caps	<u>1157.5 g</u>
therefore, MASS OF SAND	1033.3 g

Porosity = $1 - \rho_b / \rho_s$

where $\rho_b = \frac{\text{mass (sand)}}{\text{volume (total)}} = \frac{1033.3 \text{ g}}{591.6 \text{ ml}}$
 $= 1.747 \text{ g/cm}^3$

$\rho_s = 2.65 \text{ g/cm}^3$

$\epsilon = 1 - 1.747/2.65 = 0.341$

Verilite Packing Data

weight of glass column w/ end caps	1157.5 g
weight of glass column w/ end caps and fittings.	1208.0 g
weight of column and water	1810.8 g
end cap volume	11.2 ml
weight of column w/ sand	1408.1 g

Volume of Column

mass of column and water.	1799.6 g
(end cap volume eliminated)	
mass of column w/ end caps and fittings (dry)	<u>1208.0 g</u>
therefore, VOLUME OF COLUMN	591.6 mL

Mass of Sand

mass of column w/ sand	1408.1 g
mass of column w/ end caps	<u>1157.5 g</u>
therefore, MASS OF SAND	250.6 g

Porosity: $1 - \rho_b / \rho_s$

$$\text{where } \rho_b = \frac{\text{mass (sand)}}{\text{volume (total)}} = \frac{250.6 \text{ g}}{591.6 \text{ ml}}$$

$$= 0.424 \text{ g/cm}^3$$

$$\rho_s = 1.51 \text{ g/cm}^3$$

$$\epsilon = 1 - 0.424 / 1.51 = 0.720$$

Keweenaw-7 Packing Data

weight of glass column w/ end caps and fittings	1190.5 g
weight of column and water	1808.4 g
end cap volume	13.4 ml
weight of column w/ sand	2198.0 g

Volume of Column

mass of column and water	1795.0 g
(end cap volume eliminated)	
mass of column w/ end caps and fittings (dry)	<u>1190.5 g</u>
therefore, VOLUME OF COLUMN	604.5 ml

Mass of Sand

mass of column w/ sand	2198.0 g
mass of column w/ end caps	<u>1190.5 g</u>
therefore, MASS OF SAND	1007.5 g

Porosity: $1 - \rho_b / \rho_s$

$$\text{where } \rho_b = \frac{\text{mass (sand)}}{\text{volume (total)}} = \frac{1007.5 \text{ g}}{604.5 \text{ ml}}$$

$$= 1.628 \text{ g/cm}^3$$

$$\rho_s = 2.59 \text{ g/cm}^3$$

$$\epsilon = 1 - 1.628/2.59 = 0.356$$

APPENDIX C -- Chemical Properties with Sample Calculations:

Binary Gas Diffusion: Wilke-Lee Method (Reid, Prausnitz, Poling, 1987) pg 589

$$D_{AB} = \frac{[3.03 - (0.98/M_{AB})](10^{-3}) T^{3/2}}{P (M_{AB}^{3/2}) (\sigma_{AB}^2) (\Omega_0)}$$

D_{AB} = binary diffusion coefficient, cm^2/sec

with $M_{AB} = 2[1/M_A + 1/M_B]^{-1}$, g/mol

M_A = Molecular weight of A, g/mol

M_B = Molecular weight of B, g/mol

T = temperature, degrees K

P = pressure, bar

$\sigma = 1.18(V_b)^{1/3}$

V_b = molar volume, cm^3/mol (LeBas, 1915)

$e/k = 1.15(T_b)$, degrees K

T_b = Normal Boiling Pt., degrees K

$e_{AB} = (e/k_A * e/k_B)^{0.5}$

$\sigma_{AB} = (\sigma_A + \sigma_B)/2$

$\Omega_0 = A/(T^*)^B + C/\exp(DT^*) + E/\exp(FT^*) + G/\exp(HT)$

$A = 1.06036$

$B = 0.15610$

$C = 0.19300$

$D = 0.47635$

$E = 1.03587$

$F = 1.52966$

$G = 1.76474$

$H = 3.89411$

$T^* = T/e_{AB}$

Gas Diffusion Coefficients:

1,1,1-TCA (in Air) = $8.23 \cdot 10^{-2} \text{ cm}^2/\text{sec}$
 Toluene (in N_2) = $8.60 \cdot 10^{-2} \text{ cm}^2/\text{sec}$
 Toluene (in Air) = $8.25 \cdot 10^{-2} \text{ cm}^2/\text{sec}$
 Methane (in Argon) = $0.241 \text{ cm}^2/\text{sec}$
 Methane (in Air) = $0.246 \text{ cm}^2/\text{sec}$
 Argon (in Air) = $0.211 \text{ cm}^2/\text{sec}$

Liquid Diffusion: Wilke-Chang correlation (Reid, Prausnitz, Poling, 1987)
pg. 598

$$D_{AB}^0 = \frac{7.4(10^{-8})(\phi M_B)^{0.5} T}{(\eta_B) V_A^{0.6}}$$

D_{AB}^0 = mutual diffusion of solute A at very low concentrations in B, cm^2/sec

M_B = Molecular weight of solvent B, g/mol

T = temperature, degrees K

η_B = viscosity of solvent B, cp

V_A = molar volume of A at normal boiling pt., cm^3/mol

ϕ = association factor of solvent B, dimensionless

Liquid Diffusion Coefficients (in water):

1,1,1-TCA = $9.00 \times 10^{-6} \text{ cm}^2/\text{sec}$

Toluene = $1.12 \times 10^{-5} \text{ cm}^2/\text{sec}$

Density and Viscosity of Air -vs- Argon/Methane:

Reported Value for Air (78% N₂, 21% O₂, 1% Ar) = 1.184 g/L

Air Pollution Control - A Design Approach
(Cooper & Alley, 1986) pg 24

$$\rho_{Ar/Me} = P(MW)[R(T)]^{-1}$$

$$\rho_{Argon} = 1.636 \text{ g/L}$$

$$\rho_{Methane} = 0.656 \text{ g/L}$$

$$\text{therefore, } \rho_{Ar/Me} = 1.636(0.95) + 0.656(0.05) = 1.587 \text{ g/l}$$

Reported value of viscosity of air (@ 25 deg C) = 183.75 uP

Use method of Wilke (Reid, Prausnitz, and Poling - Property of Liquids and Gases pg. 407)

$$\phi_{ij} = \frac{[1 + (\eta_i/\eta_j)^{0.5}(M_j/M_i)^{0.25}]^2}{[8.0(1 + (M_i/M_j))^{0.5}]}$$

$$\phi_{ji} = (\eta_j/\eta_i)(M_i/M_j)\phi_{ij}$$

From Handbook of Chemistry and Physics - 61st Edition

viscosity of Argon at 25 deg C (η_i) = 224.69 uP

viscosity of Methane at 25 deg C (η_j) = 110.23 uP

M_i = molecular weight of Argon = 40.0

M_j = molecular weight of Methane = 16.04

$$\text{therefore } \phi_{ij} = 0.86$$

$$\phi_{ji} = 1.06$$

$$\text{for two gases } \eta_m = (y_i\eta_i)/(y_i + Y_j\phi_{ij}) + (y_j\eta_j)/(y_j + y_i\phi_{ji})$$

where y = mole fractions

for 95/5 mixture of Argon/Methane

$$\eta_{argon/methane} = 183.75 \text{ uP}$$

DATE	SOIL TYPE	CHEMICAL	INF CONC. (mg/L)	POROSITY	DEG OF SAT	FLOW RATE (MI/Min)	VELOCITY (cm/sec)	TEMPERATURE (Deg C)	Atm. Press (mm Hg)
June 28, '89	Ottawa Sand	Toluene	47.7	0.341	0	6.17	0.0154	22	746.8
June 29, '89	Ottawa Sand	Toluene	60.0	0.341	0	5.81	0.0145	20.5	748.5
June 30, '89	Ottawa Sand	Toluene	79.7	0.341	0	5.44	0.0136	21	745
July 3, '89	Ottawa Sand	Toluene	63.0	0.341	0	15.06	0.0375	25	745
July 5, '89	Ottawa Sand	Toluene	60.0	0.341	0.265	5.65	0.0191	25	744.3
July 7, '89	Ottawa Sand	Toluene	55.9	0.341	0.291	4.50	0.0158	24	746
July 10, '89	Ottawa Sand	Toluene	56.8	0.341	0.274	16.40	0.0563	24	741
July 12, '89	Ottawa Sand	Toluene	60.0	0.341	0.267	16.50	0.0562	23	745.8
July 13, '89	Verillite	Toluene	59.8	0.720	0	5.00	0.0102	22	745
July 14, '89	Verillite	Toluene	1	0.720	0	4.96	0.0098	24	745
July 17, '89	Verillite	Toluene	60.0	0.720	0	5.02	0.0097	22	743.3
July 24, '89	Verillite	Toluene	58.9	0.720	0	16.68	0.0322	24	748
July 26, '89	Verillite	Toluene	50.6	0.720	0.621	15.60	0.0482	25	746.4
July 31, '89	Verillite	Toluene	1	0.720	0.621	8.42	0.0260	22.5	745
August 9, '89	Verillite	Toluene	1	0.720	0.622	15.30	0.0475	23	743
Sept. 5, '89	Verillite	Toluene	1	0.720	0.620	5.39	0.0167	21	745
Sept. 13, '89	Verillite	Toluene	1	0.720	0.620	4.36	0.0135	26.5	744.8
Oct. 11, '89	Ottawa Sand	Ar/CH ₄	1	0.334	0	4.22, 5.02	0.0107, 0.0128	23.5	746.0
Oct. 12, '89	Ottawa sand	Ar/CH ₄	1	0.334	0	10.42, 14.53	0.0265, 0.0369	23	747
Oct. 18, '89	Keweenaw-7	Ar/CH ₄	1	0.356	0	2.51, 3.26	0.0600, 0.0559	23.5	746
Oct. 19, '89	Keweenaw-7	Ar/CH ₄	1	0.356	0	12.04, 15.87	0.0565, 0.0534	22	750
Oct. 27, '89	Ottawa Sand	Toluene (N ₂)	1	0.334	0	23.60, 22.00	0.0584, 0.0730	26	746
Oct. 28, '89	Ottawa Sand	Toluene (N ₂)	1	0.334	0	22.22, 21.02	0.0487, 0.0854	25	748
Oct. 29, '89	Ottawa Sand	Toluene (N ₂)	1	0.334	0	22.96, 28.71		25	749
Oct. 30, '89	Ottawa Sand	Toluene (N ₂)	1	0.334	0.298	19.17, 33.60		24	750
Nov. 8, '89	Verillite	Toluene (N ₂)	1	0.720	0.64	18.14, 20.78	0.0022	22	745
Nov. 13, '89	Ottawa Sand	Toluene (N ₂)	1	0.335	Humidified	14.78, 16.65	0.0009	21	745
Nov. 2-4, '88	Ottawa Sand	Toluene (H ₂ O)	15.2	0.333	0.376	4.00	0.0016	24	767.6
Aug. 8-12, '88	Verillite	Toluene (H ₂ O)	17.5	0.642	0.665	3.08	0.0012	21	764
Aug. 16-17, '88	Ottawa Sand	1,1,1-TCA (H ₂)	11.5	0.333	0.312	2.95		22	764
Aug. 19-22, '88	Verillite	1,1,1-TCA (H ₂)	30.2	0.642	0.613	4.14		22	764

DATE	MASS BALANCE		CENTER OF MASS (pv)		CENTER OF MASS ERRORS		PULSE DURATION (Hrs)
	Retained	Recovered	Breakthrough	Elution	Pore volumes	Minutes	
June 28, '89	14.0	11.6	1.45	1.20	0.25	8.2	2.653
June 29, '89	17.2	15.8	1.40	1.29	0.11	3.8	2.560
June 30, '89	21.3	22.2	1.29	1.34	-0.05	-1.9	2.400
July 3, '89	18.2	17.9	1.38	1.40	-0.02	-0.3	0.713
July 5, '89	31.6	31.1	2.63	2.66	-0.03	-0.8	
July 7, '89	18.0	14.8	2.18	2.28	-0.10	-3.2	3.883
July 10, '89	20.5	18.6	2.40	2.33	0.07	0.6	2.875
July 12, '89	0.35	0.34	2.33	2.21	0.12	1.1	1.555
July 13, '89	39.5	32.0	1.53	1.22	0.31	26.4	5.909
July 14, '89	0.61	0.52	1.42	1.22	0.20	17.2	4.827
July 17, '89	37.5	36.4	1.46	1.44	0.02	1.7	6.387
July 24, '89	39.3	36.3	1.54	1.41	0.13	3.3	3.053
July 26, '89	52.1	45.4	6.27	5.36	0.91	9.4	5.800
July 31, '89	2.0	1.6	12.4	9.6	2.82	54.1	16.472
August 9, '89	1.4	1.1	8.65	-	-	-	8.707
Sept. 5, '89	-	0.7	-	4.50	-	-	4.891
Sept. 13, '89	1.0	0.7	6.43	4.24	2.19	214.1	21.387
Oct. 11, '89	0.20	0.20	1.00	1.00	0	0	2.714
Oct. 12, '89	0.21	0.21	1.00	1.00	0	0	2.213
Oct. 18, '89	0.22	0.22	1.00	1.00	0	0	5.214
Oct. 19, '89	0.23	0.22	1.00	1.00	0	0	1.284
Oct. 27, '89	2.1	1.5	10.78	8.95	1.83	16.4	3.730
Oct. 28, '89	2.0	1.3	10.04	6.40	3.64	34.2	3.967
Oct. 29, '89	2.3	1.5	11.42	7.32	4.10	28.2	2.720
Oct. 30, '89	0.46	0.46	3.15	2.28	0.87	5.1	1.807
Nov. 8, '89	1.87	1.80	11.80	11.65	0.15	1.1	4.787
Nov. 13, '89	0.28	0.24	1.37	1.16	0.21	2.5	
Aug. 2-4, '88	31.4	36.4					
Aug. 8-12, '88	67.8	88.0					
Aug. 16-17, '88	12.6	14.7					
Aug. 19-22, '88	50.2	69.0					

DATE	Solubility (UNIFAC)		HENRY'S CONSTANT (UNIFAC) (dimensionless)	MASS BALANCE CALCULATIONS	
	Mol/L	mg/L		Retardation	Henry's Constant
June 28, '89	0.0052	476.4	0.2546	0.0889	
June 29, '89	0.0051	465.3	0.2541	0.0848	
June 30, '89	0.0051	469.0	0.2462	0.0637	
July 3, '89	0.0054	500.3	0.2811	0.0825	
July 5, '89	0.0054	500.3	0.2811		0.21
July 7, '89	0.0053	492.0	0.2721		0.33
July 10, '89	0.0053	492.0	0.2721		0.26
July 12, '89	0.0053	484.7	0.2632		0.27
July 13, '89	0.0052	476.4	0.2546	0.9396	
July 14, '89	0.0053	492.0	0.2721	0.7238	
July 17, '89	0.0052	476.4	0.2546	0.7969	
July 24, '89	0.0053	492.0	0.2721	0.9673	
July 26, '89	0.0054	500.3	0.2811		0.30
July 31, '89	0.0052	480.0	0.2589		0.14
August 9, '89	0.0053	484.7	0.2632		0.21
Sept. 5, '89	0.0051	469.0	0.2462		0.47
Sept. 13, '89	0.0056	514.1	0.2950		0.30
Oct. 11, '89					
Oct. 12, '89					
Oct. 18, '89					
Oct. 19, '89					
Oct. 27, '89	0.0055	507.7	0.2903	1.73	
Oct. 28, '89	0.0054	500.3	0.2811	1.87	
Oct. 29, '89	0.0054	500.3	0.2811	2.13	
Oct. 30, '89	0.0053	492.0	0.2721		0.19
Nov. 8, '89	0.0052	476.4	0.2546		0.23
Nov. 13, '89	0.0051	469.0	0.2462	0.0793	
Aug. 2-4, '88	0.0053	492.0	0.2721		0.19
Aug. 8-12, '88	0.0051	469.0	0.2462		0.17
Aug. 16-17, '88	0.0092	1226.0	0.6440		0.43
Aug. 19-22, '88	0.0092	1226.0	0.6440		0.40

HOMOGENEOUS HYDROLYSIS RATE CONSTANTS
FOR SELECTED CHLORINATED
METHANES, ETHANES, ETHENES, AND PROPANES

Peter M. Jeffers*, Lisa M. Ward, Lisa M. Woytowitch, and N. Lee Wolfe#

Chemistry Department, SUNY, Cortland, N.Y. 13045

Environmental Research Laboratory, USEPA, Athens, Ga. 30613

ABSTRACT. Hydrolysis rate constants for 18 chlorinated methanes, ethanes, ethenes, and propanes have been measured in dilute aqueous solutions within the temperature range of 0 to 180° C and at pH values of 3 to 14. Arrhenius parameters were determined for both neutral and alkaline hydrolysis reactions. Reactivity of these compounds in basic solution increases in accord with the expected acidity of the most reactive hydrogen atom in the molecule. Neutral hydrolysis appears to depend on both the C-Cl bond strength and the degree of steric hinderance at the reaction site. Only a neutral hydrolysis process occurs for carbon tetrachloride, 1,1,1-trichloroethane, and 2,2-dichloropropane. The chlorinated ethenes and hexachloroethane react only with hydroxide under severe conditions and exhibit no neutral hydrolysis. Some of these compounds eliminate HCl, whereas others substitute OH for Cl to form alcohols that may react further to give aldehydes or carboxylic acids as products. Environmental hydrolysis half-lives (25 C, pH 7) range from 36 hours for 2,2-dichloropropane to 1850 years for chloroform and to

over 10^6 years for hexachloroethane and the ethenes.

INTRODUCTION. Many halogenated organic compounds are found in natural waters, the result of chlorination processes, manufacturing waste discharges, household and industrial spills, and landfill leaching. A knowledge of the eventual fate of these solvents is of obvious importance, although actual rate constants for chemical transformations of many compounds of interest are not readily available. One of the early compilations of aquatic fate of priority pollutants (1) contained numerous entries stating that "No information is available on the hydrolysis of this compound" and other entries based on extrapolated behavior of similar compounds that are now recognized to be incorrect. The pioneering work of Dilling (2) was limited by experimental design because hydrolysis measurements were performed only at room temperature. Even the excellent review and compilation of homogeneous hydrolysis by Mabey and Mill (3) is far from complete, and the recent review by Vogel, Criddle, and McCarty (4) contains only limited information on these important reactions.

For several reasons, measurements of the homogeneous, abiotic hydrolysis rates are needed even for compounds that react very slowly under ordinary environmental conditions. First, because some environmental compartment residence times are long, e.g. in groundwater systems, large lakes, and the oceans, slow reactions can still be major factors in loss of a pollutant that

must travel a significant distance before it becomes a potential problem for human populations. Second, the study of any biologically mediated process or heterogeneously catalyzed reaction must allow for the amount of reaction that occurs by a purely abiotic, homogeneous pathway.

This paper presents experimental data on the neutral and base-catalyzed hydrolysis of CHCl_3 and CCl_4 along with most of the chlorinated ethanes and ethenes, plus several chlorinated propanes. (See Table I for the compound abbreviations which will be used throughout the text of this paper.)

EXPERIMENTAL. The chlorinated compounds (see Table I) were obtained from Aldrich, Eastman, or Pfaltz and Bauer, and were of the highest purity available. Aqueous solutions were prepared by shaking the organic compound vigorously by hand for 2 minutes with deionized water, which previously had been distilled and boiled to remove any traces of organic contaminants. Small amounts of these solutions were added to 0.1 molar, pH 7 phosphate buffer or to dilute NaOH or HCl solutions to achieve the desired base or acid concentrations. Most final solutions used in the hydrolysis experiments were less than 10% saturated in the organic substrate. Several of the more reactive compounds which hydrolyzed rapidly at lower base concentrations were prepared at less than 1% saturation levels to assure excess base. The solutions always were prepared with base concentrations at least ten-fold greater than that of the halogenated organic so that pseudo first-order kinetics could be assumed. The base

concentrations were attained by dilution of standardized solutions and were checked with a research quality pH meter for low $[OH^-]$ and by titration against potassium acid phthalate for more concentrated NaOH solutions. All solutions that were not used immediately after preparation were refrigerated. The less reactive solutions did not degrade at low temperatures in time periods of weeks to months.

Hydrolysis experiments utilized either zero dead-volume stainless steel tubes with about 2 mL volume, partially flattened by squeezing with a vise to allow for thermal expansion, or glass bulbs drawn from 7-mm-od borosilicate tubing to a fine tip at each end. The stainless steel tubes were washed in solvent, thoroughly rinsed with distilled water, and oven dried before they were filled using a long needle syringe. The glass bulbs were flame cleaned during fabrication and were used as soon as they had cooled. They were not reused. A set of the glass bulbs was filled by pouring the solution into a small beaker containing the bulbs in an upright position. The bulbs filled completely and simultaneously by capillary action. The ends were then flame-sealed enclosing about 350 μ L of liquid and a 10 to 15 μ L air space. Without this minimum air space, the bulbs exploded during heating.

For some reactions run below 50 C, the reactive solution was placed in a zero dead-volume septum vial capped with a teflon-lined septum and was sampled by puncturing the septum with a microliter syringe. Results using the septum vials could be matched using the glass bulbs. The lower temperatures were

achieved by using water baths. The reaction tubes/bulbs used for high temperature runs were air-thermostated using a gas chromatograph oven, which was monitored to 0.1 degree by thermocouple. Any temperature fluctuations resulting from opening the oven door to remove a sample were observed to recover within 15 seconds. At the concentrations used in these experiments, we did not expect adsorption on the steel or the glass would be a problem. We did check for adsorption, however, by filling a glass bulb with saturated 12-DCE solution, rinsing once with water, and, after gently wiping off adhering water droplets with a tissue, rinsing with a small volume of acetonitrile. Although 12-DCE is one of the most hydrophobic compounds we studied, and thus might be expected to exhibit relatively strong adsorption, the acetonitrile was found to contain only traces of 12-DCE.

All analyses were performed by gas chromatography using aqueous on-column injections. However, because this research spanned a 14-month period at three different institutions, a number of different chromatographs, columns, and conditions were used. The columns included a 0.53mm x 30m SPB-5 column and flame ionization detector, a 2mm x 2m 1% SP-1000 on Graphpak column and electron capture detector, a 2mm x 30cm 1% UCW-985 on Chromosorb W column and both flame and Hall electrolytic conductivity detectors, and a 0.334mm x 30m DB-5 column with flame and ECD. Some measurements on CCl_4 and TCE were done with each of these systems, with k values reproducible within experimental error.

KINETIC ANALYSIS. Preliminary studies of each compound were made to find appropriate temperature and base concentration ranges at which the reaction would proceed through several half-lives in 30 minutes to several days. The dependence of hydrolysis rate on concentration of base was determined by varying $[\text{OH}^-]$ by at least a factor of ten within the range pH 7 to 14. All reactions were found to be either first-order in base or pH independent. Solutions were made .001 M in HCl to measure the "neutral" hydrolysis rate in order to assure negligible reaction with OH^- . There was no evidence of any acid catalysis of these reactions. The data were reduced as first-order or pseudo first-order, with natural logarithm of reactant concentration plotted against time in minutes, the slope giving $k(\text{observed})$. Linearity of these $\ln C$ versus time plots is a good check on the first-order dependence of rate on organic substrate. Least-squares regression analysis typically showed $r^2 > 0.95$. The second-order rate constant for base-catalyzed reactions was obtained by dividing $k(\text{obs})$ by base concentration. Each individual rate constant value was determined using 5 to 20 time-concentration points, with each sample analyzed in triplicate.

Arrhenius temperature dependence was assumed, with the slope of the $\ln k$ versus $1/T$ plot set equal to $-E_a/R$, and the intercept equal to $\ln A$, where E_a is the activation energy, R the gas constant, and A the pre-exponential factor. Temperature ranges for the alkaline and "neutral" experiments are included in Table I.

RESULTS. The same rate constants were measured, within experimental error, using the zero dead-volume stainless steel tubes or the glass bulbs for study of nine of these compounds. These results provided experimental justification that no Henry's law corrections were required. Henry's law constants (Table I) have been measured from 10 to 30 C and fit by an exponential two-parameter equation by Ashworth et al. (5). Extrapolation with this equation to the conditions of our experiments is tenuous at best, but calculations showed that the worst possible case was CCl_4 , for which the calculated corrections reduced the activation energy by 8 kJ/mole, and increased the calculated environmental half-life by a factor of 2. With 1122-TCA, we calculate that less than 0.2% of the organic material will be in the vapor phase at 100 C in our bulbs. These two systems represent the extremes for the compounds we studied. Because we have no information on high temperature values for Henry's law constants, we report our rate data without corrections.

The Arrhenius parameters deduced for these systems are listed in Table II, with Figures 1 and 2 showing the $\ln k$ versus $1/T$ behavior over the actual range of temperature studied. Figure 3 shows the reduced data sets for CCl_4 assuming both first-order ($\ln \text{Conc.}$) and second-order ($1/\text{Conc.}$) kinetics. The data clearly are a linear fit to the first-order data reduction process (see discussion).

Products formed in these reactions were deduced from the GC analysis of the kinetic runs, with identification based on

retention times, and also on the results of GC-MS analysis. No volatile products were detected for the methanes. Vinyl chloride was found upon alkaline hydrolysis of both 11-DCA and 12-DCA, whereas neutral hydrolysis of 12-DCA produced ethylene glycol. No chlorinated product was observed from 111-TCA hydrolysis over the T-range 65 - 120 C, at any pH, although the relatively low ECD response to DCE may have obscured our detection of it as a low percentage product. Under alkaline conditions, 112-TCA produced 12-DCE and both tetrachloroethanes dehydrohalogenated to TCE. PCA yielded PCE quantitatively under all pH conditions. The only product identified from alkaline hydrolysis of the ethenes was chloroacetylene formed from 11-DCE.

DISCUSSION. Fells and Moellwyn-Hughes (6) studied hydrolysis of the chlorinated methanes in a set of classic papers. Our value of $k(\text{base})$ for CHCl_3 at 50 C agrees within 1% with the Moellwyn-Hughes value. His activation energy of 115.4 kJ/mole is about 10 kJ/mole higher than ours, a discrepancy within our combined experimental errors. The interesting and important difference is that Moellwyn-Hughes found CCl_4 hydrolysis to be second-order in CCl_4 and independent of base concentration. We confirm that CCl_4 hydrolysis is pH independent (pH 2 to 13), but we found the reaction to be clearly first-order in CCl_4 (see Figure 3). The second-order process for CCl_4 has been widely quoted but is apparently incorrect. The error probably stems from the fact that Fells and Moellwyn-Hughes measured appearance of chloride ion while we followed disappearance of CCl_4 .

The reaction certainly includes many steps, and some intermediate bottleneck step controlling the eventual production of chloride may appear second-order in CCl_4 . Nevertheless, the disappearance of CCl_4 is, in fact, a first-order reaction. The Fells and Moellwyn-Hughes second-order rate constant multiplied by their reported concentration gives a first-order rate constant within 40% of our experimental value at 95 C. Their activation energy of 98.6 kJ/mole is 16 kJ/mole lower than ours. This degree of agreement is probably fortuitous because we may have been observing different rate-limiting processes.

The rate constants for hydrolysis of the chlorinated ethenes appear to be the first ones reported for abiotic, homogeneous systems. Pearson and McConnell (7) estimated half-lives in water at room temperature for TCE and PCE of 2.5 and 6 years, respectively. R. B. Cain, in discussing this paper (7), suggested the loss may have been due to biodegradation, and the authors did not refute the possibility. Cline and Delfino (8) initially suggested that 11-DCE hydrolyzed more rapidly at 28 C than at 39 C, but after more extensive study (9) reported no significant degradation in over a year at either temperature. Their experiments at pH 13 indicated that 11-DCE yields chloroacetylene as an intermediate at elevated temperatures, at a rate approximately one tenth the TCA degradation rate, but they deduced no quantitative rate constant. The rate constants calculated from our parameters for any of the ethenes are all so small at environmental temperature and pH conditions (see Table II) that homogeneous hydrolysis certainly can be regarded as

negligible for any of these compounds. The extrapolated half-lives are all so great that, for practical purposes, the validity of the extrapolation process is beyond question, and extrapolation errors are irrelevant.

We found no other experimental studies of 11-DCA in either neutral or alkaline solutions. There are literature values for most of the other chlorinated ethanes, with the most extensive previous work on alkaline hydrolysis reported by Walraevens, Trouillet, and Devos (10) (WTD). For 12-DCA, WTD report an activation energy of 96.1 kJ/mole, considerably lower than our 121.6 kJ/mole, and consequently their A factor of 5.9E12 is lower than our 2.3E17. (All rate constant parameters will be in units of minutes, moles/l, and kJ/mole, unless specifically stated otherwise). However, WTD deduce their parameters from measurements at 60, 65, and 70 C combined with results of Okamoto et al. (11) for 110 and 120 C. Our value of $k_b = 0.0188$ at 70 C is in good agreement with WTD's .0136. At 120 C our rate constant is more than an order of magnitude larger than that of Okamoto et al. For the neutral reaction, Barach and Reinhard (12) found (A;E) = 4.0E11; 108.7, respectively, compared to our 2.83E10; 103.7. Their 37-year half-life at 25 C is about half our 72-year calculated value. Ehrenberg et al. (13) reported a half-life of 74 years, in excellent agreement with ours. At 80 C, Mabey, Barich, and Mill (MBM) (14) measured k_n to be 3E-7 sec⁻¹, while our calculated value is 2.1E-7 sec⁻¹.

WTD found Arrhenius parameters for 112-TCA of 5.9E13; 93.6, which compare reasonably with our 2.77E14; 88.2. MBM measured

$k_b = 0.35$ at 25 C whereas we calculate $k_b = .094$. For the neutral reaction, the only comparison is MBM at 80 C, $k_n = 9E-8 \text{ sec}^{-1}$, whereas we calculate $k_n = 0.18E-8 \text{ sec}^{-1}$. We find that even at pH 7 the alkaline reaction is the major pathway, and MBM may have measured a combined neutral and alkaline rate rather than the discrete neutral reaction.

All investigators agree that 111-TCA undergoes only neutral hydrolysis. Our Arrhenius parameters of $2.96E14$; 116.1 are bracketted by those of MBM ($9.12E13$; 112.0) and Cline and Delfino (9) ($1.2E15$; 119.3). The three studies appear to be within experimental uncertainty of one another. WTD measured this reaction only at 60 C and 65 C, and their rate-constants fall on the line connecting our results with Cline and Delfino's. The extrapolated or measured room temperature half-lives are: ours - 388 day, Cline and Delfino - 295 day, MBM - 230 day, Pearson and McConnell (7) - 273 day at 10 C, Dilling et. al. (2) - 180 day, Vogel and McCarty (15) - 2.8 year at 20 C.

Our alkaline hydrolysis activation energy for 1122-TCA of 78.2 kJ/mole is lower than that of WTD (94.3) and that of Cooper et al. (16) (91.1) although our rate constant at 11 C (6.54) is a near match for WTD's (6.48). At 40 C, we are a factor of 2 lower than WTD and Cooper et al., and we are about a factor of 2 lower than MBM's 25 C value of 72. MBM measured the "neutral" hydrolysis at pH 7, 55 C, and pH 6.2, 40 C, but their k values are more than 2000 times ours and probably are still measurements of the alkaline reaction.

For the 1112-TCA alkaline reaction, our parameters, $8.62E15$;

100.3, are a reasonable match with WTD ($1.7E17$; 107.8), whereas for the neutral reaction at 80 C, we are about four times MBM's k- value. Our alkaline hydrolysis results with PCA ($1.94E17$; 80.8) are within experimental uncertainty of Cooper et al. (17) ($1.12E17$; 77.5). WTD's activation energy of 63.5 kJ/mole appears unreasonably low, but their k at 20 C of 882 agrees well with our value of 751.

The polychlorinated propanes follow the same trends observed with the ethanes, but are more reactive. Ellington (18) has found Arrhenius constants for the base-catalyzed reactions of 12-DCP ($2.4E17$; 128.0) and 123-TCP ($1.2E21$; 126.0). Our value for 12-DCA is remarkably close to Ellington's rate constant for 12-DCP, and Ellington's propane work is consistent with the trends expected from our values for 1123-TCP and 11233-PCP, assuming the ethanes and propanes behave similarly with respect to increasing degree of chlorination.

Queen and Robertson (19) pointed out that gem-dihalides, like other compounds containing a perhalogenated C-atom, are unreactive towards nucleophilic displacement. This observation is consistent with our experiments. They measured the neutral hydrolysis rate of 22-DCP. Their data, put into Arrhenius form, yield $1.25E16$; 111.1, an almost identical match with our values.

It is clear that the ethenes as a group are very unreactive, with 12-DCE the least reactive member. The ethenes hydrolyze only under strongly basic conditions. HCA is by far the least reactive ethane, also degrading only under severe alkaline conditions. The remainder of the ethanes fit a pattern of

increasing alkaline reactivity with increasing chlorination, as long as each carbon is at least monochlorinated. There is an enormous increase in reactivity in going from 11-DCA to 112-TCA. The 'local' perhalogenation found in 111-TCA, CCl_4 , and 22-DCP results in reaction only by neutral hydrolysis. It appears that proton abstraction by OH^- is possible only if a Cl-atom is attached to the same carbon, and that OH^- has little tendency to displace Cl from a C-atom that is not also bonded to H.

The trends in neutral hydrolysis reactivity are not the result of a single simple factor. Neither the activation energies nor the frequency factors correlate exclusively with the reactivity order, implying that some combination of steric and energetic effects must be considered.

Because a number of these compounds react by parallel neutral and base catalyzed pathways, the half-lives listed in Table II are for the sum of these two processes, calculated at $[\text{OH}^-] = 1.E-7$. On the other hand, Cooper et al. (16) noted that some natural and treated waters have quite high pH values, sufficient, in some cases, to drastically decrease the observed environmental hydrolysis half-life.

ACKNOWLEDGMENTS. We gratefully acknowledge useful discussions and information provided by Tom Stauffer (HQAFESC, Tyndall AFB), and by Jackson Ellington and Paul Tratnyek (EPA, ERL-Athens). Ms. Kim Buggs assisted with early experiments. The hospitality of Tyndall AFB is sincerely appreciated.

LITERATURE CITED.

1. Callahan, M.A.; Slimak, M. W.; Gabel, N. W.; May, I. P.; Fowler, C. F.; Freed, J. R.; Jennings, P.; Durfee, R. L.; Whitmore, F. C.; Maestri, B.; Mabey, W. R.; Holt, B. R.; Gould, C., "Water Related Environ. Fate of 129 Priority Pollutants", EPA 440/4-79-029b, (1979).
2. Dilling, W.L.; Tefertiller, N.; Kallos, G. Environ. Sci. Technol., (1975), 9, 833.
3. Mabey, W.; Mill, T. J. Phys. Chem. Ref. Data, (1978), 7, 383.
4. Vogel, T.M.; Criddle, C.; McCarty, P. Environ. Sci. Technol., (1987), 21, 722.
5. Ashworth, R. A.; Howe, G. B.; Mullins, M. E.; Rogers, T. N. J. Hazardous Materials, (1988), 18, 25.
6. (a) Fells, I.; Moellwyn-Hughes, E. A. J. Chem. Soc., (1959), 398.
(b) Moellwyn-Hughes, E. A. Proc. Royal Soc., (1949), A196, 540.
(c) Moellwyn-Hughes, E. A. Proc. Royal Soc., (1953), A220, 386.

- (d) Fells, I.; Moellwyn-Hughes, E. A. J. Chem. Soc., (1958), 1326.
7. Pearson, C. R.; McConnell, G. Proc. Royal Soc. London, (1975), B189, 305.
8. Cline, P. V.; Delfino, J., Preprint Extended Abstract, ACS Nat'l meeting, (1983), Div. Env. Chem., p 577.
9. Cline, P. V.; Delfino, J. J. In Biohazards of Drinking Water; Larson, R. A., Ed.; Lewis: Chelsea, Mich., 1989; pp 47 - 56.
10. Walraevens, R.; Trouillet, P.; Devos, A. Int. J. Chem. Kinetics, (1974), 6, 777.
11. Okamoto, K.; Matsuda, H.; Kawasaki, H.; Shingu, H. Bull. Chem. Soc. Jpn., (1967), 40, 1917.
12. Barach, J. E.; Reinhard, M. Preprint, submitted to Environ. Sci. Technol., (1988).
13. Ehrenberg, L.; Osterman-Golkar, S.; Singh, D.; Lundqvist, U. Radiation Bot., (1974), 15, 185.
14. Mabey, W.; Barich, V.; Mill, T., Preprint Extended Abstract, ACS 186th. Nat'l meeting, (1983), Div. Env. Chem., p 359.
15. Vogel, T. M.; McCarty, P. L. Environ. Sci. Technol., (1987), 21, 1208.
16. Cooper, W. J.; Mehran, M.; Riusech, D.; Joens, J. Environ. Sci. Technol., (1987), 21, 1112.
17. Cooper, W. J.; Joens, J. A.; Slefker, R. A.; El-Shazby, O. A. In Biohazards of Drinking Water; Larson, R. A., Ed.; Lewis: Chelsea, Mich., 1989.
18. Ellington, J. J.; Stancil, Jr., F.; Payne, W.; Trusty, C., "Measurement of Hydrolysis Rate Constants for Evaluation of

Hazardous Waste Land Disposal", Vol. I and II, EPA/600/3-87/019, (1987).

19. Queen, A.; Robertson, R. E. J. Amer. Chem. Soc., (1966), 88, 1363

NOTE. This research was performed through sponsorship by the Air Force Office of Scientific Research/AFSC, USAF, under contract F49620-85-C-0013, through a Mini Grant from Universal Energy Systems, AFOSR, a Cortland College Faculty Research Grant, and a National Research Council Senior Fellowship.

This manuscript is submitted for publication with the understanding that the United States Government is authorized to reproduce and distribute reprints for government purposes.

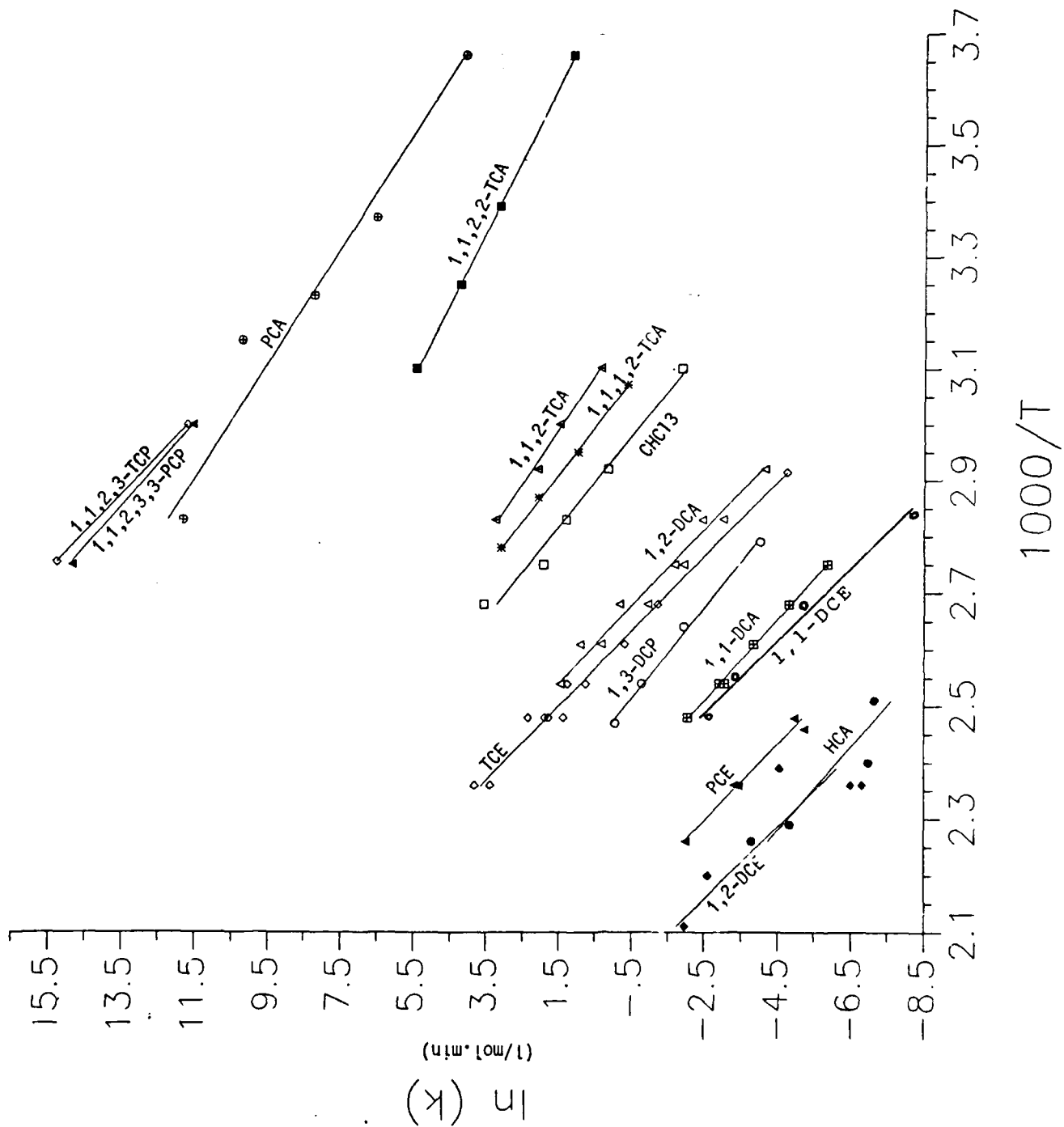
Mention of trade names or commercial products does not constitute endorsement or recommendation for use by the U. S. Environmental Protection Agency.

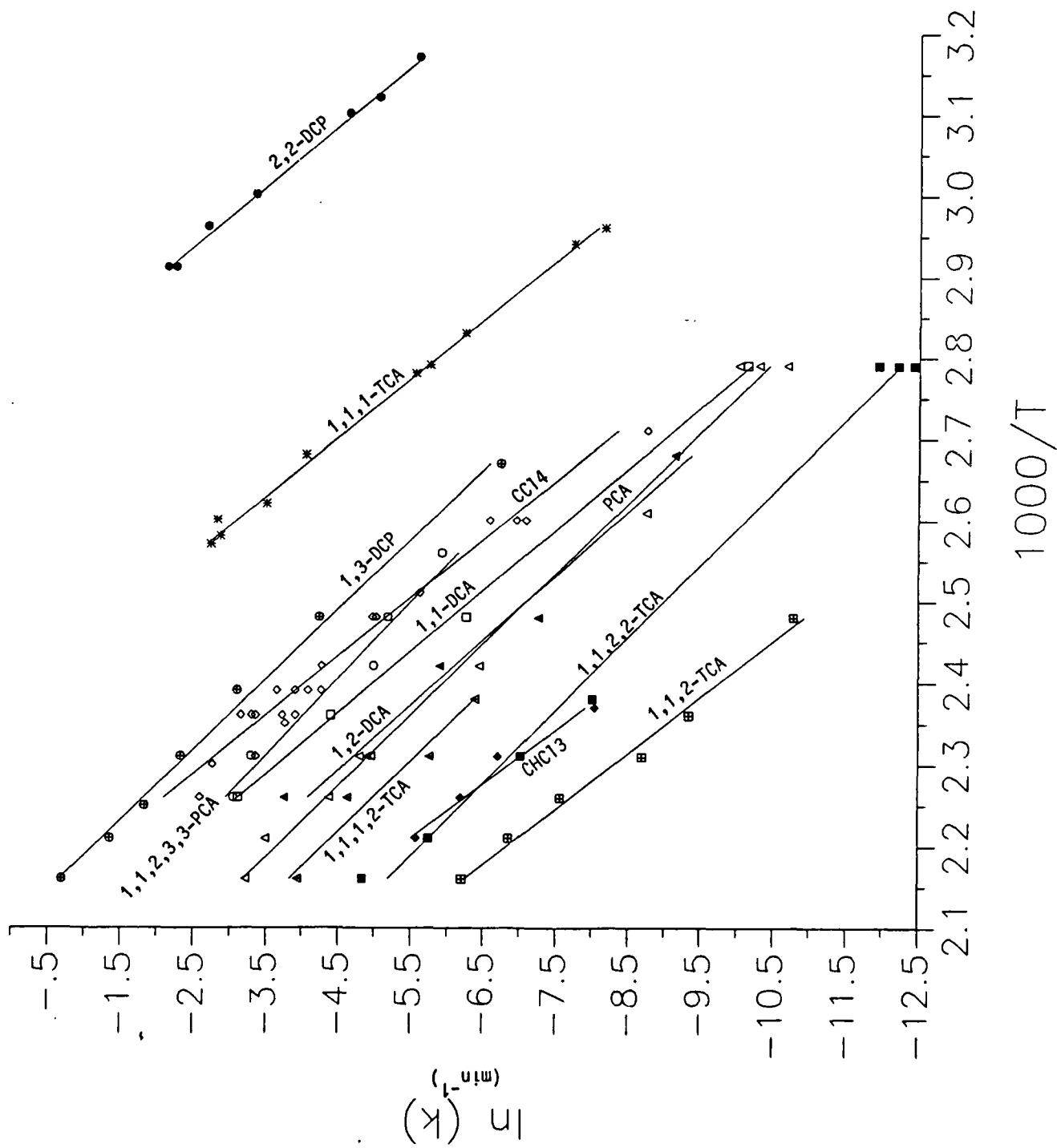
Figure Legends.

Figure 1. Arrhenius plot for all alkaline hydrolysis reactions. All k's are second-order ($L \text{ mole}^{-1} \text{ min}^{-1}$) . Lines are determined by least-squares regression.

Figure 2. Arrhenius plot for neutral hydrolysis reactions. All k's are first order. Lines are from least-squares regression.

Figure 3. Reaction order test for CCl_4 . A first-order reaction is linear in $\log (\text{conc.})$ versus time while a second-order reaction follows a linear $1/(\text{conc.})$ versus time plot. Note the curvature of the data reduced as inverse concentration dependence.





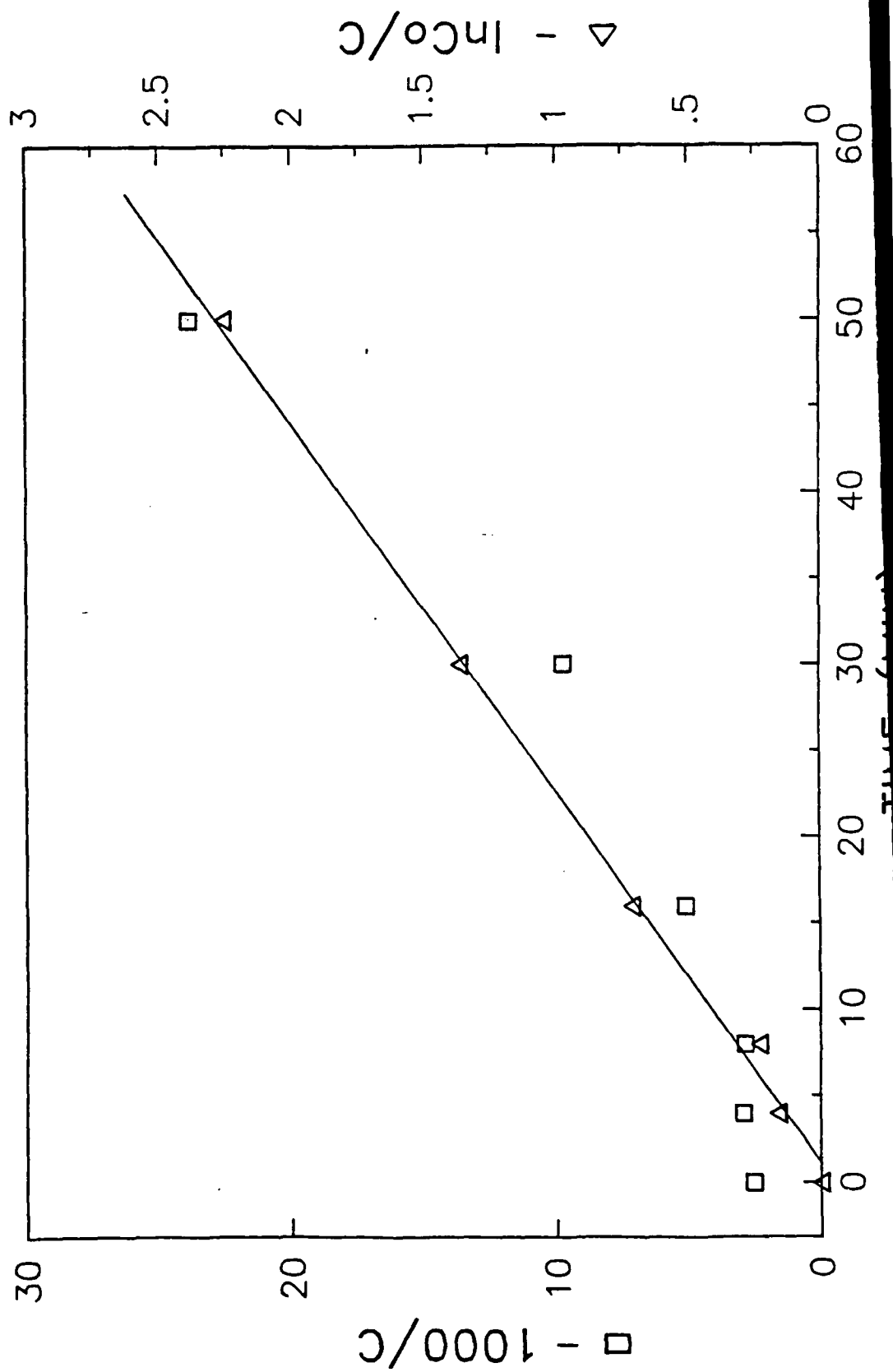


TABLE I. Experimental conditions for the compounds studied.

COMPOUND (ABBREVIATION)

COMPOUND (ABBREVIATION)	pH Range	SOL* mg/l	H(30 C) #	T-neutral Range	T-basic Range
CHLOROFORM (CHCl ₃)	3 - 13	8200	0.00554	150 - 180	50 - 90
CARBON TETRACHLORIDE (CCl ₄)	2 - 14	785	0.0378	96 - 170	95 - 170
1,1-DICHLOROETHANE (11-DCA)	3 - 12	5500	0.00776	85 - 170	90 - 130
1,2-DICHLOROETHANE (12-DCA)	3 - 14	8690	0.00174	100 - 169	70 - 120
1,1,2-TRICHLOROETHANE (112-TCA)	3 - 12	4500	0.00133	130 - 170	50 - 80
1,1,1-TRICHLOROETHANE (111-TCA)	2 - 13	720	0.0211	65 - 116	
1,1,1,2,2-TETRACHLOROETHANE (1122-TCA)	3 - 12	2900	0.0007	85 - 190	0 - 50
1,1,1,1,2-TETRACHLOROETHANE (11112-TCA)	3 - 12			147 - 190	52 - 87
PENTACHLOROETHANE (PCA)	2 - 10			85 - 190	0 - 80
HEXACHLOROETHANE (HCA)	3 - 14	50	0.0103		125 - 170
1,3-DICHLOROPROPANE (13-DCP)	3 - 13	2700	0.003	101 - 190	85 - 132
2,2-DICHLOROPROPANE (22-DCP)	3 - 13			42 - 71	
1,1,2,3-TETRACHLOROPROPANE (1123-TCP)	7 - 12				60 - 90
1,1,2,3,3-PENTACHLOROPROPANE (11233-PCP)	3 - 7			118 - 170	60 - 90
1,1-DICHLOROETHENE (11-DCE)	2 - 10	400	0.0318		70 - 130
1,2-DICHLOROETHENE (12-DCE)	2 - 14	600	0.00575		140 - 200
TRICHLOROETHENE (TCE)	2 - 14	1100	0.0128		70 - 160
TETRACHLOROETHENE (PCE)	2 - 14	200	0.0245		130 - 170

* From Ref. (1).

* atm m³/mol. From Ref. (5).

FINAL REPORT

SORPTION KINETICS OF VOLATILE ORGANIC COMPOUNDS
ON AQUIFER MATERIALS

January - December, 1989

Submitted by: Richard S. Myers, Ph.D.

Professor of Chemistry

Department of Physical Sciences

Delta State University

Cleveland, MS 38733

(601) 846-4482

Submitted to: Air Force Office of Scientific Research

UES Project S-210-9MG-047

MINI GRANT PROGRAM

Universal Energy Systems, Inc.

4401 Dayton-Xenia Road

Dayton, OH 45432

ABSTRACT

A technique for the measurement of concentration changes due to the rapid adsorption of volatile organic compounds was used to determine the speed with which these compounds are sorbed on soil and aquifer materials. Kinetics of the initial minutes and hours of adsorption of 1,2-dichlorobenzene onto a natural soil and a modified silica were investigated. Results indicated a rapid initial adsorption followed by a slower approach to equilibrium. Most of the adsorption occurred within twenty minutes. The kinetics of adsorption were described by a model consisting of a rapid step followed by a slower step, represented by two consecutive, reversible, first order reactions. The rate constants produced by the model were used to generate concentration - time curves and partition constants which agreed very closely with experimental results.

Acknowledgements

I wish to express my appreciation to the Air Force Office of Scientific Research for sponsoring this research. I also wish to thank Universal Energy Systems for effectively and efficiently administering the minigrant program.

The willing contributions of many people enhanced these research experiences. Dr. Tom Stauffer of the Air Force Engineering and Services Center gave support with direction, assistance, and fruitful discussions. The administration at Delta State University provided resources, and colleagues in the Department of Physical Sciences gave support and encouragement. Undergraduate chemistry students George Gong and Dana Renfroe provided technical and laboratory assistance. I wish to thank each of them for contributing to a successful research project.

I. INTRODUCTION

One of the major factors affecting the fate of organic contaminant materials in the soil environment is the rate at which the contaminant is sorbed on the soil particles. To better understand how organic chemicals behave in groundwater, it is necessary to understand the factors which affect the partitioning of the contaminant between the soil and water phases. A study of the kinetics of adsorption and desorption processes is of fundamental importance in understanding the transport of contaminants in the soil in general and in aquifers in particular. Knowledge of the rates of adsorption will be useful in refining various partition and transport models.

There is evidence to show that while hydrophobic compounds may adsorb rapidly, the desorption is much slower. This indicates that the sorbed compound is very strongly, or perhaps irreversibly, bound to the soil particles (Ditoro and Horzempa, 1982; Karickhoff and Morris, 1985). Most evidence comes from soil-water slurry experiments where equilibration time is on the order of hours to days (Hamaker, 1972). The literature contains few reports of the changes occurring in the first few minutes of adsorption onto a natural soil (Wahid and Sethunathan, 1978 ; Wauchope and Myers, 1985; Wu and Gschwend, 1986) and none with aquifer material. These and

other kinetic studies generally show a rapid initial adsorption followed by a slow approach to equilibrium (Karickhoff, 1980; Peel and Benedek, 1980).

This study examines the changes that occur in the first minutes of the sorption process as a result of rapid mixing of soil, contaminant, and water. The contaminant, or pollutant, material is a volatile, hydrophobic, organic compound. This type of compound is of particular interest due to environmental problems associated with spills and leakages of fuels and solvents.

II. OBJECTIVES OF RESEARCH EFFORT

In order to understand how volatile organic chemicals, specifically substituted aromatics and halogenated solvents, behave in soils and aquifers, it is necessary to measure the rates of adsorption and the rates of desorption. The contaminant in this study was a volatile, nonpolar organic compound, such as those found in jet fuels and solvents. The adsorbents include a soil and an aquifer material.

The following purposes of the research investigation were accomplished:

1. Improve the design the experimental apparatus in order to increase the sensitivity of the system so that adsorption onto materials with low organic carbon content may be more easily measured.

2. Investigate the kinetics of the initial few minutes and hours of adsorption of a contaminant onto soil.

3. Determine how well a kinetic model of adsorption fits the experimental data.

III. MATERIALS AND METHODS

Materials. The adsorbing materials were a natural soil with total organic carbon content of 0.72 % and a silica modified to contain 0.061 % total organic carbon. Both materials were passed through a 1.0 mm sieve.

In order to simulate an aquifer material, silica was coated with humic acid (Burris, MacIntyre, and Stauffer, 1989). Silica (SiO_2 , 40-100 mesh, Fisher Scientific) was washed overnight with 1 M HCl, rinsed with water, and heated at 700 °C overnight. It was then placed in a beaker and covered with an pH 10 solution of humic acid (Aldrich Chemical) with no supernatant liquid. The mixture was acidified with 1 M HCl added dropwise while stirring, then heated at 100 °C overnight. The silica was rinsed repeatedly with 0.005 M CaSO_4 until the supernatant was clear, then dried overnight. Total organic carbon of the coated particles was determined using the Walkley-Black procedure (Page, 1982)

The contaminant was 1,2-dichlorobenzene, purchased from Fisher Scientific and used without further purification. It proved to be the best contaminant among several that were

tested, giving the greatest change in photoionization detector signal as a result of the adsorption process. The Henry's Law constant of 0.064 (mol/mL air)/(mol/mL water) indicated that the measured concentration of dichlorobenzene in the gas phase would be proportional to the concentration in the liquid phase (Ashworth, et al, 1988). Reverse osmosis water was used for the preparation of slurries.

Experimental Apparatus. Kinetic measurements were made using a modification of the apparatus described by Wu and Gschwend (1986). A two-liter reaction flask with three necks, containing approximately 1.8 L slurry, was continuously stirred with a mechanical stirrer in the center neck of the flask. During the entire adsorption process, air was pumped through the slurry at a rate of 20 mL/s by a stainless steel bellows pump (model MB-21, Metal Bellows Co., Newton, MA) and recycled in an all glass and stainless steel closed loop. For analysis a small portion of the flow (20 mL/min) was passed through a closed, parallel loop containing the photoionization detector (model 52-02A, H·NU Systems, Newton Highlands, MA). The signal from the photoionization detector, measuring concentration in the gas phase, was recorded on a strip chart recorder (Microscribe 4500, Fisher Scientific) . The system was maintained at 25 ± 0.5 °C, except that the photoionization detector was maintained at 200 °C. In order to check the baseline response and to zero the detector, it was initially

connected to a similar loop containing only water-saturated air. The system was used during the adsorption experiment without detectable loss of contaminant due to leaks or decomposition by the photoionization detector.

Procedure for Adsorption Kinetics. With the reaction flask initially containing only water and air, the detector was adjusted to a zero baseline. A small amount of the contaminant was introduced with a microliter syringe and allowed to dissolve with stirring.

The solid adsorbent was mixed with a measured amount of water for at least a day to establish a natural state of wetting. To begin the adsorption process the solid-water suspension was poured into the reaction flask through the side neck. In every case the masses of water, soil, and contaminant were known. It was previously determined that opening the side neck momentarily did not result in a measurable loss of contaminant. With air circulating in the system, the concentration of the contaminant in the gas phase was measured continuously.

A typical experiment would involve a mixture with a total of 1600 mL water, 100-500 g soil or silica, and 2.0 to 10.0 uL dichlorobenzene.

Data Analysis. In order to determine the rate constants associated with the kinetic model, time-concentration data were analyzed using nonlinear least squares regression

analysis (MINSQ program, Micromath Scientific Software, Salt Lake City, Utah)

IV. A GENERAL MODEL FOR KINETICS OF ADSORPTION

The kinetics of adsorption may be represented by a rapid step followed by a slower step, sometimes called the two-box model (Karickhoff and Morris, 1985). This model consists of two consecutive, reversible, first order reactions. First the adsorbate is rapidly and loosely bound to a surface site. The second step consists of the adsorbate's being more slowly and much more tightly, but not irreversibly, bound to the surface of the adsorbent. This slower step may be due to one of several causes: the freeing of sites onto which the adsorbate can be more tightly bound, diffusion or migration to sites in which the adsorbate is more strongly bonded, a different adsorption mechanism, or other causes.

This process may be represented as a series of consecutive, reversible, first-order reactions.



A_s , A_1 , and A_n , respectively, represent the adsorbed substance in solution, adsorbed at a labile site on the soil surface, and adsorbed at a more restricted, non-labile site. No assumptions are made about the nature of these sites.

Labile refers to the adsorbate loosely bound to sites on the solid surface for which the adsorption process is readily reversed; that is, adsorption-desorption may be rapid. "Non-labile" refers to a more strongly, but not irreversibly, bound adsorbate. The k 's are the first-order rate constants. The first step in the adsorption process is usually rapid (larger rate constants), and the second is slower (smaller rate constants).

The change in concentration of adsorbate in each of the three states may be represented by the following rate equations:

$$\frac{d[A_s]}{dt} = -k_{12}[A_s] + k_{21}[A_1] \quad (2)$$

$$\frac{d[A_1]}{dt} = k_{12}[A_s] + (-k_{21} - k_{23})[A_1] + k_{23}[A_n] \quad (3)$$

$$\frac{d[A_n]}{dt} = k_{23}[A_1] - k_{32}[A_n] \quad (4)$$

Solutions to differential equations of these types have been discussed by several authors (Moore and Pearson, 1981; Szabo, 1969; Capellos and Bielski, 1980).

For the adsorption experiment the concentrations in solution, at labile sites, and at non-labile sites are expressed as follows:

$$[A_s] = [A_s]_0 \left[\frac{k_{21}k_{32} + k_{12}(\lambda_2 - k_{23} - k_{32})\exp(-\lambda_2 t)}{\lambda_2 \lambda_3} + \frac{k_{12}(k_{23} + k_{32} - \lambda_3)\exp(-\lambda_3 t)}{\lambda_3 (\lambda_2 - \lambda_3)} \right] \quad (5)$$

$$[A_1] = [A_s]_0 \left[\frac{k_{21}k_{32} + k_{12}(k_{32} - \lambda_3)\exp(-\lambda_2 t)}{\lambda_2 \lambda_3} + \frac{k_{12}(\lambda_2 - k_{32})\exp(-\lambda_3 t)}{\lambda_3 (\lambda_2 - \lambda_3)} \right] \quad (6)$$

$$[A_n] = [A_s]_0 \left[\frac{k_{21}k_{23}}{\lambda_2 \lambda_3} + \frac{k_{12}k_{23}}{\lambda_2 (\lambda_2 - \lambda_3)} \exp(-\lambda_2 t) + \frac{k_{12}k_{23}}{\lambda_3 (\lambda_2 - \lambda_3)} \exp(-\lambda_3 t) \right] \quad (7)$$

where

$$\lambda_2 = (p + q) / 2 \quad (8)$$

$$\lambda_3 = (p - q) / 2 \quad (9)$$

and

$$p = k_{12} + k_{21} + k_{23} + k_{32} \quad (10)$$

$$q = [p^2 - 4 (k_{12}k_{23} + k_{32}k_{21} + k_{12}k_{32})]^{1/2} \quad (11)$$

and $[A_s]_0$ is the initial concentration of contaminant in solution.

Equation (5) is the model for adsorption that is used with the nonlinear least squares regression program. Concentration, $[A_s]$, and time, t , are the experimental data. The data analysis finds the values of the rate constants which give the best agreement between experiment and calculation.

After the rate constants have been determined from experimental data, all concentrations, $[A_s]$, $[A_1]$, and $[A_n]$, may be determined as a function of time.

IV. RESULTS AND DISCUSSION

The initial changes in concentration of dichlorobenzene due to adsorption by soil are shown in Figures 1, 2, and 3. The rates of adsorption of dichlorobenzene by the simulated aquifer material are shown in Figures 4 and 5. In every case it appears that there is a fast initial adsorption followed by a slower approach to equilibrium. There is a greater

degree of adsorption by the soil because of the higher content of organic carbon.

The experimental systems which gave meaningful results for adsorption kinetic results are described in Table 1.

Table 1. Experimental Systems for Adsorption Kinetics

Expt. no.	Figure no.	C ₀ ppm	C _e /C ₀	Sorbent	Solid conc. g/L	K _p obs mL/g	K _p calc mL/g	K _{oc} calc mL/g
1	1	8.2	0.36	soil	250	7.1	7.7	1100
2	1	4.1	0.28	soil	250	10	9.8	1400
3	1	1.6	0.25	soil	250	13	14	1900
4	2	8.2	0.52	soil	125	6.8	7.8	1100
5	2	4.1	0.33	soil	125	16	15	2100
6	2	1.6	0.29	soil	125	20	20	2800
7	3	8.2	0.66	soil	62	6.2	7.9	1100
8	3	4.1	0.59	soil	62	11	11	1500
9	3	1.6	0.57	soil	62	12	12	1700
10	4	8.2	0.76	silica	310	1.0	1.0	1700
11	4	4.1	0.65	silica	310	2.0	2.0	3300
12	4	1.6	0.66	silica	310	1.7	1.6	2600
13	5	8.2	0.75	silica	125	2.7	2.9	4700
14	5	4.1	0.69	silica	125	3.6	2.9	4700
15	5	1.6	0.75	silica	125	2.7	2.9	4700

C₀ is the initial concentration of the dichlorobenzene (ppm). The ratio C_e/C₀ is the ratio of the concentration at the end of the kinetics run to the initial concentration. It does not represent an equilibrium concentration, because the time of adsorption varied from 40 to 500 minutes. Equilibrium

generally would not have been established in that length of time.

The partition coefficients, K_p and K_{oc} , are determined from equilibrium concentrations. They are defined by

$$K_p = \frac{x / m}{C_e} \quad (12)$$

$$K_{oc} = \frac{K_p}{F_{oc}} \quad (13)$$

where x/m is the amount of contaminant x (in ug) adsorbed by a mass m of soil (in g) at equilibrium with the solution of concentration C_e (in ug contaminant/mL solution). F_{oc} is the fraction by mass of organic carbon in the soil. The use of K_{oc} "corrects" the value of K_p , assuming organic carbon to be the actual adsorbent.

Additionally, the value of K_p may be calculated from the rate constants (Table 2).

$$K_p = \frac{k_{12}}{k_{21}} \left(1 + \frac{k_{23}}{k_{32}} \right) \frac{V}{m} \quad (14)$$

where V is the volume of solution (in mL).

In Table 1 the values $K_p(\text{obs})$ are calculated using equation (12) and the experimental values of initial and final concentrations, making the assumption that final concentrations are equilibrium concentrations. The values of $K_p(\text{calc})$

and $K_{oc}(\text{calc})$ are calculated from the rate constants generated by the kinetic model (equation 14).

There is a very good agreement between the observed values of K_p and the values calculated from the rate constants (the correlation coefficient, $r = 0.99$).

Often similar values of K_{oc} are obtained for a given soil and contaminant (Hamaker and Thompson, 1972). In this study the average value of K_{oc} for the soil is 1600, and that for the silica is 3600. The values of K_p and K_{oc} for a particular soil are not the true values and show some degree of variation because the system was not at equilibrium when the kinetics experimental run was stopped. The kinetic runs were discontinued because the detector began to show some drift after several hours of continuous operation. To discontinue the experiment after several hours was consistent the overall goal of the project to investigate the initial minutes and hours of adsorption.

The extent of adsorption is much smaller for adsorption onto the simulated aquifer material (silica), which has a much lower amount of organic carbon (average $K_p = 2.3$), than adsorption on the soil (average $K_p = 11$).

The nonlinear regression fits using the model in equations (1) and (5) resulted in four first order rate constants shown in Table 2.

Table 2. First order kinetic parameters from adsorption experiments

Expt. no.	Figure no.	C_0 ppm	Sorbent	Solid conc. g/L	k_{12} min ⁻¹	k_{21} min ⁻¹	k_{23} min ⁻¹	k_{32} min ⁻¹
1	1	8.2	soil	250	0.17	0.21	0.011	0.0080
2	1	4.1	soil	250	0.17	0.25	0.047	0.018
3	1	1.6	soil	250	0.19	0.22	0.013	0.0044
4	2	8.2	soil	125	0.21	0.44	0.060	0.057
5	2	4.1	soil	125	0.25	0.28	0.039	0.034
6	2	1.6	soil	125	0.29	0.29	0.045	0.031
7	3	8.2	soil	62	0.14	0.75	0.099	0.060
8	3	4.1	soil	62	0.14	0.32	0.022	0.038
9	3	1.6	soil	62	0.22	0.63	0.13	0.11
10	4	8.2	silica	310	0.073	0.67	0.13	0.068
11	4	4.1	silica	310	0.087	0.22	0.023	0.038
12	4	1.6	silica	310	0.054	0.18	0.015	0.023
13	5	8.2	silica	125	0.035	0.16	0.0042	0.0064
14	5	4.1	silica	125	0.089	0.47	0.099	0.11
15	5	1.6	silica	125	0.084	0.26	0.0013	0.010

The sequential-equilibria model (equation 1) gives excellent fits to the data using the parameters generated by the nonlinear regression program and presented in Table 2. Results for several experiments are shown in Figures 6 - 9. Agreement between experimental and calculated values of concentration is excellent.

Average values for the rate constants for the soil and modified silica are given in Table 3.

Table 3. Average kinetic parameters.

	percent organic carbon	k_{12} min^{-1}	k_{21} min^{-1}	k_{23} min^{-1}	k_{32} min^{-1}
SOIL	0.72 %				
Average		0.20	0.38	0.052	0.040
Standard deviation		0.050	0.20	0.040	0.033
MODIFIED SILICA	0.061 %				
Average		0.070	0.33	0.045	0.043
Standard deviation		0.022	0.20	0.055	0.040

Although there are relatively large standard deviations for the rate constants, it is interesting to note that the average rate constant for the soil is approximately equal to that for the modified silica, with the exception of k_{12} . The average value of k_{12} for the soil is considerably higher than that for the silica, consistent with the relative faster of adsorption on the soil, with its much higher organic carbon content.

Using these values of the rate constants, the model can be used to estimate changes in the concentration of contaminant adsorbed on labile sites (which usually peaks and then slowly decreases) and in the concentration of contaminant adsorbed on nonlabile, restricted sites, which slowly increases. These two concentrations cannot be measured directly. Examples of these calculations are shown in Figures 10 and 11.

Desorption of the contaminant from the surface of the sorbate would occur if the water phase were removed at equilibrium and replaced with pure, non-contaminated water.

The process described in equation (1) would be reversed, causing the concentration of contaminant in water to increase until equilibrium is once again established. Rate constants from adsorption experiments can be used to estimate the rate at which desorption occurs. The concentrations $[A_1]$ and $[A_n]$ must first be calculated after some period of adsorption. These will be the initial concentrations for desorption as the aqueous phase is removed and some noncontaminated water, equal in amount to that used in adsorption, is added. The increase in solution concentration as a function of time may then be computed. Agreement between experimental and computed desorption curves is fairly good (Wauchope and Myers, 1985). Additionally, where desorption data do not exist, desorption kinetics may be predicted (See Figure 12).

Using the average rate constants shown in Table 3, general adsorption and desorption curves may be generated. Figure 13 indicates the average rates of adsorption and of desorption for the nine experiments with various amounts of soil and contaminant. Figure 14 shows similar average calculations for the six experiments with the modified silica. The soil, with its higher organic carbon content, shows a greater extent of adsorption, as well as greater initial rates of adsorption. Desorption, following replacement of the aqueous phase, produces a higher solution concentration in the soil system

because there is more contaminant adsorbed onto the soil than onto the silica.

V. RECOMMENDATION

The rates of adsorption and of desorption should be considered when developing and refining models for the transport and partition of contaminants in surface waters and in aquifers. In some cases the rates of adsorption may be fast compared to the flow of water in aquifer systems. It appears that in well-mixed slurries of water and soil, adsorption and desorption equilibria can respond rapidly and reversibly to changes in the mixture, approaching a new equilibrium in minutes or hours. But desorption is slower for contaminants that have been in contact with soil for long periods of time, due to higher concentrations in nonlabile sites.

REFERENCES

- Ashworth, R.A., Howe, G.B., Mullins, M.E., and Rogers, T.N. 1988. Air-Water Partition Coefficients of Organics in Dilute Aqueous Solutions. Journal of Hazardous Materials, 18, p.25-36.
- Burris, D.R., MacIntyre, W.G., and Stauffer, T.B., 1989. Organic chemical sorption kinetic effects measured on columns of humic acid coated silica. To be submitted to Environmental Science and Technology.
- Ditoro, D.M. and Horzempa, L.M. 1982. Reversible and resistant components of PCB adsorption - desorption: Isotherms. Environ. Sci. Technol. 16, p. 594-602.
- Capellos, C. and Bielski, B. 1980. Kinetic Systems, Robert E. Krieger Publishing Co., New York, p. 35-38.
- Hamaker, J.W. 1972. The interpretation of soil leaching experiments. p. 115-133. In R. Haque and V.H. Freed (ed.) Environmental dynamics of pesticides. Plenum Press, New York.
- Hamaker, J.W. and Thompson, J.M. 1972. Adsorption. p. 49-143. In C.A. Goring and Hamaker, J.W. (ed.) Organic chemicals in the soil environment. Marcel Dekker, Inc., New York.
- Karickhoff, S.W. 1980. Sorption kinetics of hydrophobic pollutants in natural sediments. In R.A. Baker (ed.) Contaminants and Sediments, vol. II, Ann Arbor Science Publishers, Ann Arbor, MI, p. 193-205.
- Karickhoff, S.W. and Morris, K.R. 1985. Sorption dynamics of hydrophobic pollutants in sediment suspensions, Environ. Toxicology and Chem. 4, p. 469-479.
- Moore, J. and Pearson, R. 1981. Kinetics and Mechanism, Third Edition, Wiley-Interscience, New York, p. 296-300.
- Page, A.L., Ed. 1982. Methods of Soil Analysis, Part 2, Soil Society of America, Madison, WS, page 570.
- Peel, R.G. and Benedek, A. 1980. Attainment of equilibrium in activated carbon isotherm studies, Environ. Sci. Technol., 14 p. 66-71.
- Szabo, Z. 1969. Kinetic characterization of complex reaction systems, in Comprehensive Chemical Kinetics, vol. 2, Bamford, C. and Tipper, C., Eds., Elsevier, New York, p. 29,30.

Wahid, P.A. and Sethunathan, N. 1978. A simple method to study pesticide sorption in soils at short time intervals, Soil Sci., 126, p. 56-58.

Wauchope, R.D. and Myers, R.S. 1985. Adsorption-desorption kinetics of atrazine and linuron in freshwater-sediment aqueous slurries, J. Environ. Qual., 14 p. 132-136.

Wu, S.C. and Gschwend, P.M. 1986. Sorption kinetics of hydrophobic organic compounds to natural sediments and soils, Environ. Sci. Technol., 20 p. 717-725.

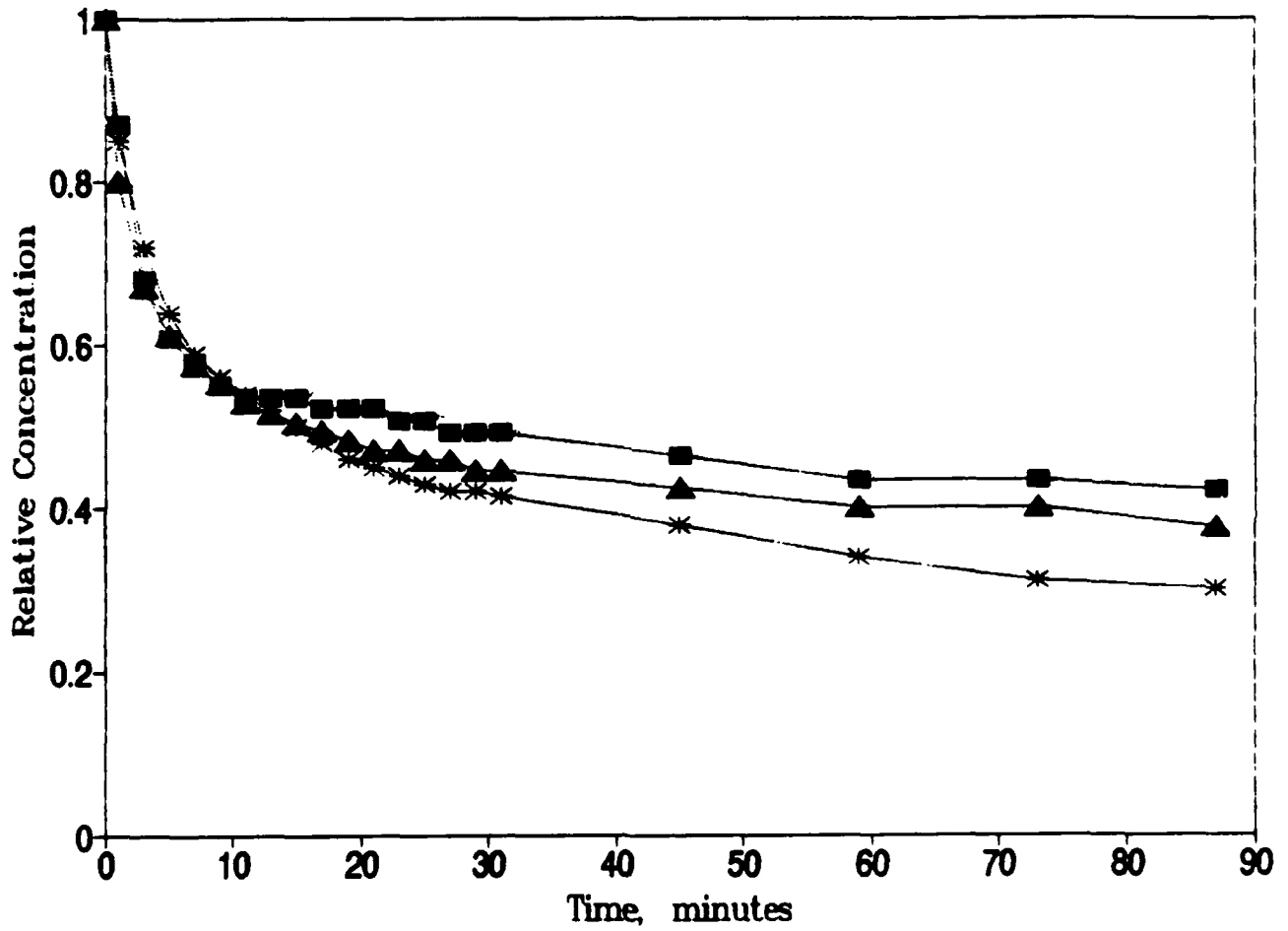


Figure 1. Adsorption of 1,2-dichlorobenzene from a mixture containing 250 g soil/Liter slurry. Initial concentrations are 8.2 ppm (■), 4.1 ppm (*), and 1.6 ppm (▲).

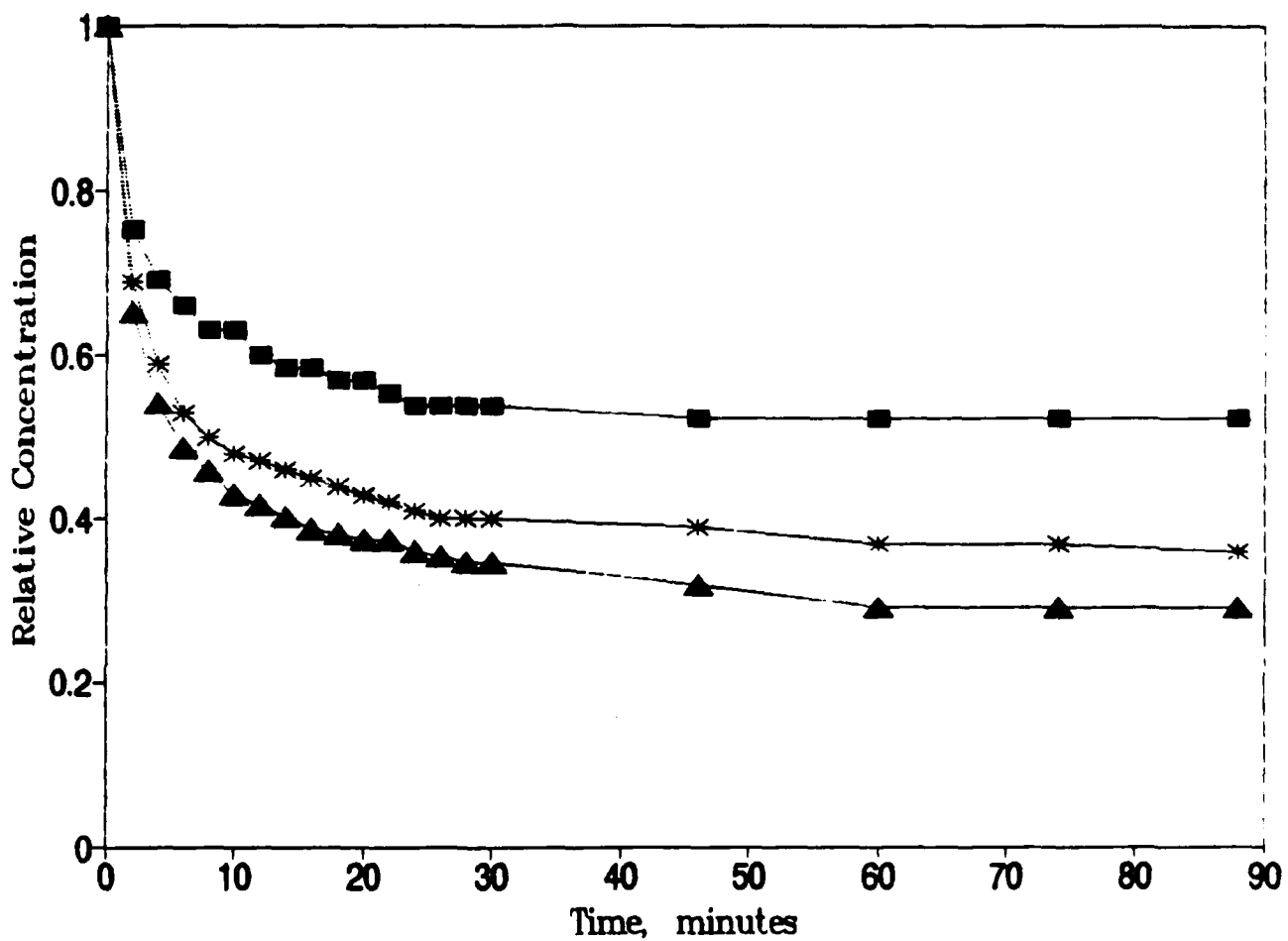


Figure 2. Adsorption of 1,2-dichlorobenzene from a mixture containing 125 g soil/Liter slurry. Initial concentrations are 8.2 ppm (●), 4.1 ppm (*), and 1.6 ppm (▲).

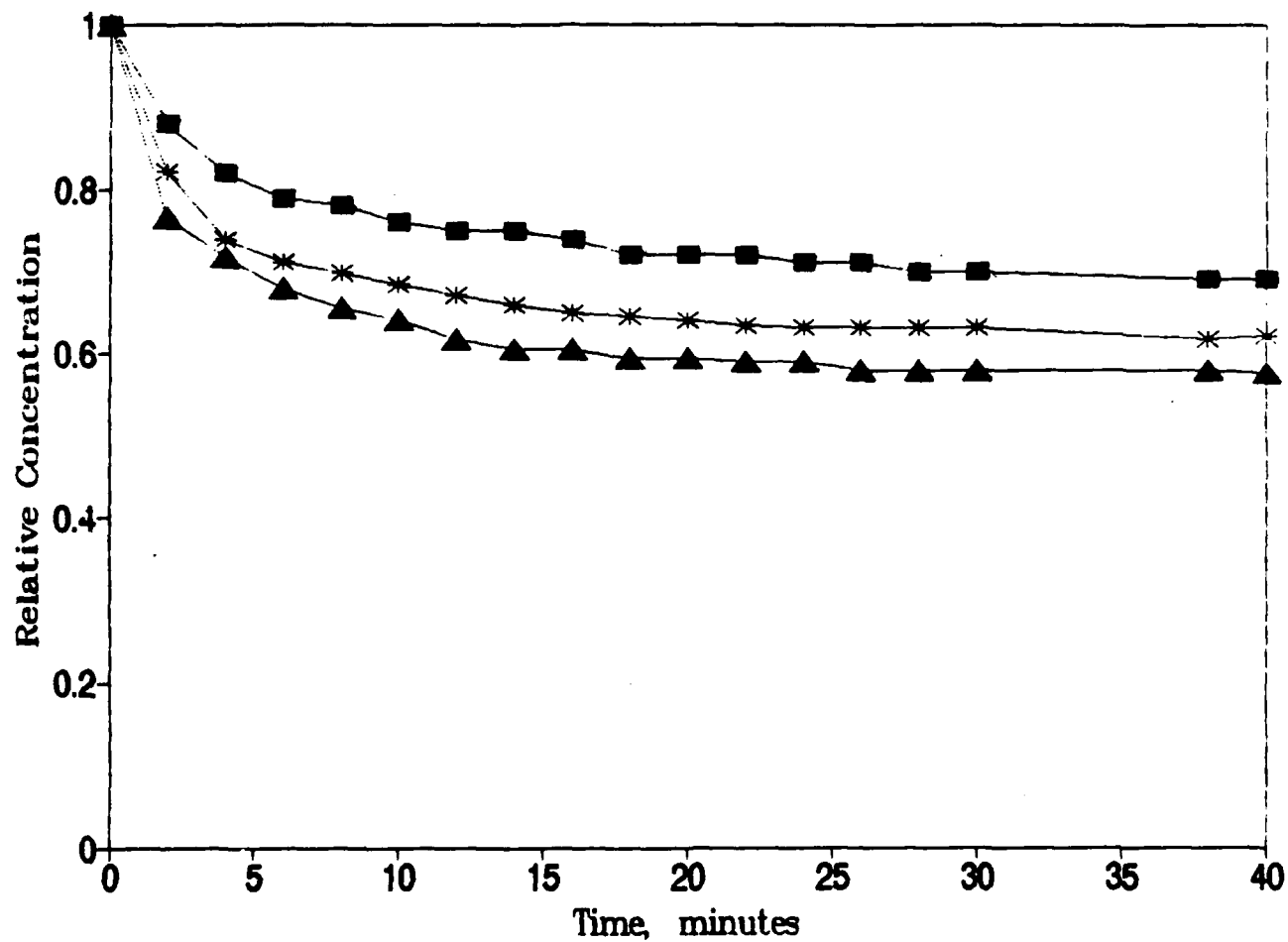


Figure 3. Adsorption of 1,2-dichlorobenzene from a mixture containing 62 g soil/Liter slurry. Initial concentrations are 8.2 ppm (■), 4.1 ppm (*), and 1.6 ppm (▲).

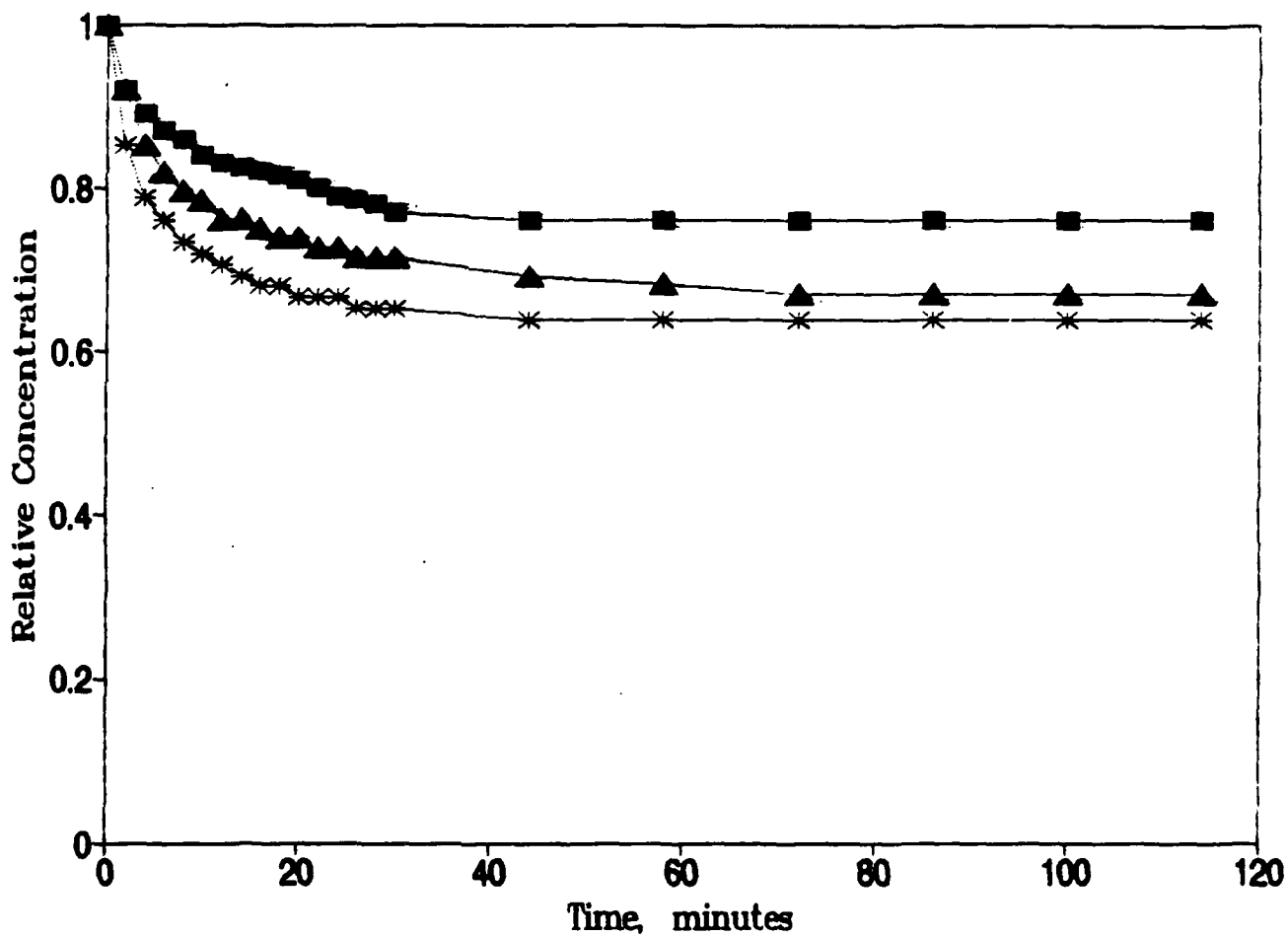


Figure 4. Adsorption of 1,2-dichlorobenzene from a mixture containing 310 g silica/Liter slurry. Initial concentrations are 8.2 ppm (■), 4.1 ppm (*), and 1.6 ppm (▲).

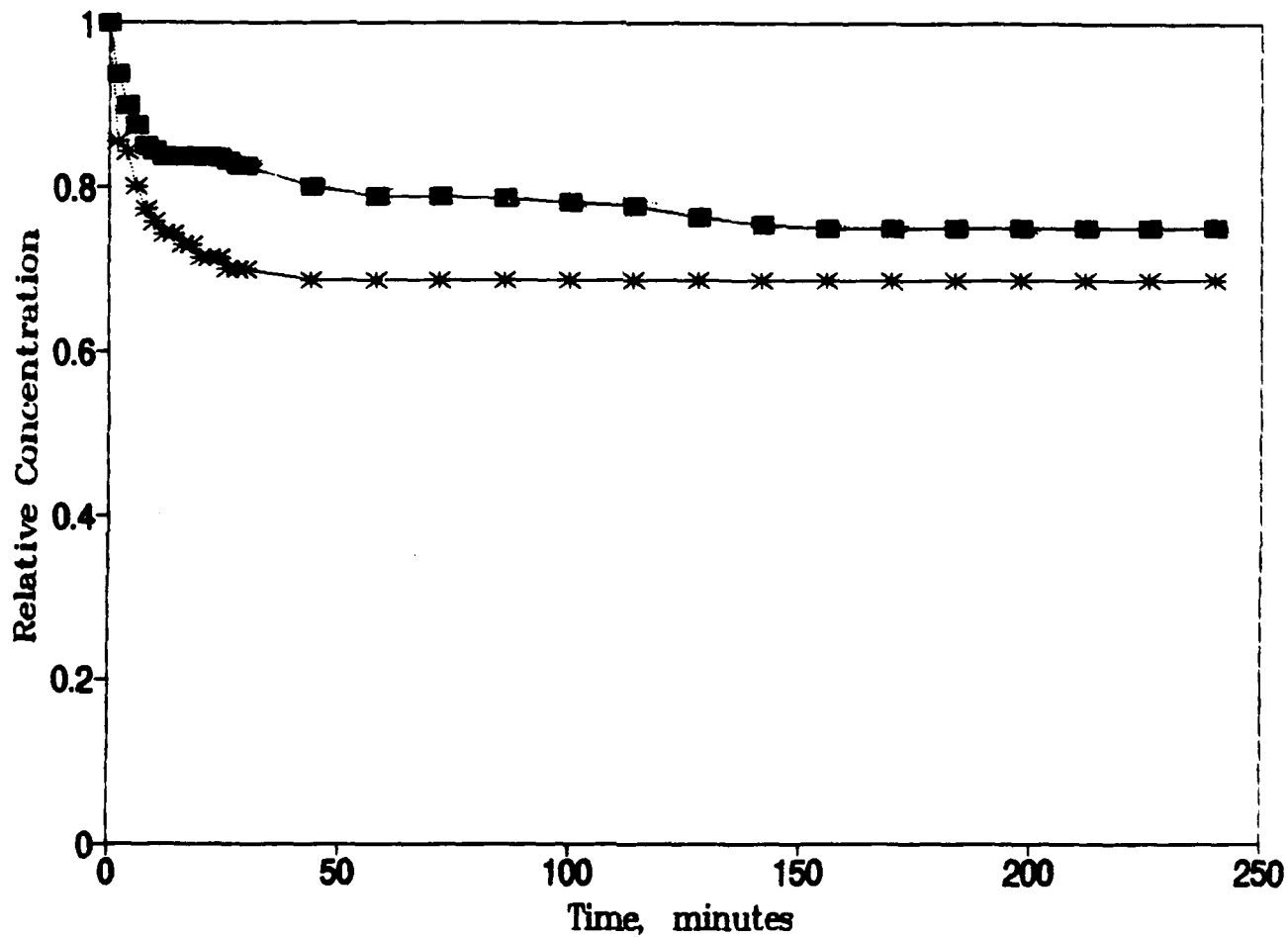


Figure 5. Adsorption of 1,2-dichlorobenzene from a mixture containing 125 g silica/Liter slurry. Initial concentrations are 8.2 ppm (■) and 4.1 ppm (*).

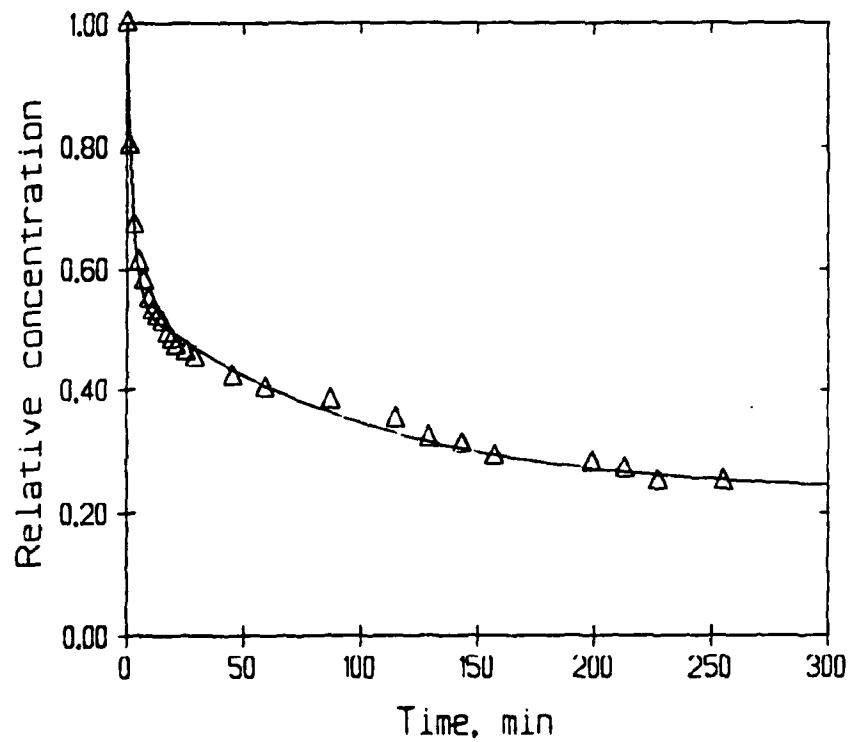
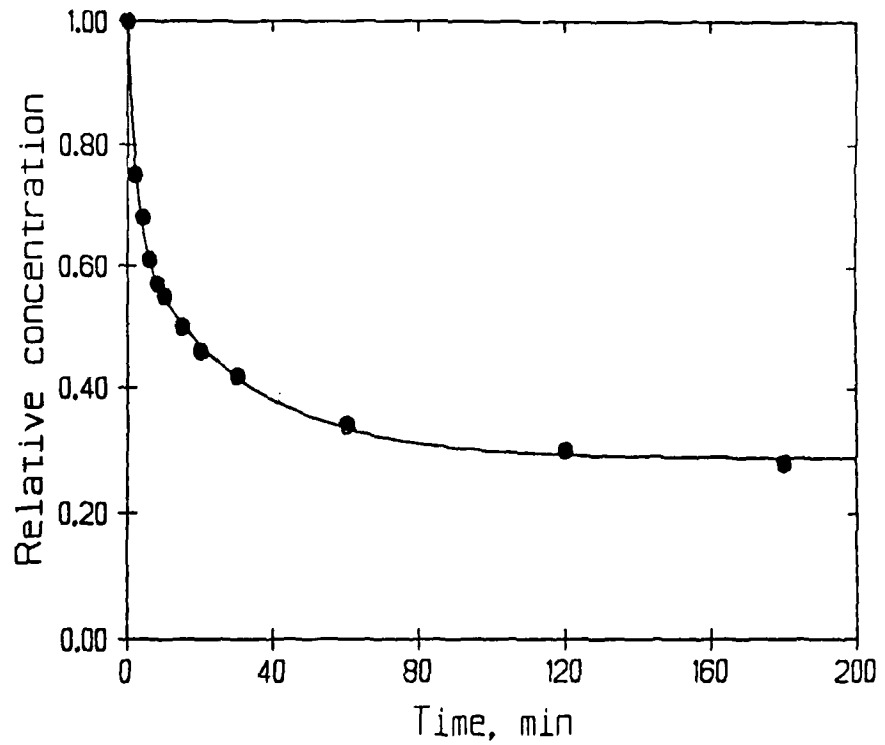


Figure 6. Adsorption of 1,2-dichlorobenzene by soil (250 g/L). (Top) Initial concentration = 4.1 ppm. (Bottom) Initial concentration = 1.6 ppm. The solid lines represent the concentrations generated by the adsorption model (equation 5).

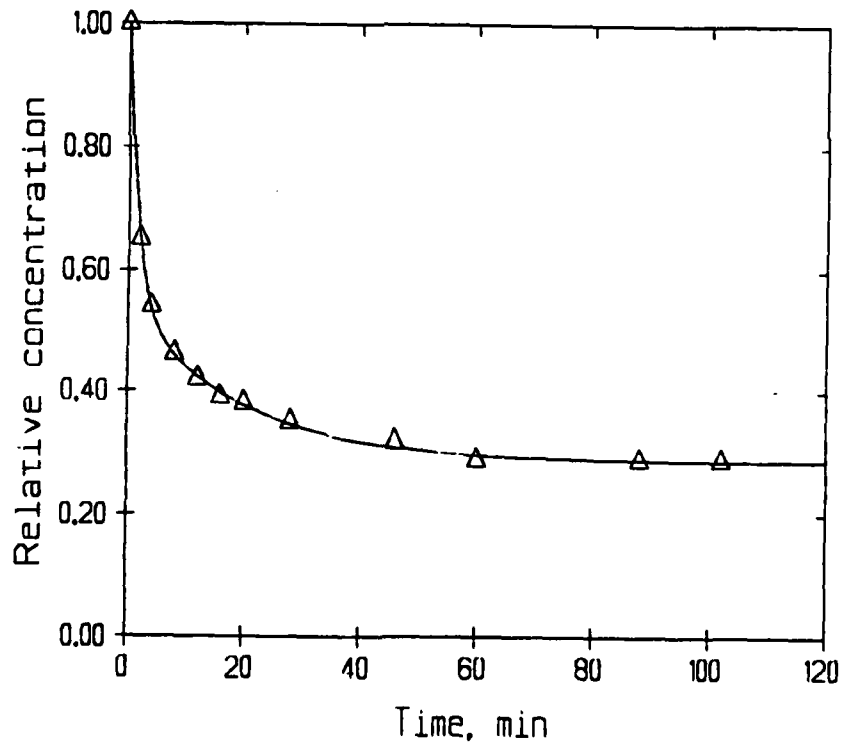
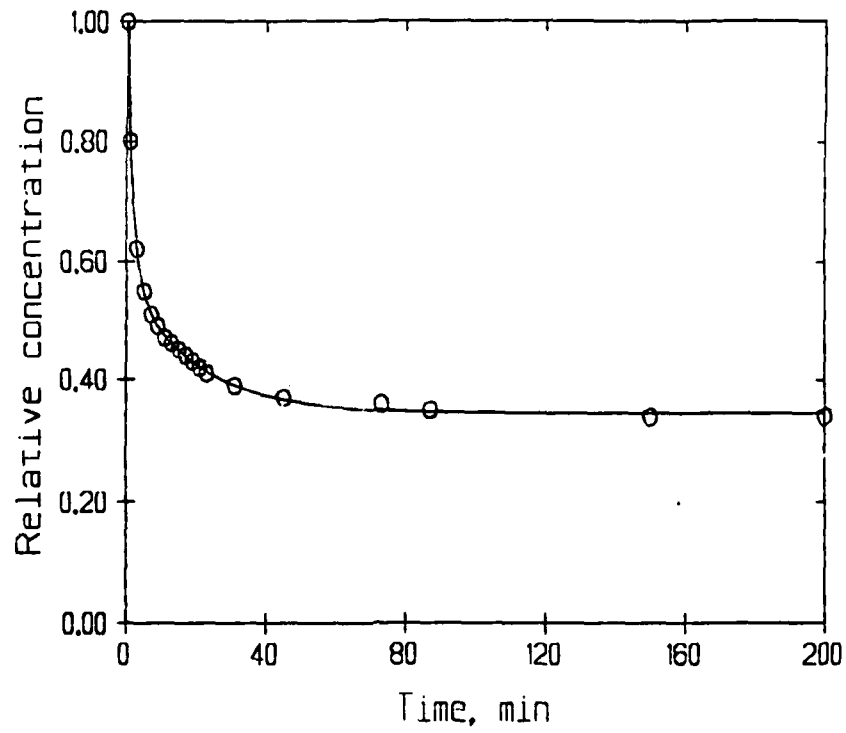


Figure 7. Adsorption of 1,2-dichlorobenzene by soil (125 g/L). (Top) Initial concentration = 4.1 ppm. (Bottom) Initial concentration = 1.6 ppm. The solid lines represent the concentrations generated by the adsorption model (equation 5).

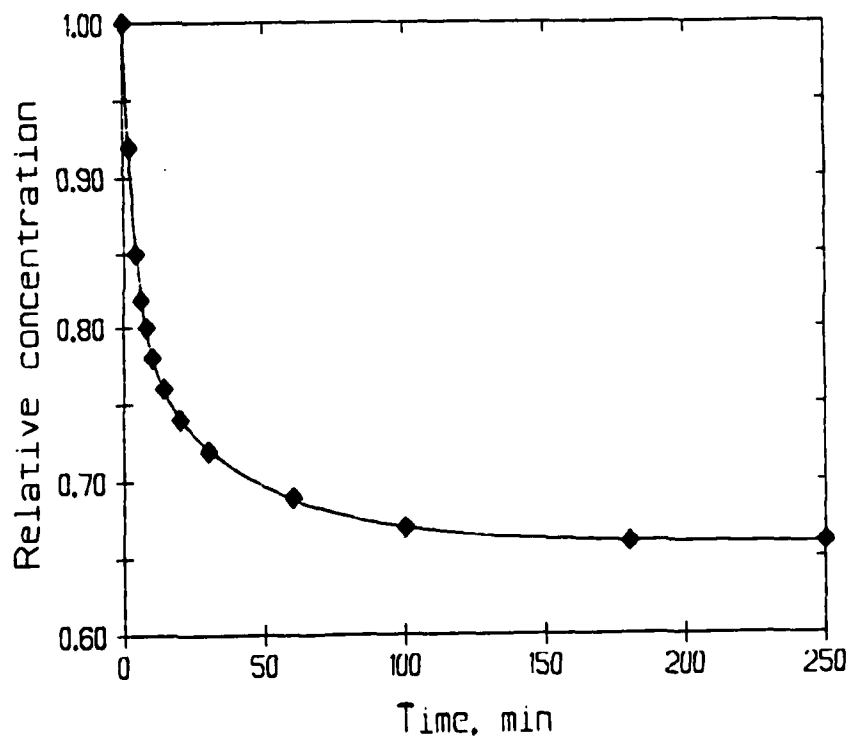
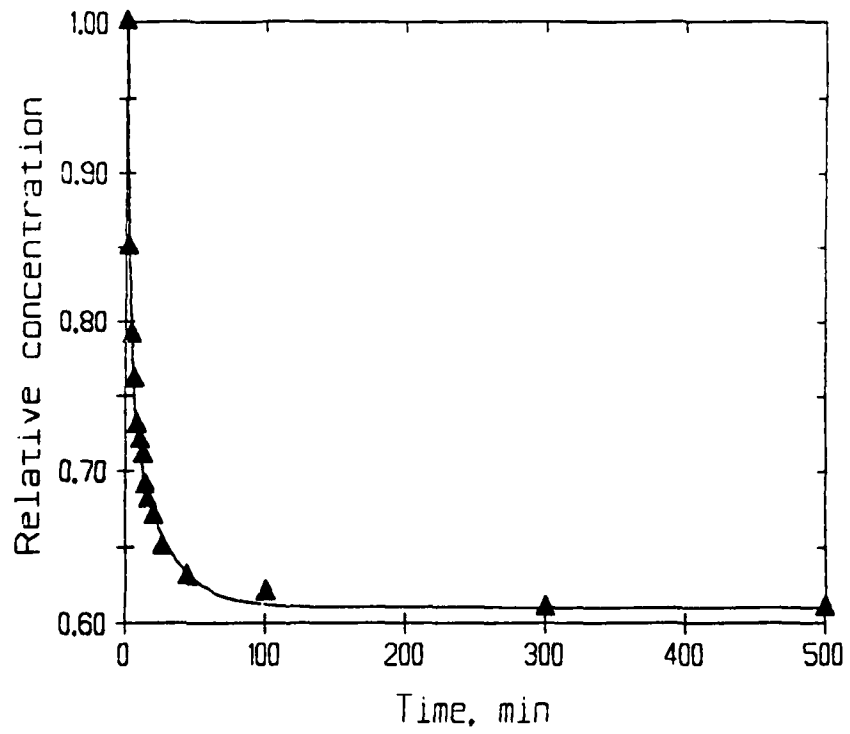


Figure 8. Adsorption of 1,2-dichlorobenzene by silica (310 g/L). (Top) Initial concentration = 4.1 ppm. (Bottom) Initial concentration = 1.6 ppm. The solid lines represent the concentrations generated by the adsorption model (equation 5).

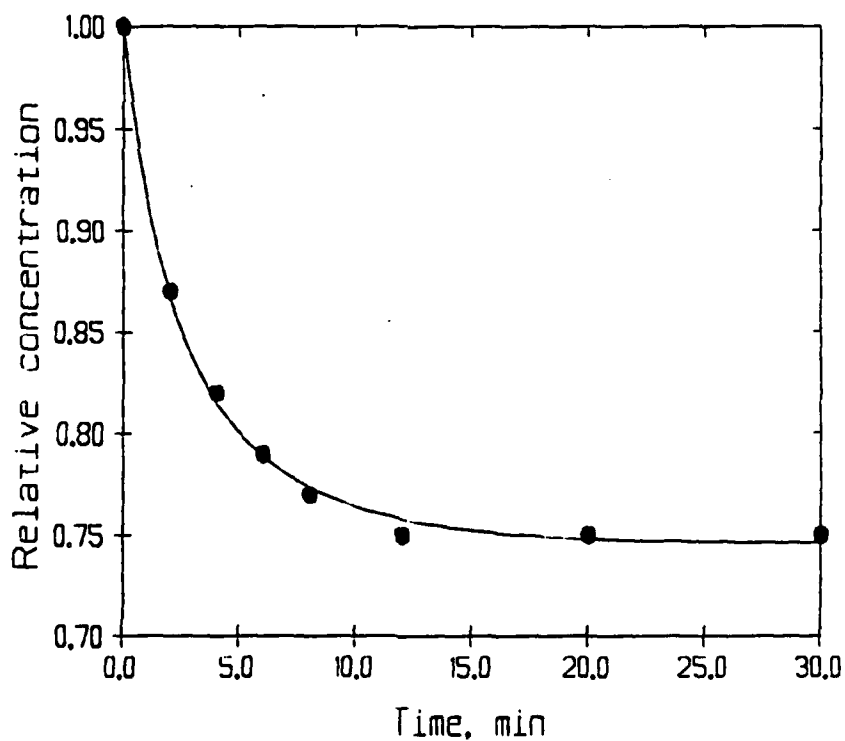
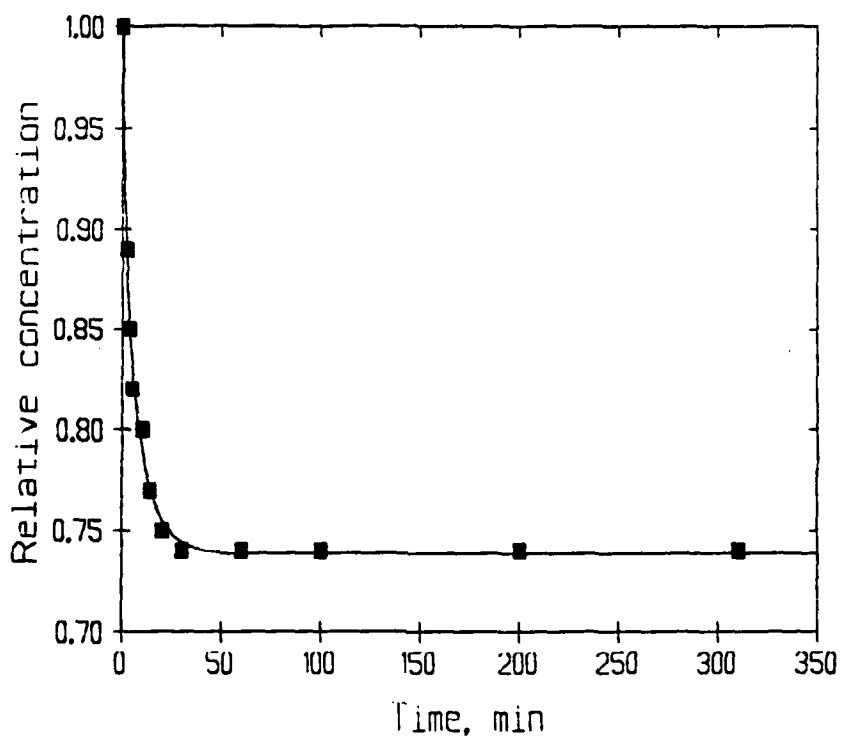


Figure 9. Adsorption of 1,2-dichlorobenzene by silica (125 g/L). (Top) Initial concentration = 4.1 ppm. (Bottom) Initial concentration = 1.6 ppm. The solid lines represent the concentrations generated by the adsorption model (equation 5).

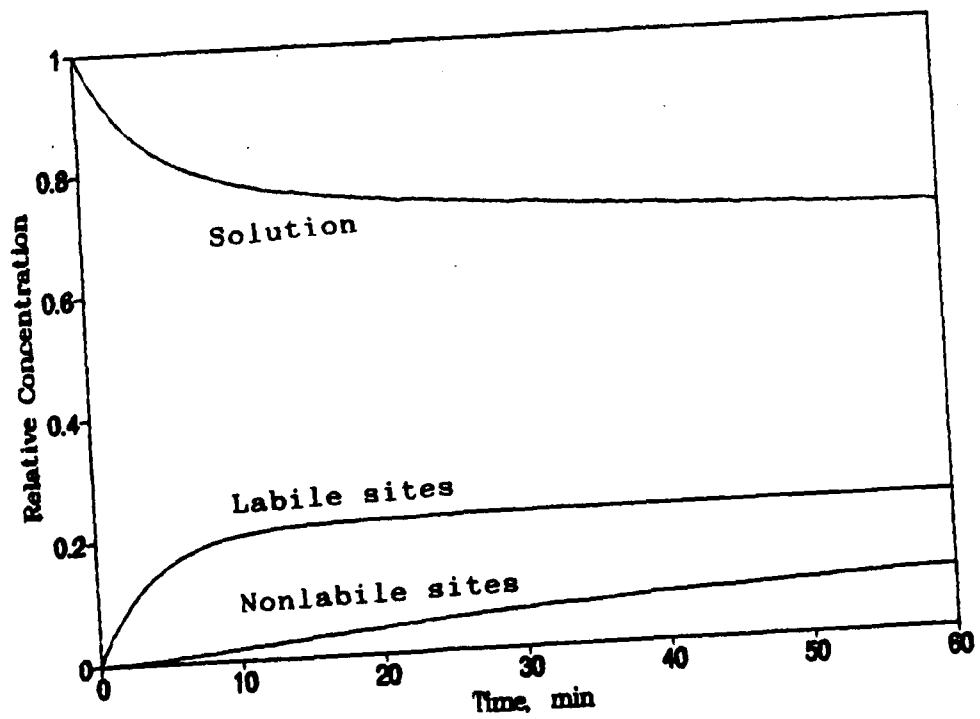
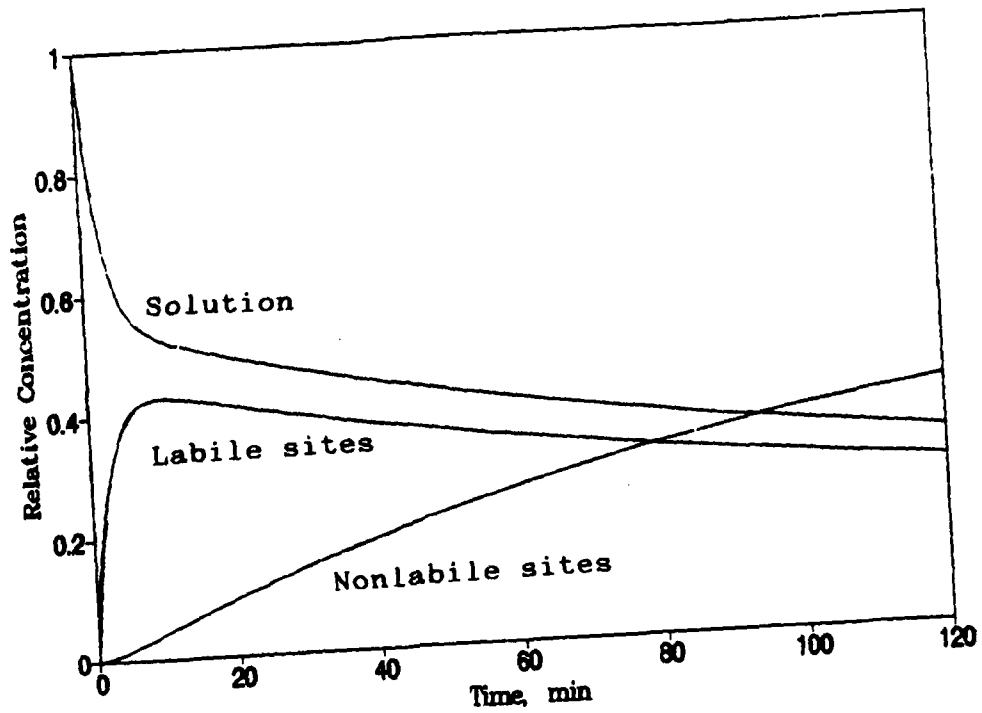


Figure 10. Calculated concentration of dichlorobenzene in solution, adsorbed onto labile sites, and adsorbed onto nonlabile sites for (Top) 250 g/L soil and (Bottom) 310 g/L silica. The initial concentration of dichlorobenzene in solution is 1.6 ppm.

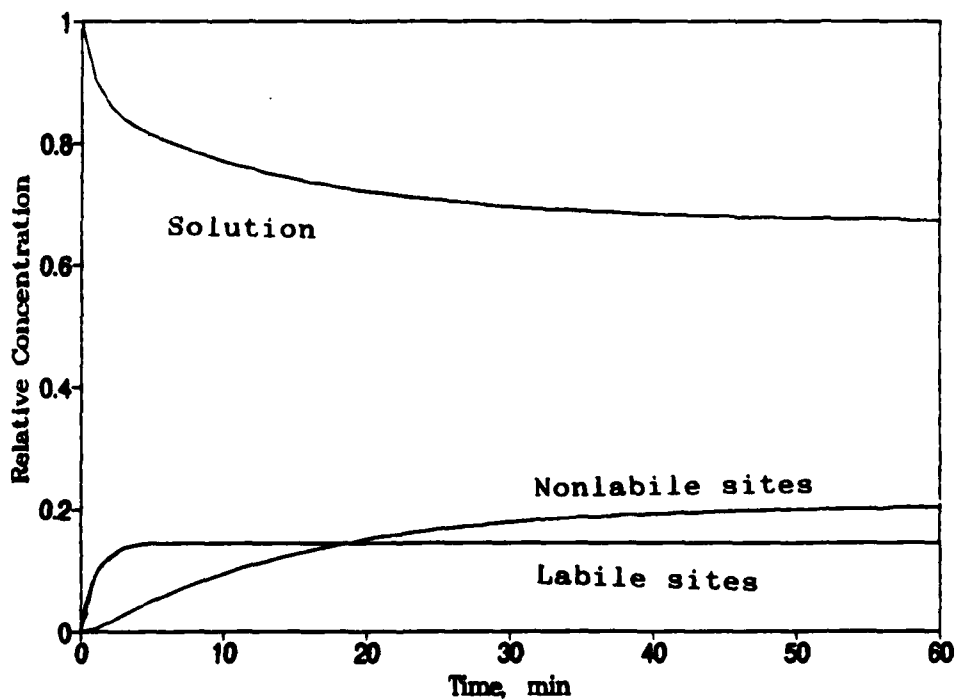
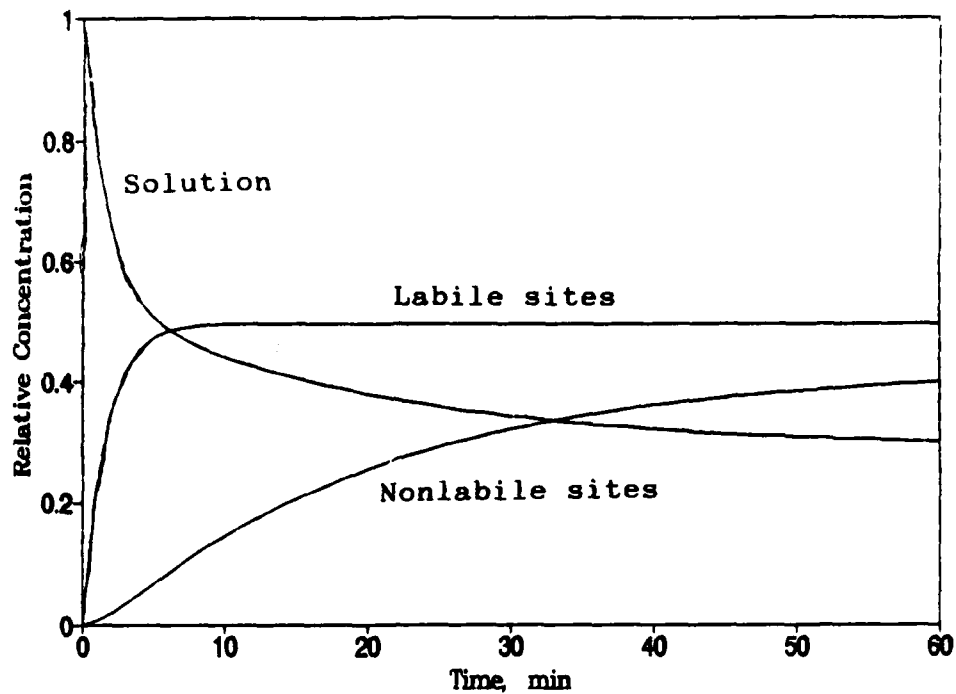


Figure 11. Calculated concentration of dichlorobenzene in solution, adsorbed onto labile sites, and adsorbed onto nonlabile sites for (Top) 125 g/L soil, initial concentration of dichlorobenzene is 4.1 ppm; and (Bottom) 62 g/L soil, initial concentration of dichlorobenzene is 8.2 ppm.

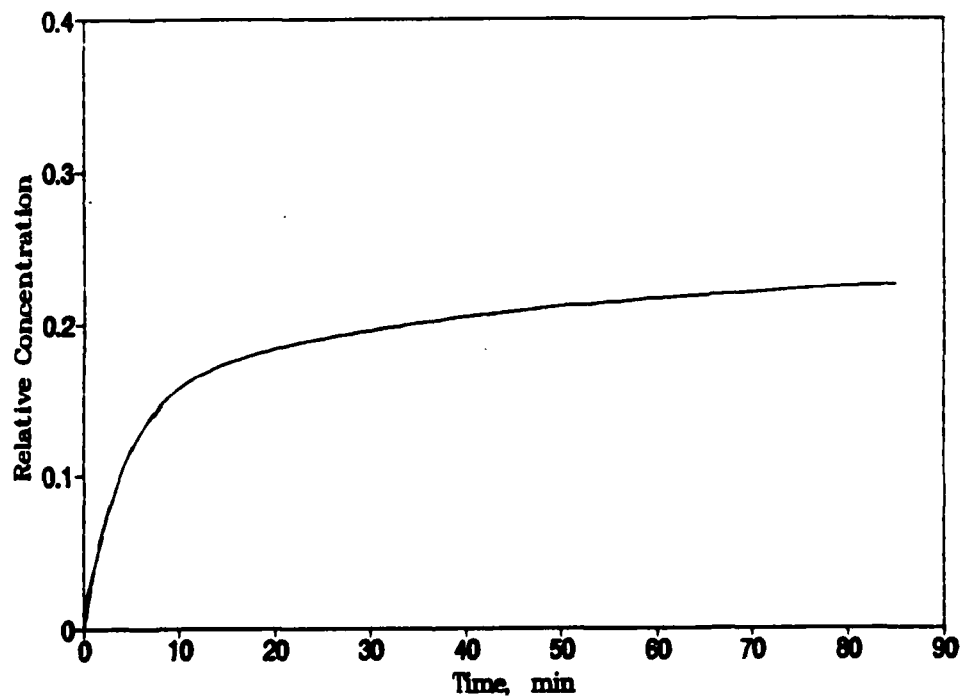
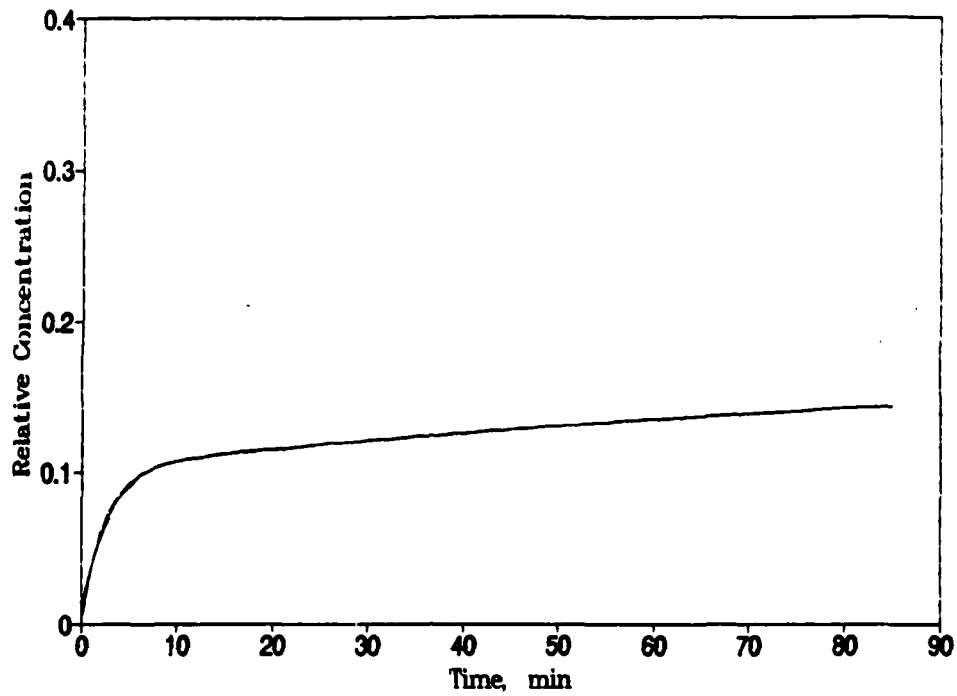


Figure 12. Predicted rates of desorption. The aqueous phase is replaced with pure water after 24 hour adsorption of 1.6 ppm dichlorobenzene onto (Top) 250 g/L soil; (Bottom) 310 g/L silica.

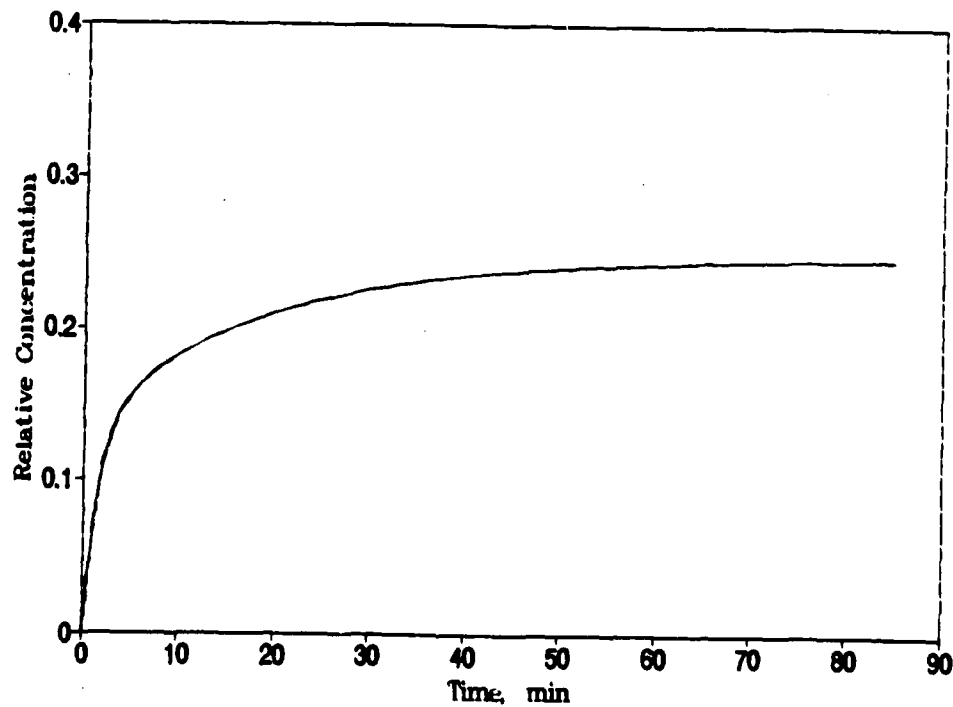
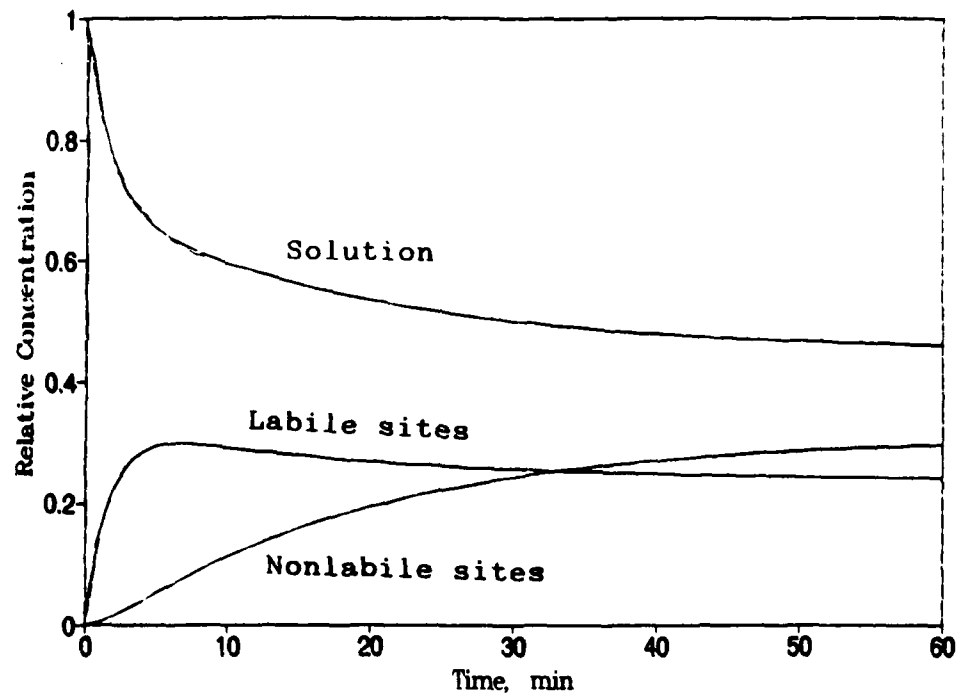


Figure 13. (Top) An "average" experiment for adsorption by soil, using average rate constants from Table 3. (Bottom) Calculated rate of desorption from soil using average kinetic parameters from Table 3.

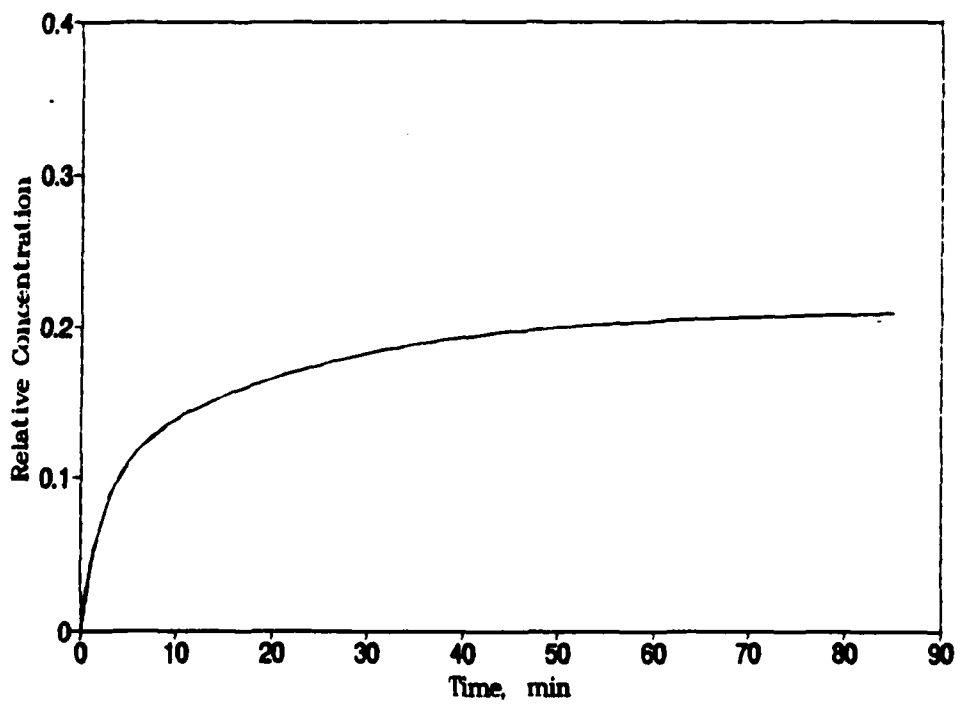
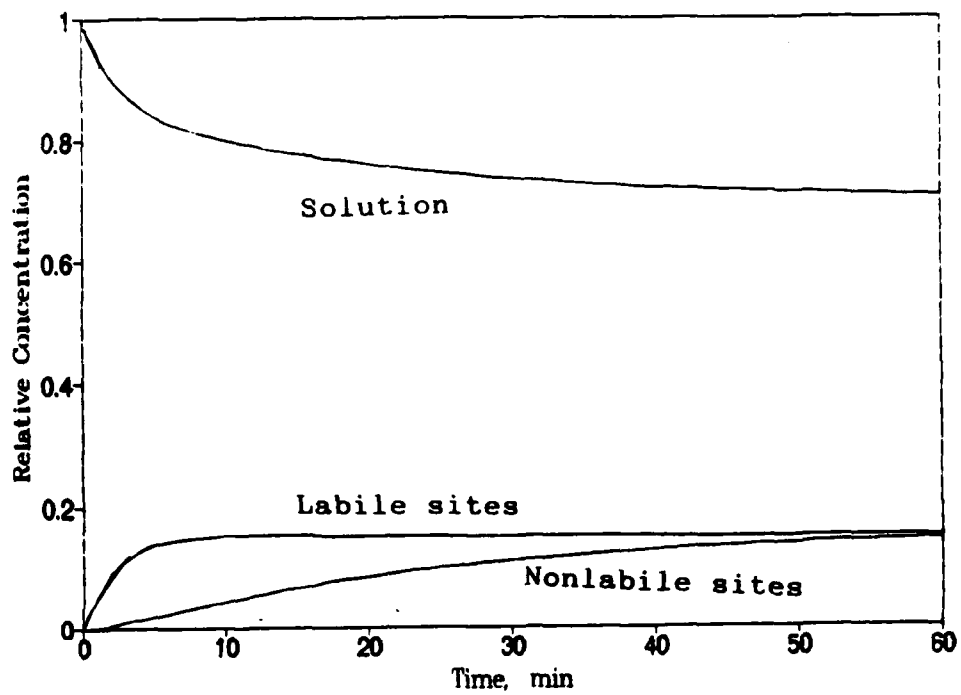


Figure 14. (Top) An "average" experiment for adsorption by silica, using average rate constants from Table 3. (Bottom) Calculated rate of desorption from silica using average kinetic parameters from Table 3.

Air Force Research Budget

Account 0220383368

	Budget amount	Transfer	Amount expended	Total expended	Balance
I. Salaries and wages					
A. Salaries					
1. Principal Investigator	9,555.00			9,555.00	0.00
2. Research assistant	2,200.00			2,200.00	0.00
B. Fringe benefits	1,718.00			1,812.19	
transfer		94.19			(0.00)
II. Permanent equipment					
A. Photoionization detector	4,500.00				
HMU 52-Q2A with accessories					
PO 015057 obj 8270			4,012.00		
" obj 6310			170.00		
" obj 6310			300.00	4,482.00	
transfer from 8270		(18.00)			0.00
B. Recorder	1,150.00				
Fisher Microscribe recorder			885.50		
PO 014433 obj 8270			93.09	978.59	
recorder paper obj 6310					
transfer from 8270		(171.41)			(0.00)
C. Metal bellows pump	400.00				
PO 014985 obj 6491			387.14	387.14	
transfer from 6491		(12.86)			0.00
D. Stirrer					
Ace heavy duty motor, stirr	450.00				
motor obj 6491			410.00	410.00	
transfer from 6491		(40.00)			0.00
III. Supplies and materials					
All object 6310					
A. Glassware, plasticware, supplies,	800.00				
Alltech Assoc PO 014676			121.09		
Alltech Assoc PO 014676			98.25		
Ace Glassware, stirrer supplies, ect.					
PO 015198			324.36		
PO 015198			154.83		
PO 015198			37.98		
Aldrich Chemical PO 017060			38.09		
Fisher Scientific PO 017181			223.26		
Nitrogen Walker W. PO 015944			25.52		
Fisher Scientific PO 019301			211.49		
Ace Glassware PO 018068			41.17	1276.04	
transfer		476.04			0.00

B. Stainless steel fittings, connec	600.00				
Little Rock Valve & Fitting					
PO 015082 obj 6290			625.85		
PO 015696 obj 6290			32.24	658.09	
transfer obj 6290		58.09			(0.00)
IV. Computer costs					
A. Software for data analysis	400.00				
"Micromath" regression analysis					
PO 015084 obj 5870			398.00		
upgrade PO 017074 obj 5870			79.00	477.00	
transfer obj 5870		77.00			0.00
B. Mathematics coprocessor chip	600.00				
PO 015945 obj 8250			136.45		
transfer obj 8250		(94.19)			
transfer obj 8250		(0.50)			
		(368.86)		136.45	0.00
V. TOTAL DIRECT COSTS	\$22,373.00			\$22,372.50	\$0.50
VI. Indirect costs	1,175.00	0.50	1,175.50	1,175.50	0.00
VII. TOTAL	\$23,548.00	0.00		\$23,548.00	\$0.00
Additional research funds provided by the Department of Physical Sciences	PO 014710			\$463.39	

BUDGET BY OBJECT NUMBER

Object number	Budget	Transfer	Expend	Expend Tot	Balance
1300 Salaries	9,555.00		9,555.00	9,555.00	0.00
2800 Student wages	2,200.00		2,200.00	2,200.00	0.00
3900 Fringe benefits	1,718.00	94.19	1,812.19	1,812.19	(0.00)
5870 Software	400.00	77.00	398.00 79.00	477.00	0.00
5910 Indirect	1,175.00	0.50	1,175.50	1,175.50	0.00
6290 Supplies, steel	600.00	58.09	625.85 32.24	658.09	(0.00)
6310 Supplies, glass	800.00	670.27 368.86	170.00 300.00 93.09 25.52 121.09 98.25 324.36 154.83 37.98 38.09 223.26 41.17 211.49	1,839.13	(0.00)
6491 Equip. related	850.00	(52.86)	387.14 410.00	797.14	0.00
8250 Computer equipment	600.00	(463.55)	136.45	136.45	0.00
8270 Scientific equip.	5,650.00	(752.50)	4,012.00 885.50	4,897.50	0.00
	23,548.00	(0.00)		23,548.00	(0.00)

FINAL REPORT NUMBER 34
REPORT WILL BE SUBMITTED UNDER MINI-GRANT 210-10MG-095
Dr. William Schulz
760-7MG-079

FINAL REPORT NUMBER 35
REPORT NOT AVAILABLE AT THIS TIME
Dr. Dennis Truax
760-7MG-105